MULTIFACETED APPROACHES COMBINING LOW OR HIGH LET RADIATION AND PHARMACOLOGICAL INTERVENTIONS IN CANCER AND RADIOPROTECTION: FROM BENCH TO BEDSIDE

EDITED BY: Pankaj Chaudhary, Sandeep Kumar Shukla and Shubhankar Suman

PUBLISHED IN: Frontiers in Oncology

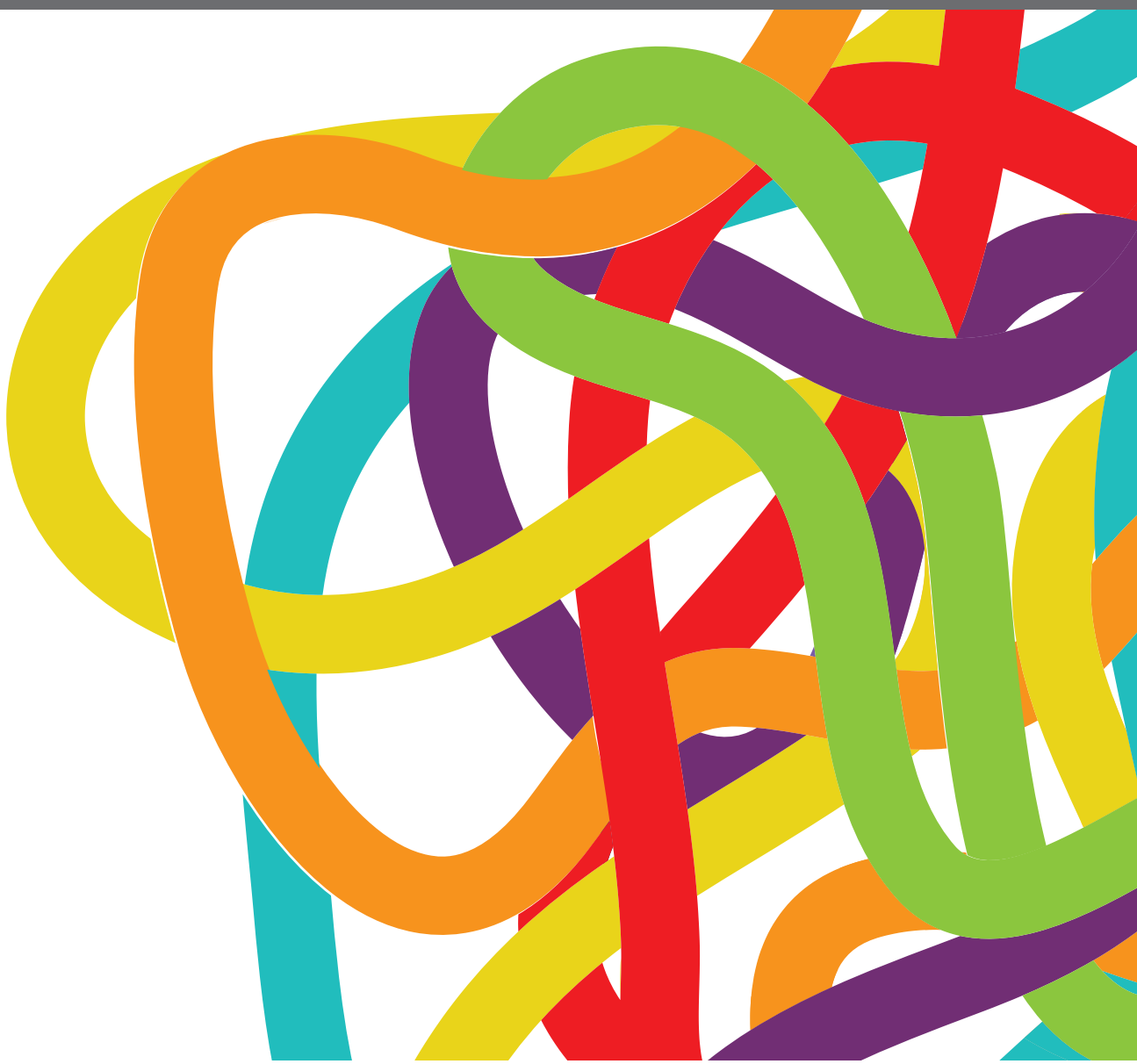

frontiers Research Topics

ISSN 1664-8714
ISBN 978-2-88974-948-5
DOI 10.3389/978-2-88974-948-5

About Frontiers

Frontiers is more than just an open-access publisher of scholarly articles: it is a pioneering approach to the world of academia, radically improving the way scholarly research is managed. The grand vision of Frontiers is a world where all people have an equal opportunity to seek, share and generate knowledge. Frontiers provides immediate and permanent online open access to all its publications, but this alone is not enough to realize our grand goals.

Frontiers Journal Series

The Frontiers Journal Series is a multi-tier and interdisciplinary set of open-access, online journals, promising a paradigm shift from the current review, selection and dissemination processes in academic publishing. All Frontiers journals are driven by researchers for researchers; therefore, they constitute a service to the scholarly community. At the same time, the Frontiers Journal Series operates on a revolutionary invention, the tiered publishing system, initially addressing specific communities of scholars, and gradually climbing up to broader public understanding, thus serving the interests of the lay society, too.

Dedication to Quality

Each Frontiers article is a landmark of the highest quality, thanks to genuinely collaborative interactions between authors and review editors, who include some of the world's best academicians. Research must be certified by peers before entering a stream of knowledge that may eventually reach the public - and shape society; therefore, Frontiers only applies the most rigorous and unbiased reviews.
Frontiers revolutionizes research publishing by freely delivering the most outstanding research, evaluated with no bias from both the academic and social point of view. By applying the most advanced information technologies, Frontiers is catapulting scholarly publishing into a new generation.

What are Frontiers Research Topics?

Frontiers Research Topics are very popular trademarks of the Frontiers Journals Series: they are collections of at least ten articles, all centered on a particular subject. With their unique mix of varied contributions from Original Research to Review Articles, Frontiers Research Topics unify the most influential researchers, the latest key findings and historical advances in a hot research area! Find out more on how to host your own Frontiers Research Topic or contribute to one as an author by contacting the Frontiers Editorial Office: frontiersin.org/about/contact

MULTIFACETED APPROACHES COMBINING LOW OR HIGH LET RADIATION AND PHARMACOLOGICAL INTERVENTIONS IN CANCER AND RADIOPROTECTION: FROM BENCH TO BEDSIDE

Topic Editors:
Pankaj Chaudhary, Queen's University Belfast, United Kingdom
Sandeep Kumar Shukla, Institute of Nuclear Medicine & Allied Sciences (DRDO), India
Shubhankar Suman, Georgetown University, United States

Citation: Chaudhary, P., Shukla, S. K., Suman, S., eds. (2022). Multifaceted Approaches Combining Low or High LET Radiation and Pharmacological Interventions in Cancer and Radioprotection: From Bench to Bedside. Lausanne: Frontiers Media SA. doi: 10.3389/978-2-88974-948-5

Table of Contents

frontiers in Oncology

EDITORIAL
published: 28 March 2022
doi: 10.3389/fonc.2022.880607

Editorial: Multifaceted Approaches Combining Low or High LET Radiation and Pharmacological Interventions in Cancer and Radioprotection: From Bench to Bedside

Pankaj Chaudhary[1*], *Sandeep Kumar Shukla*[2*] *and Shubhankar Suman*[3*]

[1] The Patrick G Johnston Centre for Cancer Research, Faculty of Medicine, Health and Life Sciences, Queen's University, Belfast, United Kingdom, [2] Institute of Nuclear Medicine & Allied Sciences, Defense Research and Development Organization (DRDO), Delhi, India, [3] Department of Oncology, Lombardi Comprehensive Cancer Center, Georgetown University Medical Center, Washington, DC, United States

OPEN ACCESS

Edited and reviewed by:
Timothy James Kinsella, Warren Alpert Medical School of Brown University, United States

****Correspondence:***
Pankaj Chaudhary
p.chaudhary@qub.ac.uk
Sandeep Kumar Shukla
sandeepshukla.inmas@gov.in
Shubhankar Suman
ss2286@georgetown.edu

Specialty section:
This article was submitted to Radiation Oncology, a section of the journal Frontiers in Oncology

Received: *21 February 2022*
Accepted: *28 February 2022*
Published: *28 March 2022*

Citation:
Chaudhary P, Shukla SK and Suman S (2022) Editorial: Multifaceted Approaches Combining Low or High LET Radiation and Pharmacological Interventions in Cancer and Radioprotection: From Bench to Bedside. Front. Oncol. 12:880607. doi: 10.3389/fonc.2022.880607

Keywords: radiotherapy, cancer, radioprotection, radiosensitization, heavy ion radiotherapy, radiobiology

Editorial on the Research Topic

Multifaceted Approaches Combining Low or High LET Radiation and Pharmacological Interventions in Cancer and Radioprotection: From Bench to Bedside

Radiotherapy (RT) using external or internal sources of ionizing radiation (IR) is a highly effective treatment modality to treat various cancer types (1, 2). Currently about half of all cancer patients receive RT during their lifetime often resulting in an overall increase in survival (3, 4). External beam radiotherapy (EBRT) mainly treat tumors employing photon (X-rays) or ion beams (proton and heavy ions) to the tumor tissue and are usually generated by a linear accelerator or cyclotron respectively, while brachytherapy (internal RT) uses internally implanted IR sources such as seeds, or capsules inside or in the close vicinity of the tumor tissue. Photon and electron beams based treatment modalities are still the most widely used form of EBRT, however, due to the high linear energy transfer (LET) characteristics protons and heavy ion radiation [such as Carbon (^{12}C) ion] have been demonstrated to deposit relatively higher IR-dose specifically to the tumor region. Therefore, EBRT using protons and heavy-ions allows achieving greater normal tissue sparing, relative to photon beams (Malouff et al.) (5). While the technological developments related to treatment planning, image-guided beam delivery, bio-dosimetry to improve photon, proton, and heavy-ion EBRT is ongoing, identification of targetable IR-induced signaling pathways and development of pharmacological radio-modifiers (radiosensitizer and radioprotectors) are also required for further advancement of RT (5, 6). This special interdisciplinary issue presents research and review papers that touch upon biophysical, biological, and clinical aspects of RT.

RT-associated side effects are often associated with errors in bio-dosimetry, dose distribution patterns and individual sensitivity to develop acute and late tissue toxicity. Scattered particles and secondary neutrons may affect bio-dosimetry resulting in unexpected side effects after proton

radiotherapy (PRT) and ^{12}C-ion radiotherapy (7). The study by Horendeck et al. confirmed that the Bragg peak and slightly shorter range of the post-Bragg peak region of proton radiation contain relatively high LET. This finding may explain the unwanted side effects, that could be improved using a narrower spread-out Bragg peak (SOBP). Additionally, the report by Buglewicz et al. demonstrates that DNA double-strand breaks (DSBs) density increases with a decrease in cell survival at the Bragg peak. Further, they demonstrate differential changes in the DSB in the post-Bragg peak tail regions, which has implications in ^{12}C-ion radiotherapy (CIRT) treatment planning to limit its late normal tissue toxicity and risk of secondary cancers.

RT with adjuvant chemotherapeutic agents is an established and classical approach for cancer therapy, however, an optimal combination of RT and targeted molecular therapy (including immunotherapy) is still not widely used (8, 9). A case report by Zhang suggests that a combination of RT and tyrosine kinase inhibitors (TKI) might be optimal in patients with brain metastasis of non-small-cell lung cancer (NSCLC) after resistance to crizotinib. Therefore, a detailed understanding of differential molecular responses in tumor and normal tissue after IR and molecular therapy is important for plausible target identification. The study by Macaeva et. al. demonstrated variable amplitude and timing of transcription response after photon and particle irradiation. A similar p53 related transcriptome was observed after photon and particle irradiation, however, immune response associated gene sets were significantly up-regulated in response to heavy ions. This indicates a higher immunogenic response of heavy ions and therefore optimization of PRT and immunotherapy combination might be required for better therapeutic outcomes. A review paper by Elbanna et. al. provides the perspective on clinical and preclinical aspects of combined RT and molecular therapy, however, most have failed primarily due to the lack of robust preclinical data. Additionally, timing and selection of molecular therapy with IR could also affect the outcome. While IR in the combination with immunotherapy could offer better control of the metastatic disease, and developing these combinations are often challenging due to discrepancies in the *in vitro*, *in vivo*, and clinical findings. The study by Reppigen et al. emphasizes such discrepancies between *in vitro* and *in vivo* studies, where despite promising *in vitro* data, no synergistic effect of cabozantinib and IR was evident.

Despite the higher relative biological effectiveness (RBE) of PRT and CIRT for tumor cell killing, radiosensitizers are required to enhance their clinical efficacy (6). The study by Johnson et al. tested the radiosensitization effect of hydroxamate-based histone deacetylase inhibitors (HDACi) and found that unlike radiosensitization observed with photon radiation, no appreciable tumor cell radiosensitization was achieved after proton and heavy-ions. Therefore, generalization of the widely used radiosensitizers with photons may not be appropriate for proton and heavy-ion therapy. In pursuit of the development of heavy-ion specific radiosensitizer, Prabhakaran et. al. studied the effects of ^{12}C-ion in combination with fused toes homolog (FTS) silencing on uterine cervical cancer cells. The ^{12}C-ion-induced overexpression of Notch signaling molecules was attenuated after silencing of FTS leading to an enhanced radiosensitization of the cervical cancer cells.

The recurrence of radioresistant tumors is also believed as one of the major factors restricting the efficacy and success of RT and some tumors respond poorly to conventional treatments after developing radioresistant phenotype (10). While several mechanisms implicated in the development of tumor radioresistance have been identified, the variation among tumor cell types is still a concern. In this direction, Yang et. al. have demonstrated that cancer-IgG regulated PI3K/AKT/DNA-PKcs signaling is associated with the development of radioresistance and poor prognosis of the lung. Using the siRNA screening approach, Nickson et. al. identified ubiquitin-specific protease 9X (USP9X) is required to stabilize key proteins involved in centrosome formation particularly in response to high-LET protons. They further demonstrated that the depletion of the (USP9X) in cancer cells (HeLa and UMSCC74A cells) using small interfering RNA (siRNA), led to a significant increase in the cell killing after high-LET radiation which can potentially increase the efficacy of protons and other high LET ions in treatment of radioresistant tumors.

Acute and late radiation toxicity is a typical adverse reaction in patients treated with RT or RT combined with chemotherapy (11), and there are no FDA-approved therapies to prevent or mitigate acute and late radiation toxicity after RT. The paper by García et. al. demonstrates that administration of recombinant Wnt5a before irradiation could confer radioprotection to normal gastrointestinal tissues. Additionally, using IR exposed mice, Sanguri and Gupta demonstrated gastrointestinal and hematopoietic tissue radioprotection by prebiotic mannan oligosaccharide pretreatment. Furthermore, using a 5-year phase-2 clinical survival study, Zhu et al., demonstrated epigallocatechin-3-Gallate as a potential treatment to alleviate esophagitis symptoms in small cell lung cancer patients exposed to IR without reducing survival.

Cancer is expected to continue threatening human life, as the number of new cancer diagnoses per year is expected to rise and RT is expected to be indispensable for cancer treatment. While EBRT is the mainstay for cancer RT, brachytherapy is still used to treat a subset of breast, prostate, cervix, and head and neck cancers. A review paper by Seniwal et al. provided an account of recent developments associated with the nanotechnology-based approach to improving brachytherapy. This paper also discusses the dosimetry protocols for nano-brachytherapy applications using radiolabeled nanoparticles (radio-NPs).

Finally, we appreciate the diverse participation from all the authors who responded to our call for this interdisciplinary issue and also extend our thanks to the esteemed reviewers who invested their valuable time to review the submitted manuscripts. We hope that this Research Topic will serve its intended purpose to give visibility and insight through important findings and ideas for the improvement of RT. We also hope that this Research Topic will gather attention from both basic radiobiologists and radiation oncologists.

AUTHOR CONTRIBUTIONS

PC, SKS, and SS equally contributed to writing, revising, and finalizing this editorial. All authors contributed to the article and approved the submitted version.

FUNDING

PC acknowledges funding support from the Department of Economy, Northern Ireland, and Engineering and Physical Sciences Research Consortium (EPSRC) grant# EP/PO10059/1. SS acknowledges funding support from the National Aeronautics and Space Administration (NASA) grants # NNX09AU95G and #80NSSC18K1649.

ACKNOWLEDGMENTS

We appreciate the participation from all the authors who responded to our call for this Research Topic and also extend our thanks to all the esteemed reviewers for their valuable time to review the submitted manuscripts.

REFERENCES

1. Petroni G, Cantley LC, Santambrogio L, Formenti SC, Galluzzi L. Radiotherapy as a Tool to Elicit Clinically Actionable Signalling Pathways in Cancer. *Nat Rev Clin Oncol* (2022) 19:114–31. doi: 10.1038/s41571-021-00579-w
2. Major T, Fröhlich G, Ágoston P, Polgár C, Takácsi-Nagy Z. The Value of Brachytherapy in the Age of Advanced External Beam Radiotherapy: A Review of the Literature in Terms of Dosimetry. *Strahlenther Onkol* (2022) 198:93–109. doi: 10.1007/s00066-021-01867-1
3. Begg AC, Stewart FA, Vens C. Strategies to Improve Radiotherapy With Targeted Drugs. *Nat Rev Cancer* (2011) 11:239–53. doi: 10.1038/nrc3007
4. Bryant AK, Banegas MP, Martinez ME, Mell LK, Murphy JD. Trends in Radiation Therapy Among Cancer Survivors in the United States 2000-2030. *Cancer Epidemiol Biomarkers Prev* (2017) 26:963–70. doi: 10.1158/1055-9965.EPI-16-1023
5. Helm A, Fournier C, Durante M. Particle Radiotherapy and Molecular Therapies: Mechanisms and Strategies Towards Clinical Applications. *Expert Rev Mol Med* (2022) 24:e8. doi: 10.1017/erm.2022.2
6. Lee Y, Okayasu R. Strategies to Enhance Radiosensitivity to Heavy Ion Radiation Therapy. *Int J Part Ther* (2018) 5:114–21. doi: 10.14338/IJPT-18-00014.1
7. Dutz A, Agolli L, Baumann M, Troost EGC, Krause M, Hölscher T, et al. Early and Late Side Effects, Dosimetric Parameters and Quality of Life After Proton Beam Therapy and IMRT for Prostate Cancer: A Matched-Pair Analysis. *Acta Oncol* (2019) 58:916–25. doi: 10.1080/0284186X.2019.1581373
8. Wrona A, Dziadziuszko R, Jassem J. Combining Radiotherapy With Targeted Therapies in Non-Small Cell Lung Cancer: Focus on Anti-EGFR, Anti-ALK and Anti-Angiogenic Agents. *Transl Lung Cancer Res* (2021) 10:2032–47. doi: 10.21037/tlcr-20-552
9. Morris ZS, Harari PM. Interaction of Radiation Therapy With Molecular Targeted Agents. *J Clin Oncol* (2014) 32:2886–93. doi: 10.1200/JCO.2014.55.1366
10. Barker HE, Paget JT, Khan AA, Harrington KJ. The Tumour Microenvironment After Radiotherapy: Mechanisms of Resistance and Recurrence. *Nat Rev Cancer* (2015) 15:409–25. doi: 10.1038/nrc3958
11. Wang K, Tepper JE. Radiation Therapy-Associated Toxicity: Etiology, Management, and Prevention. *CA Cancer J Clin* (2021) 71:437–54. doi: 10.3322/caac.21689

Conflict of Interest: The authors declare that the research was conducted in the absence of any commercial or financial relationships that could be construed as a potential conflict of interest.

Publisher's Note: All claims expressed in this article are solely those of the authors and do not necessarily represent those of their affiliated organizations, or those of the publisher, the editors and the reviewers. Any product that may be evaluated in this article, or claim that may be made by its manufacturer, is not guaranteed or endorsed by the publisher.

frontiers in Oncology

ORIGINAL RESEARCH
published: 02 June 2021
doi: 10.3389/fonc.2021.675397

High Expression of Cancer-IgG Is Associated With Poor Prognosis and Radioresistance *via* PI3K/AKT/DNA-PKcs Pathway Regulation in Lung Adenocarcinoma

Xiongtao Yang[1†], Guohui Wang[2†], Jing You[3†], Runchuan Gu[4], Xiaohong Xu[1], Changdan Xu[1], Hao Wang[5,6,7,8], Ruisong Zhao[9], Xiaoyan Qiu[10,11] and Guangying Zhu[1,5,6,7,8*]*

[1] Department of Radiation Oncology, Peking University China-Japan Friendship School of Clinical Medicine, Beijing, China, [2] Department of Radiotherapy, Second Hospital of Hebei Medical University, Shijiazhuang, China, [3] Key Laboratory of Carcinogenesis and Translational Research (Ministry of Education), Department of Radiation Oncology, Peking University Cancer Hospital and Institute, Beijing, China, [4] Department of Radiation Oncology, China-Japan Friendship Institute of Clinical Medicine, Beijing, China, [5] Department of Radiation Oncology, Center of Respiratory Medicine, China-Japan Friendship Hospital, Beijing, China, [6] Institute of Respiratory Medicine, Chinese Academy of Medical Sciences, Beijing, China, [7] Department of Radiation Oncology, National Clinical Research Center for Respiratory Diseases, Beijing, China, [8] Department of Radiation Oncology, World Health Organization (WHO) Collaborating Centre for Tobacco Cessation and Respiratory Diseases Prevention, Beijing, China, [9] Department of Pathology, China-Japan Friendship Hospital, Beijing, China, [10] Department of Immunology, School of Basic Medical Sciences, Peking University, Beijing, China, [11] Peking University Center for Human Disease Genomics, Beijing, China

OPEN ACCESS

Edited by:
Shubhankar Suman, Georgetown University, United States

Reviewed by:
Kamendra Kumar, Georgetown University, United States
Raghubendra Singh Dagur, University of Nebraska Medical Center, United States

***Correspondence:**
Xiaoyan Qiu
qiuxy@bjmu.edu.cn
Guangying Zhu
zryyfa@163.com

[†]These authors have contributed equally to this work and share first authorship

Specialty section:
This article was submitted to Radiation Oncology, a section of the journal Frontiers in Oncology

Received: *03 March 2021*
Accepted: *19 April 2021*
Published: *02 June 2021*

Citation:
Yang X, Wang G, You J, Gu R, Xu X, Xu C, Wang H, Zhao R, Qiu X and Zhu G (2021) High Expression of Cancer-IgG Is Associated With Poor Prognosis and Radioresistance via PI3K/AKT/DNA-PKcs Pathway Regulation in Lung Adenocarcinoma. Front. Oncol. 11:675397. doi: 10.3389/fonc.2021.675397

Background: Lung adenocarcinoma (LUAD) is the dominant type of lung neoplasms, and radiotherapy is its mainstay treatment, yet poor prognosis caused by radioresistance remains problematic. Cancer-derived immunoglobulin G (cancer-IgG) has been detected in multiple cancers and plays important roles in carcinogenesis. This study aimed to demonstrate that cancer-IgG is associated with poor prognosis of LUAD and to identify its role in radioresistance.

Methods: Cancer-IgG expression was detected by immunohistochemistry from 56 patients with stage III LUAD and by western blot and immunofluorescence in LUAD cell lines and in a human bronchial epithelial cell line. The effects of cancer-IgG silencing on the proliferation and apoptosis of PC9 and H292 cells were evaluated by plate cloning and apoptosis assay; the effects of cancer-IgG silencing on DNA damage repair ability and radiosensitivity were evaluated by colony-forming assay, γH2AX immunofluorescence, and neutral comet assay. Finally, we used the protein phosphorylation microarray and western blot to explore mechanisms involving cancer-IgG that increased radioresistance.

Results: Cancer-IgG is widely expressed in stage III LUAD, and the overall survival and disease-free survival of patients with positive expression are notably lower than those of patients with negative expression, indicating the associations between cancer-IgG and poor prognosis as well as radioresistance. The expression of cancer-IgG in the four LUAD cell lines was located mainly on the cell membrane and cytoplasm and not in the normal

lung epithelial cell. Knockdown of cancer-IgG in PC9 and H292 cells resulted in increased apoptosis and negatively affected cancer cell proliferation. After irradiation, silencing of cancer-IgG showed a decrease in colonies as well as increases in the Olive tail moment and γH2AX foci in nucleus, indicating that the knockdown of cancer-IgG resulted in a decrease in the damage repair ability of DNA double-strand breaks in LUAD cells and an enhanced radiosensitivity. The expression of p-AKT, p-GSK3β, and p-DNA-PKcs decreased in the knockdown group after radiotherapy, suggesting that cancer-IgG could affect radiotherapy resistance by mediating double-strand breaks damage repair in LUAD cells through the PI3K/AKT/DNA-PKcs pathway.

Conclusions: This study revealed that cancer-IgG regulates PI3K/AKT/DNA-PKcs signaling pathways to affect radioresistance of LUAD and associated with poor prognosis.

Keywords: cancer-IgG, lung adenocarcinoma, radioresistance, PI3K/AKT/DNA-PKcs pathway, RP215

INTRODUCTION

Lung cancer represents the highest cancer incidence and remains the leading cause of cancer mortality worldwide (1). More than 85% of patients with lung cancer are pathologically diagnosed as having non-small cell lung cancer (NSCLC); accounting for approximately 50% of NSCLC, lung adenocarcinoma (LUAD) is the most commonly histological subtype of NSCLC (2). The clinical application of radiation for cancer therapeutic purposes began when x-ray was discovered by a German physicist, Roentgen, in 1895, and radiation has now become one of the major approaches of malignant tumor treatment after centuries of technological and equipment-related progression (3). Many large-scale clinical studies conducted in recent years involving patients with NSCLC (including LUAD) confirmed the survival time and quality-of-life improvements gained as a result of radiotherapy, and these results consequently contributed to the definition of radiotherapy as a standard therapy for NSCLC (4–6). However, local recurrence, as well as poor prognosis of patients resulting from radioresistance observed in tumor cells, has now become a major factor restricting the efficacy and additional development of radiotherapy; the 5-year survival rate of NSCLC remains less than 30% (7). Consequently, clarification about the mechanism of radioresistance in LUAD is urgently needed, and a novel theory of radiosensitization must be established to improve the survival of patients.

Qiu confirmed that epithelial tumors can produce immunoglobulin G and so established a new field of research into cancer-derived immunoglobulin G (cancer-IgG) (8). Cancer-IgG has been confirmed in a variety of tumors and is associated with poor prognosis (9–14). The discovery of the monoclonal antibody RP215, which specifically recognizes epitopes in the cancer-IgG heavy chain, has accelerated research about cancer-IgG (15). RP215-recognizable cancer-IgG interacts with integrin α6β4 to promote oncogenic activities of lung squamous cell carcinomas *via* activation of FAK and Src signaling (11). A recent study found that cancer-IgG can be secreted into the tumor microenvironment and can bind to sialic acid–binding immunoglobulin-type lectins of CD4+ and CD8+ effector T cells to directly inhibit the proliferation of CD4+ and CD8+ T cells and significantly promote tumor growth (16). Interestingly, our studies demonstrated that cancer-IgG can affect the radiosensitivity of tumors; we hypothesized that cancer-IgG can participate in irradiation-induced DNA double-strand breaks (DSBs) repair, which is considered a critical factor for LUAD radioresistance.

Several mechanisms of radioresistance involving cancer stem cells, apoptosis, reactive oxygen species, and DNA damage repair have been reported (17). DSBs caused by radiation in tumor cells are mainly repaired *via* nonhomologous end joining (NHEJ) and homologous recombination pathways, and repair by NHEJ is dominant throughout the cell cycle (18). DNA-dependent protein kinase (DNA-PK) is a key participant in DNA damage response and is instrumental in the NHEJ pathway, which serves to detect and repair DSBs. Inhibition of DNA-PK has resulted in an observable increase in tumor radiosensitivity (19). As a key complement of DNA-PK, phosphorylation of DNA-PK catalytic subunit (DNA-PKcs) is regulated by the PI3K/AKT pathway, which suggests that specific inhibition of DNA-PKcs–dependent DSBs repair *via* an AKT target can lead to an increase in the radiosensitivity of tumor cells (20). Gao et al. (21) demonstrated that bevacizumab directly inhibits the phosphorylation of VEGR2/PI3K/AKT/DNA-PKcs signaling components in endothelial cells induced by irradiation to inhibit endothelial DSB repair and increases the radiosensitivity of xenograft tumors in NSCLC. However, the effect of cancer-IgG on the radioresistance of LUAD cells has not been determined. In this study, we aimed to demonstrate that cancer-IgG is associated with the prognosis of patients with LUAD and examine its role in radioresistance.

MATERIAL AND METHODS

Collection and Processing of Clinical Specimens

The tumor tissue of 56 patients with LUAD admitted to the Peking University Cancer Hospital from October 2008 to

January 2017 were collected. Their basic information was recorded, including age, gender, cigarette smoking history, disease stage, T classification, N classification, primary lesion diameter, visceral pleura invasion, vascular tumor thrombus, cancer-IgG expression, and disease-free survival (DFS), which was defined as the time from radical operation to disease recurrence. Patients who were alive without recurrence or lost to follow-up had their data censored at last available assessment. Patients who died from other causes without prior recurrence had their data censored at the date of death. Overall survival (OS) was defined as the date from preparation for treatment to the date of death from any cause or to the time of the last follow-up. All patients with LUAD had undergone radical operation and postoperative radiotherapy plus four cycles of chemotherapy; the radiation dose was 50 Gy in 25 fractions to the clinical target volume. All procedures were approved by the institutional review board.

Cell Culture and Transfection

The human tracheal epithelial cell line (BEAS-2B) and the LUAD cell lines H292 and A549 were purchased from the National Biomedical Laboratory Cell Resource Bank. The LUAD cell lines H1299 and PC9 were obtained from the radiation department of the Peking University Cancer Hospital (Beijing, China). The H292, PC9, and H1299 lines were cultured in RPMI-1640 (Hyclone) with 10% fetal bovine serum (FBS) (Gibco), whereas the BEAS-2B and A549 cell lines were cultured in DMEM (Hyclone) with 10% FBS at 37°C in a humidified atmosphere of 95% O_2 and 5% CO_2. SiRNAs against the constant region of the Ig γ–chain (siRNA1, 5′–GGU GGA CAA GAC AGU UGAG –3′; and siRNA2, 5′–AGU GCA AGG UCU CCA ACAA–3′) and the non-silencing control RNA (scramble, 5′–UUC UCC GAA CGU GUC ACGU–3′) were produced by Suzhou GenePharma Co., Ltd. The siRNAs and scramble-RNA were transfected into the PC9 and H292 lines for 48 hours using lipofectamine 3000 (Thermo Fisher Scientific) and then were harvested according to the manufacturer's protocol.

The pGCSIL-GFP- target short hairpin RNA (shRNA) lentiviral vectors (pGCSIL is a lentiviral vector) were purchased from Shanghai GeneChem Co., Ltd, and the shRNA sequences were the same as the siRNA2 sequences (5′–AGU GCA AGG UCU CCA ACAA–3′); the scramble shRNA sequences were the same as the non-silencing control RNA sequence (5′–UUC UCC GAA CGU GUC ACGU–3′). The shRNAs were transferred with polybrene (10 mg/mL; Sigma) into PC9 and H292 cells according to the shRNA product manual. Stable cells were screened with GFP fluorescence and puromycin (2 μg/mL). The knockdown efficiency of cancer-IgG was verified by western blot.

Immunohistochemistry and Scoring

RP215 was provided by professor Xiaoyan Qiu of Peking University. We performed the experiment according to the procedure previously described for immunohistochemistry staining and cancer-IgG staining scores calculation (22). The score for RP215 staining was described as negative when the score was 0 to 3 and as positive when the score was 4 to 12.

Immunofluorescence

Cells were grown on coverslips in four-well slides (Millicell EZ). The coverslips were fixed with 95% ethanol and permeabilized in 0.1% Triton X-100. Cells were blocked goat serum (ZLI-9056; ZSGB-Bio) and then incubated with RP215 or γH2AX (#80312; CST) antibody. After incubation with a secondary antibody for 1 h, the samples were counterstained with DAPI and imaged by a confocal microscope (Leica, Germany).

Irradiation

PC9 and H292 cells were selected for radiation in the logarithmic growth phase, with the following x-ray irradiator (Varian) parameters: 6 MV x-ray energy and a dose rate of 4 Gy/min. After setting the dose according to the purpose, we placed the cell culture dish on a horizontal bed at a distance of 100 cm from the radiation source to the cell and covered it with a 1.5-cm-thick imitation human tissue pad. According to the International Atomic Energy Agency TRS-398 Code of Practice, a calibrated ionization chamber dosimeter was used for radiation dose verification.

Cell Proliferation Assay

PC9 and H292 cells transfected with the siRNAs and scramble-RNA were cultured in six-well plates with approximately 300 cells/well and were incubated for 14 days. We discarded the medium in the six-well plates and washed with phosphate-buffered saline solution three times, adding 2 mL of 4% paraformaldehyde to each well and fixing them for 15 min at room temperature. Then, we discarded the 4% paraformaldehyde and added 2 mL of crystal violet working solution (DZ0056; Leagene) to each well for staining at room temperature for 30 min, slowly washing away the excess staining solution with running water and drying at room temperature. A colony was considered surviving when 50 or more cells were counted.

Cell Apoptosis: Flow Cytometry Analysis

PC9 and H292 cells transfected with the siRNAs and scramble-RNA were cultured in six-well plates and incubated for 24 h; the cells were harvested and then incubated with FITC-annexin V and 7-AAD/PI staining buffer (KGA1030-50; KeyGen Biotech) at room temperature for 15 min. Cell apoptosis was measured with a FACS Calibur flow cytometer (BD Biosciences). Data analysis was performed with FlowJo software (Tree Star). FITC-annexin V– and PI-negative cells were considered viable; FITC-annexin V–positive and PI-negative cells represented early apoptosis cells; and FITC-annexin V– and PI-positive cells corresponded to late apoptosis or already dead cells.

Colony-Forming Assay

After spreading the cells in a six-well plate for 24 hours, irradiate them with 0, 2, 4, 6 or 8 Gy. The subsequent steps matched those of section 2.6. The formula for the cell colony-forming rate and the cell survival score of each group is as follows: colony-forming rate plating efficiency (PE) = number of clones formed by cells after irradiation ÷ number of inoculated cells in this group. The cell survival fraction = PE of a certain dose irradiation group ÷

PE of the group with 0-Gy irradiation. The survival curve was graphed according to the survival fraction and dose in GraphPad Prism software.

Neutral Comet Assay

This assay was carried out using a Trevigen kit according to the manufacturer's instructions. Briefly, PC9 and H292 cells were resuspended and collected after 3 h of 2/4-Gy irradiation. The concentration of 2×10^5/mL cell suspension and low-melting-point agarose were mixed evenly according to the volume ratio of 1:10, and then 50 μL of the mixture was dropped into the slice hole. The solidified slices with neutral electrophoresis buffer were electrophoresis at 21V voltage for 45 min and then were dried and stained with PI. Take the image under the fluorescence microscope, download the Comet Assay Software Project (CASP) to analyze the Olive tail moment of the cell, select the comet image to be analyzed with the check box, click the analysis function key and save. The main curve of the analysis curve is unimodal, and if it is bimodal, apoptotic cells are excluded. The distribution of DNA migration distance (comet tail length) and DNA content (fluorescence intensity) are linearly related to the degree of DNA damage. Olive tail moment is defined as: the product of tail DNA content and tail length, which is the main index to evaluate the degree of DNA damage in a single cell.

Protein Phosphorylation Microarray Analysis

The Phospho Explorer Antibody Microarray was conducted by Full Moon BioSystems (Sunnyvale, CA). Whole-cell lysates from H292-sh-scramble and H292-sh-cancer-IgG treated with 6-Gy irradiation were harvested using a protein extraction buffer (Full Moon BioSystems). The protein microarray experiment was performed by Wayen Biotechnology (Shanghai, China) according to their established protocol. The fluorescence signal of each antibody was obtained from the fluorescence intensity of this antibody spot. A ratio computation was used to measure the extent of protein phosphorylation. The phosphorylation ratio was calculated as follows: phosphorylation ratio = phospho value ÷ unphospho value.

Western Blot

Whole-cell lysates were prepared using a RIPA lysis buffer, supplemented with complete EDTA-free protease inhibitor mixtures and phosphatase inhibitors (Roche Diagnostics). Protein samples were separated on SDS-polyacrylamide gels. For western blot, separated proteins were transferred into PVDF membranes (Thermo Fisher). The membranes were incubated overnight at 4°C with primary antibodies and then incubated with a corresponding secondary antibody for 1 h at room temperature, when membranes were detected with an enhanced chemiluminescence reaction kit (Thermo Scientific Pierce). The primary antibodies were as follows: DNA-PKcs (ab102970, Abcam), p-DNA-PKcs (ab103970, Abcam), AKT (#4691, CST), p-AKT (#4060, CST), GSK3β (#12456, CST), p-GSK3β (#9323, CST), RP215, and GAPDH (HX1828, HuaxingBio).

Statistical Analyses

The Kaplan-Meier method was used to analyze the correlation between cancer-IgG and OS or DFS. The survival curves were compared using a log-rank test. Univariate and multivariate Cox regression analysis evaluated the cancer-IgG significantly related to OS or DFS according to P values < 0.05. Cancer-IgG and clinicopathological features was carried out with a $\chi 2$ test. Data were presented as mean ± standard deviation. Student's t test was used for the comparison between two groups. P values < 0.05 were considered statistically significant. All statistical evaluations were performed with SPSS version. 20.0.

RESULTS

Cancer-IgG Had High Expression in LUAD and Was Associated With Poor Prognosis

Clinical data and pathological slides were collected from 56 patients with stage III LUAD for analysis of cancer-IgG expression by immunohistochemistry staining; 21 were positive and 35 were negative for cancer-IgG. Cancer-IgG is mostly located in the endoplasm and cell membrane (**Figure 1A**). The relationship between cancer-IgG expression and pathological characteristics of LUAD was analyzed (**Table 1**). Results showed that the expression of cancer-IgG was approximately correlated with N classification (P = 0.093) and vascular tumor thrombus (P = 0.069), suggesting that cancer-IgG may correlate with tumor metastasis. Such a conclusion matched that of our past analysis of cancer-IgG expression in NSCLC that involved data mining and tissue microarray (23).

Studies on cancer-IgG expression level and the survival prognosis for patients have shown that cancer-IgG expression significantly correlates with survival time. Kaplan-Meier analysis (P = 0.015, log-rank test; **Figure 1B**) and univariate/multivariate Cox regression analyses (**Figures 1C, D**) have shown that patients with positive cancer-IgG expression have poor prognoses and that positive expression of cancer-IgG could serve as an independent risk factor for OS. DFS refers to the period of time from radical operation to progress of disease, highlighting the efficacy of adjuvant radiotherapy and chemotherapy. The significant difference (P = 0.012, log-rank test; **Figure 1E**) of DFS among patients with different cancer-IgG expressions suggests a potential association between cancer-IgG expression and radioresistance. A significant difference in DFS between expression levels was found through univariate/multivariate Cox regression analyses (**Figures 1F, G**), indicating that cancer-IgG could be an independent risk factor for the prognosis of patients with stage III LUAD and could be associated with radiosensitivity.

Cancer-IgG Knockdown Suppresses LUAD Progression

Many studies have explored the expression of cancer-IgG in lung cancer (11, 12, 23). We observed the expression and location of cancer-IgG in a variety of LUAD cell lines and in normal lung epithelial cells (**Figures 2A, B**), confirming the existence of

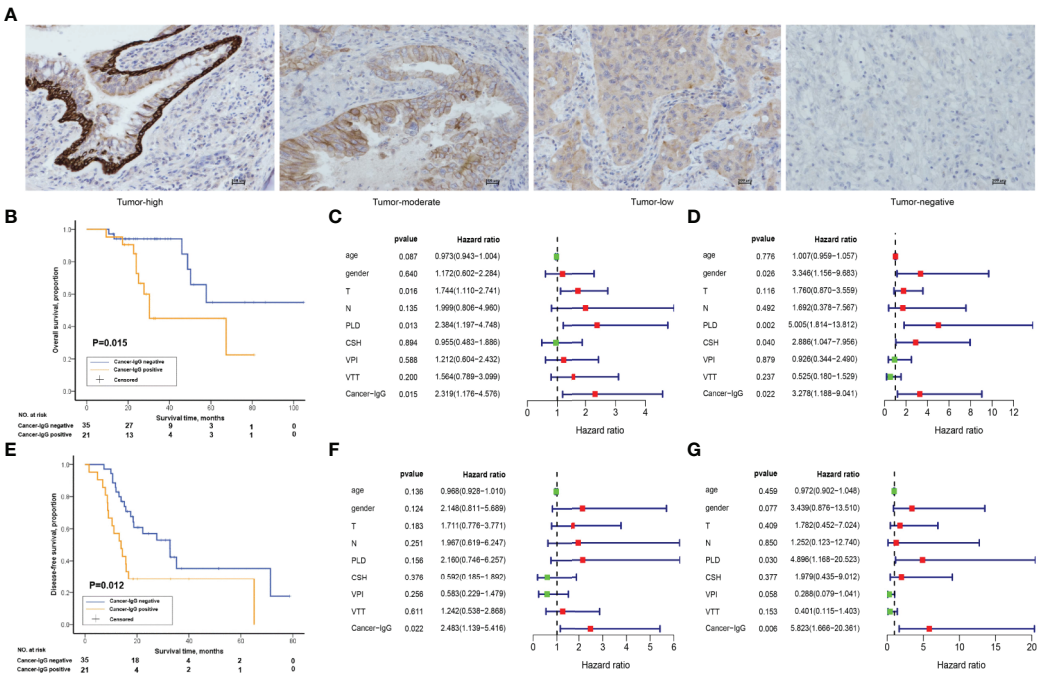

FIGURE 1 | The relationship between the expression of cancer-derived immunoglobulin G (cancer-IgG) and survival outcome in 56 patients with stage III lung adenocarcinoma (LUAD). **(A)** Different expression levels of cancer-IgG in LUAD tissue sections. Scale bar, 100 μm. **(B)** Kaplan-Meier analysis of the overall survival (OS) between positive and negative cancer-IgG expression groups. **(C, D)** Univariate and multivariate analyses using a Cox proportional hazards model for the OS of patients with LUAD. **(E)** Kaplan-Meier analysis of the disease-free survival (DFS) between positive and negative cancer-IgG expression groups. **(F, G)** Univariate and multivariate analyses using a Cox proportional hazards model for the DFS of patients with LUAD. Age; gender: 0 (female), 1 (male); T: 1, 2, 3, 4; N:1, 2, 3; primary lesion diameter (PLD): 0 (< 4 cm), 1 (≥ 4 cm or double lesions); cigarette smoking history (CSH): 0 (never), 1 (former or current); visceral pleura invasion (VPI): 0 (no), 1 (yes); vascular tumor thrombus (VTT): 0 (no), 1 (yes); cancer-IgG: 0 (negative expression), 1 (positive expression).

cancer-IgG in multiple LUAD cell lines (highest in PC9 and H292 and negative in BEAS-2B), mainly located in the endoplasm and cell membrane (consistent with previous immunohistochemistry results). By constructing siRNA that targets the *IGHG1* (immunoglobulin heavy constant gamma 1) gene, we performed cancer-IgG knockdown within PC9 and H292 cells; siRNA2 presented to be more efficient (**Figure 2C**).

A plating cloning assay was performed to evaluate cell viability and identified significant inhibition of PC9 and H292 cell proliferation as the expression of cancer-IgG was suppressed (**Figure 2D**). According to the result of a flow cyto-apoptosis assay, the ratio of cells undergoing apoptosis after cancer-IgG knockdown increased significantly, which indicated that cancer-IgG knockdown significantly promoted apoptosis of PC9 and H292 cells (**Figure 2E**). Taken together, our results suggest that reduced cancer-IgG expression attenuates LUAD cell proliferation and promotes apoptosis to prevent LUAD progression.

Cancer-IgG Silencing Attenuates LUAD Resistance to Radiation Therapy

Radiation is one of the major therapeutic measures for LUAD. High-energy x-rays induce irreversible damage to the DNA of tumor cells, which cannot be repaired in time, and thus cause tumor cell death (24). To investigate whether cancer-IgG plays a role in the damage and repair process caused by radiation within LUAD cells and consequently affects radiosensitivity, the cancer-IgG in PC9 and H292 cells was first knocked down by lentivirus (**Figure 3A**). Then, the colony-forming test was conducted under irradiation with different radiation doses (0, 2, 4, 6, and 8 Gy). The number of colonies in the cancer-IgG knockdown group was significantly reduced. The cell survival curve was simulated by the single-hit multi-target model, which showed that the sensitivity of the cancer-IgG knockdown group to radiotherapy was enhanced (**Figure 3B**).

Next, the γH2AX foci formation assay and neutral comet assay, considered critical for evaluating DNA damage process, were performed. As shown in **Figure 4A**, the number of γH2AX foci in nucleus increased 1 h after 4 Gy per fraction of irradiation in the cancer-IgG knockdown group, and the Olive tail moment was observed to have a significant increase 3 h after that irradiation (**Figure 4B**). In addition, under 2Gy irradiation, the results of the comet assay are consistent with the previous results (**Figure 4C**). The results indicated that cancer-IgG regulates the DSB damage repair process caused by radiotherapy, and cancer-IgG silencing attenuates LUAD resistance to radiation therapy.

Cancer-IgG Mediates Radioresistance to LUAD *via* PI3K/AKT/DNA-PKcs Pathway

H292 sh-scramble and sh-cancer-IgG cells were irradiated with 6 Gy. After 6 h, the total protein was extracted for phosphorylation

TABLE 1 | Association between cancer-IgG expression and clinicopathological features of patients with lung adenocarcinoma.

Characteristics	No. (%) of cases	Cancer-IgG		*P*
		Negative	Positive	
Age (years)				1.000
≥60	24 (42.9)	15	19	
<60	32 (57.1)	20	12	
Gender				0.367
Male	25 (44.6)	14	11	
Female	31 (55.4)	21	10	
Disease stage				0.659
IIIA	50 (89.3)	30	20	
IIIB	4 (7.1)	2	1	
T classification				0.594
1	22 (39.3)	15	7	
2	31 (55.3)	19	12	
3	2 (3.6)	1	1	
4	1 (1.8)	0	1	
N classification				0.093
1	4 (7.1)	4	0	
2	49 (87.5)	28	21	
3	3 (5.4)	3	0	
Primary lesion diameter (cm)				0.708
<4	39 (69.6)	25	14	
≥4 or double lesions	17 (30.4)	10	7	
Cigarette smoking history				0.664
Never	33 (58.9)	22	11	
Former	8 (14.3)	4	4	
Current	15 (26.8)	9	6	
Visceral pleura invasion				0.797
No	22 (39.3)	15	7	
Yes	32 (57.1)	19	13	
NA	2 (3.6)	1	1	
Vascular tumor thrombus				0.069
No	32 (57.1)	24	8	
Yes	16 (28.6)	8	8	
NA	8 (14.3)	3	5	

Cancer-IgG, cancer-derived immunoglobulin G; N, node; NA, not available; T, tumor.

protein microarray analysis, which found that AKT and GSK3β protein phosphorylation ratios in the sh-cancer-IgG group were reduced and that Bcl-2, BAD, caspase 3, caspase 9, and BAX apoptosis-related proteins increased (**Figure 5A**). The results indicated that cancer-IgG knockdown under irradiation leads to inhibition of the PI3K/AKT pathway and increases apoptosis in LUAD cells. Furthermore, western blot analysis on PC9 and H292 cells showed that cancer-IgG knockdown under irradiation did not affect the expression of AKT, GSK3β, or DNA-PKcs proteins. However, the expression of p-AKT and p-GSK3β decreased; this result was consistent with that of the phosphorylation protein microarray analysis. p-DNA-PKcs, a core component in the NHEJ pathway for the DSB damage repair process, is phosphorylated under cellular stress and assembled into DNA-PK with Ku70 and Ku80 heterodimers to participate in the repair process of DSBs; they also cascade to amplify repair signals and recruit more sensor proteins to repair sites to promote repair (25). The results showed that expression of the p-DNA-PKcs protein in LUAD cells increased after radiation. Knockdown of cancer-IgG inhibited the expression of the p-DNA-PKcs protein (**Figure 5B**), suggesting that the damage repair ability of DSBs in LUAD cells decreased, and radiotherapy resistance was downregulated. These results suggest that cancer-IgG can mediate radiotherapy resistance in LUAD cells *via* the PI3K/AKT/DNA-PKcs pathway and that radiosensitivity can be promoted by knocking down the expression of cancer-IgG.

DISCUSSION

In this study, we presented evidence that the absence of cancer-IgG downregulates the phosphorylation of key proteins in the PI3K/AKT/DNA-PKcs pathway and thus attenuates the radiotherapy resistance of LUAD cells. We first found that cancer-IgG is expressed in the cell membrane and endoplasm of LUAD cells; the shorter OS and DFS of patients with positive cancer-IgG expression after radical postoperative chemoradiotherapy suggested an association between cancer-IgG and the poor prognoses as well as radiotherapy resistance. Cytological experiments provided confirmation of cancer-IgG expression in LUAD cells but not in normal epithelia cells and showed that, by knocking down cancer-IgG, the proliferation of LUAD cells can be inhibited, thus promoting apoptosis of tumor cells. In addition, after irradiation of LUAD cells with cancer-IgG knockdown, the cell proliferation ability was reduced even more, and the DSB repair ability was reduced. Mechanistic studies have shown that inhibiting cancer-IgG expression affects the PI3K/AKT/DNA-PKcs pathway to downregulate the expression of repair proteins, inhibit the DSB damage and repair of LUAD cells, and enhance the radiosensitivity. To our knowledge, this study is the first to demonstrate the role of cancer-IgG in radioresistance and suggest that cancer-IgG is a potential therapeutic target for LUAD radiation therapy.

Radiotherapy, considered a standard therapeutic measures for LUAD, plays a critical role in improving the survival and prognosis of patients but is greatly hindered by the existence of radioresistance of cancer cells (26). Radiation therapy combined with targeted DSB damage repair protein inhibitors has the potential for clinical application in patients with cancer; current drug development and clinical trials for targets such as DNA-PKcs, ATM/ATR (i.e., ataxia-telangiectasia mutated and Rad3-related protein kinases), and the MRN (i.e., MRE11-Rad50-NBS1) complex are underway and may, we hope, better explain the poor efficacy caused by radiotherapy resistance (27). Although cancer-IgG was discovered in cancer cells decades ago, previous studies mainly focused on the relationship between cancer-IgG and tumorigenesis. Wang and Gan (28) found that knockdown of cancer-IgG can regulate the PTP-BAS/Src/PDK1/AKT pathway and thus significantly promote cisplatin-induced apoptosis and inhibition of oral squamous cell proliferation, migration, and invasion. Qin et al. (9) found that, in prostate cancer, cancer-IgG staining was stronger in specimens at advanced clinical stages; androgen deprivation therapy for prostate cancer–induced cancer-IgG expression maintained stemness and facilitated cancer progression through mitogen-activated protein kinase/extracellular signal–regulated kinase

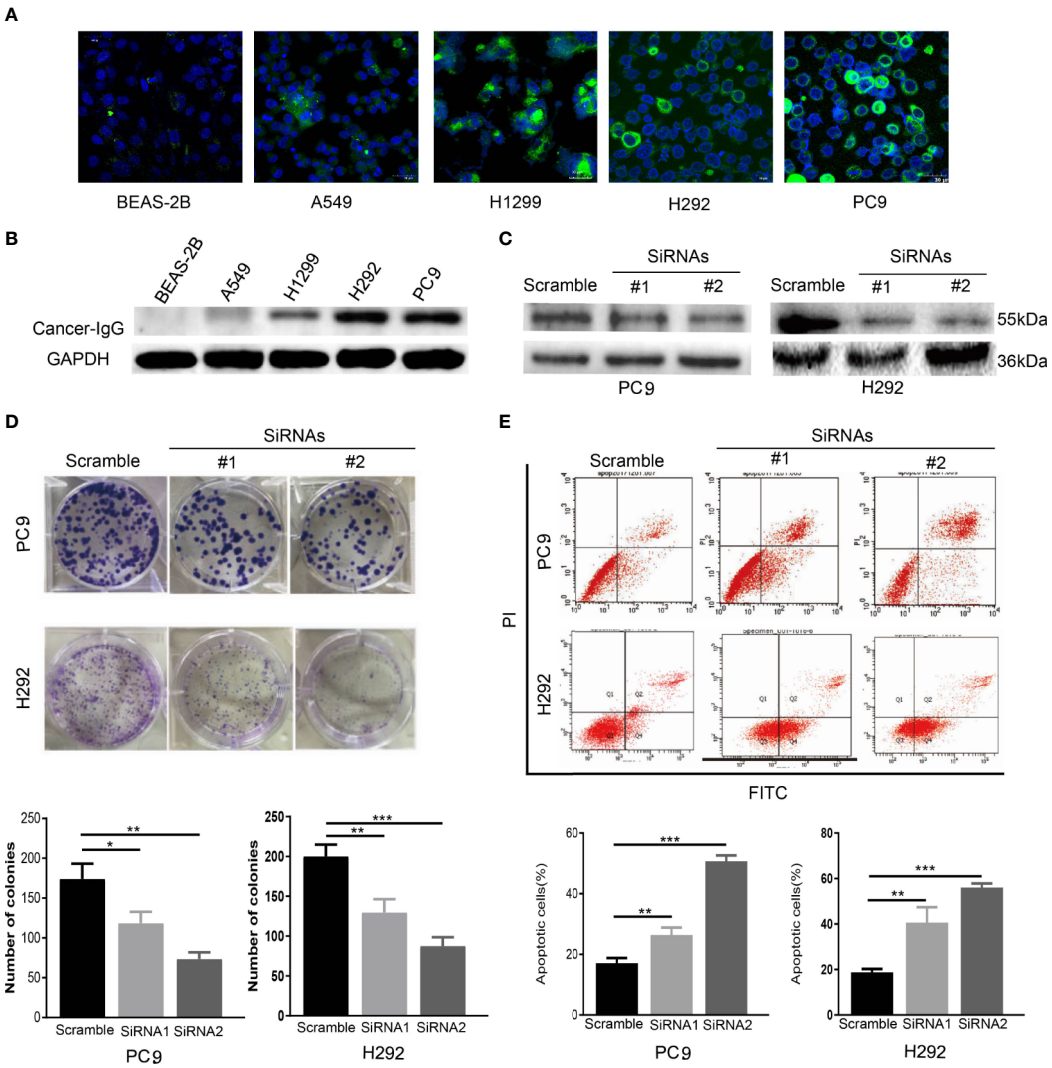

FIGURE 2 | The expression and function of cancer-IgG in LUAD cell lines and normal lung epithelial cells. **(A, B)** Immunofluorescence staining and western blot analysis are used to show cancer-IgG expression in a normal lung–derived cell line (BEAS-2B) and four LUAD cell lines (PC9, H292, H1299, A549). Scale bar, 30 μm. **(C)** Western blot is used for testing the efficiency knockdown of cancer-IgG in PC9 and H292. **(D)** Plate cloning assay to evaluate the effect of silencing cancer-IgG on the proliferation of PC9 and H292 cells (n=3). **(E)** Flow cytometry assay to evaluate the effect of silencing cancer-IgG on the apoptotic ability of PC9 and H292 cells (n=3). $^{*}p < 0.05$; $^{**}p < 0.01$; $^{***}p < 0.001$.

and AKT in prostate cancer. In our study, staining of stage III LUAD slides suggested associations between cancer-IgG and tumor invasiveness, because expression approximately correlated with N staging and vascular tumor thrombus.

Building upon previous research, this study first explored the role of cancer-IgG in tumor radiotherapy and found that it is possible to mediate radiotherapy resistance by modulating the PI3K/AKT/DNA-PKcs signaling pathway. AKT, a serine/threonine kinase, is considered a core factor in the PI3K/AKT pathway, which functions mainly according to these four steps: survival factor induction, translocation to the cell membrane, phosphorylation, and activation of downstream effectors (29). The AKT protein is frequently deregulated in a variety of human cancers, leading to overactivation and promotion of tumor cell survival, proliferation, migration, metabolism, angiogenesis, and radiochemotherapy resistance by regulating the function of multiple downstream molecules (29–31). Moreover, AKT1 interacts with DNA-PKcs through its C-terminal domain to form a functional complex, stimulates the accumulation of DNA-PKcs at DSBs, promotes the activity of DNA-PKcs, and enhances radiation-induced DSB damage repair (32). PI3K/AKT inhibitors can significantly enhance radiosensitivity of cancer cells by targeting this pathway (33, 34). Many studies have claimed that AKT binds to DNA-PKcs and participates in promotion of binding to DNA damage sites and mediation of the trans/autophosphorylation of DNA-PKcs, thereby enhancing DSB damage repair in DNA (35–37). Our study demonstrated that the expressions of p-AKT and

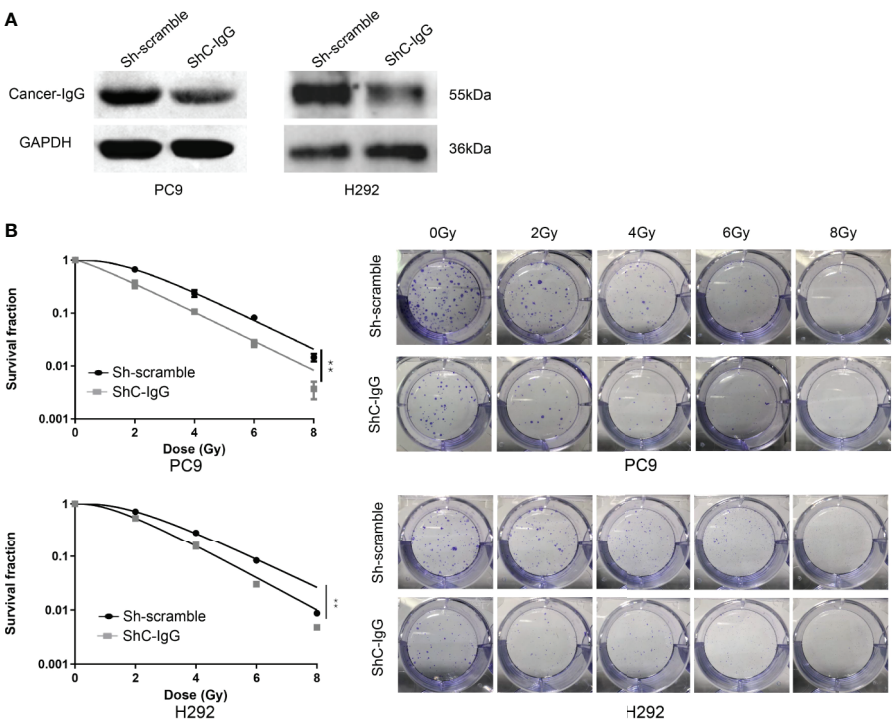

FIGURE 3 | Cancer-IgG silencing attenuates lung adenocarcinoma resistance to radiation therapy. **(A)** Western blotting was used to test the efficiency of lentiviral interfering RNA in silencing cancer-IgG in PC9 and H292. **(B)** Colony-forming assay showed that the proliferation ability of PC9 and H292 cells at silencing cancer-IgG decreased after 0, 2, 4, 6, and 8 Gy of irradiation, and the single-hit multi-target model was fitted to the survival curve. $^{**}P < 0.01$ (n=3). ShC-IgG: sh-cancer-IgG.

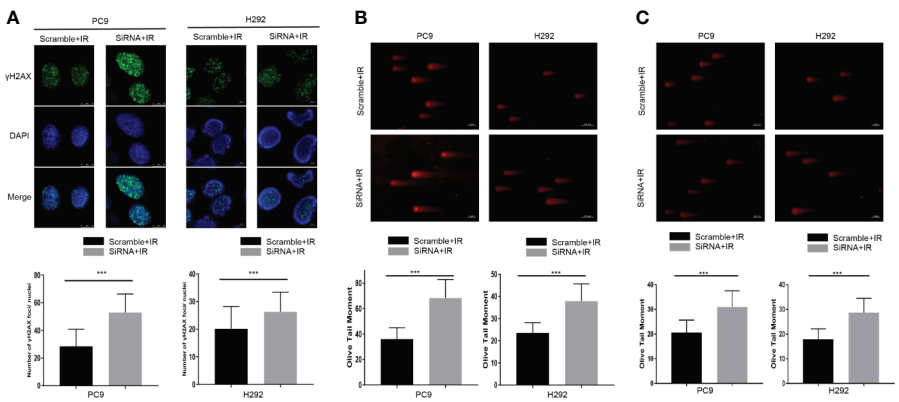

FIGURE 4 | Cancer-IgG silencing attenuates lung adenocarcinoma resistance to radiation therapy. **(A)** Silencing cancer-IgG expression inhibited the DNA double-strand break repair ability of PC9 and H292 cells, and the number of γH2AX fluorescence foci in the nucleus increased. Count 50 cells in each group in the experiment. $^{***}P < 0.001$ (n=50). **(B, C)** The DNA double-strand break repair capacity was impaired in PC9 and H292 cells with cancer-IgG knockdown, and the Olive tail moment was extended. Count 50 cells in each group in the experiment. Scale bar, 50 μm. **(B)** Irradiation 4 Gy; **(C)** Irradiation 2 Gy. $^{***}P < 0.001$ (n=50).

p-DNA-PKcs in cancer-IgG knockdown LUAD cells were decreased after radiation and that the repair ability of DSBs was decreased, as shown by results of the neutral comet assay and γH2AX immunofluorescence assay. These assays indicated that cancer-IgG can regulate the damage repair ability of DSBs in LUAD through the PI3K/AKT/DNA-PKcs pathway and upregulate radiotherapy resistance. Phosphorylation protein microarray analysis showed that, in addition to the decreased expression of damage repair proteins, apoptotic proteins of LUAD cells were increased, which may be due to the weakened repair ability and increased cell debris that enhance the mechanism of cell apoptosis.

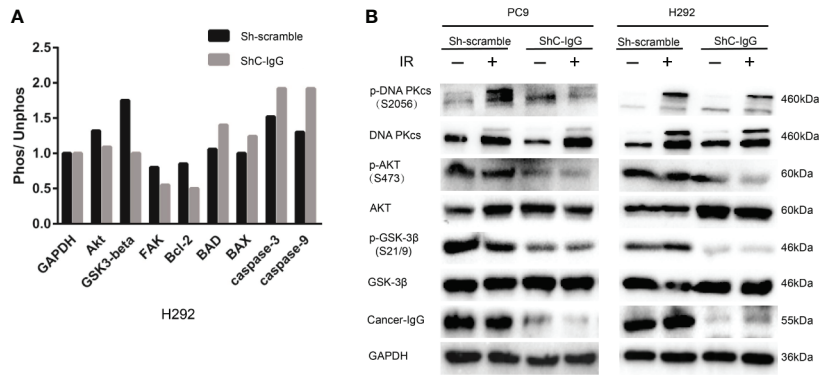

FIGURE 5 | Cancer-IgG mediates radioresistance to LUAD *via* the PI3K/AKT/DNA-PKcs pathway. **(A)** An antibody phosphorylation chip was used to detect the phosphorylation changes in key proteins of the signaling pathway after cancer-IgG was silenced. **(B)** Western blot shows the changes in the expression of DNA-PKcs, p-DNA-PKcs, AKT, p-AKT GSK3β, and p-GSK3β of knockdown cancer-IgG under irradiated and nonirradiated conditions.

To the best of our knowledge, this is the first study that explains the radiosensitization effect of cancer-IgG in LUAD. This study demonstrates that reducing the expression of cancer IgG effectively inhibits radiation-induced PI3K/AKT/DNA-PKcs signal transduction, resulting in impaired DSB damage repair ability, and leads to increased sensitivity to radiation treatments. The study provides new insights into cancer-IgG as a regulator of radiosensitivity in LUAD.

DATA AVAILABILITY STATEMENT

The raw data supporting the conclusions of this article will be made available by the authors, without undue reservation.

ETHICS STATEMENT

The studies involving human participants were reviewed and approved by Medical Ethics Committee of Beijing Cancer Hospital. The patients/participants provided their written informed consent to participate in this study.

AUTHOR CONTRIBUTIONS

XY, GW, JY, RG, XX, CX, HW and RZ conducted the research. GZ designed the study. XQ contributed the essential reagents or tools. XY and RG wrote the paper. All authors contributed to the article and approved the submitted version. XY, GW, JY contributed equally.

FUNDING

This study was supported by the grants from the National Key R&D Program of China (to GZ) (No.2018YFC1313202) and the China-Japan Friendship Hospital Scientific Research Start-up Funds (to GZ)(No.2016-RC-4).

SUPPLEMENTARY MATERIAL

The Supplementary Material for this article can be found online at: https://www.frontiersin.org/articles/10.3389/fonc.2021.675397/full#supplementary-material

REFERENCES

1. Siegel RL, Miller KD, Jemal A. Cancer Statistics, 2020. *CA: Cancer J Clin* (2020) 70(1):7–30. doi: 10.3322/caac.21590
2. Chen Z, Fillmore CM, Hammerman PS, Kim CF, Wong KK. Non-Small-Cell Lung Cancers: A Heterogeneous Set of Diseases. *Nat Rev Cancer* (2014) 14 (8):535–46. doi: 10.1038/nrc3775
3. Bernier J, Hall EJ, Giaccia A. Radiation Oncology: A Century of Achievements. *Nat Rev Cancer* (2004) 4(9):737–47. doi: 10.1038/nrc1451
4. Timmerman R, Paulus R, Galvin J, Michalski J, Straube W, Bradley J, et al. Stereotactic Body Radiation Therapy for Inoperable Early Stage Lung Cancer. *JAMA* (2010) 303(11):1070–6. doi: 10.1001/jama.2010.261
5. Curran WJ Jr., Paulus R, Langer CJ, Komaki R, Lee JS, Hauser S, et al. Sequential vs. Concurrent Chemoradiation for Stage III non-Small Cell Lung Cancer: Randomized Phase Iii Trial Rtog 9410. *J Natl Cancer Inst* (2011) 103 (19):1452–60. doi: 10.1093/jnci/djr325
6. Antonia SJ, Villegas A, Daniel D, Vicente D, Murakami S, Hui R, et al. Durvalumab After Chemoradiotherapy in Stage Iii Non-Small-Cell Lung Cancer. *N Engl J Med* (2017) 377(20):1919–29. doi: 10.1056/NEJMoa 1709937
7. Cohen AJ, Brauer M, Burnett R, Anderson HR, Frostad J, Estep K, et al. Estimates and 25-Year Trends of the Global Burden of Disease Attributable to Ambient Air Pollution: An Analysis of Data From the Global Burden of Diseases Study 2015. *Lancet* (2017) 389(10082):1907–18. doi: 10.1016/s0140-6736(17)30505-6
8. Qiu X, Zhu X, Zhang L, Mao Y, Zhang J, Hao P, et al. Human Epithelial Cancers Secrete Immunoglobulin G With Unidentified Specificity to Promote Growth and Survival of Tumor Cells. *Cancer Res* (2003) 63(19):6488–95.

9. Qin C, Sheng Z, Huang X, Tang J, Liu Y, Xu T, et al. Cancer-Driven IgG Promotes the Development of Prostate Cancer Though the SOX2-CIgG Pathway. *Prostate* (2020) 80(13):1134–44. doi: 10.1002/pros.24042
10. Peng J, Wang HC, Liu Y, Jiang JH, Lv WQ, Yang Y, et al. Involvement of non-B Cell-Derived Immunoglobulin G in the Metastasis and Prognosis of Salivary Adenoid Cystic Carcinoma. *Oncol Lett* (2017) 14(4):4491–8. doi: 10.3892/ol.2017.6782
11. Tang J, Zhang J, Liu Y, Liao Q, Huang J, Geng Z, et al. Lung Squamous Cell Carcinoma Cells Express non-Canonically Glycosylated Igg That Activates integrin-FAK Signaling. *Cancer Lett* (2018) 430:148–59. doi: 10.1016/j.canlet.2018.05.024
12. Liu Y, Liu D, Wang C, Liao Q, Huang J, Jiang D, et al. Binding of the Monoclonal Antibody RP215 to Immunoglobulin G in Metastatic Lung Adenocarcinomas is Correlated With Poor Prognosis. *Histopathology* (2015) 67(5):645–53. doi: 10.1111/his.12686
13. Babbage G, Ottensmeier CH, Blaydes J, Stevenson FK, Sahota SS. Immunoglobulin Heavy Chain Locus Events and Expression of Activation-Induced Cytidine Deaminase in Epithelial Breast Cancer Cell Lines. *Cancer Res* (2006) 66(8):3996–4000. doi: 10.1158/0008-5472.CAN-05-3704
14. Jiang H, Kang B, Huang X, Yan Y, Wang S, Ye Y, et al. Cancer IgG, a Potential Prognostic Marker, Promotes Colorectal Cancer Progression. *Chin J Cancer Res* (2019) 31(3):499–510. doi: 10.21147/j.issn.1000-9604.2019.03.12
15. Lee G. Cancer Cell-Expressed Immunoglobulins: CA215 as a Pan Cancer Marker and its Diagnostic Applications. *Cancer Biomarkers Section A Dis Markers* (2009) 5(3):137–42. doi: 10.3233/cbm-2009-0610
16. Wang Z, Geng Z, Shao W, Liu E, Zhang J, Tang J, et al. Cancer-Derived Sialylated Igg Promotes Tumor Immune Escape by Binding to Siglecs on Effector T Cells. *Cell Mol Immunol* (2019) 17(11):1148–62. doi: 10.1038/s41423-019-0327-9
17. Zhao Y, Tao L, Yi J, Song H, Chen L. The Role of Canonical Wnt Signaling in Regulating Radioresistance. *Cell Physiol Biochem Int J Exp Cell Physiol biochemistry Pharmacol* (2018) 48(2):419–32. doi: 10.1159/000491774
18. Chang HHY, Pannunzio NR, Adachi N, Lieber MR. Non-Homologous DNA End Joining and Alternative Pathways to Double-Strand Break Repair. *Nat Rev Mol Cell Biol* (2017) 18(8):495–506. doi: 10.1038/nrm.2017.48
19. Fok JHL, Ramos-Montoya A, Vazquez-Chantada M, Wijnhoven PWG, Follia V, James N, et al. AZD7648 is a Potent and Selective Dna-Pk Inhibitor That Enhances Radiation, Chemotherapy and Olaparib Activity. *Nat Commun* (2019) 10(1):5065. doi: 10.1038/s41467-019-12836-9
20. Toulany M, Kehlbach R, Florczak U, Sak A, Wang S, Chen J, et al. Targeting of AKT1 Enhances Radiation Toxicity of Human Tumor Cells by Inhibiting DNA-Pkcs-Dependent DNA Double-Strand Break Repair. *Mol Cancer Ther* (2008) 7(7):1772–81. doi: 10.1158/1535-7163.Mct-07-2200
21. Gao H, Xue J, Zhou L, Lan J, He J, Na F, et al. Bevacizumab Radiosensitizes non-Small Cell Lung Cancer Xenografts by Inhibiting Dna Double-Strand Break Repair in Endothelial Cells. *Cancer Lett* (2015) 365(1):79–88. doi: 10.1016/j.canlet.2015.05.011
22. Sheng Z, Liu Y, Qin C, Liu Z, Yuan Y, Hu F, et al. Igg is Involved in the Migration and Invasion of Clear Cell Renal Cell Carcinoma. *J Clin Pathol* (2016) 69(6):497–504. doi: 10.1136/jclinpath-2015-202881
23. Wang G, Yang X, Zhu G. Expression and Clinical Significance of Cancer-derived Immunoglobulin G in Non-small Cell Lung Cancer by Bioinformatics and Immunohistochemistry. *Zhongguo fei ai za zhi = Chin J Lung Cancer* (2019) 22(6):341–8. doi: 10.3779/j.issn.1009-3419.2019.06.03
24. Santivasi WL, Xia F. Ionizing Radiation-Induced Dna Damage, Response, and Repair. *Antioxidants Redox Signaling* (2014) 21(2):251–9. doi: 10.1089/ars.2013.5668
25. Yue X, Bai C, Xie D, Ma T, Zhou PK. Dna-Pkcs: A Multi-Faceted Player in DNA Damage Response. *Front Genet* (2020) 11:607428. doi: 10.3389/fgene.2020.607428
26. Kim BM, Hong Y, Lee S, Liu P, Lim JH, Lee YH, et al. Therapeutic Implications for Overcoming Radiation Resistance in Cancer Therapy. *Int J Mol Sci* (2015) 16(11):26880–913. doi: 10.3390/ijms161125991
27. Huang RX, Zhou PK. Dna Damage Response Signaling Pathways and Targets for Radiotherapy Sensitization in Cancer. *Signal transduction targeted Ther* (2020) 5(1):60. doi: 10.1038/s41392-020-0150-x
28. Wang LM, Gan YH. Cancer-Derived IgG Involved in Cisplatin Resistance Through Ptp-Bas/Src/Pdk1/Akt Signaling Pathway. *Oral Dis* (2020). doi: 10.1111/odi.13583
29. Revathidevi S, Munirajan AK. Akt in Cancer: Mediator and More. *Semin Cancer Biol* (2019) 59:80–91. doi: 10.1016/j.semcancer.2019.06.002
30. Song M, Bode AM, Dong Z, Lee MH. AKT as a Therapeutic Target for Cancer. *Cancer Res* (2019) 79(6):1019–31. doi: 10.1158/0008-5472.Can-18-2738
31. Toulany M, Rodemann HP. Phosphatidylinositol 3-Kinase/Akt Signaling as a Key Mediator of Tumor Cell Responsiveness to Radiation. *Semin Cancer Biol* (2015) 35:180–90. doi: 10.1016/j.semcancer.2015.07.003
32. Toulany M, Lee KJ, Fattah KR, Lin YF, Fehrenbacher B, Schaller M, et al. Akt Promotes Post-Irradiation Survival of Human Tumor Cells Through Initiation, Progression, and Termination of DNA-PKcs-dependent Dna Double-Strand Break Repair. *Mol Cancer Res MCR* (2012) 10(7):945–57. doi: 10.1158/1541-7786.Mcr-11-0592
33. Schötz U, Balzer V, Brandt FW, Ziemann F, Subtil FSB, Rieckmann T, et al. Dual PI3K/mTOR Inhibitor NVP-BEZ235 Enhances Radiosensitivity of Head and Neck Squamous Cell Carcinoma (Hnscc) Cell Lines Due to Suppressed Double-Strand Break (Dsb) Repair by Non-Homologous End Joining. *Cancers* (2020) 12(2):467. doi: 10.3390/cancers12020467
34. Park JH, Jung KH, Kim SJ, Fang Z, Yan HH, Son MK, et al. Radiosensitization of the PI3K Inhibitor HS-173 Through Reduction of DNA Damage Repair in Pancreatic Cancer. *Oncotarget* (2017) 8(68):112893–906. doi: 10.18632/oncotarget.22850
35. Palanichamy K, Patel D, Jacob JR, Litzenberg KT, Gordon N, Acus K, et al. Lack of Constitutively Active DNA Repair Sensitizes Glioblastomas to Akt Inhibition and Induces Synthetic Lethality With Radiation Treatment in a P53-Dependent Manner. *Mol Cancer Ther* (2018) 17(2):336–46. doi: 10.1158/1535-7163.Mct-17-0429
36. Lees-Miller SP. Pikk-Ing a New Partner: A New Role for PKB in the DNA Damage Response. *Cancer Cell* (2008) 13(5):379–80. doi: 10.1016/j.ccr.2008.04.010
37. Bozulic L, Surucu B, Hynx D, Hemmings BA. Pkbalpha/Akt1 Acts Downstream of DNA-PK in the DNA Double-Strand Break Response and Promotes Survival. *Mol Cell* (2008) 30(2):203–13. doi: 10.1016/j.molcel.2008.02.024

Conflict of Interest: The authors declare that the research was conducted in the absence of any commercial or financial relationships that could be construed as a potential conflict of interest.

frontiers in Oncology

ORIGINAL RESEARCH
published: 10 June 2021
doi: 10.3389/fonc.2021.686950

Evaluation of Epigallocatechin-3-Gallate as a Radioprotective Agent During Radiotherapy of Lung Cancer Patients: A 5-Year Survival Analysis of a Phase 2 Study

Wanqi Zhu[1,2,3†], Yalan Zhao[4†], Shuyu Zhang[5], Xiaolin Li[3], Ligang Xing[4], Hanxi Zhao[3*] and Jinming Yu[1,2,3*]*

[1] Tianjin Medical University Cancer Institute and Hospital, National Clinical Research Center for Cancer, Key Laboratory of Cancer Prevention and Therapy, Tianjin, Tianjin's Clinical Research Center for Cancer, Tianjin, China, [2] Department of Radiation Oncology, Tianjin Medical University, Tianjin, China, [3] Department of Radiation Oncology, Shandong Cancer Hospital and Institute, Shandong First Medical University and Shandong Academy of Medical Science, Jinan, China, [4] Department of Oncology, The Affiliated Hospital of Southwest Medical University, Luzhou, China, [5] Second Affiliated Hospital of Chengdu Medical College, China National Nuclear Corporation 416 Hospital, Chengdu, China

Background: Previous analysis of the study (NCT02577393) had demonstrated the application of epigallocatechin-3-gallate (EGCG) could be safe and effective in the prevention and treatment of acute radiation esophagitis in patients with advanced lung cancer. EGCG seemed to improve the response rate of small cell lung cancer (SCLC) to radiotherapy in a subgroup analysis. This research continued to analyze the impact of EGCG application on cancer-radiation efficacy and patient survival.

Methods: All patients with SCLC in the NCT02577393 study were included. Patients were randomized into EGCG group or conventional therapy group as protocol. The primary endpoints of the study were radiation response rate and progression-free survival (PFS). Overall survival (OS) and the efficacy of EGCG in the treatment of esophagitis were assessed as secondary endpoints.

Results: A total of 83 patients with lung cancer in the NCT02577393 study were screened, and all 38 patients with SCLC were eligible for analysis. No significant differences with regard to baseline demographic and clinical characteristics were observed between the two groups. The objective response rate (ORR) was higher than that of conventionally treated patients (84.6 *vs* 50%, $P = 0.045$), while the median PFS and OS were not significantly prolonged. At data cut-off (1 January 2021), 5-year PFS was 33% with EGCG *versus* 9.3% with conventional treatment, and 5-year OS was 30.3% *versus* 33.3%, respectively. The mean adjusted esophagitis index and pain index of patients with EGCG application were lower than conventional treatment (5.15 ± 2.75 *vs* 7.17 ± 1.99, $P = 0.030$; 8.62 ± 5.04 *vs* 15.42 ± 5.04, $P < 0.001$).

OPEN ACCESS

Edited by:
Sandeep Kumar Shukla,
Institute of Nuclear Medicine & Allied Sciences (DRDO), India

Reviewed by:
Aseem Bhatnagar,
Retired, Delhi, India
Badri Pandey,
Bhabha Atomic Research Centre (BARC), India

***Correspondence:**
Ligang Xing
sdcancerhospital@163.com
Hanxi Zhao
zhx87520052@163.com
Jinming Yu
sdyujinming@163.com

[†]These authors have contributed equally to this work and share first authorship

Specialty section:
This article was submitted to Radiation Oncology, a section of the journal Frontiers in Oncology

Received: 28 March 2021
Accepted: 10 May 2021
Published: 10 June 2021

Citation:
Zhu W, Zhao Y, Zhang S, Li X, Xing L, Zhao H and Yu J (2021) Evaluation of Epigallocatechin-3-Gallate as a Radioprotective Agent During Radiotherapy of Lung Cancer Patients: A 5-Year Survival Analysis of a Phase 2 Study. Front. Oncol. 11:686950. doi: 10.3389/fonc.2021.686950

Conclusion: The study indicates EGCG may alleviate some esophagitis-related indexes in SCLC patients exposed to ionizing radiation without reducing survival. However, this conclusion should be confirmed by further studies with large sample size.

Keywords: Epigallocatechin-3-gallate, lung cancer, radiation-induced esophagitis, radioprotective agent, long-term follow-up

BACKGROUND

Acute radiation-induced esophagitis (ARIE) is a typical adverse reaction that occurs in patients with chemo-radiotherapy/radiotherapy, which is more common in lung cancer (1). The incidence of grade 2–3 acute esophagitis caused by CCRT is 20–53.4% in pulmonary carcinoma (2, 3). The most common symptoms in patients with ARIE are odynophagia and dysphagia two or three weeks after radiation (4). With increasing attention to ARIE, new strategies for preventing and mitigating it have become an active research field. Assuredly, severe ARIE is positively correlated with the high-dose radiation per unit volume of the esophageal mucosa (5). Great efforts are being made to overcome its risk through the development of novel radiation technology and treatment targeting related signaling pathways (6).

Epigallocatechin-3-gallate (EGCG) is the main component of tea polyphenols, accounting for an average of 65% in the total tea polyphenols. It has been proved to have a strong protective effect against radiation-induced damages in the normal tissue on the cellular and animal level (7–9). Recently, the anti-irradiation damage activity of EGCG has been preliminarily proved in clinical trials, with our data confirming that the application of plant-derived polyphenol can ameliorate ARIE, radiation mucositis, and radiation dermatitis (10–16). The safety and effectiveness of EGCG make it one of the promising candidates for radioprotection. No tumor-damaged repair is also an important consideration for developing the agent, just like ensuring efficacy and acceptable toxicity. Interesting, EGCG seems to have a certain radio-enhancing effect on SCLC during radiotherapy in clinical practice. Therefore, the radiation efficacy and survival follow-up of patients with SCLC in the published trial (NCT02577393) were analyzed for verifying the overall role of EGCG in tumor radiotherapy.

METHODS

Study Population and Study Design

NCT02577393 study as a three-arm, controlled, randomized, prospective study was conducted to explore the preventive and therapeutic action of EGCG against ARIE in patients with the combination of chemoradiotherapy. The protocol was available at *Oncology and Radiotherapy* online (10). EGCG was purchased from NINGBO HEP Biotech Co., Ltd and dissolved in 0.9% saline solution to make the concentration up to 440 umol/L with reference to the results of phase I study (16).

The analysis described here included patients with SCLC who received EGCG or conventional treatment in the NCT02577393 study. Patients who slowly swallowed EGCG solution with 10 ml three times daily, whether at the beginning of radiation or at the appearance of grade I esophagitis, were included in the EGCG group. The patients in the conventional treatment group were those who were treated with a solution containing 0.16 mg/ml lidocaine, 0.02 mg/ml dexamethasone, and 0.16 mg/ml gentamicin (mLDG) for symptomatic support when esophagitis occurred. Patients in both groups stopped EGCG or mLDG solution two weeks after radiotherapy. This research design had been approved by our local study review board. All patients were included with written informed consent. **Figure 1** showed an overview of the study design. In the NCT02577393 study, there were 83 patients with lung cancer, including 38 patients with SCLC and 45 patients with non-small cell lung cancer. All 38 patients with SCLC were included in this observational non-interventional study and followed up. Follow-up visits with H&P and chest CT occurred every 3–4 months for the first two years, every 6 months for the following three years, and annually thereafter.

RADIOTHERAPY DETAILS

Radiotherapy was administered through three-dimensional conformal or intensity-modulated techniques. All patients underwent CT simulation and were immobilized supinely on thermoplastic masks or vacuum molded bags. Gross target volume included post-chemotherapy primary tumor and pre-chemotherapy nodal volume. The total dose was 50.4–60 Gy (a fraction of 1.8–2Gy once a day) or 45 Gy (1.5 Gy twice a day) for five days weekly. Planning target volume was encompassed by the 95% isodose, and the maximum dose is below 107%. The dose limits for organ at risk were as before, such as less than 18 Gy mean lung dose (10).

Study Assessments

The tumor (T), node (N), and metastasis (M) of SCLC were graded by the eighth edition AJCC/UICC stage classification. ARIE was assessed according to RTOG scoring criteria weekly from onset of radiation to 2 weeks after completion of radiation. Esophagitis-related pain and dysphagia were graded by the numerical rating scale. Esophagitis-related indexes (adjusted esophagitis index, AEI; adjusted pain index, API; adjusted dysphagia index, ADI) were calculated as previously reported (10) and shown in **Supplementary Figure 1**. The curve of each patient was drawn with the grade of esophagitis-related parameters (ARIE, pain, and dysphagia score) as ordinate and the observation completion rate as abscissa. The area under the three curves, namely AEI, API, or ADI, was an integrated measurement of severity and duration of esophagitis from different perspectives.

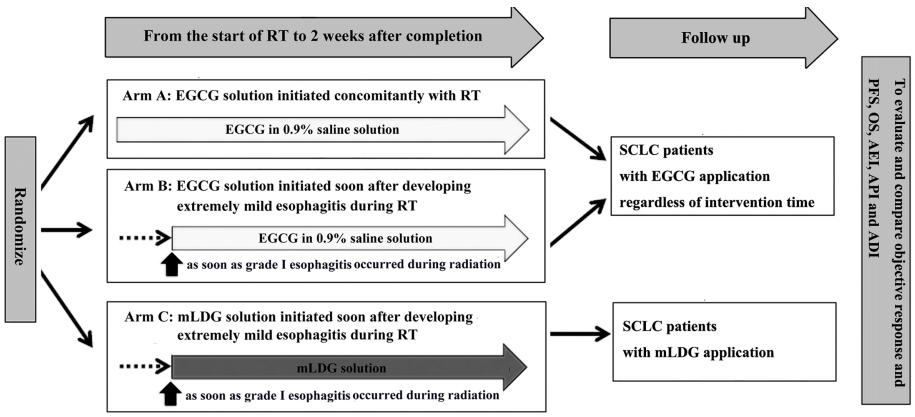

FIGURE 1 | An overview of the study design. EGCG, Epigallocatechin-3-gallate; PFS, progression-free survival; OS, overall survival; AEI, adjusted esophagitis index; API, adjusted pain index; ADI, adjusted dysphagia index.

Tumor response was assessed by RECIST criteria. ORR included complete and partial response (CR and PR) rate. PFS referred to the time from randomization until tumor progression or death from any reasons or the last medical observation. OS encompassed the intervening time from randomization to death or the last medical observation.

In this study, we primarily assessed the differences between the two groups in terms of objective response rate (ORR) and progression-free survival (PFS). The secondary endpoints included OS and three adjusted esophagitis-related indexes. In order to avoid subjective deviation, an independent evaluation group composed of two senior and well-equipped doctors assessed the above endpoints without knowing the treatment allocation.

Data Statistics

Updated data, covering the period until January 1, 2021, were used for this assessment. The calculation method of the sample size had been clarified in the previously released NCT02577393 research report, while the current analysis of ORR, PFS, and OS in SCLC was not informed. Kaplan–Meier curves and estimates were used to deal with differing survival data including PFS, OS and follow-up time. The 1-, 2-, and 5-years PFS rates were compared by Z test. Univariate and multivariate Cox regression analyses were applied to analyzed variables affecting survival time. The differences between categorical variates were tested by Fisher's exact test. The measurement data of the different groups were analyzed by t-test. Statistical significance for the hypothesis was set at a *P*-value less than 0.05 with a two-sided version. The statistical analysis was carried out using statistical package for the social sciences software systems (v. 17.0).

RESULT

Baseline Characteristics

In this report, the first patient was enrolled in April 2015 and the last one in April 2018. Thirty-eight patients with SCLC were eligible for analysis. The differences in baseline characteristic variables between the two groups were not significant (**Table 1**). Eight (21.1%) of them were female. Their age was 41 to 75 years old (median 58 years). 44.7% of the patients undertook radiotherapy and chemotherapy at the same time. Dosimetry parameters predicting potential radiation toxicities for esophagus were described in detail: the mean and maximum values were 32.7 Gy (20.3–51.9) and 65.3 Gy (51.2–68.6); V30, V35, and V50 were 57.3, 54.5, and 42.0%, respectively.

Acute Esophagitis

The median onset time of ARIE and pain symptom for patients was 3 weeks (range, 2–5 weeks) and that of dysphagia symptom was 3 weeks (range, 2–7 weeks). **Table 2** showed the highest grades of ARIE, pain, and dysphagia endured by patients in the two groups during treatment, and there were no statistical differences (P = 0.441; P = 0.796; P = 0.394). The mean AEI and API of patients with EGCG application were significantly lower than those of patients with mLDG mixture solution (5.15 ± 2.75 *vs* 7.17 ± 1.99, P = 0.030; 8.62 ± 5.04 *vs* 15.42 ± 5.04, P < 0.001 **Figure 2**). However, no statistical difference was observed in ADI (2.88 ± 2.47 *vs* 4.08 ± 2.84, P = 0.193; **Figure 2**). There was no significant difference in AEI, API, and ADI between patients receiving concurrent radio-chemotherapy and patients receiving sequential radio-chemotherapy in mLDG group and/or EGCG group (all P > 0.05).

Response Rates to Cancer Therapy

Overall, radiographic remission was observed in 73.7% of patients after the end of tumor treatment. No significant difference was noted between the groups in terms of CR or PR separately (three of 26 in EGCG group *vs* one of 12 in the placebo group, P = 1.000; 19 of 26 in EGCG group *vs* five of 12 in the placebo group, P = 0.081). The ORR of patients with EGCG was slightly higher than that of patients with conventional therapy (P = 0.045, **Table 2**). In the univariate regression analysis, EGCG

TABLE 1 | Pretreatment characteristics.

Characteristic	EGCG application (n = 26)	conventional treatment (n = 12)	*P*
Age (years)			
Median (range)	56.5 (41–75)	62.5 (50–70)	0.282
Sex (n)			
Male	22	8	0.23
Female	4	4	2
KPS score (n)			
80	10	3	0.48
90	16	9	6
Smoking index (years*root)			
Median (range)	400 (0–1,600)	500.00 (0–1,600)	0.790
T (n)			
1	0	1	0.17
2	5	3	7
3	12	2	
4	9	6	
N (n)			
1	1	0	0.185
2	11	2	
3	14	10	
Treatment (n)			
Sequential CRT	14	7	1.00
Concomitant CRT	12	5	0
Esophageal dosimetric parameters			
Mean value (Gy)			
Median (range)	31.0 (20.3–51.9)	34.2 (20.3–43.5)	0.505
Maximum value (Gy)			
Median (range)	65.8 (51.2–68.6)	64.9 (57.2–67.8)	0.711
V30 value (%)			
Median (range)	54.8 (27.0–80.0)	57.8 (30.0–72.0)	0.493
V35 value (%)			
Median (range)	52.0 (22.0–75.0)	55.0 (25.0–65.0)	0.449
V50 value (%)			
Median (range)	37.0 (19.0–70.0)	46.0 (10.0–58.0)	0.532

application was positively correlated with ORR (t =2.355, P = 0.024), and N stage was negatively correlated with ORR (t = −2.071, P = 0.046). In multivariate stepwise logistic regression analysis, only EGCG application was still significantly correlated with ORR.

PFS and OS Analyses

At the deadline for data collection, the median follow-up was 56.0 months [95% confidence interval (CI): 37.1–74.9] for patients in the EGCG group. Whereas for patients in the mLDG group, it was 50.0 months (95% CI: 28.2–71.8). Twenty-three patients died, twenty from disease progression, two from heart failure, and one from radiation pneumonia. One patient in each group was lost to follow-up.

The median time to PFS was 16.0 months (95% CI, 2.3–29.7) for EGCG and 18.0 months (95% CI, 11.6–24.4) for mLDG. Mean (standard error) PFS time was 31.9 (5.5) months for EGCG and 21.2 (5.0) months for mLDG. There was no statistical difference in PFS between the two group (chi-Square = 0.981, P = 0.322, **Figure 3**). The 1-, 2- and 5-year PFS rates in patients with EGCG solution were 53.8, 38.5, and 33.0%, respectively, and those in patients with mLDG solution were 64.8, 27.8, and 9.3%, respectively. The differences in PFS rates from 1 to 5 years were also insignificant (P = 0.320; P = 0.257; P = 0.076). The median OS in the EGCG group was 22.0 months (95% CI: 3.0–41.0), and the OS at 1, 2, and 5 years was 84.6, 50.0, and 30.3%, respectively. While the median OS of patients with mLDG was 23.0 months (95% CI: 12.8–33.2), and the OS at 1, 2, and 5 years was 75.0, 50.0, and 33.3%, respectively. Mean (standard error) OS times for EGCG and mLDG were 36.2 (4.9) and 33.6 (6.6) months, respectively. There was also no statistical difference in OS between the two groups (chi-Square = 0.007, P = 0.936, **Figure 4**).

Baseline and on-treatment factors associated with survival were analyzed. The correlation was only observed between the ORR and PFS (P = 0.002; hazard ratio (HR): 3.7, 95% CI: 1.6 to 8.3). For all subsets of participants examined, those with ORR had the higher PFS rates (1 year: 66.9 *vs* 30%; 2 years: 44.6 *vs* 10%; 5 years: 35.8 *vs* 0%). Additionally, low smoking index was associated with a prolonged OS (P = 0.044; HR: 1.0, 95% CI: 1.0 to 1.1) in a Cox proportional hazards regression analysis. The 1-, 2-, and 5-year overall survival rates separately were 94.7, 68.4, and 51.0% for patients with smoking index less than 500.

Updated Adverse Event Data

Most of the adverse events (AEs) were similar to previously published data, and the EGCG-related AE were expected (10).

TABLE 2 | Distribution of maximum grade of esophagitis-related parameters and tumor response.

	EGCG application	conventional treatment	Total	*P*
Tumor response				
Complete response	3(11.5%)	1(8.3%)	4(10.5%)	
Partial response	19(73.1%)	5(41.7%)	24(63.2%)	
Stable disease	2(7.7%)	3(25.0%)	5(13.2%)	
Progressive disease	2(7.7%)	3(25.0%)	5(13.2%)	$P = 0.145$
Overall response	22(84.6%)	6(50%)	28(73.7%)	
Overall non-response	4(15.4%)	6(50%)	10(26.3%)	$P = 0.045$
Maximum acute radiation-induced esophagitis grade				
1	21(80.8%)	9(75.0%)	30(78.9%)	
2	5(19.2%)	2(16.7%)	7(18.4%)	
3	0(0%)	1(8.3%)	1(2.6%)	$P = 0.441$
Maximum pain grade				
1	1(3.8%)	0(0%)	1(2.6%)	
2	6(23.1%)	1(8.3%)	7(18.4%)	
3	15(57.7%)	8(66.7%)	23(60.5%)	
4	2(7.7%)	2(16.7%)	4(10.5%)	
5	1(3.8%)	0(0%)	1(2.6%)	
6	1(3.8%)	1(8.3%)	2(5.3%)	$P = 0.796$
Maximum dysphagia grade				
1	5(19.2%)	0(0%)	5(13.2%)	
2	18(69.2%)	10(83.3%)	28(73.7%)	
3	3(11.5%)	2(16.7%)	5(13.2%)	$P = 0.394$

The most common adverse event in patients was leukopenia. No Grade >3 hematological adverse event was perceived including deficiency of hemoglobin, leukocyte, and platelet. In addition to hematological toxicity, other grade ≥3 AEs were gastrointestinal reactions (two cases) and radiation-induced pneumonitis (one case), which were considered to be induced by radiotherapy and chemotherapy. Weight loss of more than 5% was seen in 10.5% of individuals, and weight increase of more than 5% was seen in 7.9%. There was no significant difference in weight change between EGCG and mLDG groups. A low rate of late radiation-induced dysphagia of 5.3% was observed but without statistical difference between the two groups. All adverse reactions mentioned above should be absent from the EGCG or mLDG applications. Only one case experienced mild queasiness while swallowing the EGCG solution, which could be associated with EGCG and attributed to its weird uncomfortable taste. No other adverse effects of EGCG were noted.

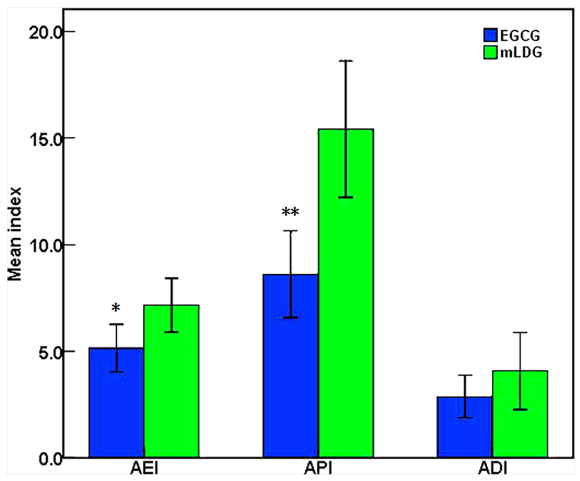

FIGURE 2 | EGCG significantly improved the patient's esophagitis and pain compared with conventional treatment. The statistical differences were observed in the mean value of AEI and API between EGCG and mLDG groups (*P = 0.030; **P < 0.001).

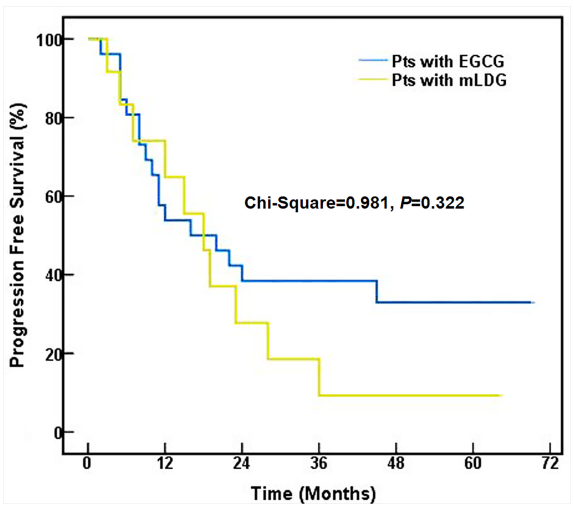

FIGURE 3 | Progression-free survival of SCLC patients (pts) treated with EGCG (blue) or mLDG (gold) solution.

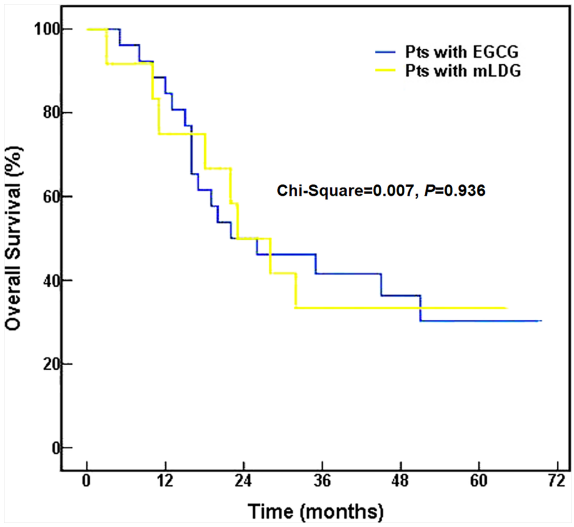

FIGURE 4 | Overall survival of SCLC patients (pts) treated with EGCG (blue) or mLDG (gold) solution.

DISCUSSION

Until now, the standard initial therapy remains concurrent chemoradiotherapy (CRT) in most limited stage SCLC cases (17, 18). ARIE, as a frequent acute complication of CRT, can continuously reduce the quality of life of patients. The advanced radiotherapy approaches cannot solve this problem completely (19, 20). Radioprotectants may shed new light on potential breakthroughs. The four key requirements for the development of radioprotectants are effective protection of normal tissue, low drug toxicity, convenience for clinical applicability, and no repair of radiation-damaged cancer (21). Due to the failure to meet all the above conditions, amifostine, the only radiation protective agent approved by FDA, is not widely used in clinical practice (22, 23). EGCG, as a representative bioactive ingredient from medicine food homology, gradually stands out among many potential new radioprotectants (24). The safe pharmacology spectrum of EGCG was determined at six escalated dose levels in our previous phase I study, resulting in a recommended concentration of 440 umol/L (16). A subsequent single-arm study was launched to ensure its efficacy in the treatment of ARIE (15). Our prospective controlled trial NCT02577393 confirmed that EGCG had significantly reduced esophagitis than conventional treatment (mLDG) during chemoradiotherapy for lung cancer, especially when used for prophylaxis (10). The above studies preliminarily proved that EGCG could meet the first three of the mentioned four key requirements. The minimum requirement for the application of protectors was not to reduce the anti-tumor effect of radiation, preferably to enhance it. This study was the first to report the long-term follow-up data of EGCG in patients with SCLC after chemoradiotherapy. To explore whether ECGC as a radioprotective agent for esophageal tissue would affect the short-term and long-term efficacy of radiotherapy for lung cancer, the differences of objective tumor remission rate and the follow-up survival time between EGCG group and placebo group were taken as the clinical endpoints (25–27).

The observations on EGCG efficacy in improving radiation-induced esophagitis were generally consistent with previous studies (10). Even if the number of participants was small, there was a significant difference in the AEI. The statistical difference was also found in the pain index. The significant difference was not found between the EGCG and mLDG groups with regard to ADI and the maximum grade of ARIE. Similar to previous studies, there was an increasing trend in the severity of esophagitis with concurrent CRT compared with sequential CRT (28). It did not reach statistical significance due to the small number of participants; therefore no attempt was made in the study to evaluate the effect of EGCG on the toxicity of concurrent chemotherapy. Our data showed a low rate of late radiation-induced dysphagia in both groups. No new adverse reactions related to EGCG had been found.

In terms of short-term response, we separately compared tumor CR and PR between patients with EGCG or mLDG solution, but found no statistical significance. However, the ORR (CR plus PR rate) was higher in patients receiving EGCG solution than that in patients undertaking the conventional treatment. It had also been reported that EGCG can improve the short-term efficacy of radiotherapy in patients with breast cancer (29). In the long-term follow-up, EGCG-treated group had a shorter median PFS but a longer mean PFS compared to the mLDG-treated group, and the difference was not statistically significant. The 1-year PFS of mLDG was higher than that of the EGCG group while the 2- and 5-year PFS rates show reversal. The 5-year PFS rate difference between EGCG and the control group was 27% (33 *vs* 9%). The undesirable performance of 1-year PFS in the EGCG group could be caused by non-cancer death and the insufficient number of participants. The association between EGCG application and ORR or between ORR and PFS appeared, but the association between EGCG application and PFS was not shown. The differences of OS between EGCG and mLDG groups also failed to reveal an obvious statistical difference. Though an overall statistically beneficial effect of EGCG was not found in the study, the trends suggested that it could bring a clinical benefit in SCLC patients with RT. EGCG remarkably enhanced the efficacy of tumor radiotherapy in the short-term and had a tendency to increase it in the long-term.

The mechanism of EGCG is complicated. Radiation essentially destroys the living organism by the deposition of energy directly into key biological macromolecules such as desoxyribonucleic acid (DNA), and a series of cascading reactions are triggered by the production of reactive oxygen species (30). EGCG can directly reduce radiation-induced DNA breaks and has the anti-ROS activity, anti-inflammatory response, anti-apoptosis function (31–33). EGCG also influences epigenetic changes through altering histone acetylation and DNA methylation (34–36). Surprisingly, it has

been reported that EGCG can significantly reduce the damage of normal mouse liver cell lines induced by radiation and effectively increase the radiosensitivity of mouse liver cancer cells at the same time. EGCG combined with radiotherapy can further reduce the expression of the apoptosis suppressor bcl-2 and increase the expression of apoptosis-related proteins in hepatocellular carcinoma cell lines. However, the opposite effects are exerted on mouse liver cell line. The regulatory effect of EGCG may be attributed to the different expression of miR-34a in two cells (37). The researchers also discovered that miR-34 methylation in small cell lung cancer is lower than that in normal cells (38). Further *in vivo* and *in vitro* tests are needed to control the influencing factors, examine the conclusions, and explore possible mechanisms.

Based on the above discussion, EGCG is very suitable as a radioprotectant for patients with SCLC who undergo radiotherapy. Still, several weaknesses of the research should be pointed out. At first, the number of patients in the study is small. As a follow-up observational study on a new drug, the study here cannot continue to recruit more patients, and only patients from the NCT02577393 study are screened for analysis. Evaluating with fewer patients sometimes fails to reach statistical significance (39). For example, the 5-year PFS rate difference between the two groups was 27% with P >0.05. Moreover, the absence of stratified randomization by chemoradiotherapy scheme could also affect the accuracy of prognostic conclusions, though the clinical features of patients between EGCG and mLDG group are well balanced at baseline. Lastly, there is a lack of research on the intricate molecular mechanism underlying different effects of EGCG on tumor and esophageal tissue. Nonetheless, it may be stated that the results of the pilot study support further exploration of the EGCG application in patients with ARIE.

CONCLUSION

Consistent with previous reports, EGCG could alleviate some esophagitis-related indexes in SCLC patients receiving radiotherapy with an acceptable toxicity. Furthermore, EGCG may increase the ORR without reducing PFS or OS. Further basic and clinical studies should be conducted to testify and clarify the mechanisms of differential effect of EGCG on cancer and normal tissues during radiation.

DATA AVAILABILITY STATEMENT

The datasets used and analyzed during the current study are available from the corresponding authors on reasonable request. Requests to access these datasets should be directed to HZ, zhx87520052@163.com.

ETHICS STATEMENT

The studies involving human participants were reviewed and approved by the ethics committee of Shandong Cancer Hospital and Institute. The patients/participants provided their written informed consent to participate in this study.

AUTHOR CONTRIBUTIONS

HZ and JY contributed to the design of the research. WZ and YZ were involved in collecting data and drafting of the manuscript. XL, SZ, and LX planned the therapy. HZ, XL, LX, and SZ devoted to collecting information, analyzing data, and modifying content. All authors contributed to the article and approved the submitted version.

FUNDING

This research was funded by National Natural Science Foundation of China (82003233), Shandong Provincial Natural Science Foundation (No. ZR2016HM35), Key Scientific and Technological Projects of Shandong Province (2018GSF118232), and Jinan Science and Technology Plan Project (202019163).

SUPPLEMENTARY MATERIAL

The Supplementary Material for this article can be found online at: https://www.frontiersin.org/articles/10.3389/fonc.2021.686950/full#supplementary-material

Supplementary Figure 1 | Calculation methods of adjusted ARIE-related indexes. The trapezoid formula was used to calculate the area beneath the curve graph of each patient. Taking the AEI of a case in the figure as an example, when the horizontal axis was the percentage of observation completion and the vertical axis was the grade of ARIE, the calculated value was 14.

REFERENCES

1. Suzuki R, Wei X, Allen PK, Welsh JW, Cox JD, Komaki R, et al. Twice-Daily Thoracic Radiotherapy for Limited-Stage Small-Cell Lung Cancer Does Not Increase the Incidence of Acute Severe Esophagitis. *Clin Lung Cancer* (2018) 19:e885–e91. doi: 10.1016/j.cllc.2018.08.012
2. Chang SC, Lai YC, Hung JC, Chang CY. Oral Glutamine Supplements Reduce Concurrent Chemoradiotherapy-Induced Esophagitis in Patients With Advanced Non-Small Cell Lung Cancer. *Med (Baltimore)* (2019) 98:e14463. doi: 10.1097/MD.0000000000014463
3. Pan Y, Brink C, Knap M, Khalil AA, Nyhus CH, McCulloch T, et al. Acute Esophagitis for Patients With Local-Regional Advanced Non Small Cell Lung Cancer Treated With Concurrent Chemoradiotherapy. *Radiother Oncol* (2016) 118:465–70. doi: 10.1016/j.radonc.2016.01.007
4. Murro D, Jakate S. Radiation Esophagitis. *Arch Pathol Lab Med* (2015) 139:827–30. doi: 10.5858/arpa.2014-0111-RS
5. Stinchcombe TE, Zhang Y, Vokes EE, Schiller JH, Bradley JD, Kelly K, et al. Pooled Analysis of Individual Patient Data on Concurrent Chemoradiotherapy for Stage III Non-Small-Cell Lung Cancer in Elderly Patients Compared With Younger Patients Who Participated in US National Cancer Institute Cooperative Group Studies. *J Clin Oncol* (2017) 35:2885–92. doi: 10.1200/JCO.2016.71.4758
6. Luna JM, Chao HH, Shinohara RT, Ungar LH, Cengel KA, Pryma DA, et al. Machine Learning Highlights the Deficiency of Conventional Dosimetric

Constraints for Prevention of High-Grade Radiation Esophagitis in Non-Small Cell Lung Cancer Treated With Chemoradiation. *Clin Transl Radiat Oncol* (2020) 22:69–75. doi: 10.1016/j.ctro.2020.03.007
7. Zhu W, Xu J, Ge Y, Cao H, Ge X, Luo J, et al. Epigallocatechin-3-Gallate (EGCG) Protects Skin Cells From Ionizing Radiation Via Heme Oxygenase-1 (HO-1) Overexpression. *J Radiat Res* (2014) 55:1056–65. doi: 10.1093/jrr/rru047
8. You H, Wei L, Sun WL, Wang L, Yang ZL, Liu Y, et al. The Green Tea Extract epigallocatechin-3-Gallate Inhibits Irradiation-Induced Pulmonary Fibrosis in Adult Rats. *Int J Mol Med* (2014) 34:92–102. doi: 10.3892/ijmm.2014.1745
9. Xie LW, Cai S, Zhao TS, Li M, Tian Y. Green Tea Derivative (-)-epigallocatechin-3-Gallate (EGCG) Confers Protection Against Ionizing Radiation-Induced Intestinal Epithelial Cell Death Both In Vitro and In Vivo. *Free Radic Biol Med* (2020) 161:175–86. doi: 10.1016/j.freeradbiomed.2020.10.012
10. Zhao H, Jia L, Chen G, Li X, Meng X, Zhao X, et al. A Prospective, Three-Arm, Randomized Trial of EGCG for Preventing Radiation-Induced Esophagitis in Lung Cancer Patients Receiving Radiotherapy. *Radiother Oncol* (2019) 137:186–91. doi: 10.1016/j.radonc.2019.02.022
11. Li X, Xing L, Zhang Y, Xie P, Zhu W, Meng X, et al. Phase II Trial of Epigallocatechin-3-Gallate in Acute Radiation-Induced Esophagitis for Esophagus Cancer. *J Med Food* (2020) 23:43–9. doi: 10.1089/jmf.2019.4445
12. Zhu W, Mei H, Jia L, Zhao H, Li X, Meng X, et al. Epigallocatechin-3-Gallate Mouthwash Protects Mucosa From Radiation-Induced Mucositis in Head and Neck Cancer Patients: A Prospective, Non-Randomised, Phase 1 Trial. *Invest New Drugs* (2020) 38:1129–36. doi: 10.1007/s10637-019-00871-8
13. Zhao H, Zhu W, Jia L, Sun X, Chen G, Zhao X, et al. Phase I Study of Topical epigallocatechin-3-Gallate (EGCG) in Patients With Breast Cancer Receiving Adjuvant Radiotherapy. *Br J Radiol* (2016) 89:20150665. doi: 10.1259/bjr.20150665
14. Zhu W, Jia L, Chen G, Zhao H, Sun X, Meng X, et al. Epigallocatechin-3-Gallate Ameliorates Radiation-Induced Acute Skin Damage in Breast Cancer Patients Undergoing Adjuvant Radiotherapy. *Oncotarget* (2016) 7:48607–13. doi: 10.18632/oncotarget.9495
15. Zhao H, Xie P, Li X, Zhu W, Sun X, Sun X, et al. A Prospective Phase II Trial of EGCG in Treatment of Acute Radiation-Induced Esophagitis for Stage III Lung Cancer. *Radiother Oncol* (2015) 114:351–6. doi: 10.1016/j.radonc.2015.02.014
16. Zhao H, Zhu W, Xie P, Li H, Zhang X, Sun X, et al. A Phase I Study of Concurrent Chemotherapy and Thoracic Radiotherapy With Oral epigallocatechin-3-Gallate Protection in Patients With Locally Advanced Stage III Non-Small-Cell Lung Cancer. *Radiother Oncol* (2014) 110(1):132–6. doi: 10.1016/j.radonc.2013.10.014
17. Tjong MC, Mak DY, Shahi J, Li GJ, Chen H, Louie AV. Current Management and Progress in Radiotherapy for Small Cell Lung Cancer. *Front Oncol* (2020) 10:1146. doi: 10.3389/fonc.2020.01146
18. Simone CB2nd, Bogart JA, Cabrera AR, Daly ME, DeNunzio NJ, Detterbeck F, et al. Radiation Therapy for Small Cell Lung Cancer: An Astro Clinical Practice Guideline. *Pract Radiat Oncol* (2020) 10(3):158–73. doi: 10.1016/j.prro.2020.02.009
19. Sprave T, Verma V, Förster R, Schlampp I, Bruckner T, Bostel T, et al. Radiation-Induced Acute Toxicities After Image-Guided Intensity-Modulated Radiotherapy Versus Three-Dimensional Conformal Radiotherapy for Patients With Spinal Metastases (IRON-1 Trial): First Results of A Randomized Controlled Trial. *Strahlenther Onkol* (2018) 194:911–20. doi: 10.1007/s00066-018-1333-z
20. Lu L, Sun C, Su Q, Wang Y, Li J, Guo Z, et al. Radiation-Induced Lung Injury: Latest Molecular Developments, Therapeutic Approaches, and Clinical Guidance. *Clin Exp Med* (2019) 19:417–26. doi: 10.1007/s10238-019-00571-w
21. Kuran D, Pogorzelska A, Wiktorska K. Breast Cancer Prevention-Is There a Future for Sulforaphane and Its Analogs? *Nutrients* (2020) 12:1559. doi: 10.3390/nu12061559
22. Singh VK, Seed TM. The Efficacy and Safety of Amifostine for the Acute Radiation Syndrome. *Expert Opin Drug Saf* (2019) 18(11):1077–90. doi: 10.1080/14740338.2019.1666104
23. King M, Joseph S, Albert A, Thomas TV, Nittala MR, Woods WC, et al. Use of Amifostine for Cytoprotection During Radiation Therapy: A Review. *Oncology* (2020) 98:61–80. doi: 10.1159/000502979
24. Ding S, Xu S, Fang J, Jiang H. The Protective Effect of Polyphenols for Colorectal Cancer. *Front Immunol* (2020) 11:1407. doi: 10.3389/fimmu.2020.01407
25. Bonvalot S, Rutkowski PL, Thariat J, Carrère S, Ducassou A, Sunyach MP, et al. NBTXR3, A First-in-Class Radioenhancer Hafnium Oxide Nanoparticle, Plus Radiotherapy Versus Radiotherapy Alone in Patients With Locally Advanced Soft-Tissue Sarcoma (Act.In.Sarc): A Multicentre, Phase 2-3, Randomised, Controlled Trial. *Lancet Oncol* (2019) 208:1148–59. doi: 10.1016/S1470-2045(19)30326-2
26. Scarantino CW, McCunniff AJ, Evans G, Young CW, Paggiarino DA. A Prospective Randomized Comparison of Radiation Therapy Plus Lonidamine Versus Radiation Therapy Plus Placebo as Initial Treatment of Clinically Localized But Nonresectable Nonsmall Cell Lung Cancer. *Int J Radiat Oncol Biol Phys* (1994) 29(5):999–1004. doi: 10.1016/0360-3016(94)90394-8
27. Zeng YC, Wu R, Xu ZG, Zhang XY, Fan GL, Wu LN, et al. Safety and Radiation-Enhancing Effect of Sodium Glycididazole in Locoregionally Advanced Laryngeal Cancers Previously Treated With Platinum-Containing Chemotherapy Regimens: A Preliminary Report. *Cancer Radiother* (2010) 14 (1):59–64. doi: 10.1016/j.canrad.2009.06.022
28. Zhao J, Zhang W, Er P, Chen X, Guan Y, Qian D, et al. Concurrent or Sequential Chemoradiotherapy After 3-4 Cycles Induction Chemotherapy for LS-SCLC With Bulky Tumor. *J Cancer* (2020) 11(17):4957–64. doi: 10.7150/jca.41136
29. Zhang G, Wang Y, Zhang Y, Wan X, Li J, Liu K, et al. Anti-Cancer Activities of Tea epigallocatechin-3-Gallate in Breast Cancer Patients Under Radiotherapy. *Curr Mol Med* (2012) 12:163–76. doi: 10.2174/156652412798889063
30. Smith TA, Kirkpatrick DR, Smith S, Smith TK, Pearson T, Kailasam A, et al. Radioprotective Agents to Prevent Cellular Damage Due to Ionizing Radiation. *J Transl Med* (2017) 15:232. doi: 10.1186/s12967-017-1338-x
31. Hsieh TC, Chao HH, Wu JM. Control of DNA Structure and Function by Phytochemicals/DNA Interaction: Resveratrol/piceatannol Induces Cu2+-Independent, Cleavage of Supercoiled Plasmid DNA. *Free Radic Biol Med* (2020) 147:212–9. doi: 10.1016/j.freeradbiomed
32. Mun GI, Kim S, Choi E, Kim CS, Lee YS. Pharmacology of Natural Radioprotectors. *Arch Pharm Res* (2018) 41:1033–50. doi: 10.1007/s12272-018-1083-6
33. Lecumberri E, Dupertuis YM, Miralbell R, Pichard C. Green Tea Polyphenol epigallocatechin-3-Gallate (EGCG) as Adjuvant in Cancer Therapy. *Clin Nutr* (2013) 32:894–903. doi: 10.1016/j.clnu.2013.03.008
34. Yi J, Chen C, Liu X, Kang Q, Hao L, Huang J, et al. Radioprotection of EGCG Based on Immunoregulatory Effect and Antioxidant Activity Against ^{60}Coγ Radiation-Induced Injury in Mice. *Food Chem Toxicol* (2020) 135:111051. doi: 10.1016/j.fct.2019.111051
35. Daniel M, Tollefsbol TO. Epigenetic Linkage of Aging, Cancer and Nutrition. *J Exp Biol* (2015) 218:59–70. doi: 10.1242/jeb.107110
36. Negri A, Naponelli V, Rizzi F, Bettuzzi S. Molecular Targets of Epigallocatechin-Gallate (EGCG): A Special Focus on Signal Transduction and Cancer. *Nutrients* (2018) 10:1936. doi: 10.3390/nu10121936
37. Kang Q, Zhang X, Cao N, Chen C, Yi J, Hao L, et al. EGCG Enhances Cancer Cells Sensitivity Under ^{60}Coγ Radiation Based on Mir-34a/Sirt1/P53. *Food Chem Toxicol* (2019) 133:110807. doi: 10.1016/j.fct.2019.110807
38. Tanaka N, Toyooka S, Soh J, Kubo T, Yamamoto H, Maki Y, et al. Frequent Methylation and Oncogenic Role of microRNA-34b/c in Small-Cell Lung Cancer. *Lung Cancer* (2012) 76:32–8. doi: 10.1016/j.lungcan.2011.10.002
39. Hupé JM. Statistical Inferences Under the Null Hypothesis: Common Mistakes and Pitfalls in Neuroimaging Studies. *Front Neurosci* (2015) 9:18. doi: 10.3389/fnins.2015.00018

Conflict of Interest: The authors declare that the research was conducted in the absence of any commercial or financial relationships that could be construed as a potential conflict of interest.

frontiers in Oncology

ORIGINAL RESEARCH
published: 10 June 2021
doi: 10.3389/fonc.2021.690042

High LET-Like Radiation Tracks at the Distal Side of Accelerated Proton Bragg Peak

Dakota Horendeck[1†], Kade D. Walsh[1†], Hirokazu Hirakawa[2], Akira Fujimori[2], Hisashi Kitamura[3] and Takamitsu A. Kato[1]*

[1] Department of Environmental & Radiological Health Sciences, Colorado State University, Fort Collins, CO, United States, [2] National Institute of Radiological Sciences, National Institutes for Quantum and Radiological Science and Technology, Chiba, Japan, [3] Radiation Emergency Medical Assistance Team, National Institutes for Quantum and Radiological Science and Technology, Chiba, Japan

OPEN ACCESS

Edited by:
Sandeep Kumar Shukla,
Institute of Nuclear Medicine & Allied Sciences (DRDO), India

Reviewed by:
Pradeep Goswami,
Institute of Nuclear Medicine & Allied Sciences (DRDO), India
Sunil Dutt Sharma,
Bhabha Atomic Research Centre (BARC), India
Walter Tinganelli,
GSI Helmholtz Center for Heavy Ion Research, Germany

***Correspondence:**
Takamitsu A. Kato
Takamitsu.Kato@Colostate.edu

[†]These authors have contributed equally to this work

Specialty section:
This article was submitted to Radiation Oncology, a section of the journal Frontiers in Oncology

Received: 02 April 2021
Accepted: 10 May 2021
Published: 10 June 2021

Citation:
Horendeck D, Walsh KD, Hirakawa H, Fujimori A, Kitamura H and Kato TA (2021) High LET-Like Radiation Tracks at the Distal Side of Accelerated Proton Bragg Peak. Front. Oncol. 11:690042. doi: 10.3389/fonc.2021.690042

Proton therapy is a type of hadron radiotherapy used for treating solid tumors. Unlike heavy charged elements, proton radiation is considered to be low LET (Linear Energy Transfer) radiation, like X-rays. However, the clinical SOBP (Spread Out Bragg Peak) proton radiation is considered to be higher in relative biological effectiveness (RBE) than both X-ray and their own entrance region. The RBE is estimated to be 1.1–1.2, which can be attributed to the higher LET at the SOBP region than at the entrance region. In order to clarify the nature of higher LET near the Bragg peak of proton radiation and its potential cytotoxic effects, we utilized a horizontal irradiation system with CHO cells. Additionally, we examined DNA repair mutants, analyzed cytotoxicity with colony formation, and assessed DNA damage and its repair with γ-H2AX foci assay in a high-resolution microscopic scale analysis along with the Bragg peak. Besides confirming that the most cytotoxic effects occurred at the Bragg peak, extended cytotoxicity was observed a few millimeters after the Bragg peak. γ-H2AX foci numbers reached a maximum at the Bragg peak and reduced dramatically after the Bragg peak. However, in the post-Bragg peak region, particle track-like structures were sporadically observed. This region contains foci that are more difficult to repair. The peak and post-Bragg peak regions contain rare high LET-like radiation tracks and can cause cellular lethality. This may have caused unwanted side effects and complexities of outputs for the proton therapy treatment.

Keywords: DNA damage, proton radiotherapy, linear energy transfer, Bragg peak, gamma-H2AX

INTRODUCTION

Proton therapy (PT) is a type of hadron radiotherapy for treating mainly solid tumors (1). Accelerated protons have a unique dose distribution along their path due to the nature of hadron radiation. The initial radiation dose is small at the entrance region. However, when protons reach the end of their path, all of the energy is deposited in a region known as the Bragg peak (2). In the post-Bragg peak region, a small amount of dose is produced by the reaction products

(2). Therefore, protons can target tumors located in the body without harming the surrounding normal tissues. In general, hadron radiation has a superior dose distribution than conventional photon radiation therapy (3). Among hadron radiation, proton radiation has less of a tail region than carbon-ion radiotherapy and less uncertainty for side effects due to the higher biological effectiveness of carbon ion radiotherapy (4). Therefore, PT is the preferred modality for patients with younger ages to avoid potential secondary tumors (5, 6). However, the proton beam can contains neutron contamination and scattered particles, leading to poorer beam profile (7). Unexpected side effects were recently reported after PT, such as brain injury (6, 8–11).

The proton beam has less tail regions than carbon-ions (12, 13), but utilizing a computer simulation by Monte Carlo calculation suggested some dose distribution after the Bragg peak (14, 15). These tail regions in the proton beam contain relatively high LET particles in a range up to 10 keV/μm, but up to 30 keV/μm (16) or 40 keV/um (17) were also reported. The LET range around 30–40 keV/μm is still not considered as high as the biological maximum LET value of 100 keV/μm, but it can cause a significant increase of relative biological effectiveness (RBE). In our previous studies, carbon-ion monoenergetic beams with LET values between 13 and 30 keV/μm could produce RBE values of 1.1–1.5 (18, 19). Besides RBE, other important cellular responses such as the oxygen enhancement ratio (OER) can also be slightly affected by radiation within this range of LET (18). LET values in the proton entrance region are approximately 1 keV/μm and cannot result in high RBE or low OER (20). Currently, the RBE of clinical proton beams in the proton SOBP region is estimated to be approximately 1.1 to 1.2 (7, 21–23).

In order to clarify the true nature of the proton RBE from biological responses at the Bragg peak and the surrounding area, a position dependent analysis was carried out with 0.5 mm to a few millimeter increments to cover the proton beam paths (24–27). We utilized a horizontal irradiation system, which we previously developed (28). This irradiation system can visually show cellular cytotoxic locations in the flasks. Additionally, we combined it with a microscopic analysis to clarify DNA damage and distribution near the Bragg peak to detect any specific changes in this narrow area. Interestingly, DNA damage with track structures produced by protons and fragments can be a good indicator of energy deposition/LET of the fragments (29). Without using expensive deconvolution software or super high-resolution microscopy, clustered foci can be denoted as a particle track-like structures by using this method (30, 31). Monoenergetic proton beams in this study will provide clear dose and LET distribution along their path. The findings in this study will provide micro-bio-dosimetry analysis for the biological significance of the proton beam.

MATERIALS AND METHODS

Cell Culture

CHO wild type (CHO 10B2) was kindly supplied by Dr. Joel Bedford of Colorado State University (Fort Collins, CO, USA). DNA repair deficient CHO mutants, V3 (DNA-PKcs, non-homologous end joining repair deficient) (32) and 51D1 (Rad51D, homologous recombination repair deficient) (33) were kindly supplied by Dr. Larry Thompson at the Lawrence Livermore National Laboratory (Livermore, CA, USA). Cells were maintained in Alpha-MEM (ThermoFisher, Waltham, MA) with 10% heat inactivated Fetal Bovine Serum (Sigma, St. Louis, MO), antibiotics (Anti-Anti; Invitrogen, Grand Island, NY) and were cultured in 37°C incubators with 5% CO_2 and humidity. We utilized CHO cells rather than human cells for the following reasons (1): colony size and shape: CHO cells produce dense, tightly packed colonies and the colony shape of CHO cells is very circular. On the other hand, colonies of many cells of human origin often spread flat and large and form uneven shapes. In this manuscript, the location of survival colonies has to be accurately recorded. Therefore, using CHO cells was of the utmost importance.

Irradiation

Proton beam irradiation was conducted at the QST (National Institutes for the Quantum and Radiological Sciences and Technology) in Chiba, Japan. Protons were accelerated to 70 MeV using the NIRS-930 cyclotron (24). Proton beam was delivered for the circular field of 7 cm diameter with 95% uniformity. Dose rate was set at 3 Gy/min. Monoenergetic 70 MeV protons have a LET value of 1 keV/μm on entrance. Exponentially growing cells were irradiated at room temperature. Dosimetry was carried out with a Markus ion chamber (PTW 23343, PTW, Freiburg GmbH, Germany) with the container filled with water or complete cell culture media. The LET values were calculated by SRIM (Stopping and Range of Ions in Matter) program from the range of the proton beam (16).

Irradiation was carried out as previously described (28) (**Figure 1**). Prior to irradiation, cell culture flasks or SlideFlasks were placed upright with the capped end opposite to the proton beam source. The thickness of the flask and SlideFlask was 1 mm of polystyrene, which is equivalent to water thickness of 1.0368 mm (34). Therefore, the analysis started 1 mm from the proton entrance for cell survival analysis. The geometric location of the SlideFlask was matched with a micrometer and an M Processor (LASICO, Los Angeles, CA) geometric recorder.

Colony Formation and Manual Colony Distribution Analysis

Two hours before irradiation, 10,000 cells were plated onto a T25 flask, which has 25 cm^2 of growing area to produce a density of an average of four cells per mm^2. After irradiation, cells were disturbed minimally during transportation from the irradiator to the incubator and kept in an incubator for 8 days to form colonies. Colonies were fixed and stained 8 days later using 100% ethanol followed by 0.1% crystal violet. Macroscopic colonies containing more than 50 cells were marked as survivors (35). The cellular attachment was confirmed after testing medium changes at different times. No colonies were observed at the highest dose Bragg peak region, which supports that there were no-floating cells during the trip from irradiation to incubation.

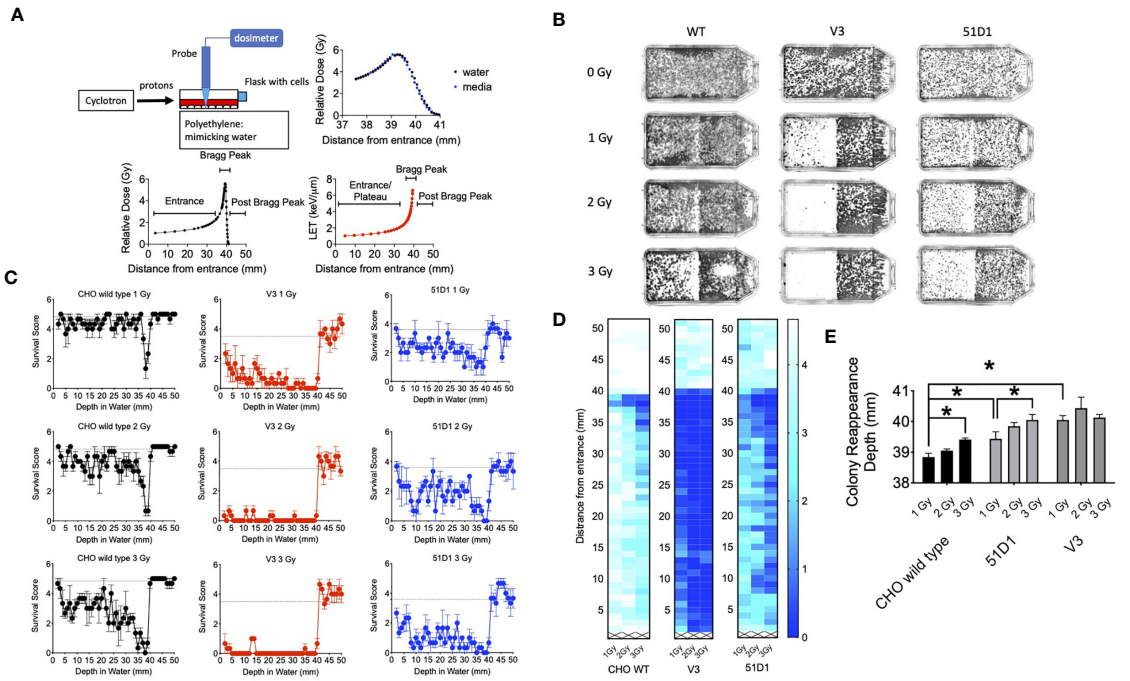

FIGURE 1 | Colony formation after horizontal proton irradiation. **(A)** Proton irradiation set-up and dose distribution measurement and calculated LET values of protons from the entrance, Bragg peak, and post-Bragg peak. The black lines indicate relative doses in water; the blue points indicate relative doses in cell culture media, and the red line indicates the calculated LET values. **(B)** Representative images of colony distribution after 0–3 Gy of initial proton irradiation to CHO wild type, V3, and 51D1 cells. The proton beam traveled from left to right. **(C)** Cell survival score after 0–3 Gy of initial proton irradiation to CHO wild type, V3, and 51D1 cells. Dashed lines represent the unirradiated control. **(D)** Heat map of cytotoxicity after proton radiation. Maximum cytotoxicity was observed at 38 mm with 35–41 mm from the entrance. The first 1 mm represents the flask wall. The right bar, scaled 0–4, indicates that a cell survival of 0 represents cell death, while 4 indicates the highest cell survival. **(E)** Colony reappearance range in different radiosensitive cells. Error bars indicate the standard error of the means. * means statistically significant differences ($P < 0.05$).

For a rough geometrical analysis of colony distribution, locations of survivors were recorded with a ruler. The flasks used have a wall that is 1 mm thick. From the end of the flask, the proton beam entry side for every 1 mm of colony existence was judged and recorded from the entrance up to 50 mm. Five lines were analyzed per flask. The survival score was defined as the presence of colonies at each distance. Five evenly different locations were analyzed with a ruler for the presence or absence of colonies. The survival score of five indicated the representation of all of the colonies that survived. The colony distribution was presented in graphs and in a heat map with Graphpad Prism 8 software (GraphPad, La Jolla, CA, USA).

In order to evaluate the cytotoxic range of the proton beam and maintain a fine geometrical analysis of the colony distribution, the reappearance of colony formation following the Bragg peak was recorded with a ruler. Colony reappearance was defined as the average distance from the entrance for the first observable colonies after the Bragg peak. Thirteen lines were analyzed for each flask to obtain a sensitive analysis of the extension of the cytotoxic range.

Digital Colony Distribution Analysis With MATLAB

To eliminate the risk of subjective analysis of manual counting, three-dimensional surface plots were created using MATLAB software. Flasks were imaged with the BIO-RAD ChemiDoc chemiluminescent imager (BIO-RAD, Hercules, CA) *via* ImageLab 2.0.1 software (BIO-RAD, Hercules, CA) under epi-white, trans-white illumination utilizing a copper stain emission filter. These images were visualized using intense bands and converted into black and white .JPG formats. The files were cropped to exclude ridges of the T-25 flasks and narrowing neck of the bottle. These images were entered into an executable script created previously (28) *via* the MATLAB software (MATHWORKS, Natick, MA). The script allows .JPG files to be analyzed by pixel shade to create three-dimensional surface plots that can be adjusted to create virtual cell survival plots.

DNA Damage Distribution Analysis

In order to estimate proton irradiation induced DNA damage and repair, γ-H2AX foci were used for a DNA double strand

break marker (36–38). CHO wild type cells were plated on a SlideFlask (ThermoFisher) the day before irradiation. This did not change the cell cycle distribution compared to re-plating 2 h before irradiation. At 30 min and 24 h after irradiation, cells were fixed in 4% paraformaldehyde for 15 min, washed three times in PBS for 10 min each, permeabilized for 5 min in 0.2% Triton X-100, and blocked with 10% goat serum in PBS overnight at 4°C. The cells were incubated with anti-γ-H2AX mouse monoclonal antibody (Upstate, Charlottesville, VA) for 1 h, washed three times in PBS for 10 min each, and incubated with Alexa Fluor-conjugated goat anti-mouse secondary antibody (Molecular Probes, Eugene, OR) for 1 h at 37°C. Cells were washed four times in PBS for 10 min each and mounted by using DAPI in Prolong Gold (Molecular Probes). Multi-dimensional fluorescence images were captured by using a Zeiss Axioplan fluorescent microscope (Zeiss, Jena, Germany) with a motorized z-stage and CoolSNAP HQ Cooled CCD camera (Photometrics, Tucson, AZ) and Metamorph software (Molecular Devices, San Jose, CA). The microscope was equipped with an M Processor (LASICO, Los Angeles, CA) to record the geometric location of slides.

Images were captured every 3.69 mm from the entrance of the protons to near the Bragg peak and every 0.46 mm or 0.92 mm from the Bragg peak to the post-Bragg peak. At each data point, the number of γ-H2AX per cell was manually obtained from at least 30 cells per experiment for the quantitative analysis. In order to investigate the repair-ability of foci at the different depths, the residual foci number was divided by the initial foci number. A track-like structure of DNA damage distribution was visually observed as a solid or dashed line of foci, which was also obtained quantitatively, per cell to estimate intermediate-high LET radiation induced damage.

Statistical Analysis

Experiments were conducted independently three times. The survival score was obtained from five locations. The colony reappearance was obtained from 13 locations, and at least 30 cells were analyzed for foci analysis. All experimental data was analyzed *via* Prism 8 software. One-way analysis of variance (ANOVA) and Dunnett's multiple comparison test were conducted for statistical significance. P-values of <0.05 were considered to indicate differences that were statistically significant.

RESULTS

Extension of Cytotoxicity Beyond Bragg Peak of Proton Beam

The 70 MeV proton beam has approximately 39 mm of range in water (**Figure 1A**). At 39.4 mm, the relative dose reached 4.12 Gy, and the mean LET values were calculated by SRIM software as 6.59 keV/μm (**Figure 1A**). The horizontal irradiation system visually presented the cell death at the Bragg peak of the proton beam as a gap devoid of colonies with the colony formation assay (**Figure 1B**). The cell survival score test and heat map analysis presented that CHO wild type had maximum cytotoxicity between 37 and 39 mm, where the lowest survival scores were found (**Figures 1C, D**). At 3 Gy of initial irradiation, elevated cytotoxicity was observed from 34 to 39 mm. There are no clear signs of cellular cytotoxicity after 41 mm for the CHO wild type. Radiosensitive DNA repair deficient mutants V3 and 51D1 showed an even greater reduction of surviving colonies. Overall, they denoted the extension of the cytotoxic range. At 40 mm, the survival scores decreased a statistically significant amount compared to the un-irradiated control ($P < 0.01$).

Additionally, the extension of the cytotoxic range was analyzed more precisely based on the reappearance of colonies after the Bragg peak (**Figure 1E**). CHO wild type showed the reappearance of colonies at 38.5 mm for 1 Gy and 39.5 mm for 3 Gy. Statistically significant extension was observed between them ($p < 0.05$). 51D1 also showed reappearance of colonies at 3.93 mm for 1 Gy and 40 mm for 3 Gy, and increased doses extended the cytotoxic range with statistical significance ($p < 0.05$). Additionally, the location of reappearance for 51D1 cells was extended compared to the CHO wild type ($p < 0.05$). V3 showed reappearance of colonies at 40 mm for 1 Gy with statistically significant extension compared to the CHO wild type, but 3 Gy of initial irradiation did not extend the reappearance of colony location. This geometric recording of the survival analysis data showed that proton induced cellular lethality was produced beyond the Bragg peak. The additional lethality was observed in the 39 to 40.5 mm region. Since double strand break repair deficient mutants showed additional cytotoxicity compared to repair proficient wild type cells, involvement of DNA double strand break formation is suggested. Since V3 did not show any additional cytotoxicity after 2Gy, it may suggest that the "dose" of fragments causing DNA damage are rapidly decreased after the end of the Bragg peak.

The survival analysis was confirmed with a digital image analysis to avoid any subjective colony counting (**Figure 2**). This analysis is based on the survived cellular density, not the clonogenic activity measured by colony formation as manual scores. Ultimately, while survivor colonies provide cellular density, both analyses should be very close together. The most cell deaths were observed at the site on the monoenergetic Bragg peak, at 38 mm. Survival plots show a strong correlation with the data obtained from survival score graphs. This shows the ability of the MATLAB software to make an effective analytical tool for rapid analysis. The biggest difference between manual analysis and computer analysis is the tail region. After the Bragg peak, manual counting showed a complete return to background level of clonogenic ability at 40 mm even for radiosensitive cells. On the other hand, the recovery of the computer analysis of the density of cells was slower. This implies that colonies are formed, but may be smaller in size due to the small amount of non-lethal DNA damage and additional support for fragment induced damage after the Bragg peak.

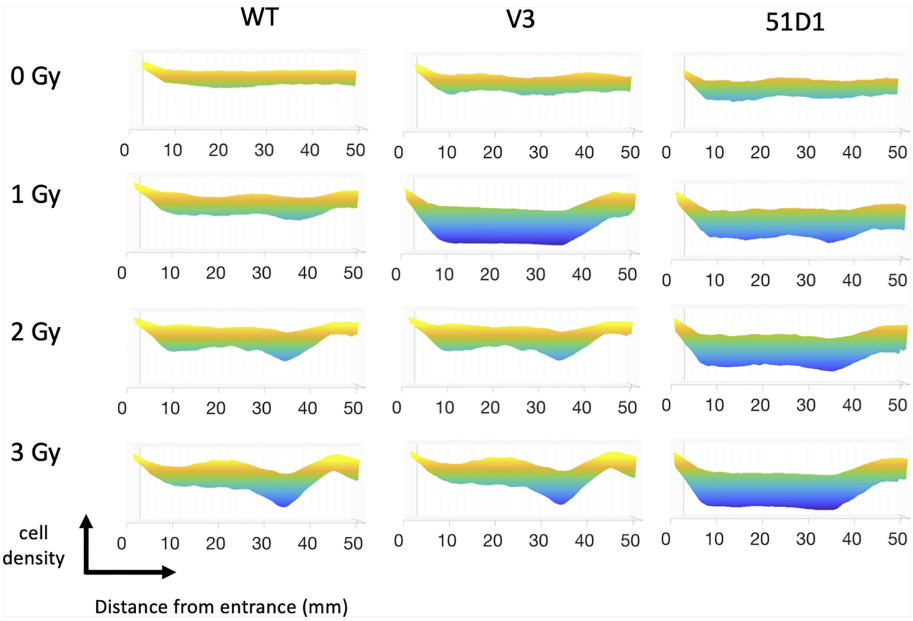

FIGURE 2 | MATLAB image analysis of cell survival after proton irradiation. Yellow color indicates more cells; blue color indicates less cells. Three flasks were merged for analysis.

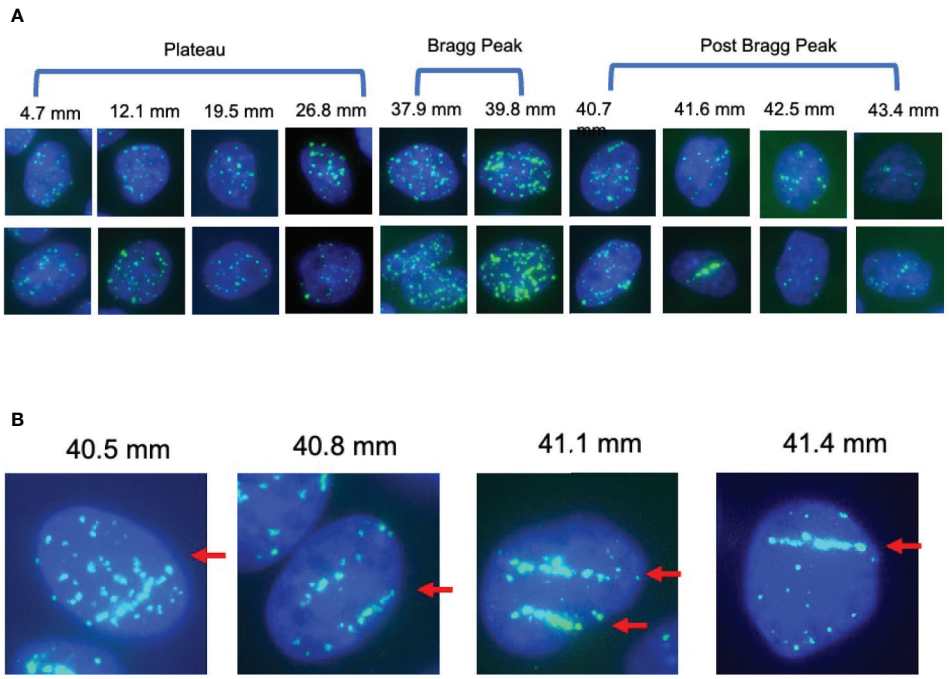

FIGURE 3 | γ-H2AX foci after 1 Gy of proton beam irradiation for CHO wild type cells. **(A)** Representative images of foci number and patterns at the specific distance for CHO wild type cells after proton 1 Gy irradiation. Two images were chosen for each distance. **(B)** Representative images of foci alignment like a track structure for CHO wild type cells after 1 Gy of proton beam. Green signals indicate γ-H2AX foci. Blue signals are nuclei stained with DAPI. Arrows indicate track like structures of foci distribution.

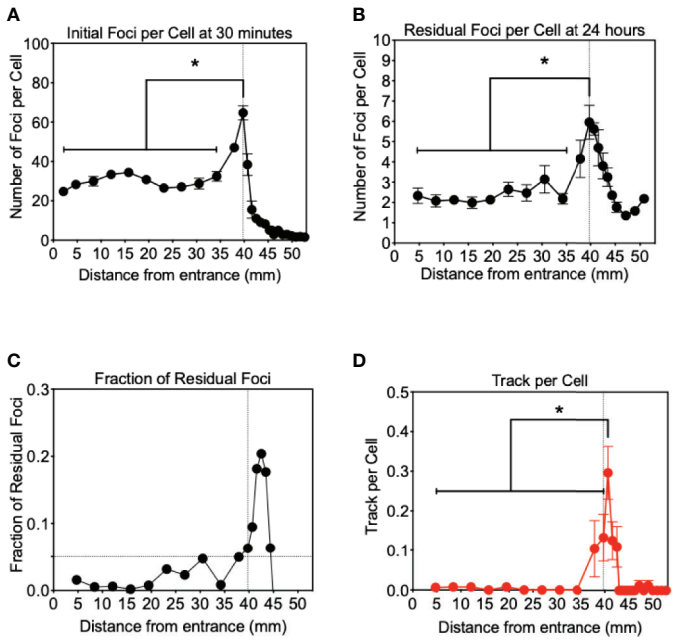

FIGURE 4 | Analysis of γ-H2AX foci after proton beam irradiation for CHO wild type cells. **(A)** Initial DNA damage 30 min after 1 Gy of irradiation. **(B)** Residual DNA damage 24 h after 1 Gy of irradiation. **(C)** Fraction of residual DNA damage obtained by residual foci number divided by initial foci number. **(D)** Track like foci pattern formation at 30 min after irradiation. Vertical lines indicate the peak of Bragg peak at 39.75 mm of initial foci formation. Horizontal line indicates the fraction of residual foci of 0.05. Error bars indicate the standard error of the means. * indicates statistically significant differences ($P < 0.05$).

γ-H2AX Foci Distribution Beyond Bragg Peak of Proton Beam

DNA damage, especially in the form of DNA double strand break, is the most reasonable way to cause cytotoxicity beyond the Bragg peak of the proton beam. The fragments of targets including proton, neutron and electrons can cause ionization and DNA breaks (2). Therefore, DNA damage was quantitatively or qualitatively analyzed, with number and distribution of γ-H2AX foci at the specific location corresponding to the proton beam path (**Figure 3A**). Track-like line alignments were sporadically in 10–30% of cells observed near the Bragg peak, especially between 39 and 42 mm, where clear line-like foci alignment was visible (**Figure 3B**).

For the initial DSB formation after 1 Gy, γ-H2AX foci formation was analyzed 30 min after irradiation (**Figure 4A**). From the entrance of the proton beam to 34.2 mm, the number of γ-H2AX foci was steady at approximately 30 foci per cell. At the Bragg peak region, 49 foci per cell at 37.9 mm and 64 foci per cell at 39.7 mm were observed and increases were statistically significant when compared to the entrance region ($P < 0.05$). After the Bragg peak, the foci number rapidly decreased and returned close to the background level of 3.5 foci per cell. At 40.7 mm, 36 foci per cell and 15 foci at 41.6 mm were observed. Generally, not many foci were observed after the Bragg peak.

Twenty four hours after irradiation, the number of residual foci was analyzed in the same manner (**Figure 4B**). Foci number was dramatically reduced at all points compared to initial number of damages. From the entrance to 34.2 mm, approximately two foci per cell were observed and no statistically significant increase was observed compared to the foci number of the control. At the Bragg peak region, 39.7 mm, a statistically significant greater number of foci than the entrance were observed as 6.0 foci per cell ($P < 0.05$). Beyond the Bragg peak, a noticeably greater number of foci were seen compared to the initial foci, which rapidly decreased after the Bragg peak. Track-like foci alignments were not observed in the cells 24 h after irradiation.

The greater number of residual foci may be simply attributed to the higher doses initially irradiated near the Bragg peak. In order to normalize and obtain a fraction of residual foci, we divided the residual foci number by the initial foci number (**Figure 4C**). These un-repaired residual foci are highly associated with complex or clusters of DNA damage that can resemble HZE (high atomic number and energy) particle irradiations. The fraction of residual foci was approximately 0.01 to 0.1 at the entrance region. The fraction of residual foci was increased near the Bragg peak. In particular, a fraction of 0.05 and above was observed from 39.7 to 44.4 mm. It was similar to the Bragg peak of the proton beam observed with initial damage at 39.7 mm, but shifted beyond the Bragg peak. This may be associated with DNA damage produced at the Bragg peak, while the slightly extended post-Bragg peak contained complex DNA damage that is difficult to be repaired.

In order to understand unrepaired residual foci at the post-Bragg peak region, foci distribution was qualitatively analyzed. Sporadically track-like structures of DNA damage were observed

in 10–30% of cells near the Bragg peak (**Figure 4D**). The track number per cell was obtained to estimate DNA damage with the track structure, which may be associated with higher LET than regular 1 keV/μm. The track structure was seen exclusively from 37.9 to 42.5 mm with the highest fraction at 40.7 mm. The distribution of the tracks per cell was also shifted to the post-Bragg peak region. This suggests that track DNA damage should contribute to the stronger biological effectiveness of protons. The distribution of unrepaired foci and track was seen up to 42.5 mm. This is matched with the cellular toxicity observed in DNA repair deficient cells (**Figure 1C**).

DISCUSSION

Proton therapy (PT) is favorable when compared to photon therapy because PT uses the same low LET radiation and focuses dose distribution to tumors more effectively (2). For CIRT, (Carbon Ion Radiotherapy) it may be dangerous to have high LET components with unexpected side effects, including secondary tumors and stronger late effects with a longer tail range and uncertainty of biological effects (3). The present work with horizontal irradiation to a monolayer cell culture showed that the proton beam has minimal effects, but enough to cause cytotoxicity in the post-Bragg peak region (**Figure 1**). As previously shown, our results confirmed that a LET increase occurs at a greater depth slightly beyond the Bragg peak, resulting in a small extension of the biologically effective dose (12). The nature of the post-Bragg peak region of the proton seems interesting. It is obviously much lower in dose than the entrance and the Bragg peak region. However, within a few millimeters after the Bragg peak of a 70 MeV proton beam, it delivers relatively higher LET radiation and damage that effectively cause lethality to cells. Using a clinical proton SOBP beam with stronger energy and longer paths of protons, the post-Bragg peak effect may be observed in a wider area than that currently studied. Horizontal irradiation to the three dimensional target systems such as phantom will provide more information in future. Although the track-like structure of foci produced by proton radiation at the distal edge and the post-Bragg peak region was not as frequently observed as carbon ion or other HZE particles (**Figure 3**), some of them resembled HZE induced dense track-like foci patterns (29), which may explained previously reported higher RBE along distal edge of proton Bragg peak (39, 40). In the clinically relevant doses of irradiation tested in this study, an average of 6.59 keV/μm of LET values was calculated at the Bragg peak (**Figure 1A**), but not all cells had tracks and are relatively rare and sporadic events. This suggests that the cells at the Bragg peak and the post-Bragg peak regions would be irradiated with very heterogenic LET qualities of radiation and might respond differently depending on the damages produced by low to high LET irradiation. It is not a surprise that researchers could not find the significant biological effectiveness in the post-Bragg peak region with the standard colony formation assay, that is unless the dose distribution profile of irradiation was conducted with at least a millimeter sensitivity or horizontal irradiation (24, 25), both of which were successfully achieved in this study. Heterogenic DNA damage amount and distribution were observed by foci analysis near the Bragg peak. These damages cause not only cytotoxicity but also genotoxicity, which may increase normal tissue complication probability. Further analysis needs a low background and high induction assay such as reporter assays to confirm the biological effects other than cytotoxicity at the post-Bragg peak. Moreover, the nature of fragments should be clarified because the proton cannot be disintegrated into smaller fragments as heavy charged particles. The particles causing high LET track-like structures at the post-Bragg peak region may be recoiled neutrons or scattered protons. This needs to be confirmed with advanced physics instruments (41).

With slightly higher LET values, should PT be discouraged? The secondary tumor risk from this middle range LET radiation may answer this (4). However, this finding provides useful information for proton radiotherapy. If the Bragg peak contains a significant fraction of intermediate range LET (10–30 keV/μm) or higher LET as observed for foci patterns, this will answer why RBE values are 1.1–1.2 and slightly higher than the plateau region and photon radiation (7, 21, 22). From the foci patterns, the intermediately high LET portion of the proton beam is limitedly distributed at the narrow region near the Bragg peak. Therefore, the distal portion of the SOBP should be rich in high LET radiation and is expected to have higher RBE as previously shown (39, 42). However, within the SOBP region getting wider, this high LET radiation would be diluted with abundant low LET protons. If treatment can be conducted with multiple short SOBP from multiple directions, proton therapy could gain the advantage over CIRT partially. It will have lower oxygen effects and higher RBE effects. Due to limited LET value, it is hard to expect the same degree of advantage from CIRT. The degree of improvement is still unclear, but it is worth investigating for the future. Additionally, in order to decrease the potential side effects, the distal portion after the SOBP should be monitored with extra caution to determine the irradiation volume.

In conclusion, the horizontal irradiation confirmed that the Bragg peak and slightly shorter range of the post-Bragg peak region of proton radiation contain relatively high LET radiation and induce significant biological effectiveness. This may be due to complex DNA damage produced with a track-like structure observed near the Bragg peak. This finding may explain the partially unwanted side effect observations, but proton therapy can be improved with a narrower SOBP treatment.

DATA AVAILABILITY STATEMENT

The original contributions presented in the study are included in the article/supplementary material. Further inquiries can be directed to the corresponding author.

AUTHOR CONTRIBUTIONS

Conceptualization, TK. Methodology and formal analysis, DH, KW, HK, TK, and AF. Resources data curation, DH, KW, HH, HK, and TK. Writing—original draft preparation, DH and TK. Writing—review and editing, KW and TK. Funding acquisition,

AF and TK. All authors contributed to the article and approved the submitted version.

FUNDING

This research was partially funded by Dr. Akiko Ueno Radiobiology Fund (TK) and Japan Ministry of Education, Culture, Science and Technology (MEXT) Grants-in-Aid for Scientific Research on Innovative Areas (JP15K21745, AF).

ACKNOWLEDGMENTS

We thank to QST Cyclotron facility. We thank Dr. Joel Bedford and Dr. Larry Thompson for kindly supplying cell lines. We thank Mr. Austin Bank for his technical assistants.

REFERENCES

1. Mohan R, Grosshans D. Proton Therapy - Present and Future. *Adv Drug Delivery Rev* (2017) 109:26–44. doi: 10.1016/j.addr.2016.11.006
2. Zeitlin C. Physical Interactions of Charged Particles for Radiotherapy and Space Applications. *Health Phys* (2012) 103:540–6. doi: 10.1097/HP.0b013e3182611125
3. Tsujii H, Kamada T. A Review of Update Clinical Results of Carbon Ion Radiotherapy. *Jpn J Clin Oncol* (2012) 42:670–85. doi: 10.1093/jjco/hys104
4. Imaoka T, Nishimura M, Daino K, Takabatake M, Moriyama H, Nishimura Y, et al. Risk of Second Cancer After Ion Beam Radiotherapy: Insights From Animal Carcinogenesis Studies. *Int J Radiat Biol* (2019) 95:1431–40. doi: 10.1080/09553002.2018.1547848
5. Bagley AF, Grosshans DR, Philip NV, Foster J, McAleer MF, McGovern SL, et al. Efficacy of Proton Therapy in Children With High-Risk and Locally Recurrent Neuroblastoma. *Pediatr Blood Cancer* (2019) 66:e27786. doi: 10.1002/pbc.27786
6. Indelicato DJ, Bradley JA, Rotondo RL, Nanda RH, Logie N, Sandler ES, et al. Outcomes Following Proton Therapy For Pediatric Ependymoma. *Acta Oncol* (2018) 57:644–8. doi: 10.1080/0284186X.2017.1413248
7. Paganetti H. Nuclear Interactions in Proton Therapy: Dose and Relative Biological Effect Distributions Originating From Primary and Secondary Particles. *Phys Med Biol* (2002) 47:747–64. doi: 10.1088/0031-9155/47/5/305
8. Gentile MS, Yeap BY, Paganetti H, Goebel CP, Gaudet DE, Gallotto SL, et al. Brainstem Injury in Pediatric Patients With Posterior Fossa Tumors Treated With Proton Beam Therapy and Associated Dosimetric Factors. *Int J Radiat Oncol Biol Phys* (2018) 100:719–29. doi: 10.1016/j.ijrobp.2017.11.026
9. Giantsoudi D, Sethi RV, Yeap BY, Eaton BR, Ebb DH, Caruso PA, et al. Incidence of CNS Injury for a Cohort of 111 Patients Treated With Proton Therapy for Medulloblastoma: LET and RBE Associations for Areas of Injury. *Int J Radiat Oncol Biol Phys* (2016) 95:287–96. doi: 10.1016/j.ijrobp.2015.09.015
10. McGovern SL, Okcu MF, Munsell MF, Kumbalasseriyil N, Grosshans DR, McAleer MF, et al. Outcomes and Acute Toxicities of Proton Therapy for Pediatric Atypical Teratoid/Rhabdoid Tumor of the Central Nervous System. *Int J Radiat Oncol Biol Phys* (2014) 90:1143–52. doi: 10.1016/j.ijrobp.2014.08.354
11. Haas-Kogan D, Indelicato D, Paganetti H, Esiashvili N, Mahajan A, Yock T, et al. National Cancer Institute Workshop on Proton Therapy for Children: Considerations Regarding Brainstem Injury. *Int J Radiat Oncol Biol Phys* (2018) 101:152–68. doi: 10.1016/j.ijrobp.2018.01.013
12. Suit H, DeLaney T, Goldberg S, Paganetti H, Clasie B, Gerweck L, et al. Proton vs Carbon Ion Beams in the Definitive Radiation Treatment of Cancer Patients. *Radiother Oncol* (2010) 95:3–22. doi: 10.1016/j.radonc.2010.01.015
13. Cheng CW, Das IJ, Srivastava SP, Zhao L, Wolanski M, Simmons J, et al. Dosimetric Comparison Between Proton and Photon Beams in the Moving Gap Region in Cranio-Spinal Irradiation (CSI). *Acta Oncol* (2013) 52:553–60. doi: 10.3109/0284186X.2012.681065
14. Parisi A, Chiriotti S, De Saint-Hubert M, Van Hoey O, Vandevoorde C, Beukes P, et al. A Novel Methodology to Assess Linear Energy Transfer and Relative Biological Effectiveness in Proton Therapy Using Pairs of Differently Doped Thermoluminescent Detectors. *Phys Med Biol* (2019) 64:085005. doi: 10.1088/1361-6560/aaff20
15. Jiang B, Wang X, Zhang Y, Guan F, Li Y, Wang X, et al. Power-Law Relationship in the Long-Tailed Sections of Proton Dose Distributions. *Sci Rep* (2018) 8:10413. doi: 10.1038/s41598-018-28683-5
16. Jones B, Hill MA. Physical Characteristics at the Turnover-Points of Relative Biological Effect (RBE) With Linear Energy Transfer (LET). *Phys Med Biol* (2019) 64:225010. doi: 10.1088/1361-6560/ab52a5
17. Dahle TJ, Rykkelid AM, Stokkevag CH, Mairani A, Gorgen A, Edin NJ, et al. Monte Carlo Simulations of a Low Energy Proton Beamline for Radiobiological Experiments. *Acta Oncol* (2017) 56:779–86. doi: 10.1080/0284186X.2017.1289239
18. Cartwright IM, Su C, Haskins JS, Salinas VA, Sunada S, Yu H, et al. Dna Repair Deficient Chinese Hamster Ovary Cells Exhibiting Differential Sensitivity to Charged Particle Radiation Under Aerobic and Hypoxic Conditions. *Int J Mol Sci* (2018) 19(8):2228. doi: 10.3390/ijms19082228
19. Maeda J, Fujii Y, Fujisawa H, Hirakawa H, Cartwright IM, Uesaka M, et al. Hyperthermia-Induced Radiosensitization in CHO Wild-Type, NHEJ Repair Mutant and HR Repair Mutant Following Proton and Carbon-Ion Exposure. *Oncol Lett* (2015) 10:2828–34. doi: 10.3892/ol.2015.3732
20. Luo WR, Chen FH, Huang RJ, Chen YP, Hsiao YY. Effects of Indirect Actions and Oxygen on Relative Biological Effectiveness: Estimate of DSB Inductions and Conversions Induced by Therapeutic Proton Beams. *Int J Radiat Biol* (2020) 96:187–96. doi: 10.1080/09553002.2020.1688883
21. Paganetti H. Relative Biological Effectiveness (RBE) Values for Proton Beam Therapy. Variations as a Function of Biological Endpoint, Dose, and Linear Energy Transfer. *Phys Med Biol* (2014) 59:R419–472. doi: 10.1088/0031-9155/59/22/R419
22. Guan F, Geng C, Ma D, Bronk L, Kerr M, Li Y, et al. Rbe Model-Based Biological Dose Optimization for Proton Radiobiology Studies. *Int J Part Ther* (2018) 5:160–71. doi: 10.14338/IJPT-18-00007.1
23. Bright SJ, Flint DB, Chakraborty S, McFadden CH, Yoon DS, Bronk L, et al. Nonhomologous End Joining Is More Important Than Proton Linear Energy Transfer in Dictating Cell Death. *Int J Radiat Oncol Biol Phys* (2019) 105:1119–25. doi: 10.1016/j.ijrobp.2019.08.011
24. Fujisawa H, Genik PC, Kitamura H, Fujimori A, Uesaka M, Kato TA. Comparison of Human Chordoma Cell-Kill for 290 MeV/n Carbon Ions Versus 70 MeV Protons In Vitro. *Radiat Oncol* (2013) 8:91. doi: 10.1186/1748-717X-8-91
25. Genet SC, Maeda J, Fujisawa H, Yurkon CR, Fujii Y, Romero AM, et al. Comparison of Cellular Lethality in DNA Repair-Proficient or -Deficient Cell Lines Resulting From Exposure to 70 MeV/n Protons or 290 MeV/n Carbon Ions. *Oncol Rep* (2012) 28:1591–6. doi: 10.3892/or.2012.1982
26. Chaudhary P, Marshall TI, Perozziello FM, Manti L, Currell FJ, Hanton F, et al. Relative Biological Effectiveness Variation Along Monoenergetic and Modulated Bragg Peaks of a 62-MeV Therapeutic Proton Beam: A Preclinical Assessment. *Int J Radiat Oncol Biol Phys* (2014) 90:27–35. doi: 10.1016/j.ijrobp.2014.05.010
27. Britten RA, Nazaryan V, Davis LK, Klein SB, Nichiporov D, Mendonca MS, et al. Variations in the RBE for Cell Killing Along the Depth-Dose Profile of a Modulated Proton Therapy Beam. *Radiat Res* (2013) 179:21–8. doi: 10.1667/RR2737.1
28. Buglewicz DJ, Banks AB, Hirakawa H, Fujimori A, Kato TA. Monoenergetic 290 MeV/n Carbon-Ion Beam Biological Lethal Dose Distribution Surrounding the Bragg Peak. *Sci Rep* (2019) 9:6157. doi: 10.1038/s41598-019-42600-4
29. Jakob B, Splinter J, Taucher-Scholz G. Positional Stability of Damaged Chromatin Domains Along Radiation Tracks in Mammalian Cells. *Radiat Res* (2009) 171:405–18. doi: 10.1667/RR1520.1
30. Noon AT, Shibata A, Rief N, Lobrich M, Stewart GS, Jeggo PA, et al. 53BP1-Dependent Robust Localized KAP-1 Phosphorylation is Essential for Heterochromatic DNA Double-Strand Break Repair. *Nat Cell Biol* (2010) 12:177–84. doi: 10.1038/ncb2017
31. Bewersdorf J, Bennett BT, Knight KL. H2AX Chromatin Structures and Their Response to DNA Damage Revealed by 4Pi Microscopy. *Proc Natl Acad Sci USA* (2006) 103:18137–42. doi: 10.1073/pnas.0608709103
32. Whitmore GF, Varghese AJ, Gulyas S. Cell Cycle Responses of Two X-ray Sensitive Mutants Defective in DNA Repair. *Int J Radiat Biol* (1989) 56:657–65. doi: 10.1080/09553008914551881

33. Hinz JM, Tebbs RS, Wilson PF, Nham PB, Salazar EP, Nagasawa H, et al. Repression of Mutagenesis by Rad51D-mediated Homologous Recombination. *Nucleic Acids Res* (2006) 34:1358–68. doi: 10.1093/nar/gkl020
34. Lourenco A, Shipley D, Wellock N, Thomas R, Bouchard H, Kacperek A, et al. Evaluation of the Water-Equivalence of Plastic Materials in Low- and High-Energy Clinical Proton Beams. *Phys Med Biol* (2017) 62:3883–901. doi: 10.1088/1361-6560/aa67d4
35. Maeda J, Roybal EJ, Brents CA, Uesaka M, Aizawa Y, Kato TA. Natural and Glucosyl Flavonoids Inhibit Poly(ADP-Ribose) Polymerase Activity and Induce Synthetic Lethality in BRCA Mutant Cells. *Oncol Rep* (2014) 31:551–6. doi: 10.3892/or.2013.2902
36. Rogakou EP, Boon C, Bonner WM. Formation of a Novel Histone Derivative, H2AX Phosphorylated on serine-139, is an Immediate Cellular Response to non-Lethal and Lethal Amounts of Ionizing Radiation, and is Also Found During Apoptosis and in Germ Cells. *Mol Biol Cell* (1997) 8:1858–8. doi: 10.1074/jbc.273.10.5858
37. Costes SV, Chiolo I, Pluth JM, Barcellos-Hoff MH, Jakob B. Spatiotemporal Characterization of Ionizing Radiation Induced DNA Damage Foci and Their Relation to Chromatin Organization. *Mutat Res* (2010) 704(1–3):78–87. doi: 10.1016/j.mrrev.2009.12.006
38. Jakob B, Scholz M, Taucher-Scholz G. Biological Imaging of Heavy Charged-Particle Tracks. *Radiat Res* (2003) 159:676–84. doi: 10.1667/0033-7587(2003)159[0676:BIOHCT]2.0.CO;2
39. Cuaron JJ, Chang C, Lovelock M, Higginson DS, Mah D, Cahlon O, et al. Exponential Increase in Relative Biological Effectiveness Along Distal Edge of a Proton Bragg Peak as Measured by Deoxyribonucleic Acid Double-Strand Breaks. *Int J Radiat Oncol Biol Phys* (2016) 95:62–9. doi: 10.1016/j.ijrobp.2016.02.018
40. Guan FD, Bronk L, Titt U, Lin SH, Mirkovic D, Kerr MD, et al. Spatial Mapping of the Biologic Effectiveness of Scanned Particle Beams: Towards Biologically Optimized Particle Therapy. *Sci Rep* (2015) 5:9850. doi: 10.1038/srep09850
41. Halg RA, Schneider U. Neutron Dose and its Measurement in Proton Therapy-Current State of Knowledge. *Br J Radiol* (2020) 93:20190412. doi: 10.1259/bjr.20190412
42. Jones B, McMahon SJ, Prise KM. The Radiobiology of Proton Therapy: Challenges and Opportunities Around Relative Biological Effectiveness. *Clin Oncol (R Coll Radiol)* (2018) 30:285–92. doi: 10.1016/j.clon.2018.01.010

Conflict of Interest: The authors declare that the research was conducted in the absence of any commercial or financial relationships that could be construed as a potential conflict of interest.

frontiers in Oncology

ORIGINAL RESEARCH
published: 24 June 2021
doi: 10.3389/fonc.2021.677781

Prebiotic Mannan Oligosaccharide Pretreatment Improves Mice Survival Against Lethal Effects of Gamma Radiation by Protecting GI Tract and Hematopoietic Systems

Sweta Sanguri[†] *and Damodar Gupta*[*]

Division of Metabolic Cell Signaling Research, Institute of Nuclear Medicine & Allied Sciences, Delhi, India

Total body irradiation (TBI) results in critical injuries in a dose dependent manner that primarily damages highly proliferating tissues including hematopoietic stem cells (HSCs) and intestinal crypt stem cells *etc.* This may result in hematopoietic syndrome leading to bone marrow failure and gastrointestinal syndrome leading to chronic intestinal functional alterations. Death results from the gastrointestinal syndrome due to sepsis, bleeding, dehydration, and multi-system organ failure. We demonstrate that the prebiotic mannan oligosaccharide (MOS) pretreatment substantially prolongs survival in both male and female mice when administered 2 h prior to radiation either through oral or intraperitoneal route. The radioprotective efficacy of MOS was found to be age dependent and improves survival even in aged mice (12–13 months old). MOS pretreatment effectively abrogates radiation-induced hematopoietic injury and accelerates recovery of lymphocytes and WBCs and alleviates depletion of circulatory blood cells. Results also illustrate that MOS pretreatment abolishes crypt cell death and denudation of villi in comparison to the respective irradiated animals and ameliorates the overall radiation-induced damage to the GI system. MOS pretreatment facilitates intestinal recovery leading to enhanced animal survival demonstrating its protection efficacy against TBI induced mortality. Moreover, MOS pretreated animals show signs of accelerated recovery in terms of severity of radiation sickness symptoms including weight loss and completely abolish TBI associated mortality.

Keywords: total body irradiation, gastrointestinal syndrome, hematopoietic syndrome, radiation countermeasure agents, mannan oligosaccharide, prebiotics, mitochondria

Abbreviations: IR, ionising radiation; ARS, acute radiation syndrome; MOS, mannan oligosaccharide; H-ARS, hematopoietic acute radiation syndrome; GI-ARS, gastrointestinal acute radiation syndrome; HSCs, hematopoietic stem cells; TBI, total body irradiation; TLR, toll-like receptor; RCAs, radiation countermeasure agents; BM, bone marrow.

OPEN ACCESS

Edited by:
Shubhankar Suman,
Georgetown University, United States

Reviewed by:
Shardul Kulkarni,
Pennsylvania State University (PSU), United States
Amit Kunwar,
Bhabha Atomic Research Centre (BARC), India

****Correspondence:***
Damodar Gupta
damodar.gupta@gmail.com;
damodar@inmas.drdo.in

[†]Present address:
Sweta Sanguri,
Department of Radiation Biology, Inter-University Accelerator Centre (IUAC), New Delhi, India

Specialty section:
This article was submitted to Radiation Oncology, a section of the journal Frontiers in Oncology

Received: *16 March 2021*
Accepted: *27 May 2021*
Published: *24 June 2021*

Citation:
Sanguri S and Gupta D (2021) Prebiotic Mannan Oligosaccharide Pretreatment Improves Mice Survival Against Lethal Effects of Gamma Radiation by Protecting GI Tract and Hematopoietic Systems. Front. Oncol. 11:677781. doi: 10.3389/fonc.2021.677781

INTRODUCTION

Development of safe and effective radiation countermeasure approaches, including radio-protectors, mitigators, and therapeutics, are crucial and vital for the management of prospective disaster scenarios comprising low and high dose radiation exposure (1). Radiation exposure can result in mortality or can cause long-term adverse health effects depending upon the exposure dose, dose rate, and time of exposure (2). Acute radiation syndrome (ARS) arises mainly due to the intense enormity of injury to the actively proliferating cells including hematopoietic stem cells (HSCs) and intestinal crypts stem cells *etc.* resulting in hematopoietic acute radiation syndrome (H-ARS; leading to bone marrow failure) and gastrointestinal acute radiation syndrome (GI-ARS; leading to chronic intestinal functional alterations) respectively. High dose TBI can result in neurovascular acute radiation syndrome (NV-ARS) leading to death generally within 24–48 h. NV-ARS is considered fatal due to irreversible damage to organs. Therefore, only H-ARS and GI-ARS are being focused for the development of radiation countermeasures (3). Radiation exposure induces damage to the intestinal crypt cells in the gastrointestinal tract, compelling crypt cells to undergo apoptosis within hours after ionizing radiation (IR) exposure (4). Since GI tract is an extremely rapid cell turnover tissue, depletion of crypt cells results in homeostasis imbalance, and restoration of intestinal villi is impaired, leading to loss of villi cellularity and denudation of the villi (5, 6). Consequently, other morphological changes including disruption of the epithelial barrier manifest along with compromised functional capacity leading to chronic intestinal functional alterations comprising GI-ARS. Hence, it is obligatory to identify efficient, medically safe, and affordable radiation countermeasure agents (RCAs) that can potentially prevent or manage both H-ARS and GI-ARS.

Toll-like receptor (TLR) family is one of the imperative components of innate immune system, which is the first line of defense against microbial invasion (7). TLRs can recognize pathogens, molecular patterns and/or danger signals and induce immune signaling for evasion of infection. Stimulation of TLR2, 4, 5 or 9 by corresponding ligand(s) has been shown to reduce radiation-induced cell death in crypt cells, resulting in improved radiation-induced GI-ARS symptoms (7). Consequently, different TLR ligands are currently under different stages of development as RCAs for ARS. Manipulation of TLR functions has been shown to activate NF-κB pathway and reduce radiation-induced cell death. Entolimod (CBLB502, a TLR5 agonist) has been granted both Fast Track and Orphan Drug status by the US FDA during or after a radiation disaster to reduce risk of death. Entolimod has been shown to reduce radiation damage to both hematopoietic (HP) and gastrointestinal (GI) tissues and improve tissue regeneration (2, 8, 9).

Mannan oligosaccharide (MOS) is a TLR agonist and is used as prebiotic nutritional supplement in several living organisms including farm animals, cattle, pigs, dogs, chicken, fishes *etc.* for its gastrointestinal and immunological responses (10, 11). MOS is reported to improve health, growth status, and overall performance in animals (12–14). It is known to support the gut microflora and stimulates epithelial barrier structure and functionality of intestinal mucosa (12). MOS is shown to increase microvilli surface area and goblet cell numbers in small intestine of animals (15). It stimulates the immune system of the host and has adsorbent capacity against toxins and it is non-toxic when administered orally, even in very large concentration (16, 17). Under *in vitro* conditions, we have demonstrated that MOS mediates alteration in mitochondrial physiology in immortalized normal cells and offer advantages in reducing biological effects of γ-radiation *in vitro* and thereby enhances cell survival (18, 19). TLRs have been reported to express in humans and mice (3, 18, 20), we intend to utilize the benefits of MOS supplementation against radiation induced ARS. Since mitochondrial respiratory activity is reported to decline during the natural aging process, we investigated the effects of MOS pretreatment (50 mg/kg/B.W i.p. and 200 mg/kg B.W. orally; 2 h prior to irradiation) on IR-induced injury in different age groups of BALB/c mice at lethal (7.5 Gy) and sub-lethal (3 and 5 Gy) doses of TBI. In our preliminary experiments, we administered MOS intraperitoneally (50 mg/kg/B.W i.p; 2 h prior to irradiation) and observed 100% survival advantage in mice at lethal dose of TBI. MOS as a prebiotic is non-toxic orally and has beneficial effects in overall health of an organism. Remarkably, MOS oral pretreatment (200 mg/kg B.W. orally; 2 h prior to TBI; 7.5 Gy) also confers 100% radiation protection at lethal dose of TBI despite having a different biodistribution pattern than through intraperitoneal route as studied earlier (14). TBI instigates bone marrow (BM) suppression resulting in loss of circulating blood cells. It also causes significant loss of viable crypt cells in the intestine, perturbs villus structure, disrupts mucosal layer integrity thereby compromising proper absorption of essential nutrients. The immune-suppression and thrombocytopenia associated with the H-ARS favor opportunistic infections and hemorrhage. MOS pretreatment to mice effectively minimizes radiation-induced hematopoietic and gastrointestinal injury, accelerates recovery of circulating blood cells, minimizes oxidative damage to important cellular biomolecules, restores intestinal integrity and consequently abrogates TBI-induced lethality.

MATERIALS AND METHODS

Chemicals

All chemicals used in the study were of analytical grade and were either procured from an Indian manufacturer (SRL India, HiMedia chemicals) or obtained from Sigma Aldrich (St Louis, MO), Thermo Fisher Scientific Inc (USA) *etc.* Mannan oligosaccharide (MOS), 1,3,5-trihydroxybenzene, phloroglucinol, D-xylose, ethylene diaminetetracetic acid (EDTA), BCA kit, hematoxylin, eosin, thiobarbituric acid, BSA, Mops, Sucrose, TBA, DTNB, NEM, neutral buffered formalin, decalcifying solution-Lite, were obtained from Sigma-Aldrich Chemical Co., St. Louis, MO, USA. Phosphate buffer saline (PBS), acetic acid, hydrochloric acid, and all other chemicals obtained were of analytical grade from SRL India. Reagents for hematology analyzer (Isotonac 3, Hemolynac 5,

Hemolyzing Reagent, Hemolynac 3, Cleanac 3) were procured from Nihon Kohden, Japan.

Mice

Inbred BALB/c mice were obtained from the central experimental animal facility of the Institute of Nuclear Medicine & Allied Sciences (INMAS), Defence Research and Development Organization (DRDO). Both male and female mice of different age groups *viz.* 8–12 weeks, 6–8 months, and 12–13 months old acclimatized and healthy animals were chosen for studies. Mice were housed in the facility maintained at 21 ± 2°C with 50 ± 10% humidity on a 12 h light/dark cycle and were fed standard rodent feed (from Golden Feeds, Delhi, India) and water *ad libitum*. All surviving mice were euthanized at the completion of the observation period.

Irradiation

Mice were subjected to total body irradiation (TBI) in 60Co Gamma Teletherapy unit (Bhabhatron II, Panacea Medical Technologies, Bangalore, India) at a dose rate of 2.25–2.55 Gy/min. (dose rate of the 60Co Gamma irradiation source was calibrated using physical dosimetry). Mice were subjected to radiation exposure of either 3 or 5 Gy and/or lethal dose of 7.5 Gy separately with or without MOS pretreatment.

Preparation and Administration of MOS

MOS was dissolved (20 mg/ml stock) in sterile phosphate buffered saline (PBS; 1×) under aseptic conditions. MOS was administered (intra-peritoneally 50 mg/kg body weight or orally 200 mg/kg body weight separately as indicated) 2 h prior to total body irradiation (TBI) in mice for radioprotection efficacy studies.

Survival Studies

To study radio-protective efficacy of MOS, mice were divided into the following groups: Control (sham irradiated; vehicle treated), MOS alone, Radiation (3 or 5 or 7.5 Gy) alone, and mice that received MOS 2 h before TBI (3 or 5 or 7.5 Gy; n = 8/group). MOS was administered intra-peritoneally (50 mg/kg body weight) or orally (200 mg/kg body weight) 2 h prior to TBI in a single fraction as per groups, as indicated. All animals were weighed, and their well-being was inspected daily from the initiation of treatment to the end of the study.

Evaluation of Biological Effects of Radiation

To evaluate effects of MOS pretreatment in radiation protection and minimize biological effects of radiation, mice were exposed to different doses of IR (3 and 5 Gy) separately. Mice were divided into the following six groups: Control (sham irradiated, vehicle treated), MOS alone (oral; 20 0mg/kg body weight), radiation alone (3 or 5 Gy alone), mice that received MOS 2 h before 3 or 5 Gy TBI (n = 8/group). MOS was administered orally at 200 mg/kg body weight 2 h prior to TBI (3 or 5 Gy) in a single fraction as per group. The mice were sacrificed on days 3, 7, 15, and 40 as per ethical guidelines (by cervical dislocation), and tissues were collected. The tissues were washed in PBS and either fixed for histology or flashed frozen in liquid N_2, and stored for further assays.

Peripheral Blood Analysis

Blood was withdrawn from the retro-orbital plexus and collected in heparinized blood collection tubes (BD Biosciences, San Jose, CA) on days 3, 5, 15, and 21 following various treatments. Blood was mixed gently on a rotary shaker until acquisition and analysis for red blood cells, hemoglobin, platelets, leukocytes, and lymphocytes by using hematology analyzer (MEK-6400; Nihon Kohden, Japan), and data was generated using Data Management Software (DMS-Lite software).

Histological Examination of Bone Marrow

Mice were euthanized humanely, and femurs were isolated on days 3, 7, 15, and 40-post IR exposure or/and MOS treatment. Histological examination of bone marrow was done as described by Travlos et al. with minor modifications (21). Briefly, femurs were fixed in 10% formalin, neutral buffered (Sigma) for 12–14 h at RT with gentle rocking followed by incubation in decalcifying solution-Lite (Sigma) at RT with gentle rocking for 14–16 h. Femurs were then washed thoroughly in tap water and thereafter processed for dehydration, and paraffin blocks were made. The micro-sections (3 μm) of tissue were prepared and stained with hematoxylin and eosin (H&E). Slides were examined by microscopy, and brightfield image acquisition was done using Cell imager, Optika, Italy.

Histological Examination of Small Intestine

Histological examination of small intestine was done as described by Morson et al. (22) with minor modifications. Briefly, the mice were euthanized humanely, and intestine of each animal was dissected, washed with PBS to remove intestinal contents (on days 3, 7, 15 and 40-post IR exposure). Following washing, jejunums were fixed in 10% neutral-buffered formalin (Sigma) at 37°C for 24 h. The fixed tissue was thereafter processed for dehydration, and paraffin blocks were made. The micro-sections (5 μm) of tissue were prepared and placed on slides for staining with hematoxylin and eosin (H&E). Slides were examined by microscopy and brightfield image acquisition was done using Cell imager, Optika Italy. Villus height and crypt depth were measured and compared with that of control. Villus height was determined by measuring the distance from the tip of the villus up to the crypt. Spatial scale of the active image was defined and presented in micrometer (calibrated unit, 2.55 pixels/micrometer) by converting pixels to μm using ImageJ software for mac (Version 1.50i, NIH USA).

Crypt Microcolony Survival Assay

Non-serial transverse sections of jejunum were studied for the number of cells per crypt and surviving crypt per T.S. Each section was separated from the previous one by a minimum of 50 μm of tissue. Surviving crypts with ≥10 cells for each T.S. were counted, and results are expressed as number of surviving crypt/T.S. jejunum (23). A surviving crypt was defined as one that had ten or more tightly and strongly packed H & E stained cells

(excluding Paneth cells). Only regions that were orientated correctly and did not contain Payer's patches were scored (Payer's patches influence both the number of crypts in a normal circumference and the ability of a crypt to survive insult). Number of cells per crypt was also counted, and results were expressed as number of cells/crypt. Data were pooled from three to four separate T.S. of jejunum from each mouse. Only those crypts which were seen directly against the inner muscle layer were counted. All counts and measurements from each tissue specimen were obtained "blind" from a minimum of four coded sections.

D-Xylose Absorption Assay

To quantify absorption efficacy of intestine as a physiological indicator of mucosal barrier integrity in mice (n = 8/group) after various treatments, a D-xylose uptake assay was performed at various time points (0, 3, 7, 10, 15 and 40 days post 3, 5, and 7.5 Gy TBI). A 5% w/v solution of D-xylose (100 µl/mouse) in deionized water was administered orally, and blood samples were collected 2 h post administration. Blood was withdrawn from the retro-orbital plexus and collected in microtainer tubes (BD Microtainer Gold tube, BD Biosciences, San Jose, CA). Following 30 min coagulation at room temperature, the sera were well separated from the gel by 10 min-centrifugation at 10,000g, collected and stored at −80°C for later study. Serum D-xylose concentration was determined according to Eberts et al. with minor modifications (24). Then 5 ml phloroglucinol (1,3,5-trihydroxybenzene, Sigma Chemical Co., St. Louis, MO) reagent (0.5 g of phloroglucinol, 100 ml glacial acetic acid, and 10 ml of conc. HCl) was added to 50 µl of plasma. This solution was heated to 100°C in a water bath for 4 min to allow optimum color development. After equilibration to room temperature, sample absorption was measured using spectrophotometer at 554 nm, and D-xylose concentration in each serum sample was calculated using D-xylose standard calibration curve.

Isolation of Mitochondria

Kidney and liver tissues stored at −80°C were taken out, and homogenate (10%) was prepared in ice-cold isolation medium (0.3 M sucrose, 0.1% BSA, 1 mM EGTA, 5 mM Mops, 5 mM KH_2PO_4, pH 7.4) using a Potter Elvjham homogenizer, and mitochondria were isolated using the method of Goel et al. (25). Briefly, the homogenate was centrifuged at 1,000g for 10 min at 4°C. The supernatant was collected and centrifuged at 10,000g for 20 min at 4°C to obtain the mitochondrial pellet. The mitochondrial pellet was washed three times with 50 mM potassium phosphate buffer (pH 7.4) to remove traces of sucrose, and integrity of mitochondria was determined by measuring the monoamine oxidase enzyme activity (26, 27).

Mitochondrial Lipid Peroxidation

Thiobarbituric acid reactive substances (TBARSs) were measured spectrophotometrically in liver and kidney homogenates as described by (28) with minor modifications. Briefly, mitochondrial protein (4 mg/ml) was mixed with an equal volume of Buege & Aust reagent (TCA, 15% (w/v) in 0.25 M HCl; TBA, 0.37% (w/v) in 0.25 M HCl) and heated for 15 min in boiling water. After cooling, the precipitate was removed by centrifugation at 1,000g in a refrigerated centrifuge (Sigma 3-18K, St. Louis, MO, USA) for 10 min at room temperature. The absorbance of the supernatant was recorded at 532 nm (IMPLEN nanodrop, Germany) against a sample containing reagents but no sample. The concentration of TBARS was determined using an extinction coefficient of 1.56×105 mol^{-1} cm^{-1} and results are expressed as nmoles of MDA per mg of mitochondrial protein. Protein concentration in each sample was measured by using BCA kit (Sigma-Aldrich Chemical Co., St. Louis, MO, USA) as per manufacturers' protocol using bovine serum albumin (BSA) as standard.

Thiol Estimation

Acid soluble thiol was measured spectrophotometrically in liver and kidney homogenates as described by *Ellman* with minor modifications (29). Briefly, 0.3 ml mitochondrial protein (4 mg/ml) was mixed with an equal volume of SDS (10%) and mixed thoroughly. A 2.4 ml sodium phosphate buffer (5 mM) was added, and the solutions were mixed properly. The background absorbance of the solution was recorded at 412 nm using spectrophotometer. A 0.3 ml DTNB (1 mM) was then added, and the solutions were incubated for 1 h at 37°C, and absorbance was measured at 412 nm. The concentration of sulfhydryls in the sample was determined using molar extinction coefficient of TNB (14,150 M^{-1} cm^{-1}), and results are expressed as nmol of TNB per mg of mitochondrial protein. Protein concentration in each sample was measured by using BCA kit (Sigma-Aldrich Chemical Co., St. Louis, MO, USA) as per manufacturers' protocol using bovine serum albumin (BSA) as standard.

Statistical Analysis

All the data were analyzed using Graph Pad Prism (version 5.01) and were presented as mean ± standard deviation (SD). Significance of difference between groups was determined by Student's t-test and one-way or two-way ANOVA with Newman–Keuls' multiple composite-tests. Survival studies' data were analyzed using the Kaplan–Meier method followed by Mantel–Cox (log-rank) test for assessment of significant differences. Results were considered significant at $P < 0.05$.

RESULTS

Survival Studies of Mice Following Treatment With MOS

Survival studies performed on Balb C mice showed that all the mice exposed to lethal doses of gamma radiation (7.5 Gy) alone died within 14 days (LD-100/14). Treatment of mice with MOS alone (IP 50 mg/kg BW or oral 200 mg/kg BW) did not influence the survival of mice. Moreover, oral administration of MOS showed no toxicity in terms of survival up to 5 g/kg BW. Pre-irradiation treatment of mice with MOS (−2 h; 50 mg/kg bw; IP) conferred remarkable protection of mice resulting in the 100% survival of mice (both male and female mice, age 8–12 weeks) as

observed till 30 days (**Figure 1A**; $p < 0.001$). Interestingly, pre-irradiation treatment of mice with MOS (−2 h; 200 mg/kg bw; orally) also conferred 100% survival of mice (both males and females, age 8–12 weeks and female, 6–8 months, **Figures 1B, C**; $p< 0.001$) as observed till 30 days and thereafter also (up to 6 months) with respect to group exposed to radiation (7.5 Gy) alone. The radioprotective efficacy of MOS was found to be age dependent with 90, 60, and 50% survival in 6–8 months male mice, 12–13 months old female mice, and 12–13 months old male mice respectively (**Figures 1C, D**; $p < 0.001$) observed till 30 days. At 7.5 Gy TBI dose, the radiation alone group experienced absolute mortality and the entire cohort of animals died on (or before) 15–16 days post TBI accompanied with symptoms of radiation sickness such as weight loss, diarrhea, anorexia, and lethargy. The animals treated with MOS prior to TBI showed significantly less severity of symptoms or no symptoms at all.

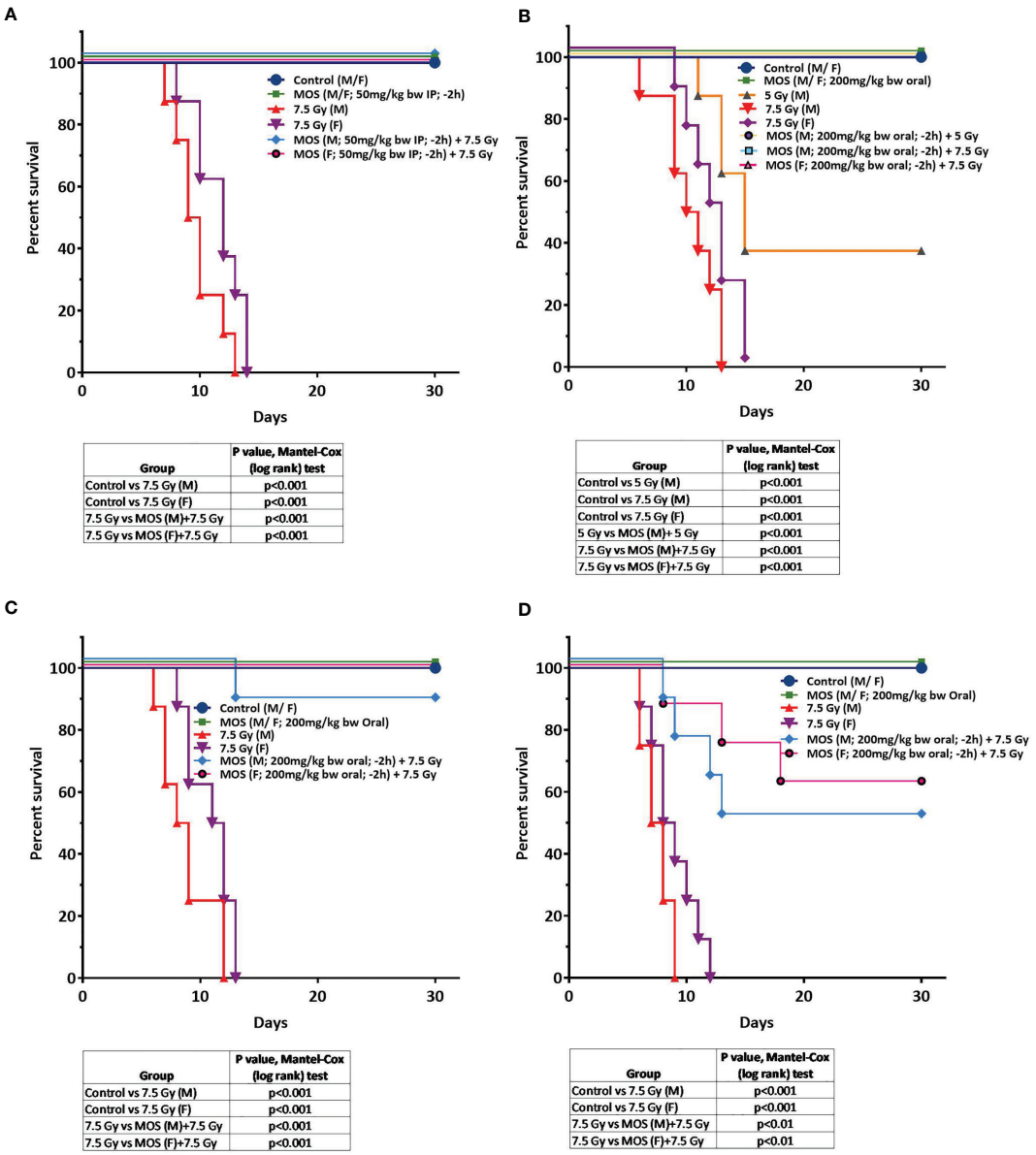

Group	P value, Mantel-Cox (log rank) test
Control vs 7.5 Gy (M)	p<0.001
Control vs 7.5 Gy (F)	p<0.001
7.5 Gy vs MOS (M)+7.5 Gy	p<0.001
7.5 Gy vs MOS (F)+7.5 Gy	p<0.001

Group	P value, Mantel-Cox (log rank) test
Control vs 5 Gy (M)	p<0.001
Control vs 7.5 Gy (M)	p<0.001
Control vs 7.5 Gy (F)	p<0.001
5 Gy vs MOS (M)+ 5 Gy	p<0.001
7.5 Gy vs MOS (M)+7.5 Gy	p<0.001
7.5 Gy vs MOS (F)+7.5 Gy	p<0.001

Group	P value, Mantel-Cox (log rank) test
Control vs 7.5 Gy (M)	p<0.001
Control vs 7.5 Gy (F)	p<0.001
7.5 Gy vs MOS (M)+7.5 Gy	p<0.001
7.5 Gy vs MOS (F)+7.5 Gy	p<0.001

Group	P value, Mantel-Cox (log rank) test
Control vs 7.5 Gy (M)	p<0.001
Control vs 7.5 Gy (F)	p<0.001
7.5 Gy vs MOS (M)+7.5 Gy	p<0.01
7.5 Gy vs MOS (F)+7.5 Gy	p<0.01

FIGURE 1 | **(A–D)** MOS pretreatment protects mice from TBI-induced lethality. Protective effects of MOS (*i.e.* administered 2 h prior to irradiation) against lethal TBI (7.5 Gy). **(A)** Mice (8 to 12 weeks old, both male and female) were injected MOS (50 mg/kg/B.W.; i.p.) and irradiated 2 h post treatment. **(B)** Protective effects of MOS (*i.e.* administered orally 200 mg/kg B.W.; 2 h prior to irradiation) against lethal TBI (7.5 Gy) and sub-lethal TBI (5 Gy). Mice (8 to 12 weeks old, both male and female) were administered MOS orally and irradiated 2 h post treatment. **(C)** Mice (6–8 months old, both male and female) were administered MOS orally (200 mg/kg B.W.) and irradiated 2 h post treatment. **(D)** Mice (12–13 months old, male) were administered MOS orally (200 mg/kg B.W. and irradiated 2 h post treatment. Kaplan–Meier survival curve depicts the 30-day survival (n = 8 in all the groups). The table summarizes the findings of Mantel–Cox (log-rank) test comparing survival responses between un-irradiated and TBI cohorts, TBI and MOS (−2h) +TBI cohorts.

The studies were also performed to measure survival at sub-lethal dose of TBI (5Gy). Exposure of mice to 5 Gy radiation also found to reduce survival by 60% (LD-60/21) with respect to control group. Administration of MOS (male; 200 mg/kg bw orally; −2 h) conferred 100% protection with respect to 5 Gy alone ($p < 0.001$).

The result suggests that MOS treatment prior to radiation protects animal from deleterious effects of radiation and confers 100% survival when administered from either of the two routes.

MOS Pretreatment Amends Hematological Indices in the Peripheral Blood Post TBI

The kinetics of hematopoietic recovery in sub-lethally irradiated mice treated with MOS was followed for 30 days post-TBI. MOS significantly increased survival from 60 to 100% in combination (MOS + 5Gy) cohorts compared to the TBI (5 Gy) group. Assessment of the peripheral blood for various hematological parameters exhibited significant decrease in peripheral blood components (**Figures 2A–E**). The results revealed that exposure to TBI significantly decreased the number of circulating leukocytes in animals exposed to TBI ($3.87 \times 10^3 \pm 0.35$ cells/μl, $p < 0.001$) and $3.43 \times 10^3 \pm 0.45$, $p < 0.001$) cells/μl in 3 and 5Gy TBI cohorts respectively) in comparison to $6.63 \times 10^3 \pm 0.5$ cells/μl in un-irradiated control cohorts, with nadir observed at day 15 post-irradiation ($0.62 \times 10^3 \pm 0.1$ cells/μl, $p < 0.001$ and $0.217 \times 10^3 \pm 0.08$ cells/μl, $p < 0.001$) in 3 and 5Gy TBI, respectively). Decrease in circulating leukocytes can compromise the health status of animals and can result in immunosuppression. Leukocyte levels did not recover till day 30 in the TBI mice. On the contrary, MOS pretreatment augmented the WBC count by accelerated recovery in the leukocyte counts at day 22 ($4.23 \times 10^3 \pm 0.42$ cells/μl, $p < 0.001$ and $3.74 \times 10^3 \pm 0.73$ cells/μl, $p < 0.001$) in MOS +3 Gy and MOS + 5 Gy group respectively), and recovered to almost normal levels by day 30 in animals of both MOS + 3 Gy and MOS + 5 Gy groups. The lymphocyte percentage significantly decreased at day 3 ($34.03 \pm 5.43\%$, $p < 0.001$ and $31.78 \pm 5.20\%$, $p < 0.001$) and reached their nadir around day 5 ($20.20 \pm 0.73\%$, $p < 0.001$ and $19.82 \pm 2.85\%$, $p < 0.001$) and did not recover until after day 30 post-TBI [($49.0 \pm 1.97\%$, $p < 0.001$) and ($43.50 \pm 3.95\%$, $p < 0.001$)], in both 3 and 5 Gy cohorts, respectively (**Figure 2B**). Contrarily, in MOS pretreated cohorts, the initial decrease in lymphocyte percentage was rapid till day 5 post TBI, after which accelerated recovery was observed and approximately normal percentage was reached by day 30 post TBI. Erythrocytes and hemoglobin were slower to reach their nadir (day 22), and both recovered to almost normal levels by day 30 (**Figures 2C, D**) both in TBI and MOS + TBI cohorts. Exposure to TBI in irradiated group resulted in initial gradual decrease in platelet count at day 3 ($784.07 \times 10^3 \pm 32.42$ cells/μl, p = ns and $697 \times 10^3 \pm 12.00$ cells/μl, $p < 0.01$) followed by a subsequent sharp decrease at day 5, reached nadir ($325.60 \times 10^3 \pm 26.66$ cells/μl, $p < 0.001$ and $259.10 \times 10^3 \pm 47.92$ cells/μl, $p < 0.001$) at day 15 post TBI, and recovered levels were seen in 3 and 5 Gy irradiated cohorts respectively, by day 30 post TBI (**Figure 2E**). Hematopoietic suppression was significantly lesser in TBI mice pretreated with MOS in all studied parameters. Thus, these results suggest that MOS could be a potential countermeasure for the reduced number of circulating blood cells in irradiated animals.

MOS Pretreatment Restores Bone Marrow Cellularity in TBI Mice

TBI above a threshold dose induces hematopoietic injury and is characterized by depletion of the bone marrow cellular content (7, 30). Effects of MOS pretreatment on the radiation-induced damage to the bone marrow were analyzed by histological analysis of the mice femurs on days 3, 7, 15, and 40 post TBI (3 and 5 Gy). In TBI mice, hematopoietic stem cells and vasculature are disrupted to a large extent, and results show dramatic decrease in bone marrow cellularity in TBI mice. The bone marrow appears necrotic and highly hemorrhagic, and the marrow space shows high content of RBCs (anuclear pink cells). Scattered islands of hematopoietic cells were found to occupy the marrow cavity with variable cellularity and decreased hematopoiesis, till day 15 post 3 and 5 Gy TBI; (**Figures 3B, C**) in comparison to un-irradiated animals that show hypercellular marrow, with more than 90% cellularity with trilineage hematopoiesis. Erythroid series is visible; myeloid series show complete maturation, and megakaryocytes are adequate in number and morphology; **Figure 3A**. Contrarily, MOS pretreatment abrogated the radiation-induced cellular depletion to a large extent with cell numbers and cellular content almost similar to levels in the control animals, and accelerated recovery. The data corroborates well with peripheral blood analysis and indicate that MOS pretreatment alleviates the TBI-induced BM suppression resulting in enhanced hematopoietic recovery.

Histological Examination of Small Intestine

H&E stained sections of the jejunum were analyzed on days 3, 7, 15, and 40-post irradiation. Jejuna from MOS treated animals prior to TBI (both 3 and 5 Gy) and irradiated animals (both 3 and 5 Gy TBI) showed shortening of the villi and loss of structural integrity at days 3 and 7 (**Figure 4**). However, the villi blunting and loss of structure were significantly less in MOS-pretreated animals in comparison to the respective irradiated animals. Similarly, there was significant decline in crypt depth post TBI in comparison to un-irradiated control, and the decrease was less in MOS-pretreated animals. MOS pretreated animals showed signs of accelerated recovery as demonstrated by the increase in villi length (427 ± 48.5 μm, $p < 0.05$ and 359 ± 31.09 μm, $p < 0.05$; **Figure 5A**), crypt depth (**Figure 5B**), and the substantial decline in blunting in comparison to the irradiated group (villi length; 237 ± 84.2 μm, $p < 0.05$ and 206.66 ± 23.094 μm, $p < 0.05$, crypt depth) day 15, post 3 and 5 Gy TBI respectively. By day 40 the morphology of jejuna in both irradiated and MOS-pretreated animals had returned to normal. The number of surviving and regenerating crypts per intestinal circumference was scored, and the average per mouse and per group was determined. The average viable crypts per T.S. of jejunum in the untreated control were about 120.5 ± 3.56 (**Figure 5C**). MOS treatment alone exhibited non-significant changes in the number of crypts (125 ± 3.53, 125 ± 6.36, 128 ± 3.6, and 123 ± 4.7) than that of control (on days 3, 7, 15, and 40 respectively). The 3 and 5 Gy cohorts exhibited reduced number

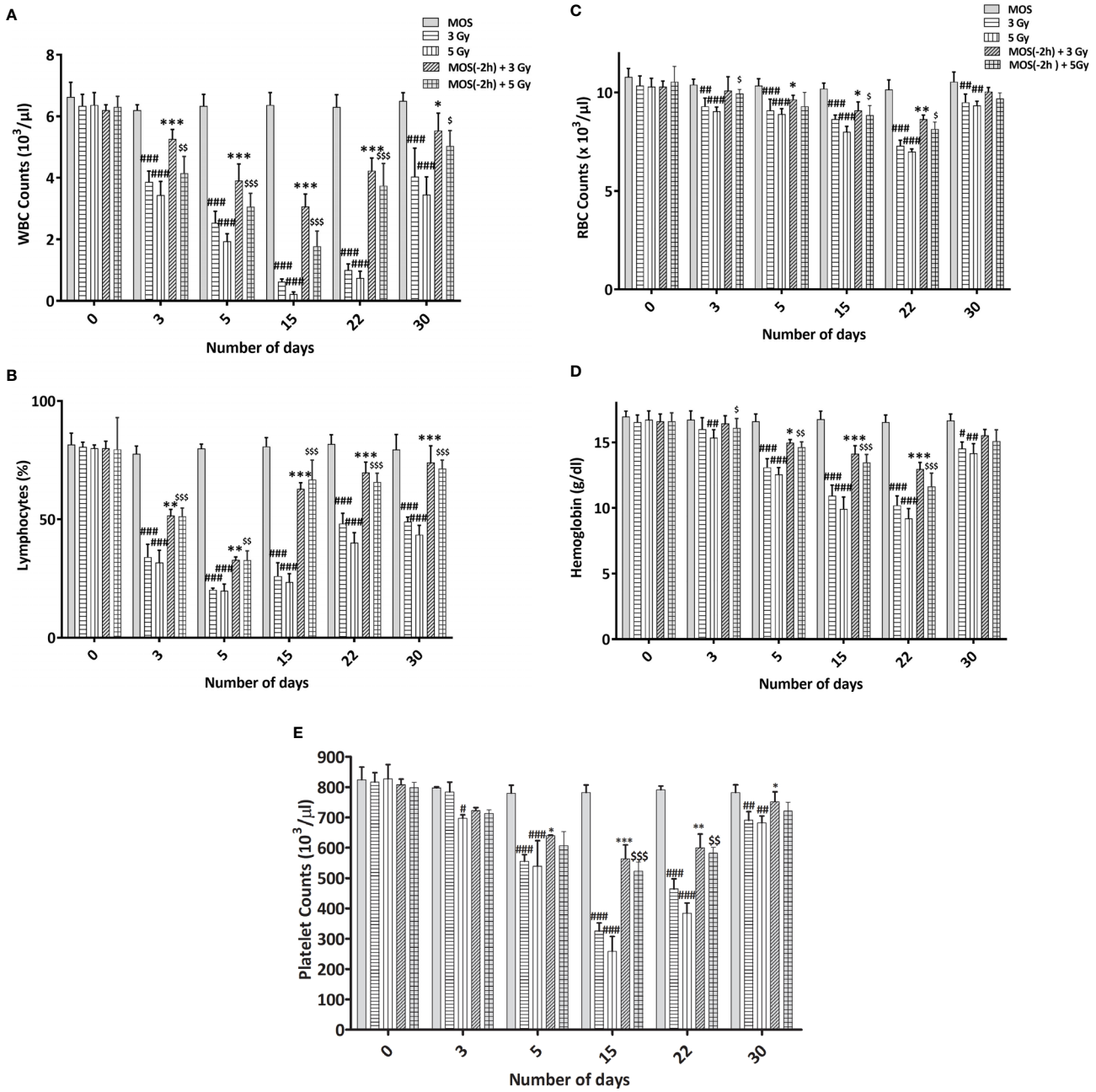

FIGURE 2 | **(A–E)** MOS mediated alterations in the hematological indices in the peripheral blood. Mice were treated with MOS and/or subjected to exposure of radiation (3 and 5 Gy) and assessed for blood cell parameters as described in *Materials and Methods*. Blood counts representing **(A)** WBC, **(B)** lymphocyte, **(C)** RBC, **(D)** hemoglobin, and **(E)** platelets at days 3, 5, 15, 22, and 30 post TBI. (n = 10). Error bars represent mean ± SD, and $^{*}p < 0.05$, $^{**}p < 0.01$, and $^{***}p < 0.001$, $^{\#}p < 0.05$, $^{\#\#}p$ 0.01, $^{\#\#\#}p < 0.001$, $^{\$}p < 0.05$, $^{\$\$}p < 0.01$ and $^{\$\$\$}p < 0.001$ were considered significant, #compared to unirradiated control, *compared to 3 Gy irradiated cohorts and $compared to 5 Gy irradiated cohorts.

of viable crypts to 81 ± 2.82, $p < 0.001$, 82.5 ± 3.53, $p < 0.001$, 86 ± 4.24, $p < 0.001$, 100.5 ± 3.53, $p < 0.001$, and 66 ± 3.53, $p < 0.001$, 64 ± 5.65, $p < 0.001$, 81 ± 2.9, $p < 0.001$, 94.5 ± 6.36, $p < 0.001$ on days 3, 7, 15, and 40 post TBI respectively. Pre-irradiation administration of MOS in 3 and 5 Gy TBI cohorts showed significantly higher number of viable crypts on day 3 (113 ± 4.23, $p < 0.01$ and 90 ± 2.82, $p < 0.01$) and day 7 (94 ± 2.82, $p < 0.01$ and 87± 2.9, $p < 0.01$) respectively in comparison to irradiated control group.

Numbers of cells per crypt were counted and shown in **Figure 5D**. The average cells per crypt of jejunum in the untreated control were about 35.5 ± 2.32. MOS treatment alone

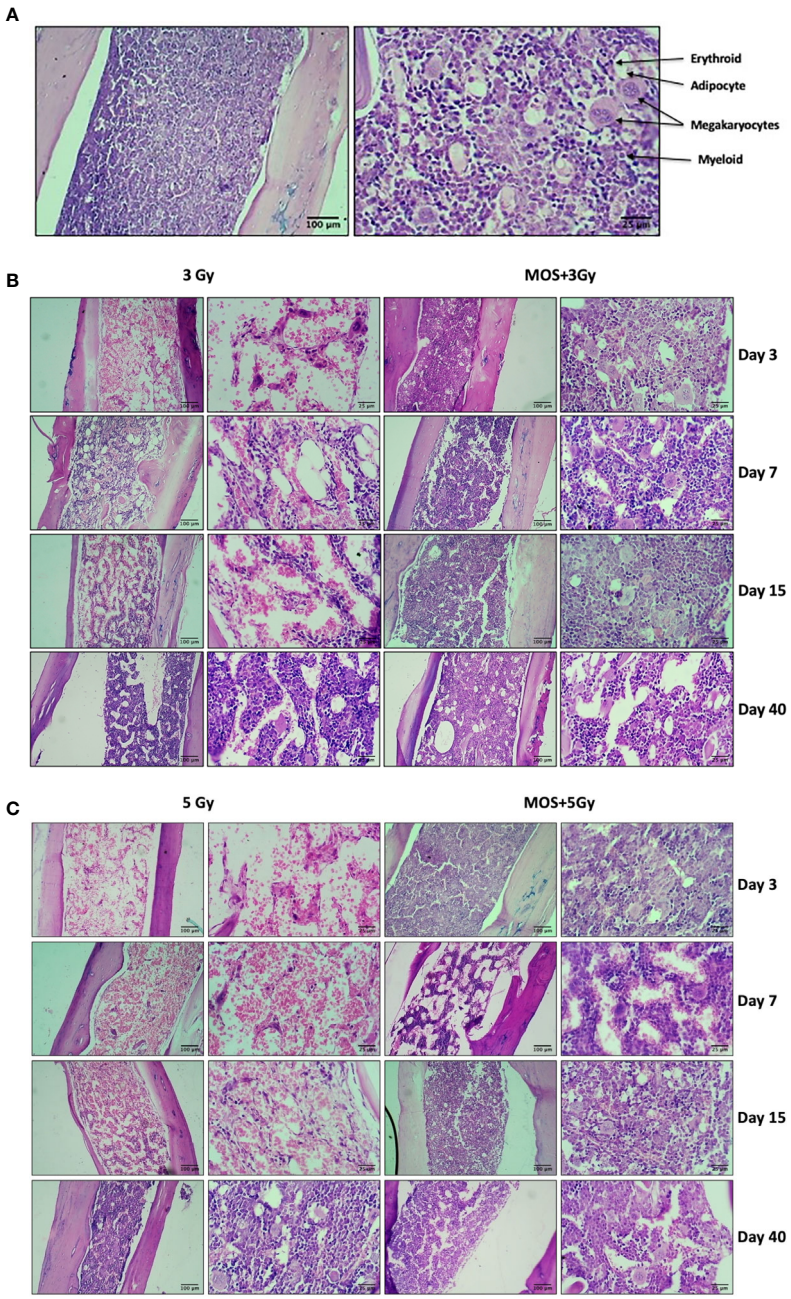

FIGURE 3 | Histological examination of bone marrow. Mice were treated with MOS and/or subjected to TBI (3 and 5 Gy) and assessed for histological examination of small intestine on days 3, 7, 15, and 40-post MOS treatment and/or TBI as described in *Materials and Methods*. **(A)** Representative image of H&E stained femur section of un-irradiated control mice. **(B)** Representative image of H&E stained femur section of 3 Gy TBI and 3 Gy +M mice. **(C)** Representative image of H&E stained femur section of 5 Gy TBI and 5 Gy +M mice.

exhibited non-significant changes in the number of crypts than that of control in all the time points studied. The number of cells was reduced to 20 ± 2.82, $p < 0.001$, 23.5 ± 2.12, $p < 0.001$, 24 ± 2.9, $p < 0.001$, 29.5 ± 2.12, *ns* and 17.5 ± 2.12, $p < 0.001$, 16 ± 1.41, $p < 0.001$, 20 ± 2.9, $p < 0.001$ 24 ± 2.2, *ns* on days 3,7, 15, 40 post (3 and 5 Gy) TBI respectively. MOS pretreatment showed higher number of cells per crypt in MOS + 3 Gy and MOS + 5Gy cohorts on day 3 (113 ± 4.23 and 90 ± 2.82, $p < 0.05$) and day 7 (94 ± 2.82, $p < 0.01$ and 87± 2.9, $p < 0.01$) in comparison to irradiated cohorts respectively. Significant recovery was evident in MOS-pretreated cohorts in terms of villi height, crypt depth, number of surviving crypts, and cells per crypt 15 days post TBI.

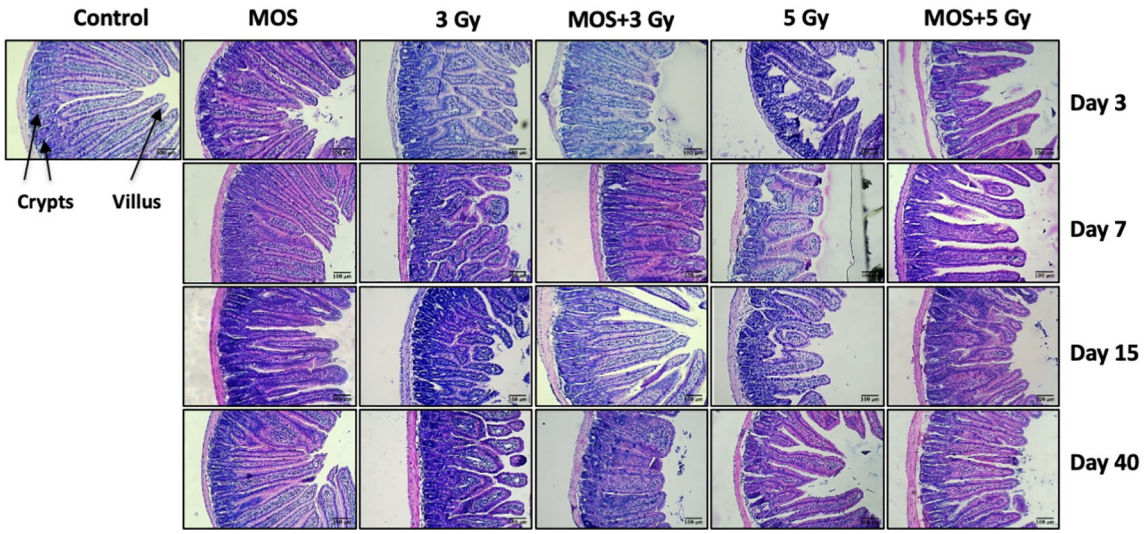

FIGURE 4 | Histological examination of small intestine. Mice were treated with MOS and/or subjected to TBI (3 and 5 Gy) and assessed for histological examination of small intestine on days 3, 7, 15, and 40-post MOS treatment and/or TBI as described in *Materials and Methods*. Scale bar equals 100 μm with an original magnification of ×400.

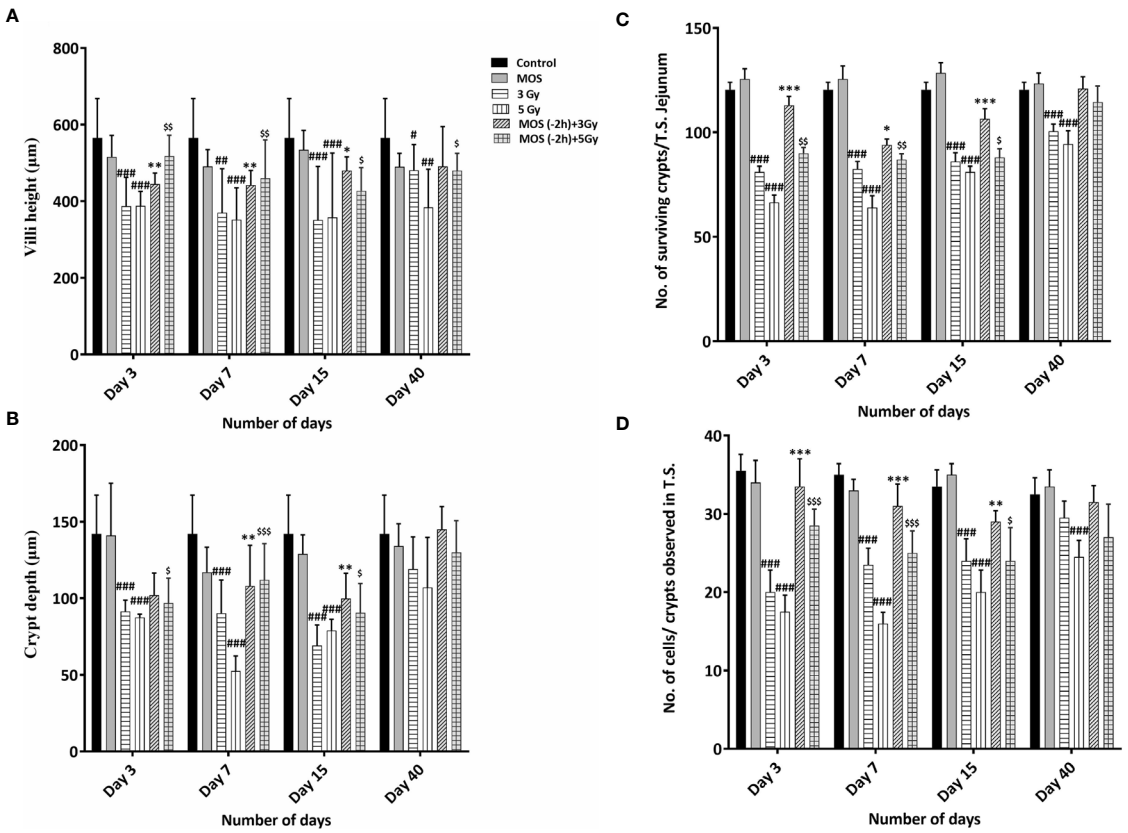

FIGURE 5 | **(A–D)** Histological examination of small intestine: Mice were treated with MOS (200 mg/kg bw) and/or subjected TBI (3 Gy and 5 Gy) and thereafter assessed for histological examinations of small intestine on days 3, 7, 15 and 40-post MOS treatment and/or TBI as described in materials and methods. Representation of **(A)** Villi height (mm) **(B)** Crypt depth (mm) **(C)** No. of surviving crypts/T.S. Jejunum **(D)** No. of cells present per crypt observed in T.S. Error bars represent mean ± SD, and $^{*}p < 0.05$, $^{**}p < 0.01$, $^{***}p < 0.001$, $^{\#}p < 0.05$, $^{\#\#}p < 0.01$, and $^{\#\#\#}p < 0.001$, $^{\$}p < 0.05$, $^{\$\$}p < 0.01$ and $^{\$\$\$}p < 0.001$ were considered significant, $^{\#}$compared to unirradiated control, *compared to 3 Gy irradiated cohorts and $^{\$}$compared to 5 Gy irradiated cohorts.

Xylose Absorption Assay

Functional regeneration and absorptive capacity of the intestines in TBI mice were determined by measuring intestinal absorption of D-xylose. Serum D-xylose level in non-irradiated group was 148 ± 8.88 µg/ml, and there was progressive reduction in xylose absorption in 3 Gy TBI mice (111 ± 8.5 µg/ml, $p < 0.01$), 5 Gy TBI mice (74.66 ± 5.5 µg/ml, $p < 0.001$), and 7.5 Gy irradiated mice (63.66 ± 11.84 µg/ml, $p < 0.001$). MOS pretreatment exhibits significant recovery in the xylose absorption 3 days post TBI in mice exposed to 3 Gy (135 ± 4.16 µg/ml, $p < 0.01$), 5 Gy (134 ± 5.56 µg/ml, $p < 0.001$), and 7.5 Gy (112 ± 9.84 µg/ml, $p < 0.001$); (**Figures 6A–C**). Xylose absorption further declined on day 7 post TBI in the irradiated cohorts 3 Gy (94.33 ± 6.02 µg/ml, $p < 0.001$), 5 Gy (64 ± 6.02 µg/ml, $p < 0.001$), and 7.5 Gy (43.44 ± 4.9 µg/ml, $p < 0.001$) respectively as well as the MOS-pretreated cohorts 3 Gy (125.21 ± 6.32 µg/ml, $p < 0.01$), 5 Gy (113.41 ± 6.02 µg/ml, $p < 0.001$), and 7.5 Gy (90.33 ± 9.29 µg/ml, $p < 0.001$). A time course study (1–40 days) showed significant recovery of xylose absorption in MOS-pretreated cohorts at day 15 post 3 Gy (125.31 ± 6.11 µg/ml, $p < 0.001$), 5 Gy (117.51 ± 6.02 µg/ml, $p < 0.001$) 7.5 Gy TBI (102 ± 8.0 µg/ml, $p < 0.001$) and continued to improve till day 40 post 3 Gy (142.31 ± 7.03 µg/ml, $p < 0.001$), 5 Gy (144.51 ± 7.02 µg/ml, $p < 0.001$), and 7.5 Gy TBI (109.37 ± 19 µg/ml, $p < 0.001$) thereby, indicating the functional regeneration of intestine after radiation injury. The 7.5 TBI cohorts exhibited surplus decline in xylose absorption at day 10 (35.33 ± 5.51 µg/ml, $p < 0.001$) and day 15 (31 ± 3.6 µg/ml, $p < 0.001$) with no surviving animals in the group after day 15. The 7.5 Gy TBI animals were incapable of demonstrating adequate xylose absorption after radiation injury, further contributing to animal mortality. The 3 Gy (84 ± 6.65 µg/ml, $p < 0.001$) and 5 Gy (55.51 ± 6.32 µg/ml, $p < 0.001$) TBI cohorts exhibited further decline in the intestinal absorptive capacity on day 15, with improvement in xylose absorption on day 40 (127.67 ± 7.50 µg/ml, $p < 0.001$) and (101.82 ± 11.21 µg/ml, $p < 0.001$) respectively.

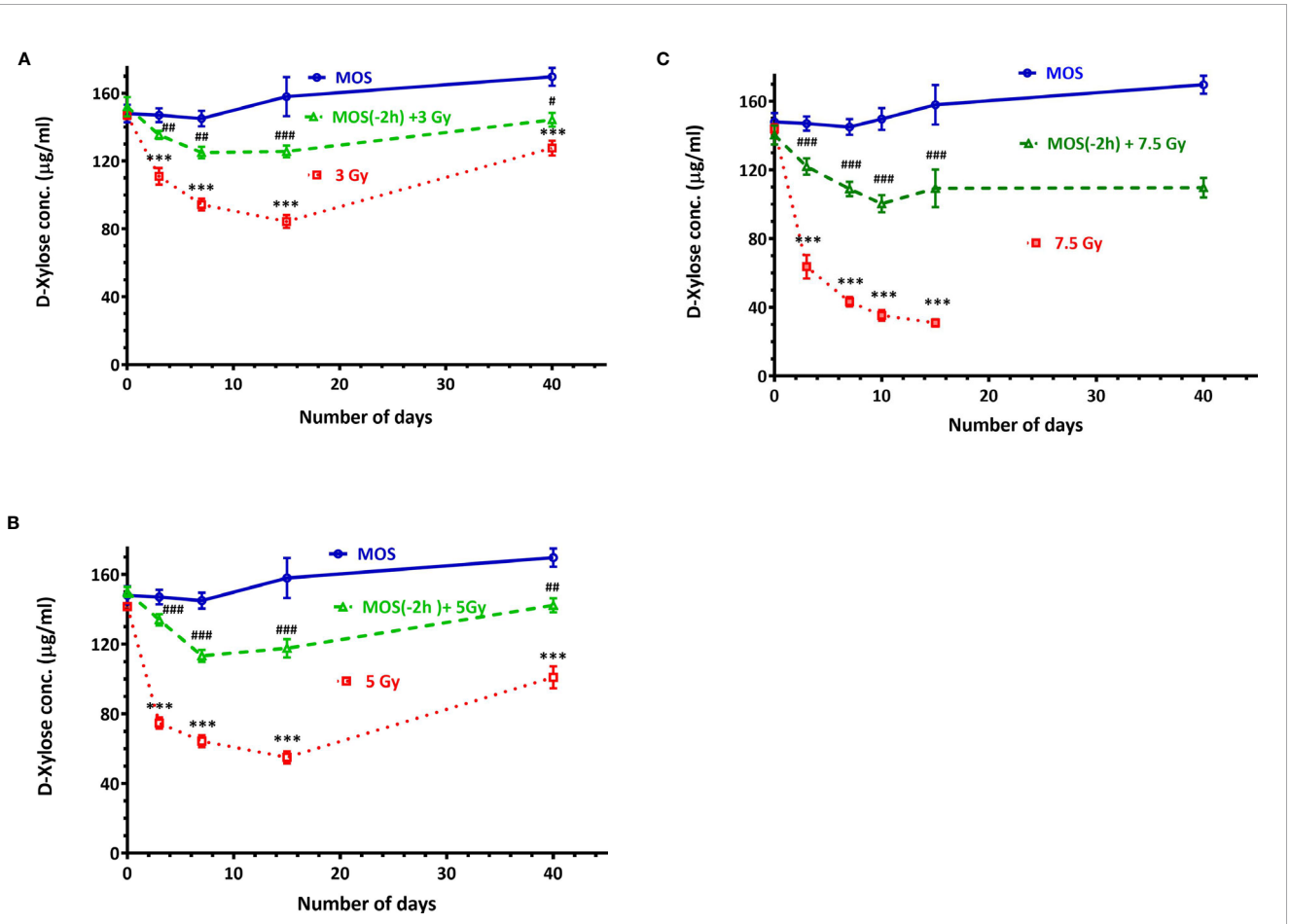

FIGURE 6 | D-Xylose absorption assay: Mice were treated with MOS (200 mg/kg bw) and/or subjected to **(A)** TBI (3 Gy) and assessed for absorptive capacity of the small intestine on days 0, 3, 7, 15, and 40; **(B)** TBI (5 Gy) assessed for absorptive capacity of the small intestine on days 0, 3, 7, 15, and 40; **(C)** TBI (7.5 Gy) assessed for absorptive capacity of the small intestine on days 0, 3, 7, 10, 15, and 40 post TBI as described in *Materials and Methods*. Error bars represent mean ± SD, $^{***}p < 0.001$ were considered significant compared to un-irradiated control group and $^{###}p < 0.001$were considered significant compared to irradiated group.

MOS Pretreatment Lowers MDA Levels in the Kidney and Liver Mitochondria

Ionizing radiation causes extensive damage to lipid component of biological membrane due to initiation of chain reaction of free radical formation (31). Phospholipids along with protein components of the biological membrane are also equally vulnerable to the free radical mediated attack resulting in oxidative modification rendering them non-functional (25, 32). Lipid peroxidation leads to formation of mutagenic MDA, compromising membrane fluidity, integrity, and biological functioning.

Results show intensive increase in MDA concentration 3 days post 3 and 5 Gy TBI mice kidney (72 ± 4.24, $p < 0.001$ and 86.5 ± 6.36, $p < 0.001$ nM/L/mg of mitochondrial protein) in comparison to un-irradiated control (33 ± 4.2, $p < 0.001$); **Figure 7**. MDA concentration remained significantly high in TBI mitochondria (of mice kidney). MOS pretreatment in combination cohorts has shown significant decrease in MDA levels in the kidney mitochondria in comparison to that of irradiated animals at all the studied time points.

MOS Administration Prior to TBI Ameliorates Free Thiol Levels in Mitochondria

Presence of thiols in the biological system is of great significance in redox metabolism both as components of protein structures and as metabolic intermediates. Protein thiols play an important role in many cellular functions, including protein folding, enzyme catalysis, and metabolic regulation. Thiols are present as protein thiols and non-protein thiols and have ability to directly scavenge free radicals. Exposure to IR is known to deplete GSH and other thiols in animal tissues in dose dependent manner. Therefore, measurement of the biological thiols is important to investigate their roles in IR induced oxidative stress. Results show dramatic decrease in thiol concentration 3 days post 3 and 5 Gy TBI mice kidney (3.05 ± 0.778, $p < 0.001$ and 2.25 ± 0.354, $p < 0.001$ nM/L/mg of mitochondrial protein) in comparison to un-irradiated control (6.050 ± 0.35, $p < 0.001$); **Figure 8**. Acid soluble thiol levels remained significantly lesser in TBI mitochondria (of mice kidney) at all time points studied in comparison to that of control.

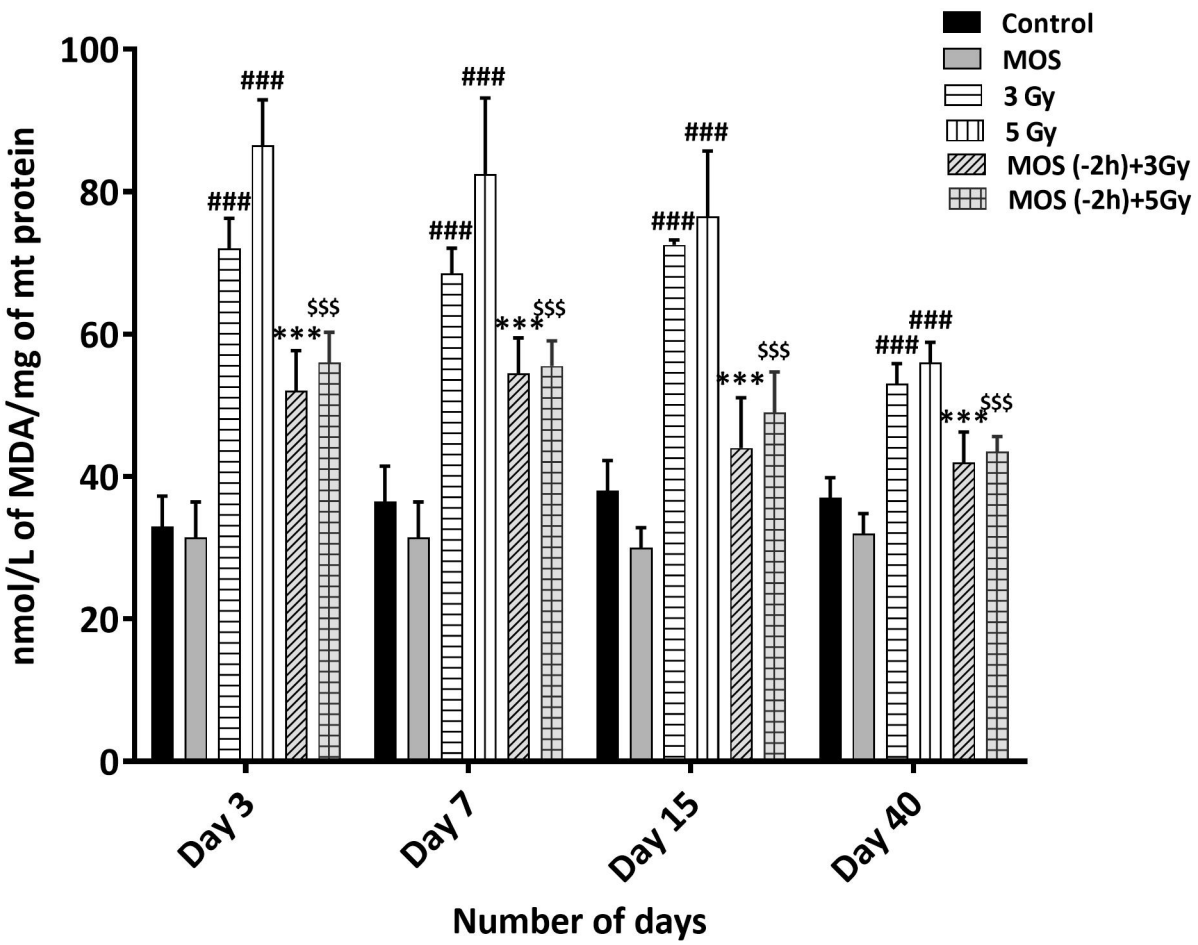

FIGURE 7 | Lipid peroxidation assay: Mice were treated with MOS (200 mg/kg bw) and/or subjected to TBI (3 and 5 Gy) and assessed for MDA levels in mice kidney mitochondria as described in *Materials and Methods*. Error bars represent mean ± SD, $^{###}p < 0.001$ were considered significant compared to un-irradiated control group, $^{***}p < 0.001$ were considered significant compared to irradiated group and $^{\$\$\$}p < 0.001$ were considered significant compared to 5 Gy irradiated group.

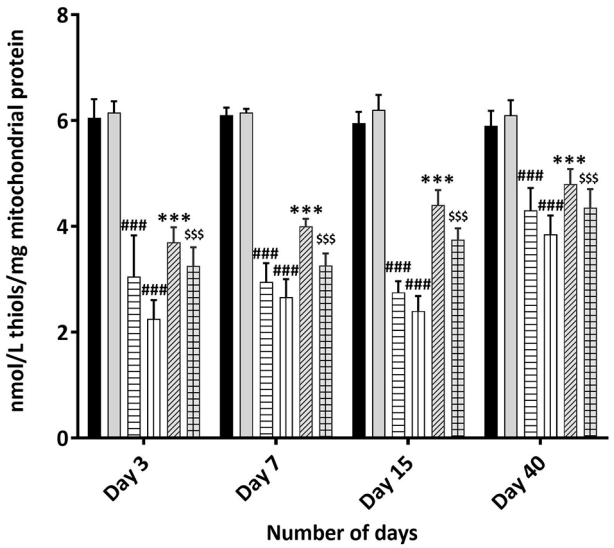

FIGURE 8 | Total Thiol estimation using Ellman's reagent: Mice were treated with MOS (200 mg/kg bw) and/or subjected TBI (3 and 5 Gy) and assessed for total thiol levels in mice kidney mitochondria as described in *Materials and Methods*. Error bars represent mean ± SD, $^{###}p < 0.001$ were considered significant compared to un-irradiated control group, $^{***}p < 0.001$ were considered significant compared to irradiated group and $^{\$\$\$}p < 0.001$ were considered significant compared to 5 Gy irradiated group.

MOS pretreatment in combination cohorts has shown significant increased thiol levels in the kidney mitochondria in comparison to that of irradiated animals at all the studied time points. MOS administration prior to TBI improved thiol levels in mitochondria (kidney) of animals in comparison to that of irradiated group.

DISCUSSION

Prebiotic MOS is reported to have beneficial effects in overall health of an organism, possess intestinal stimulatory capability, and immune modulation potential. And we have earlier reported *in vitro* radiation protection efficacy of MOS in normal cells with intact respiratory function (**Figure 9**) (19). The present study focuses on demonstrating radioprotective effects of MOS, a prebiotic and understanding its role in reducing deleterious effects of TBI on hematopoietic and gastrointestinal system. Mannan pretreatment (IP 50 mg/kg BW or oral 200 mg/kg BW, separately) confers 100% survival advantage to 8–2 weeks old mice (both male and female) against lethal dose of TBI (7.5 Gy) compared to 100% mortality within 14 days after IR exposure alone group (**Figures 1A, B**). Moreover, improved survival (approximately 62 and 50%) in MOS pretreated BALB/c mice (12–13 months old female and male mice respectively) receiving lethal dose (7.5 Gy) of TBI was also observed (**Figure 1D**). There was less decline and consequently prompt recovery of the radiation-induced loss of body weight in MOS pretreated cohort post total body irradiation (TBI) in comparison to irradiated animals (data not shown).

Hematopoietic stem cells and intestinal crypt stem cells are extremely sensitive to damage by IR because of their highly proliferative nature (30). Sensitivity of bone marrow against TBI has been well documented, and pancytopenia is a major factor in radiation-induced morbidity and mortality (33). We assessed the effects of MOS pretreatment on bone marrow and radiation-induced suppression in the number of circulating blood cells by exposing mice to 3 and 5 Gy TBI at days 3, 7, 15, and 40. There was massive ablation of cellular content of the bone marrow and consequent decrease in number of circulating blood cells after 3 and 5 Gy TBI (**Figures 2A–E**). Damage to hematopoietic stem cells results in depletion of peripheral blood lymphocytes and consequently enhances the susceptibility of organism to opportunistic secondary infections. Results reveal reduction in various hematological parameters post TBI, and the baseline levels for most were never achieved in TBI mice. On the other hand, MOS modulated rapid recovery of the constituent parameters leading to attainment almost baseline levels of most peripheral blood cells by day 30 (**Figures 2A–E**). MOS pretreatment in mice reduced radiation induced damage to

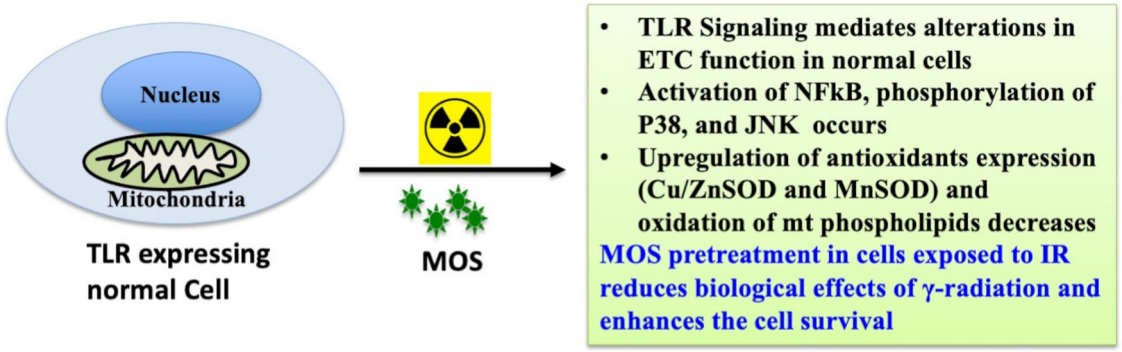

FIGURE 9 | MOS mediated radiation protection *in vitro*: MOS mediated radiation protection in normal cells requires TLR and ETC function. Under *in vitro* system, mannan counters radiation response through activation of NFκB, p38 and JNK, alteration in mitochondrial physiology, increase in MnSOD and Cu/ZnSOD expression, and decrease in peroxidation of cardiolipin inside mitochondrial inner membrane.

hematopoietic stem cells and instigated rapid restoration of bone marrow cellular content (**Figure 3**) resulting in substantial increase in the number of circulating blood cells (**Figures 2A–E**). Stimulation of hematopoietic stem cells might be involved in promoting prompt recovery of hematopoietic system in comparison to irradiated group. IR poses damage to both gastrointestinal system and hematopoietic system and both of these losses can independently or synergistically result in mortality. It has been shown that doses that manifest GI-ARS also impact bone marrow tremendously and lower ability of the body to manage the infections caused by intrusions in intestinal mucosal barrier (34). Contrarily, findings from another study clearly separate the effects of radiation on the GI epithelium from those on the BM or BM-derived cells and have shown that the radio-sensitivity of the BM does not influence radio-sensitivity of the GI epithelium (30). The effects of MOS pretreatment on the radiation-induced damage to the GI system were analyzed by histological examination of the jejunum on days 3, 7, 15, and 40 post TBI. Results depict that MOS pretreatment followed by TBI minimizes crypt cell death and denudation of villi in comparison to the respective irradiated animals. Moreover, MOS pretreated animals showed signs of accelerated overall recovery as demonstrated by substantial decline in blunting, early restoration of normal morphology, and absorption function of small intestine (**Figures 4–6**).

Presence of thiols in biological system is of great significance in redox metabolism both as components of protein structures and as metabolic intermediates (35). Thiols play an important role in many cellular functions, including protein folding, enzyme catalysis, and metabolic regulation (36–38). Thiols have the ability to directly scavenge free radicals and may act as cofactor for enzymes involved in management of oxidative stress (38, 39). Exposure to IR is known to deplete GSH and other thiols in animal tissues in a dose dependent manner. Therefore, we measured acid soluble thiols to investigate their roles in IR induced oxidative stress. MOS administration prior to TBI ameliorated acid soluble thiol levels in mitochondria (of liver and kidney) of animals in comparison to that of irradiated group (**Figure 8**). Ionizing radiation causes extensive damage to lipid component of biological membrane due to initiation of chain reaction of free radical formation (31). Phospholipids along with protein components of the biological membrane are also equally vulnerable to the free radical attack resulting in oxidative modification rendering them non-functional (40). Lipid peroxidation leads to formation of mutagenic MDA, compromising membrane fluidity, integrity, and biological functioning (41). MOS pretreatment in combination cohorts has shown significant decrease in MDA levels in the kidney and liver mitochondria in comparison to that of irradiated animals (**Figure 7**). Mitochondria is an important cell

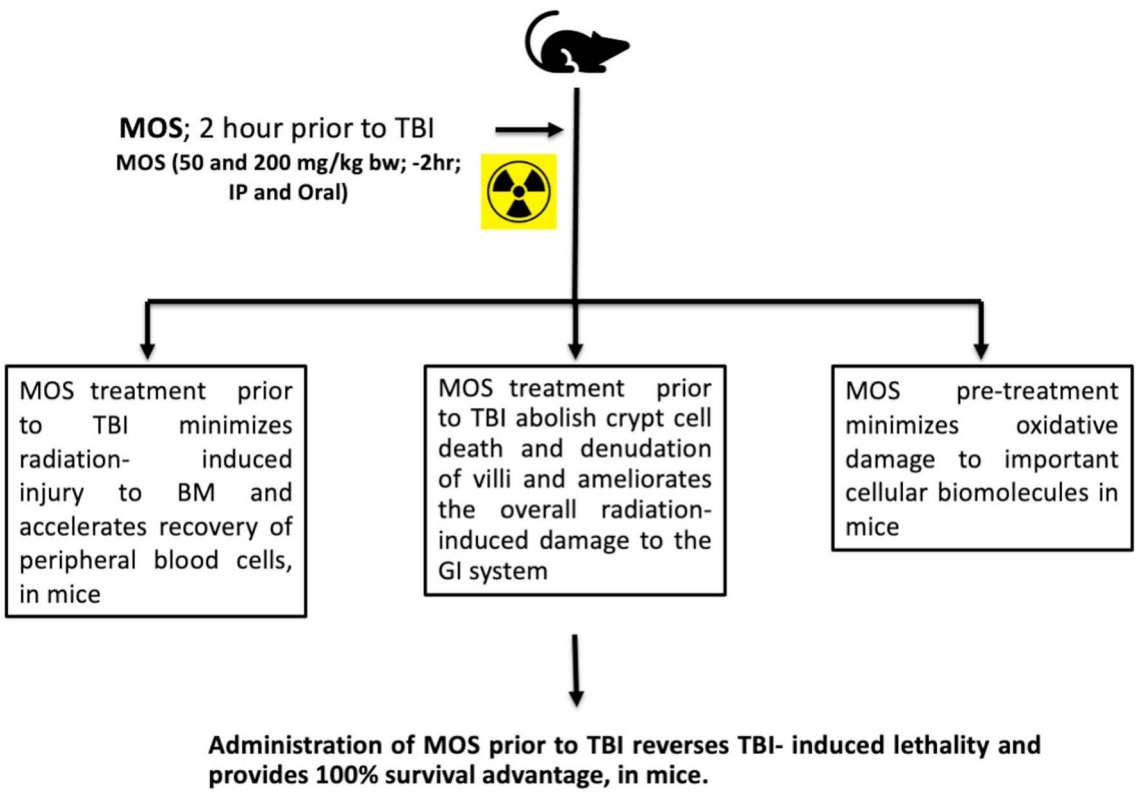

FIGURE 10 | MOS mediated radiation protection *in vivo*: Under *in vivo* condition, MOS pretreatment abates radiation-induced damage to hematopoietic system and gastrointestinal system, accelerates recovery, and consequently abrogates TBI-induced lethality in mice.

organelle that is both a potential source as well as target of ROS. Correspondingly, under *in vitro* system, we have demonstrated that MOS counters IR induced ROS through alteration in mitochondrial physiology, increase in MnSOD and Cu/ZnSOD expression, and decrease in peroxidation of cardiolipin inside mitochondrial inner membrane (19). As aging progresses, there is more damage accumulation in mitochondria, and there is decline in electron transport chain function. Since mitochondrial respiratory capacity is known to decline with age, reduction in survival percent in mannan pretreated aged mice (50–60% in 12–13 months old mice with respect to 100% survival in 8–12 weeks old mice) was well expected after TBI. Another independent study was done in our laboratory to assess the effects of ionizing radiation on GI tract microflora in MOS treated mice post TBI. Mice gut microflora was cultured from the fecal matter followed by characterization of bacteria based on morphology and differential staining. The gut microflora largely remains unperturbed in MOS pretreated mice, and there was decline in microflora type and number in TBI mice. The results of the study will be discussed in detail elsewhere (unpublished data). Results demonstrate that MOS ameliorates the radiation-induced damage to the hematopoietic and GI system, accelerates recovery leading to enhanced animal survival demonstrating its protection efficacy against TBI induced mortality (**Figure 10**).

In summary, MOS treatment prior to TBI effectively minimizes radiation-induced hematopoietic and gastrointestinal injury, accelerates recovery of circulating blood cells, minimizes oxidative damage to important cellular biomolecules, restores intestinal integrity, and consequently abrogates TBI-induced lethality. Earlier, we have shown that TLR and mitochondrial ETC functions are inevitable in radio-protective efficacy exhibited by mannan. These observations clearly demonstrate the potential of MOS as a countermeasure agent to ameliorate biological effects of radiation. Abrogation of damage to both GI and hematopoietic system may play a major role in enhanced recovery of organism and thereby improved overall survival. Further studies are necessary to unravel the mechanisms underlying decrease in the radiation-induced damage to stem cell compartments of tissue and accelerated repair of tissue damage by mannan pretreatment, besides its ability to abolish cellular oxidative stress. In recent years, numerous radiation countermeasure agents have been reported, most of which are efficient but relatively toxic. MOS, as a radiation countermeasure agent, may be beneficial in case of planned radiotherapy events. However, the present study was done on single strain of mice model, and the results need to be validated in other more suitable animal model at pre-clinical levels.

DATA AVAILABILITY STATEMENT

The original contributions presented in the study are included in the article/supplementary material. Further inquiries can be directed to the corresponding author.

ETHICS STATEMENT

The animal study was reviewed and approved by the Animal Ethical Committee, Institute of Nuclear Medicine & Allied Sciences (INMAS), Defence Research and Development Organization (DRDO).

AUTHOR CONTRIBUTIONS

SS and DG designed research, performed research, analyzed data, and wrote the paper. All authors contributed to the article and approved the submitted version.

FUNDING

This study was supported by Defence Research and Development Organization (DRDO), Ministry of Defence, India.

ACKNOWLEDGMENTS

SS is grateful to CSIR for the award of research fellowship. We are grateful to Director, INMAS for providing opportunity to carry out this research work and Defence Research and Development Organization (DRDO), Ministry of Defence, India for providing necessary infrastructure and financial support for research. Cooperation and support of Experimental animal facility INMAS for providing and maintaining animals and Ms. Anjali Sharma for radiation exposure of cells using Bhabhatron II Irradiation facility are acknowledged.

REFERENCES

1. Singh V, Gupta D, Almasan A. Development of Novel anti-CD20 Monoclonal Antibodies and Modulation in CD20 Levels on Cell Surface: Looking to Improve Immunotherapy Response. *J Cancer Sci Ther* (2015) 7(11):347. doi: 10.4172/1948-5956.1000373
2. Singh VK, Romaine PL, Newman VL, Seed TM. Medical Countermeasures for Unwanted CBRN Exposures: Part II Radiological and Nuclear Threats With Review of Recent Countermeasure Patents. *Expert Opin Ther Pat* (2016) 26 (12):1399–408. doi: 10.1080/13543776.2016.1231805
3. Singh VK, Seed TM. A Review of Radiation Countermeasures Focusing on Injury-Specific Medicinals and Regulatory Approval Status: Part I. Radiation Sub-Syndromes, Animal Models and FDA-approved Countermeasures. *Int J Radiat Biol* (2017) 93(9):851–69. doi: 10.1080/09553002.2017.1332438
4. Potten CS, Merritt A, Hickman J, Hall P, Faranda A. Characterization of Radiation-Induced Apoptosis in the Small Intestine and Its Biological Implications. *Int J Radiat Biol* (1994) 65(1):71–8. doi: 10.1080/09553009414550101
5. Ijiri K, Potten CS. The Re-Establishment of Hypersensitive Cells in the Crypts of Irradiated Mouse Intestine. *Int J Radiat Biol Relat Stud Phys Chem Med* (1984) 46(5):609–23. doi: 10.1080/09553008414551801.
6. Potten CS. The Significance of Spontaneous and Induced Apoptosis in the Gastrointestinal Tract of Mice. *Cancer Metastasis Rev* (1992) 11(2):179–95. doi: 10.1007/BF00048063

7. Singh VK, Ducey EJ, Fatanmi OO, Singh PK, Brown DS, Purmal A, et al. CBLB613: A TLR 2/6 Agonist, Natural Lipopeptide of Mycoplasma Arginini, as a Novel Radiation Countermeasure. *Radiat Res* (2012) 177(5):628–42. doi: 10.1667/RR2657.1
8. Burdelya LG, Krivokrysenko VI, Tallant TC, Strom E, Gleiberman AS, Gupta D, et al. An Agonist of Toll-Like Receptor 5 Has Radioprotective Activity in Mouse and Primate Models. *Science* (2008) 320(5873):226–30. doi: 10.1126/science.1154986
9. Singh VK, Seed TM. Entolimod as a Radiation Countermeasure for Acute Radiation Syndrome. *Drug Discov Today* (2021) 26(1):17–30. doi: 10.1016/j.drudis.2020.10.003
10. Momeni-Moghaddam P, Keyvanshokooh S, Ziaei-Nejad S, Parviz Salati A, Pasha-Zanoosi H. Effects of Mannan Oligosaccharide Supplementation on Growth, Some Immune Responses and Gut Lactic Acid Bacteria of Common Carp (Cyprinus Carpio) Fingerlings. *Veterinary Res Forum: An Int Q J* (2015) 6(3):239–44.
11. Hutsko SL, Meizlisch K, Wick M, Lilburn MS. Early Intestinal Development and Mucin Transcription in the Young Poult With Probiotic and Mannan Oligosaccharide Prebiotic Supplementation. *Poultry Sci* (2016) 95(5):1173-8. doi: 10.3382/ps/pew019
12. Razeghi Mansour M, Akrami R, Ghobadi SH, Amani Denji K, Ezatrahimi N, Gharaei A. Effect of Dietary Mannan Oligosaccharide (MOS) on Growth Performance, Survival, Body Composition, and Some Hematological Parameters in Giant Sturgeon Juvenile (Huso Huso Linnaeus, 1754). *Fish Physiol Biochem* (2012) 38(3):829–35. doi: 10.1007/s10695-011-9570-4
13. Halas V, Nochta I. Mannan Oligosaccharides in Nursery Pig Nutrition and Their Potential Mode of Action. *Anim: An Open Access J MDPI* (2012) 2 (2):261–74. doi: 10.3390/ani2020261
14. Sanguri S, Gupta D, Singh T, Singh AK. Biodistribution and Scintigraphic Evaluation of 99mTc-Mannan Complex. *Discov September* (2016) 4:e65. doi: 10.15190/d.2016.12
15. Santos EG, Costa FG, Silva JH, Martins TD, Figueiredo-Lima DF, Macari M, et al. Protective Effect of Mannan Oligosaccharides Against Early Colonization by Salmonella Enteritidis in Chicks Is Improved by Higher Dietary Threonine Levels. *J Appl Microbiol* (2013) 114(4):1158–65. doi: 10.1111/jam.12108
16. Torrecillas S, Montero D, Caballero MJ, Robaina L, Zamorano MJ, Sweetman J, et al. Effects of Dietary Concentrated Mannan Oligosaccharides Supplementation on Growth, Gut Mucosal Immune System and Liver Lipid Metabolism of European Sea Bass (Dicentrarchus Labrax) Juveniles. *Fish Shellfish Immunol* (2015) 42(2):508–16. doi: 10.1016/j.fsi.2014.11.033
17. Madrigal-Santillan E, Alvarez-Gonzalez I, Marquez-Marquez R, Velazquez-Guadarrama N, Madrigal-Bujaidar E. Inhibitory Effect of Mannan on the Toxicity Produced in Mice Fed Aflatoxin B1 Contaminated Corn. *Arch Environ Contamination Toxicol* (2007) 53(3):466–72. doi: 10.1007/s00244-006-0074-7
18. Sanguri S, Gupta D. Role of Toll Like Receptor(s) in Tumor Biology. *J Tumor Med Prev* (2017) 1(7):0013-0019. doi: 10.19080/JTMP.2017.01.555554
19. Sanguri S, Gupta D. Mannan Oligosaccharide Requires Functional ETC and TLR for Biological Radiation Protection to Normal Cells. *BMC Cell Biol* (2018) 19(1):9. doi: 10.1186/s12860-018-0161-4
20. Huhta H, Helminen O, Kauppila JH, Salo T, Porvari K, Saarnio J, et al. The Expression of Toll-Like Receptors in Normal Human and Murine Gastrointestinal Organs and the Effect of Microbiome and Cancer. *J Histochem Cytochem* (2016) 64(8):470–82. doi: 10.1369/0022155416656154
21. Travlos GS. Normal Structure, Function, and Histology of the Bone Marrow. *Toxicol Pathol* (2006) 34(5):548–65. doi: 10.1080/01926230600939856
22. Morson BC. Histopathology of the Small Intestine. *Proc R Soc Med* (1959) 52 (1):6–10. doi: 10.1177/003591575905200102
23. Potten CS. Protection of the Small Intestinal Clonogenic Stem Cells From Radiation-Induced Damage by Pretreatment With Interleukin 11 Also Increases Murine Survival Time. *Stem Cells* (1996) 14(4):452–9. doi: 10.1002/stem.140452
24. Eberts TJ, Sample RH, Glick MR, Ellis GH. A Simplified, Colorimetric Micromethod for Xylose in Serum or Urine, With Phloroglucinol. *Clin Chem* (1979) 25(8):1440–3. doi: 10.1093/clinchem/25.8.1440
25. Goel HC, Gupta D, Gupta S, Garg AP, Bala M. Protection of Mitochondrial System by Hippophae Rhamnoides L. Against Radiation-Induced Oxidative Damage in Mice. *J Pharm Pharmacol* (2005) 57(1):135–43. doi: 10.1211/0022357055218
26. Gupta D, Arora R, Garg AP, Goel HC. Radiation Protection of Mitochondrial System by Podophyllum Hexandrum Royale *In Vivo*. *Mol Cell Biochem* (2004) 266:65–77. doi: 10.1023/B:MCBI.0000049139.05337.40
27. Gupta D, Arora R, Garg AP, Bala M, Goel HC. Modification of Radiation Damage to Mitochondrial System *In Vivo* by Podophyllum Hexandrum: Mechanistic Aspects. *Mol Cell Biochem* (2004) 266(1-2):65–77. doi: 10.1023/B:MCBI.0000049139.05337.40
28. Buege JA, Aust SD. Microsomal Lipid Peroxidation. *Methods Enzymol* (1978) 52:302–10. doi: 10.1016/S0076-6879(78)52032-6
29. Ellman GL. Tissue Sulfhydryl Groups. *Arch Biochem Biophys* (1959) 82(1):70–7. doi: 10.1016/0003-9861(59)90090-6
30. Leibowitz BJ, Wei L, Zhang L, Ping X, Epperly M, Greenberger J, et al. Ionizing Irradiation Induces Acute Haematopoietic Syndrome and Gastrointestinal Syndrome Independently in Mice. *Nat Commun* (2014) 5:3494. doi: 10.1038/ncomms4494
31. Cordeiro RM. Reactive Oxygen Species at Phospholipid Bilayers: Distribution, Mobility and Permeation. *Biochim Biophys Acta* (2014) 1838(1 Pt B):438–44. doi: 10.1016/j.bbamem.2013.09.016
32. Gupta D, Arora R, Garg AP, Goel HC. Radiation Protection of HepG2 Cells by Podophyllum Hexandrum Royale. *Mol Cell Biochem* (2003) 250(1-2):27–40. doi: 10.1023/a:1024925612233
33. Kulkarni S, Singh PK, Ghosh SP, Posarac A, Singh VK. Granulocyte Colony-Stimulating Factor Antibody Abrogates Radioprotective Efficacy of Gamma-Tocotrienol, a Promising Radiation Countermeasure. *Cytokine* (2013) 62 (2):278–85. doi: 10.1016/j.cyto.2013.03.009
34. Booth C, Tudor G, Tudor J, Katz BP, MacVittie TJ. Acute Gastrointestinal Syndrome in High-Dose Irradiated Mice. *Health Phys* (2012) 103(4):383–99. doi: 10.1097/HP.0b013e318266ee13
35. Liu Y, Song Y, Rockenbauer A, Sun J, Hemann C, Villamena FA, et al. Synthesis of Trityl Radical-Conjugated Disulfide Biradicals for Measurement of Thiol Concentration. *J Org Chem* (2011) 76(10):3853–60. doi: 10.1021/jo200265u
36. Klomsiri C, Karplus PA, Poole LB. Cysteine-Based Redox Switches in Enzymes. *Antioxid Redox Signaling* (2011) 14(6):1065–77. doi: 10.1089/ars.2010.3376
37. Biaglow JE, Varnes ME, Clark EP, Epp ER. The Role of Thiols in Cellular Response to Radiation and Drugs. *Radiat Res* (1983) 95(3):437–55. doi: 10.2307/3576092
38. Poole LB. The Basics of Thiols and Cysteines in Redox Biology and Chemistry. *Free Radical Biol Med* (2015) 80:148–57. doi: 10.1016/j.freeradbiomed.2014.11.013
39. Mari M, Colell A, Morales A, von Montfort C, Garcia-Ruiz C, Fernandez-Checa JC. Redox Control of Liver Function in Health and Disease. *Antioxid Redox Signaling* (2010) 12(11):1295–331. doi: 10.1089/ars.2009.2634
40. Orrenius S, Gogvadze V, Zhivotovsky B. Mitochondrial Oxidative Stress: Implications for Cell Death. *Annu Rev Pharmacol Toxicol* (2007) 47:143–83. doi: 10.1146/annurev.pharmtox.47.120505.105122
41. Gulbahar O, Aricioglu A, Akmansu M, Turkozer Z. Effects of Radiation on Protein Oxidation and Lipid Peroxidation in the Brain Tissue. *Transplant Proc* (2009) 41(10):4394–6. doi: 10.1016/j.transproceed.2009.09.076

Conflict of Interest: The authors declare that the research was conducted in the absence of any commercial or financial relationships that could be construed as a potential conflict of interest.

frontiers in Oncology

CASE REPORT
published: 28 June 2021
doi: 10.3389/fonc.2021.709188

Case Report: Treatment of Alectinib in NSCLC With Brain Metastasis Patient Refractory to Radiotherapy After Resistance to Crizotinib

*Chunzhi Zhang**

Department of Radiation Oncology, Tianjin Hospital, Tianjin, China

Background: Brain metastasis is the most common form of tumor recurrence after resistance to crizotinib in patients with anaplastic lymphoma kinase (ALK)-positive non-small-cell lung cancer (NSCLC). The treatment of brain metastasis in patients with ALK-positive NSCLC requires a multidisciplinary approach, including targeted therapy, chemotherapy, and radiotherapy. At present, no optimal treatment for these patients has been identified, although radiotherapy has remained a vital treatment.

Case Presentation: We experienced a patient with ALK-positive NSCLC who developed brain metastasis after crizotinib therapy. ALK rearrangement was not detected in a blood sample using next-generation sequencing. In accordance with National Comprehensive Cancer Network guidance, the patient underwent whole-brain radiotherapy. However, the number of metastatic sites unexpectedly increased. In desperation, the patient was empirically given alectinib after radiotherapy failure, and unanticipated success was achieved.

Conclusions: This case revealed some new insights. First, liquid biopsy is complementary to tissue biopsy in patients with NSCLC, mainly in those with EGFR mutation. However, ALK rearrangement should be assessed using tissue biopsy as much as possible. Second, brain metastasis of NSCLC might respond to second-generation tyrosine kinase inhibitors (TKIs), such as alectinib and ceritinib, after resistance to crizotinib regardless of the presence or absence of ALK rearrangement in liquid biopsy. Finally, combined radiotherapy and TKI therapy appears optimal in patients with brain metastasis of NSCLC after resistance to crizotinib in the absence of a definitive driver gene.

Keywords: anaplastic lymphoma kinase, non-small-cell lung cancer, brain metastasis, radiotherapy, alectinib

Abbreviations: NSCLC, non-small-cell lung cancer; ALK, anaplastic lymphoma kinase; ALKr, anaplastic lymphoma kinase gene rearrangement; BM, brain metastasis; TKIs, tyrosine-kinase inhibitors; CEA, carcinoembryonic antigen; NGS, next-generation sequencing; FISH, fluorescence *in situ* hybridization; WBRT, whole brain radiation therapy; SIB, simultaneous integrated boost; MR, magnetic resonance; CEA, carcinoembryonic antigen.

OPEN ACCESS

Edited by:
Shubhankar Suman, Georgetown University, United States

Reviewed by:
Akshay Pandey, Stanford University, United States
Ashish Kumar, Wake Forest Baptist Medical Center, United States

***Correspondence:**
Chunzhi Zhang
zhchzh_6@hotmail.com

Specialty section:
This article was submitted to Radiation Oncology, a section of the journal Frontiers in Oncology

Received: *13 May 2021*
Accepted: *10 June 2021*
Published: *28 June 2021*

Citation:
Zhang C (2021) Case Report: Case Report: Treatment of Alectinib in NSCLC With Brain Metastasis Patient Refractory to Radiotherapy After Resistance to Crizotinib. Front. Oncol. 11:709188. doi: 10.3389/fonc.2021.709188

INTRODUCTION

As a drive gene mutation, anaplastic lymphoma kinase (ALK) gene rearrangement (ALKr) accounts for 2% to 7% of all cases of non-small-cell lung cancer (NSCLC) (1). Therefore, agents targeting ALKr might precisely treat this subtype of NSCLC. As a first-generation drug targeting ALKr, crizotinib has proven effective in patients with NSCLC harboring ALKr (2). However, most patients experience tumor recurrence within 1 year after crizotinib therapy. Moreover, brain metastasis (BM), which remains a substantial cause of morbidity and mortality, is the most common type of recurrence (3). The treatment of BM of ALK-positive NSCLC requires a multidisciplinary approach, including targeted therapy, chemotherapy, and radiotherapy. To date, no definitive treatment has been established. Haihong et al. reported that patients with BM of ALK-positive lung adenocarcinoma had better overall survival following tyrosine-kinase inhibitor (TKI) treatment or cranial radiotherapy. Moreover, cranial radiotherapy plays an important role in the treatment of these patients (4). A lack of response to radiotherapy has not been previously reported in patients with BM of ALK-positive lung adenocarcinoma. In this study, we found that alectinib was effective in a patient with BM of NSCLC refractory to radiotherapy that was negative for ALKr after resistance to crizotinib. In addition, we discuss the effects of different treatments for BM of ALK-positive lung adenocarcinoma by reviewing the relevant literature.

CASE DESCRIPTION

A 67-year-old man had a greater than 20-year history of smoking 20 cigarettes/day, although he quit smoking 10 years before presentation. In July 2015, he sought medical advice for right supraclavicular lymph node enlargement. Physical examination identified right supraclavicular lymph node enlargement that was not painful. Laboratory data were normal excluding elevation of carcinoembryonic antigen (CEA) levels (8.7). Positron emission tomography (PET) revealed one occupying lesion in the left lung, as well as right supraclavicular lymph node enlargement and multiple mediastinal lymphadenopathies. Moreover, there were multiple bone metastases, including metastases in the fourth cervical vertebra, left first rib, and left pubis (**Figure 1A**). According to the eighth edition of the classification of lung cancer, the stage of this malignancy was IV (T1cN3M1b). Transcutaneous needle biopsy was performed at the site of right supraclavicular lymph node enlargement. Based on the result of immunohistochemical analysis, a diagnosis of poorly differentiated adenocarcinoma was made (**Figure 1B**). Via next-generation sequencing (NGS) and fluorescence *in situ* hybridization, ALKr was detected in biopsy samples. Therefore, crizotinib therapy was started, which resulted in the shrinkage of all lesions after 3 months. In addition, CEA levels had declined to 6.7 at this time. At the end of the follow-up period, all lesions exhibited further shrinkage excluding the left lung lesion,

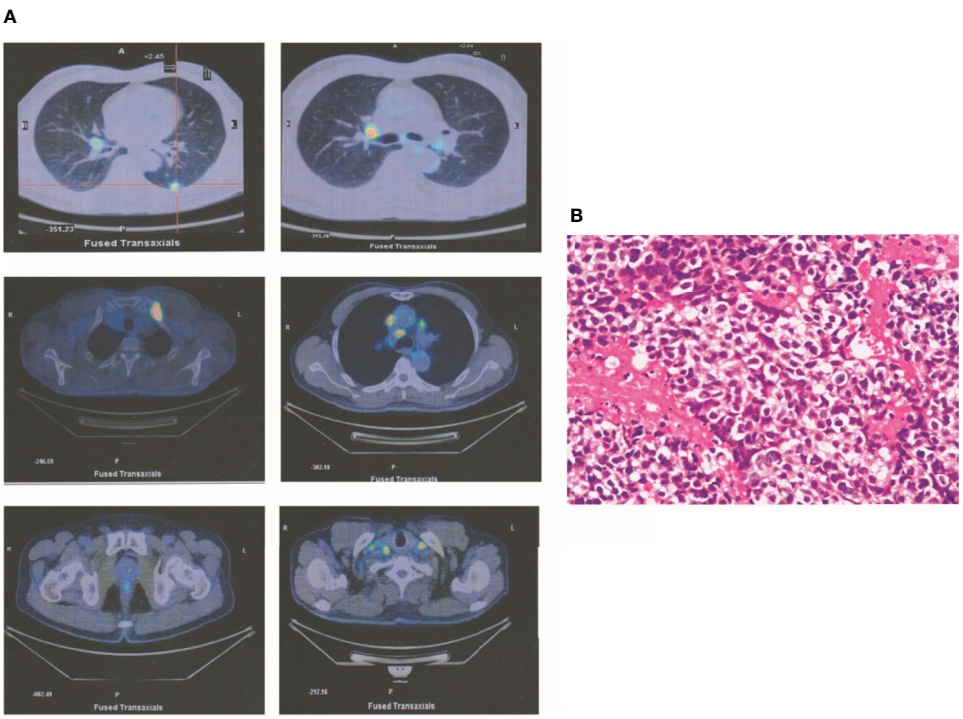

FIGURE 1 | A T1cN3M1b NSCLC patient. **(A)** PET revealed that one occupying lesion is in left lung. There is one right supraclavicular lymph node enlargement and multiple mediastinal lymphadenopathies. Moreover, there were multiple bone metastases, including the fourth cervical vertebra, the left first rib, and the left pubis. **(B)** According to the immunohistochemical analysis, a diagnosis of poorly differentiated adenocarcinoma was made.

which was stable. Laboratory analysis revealed normal CEA levels (<5.0).

In October 2019, the patient experienced dizziness and right hip pain. PET revealed multiple bone metastases in the right ilium and right ischium (**Figure 2A**). Moreover, there were multiple metastatic foci in the brain (**Figure 2A**). Contrast-enhanced magnetic resonance imaging (MRI) disclosed nine BMs (**Figure 2B**). Laboratory analysis revealed a CEA level of 3.6. We recommended biopsy of the right iliac bone. Because the patient had high intracranial pressure and worsening dizziness, he and his family refused biopsy. ALKr was not detected in a blood sample examined *via* NGS. Following Liu's report (5), the patient received whole-brain radiotherapy (WBRT) combined with simultaneous integrated boost (SIB) directed at the metastatic foci. The dose of WBRT was 39.6 Gy delivered in 22 fractions, and that of SIB was 55 Gy delivered in 22 fractions (**Figure 2C**). The patient also received radiotherapy of the right iliac bone lesion (60 Gy in 24 courses, **Figure 2D**). Although radiotherapy resulted in improvement of the patient's right hip pain, his intracranial pressure worsened. The patient underwent MRI after completing 10 fractions of cranial radiotherapy. MRI indicated that the number of BMs had increased to approximately 50 (**Figure 3A**). After careful consideration, we decided to finish WBRT. After finishing WBRT, the patient became comatose, and MRI revealed approximately 80 BMs, including some in the brain stem (**Figure 3B**). Satoh et al. reported that the overall concordance rate of the ALK status was 100% according to immunostaining between histologic and paired liquid-based cytology specimens (6). However, Aldea et al. found that the detection rate of genomic alterations was lower in patients with isolated central nervous system (CNS) progression (7). Because the result of blood testing was doubtful, the patient received alectinib 600 mg twice daily. After a week of oral alectinib treatment, the patient gradually regained consciousness, and his physical symptoms had gradually improved after a month of therapy. MRI revealed a reduction in the number of BMs to approximately 60 and a decrease in the total metastatic tumor volume (**Figure 4A**). Some metastatic foci vanished, especially in the brain stem. However, the right thalamus hemorrhaged and ruptured into the ventricle because the patient autonomously terminated antihypertensive therapy, resulting in cerebral hemorrhage. The patient was treated for cerebral hemorrhage. Meanwhile, the patient continued to take alectinib. After a month of treatment following the development of hemorrhage, the patient's condition had gradually stabilized. MRI illustrated that most of the hematoma was absorbed and the number of BMs had further decreased to approximately 20 (**Figure 4B**). The total metastatic tumor volume had also further decreased.

DISCUSSION AND CONCLUSIONS

BM, which is a frequent complication in patients with NSCLC, is associated with poor survival outcomes, and it poses clinical challenges for oncologists (8). At the initial diagnosis, 10% of patients with NSCLC have BM, and the brain is the only site of tumor relapse in 50% of patients with NSCLC (9). However, the risk of BM is higher in patients with NSCLC harboring ALKr. The rate of BM is approximately 20% in patients with NSCLC harboring ALKr at the initial diagnosis and up to 75% in patients after resistance to crizotinib (10). Therefore, the therapeutic effect on BM plays an important role in prolonging overall survival and improving patient quality of life. However, there is no standard treatment for BM of NSCLC. Prior studies used different strategies to treat BM of NSCLC, including surgery, radiotherapy, chemotherapy, targeted therapy, immunotherapy, and combinations of different modalities (11–15).

Radiotherapy, including WBRT (13, 16, 17) and stereotactic radiosurgery (SRS) (16–18), plays an important role in treating BM of NSCLC harboring driver gene mutations. In accordance with National Comprehensive Cancer Network recommendations,

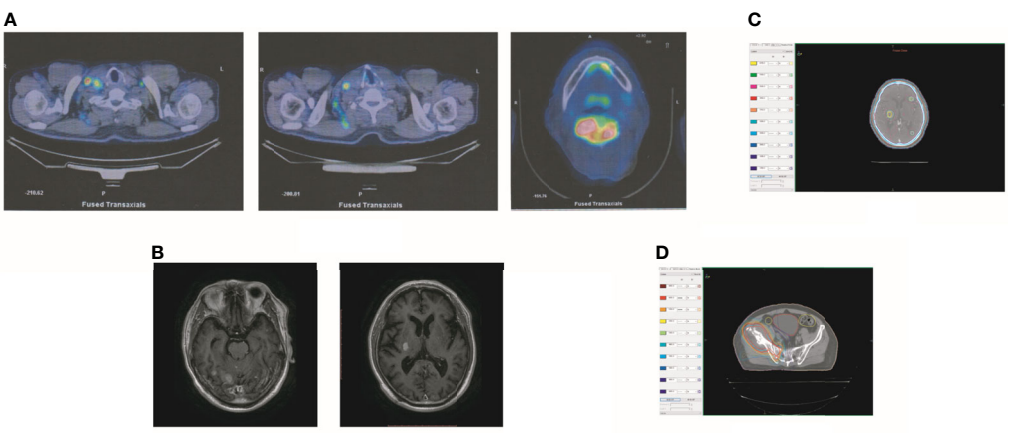

FIGURE 2 | Tumor recurrence after treatment of crizotinib. **(A)** PET revealed multiple bone metastases in the right ilium and the right ischium. Moreover, there were multiple metastatic focuses in the brain. **(B)** The contrasted MR showed that the patient had BM. **(C)** The dose distribution of radiotherapy in BM. **(D)** The dose distribution of radiotherapy in the lesion of the right iliac bone.

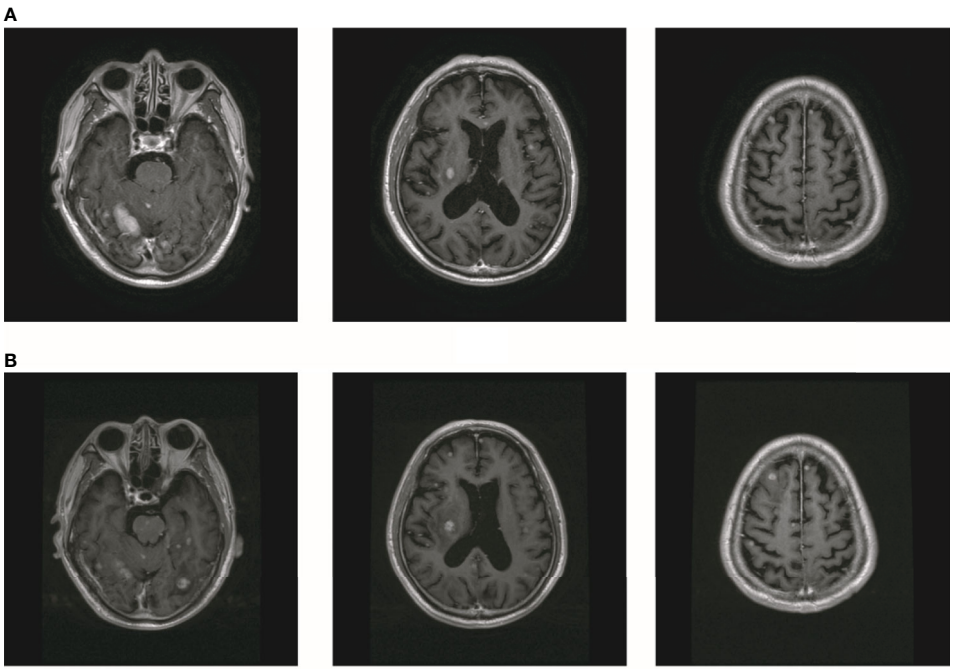

FIGURE 3 | The number of BM increased after radiotherapy. **(A)** The MR showed that the number of brain metastasis increased to about 50. **(B)** MR showed that the number of BM increased to about 80.

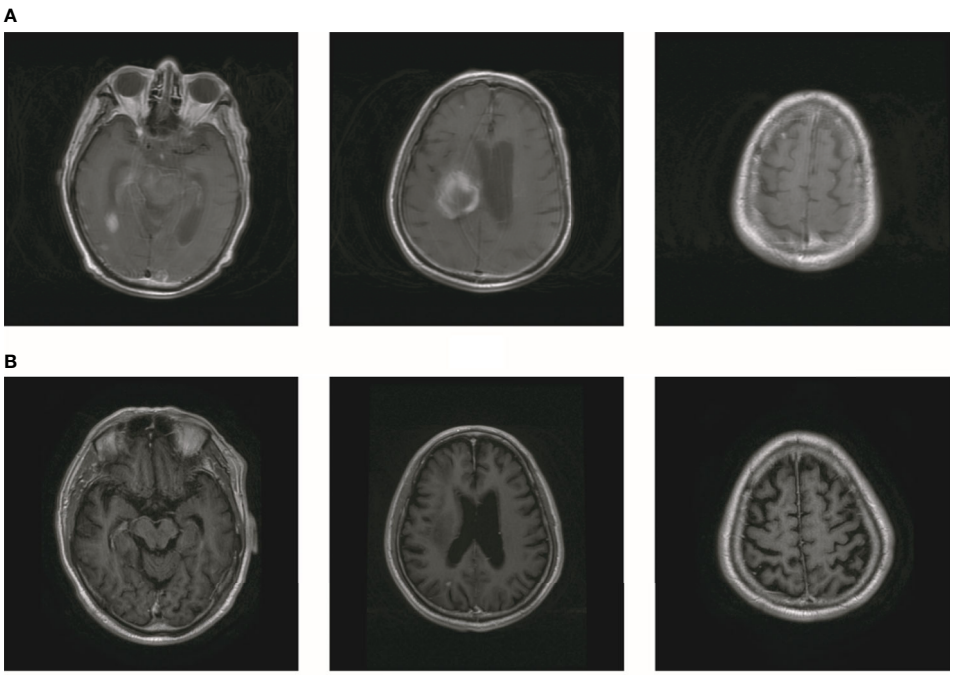

FIGURE 4 | The number of BM decreased after treatment of alectinib. **(A)** MR showed that the number of brain metastasis decreased to about 60. **(B)** The number of brain metastasis further decreased to about 20.

the patient received WBRT. To increase local control, we used SIB to increase the dose delivered to metastatic foci. However, during the course of radiotherapy, the number of BMs inexplicably increased in this patient. This phenomenon has not been reported previously. Prior studies mainly found that WBRT impairs cognitive function and quality of life and cited SRS as an alternative therapy for patients with BM. Some studies reported that SRS achieved good local control and resulted in less cognitive deterioration in patients with one to three BMs (19, 20). Hughes et al. reported that SRS alone could be adapted to treat patients with five to 15 BMs (21). Recently, Robin et al. found that patients with BM and ALKr could uniquely benefit from SRS (20). Thus, SRS alone may become a preferred strategy for treating BMs.

NGS did not identify ALKr in a blood sample from the patient. Therefore, the patient did not continue in using ALK inhibitor. Because of the poor accumulation of crizotinib in the CNS, many NSCLC patients with ALKr frequently develop BM after treatment with the drug. Second-generation ALK inhibitors, such as alectinib, can achieve a higher concentration in the CNS, resulting in enhanced efficacy against BM in NSCLC patients with ALKr (22). After crizotinib failure in patients with ALK-positive NSCLC, Novello et al. reported that alectinib had significantly better efficacy against BM than chemotherapy (3). It is unclear whether the combination of radiotherapy and TKIs has better efficacy against BM than either treatment alone. In a meta-analysis, Singh et al. reported no significant difference in efficacy between combined radiotherapy and TKI therapy and radiotherapy alone. Similarly, there was no significant difference in median overall survival between the TKI, radiotherapy, and combination alternatives (23). Thus, treatment should be selected according to the specific situation of the patient. In our case, the patient empirically received alectinib after radiotherapy failure, and unexpected success was achieved.

In summary, some new insights were revealed in this study. First, liquid biopsy is complementary to tissue biopsy in patients with NSCLC, mainly in those with EGFR mutation. However, ALK rearrangement should be assessed using tissue biopsy as much as possible. Second, brain metastasis of NSCLC might respond to second-generation TKIs, such as alectinib and ceritinib, after resistance to crizotinib regardless of the presence or absence of ALK rearrangement in liquid biopsy. Finally, combined radiotherapy and TKI therapy appears optimal in patients with brain metastasis of NSCLC after resistance to crizotinib in the absence of a definitive driver gene.

DATA AVAILABILITY STATEMENT

The original contributions presented in the study are included in the article/supplementary material. Further inquiries can be directed to the corresponding author.

ETHICS STATEMENT

Written informed consent was obtained from the individual(s) for the publication of any potentially identifiable images or data included in this article.

AUTHOR CONTRIBUTIONS

CZ is responsible for all the work of this manuscript.

ACKNOWLEDGMENTS

We acknowledge the work of colleagues in the Pathology and X-ray Department in offering the original images and data related to this article. We thank Joe Barber Jr., PhD, from Liwen Bianji (Edanz) (https://www.liwenbianji.cn/), for editing the English text of a draft of this manuscript.

REFERENCES

1. Dagogo-Jack I, Yoda S, Lennerz JK, Langenbucher A, Lin JJ, Rooney MM, et al. Met Alterations Are a Recurring and Actionable Resistance Mechanism in ALK-Positive Lung Cancer. *Clin Cancer Res* (2020) 26:2535–45. doi: 10.1158/1078-0432.CCR-19-3906
2. Yang Y, Zhou J, Zhou J, Feng J, Zhuang W, Chen J, et al. Efficacy, Safety, and Biomarker Analysis of Ensartinib in Crizotinib-Resistant, ALK-Positive Non-Small-Cell Lung Cancer: A Multicentre, Phase 2 Trial. *Lancet Respir Med* (2020) 8:45–53. doi: 10.1016/S2213-2600(19)30252-8
3. Novello S, Mazieres J, Oh IJ, de Castro J, Migliorino MR, Helland A, et al. Alectinib Versus Chemotherapy in Crizotinib-Pretreated Anaplastic Lymphoma Kinase (ALK)-Positive Non-Small-Cell Lung Cancer: Results From the Phase III ALUR Study. *Ann Oncol* (2018) 29:1409–16. doi: 10.1093/annonc/mdy121
4. Yang H, He D, Wang F, Deng Q, Xie Z. A Study on Different Therapies and Prognosis-Related Factors for Brain Metastases in Lung Adenocarcinoma Patients With Driver Mutation. *Clin Exp Metastasis* (2020) 37:391–9. doi: 10.1007/s10585-020-10026-2
5. Liu H, Xu X, Wang J, Wang W, Ma C, Sun T, et al. Clinical Study on Different Doses and Fractionated Radiotherapies for Multiple Brain Metastases of Non-EGFR Mutant Lung Adenocarcinoma. *Ann Palliat Med* (2020) 9:2003–12. doi: 10.21037/apm-20-1203
6. Satoh Y, Matsuo Y, Kuba T, Yamashita K, Sawano M, Tozaka S, et al. EGFR Mutation Genotyping and ALK Status Determination in Liquid-Based Cytology Samples of Non-Small Cell Lung Cancer. *Virchows Arch* (2020) 476:753–62. doi: 10.1007/s00428-019-02692-9
7. Aldea M, Hendriks L, Mezquita L, Jovelet C, Planchard D, Auclin E, et al. Circulating Tumor DNA Analysis for Patients With Oncogene-Addicted Nsclc With Isolated Central Nervous System Progression. *J Thorac Oncol* (2020) 15:383–91. doi: 10.1016/j.jtho.2019.11.024
8. Boire A, Brastianos PK, Garzia L, Valiente M. Brain Metastasis. *Nat Rev Cancer* (2020) 20:4–11. doi: 10.1038/s41568-019-0220-y
9. Munsterberg J, Loreth D, Brylka L, Werner S, Karbanova J, Gandrass M, et al. ALCAM Contributes to Brain Metastasis Formation in Non-Small-Cell Lung Cancer Through Interaction With the Vascular Endothelium. *Neuro Oncol* (2020) 22:955–66. doi: 10.1093/neuonc/noaa028
10. Itchins M, Lau B, Hudson AL, Westman H, Xia CY, Hayes SA, et al. Alk-Rearranged Non-Small Cell Lung Cancer in 2020: Real-World Triumphs in an Era of Multigeneration Alk-Inhibitor Sequencing Informed by Drug Resistance Profiling. *Oncologist* (2020) 25:641–9. doi: 10.1634/theoncologist.2020-0075

11. Qing D, Zhao B, Zhou YC, Zhu HL, Ma DY. Whole-Brain Radiotherapy Plus Sequential or Simultaneous Integrated Boost for the Treatment of a Limited Number of Brain Metastases in Non-Small Cell Lung Cancer: A Single-Institution Study. *Cancer Med* (2020) 9:238–46. doi: 10.1002/cam4.2696
12. Goldberg SB, Schalper KA, Gettinger SN, Mahajan A, Herbst RS, Chiang AC, et al. Pembrolizumab for Management of Patients With NSCLC and Brain Metastases: Long-Term Results and Biomarker Analysis From a Non-Randomised, Open-Label, Phase 2 Trial. *Lancet Oncol* (2020) 21:655–63. doi: 10.1016/S1470-2045(20)30111-X
13. Singh R, Lehrer EJ, Ko S, Peterson J, Lou Y, Porter AB, et al. Brain Metastases From non-Small Cell Lung Cancer With EGFR or ALK Mutations: A Systematic Review and Meta-Analysis of Multidisciplinary Approaches. *Radiother Oncol* (2020) 144:165–79. doi: 10.1016/j.radonc.2019.11.010
14. Lin JJ, Schoenfeld AJ, Zhu VW, Yeap BY, Chin E, Rooney M, et al. Efficacy of Platinum/Pemetrexed Combination Chemotherapy in ALK-Positive Nsclc Refractory to Second-Generation Alk Inhibitors. *J Thorac Oncol* (2020) 15:258–65. doi: 10.1016/j.jtho.2019.10.014
15. Ramalingam SS, Vansteenkiste J, Planchard D, Cho BC, Gray JE, Ohe Y, et al. Overall Survival With Osimertinib in Untreated, EGFR-Mutated Advanced Nsclc. *N Engl J Med* (2020) 382:41–50. doi: 10.1056/NEJMoa1913662
16. Glatzer M, Faivre-Finn C, De Ruysscher D, Widder J, Van Houtte P, Troost EGC, et al. Role of Radiotherapy in the Management of Brain Metastases of NSCLC - Decision Criteria in Clinical Routine. *Radiother Oncol* (2021) 154:269–73. doi: 10.1016/j.radonc.2020.10.043
17. Arrieta O, Ramirez-Tirado LA, Caballe-Perez E, Mejia-Perez A, Zatarain-Barron ZL, Cardona AF, et al. Response Rate of Patients With Baseline Brain Metastases From Recently Diagnosed Non-Small Cell Lung Cancer Receiving Radiotherapy According to EGFR, ALK and KRAS Mutation Status. *Thorac Cancer* (2020) 11:1026–37. doi: 10.1111/1759-7714.13359
18. Borghetti P, Bonu ML, Giubbolini R, Levra NG, Mazzola R, Perna M, et al. Concomitant Radiotherapy and TKI in Metastatic EGFR- or ALK-Mutated Non-Small Cell Lung Cancer: A Multicentric Analysis on Behalf of AIRO Lung Cancer Study Group. *Radiol Med* (2019) 124:662–70. doi: 10.1007/s11547-019-00999-w
19. Brown PD, Jaeckle K, Ballman KV, Farace E, Cerhan JH, Anderson SK, et al. Effect of Radiosurgery Alone vs Radiosurgery With Whole Brain Radiation Therapy on Cognitive Function in Patients With 1 to 3 Brain Metastases: A Randomized Clinical Trial. *JAMA* (2016) 316:401–9. doi: 10.1001/jama.2016.9839
20. Robin TP, Camidge DR, Stuhr K, Nath SK, Breeze RE, Pacheco JM, et al. Excellent Outcomes With Radiosurgery for Multiple Brain Metastases in ALK and EGFR Driven Non-Small Cell Lung Cancer. *J Thorac Oncol* (2018) 13:715–20. doi: 10.1016/j.jtho.2017.12.006
21. Hughes RT, McTyre ER, LeCompte M, Cramer CK, Munley MT, Laxton AW, et al. Clinical Outcomes of Upfront Stereotactic Radiosurgery Alone for Patients With 5 to 15 Brain Metastases. *Neurosurgery* (2019) 85:257–63. doi: 10.1093/neuros/nyy276
22. Yang YL, Xiang ZJ, Yang JH, Wang WJ, Xiang RL. Effect of Alectinib Versus Crizotinib on Progression-Free Survival, Central Nervous System Efficacy and Adverse Events in ALK-Positive Non-Small Cell Lung Cancer: A Systematic Review and Meta-Analysis. *Ann Palliat Med* (2020) 9:1782–96. doi: 10.21037/apm-19-643
23. Nakashima T, Nonoshita T, Hirata H, Inoue K, Nagashima A, Yoshitake T, et al. Adverse Events of Concurrent Radiotherapy and ALK Inhibitors for Brain Metastases of ALK-Rearranged Lung Adenocarcinoma. *In Vivo* (2020) 34:247–53. doi: 10.21873/invivo.11767

Conflict of Interest: The author declares that the research was conducted in the absence of any commercial or financial relationships that could be construed as a potential conflict of interest.

frontiers in Oncology

ORIGINAL RESEARCH
published: 01 July 2021
doi: 10.3389/fonc.2021.671431

USP9X Is Required to Maintain Cell Survival in Response to High-LET Radiation

Catherine M. Nickson[1†], Maria Rita Fabbrizi[1†], Rachel J. Carter[1], Jonathan R. Hughes[1], Andrzej Kacperek[2], Mark A. Hill[3] and Jason L. Parsons[1,2]*

[1] Cancer Research Centre, Department of Molecular and Clinical Cancer Medicine, University of Liverpool, Liverpool, United Kingdom, [2] Clatterbridge Cancer Centre NHS Foundation Trust, Bebington, United Kingdom, [3] Department of Oncology, CRUK/MRC Oxford Institute for Radiation Oncology, University of Oxford, Gray Laboratories, Oxford, United Kingdom

Ionizing radiation (IR) principally acts through induction of DNA damage that promotes cell death, although the biological effects of IR are more broad ranging. In fact, the impact of IR of higher-linear energy transfer (LET) on cell biology is generally not well understood. Critically, therefore, the cellular enzymes and mechanisms responsible for enhancing cell survival following high-LET IR are unclear. To this effect, we have recently performed siRNA screening to identify deubiquitylating enzymes that control cell survival specifically in response to high-LET α-particles and protons, in comparison to low-LET X-rays and protons. From this screening, we have now thoroughly validated that depletion of the ubiquitin-specific protease 9X (USP9X) in HeLa and oropharyngeal squamous cell carcinoma (UMSCC74A) cells using small interfering RNA (siRNA), leads to significantly decreased survival of cells after high-LET radiation. We consequently investigated the mechanism through which this occurs, and demonstrate that an absence of USP9X has no impact on DNA damage repair post-irradiation nor on apoptosis, autophagy, or senescence. We discovered that USP9X is required to stabilize key proteins (CEP55 and CEP131) involved in centrosome and cilia formation and plays an important role in controlling pericentrin-rich foci, particularly in response to high-LET protons. This was also confirmed directly by demonstrating that depletion of CEP55/CEP131 led to both enhanced radiosensitivity of cells to high-LET protons and amplification of pericentrin-rich foci. Our evidence supports the importance of USP9X in maintaining centrosome function and biogenesis and which is crucial particularly in the cellular response to high-LET radiation.

Keywords: centrosome, DNA damage, DNA repair, ionizing radiation, protons, ubiquitin, USP9X

OPEN ACCESS

Edited by:
Pankaj Chaudhary, Queen's University Belfast, United Kingdom

Reviewed by:
Rupak Pathak, University of Arkansas for Medical Sciences, United States
Paul F. Wilson, University of California, Davis, United States

***Correspondence:**
Jason L. Parsons
j.parsons@liverpool.ac.uk

[†]These authors have contributed equally to this work

Specialty section:
This article was submitted to Radiation Oncology, a section of the journal Frontiers in Oncology

Received: *23 February 2021*
Accepted: *15 June 2021*
Published: *01 July 2021*

Citation:
Nickson CM, Fabbrizi MR, Carter RJ, Hughes JR, Kacperek A, Hill MA and Parsons JL (2021) USP9X Is Required to Maintain Cell Survival in Response to High-LET Radiation. Front. Oncol. 11:671431. doi: 10.3389/fonc.2021.671431

INTRODUCTION

Ionizing radiation (IR) is a major cancer treatment modality for primary and metastatic cancers. Although conventional radiotherapy (e.g. X-rays) is largely employed, there is an increase in the utilization of precision proton beam therapy (PBT) that can more accurately deliver the radiation dose to the tumor, thus limiting any adverse side effects. In particular, PBT is used for the treatment of solid tumors, such as head and neck squamous cell carcinoma (1). The therapeutic effect of IR is

predominantly through the induction of DNA damage that ultimately drives cancer cell death. As well as DNA double strand breaks (DSBs), IR causes the formation of complex DNA damage (CDD), which is defined as two or more DNA lesions within one or two DNA helical turns, that contribute to the cell killing effects of the radiation (2–4). This is particularly relevant following high-linear energy transfer (LET) radiation that generates increased quantities and complexity of CDD. Indeed, PBT displays increases in LET at the Bragg peak and at the distal edge where the majority of the radiation dose is delivered, which creates uncertainty in the treatment because of the different biological effects (5). Specifically within cultured cells, CDD has been shown to persist for several hours post-irradiation (6, 7), and therefore, its importance in promoting genome instability and cell death following IR is recognized (5, 8). Although the biological impact of high-LET radiation is largely associated with the direct effects of irreparable CDD induction, this has also been demonstrated to promote disruption and persistent changes to chromatin structure (9, 10), enhance cellular senescence (11), and to increase apoptotic signaling (12). This reflects, to some degree, the potentially diverse mechanisms through which high-LET radiation may act.

The ubiquitin proteasome pathway, catalyzed by E3 ubiquitin ligases and deubiquitylation enzymes (DUBs), is known to be important in the regulation of several DNA repair pathways where it acts to control the cellular levels of key proteins that co-ordinate the repair of the DNA damage (13–15). Recently, we discovered that ubiquitylation is a key factor in the cellular response to high-LET radiation, including high-LET α-particles and protons. Specifically, we identified that histone H2B ubiquitylation on lysine 120, which is catalyzed by the E3 ubiquitin ligases ring finger protein 20/40 (RNF20/40) and male-specific lethal-2 homolog (MSL2), is induced following high-LET radiation. Induction of histone H2B ubiquitylation in turn promotes the repair of CDD required for cell survival (6). Subsequently, we utilized an siRNA screening strategy to identify that ubiquitin specific protease 6 (USP6) is important for maintaining levels of the DNA repair protein poly (ADP-ribose) polymerase-1 (PARP-1), which is similarly essential for efficient repair of CDD and thus survival of cells following irradiation with high-LET α-particles and protons (7). Our findings also highlighted the involvement of other DUBs in controlling cell survival under these conditions, although their precise roles and mechanisms of action in response to high-LET radiation are yet to be determined.

The ubiquitin-specific protease 9X (USP9X) is a highly conserved DUB, which has been suggested to play several important roles, particularly in maintaining cell survival, development, and polarity, as well as in protein trafficking (16). Specifically, USP9X has been shown to regulate apoptosis by initiating the apoptotic c-Jun N-terminal kinase (JNK) signaling cascade in neurons and embryonic kidney cells (17, 18). Conversely, USP9X is also proposed to be involved in the stabilization of the anti-apoptotic protein Mcl-1 by protecting it from ubiquitylation-dependent proteasomal degradation (19, 20), indicating that the role of USP9X in cell death regulation may be cell-type and disease specific. In fact, a role for USP9X in cancer development is not yet clear, having been found to act both as an oncogene and a tumor suppressor, depending on the type and stage of cancer (16). More recently, there has been accumulating evidence identifying USP9X as a major player in the maintenance and stability of key centriolar satellite proteins, consequently involved in promoting centrosome duplication (21–24). However, a role for USP9X in the cellular response to IR, and specifically the impact of the enzyme following high-LET radiation, has not been previously reported.

In this study, we have now further examined the roles of other DUBs that are required to promote cell survival specifically in response to high-LET radiation, with a focus on PBT that generates increasing LET particularly at the Bragg peak distal end. We demonstrate that an siRNA knockdown of USP9X leads to increased cell death specifically in response to high-LET protons and α-particle irradiation, but not to low-LET protons and X-rays. We further show that this reduction in cell survival in USP9X-depleted cells does not correlate with alterations in the efficiency of CDD repair or with the activation of cell death pathways, but is in fact mediated by centriolar satellite accumulation.

MATERIALS AND METHODS

Antibodies and siRNA

The DUB siRNA library (ON-TARGETplus), USP9X siRNA pool and individual siRNA targeting USP9X (USP9X_6 5′-AGAAAUCGCUGGUAUAAAU-3′ and USP9X_8 5′-GUACGACGAUGUAUUCUCA-3′) were from Horizon Discovery (Cambridge, UK). The non-targeting control siRNA (AllStars Negative Control siRNA) was from Qiagen (Manchester, UK). The following antibodies were used: PARP-1 (sc-53643) and Mcl-1 (sc-819; both Santa Cruz Biotechnology, Heidelberg, Germany), γH2AX (05-636; Merck-Millipore, Watford, UK), USP9X (A301-350A) and 53BP1 (A300-272A; both Bethyl Labs, Montgomery, AL), LC3B (2775) and β-Galactosidase (9860; both Cell Signaling Technology, London, UK), Pericentrin (ab4448; Abcam, Cambridge, UK), CEP55 (23891-1-AP) and CEP131 (25735-1-AP; both Proteintech, Manchester, UK) and tubulin (T6199; Sigma-Aldrich, Gillingham, UK). Goat anti-mouse Alexa Fluor 555 (A21422) or goat anti-rabbit Alexa Fluor 488 (A11008) secondary antibodies for immunofluorescence were from Life Technologies (Paisley, UK).

Cell Culture and Irradiation Sources

Oropharyngeal squamous cell carcinoma cells (UMSCC74A) were kindly provided by Prof T. Carey, University of Michigan, USA. HeLa and UMSCC74A cells were routinely cultured as monolayers in Dulbecco's Modified Eagle Medium (DMEM) supplemented with 10% fetal bovine serum, 2 mM L-

glutamine, 1× penicillin-streptomycin and 1× non-essential amino acids. siRNA knockdowns were performed for 48 h using Lipofectamine RNAiMAX (Life Technologies, Paisley, UK). Irradiation sources are as previously described (6). In brief, cells were exposed to either low-LET X-rays (100 kV; CellRad X-ray irradiator, Faxitron Bioptics, Tucson, USA; dose rate of ~3 Gy/min), or with a horizontal, passive-scattered proton beam line of 60 MeV maximal energy at the Clatterbridge Cancer Centre. These low-energy X-rays will generate higher LET photoelectrons and therefore a raised RBE when compared to higher energy photon sources (25, 26). For low-LET proton irradiations, cells were irradiated directly by a ~1 keV/μm pristine beam of 58 MeV effective energy (dose rate of ~5 Gy/min). For high-LET proton irradiations, a modulator was utilized to generate a 27-mm spread-out Bragg peak and a 24.4-mm absorber was used to position the cells at the distal edge, corresponding to a mean proton energy of 11 MeV at a dose averaged LET of 12 keV/μm (dose rate of ~5 Gy/min). The LET was an estimation based on previous work utilizing the Clatterbridge beam (27) and considering the proton stopping power at this range. RBE values of 1.67 ± 0.14 (Hela) and 1.85 ± 0.15 (UMSCC74A), comparing high-LET *versus* low-LET protons, have been previously determined (6). High-LET α-particle irradiations (3.26 MeV, 121 keV/μm) were performed on cells grown on Mylar sealed on glass cylinders using a ^{238}Pu irradiator at the CRUK/MRC Oxford Institute for Radiation Oncology, as previously described (28, 29). Assuming a typical cross-sectional nuclear area of an attached Hela and UMSCC74A cell of ~150 μm^2, these irradiations correspond to a mean of ~940, 78, and 7.7 nuclear traversals per Gy for low-LET protons, high-LET protons, and α-particle irradiations, respectively (29), with the number following a Poisson distribution and dependent on the natural variation in nuclear cross-sectional area with the cell cycle.

Clonogenic Assays

Clonogenic assays were performed as recently described (6, 7). In brief, following siRNA treatments, cells were irradiated in 35-mm dishes, harvested and a defined number seeded in triplicate into 6-well plates. Plating efficiencies for the untreated cells were as follows: HeLa (~40%), UMSCC74A (~10%). Plating efficiencies for USP9X siRNA-treated cells were as follows: HeLa (~30%), UMSCC74A (~4%). Increasing cell numbers were plated for increasing IR doses to allow for reductions in plating efficiencies. Colonies were allowed to grow for 7 to 10 days prior to fixing and staining with 6% glutaraldehyde and 0.5% crystal violet for 30 min. Dishes were washed, left to air dry overnight and colonies counted using the GelCount colony analyzer (Oxford Optronics, Oxford, UK). Colony counting settings were optimized for both cell lines, based on inclusion of distinct colonies of specific size and intensity, although the same settings were used across the various treatments. A colony is defined as containing 50 or more cells. Relative colony formation (surviving fraction) was expressed as colonies per treatment level *versus* colonies that appeared in the untreated control. Results were accumulated from at least three independent biological experiments, apart from the siRNA screen which was from a single experiment (but containing triplicate samples).

Cell Cycle Analysis and Immunoblotting

For cell cycle analysis, cells were trypsinized, washed twice with ice-cold PBS (100 × *g* for 5 min at 4°C), fixed with ice cold 70% ethanol and kept at 4°C until analysis. Fixed cells were centrifuged (200 × *g* for 5 min at 4°C), washed with PBS containing 0.05% Tween-20, and then resuspended in PBS containing 0.05% Tween-20, 10 μg/ml propidium iodide and 0.1 mg/ml RNase A for 1 h at room temperature. Analysis was performed using the Attune NxT Flow Cytometer (Life Technologies, Paisley, UK). Whole-cell extracts were prepared, separated by SDS-PAGE electrophoresis, and analyzed by quantitative immunoblotting using the Odyssey image analysis system (Li-cor Biosciences, Cambridge, UK), as previously described (30, 31).

Enzyme-Modified Neutral Comet Assay

Detection of CDD was achieved using enzyme treatment of DNA originally described by Sutherland et al. (32, 33), but which has been employed in development of the enzyme-modified neutral comet assay, as recently described (34). In brief, cells were trypsinized, diluted to 1 × 10^5 cells/ml and 250-μl aliquots of the cell suspension placed into the wells of a 24-well plate, which was placed on ice. Cells were irradiated (4 Gy) and embedded on a microscope slide in low melting agarose (Bio-Rad, Hemel Hempstead, UK). The slides were incubated for up to 4 h at 37°C in a humidified chamber to allow for DNA repair, prior to cell lysis in buffer containing 2.5 M NaCl, 100 mM EDTA, 10 mM Tris-HCl pH 10.5, 1% N-lauroylsarcosine, 1% DMSO, and 1% (v/v) Triton X-100. Slides were washed three times with enzyme reaction buffer (40 mM HEPES-KOH, 100 mM KCl, 0.5 mM EDTA and 0.2 mg/ml BSA, pH 8.0), and then incubated with either buffer alone (mock-treated; revealing levels of DNA DSBs) or with buffer containing 5 pmol OGG1, 6 pmol NTH1, and 0.6 pmol APE1 (enzyme-treated; revealing levels of DNA DSBs plus CDD) for 1 h at 37°C in a humidified chamber. Following treatment, slides were placed in cold electrophoresis buffer [1 × TBE buffer (pH 8.3)] in the dark for 25 min to allow the DNA to unwind, prior to electrophoresis at 25 V, ~20 mA for 25 min. Slides were washed three times with 1× PBS before allowing to dry overnight. Slides were rehydrated for 30 min in water (pH 8.0), stained for 30 min with SYBR Gold (Life Technologies, Paisley, UK), diluted 1:10,000 in water (pH 8.0), and again dried overnight. Cells (50 per slide, in duplicate) were analyzed from the dried slides using the Komet 6.0 image analysis software (Andor Technology, Belfast, Northern Ireland) and % tail DNA values averaged from at least three independent biological experiments.

Immunofluorescence and β-Galactosidase Staining

Measurement of DNA repair protein foci (γH2AX and 53BP1) was examined as previously described (30). In brief, cells were grown on 13-mm coverslips until ~70% to 80% confluent, irradiated at 4 Gy and incubated for up to 8 h in 5% CO_2 at

37°C to allow for DNA repair. Cells were washed with PBS at room temperature for 5 min, before being fixed using 4% paraformaldehyde for 10 min. Cells were permeabilized with 0.2% Triton X-100 in PBS for 10 min, washed three times with 0.1% Tween-20 for 10 min, and blocked to avoid non-specific staining *via* incubation with 2% BSA for 30 min at room temperature on a rocking platform. γH2AX or 53BP1 antibodies in 2% BSA were subsequently added and coverslips incubated overnight at 4°C. Following three washes with PBS, coverslips were incubated with either goat anti-mouse Alexa Fluor 555 or goat anti-rabbit Alexa Fluor 488 secondary antibodies in 2% BSA for 1 h at room temperature in the dark. Finally, samples were washed with PBS for 10 min on a rocking platform and mounted on a microscope slide using Fluoroshield containing DAPI (Sigma-Aldrich, Gillingham, UK). Cells were examined using an Olympus BX61 fluorescent microscope with a Photometrics CoolSNAP HQ2 CCD camera. MicroManager software was used to capture images (~20 images/cell line/antibody). Similarly, cells were fixed on coverslips post-irradiation (4 Gy) and incubation (48 h), but then stained using Pericentrin antibodies prior to incubation with AlexaFluor488 secondary antibodies, and pericentrin-rich foci scored using fluorescence microscopy. Analysis of senescence was carried out using the β-Galactosidase Staining kit (Cell Signaling Technology, London, UK) and where hydrogen peroxide (100 μM for 2 h) was used as a positive control.

Statistical Analysis

All experiments (unless defined above) were performed in at least triplicate as separate independent, biological experiments. Statistical analysis of clonogenic survival data was performed using a one-way ANOVA and comparing surviving fractions at 2 Gy (SF2) or 4 Gy (SF4). Statistical analysis of DNA damage quantified through neutral comet assays and pericentrin-rich foci through immunofluorescence staining was performed using either a one-sample or two-sample *t* test.

RESULTS

Screening for DUBs Involved in Response to High-LET IR

In our recent work, we performed an siRNA screen of 84 DUBs analyzing the survival of HeLa cells after a single dose of IR, with a particular focus on high-LET IR, which generates increased levels and complexity of CDD consisting of two or more DNA lesions within one or two helical turns of the DNA (7). We have now further interrogated these data, which demonstrates the wide range of changes in HeLa cell survival in response to a single dose of high-LET α-particles (121 keV/μm) *versus* low-LET X-rays following individual DUB knockdowns (**Figure 1A**). Similarly, a variability in cell survival in the absence of the DUBs is observed in response to relatively high-LET protons (12 keV/μm) generated at the Bragg peak distal edge, *versus* low-LET protons (1 keV/μm) at the entrance dose of a pristine beam (**Figure 1B**). Survival was normalized to the irradiated mock-treated control sample (generating ~40% cell survival), which was set to 1.0, and the data subsequently plotted (on a $\log_2$ scale). The top 10 DUB candidates reducing cell survival in response to high-LET α-particles (**Table 1**) and relatively high-LET protons (**Table 2**), in addition to their impact on survival following low-LET protons and X-rays, are shown. We focused our attention on candidate enzymes whose depletion led to a specific reduction in cell survival following high-LET radiation. This led us to identify that depletion of USP9X caused no reduction in cell survival after low-LET X-ray or proton irradiation, whereas survival after high-LET α-particles and protons was reduced by ~20% and ~40%, respectively (**Tables 1**, **2**).

USP9X Modulates Cell Survival in Response to High-LET IR

Following siRNA screening, we aimed to validate that depletion of USP9X caused a decrease in cell survival following high-LET radiation, but had no impact in response to low-LET protons, in

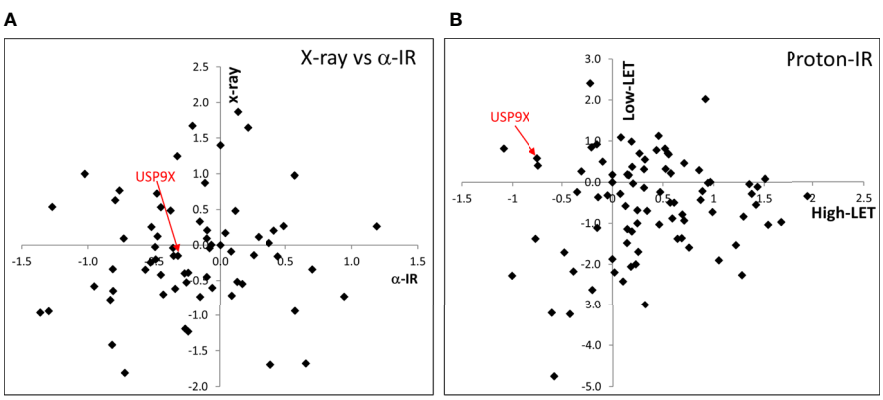

FIGURE 1 | siRNA screen of DUBs modulating cell survival following high and low LET radiation. HeLa cells were transfected with siRNA (pool of 4 oligonucleotides) targeting individual DUBs for 48 h, and irradiated with either **(A)** 0.5 Gy α-particles or 1 Gy X-rays, or **(B)** 2 Gy relatively high-LET protons or 2 Gy low-LET protons. Clonogenic survival was analyzed from a single experiment (using triplicate samples) and normalized against the mock-treated control. Results are shown as a $\log_2$ plot, and indicated is the clonogenic survival following USP9X depletion. Data has been adapted from (7).

TABLE 1 | Candidate DUBs whose siRNA-mediated depletion enhance radiosensitivity of cells in response to α-particle radiation.

DUB enzyme	α-particles	X-rays	High-LET protons	Low-LET protons
USP6	0.39	0.51*	0.60	1.32
USP21	0.41	0.52	1.06	0.82
USP36	0.41	1.45	0.66	0.11
DUB3	0.49	2.00	0.90	1.89
STAMBPL1	0.52	0.67	0.72	0.31
UCHL3	0.56	0.59	1.69	0.33
AMSH	0.57	0.37	1.47	1.59
CYLD	0.57	0.79	0.47	1.76
UCHL5	0.57	0.64	1.51	0.54
OTUB1	0.58	1.55	1.99	0.61
USP9X	**0.80**	**0.90**	**0.60**	**1.50**

*Surviving fractions from a single experiment containing triplicate samples were normalized against the mock-treated control, which was set to 1.0. Survival data acquired in response to USP9X depletion is highlighted in bold. *Previously identified as a false positive result, data adapted from (7).*

TABLE 2 | Candidate DUBs whose siRNA-mediated depletion enhance radiosensitivity of cells in response to high-LET protons.

DUB enzyme	High-LET protons	Low-LET protons	α-particles	X-rays
CYLD	0.47	1.76	0.57	0.79
USP7	0.50	0.21	1.30	1.02
USP31	0.59	0.38	n.d.	n.d.
USP9X	**0.60**	**1.50**	**0.80**	**0.90**
USP6	0.60	1.32	0.39	0.51*
USP36	0.66	0.11	0.41	1.45
USP39	0.67	0.04	n.d.	2.64
STAMBPL1	0.72	0.31	0.52	0.67
USP43	0.74	0.11	n.d.	n.d.
YOD1	0.77	0.22	0.78	0.90

*Surviving fractions from a single experiment containing triplicate samples were normalized against the mock-treated control, which was set to 1.0. n.d. indicates not determined. Survival data acquired in response to USP9X depletion is highlighted in bold. *Previously identified as a false positive result, data adapted from (7).*

both HeLa cells and also cells derived from head and neck squamous cell carcinoma. In response to USP9X siRNA (pool of 4 siRNAs utilized in the screen), there was no impact on cell survival following a dose titration of low-LET X-rays (**Figures 2A, B**) or low-LET protons (**Figures 2E, F**) in comparison to non-targeting (NT) control siRNA-treated cells. In fact, depletion of USP9X appeared to cause a mild increase in radioresistance following low-LET protons. However, in contrast to low-LET radiation, USP9X siRNA led to reduced survival in response to high-LET α-particles (**Figures 2C, D**), and more dramatically in response to relatively high-LET protons (**Figures 2G, H**). To further validate that our observations were specific, we utilized two single siRNA sequences (USP9X_6 and USP9X_8) that were demonstrated to be effective in suppressing USP9X protein levels in both HeLa (**Figure 3A**) and UMSCC74A oropharyngeal squamous cell carcinoma cells (**Figure 3B**). We focused on the impact of protons, particularly as PBT is employed clinically for the treatment of tumors, including head and neck squamous cell carcinoma. We confirmed that targeting USP9X had no effect on the survival of HeLa cells (**Figures 3C, D**) or UMSCC74 cells (**Figures 3G, H**) following low-LET protons, in comparison to NT control siRNA-treated cells. However, significantly reduced survival of HeLa (**Figures 3E, F**) and UMSCC74A (**Figures 3I, J**) cells was observed following USP9X depletion in response to high-LET protons, compared with NT control siRNA cells. These data confirmed the importance of USP9X in maintaining cell survival following treatment with relatively high-LET protons.

USP9X Does Not Interfere With CDD Repair or Cell Cycle Progression Following High-LET Protons

Given our demonstration that USP9X is required for maintaining cell survival specifically in response to relatively high-LET protons, we sought to define its mechanism of action. In the first instance, and given the propensity for high-LET radiation to cause increases in the levels of CDD, we utilized an enzyme-modified neutral comet assay (34) to monitor the levels and kinetics of repair of CDD. This assay also has the added advantage of revealing the levels and repair of DNA DSBs (in the absence of modifying enzymes). We demonstrate that DNA DSB levels are not significantly different in USP9X siRNA *versus* NT control siRNA-treated cells in response to relatively high-LET protons at any time points (0-4 h) post-irradiation (**Figure 4A**; compare black and red, and **Figure 4B**). We were able to confirm that relatively high-LET protons caused a significant increase in the levels of CDD in NT control siRNA-treated cells immediately post-irradiation, followed by significantly slower kinetics of repair from 1 to 4 h post-irradiation (**Figure 4A**; compare black and grey bars, and **Figure 4B**), consistent with our

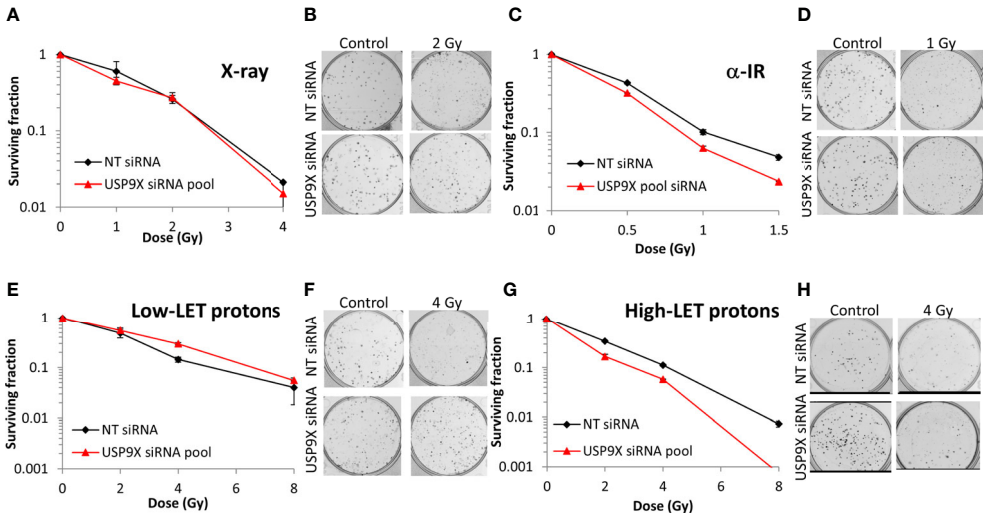

FIGURE 2 | Validation of USP9X in enhancing cellular radiosensitivity in response to high-LET α-particles and protons. HeLa cells were treated with USP9X siRNA (pool of 4 oligonucleotides) or a non-targeting (NT) control siRNA for 48 h and irradiated with increasing doses of **(A, B)** X-rays, **(C, D)** α-particles, **(E, F)** low-LET protons, or **(G, H)** relatively high-LET protons. Clonogenic survival of cells was analyzed from 2 independent experiments, and shown is the mean surviving fraction ± S.E. (**B, D, F, H**) Shown are representative images of colonies in non-irradiated and irradiated plates, the latter of which contained four times the number of cells seeded.

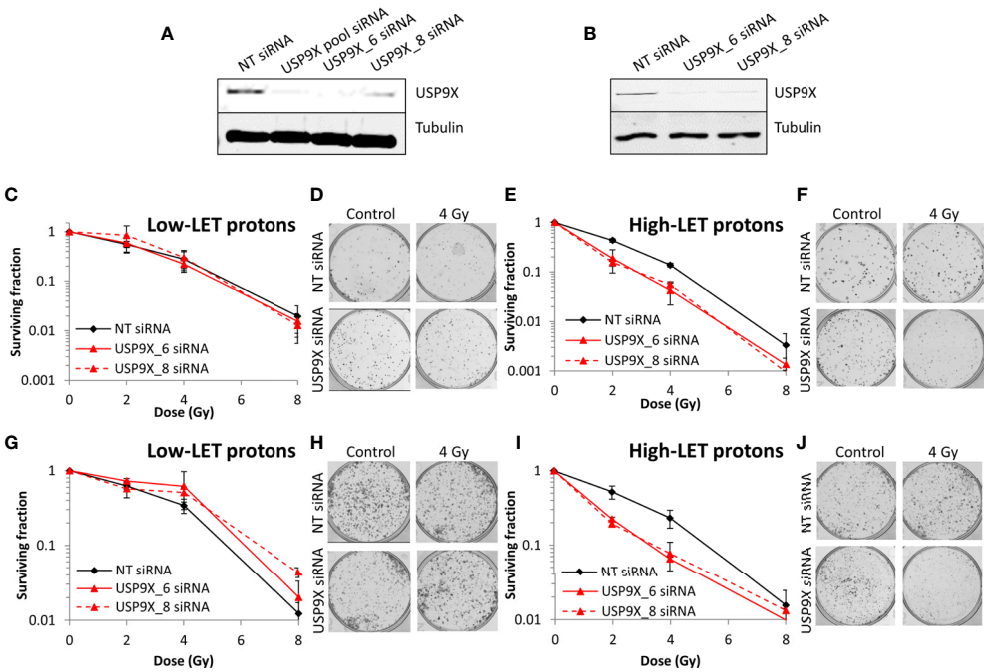

FIGURE 3 | Specific targeting of USP9X leads to enhanced cellular radiosensitivity after relatively high-LET protons. **(A–J)** Cells were treated with individual USP9X siRNAs (USP9X_6 and USP9X_8) or a non-targeting (NT) control siRNA for 48 h. Whole cell extracts prepared from **(A)** HeLa or **(B)** UMSCC74A cells were analyzed by immunoblotting using USP9X or tubulin antibodies. HeLa cells were subsequently irradiated with increasing doses of **(C, D)** low-LET protons or **(E, F)** relatively high-LET protons. UMSCC74A cells were also treated with increasing doses of **(G, H)** low-LET protons or **(I, J)** relatively high-LET protons. Clonogenic survival of cells was analyzed from 3 independent experiments, and shown is the mean surviving fraction ± S.E. Shown are representative images of colonies from **(D, F)** HeLa cells or **(H, J)** UMSCC74A cells in non-irradiated and irradiated plates, the latter of which contained four times the number of cells seeded. A comparison of the surviving fractions at 2 Gy (SF2) by one-way ANOVA in HeLa cells reveals $p < 0.05$ (NT siRNA *vs* USP9X_6), $p < 0.001$ (NT siRNA *vs* USP9X_8) and in UMSCC74A cells, $p < 0.05$ (NT siRNA *vs* USP9X_6 and NT siRNA *vs* USP9X_8). At 4 Gy (SF4), one-way ANOVA values in HeLa cells are $p < 0.01$ (NT siRNA *vs* USP9X_6), $p < 0.005$ (NT siRNA *vs* USP9X_8) and in UMSCC74A cells, $p < 0.05$ (NT siRNA *vs* USP9X_6 and NT siRNA *vs* USP9X_8).

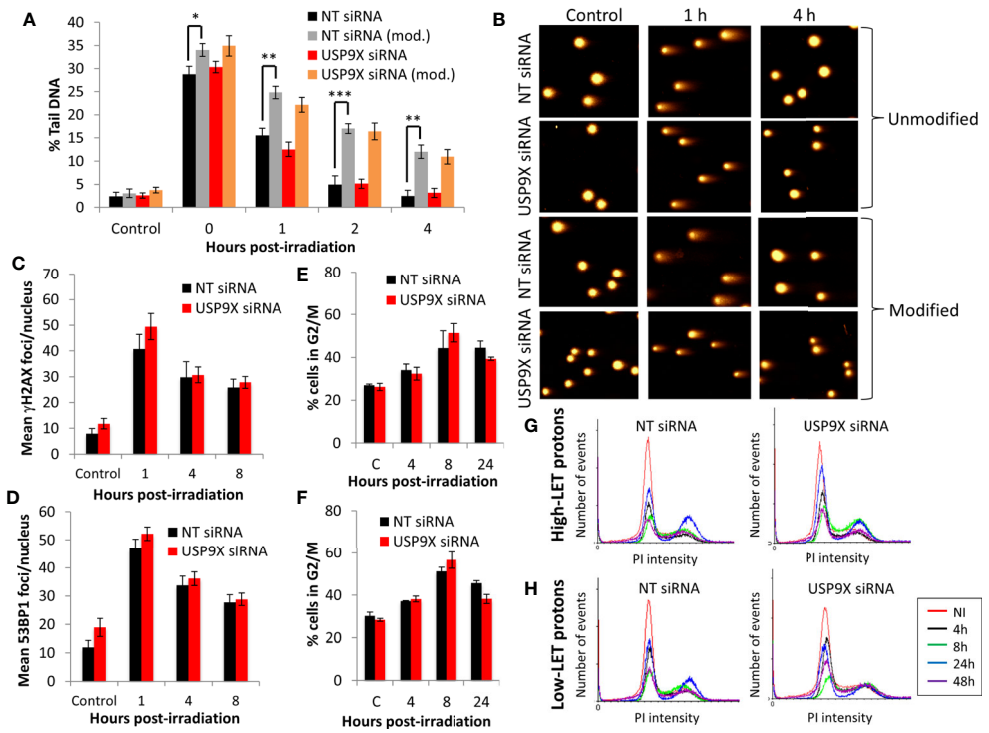

FIGURE 4 | USP9X depletion does not affect the repair of CDD or cell cycle progression in response to relatively high-LET protons. HeLa cells were treated with USP9X or a non-targeting (NT) control siRNA for 48 h. **(A)** Cells were irradiated with 4 Gy relatively high-LET protons, and DNA damage measured at various time points post-irradiation using the enzyme-modified neutral comet assay in the absence (revealing DSBs) or presence (revealing CDD; as indicated by mod) of the recombinant enzymes APE1, NTH1, and OGG1. Shown is the mean percentage tail DNA ± S.D plus **(B)** representative images of comets. *p < 0.02, **p < 0.005, ***p < 0.002 as analyzed by a one-sample *t*-test. **(C)** γH2AX or **(D)** 53BP1 foci were analyzed by immunofluorescence staining at various time points post-irradiation. Shown is the mean number of foci/nucleus ± S.D. **(E–H)** Cell cycle profiles were determined by flow cytometry analysis post-irradiation with **(E, G)** high-LET or **(F, H)** low-LET protons. C refers to control, unirradiated cells. **(E, F)** Shown is the mean percentage of cells in G2/M phase ± S.E.

previously published data (6, 7). Following depletion of USP9X, we observed that the efficiency of CDD repair in comparison to NT control siRNA-treated cells was not significantly different, at least at 1 to 4 h post-irradiation (**Figure 4A**; compare grey and orange bars, and **Figure 4B**). Data, demonstrating a lack of effect of USP9X depletion on the repair of DNA DSBs induced by relatively high-LET protons, were supported by an absence of any differences in the induction and resolution of γH2AX and 53BP1 foci, as surrogate markers, up to 8 h post-irradiation relative to NT control siRNA-treated cells (**Figures 4C, D**). We also analyzed the progression of cells through the cell cycle post-irradiation. Similarly, this revealed no significant differences in G2/M accumulation in USP9X siRNA-treated cells either before or after high-LET proton irradiation compared to NT control siRNA-treated cells (**Figure 4E**), or in the overall cell cycle profiles (**Figure 4G**). Similar numbers of cells in G2/M phase (**Figure 4F**) and in cell cycle profiles (**Figure 4H**) were also observed in USP9X-depleted and NT control siRNA-treated cells in response to low-LET protons. These data suggest that there is no significantly different checkpoint activation or cell cycle arrest in USP9X-depleted cells following either relatively high- or low-LET protons.

USP9X Does Not Impact Apoptosis, Autophagy or Senescence Following High-LET Protons

To examine the potential impact of USP9X on triggering apoptosis post-irradiation with relatively high-LET protons, we analyzed the cellular protein levels of PARP-1 (including cleaved PARP-1) and Mcl-1. However, we did not observe any differences in these proteins 1 to 24 h post-irradiation, nor in the accumulation of cleaved PARP-1, in USP9X siRNA-treated cells compared to NT control siRNA-treated cells (**Figure 5A**), suggesting that apoptosis does not play a role in the differential cellular response. We also compared the expression of LC3B (**Figure 5B**; red text refers to time following relatively high-LET protons) and β-Galactosidase by both microscopy (**Figure 5C**; utilizing H2O2 as a positive control) and immunoblotting (**Figure 5D**), as markers of autophagy and senescence, respectively. Similarly, we observed no obvious differences in LC3B or β-galactosidase levels between USP9X-depleted and NT control siRNA-treated cells post-irradiation with either relatively high- or low-LET protons, suggesting that neither autophagy nor senescence are responsible for decreased cell survival specifically following relatively high-LET protons.

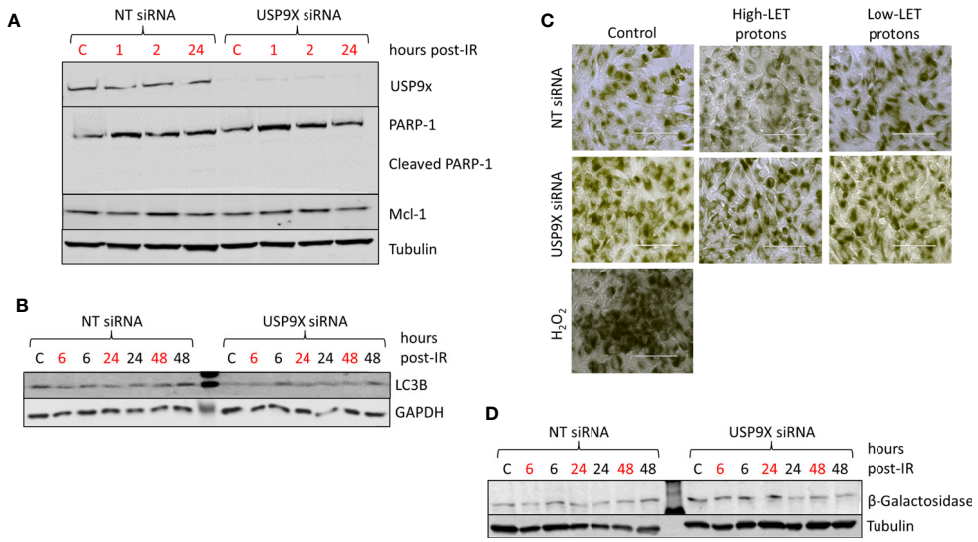

FIGURE 5 | USP9X depletion does not affect cellular levels of apoptosis, autophagy and senescence in response to relatively high-LET protons. HeLa cells were treated with USP9X or a non-targeting (NT) control siRNA for 48 h, and unirradiated (designated C) or irradiated with 4 Gy relatively high-LET or low-LET protons and allowed to repair for the time points indicated post-irradiation. **(A, B, D)** Whole cell extracts were analyzed by immunoblotting using the indicated antibodies. **(C)** Cells were fixed 48 h post-irradiation and stained for β-Galactosidase, with 100 μM H_2O_2 used as a positive control.

USP9X Inhibition Causes Amplification of Pericentrin-Rich Bodies After High-LET Protons

Since recent data have shown that USP9X is an integral component of centrosomal protein maintenance, we analyzed the impact of USP9X depletion on stabilization of centrosomal proteins. We observed that an absence of USP9X alone in HeLa cells caused reduced levels of the centrosome proteins CEP55 (~60%) and CEP131 (~40%) in comparison to NT control siRNA-treated cells (**Figure 6A**; compare lanes 1 and 4). Reduced levels of CEP55 and CEP131 (by ~50–60%) were maintained in USP9X-depleted cells 24 h post-irradiation with both low- and high-LET protons (**Figure 6A**; compare lanes 2–3 and 5–6). Similar observations were seen in UMSCC74A cells, whereby CEP55 and CEP131 protein levels were reduced by 50% and 30%, respectively, in USP9X-depleted cells (**Figure 6B**; compare lanes 1 and 4). CEP55 and CEP131 protein levels were further reduced (by ~60–90%) in USP9X-depleted cells compared to NT control siRNA-treated cells 24 h post-irradiation with both low- and high-LET protons (**Figure 6B**; compare lanes 2–3 and 5–6). In addition to reduced centrosome protein stability, we discovered a ~2.6- to 2.9-fold increase in pericentrin-rich foci in NT control siRNA-treated HeLa cells 48 h post-irradiation with both low and high LET protons (**Figures 6C, D**). However, we observed that there was an additional ~1.9-fold statistically significant increase in foci in USP9X-depleted cells specifically in response to high-LET protons, but not following low-LET protons (**Figures 6C, D**). Similarly, in UMSCC74A cells, there was a ~1.8-fold increase in pericentrin-rich foci in NT control siRNA-treated HeLa cells 48 h post-irradiation with both low- and high-LET protons, but this further increased by ~2.2-fold in USP9X-depleted cells (**Figures 6E, F**). Amplification of pericentrin-foci was consequently ~6.7-fold (HeLa) and ~4.9-fold (UMSCC74A) higher in USP9X-depleted cells irradiated with high-LET protons compared with unirradiated cells.

To recapitulate the impact of USP9X in controlling sensitivity of cells to high-LET protons mediated *via* centrosomal protein maintenance, we specifically targeted CEP55 and CEP131 using siRNA. We identified conditions that led to ~50% reduced CEP55 and CEP131 protein levels in HeLa cells (**Figure 7A**; lanes 4 and 8), which mimic those of USP9X depletion (**Figure 6A**). We observed under these conditions that cells do not display any increase in radiosensitivity to low-LET protons (**Figure 7B**), but that there is reduced survival to relatively high-LET protons (**Figure 7C**). Additionally, we discovered that there was an a ~1.4-fold statistically significant increase in pericentrin-rich foci in USP9X-depleted cells *versus* NT control siRNA-treated cells specifically in response to high-LET protons, but not following low-LET protons (**Figures 7D, E**). This suggests that USP9X is required for maintenance of centrosomal proteins and for controlling pericentrin-rich foci, which is important for cell survival particularly in response to high-LET radiation.

DISCUSSION

IR, particularly at high-LET, can generate CDD known to compromise genome integrity and to contribute to cell death due to the inability of the cellular DNA repair machinery to accurately repair the damage. However, high-LET radiation has also been shown to promote persistent alterations to the structure of chromatin (9, 10), and to enhance senescence and apoptosis (11, 12). We recently demonstrated using a DUB siRNA screen, that

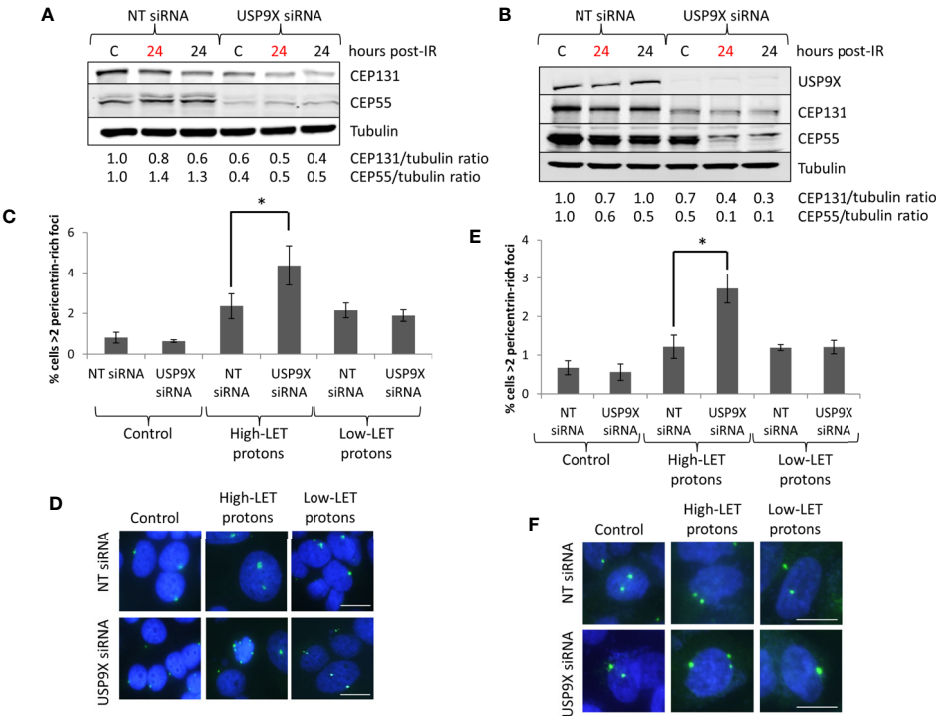

FIGURE 6 | USP9X depletion destabilizes centrosomal proteins, and induces pericentrin-rich foci amplification in response to relatively high-LET protons. **(A, C, D)** HeLa or **(B, E, F)** UMSCC74A cells were treated with USP9X or a non-targeting (NT) control siRNA for 48 h, and unirradiated designated **(C)** or irradiated with 4 Gy relatively high-LET or low-LET protons and allowed to repair for the time points indicated post-irradiation. **(A, B)** Whole cell extracts were analyzed by immunoblotting using the indicated antibodies. Red and black text refers to time post-irradiation following relatively high-LET and low-LET protons, respectively. Protein levels of CEP131 and CEP55 relative to tubulin and normalized to the unirradiated NT siRNA control treated cells which was set to 1.0 are shown. **(C, E)** Analysis of pericentrin was performed by immunofluorescence 48 h post-irradiation. Shown is the mean percentage of cells with >2 pericentrin-rich foci/nucleus ± S.D. *p < 0.03 as analyzed by a two-sample *t*-test. **(D, F)** Representative images of pericentrin staining (green stain) and nuclei (blue stain; DAPI).

depletion of USP6 causes significantly increased radiosensitivity to high-LET IR (relatively high-LET protons and α-particles) but not low-LET IR (protons or X-rays), which was mediated by instability of PARP-1 required for CDD repair (7). In the current study, we discovered that another DUB enzyme, USP9X, is similarly required for maintaining cell survival specifically in response to high-LET IR, particularly high-LET protons. We demonstrated that this phenotype was not caused by interference with CDD repair, cell cycle progression, apoptosis, autophagy or senescence. In fact, we discovered that an absence of USP9X caused destabilization of centrosomal proteins, and enhanced amplification of pericentrin-rich foci in response to relatively high-LET protons. This suggests that maintenance of CEP55 and CEP131 is the major factor contributing to reduced cell survival following relatively high-LET protons in the absence of USP9X.

Our findings that USP9X does not affect cell cycle progression is in agreement with a previous study, which demonstrated that USP9X depletion was linked to an increased loss of anaphase-promoting complex/cyclosome (APC/C) substrates, in particular cyclin A, but also cyclin B and NEK2A, and that cells consequently failed to arrest mitosis after microtubule poisoning in HeLa cells and U2OS cells (35). USP9X has been shown to promote Mcl-1 stabilization and to increase tumor cell survival in response to radiation and chemotherapy in several tumor types (19, 36–39). This is in contrast to our findings, where we observed no evidence of a role for Mcl-1, and therefore apoptosis through lack of PARP-1 cleavage, in the USP9X-dependent radiosensitisation of HeLa and UMSCC74A cells following relatively high-LET protons. Indeed, in certain glioblastoma cell lines, it has been demonstrated that USP9X loss regulates radiosensitivity by Mcl-1-independent mechanisms (40). USP9X interacts with VMP1, indicating that there is a close cooperation between the autophagy pathway and the ubiquitin recognition machinery required for selective autophagosome formation (41). On analysis of the levels of LC3B, as a marker of autophagy, after relatively high-LET *versus* low-LET protons, we did not find any evidence indicating that autophagy plays a significant role in cell survival in response to these conditions. USP9X has recently been suggested to stabilize the breast cancer protein-1 (BRCA1) required for DSB repair by homologous recombination through its DUB enzymatic activity, and which is required for resistance to the PARP inhibitor olaparib in HeLa and breast cancer cells (42). These data are supported by another study, although it was proposed that USP9X actually regulates BRCA1 (and RAD51) at the transcriptional level in U2OS cells, which was independent of its catalytic activity (43). This study also presented limited data showing increased levels of 53BP1 foci both in the absence and presence of IR (1 h post-irradiation), in USP9X-depleted cells. Despite this evidence, we observed that an absence of USP9X did

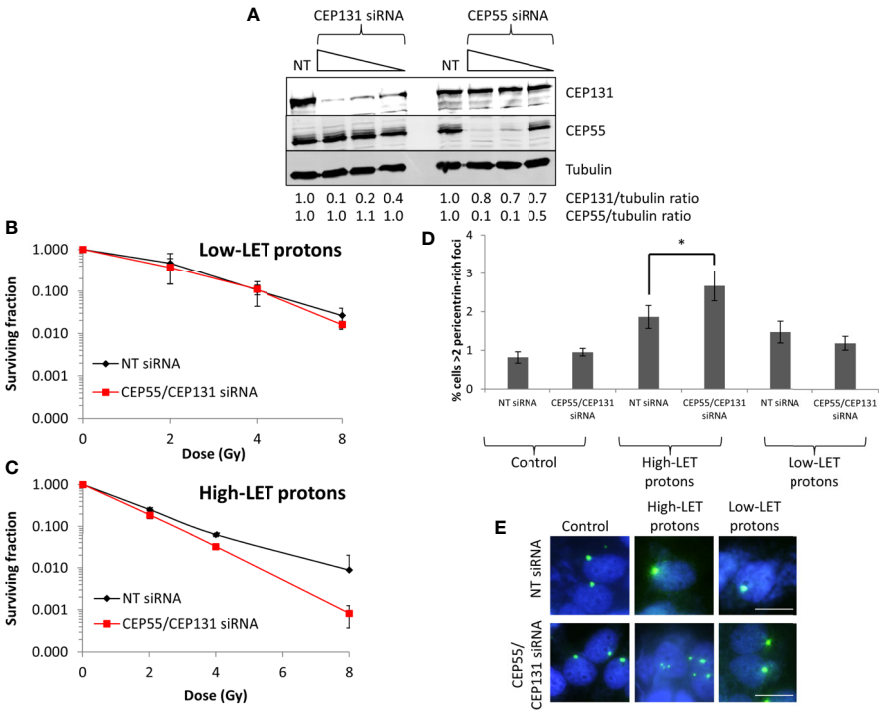

FIGURE 7 | CEP55 and CEP131 depletion induces pericentrin-rich foci amplification and reduces cell survival in response to relatively high-LET protons. **(A)** HeLa cells were treated with CEP55 or CEP131 siRNA (0.01, 0.1 and 1 nM) or a non-targeting (NT) control siRNA for 48 h, and whole cell extracts were analyzed by immunoblotting using the indicated antibodies. Protein levels of CEP131 and CEP55 relative to tubulin and normalized to the NT siRNA control-treated cells which was set to 1.0 are shown. **(B–E)** HeLa cells were treated with CEP55 and CEP131 siRNA (0.01 nM) or a non-targeting (NT) control siRNA for 48 h. Cells were irradiated with increasing doses of **(B)** low-LET protons or **(C)** relatively high-LET protons. Clonogenic survival of cells was analyzed from 2 independent experiments, and shown is the mean surviving fraction ± S.E. **(D, E)** Alternatively, analysis of pericentrin was performed by immunofluorescence 48 h post-irradiation (with 4 Gy). **(D)** Shown is the mean percentage of cells with >2 pericentrin-rich foci/nucleus ± S.D. *p < 0.05 as analyzed by a two-sample *t*-test. **(E)** Representative images of pericentrin staining (green stain) and nuclei (blue stain; DAPI).

not cause any significant differences in the repair of DSBs, using γH2AX and 53BP1 foci analysis, or in the kinetics of DSB or CDD repair after relatively high-LET protons. This would indicate that the ability of the cells, at least the ones utilized in our study (HeLa and UMSCC74A), to repair DNA damage was not heavily compromised.

USP9X has more recently been observed in U2OS and HeLa cells to localize to centrosomes in association with PCM1, CEP55 and CEP131, where the enzyme antagonizes proteosomal degradation of these key centriolar satellite proteins to promote centrosome duplication (21–23). Interestingly, in MRXS99F fibroblasts USP9X was also found to localize to the centrosome, but had no impact on controlling the protein levels of PCM1 or CEP131 (24). This suggests that there are cell-type–specific roles and targets for USP9X. Here, we observed that USP9X-depleted HeLa and UMSCC74A oropharyngeal squamous cell carcinoma cells have reduced levels of CEP55 and CEP131. Furthermore, we observed an increased number of pericentrin-rich foci after proton irradiation in both non-targeting and USP9X-depleted cells, but that this phenotype was further exacerbated specifically after high-LET protons in USP9X-depleted cells. We also targeted CEP55 and CEP131 directly and demonstrated that their moderate depletion (by ~50%, consistent with effects seen following USP9X depletion) also led to amplification of pericentrin-rich foci and enhanced sensitivity of cells specifically to high LET protons. Pericentrin is not only a component of centrosomes but also a feature of centriolar satellites and cilia, which are associated with centrosome biology. Our data therefore indicate that USP9X could play a role in centriolar satellite generation, which ultimately maintains centrosome stability. Centriolar satellites are small, granular structures that cluster around centrosomes and are thought to play important roles in both centrosome assembly and in cilia formation (44, 45). There is also evidence demonstrating that cellular stresses, such as UV radiation, disrupt centriolar satellites and stimulate ciliogenesis (46). Furthermore, and consistent with our data, DNA damage induction by IR and bleomycin has been shown to lead to excessive formation of centriolar satellites, which is a prerequisite for centrosome amplification (47). It is possible, therefore, that following high-LET protons, which is more densely ionizing leading to increased protein as well as DNA damage, there is uncontrolled centrosome biogenesis, which is likely to contribute to increased genome instability through chromosomal aberrations and therefore reduced cell survival. It is important to note that the UMSCC74A cells employed in our study contain wild type p53 tumor suppressor protein, whereas

HeLa cells have significantly reduced levels of p53 due to human papillomavirus type 18 infection that ultimately leads to p53 degradation. The phenotype of increased radiosensitivity and elevated levels of pericentrin-rich foci in cells in response to high-LET radiation therefore does not appear to be dependent on loss of p53. Given that p53 is frequently mutated in human cancers, and particularly in head and neck squamous cell carcinoma (48), more expansive studies using cells containing different p53 status are required to fully investigate this. Nevertheless, and at this stage, the precise mechanism underlying the impact of USP9X in regulating centrosome biology specifically in response to relatively high-LET protons is unclear. Further ongoing experiments are necessary to fully understand centrosome biology (>100 centrosome proteins exist) in multiple cell lines lacking USP9X pre- and post-irradiation, particularly those originating from head and neck cancers, which is our research and clinical focus. We also aim to analyze more the impact of low- *versus* high-LET radiation at the chromosome level, and the dependence on USP9X, which is likely to be contributing to the increased radiosensitivity of cells lacking USP9X specifically in response high-LET radiation. Nevertheless, our data suggest that USP9X is essential for maintaining cell survival, particularly following high-LET radiation.

DATA AVAILABILITY STATEMENT

The raw data supporting the conclusions of this article will be made available by the authors, without undue reservation.

AUTHOR CONTRIBUTIONS

JP conceptualized and designed the project. AK, MH, and JP designed the experimental setup. CN, MF, RC, and JH performed experiments. CN, MF, RC, and JP performed data analysis and validation. CN, MF, RC, and JP wrote the manuscript and all authors contributed to reviewing and editing. JP and MH coordinated funding acquisition. All authors contributed to the article and approved the submitted version.

FUNDING

This research was funded by North West Cancer Research (CR1074 and CR1197) and by the Medical Research Council *via* a New Investigator Research Grant (MR/M000354/1) awarded to JP. Funding from Medical Research Council Strategic Partnership Funding (MC-PC-12004) for the CRUK/MRC Oxford Institute for Radiation Oncology is also gratefully acknowledged.

ACKNOWLEDGMENTS

The authors thank Prof T. Carey for providing the UMSCC74A cells and Prof G. Dianov for providing APE1, NTH1, and OGG1 bacterial expression plasmids. The authors also thank Brian Marsland and Ian Taylor at the Clatterbridge Cancer Centre for technical assistance with proton irradiation of cells, and Dr Urszula McClurg for critically reviewing the manuscript.

REFERENCES

1. Holliday EB, Frank SJ. Proton Radiation Therapy for Head and Neck Cancer: A Review of the Clinical Experience to Date. *Int J Radiat Oncol Biol Phys* (2014) 89:292–302. doi: 10.1016/j.ijrobp.2014.02.029
2. Goodhead DT. Initial Events in the Cellular Effects of Ionizing Radiations: Clustered Damage in DNA. *Int J Radiat Biol* (1994) 65:7–17. doi: 10.1080/09553009414550021
3. Ward JF. The Complexity of DNA Damage: Relevance to Biological Consequences. *Int J Radiat Biol* (1994) 66:427–32. doi: 10.1080/09553009414551401
4. Hill MA. Radiation Track Structure: How the Spatial Distribution of Energy Deposition Drives Biological Response. *Clin Oncol (R Coll Radiol)* (2020) 32:75–83. doi: 10.1016/j.clon.2019.08.006
5. Vitti ET, Parsons JL. The Radiobiological Effects of Proton Beam Therapy: Impact on DNA Damage and Repair. *Cancers (Basel)* (2019) 11:946. doi: 10.3390/cancers11070946
6. Carter RJ, Nickson CM, Thompson JM, Kacperek A, Hill MA, Parsons JL. Complex DNA Damage Induced by High Linear Energy Transfer Alpha-Particles and Protons Triggers a Specific Cellular DNA Damage Response. *Int J Radiat Oncol Biol Phys* (2018) 100:776–84. doi: 10.1016/j.ijrobp.2017.11.012
7. Carter RJ, Nickson CM, Thompson JM, Kacperek A, Hill MA, Parsons JL. Characterisation of Deubiquitylating Enzymes in the Cellular Response to High-LET Ionizing Radiation and Complex Dna Damage. *Int J Radiat Oncol Biol Phys* (2019) 104:656–65. doi: 10.1016/j.ijrobp.2019.02.053
8. Mavragani IV, Nikitaki Z, Souli MP, Aziz A, Nowsheen S, Aziz K, et al. Complex DNA Damage: A Route to Radiation-Induced Genomic Instability and Carcinogenesis. *Cancers (Basel)* (2017) 9:91. doi: 10.3390/cancers9070091
9. Timm S, Lorat Y, Jakob B, Taucher-Scholz G, Rube CE. Clustered DNA Damage Concentrated in Particle Trajectories Causes Persistent Large-Scale Rearrangements in Chromatin Architecture. *Radiother Oncol* (2018) 129:600–10. doi: 10.1016/j.radonc.2018.07.003
10. Anderson RM, Stevens DL, Sumption ND, Townsend KM, Goodhead DT, Hill MA. Effect of Linear Energy Transfer (LET) on the Complexity of Alpha-Particle-Induced Chromosome Aberrations in Human CD34+ Cells. *Radiat Res* (2007) 167:541–50. doi: 10.1667/RR0813.1
11. Zhang X, Ye C, Sun F, Wei W, Hu B, Wang J. Both Complexity and Location of DNA Damage Contribute to Cellular Senescence Induced by Ionizing Radiation. *PloS One* (2016) 11:e0155725. doi: 10.1371/journal.pone.0155725
12. Niemantsverdriet M, Van Goethem MJ, Bron R, Hogewerf W, Brandenburg S, Langendijk JA, et al. High and Low LET Radiation Differentially Induce Normal Tissue Damage Signals. *Int J Radiat Oncol Biol Phys* (2012) 83:1291–7. doi: 10.1016/j.ijrobp.2011.09.057
13. Edmonds MJ, Parsons JL. Regulation of Base Excision Repair Proteins by Ubiquitylation. *Exp Cell Res* (2014) 329:132–8. doi: 10.1016/j.yexcr.2014.07.031
14. Carter RJ, Parsons JL. Base Excision Repair, a Pathway Regulated by Posttranslational Modifications. *Mol Cell Biol* (2016) 36:1426–37. doi: 10.1128/MCB.00030-16
15. Dianov GL, Meisenberg C, Parsons JL. Regulation of DNA Repair by Ubiquitylation. *Biochem (Mosc)* (2011) 76:69–79. doi: 10.1134/S0006297911010093
16. Murtaza M, Jolly LA, Gecz J, Wood SA. La FAM Fatale: USP9X in Development and Disease. *Cell Mol Life Sci* (2015) 72:2075–89. doi: 10.1007/s00018-015-1851-0
17. Huntwork-Rodriguez S, Wang B, Watkins T, Ghosh AS, Pozniak CD, Bustos D, et al. JNK-Mediated Phosphorylation of DLK Suppresses its Ubiquitination to Promote Neuronal Apoptosis. *J Cell Biol* (2013) 202:747–63. doi: 10.1083/jcb.201303066
18. Nagai H, Noguchi T, Homma K, Katagiri K, Takeda K, Matsuzawa A, et al. Ubiquitin-Like Sequence in ASK1 Plays Critical Roles in the Recognition and

Stabilization by USP9X and Oxidative Stress-Induced Cell Death. *Mol Cell* (2009) 36:805–18. doi: 10.1016/j.molcel.2009.10.016
19. Schwickart M, Huang X, Lill JR, Liu J, Ferrando R, French DM, et al. Deubiquitinase USP9X Stabilizes MCL1 and Promotes Tumour Cell Survival. *Nature* (2010) 463:103–7. doi: 10.1038/nature08646
20. Sun H, Kapuria V, Peterson LF, Fang D, Bornmann WG, Bartholomeusz G, et al. Bcr-Abl Ubiquitination and Usp9x Inhibition Block Kinase Signaling and Promote CML Cell Apoptosis. *Blood* (2011) 117:3151–62. doi: 10.1182/blood-2010-03-276477
21. Li X, Song N, Liu L, Liu X, Ding X, Song X, et al. USP9X Regulates Centrosome Duplication and Promotes Breast Carcinogenesis. *Nat Commun* (2017) 8:14866. doi: 10.1038/ncomms14866
22. Wang Q, Tang Y, Xu Y, Xu S, Jiang Y, Dong Q, et al. The X-linked Deubiquitinase USP9X Is an Integral Component of Centrosome. *J Biol Chem* (2017) 292:12874–84. doi: 10.1074/jbc.M116.769943
23. Han KJ, Wu Z, Pearson CG, Peng J, Song K, Liu CW. Deubiquitylase USP9X Maintains Centriolar Satellite Integrity by Stabilizing Pericentriolar Material 1 Protein. *J Cell Sci* (2019) 132:jcs221663. doi: 10.1242/jcs.221663
24. Kodani A, Moyer T, Chen A, Holland A, Walsh CA, Reiter JF. SFI1 Promotes Centriole Duplication by Recruiting USP9X to Stabilize the Microcephaly Protein STIL. *J Cell Biol* (2019) 218:2185–97. doi: 10.1083/jcb.201803041
25. Hill MA. The Variation in Biological Effectiveness of X-Rays and Gamma Rays With Energy. *Radiat Prot Dosimetry* (2004) 112:471–81. doi: 10.1093/rpd/nch091
26. Task Group on Radiation Quality Effects in Radiological Protection, C.O.R.E and I.C.O.R.P. Relative Biological Effectiveness (RBE), Quality Factor (Q), and Radiation Weighting Factor (W(R)). A Report of the International Commission on Radiological Protection. *Ann ICRP* (2003) 33:1–117. doi: 10.1016/S0146-6453(03)00024-1
27. Chaudhary P, Marshall TI, Currell FJ, Kacperek A, Schettino G, Prise KM. Variations in the Processing of DNA Double-Strand Breaks Along 60-Mev Therapeutic Proton Beams. *Int J Radiat Oncol Biol Phys* (2016) 95:86–94. doi: 10.1016/j.ijrobp.2015.07.2279
28. Goodhead DT, Bance DA, Stretch A, Wilkinson RE. A Versatile plutonium-238 Irradiator for Radiobiological Studies With Alpha-Particles. *Int J Radiat Biol* (1991) 59:195–210. doi: 10.1080/09553009114550181
29. Tracy BL, Stevens DL, Goodhead DT, Hill MA. Variation in RBE for Survival of V79-4 Cells as a Function of Alpha-Particle (Helium Ion) Energy. *Radiat Res* (2015) 184:33–45. doi: 10.1667/RR13835.1
30. Nickson CM, Moori P, Carter RJ, Rubbi CP, Parsons JL. Misregulation of DNA Damage Repair Pathways in HPV-Positive Head and Neck Squamous Cell Carcinoma Contributes to Cellular Radiosensitivity. *Oncotarget* (2017) 8:29963–75. doi: 10.18632/oncotarget.16265
31. Edmonds MJ, Carter RJ, Nickson CM, Williams SC, Parsons JL. Ubiquitylation-Dependent Regulation of NEIL1 by Mule and TRIM26 Is Required for the Cellular DNA Damage Response. *Nucleic Acids Res* (2017) 45:726–38. doi: 10.1093/nar/gkw959
32. Sutherland BM, Bennet PV, Sidorkina O, Laval J. Clustered DNA Damages Induced in Isolated DNA and in Human Cells by Low Doses of Ionizing Radiation. *Proc Natl Acad USA* (2000) 97:103–8. doi: 10.1073/pnas.97.1.103
33. Sutherland BM, Bennett PV, Sutherland JC, Laval J. Clustered DNA Damages Induced by X Rays in Human Cells. *Radiat Res* (2002) 157:611–6. doi: 10.1667/0033-7587(2002)157[0611:CDDIBX]2.0.CO;2
34. Fabbrizi MR, Hughes JR, Parsons JL. The Enzyme-Modified Neutral Comet (Emnc) Assay for Complex Dna Damage Detection. *Methods Protoc* (2021) 4:14. doi: 10.3390/mps4010014
35. Skowyra A, Allan LA, Saurin AT, Clarke PR. Usp9x Limits Mitotic Checkpoint Complex Turnover to Strengthen the Spindle Assembly Checkpoint and Guard Against Chromosomal Instability. *Cell Rep* (2018) 23:852–65. doi: 10.1016/j.celrep.2018.03.100
36. Peddaboina C, Jupiter D, Fletcher S, Yap JL, Rai A, Tobin RP, et al. The Downregulation of Mcl-1 Via USP9X Inhibition Sensitizes Solid Tumors to Bcl-xl Inhibition. *BMC Cancer* (2012) 12:541. doi: 10.1186/1471-2407-12-541
37. Habata S, Iwasaki M, Sugio A, Suzuki M, Tamate M, Satohisa S, et al. BAG3-Mediated Mcl-1 Stabilization Contributes to Drug Resistance Via Interaction With USP9X in Ovarian Cancer. *Int J Oncol* (2016) 49:402–10. doi: 10.3892/ijo.2016.3494
38. Cui J, Sun W, Hao X, Wei M, Su X, Zhang Y, et al. EHMT2 Inhibitor BIX-01294 Induces Apoptosis Through PMAIP1-USP9X-MCL1 Axis in Human Bladder Cancer Cells. *Cancer Cell Int* (2015) 15:4. doi: 10.1186/s12935-014-0149-x
39. Trivigno D, Essmann F, Huber SM, Rudner J. Deubiquitinase USP9x Confers Radioresistance Through Stabilization of Mcl-1. *Neoplasia* (2012) 14:893–904. doi: 10.1593/neo.12598
40. Wolfsperger F, Hogh-Binder SA, Schittenhelm J, Psaras T, Ritter V, Bornes L, et al. Deubiquitylating Enzyme USP9x Regulates Radiosensitivity in Glioblastoma Cells by Mcl-1-Dependent and -Independent Mechanisms. *Cell Death Dis* (2016) 7:e2039. doi: 10.1038/cddis.2015.405
41. Grasso D, Ropolo A, Lo Re A, Boggio V, Molejon MI, Iovanna JL, et al. Zymophagy, a Novel Selective Autophagy Pathway Mediated by VMP1-USP9x-p62, Prevents Pancreatic Cell Death. *J Biol Chem* (2011) 286:8308–24. doi: 10.1074/jbc.M110.197301
42. Lu Q, Zhang FL, Lu DY, Shao ZM, Li DQ. USP9X Stabilizes BRCA1 and Confers Resistance to DNA-Damaging Agents in Human Cancer Cells. *Cancer Med* (2019) 8:6730–40. doi: 10.1002/cam4.2528
43. O'dea R, Santocanale C. Non-Canonical Regulation of Homologous Recombination DNA Repair by the USP9X Deubiquitylase. *J Cell Sci* (2020) 133:jcs.233437. doi: 10.1242/jcs.233437
44. Hori A, Toda T. Regulation of Centriolar Satellite Integrity and its Physiology. *Cell Mol Life Sci* (2017) 74:213–29. doi: 10.1007/s00018-016-2315-x
45. Odabasi E, Gul S, Kavakli IH, Firat-Karalar EN. Centriolar Satellites Are Required for Efficient Ciliogenesis and Ciliary Content Regulation. *EMBO Rep* (2019) 20:e47723. doi: 10.15252/embr.201947723
46. Villumsen BH, Danielsen JR, Povlsen L, Sylvestersen KB, Merdes A, Beli P, et al. A New Cellular Stress Response That Triggers Centriolar Satellite Reorganization and Ciliogenesis. *EMBO J* (2013) 32:3029–40. doi: 10.1038/emboj.2013.223
47. Loffler H, Fechter A, Liu FY, Poppelreuther S, Kramer A. DNA Damage-Induced Centrosome Amplification Occurs Via Excessive Formation of Centriolar Satellites. *Oncogene* (2013) 32:2963–72. doi: 10.1038/onc.2012.310
48. Cancer Genome Atlas N. Comprehensive Genomic Characterization of Head and Neck Squamous Cell Carcinomas. *Nature* (2015) 517:576–82. doi: 10.1038/nature14129

Conflict of Interest: The authors declare that the research was conducted in the absence of any commercial or financial relationships that could be construed as a potential conflict of interest.

frontiers in Oncology

ORIGINAL RESEARCH
published: 26 August 2021
doi: 10.3389/fonc.2021.735940

Evaluation of Histone Deacetylase Inhibitors as Radiosensitizers for Proton and Light Ion Radiotherapy

Alicia M. Johnson[1], *Paula V. Bennett*[1], *Katherine Z. Sanidad*[1], *Anthony Hoang*[1], *James H. Jardine*[1], *Deborah J. Keszenman*[1,2] *and Paul F. Wilson*[1,3]*

[1] Biology Department, Brookhaven National Laboratory, Upton, NY, United States, [2] Laboratorio de Radiobiología Médica y Ambiental, Grupo de Biofisicoquímica, Centro Universitario Regional Litoral Norte, Universidad de la República (UdelaR), Salto, Uruguay, [3] Department of Radiation Oncology, University of California–Davis, Sacramento, CA, United States

OPEN ACCESS

Edited by:
Sandeep Kumar Shukla, Institute of Nuclear Medicine & Allied Sciences (DRDO), India

Reviewed by:
Paban K. Agrawala, Institute of Nuclear Medicine & Allied Sciences (DRDO), India
Takamitsu A. Kato, Colorado State University, United States

***Correspondence:**
Paul F. Wilson
pfwilson@ucdavis.edu

Specialty section:
This article was submitted to Radiation Oncology, a section of the journal Frontiers in Oncology

Received: 04 July 2021
Accepted: 29 July 2021
Published: 26 August 2021

Citation:
Johnson AM, Bennett PV, Sanidad KZ, Hoang A, Jardine JH, Keszenman DJ and Wilson PF (2021) Evaluation of Histone Deacetylase Inhibitors as Radiosensitizers for Proton and Light Ion Radiotherapy. Front. Oncol. 11:735940. doi: 10.3389/fonc.2021.735940

Significant opportunities remain for pharmacologically enhancing the clinical effectiveness of proton and carbon ion-based radiotherapies to achieve both tumor cell radiosensitization and normal tissue radioprotection. We investigated whether pretreatment with the hydroxamate-based histone deacetylase inhibitors (HDACi) SAHA (vorinostat), M344, and PTACH impacts radiation-induced DNA double-strand break (DSB) induction and repair, cell killing, and transformation (acquisition of anchorage-independent growth in soft agar) in human normal and tumor cell lines following gamma ray and light ion irradiation. Treatment of normal NFF28 primary fibroblasts and U2OS osteosarcoma, A549 lung carcinoma, and U87MG glioma cells with 5–10 μM HDACi concentrations 18 h prior to cesium-137 gamma irradiation resulted in radiosensitization measured by clonogenic survival assays and increased levels of colocalized gamma-H2AX/53BP1 foci induction. We similarly tested these HDACi following irradiation with 200 MeV protons, 290 MeV/n carbon ions, and 350 MeV/n oxygen ions delivered in the Bragg plateau region. Unlike uniform gamma ray radiosensitization, effects of HDACi pretreatment were unexpectedly cell type and ion species-dependent with C-12 and O-16 ion irradiations showing enhanced G0/G1-phase fibroblast survival (radioprotection) and in some cases reduced or absent tumor cell radiosensitization. DSB-associated foci levels were similar for proton-irradiated DMSO control and SAHA-treated fibroblast cultures, while lower levels of induced foci were observed in SAHA-pretreated C-12 ion-irradiated fibroblasts. Fibroblast transformation frequencies measured for all radiation types were generally LET-dependent and lowest following proton irradiation; however, both gamma and proton exposures showed hyperlinear transformation induction at low doses (≤25 cGy). HDACi pretreatments led to overall lower transformation frequencies at low doses for all radiation types except O-16 ions but generally led to higher transformation frequencies at higher doses (>50 cGy). The results of these *in vitro* studies cast doubt on the clinical efficacy of using HDACi as radiosensitizers for light

ion-based hadron radiotherapy given the mixed results on their radiosensitization effectiveness and related possibility of increased second cancer induction.

Keywords: HDAC inhibitor, SAHA, radiosensitization, double-strand break, ionizing radiation, protons, carbon ions, transformation

INTRODUCTION

Despite the improved dose distributions and increased relative biological effectiveness (RBE) afforded by accelerated proton and carbon ion-based hadron radiotherapies (1), significant opportunities remain for enhancing their clinical effectiveness through pharmacological means to achieve tumor cell radiosensitization and normal tissue radioprotection. Identifying effective radiosensitizers that synergistically enhance charged particle-induced tumor cell killing would allow for lower doses per fraction to be used, thereby reducing normal tissue exposures. Alternatively, an increased therapeutic index could be achieved using charged particle normal tissue radioprotectors that would allow for boosting of tumor doses (assuming the agent does not likewise radioprotect tumor cells). Charged particles have been shown to induce higher relative frequencies of closely localized DNA double-strand breaks (DSBs) and clustered DNA damages along their tracks compared to low linear energy transfer (LET) photon radiations (2, 3). This feature underlies their higher RBE for cell killing *in vitro* and tumor control *in vivo* (4). The density and complexity of these lesions activate several cellular DNA damage response (DDR) pathways, and their repair and restitution require the participation of multiple DNA signaling and repair pathways to properly identify them and coordinate their repair as cells progress through the cell cycle (5–7). Compared to low LET X- and γ-rays, it has been shown the repair of intermediate to high LET HZE ion-induced DNA damage requires relatively more reliance on homologous recombinational repair (HRR) as damages that were not repaired in G0/G1 phase by non-homologous end-joining (NHEJ) and base excision repair (BER) present themselves during subsequent chromatin decondensation and DNA replication in S phase (8–11). Exposures to charged particles, including low LET protons, are consistently associated with higher relative induction of DSB-associated foci, prematurely condensed chromosomal breaks, and simple and complex chromosomal aberrations measured *in vitro* post-irradiation compared to X- and γ-rays (9, 12–15).

Targeting the charged particle-induced DDR offers multiple promising radiosensitization approaches for hadron radiotherapies by directly inhibiting DNA damage signaling and repair pathways using, *e.g.*, PARP, ATM, and DNA-PK-specific inhibitors, or by treating cells with agents that modulate chromatin compaction and epigenetic status such as histone deacetylase inhibitors (HDACi) (16, 17). HDACi prevent the deacetylation of lysines on histone tails by different HDACs by directly binding their catalytic site, functionally maintaining chromatin in a hyperacetylated state that results in decondensation and altered rates of gene expression (18, 19). They have been shown to likewise affect the expression and acetylation status of a number of non-histone nuclear and cytoplasmic proteins involved in DNA repair, apoptosis induction, cell cycle progression, proliferation, and differentiation (20). The HDACi SAHA (suberoylanilide hydroxamic acid; vorinostat), M344 (4-(dimethylamino)-N-[7-(hydroxyamino)-7-oxoheptyl]-benzamide), and PTACH (S-[6-(4-phenyl-2-thiazolylcarbamoyl)hexyl] thioisobutyrate) are hydroxamate analogues that effectively inhibit both class I and II HDACs at nanomolar concentrations, but not other HDAC classes (21). SAHA is US FDA-approved as a stand-alone treatment for cutaneous T-cell lymphoma in patients with progressive or recurrent disease on or following two systemic therapies (22) and shows promise for the treatment of other hematological and solid malignancies alone or in combination therapies (23, 24). Patients receiving 200–600 mg vorinostat either orally or intravenously reach plasma/serum concentrations of ~1–2 μM approximately 1–2.5 h following administration (25–27). In (28), 5 μM SAHA treatments of HFS normal human fibroblasts, A549 lung carcinoma, and LNCaP prostate cancer cells *in vitro* resulted in γ-H2AX foci formation, indicating HDACi are capable of inducing DSBs. DSBs were effectively repaired in the normal cells during continuous culture with SAHA and after washout; however, both tumor cell lines demonstrated a persistence of foci and decreased expression of several key DNA damage signaling and repair proteins including Rad50, Mre11, and ATM. HDACs and other acetyltransferases also impact HRR and cellular radiosensitivity by modulating acetylation status and activity of HRR proteins directly. A report by (29) demonstrated the acetylation of Rad52 on multiple sites by p300/CBP acetyltransferase and their impact on Rad52 foci formation, a key step for Rad51 recruitment to IR-induced DSBs. Increased SAHA-mediated cytotoxicity was observed by (30) in U251tk glioblastoma cells expressing herpes simplex thymidine kinase exposed to the nucleoside analogue ganciclovir. In cells treated with 0.3–20 μM SAHA, Rad51 expression was significantly reduced in a concentration-dependent manner, and Rad51 foci formation was nearly completely inhibited at sites of replication-associated DSBs following two cycles of ganciclovir incorporation.

Abbreviations: BER, base excision repair; CIRT, carbon ion radiation therapy; DDR, DNA damage response; DSB, double-strand break; DMSO, dimethyl sulfoxide; HDACi, histone deacetylase inhibitor; HRR, homologous recombinational repair; HZE, high *Z* and *E*; IMRT, intensity-modulated radiation therapy; M344, 4-(dimethylamino)-N-[7-(hydroxyamino)-7-oxoheptyl]-benzamide; NHEJ, non-homologous end-joining; PBRT, proton beam radiation therapy; PTACH, S-[6-(4-phenyl-2-thiazolylcarbamoyl)hexyl] thioisobutyrate; RBE, relative biological effectiveness; SAHA, suberoylanilide hydroxamic acid; SER, sensitizer enhancement ratio.

Pretreatments with SAHA and other hydroxamate-based "pan-HDAC" inhibitors such as M344 and panobinostat have been shown to effectively sensitize human tumor cells *in vitro* to X- and γ-rays and *in vivo* in various chemotherapy and radiotherapy clinical trials (20, 21, 31–33). Mechanisms by which HDACi radiosensitize tumor cells include increasing apoptosis induction, altering relative cell cycle distributions, and downregulating the expression of key NHEJ and HRR repair genes. In (34), SAHA pretreatments of DU145 prostate cancer and U373vIII glioma cells (1 and 0.75 μM, respectively) synergistically increased cell killing and apoptosis induction and reduced Rad51 and DNA-PK expression post-IR in 6 Gy-irradiated DU145 cells. This was likewise observed in (31) in which SAHA-mediated radiosensitization of SAOS2 and KHOS-24S osteosarcoma and RD and A-204 rhabdomyosarcoma cell lines was associated with reduced Rad51 and Ku80 expression, increased histone H3 acetylation, and higher levels of both G2/M-phase cell cycle arrest and apoptosis induction following X-irradiation. Interestingly, in this same report, 24 h pretreatment with 1 μM SAHA did not affect the survival of normal human osteoblasts (hFOB 1.19) or diploid fibroblasts (NHDFc).

Fewer reports exist on the responses of human normal and tumor cells treated with HDACi and exposed to accelerated protons or C-12 ions at energies typically employed in hadron radiotherapy. A report by (35) showed increased C-12 ion-induced cell killing and apoptosis, along with higher expression of p21 and γ-H2AX and proportions of G2/M-phase arrested cells, in KHOS-24S osteosarcoma and A-204 rhabdomyosarcoma cells pretreated with 0.5–1 μM SAHA. A radioprotective effect of 1 μM SAHA pretreatment was seen for these same endpoints measured in C-12 ion-irradiated hFOB 1.10 osteoblasts. In (36), 24 h pretreatment of human glioblastoma LN18 and U251 cell lines with 0.5 μM SAHA prior to irradiation with 250 kVp X-rays or 290 MeV/n SOBP C-12 ions resulted in delayed kinetics of γ-H2AX foci resolution and increased cell killing with sensitizer enhancement ratios (SER) of ~1.2–1.55 reported. In (37), 3 h pretreatment with 1 mM valproic acid (VPA) sensitized hepatocellular carcinoma (HCC) cells to 230 MeV SOBP proton-induced cell killing and apoptosis induction. In (38), 24 h pretreatment with 0.2 or 2 μM SAHA sensitized A549 lung carcinoma cells to cesium-137 γ-rays, 200 MeV SOBP protons, and 290 MeV/n SOBP C-12 ions, but did not radiosensitize log-phase or quiescent G0/G1-phase normal AG01522 fibroblasts (aside from perhaps a modest degree of proton radiosensitization). Pretreatment with 2 μM SAHA also significantly reduced Rad51 and RPA foci formation in γ-ray and proton-irradiated A549 cells. Results of these studies suggest a greater potential for HDACi-mediated charged particle tumor cell radiosensitization given the greater reliance on HRR for repairing charged particle-induced clustered DNA damage.

We hypothesized that HDACi pretreatment would lead to effective *in vitro* charged particle radiosensitization of human normal and tumor cell lines similar to (or greater than) levels achieved following X- and γ-ray irradiation. We focused a portion of our studies on the radiation responses of non-transformed cells using low-passage NFF28 primary human fibroblasts as a model normal cell type, given fibroblasts are primary constituents of both normal tissue stroma and tumor microenvironments and contribute significantly to tissue-level IR responses through paracrine and endocrine signaling mechanisms (39). We first identified the most effective concentrations of SAHA, M344, and PTACH for cesium-137 γ-ray radiosensitization of quiescent G0/G1-phase NFF28 fibroblasts and asynchronously growing A549 lung carcinoma, U2OS osteosarcoma, and U87MG malignant glioma cells using single-cell colony formation assays. We then investigated impacts of HDACi pretreatment on cell killing following irradiation with accelerated 200 MeV protons, 290 MeV/n C-12 ions, and 350 MeV/n O-16 ions in the same cell strain/lines, with DSB-associated γ-H2AX/53BP1 foci assays conducted with quiescent NFF28 fibroblasts and cellular transformation (acquisition of anchorage-independent growth in soft agar) assays conducted with asynchronously growing NFF28 cultures. Charged particle irradiations were conducted in the initial entrance/plateau region of the charged particle Bragg curves, as opposed to the much higher relative LET (and associated RBE) portions of the Bragg peak region typically used for clinical hadron radiotherapies (40–43), as these more specifically relate to clinically relevant normal tissue exposures in proximal entrance regions prior to SOBP-targeted tumor volumes.

MATERIALS AND METHODS

Cell Culture and Irradiations

Cultures of NFF28 normal diploid primary human fibroblasts (passage levels 3–8), A549 lung carcinoma (CRL-CCM-185), U2OS osteosarcoma (HTB-96), and U87MG (HTB-14) malignant glioma cells were used in these experiments. The tumor cell lines were obtained from the American Type Culture Collection (ATCC). Strain NFF28 was originally isolated from neonatal foreskin by Dr. Betsy Sutherland's laboratory at Brookhaven National Laboratory (BNL) (44), and photon and charged particle radiation survival and transformation datasets are available for this fibroblast strain as reported previously (45–48). Cells were grown in αMEM medium supplemented with 15% fetal bovine serum (Hyclone), 100 U/ml penicillin, 100 μg/ml streptomycin, vitamins, amino acids, and GlutaMAX™-I (GIBCO/Invitrogen) in a 37°C incubator supplied with 95% air/5% CO_2 in standard T-25 tissue culture flasks or Nalge-Nunc™ flaskettes. Cells were maintained in asynchronous log-phase growth for survival and transformation assays or allowed to reach density-inhibited confluence (quiescence) for assessing NFF28 G0/G1-phase survival and DSB-associated foci induction and repair kinetics. For foci assays, NFF28 cells were passaged regularly prior to reaching confluency, seeded at ~30% density into microscope flaskettes (Nalge-Nunc™), and grown for 5 days to full confluency with a medium change on day 2. Suberoylanilide hydroxamic acid (SAHA), 4-(dimethylamino)-N-[7-(hydroxyamino)-7-oxoheptyl]-benzamide (M344), and S-[6-(4-phenyl-2-thiazolylcarbamoyl) hexyl] thioisobutyrate (PTACH) were purchased from

Sigma-Aldrich and prepared as 10 or 100 mM stocks dissolved in DMSO. Cultures were pretreated with 1–20 μM concentrations of HDACi or 0.1% DMSO as a vehicle control for 18 h prior to irradiation.

Cesium-137 662-keV γ-ray irradiations were conducted using the BNL Biology Department's J.L. Shepherd Mark I Model 68A cabinet irradiator at a dose-rate of ~0.7 Gy/min (dosimetry verified by J.L. Shepherd). Charged particle irradiations were conducted at the NASA Space Radiation Laboratory (NSRL) at BNL. Accelerated beams of 200 MeV protons (LET = 0.45 keV/μm in H_2O), 290 MeV/n C-12 ions (LET = 13.02 keV/μm), and 350 MeV/n O-16 ions (LET = 20.90 keV/μm) were delivered in the entrance/plateau region of the Bragg curve (as opposed to the higher LET Bragg peak or as a SOBP) at dose-rates of ~0.1–0.6 Gy/h. Doses were confirmed by NSRL physicists at the flask position using a NIST-traceable tissue-equivalent ion chamber (EG&G model IC-17) used to calibrate a series of custom parallel-plate beamline ionization chambers to control beam delivery (49). Cell cultures were irradiated at room temperature in sealed flasks or microscope chamber slides. After irradiation, cells were subcultured and plated immediately for survival, or the medium changed and cells incubated at 37°C until subculture for transformation assays. For measurements of DSB-associated foci levels, fibroblast cultures in flaskettes were returned to the NSRL 37°C incubator until collection/fixation from 10 min to 24 h post-irradiation. Sham-irradiated cells for all assays were harvested by identical procedures.

Immunocytochemistry and DSB-Associated γ-H2AX pS139/53BP1 Foci Imaging/Scoring

DSB-associated colocalized γ-H2AX/53BP1 foci formation was evaluated as described previously (50, 51). The medium in SAHA-treated cultures was not changed post-irradiation, so cells were treated continuously with 10 μM SAHA until being collected at the following time points. At 10 min, 30 min, 2 h, 6 h, and 24 h post-irradiation, flaskettes were removed from the 37°C incubator, rinsed with PBS, and fixed with fresh 4% formaldehyde at room temperature for 15 min. Slides were then permeabilized with 0.5% Triton X-100 on ice for 10 min, and washed with PBS. Slides were blocked in PBS with 1% BSA, 2% fetal bovine and goat sera, 0.1% Triton X-100, and 0.05% Tween-20 for 30 min at room temperature followed by incubation in a 37°C humid chamber for 30 min with one of the following primary antibody combinations diluted 1:400 in PBS with 1% BSA: mouse monoclonal anti-γ-H2AX pS139 (JBW301, Upstate/Millipore) and rabbit polyclonal anti-53BP1 (NB100-304, Novus Biologicals). Slides were rinsed in PBS and incubated in a 37°C humid chamber for 30 min with Alexa Fluor® 488 and 594-conjugated goat anti-mouse and anti-rabbit F(ab′)2 fragments (Molecular Probes/Invitrogen) diluted 1:500 in PBS. Slides were rinsed in PBS, treated with 3.7% formaldehyde to immobilize the antibodies at their target locations, and mounted with ProLong Gold antifade reagent with 0.2 μg/ml 4′, 6-diamidino-2-phenylindole (DAPI; Molecular Probes/Invitrogen). Images were captured using a Zeiss Axio Observer Z1 epifluorescence microscope equipped with a 63× oil immersion objective and appropriate filter sets, and processed using Zeiss AxioVision image analysis software. For two to three independent experiments, ≥50 cells per time-point were scored by eye by two cross-corroborated scorers to minimize any observer bias. Nuclei of atypical size or morphology or those with very high foci counts (*e.g.*, S-phase cells) were not scored.

Survival and Transformation Assays

Post-irradiation cell survival was determined by single-cell colony formation assays as described previously (52). Immediately following irradiation, appropriate numbers of cells were plated in triplicate in 10-cm culture dishes or T-25 flasks with complete medium to yield ~50–100 viable colonies after 14 days of undisturbed growth at 37°C. Dishes were then aspirated and rinsed with PBS, fixed with 95% ethanol, and stained with a solution of 50% (v/v) Kopykake blue food dye (Kopykake Enterprises), 40% methanol, and 10% glacial acetic acid. Colonies of ≥50 viable cells were scored as survivors. Post-irradiation transformation frequencies were assessed by measurement of anchorage-independent (A-I) growth in soft agar, a selective condition in which untransformed fibroblasts do not proliferate, per established Sutherland lab protocols (45, 47, 53). For A-I growth, 8 ml of agar mix consisting of 80 ml 1.25% Difco Bacto agar, 80 ml 2X DMEM, 20 ml iron-supplemented FCS, 20 ml Difco tryptose phosphate broth (29.5 g/l ddH_20) was aliquoted in 60-mm culture dishes and allowed to set. They were then overlaid with a mixture of 1 ml of medium plus serum containing 10^5 cells plus 2 ml agar mix and allowed to solidify at RT. Plates were incubated at 37°C for 20 days with weekly medium changes to maintain proper humidity, after which A-I colonies of ≥50 cells were counted under a dissecting microscope. The frequency of transformants per survivor was determined from the ratio of A-I colonies per number of surviving cells plated, with ≥6 replicate dishes counted per data point in at least two independent experiments.

Statistical Analyses

Statistical analyses were performed using Prism (GraphPad Software). Survival data were fit using Prism's weighted least-squares linear-quadratic survival curve-fitting function; survival datasets were best fit by either a linear-quadratic (LQ; $S = e^{-\alpha D-\beta D\wedge 2}$) or linear ($S = e^{-\alpha D}$) exponential function. Transformation data were best fit by Prism using weighted least-squares regression hyperbolic curve fitting over the full dose range and linearly for low doses ≤25 cGy. Low dose DSB-associated foci induction data at low doses were also fitted by linear regression curve fits. Statistical differences among datasets were tested using unpaired two-tailed Student's *t*-tests with Welch's correction and one-way or two-way ANOVA with Tukey's HSD *post hoc* test (Prism) used to identify statistically significant differences among groups; *p*-values ≤0.05 were considered statistically significant differences.

RESULTS

Gamma Ray Survival Assays

Single-cell colony formation assays were first performed with 1–20 μM concentrations of SAHA, M344, and PTACH to determine their optimum concentrations for cesium-137 γ-ray radiosensitization of NFF28 fibroblasts and A549 lung carcinoma, U2OS osteosarcoma, and U87MG malignant glioma cells. Sham-irradiated plating (cloning) efficiencies (PE) for 1–20 μM HDACi 18 h pretreatments for all four cell types are shown in **Supplementary Figure 1**. Quiescent G0/G1-phase NFF28 fibroblasts showed increased PE values following pretreatment with all three HDACi at the concentrations tested, and the three tumor lines generally showing reduced plating efficiencies with increasing inhibitor concentrations. Survival curves for NFF28, A549, U2OS, and U87MG cells irradiated with 0.5–6 Gy γ-rays are shown in **Figure 1** for cultures pretreated with SAHA and **Supplementary Figures 2**, **3** for cultures pretreated with M344 and PTACH, respectively. Significant radiosensitization of NFF28 fibroblasts was observed for all three HDACi at higher doses of 1–6 Gy (p = <0.0001–0.0221 for SAHA, 0.0008–0.0457 for M344, 0.0009–0.0161 for PTACH by one-way ANOVA). Of the three HDACi tested, SAHA provided the highest degree of γ-ray radiosensitization for the three tumor lines (p = 0.0037–0.0406 for A549 for doses of 2–6 Gy, 0.0018–0.0317 for U2OS at 6 Gy, and 0.0466 for 2 Gy-irradiated U87MG cells pretreated with 20 μM SAHA). M344 was only effective at significantly radiosensitizing A549 cells at 2 Gy only (10 μM M344; p = 0.0202) and U2OS and U87MG cells at the highest dose of 6 Gy (p=0.0013–0.0027 for 5–20 μM M344 and p=0.0293 and 0.0374 for 10 and 20 μM M344, respectively). The results of the γ-ray clonogenic survival assays are summarized in **Supplementary Table 1** with D_{10} (doses required to reduce relative survival to 10%) and SER values (calculated as the ratios of D_{10} values of HDACi-pretreated cells to DMSO vehicle controls) reported.

SER values for 1–20 μM concentrations of the three HDACi are shown in **Supplementary Figure 4** with levels of γ-ray

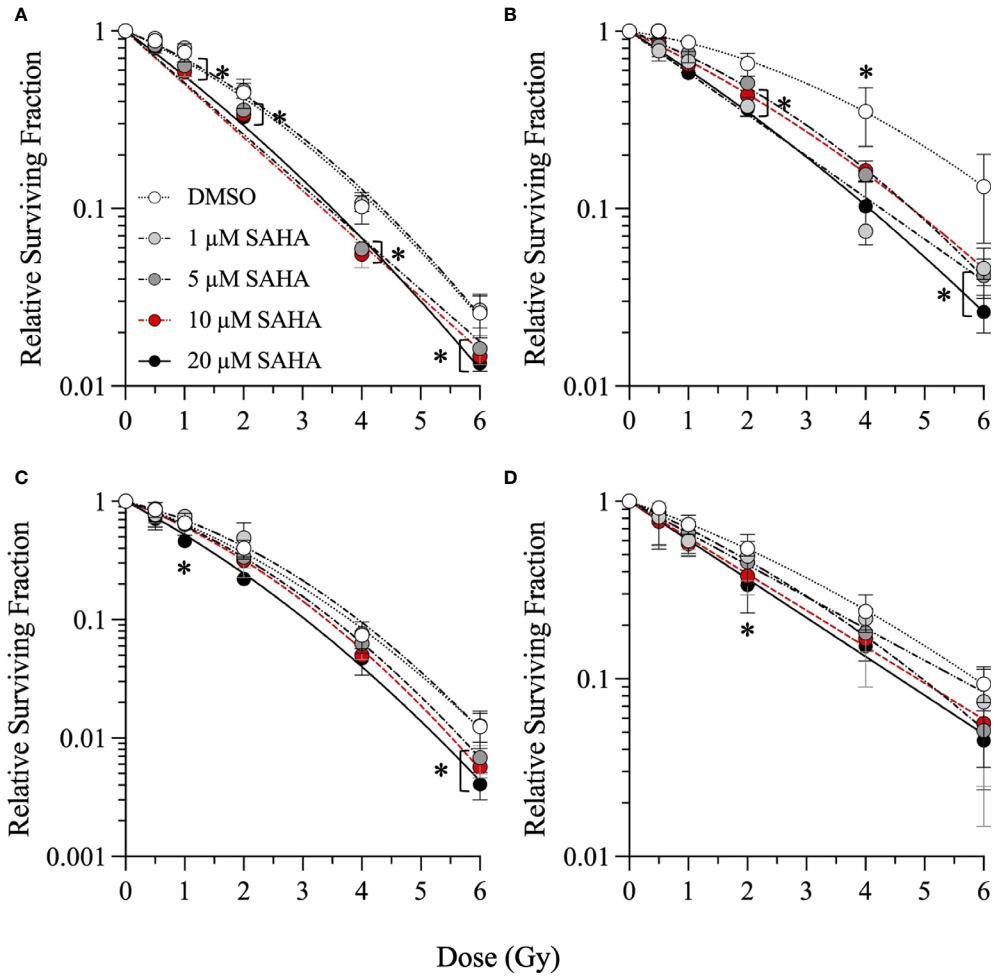

FIGURE 1 | Clonogenic survival of G0/G1-phase normal NFF28 primary fibroblasts **(A)** and asynchronously growing A549 lung carcinoma **(B)**, U2OS osteosarcoma **(C)**, and U87MG malignant glioma cells **(D)** pretreated for 18 h with 1–20 μM SAHA and exposed to 0.5–6 Gy cesium-137 γ-rays (LET = 0.91 keV/μm). Data reported as mean ± SD; where error bars are not visible, they are smaller than the data point. Asterisks mark significant differences compared to DMSO controls at p-values of ≤0.05 (*) by one-way ANOVA.

radiosensitization in the four cell types generally increasing in a concentration-dependent manner. A549 lung carcinoma cells showed the greatest degree of radiosensitization with SER values of 1.36–1.6 following 1–20 μM SAHA pretreatment ($p = 0.0359$ and 0.0133 for 1 and 20 μM SAHA, respectively, by two-way ANOVA), along with values of 1.32 and 1.16 for 10 μM M344 and 5 μM PTACH, respectively. SER values ranged from 1.16 to 1.33 for quiescent NFF28 fibroblasts, 1.03–1.25 for U2OS osteosarcoma cells and 1.08–1.31 for U87MG cells ($p = 0.0065$ for 20 μM SAHA and 0.0072 for 10 μM M344). Both SAHA and M344 showed more efficient γ-ray radiosensitization than PTACH in all three tumor cell lines, while all three compounds equally radiosensitized NFF28 fibroblasts. Interestingly, slightly increased survival (*i.e.*, mild radioprotection) was observed for quiescent NFF28 fibroblasts pretreated with 1 μM concentrations of all three HDACi and also for U2OS osteosarcoma cells pretreated with 1 μM SAHA and PTACH (both are mesenchymal-derived cell types). Based on results of these assays, we chose 10 μM SAHA, 10 μM M344, and 5 μM PTACH as the most effective radiosensitizer concentrations (that did not likewise appreciably decrease PE per **Supplementary Figure 1**) for the subsequent charged particle irradiations.

Proton, Carbon, and Oxygen Ion Survival Assays

Single-cell colony formation assays were next performed with 10 μM SAHA, 10 μM M344, and 5 μM PTACH concentrations to determine their ability to radiosensitize all four cell types to charged particle irradiation delivered at typical hadron RT energies. Unlike clinical SOBP irradiations employing the higher LET portion of the Bragg peak, these irradiations were conducted using the initial Bragg plateau region since a major focus of this study was modeling proximal (entrance) normal tissue effects of irradiated stromal fibroblasts. Survival curves are shown in **Figures 2–4** for low-passage G0/G1-phase NFF28 fibroblasts (**panel A**) and asynchronously growing A549 lung carcinoma (**B**), U2OS osteosarcoma (**C**), and U87MG malignant glioma cells (**D**) irradiated with 0.5–4 Gy of 200 MeV protons (LET = 0.45 keV/μm in H_2O; **Figure 2**), 290 MeV/n carbon-12 ions (13.02 keV/μm; **Figure 3**), or 350 MeV/n oxygen-16 ions (20.90 keV/μm; **Figure 4**), respectively. All three HDACi were able to significantly radiosensitize NFF28 fibroblasts at higher proton doses of 3–4 Gy ($p = 0.0001$–0.0311; **Figure 2A**) and for 2 Gy of O-16 ions ($p = 0.0179$–0.0386; **Figure 4A**); however, no significant differences were noted for C-12 ion irradiations (**Figure 3A**). Significant HDACi-mediated radiosensitization was not observed for A549 cells exposed to any of the three charge particle types except for 50 cGy O-16 ion irradiations ($p = 0.0193$ for 10 μM SAHA and 0.025 for 10 μM M344; **Figure 4B**). The only significant difference observed for U2OS survival was for 5 μM PTACH-pretreated cells exposed to 2 Gy C-12 ions ($p = 0.00422$; **Figure 3C**). For U87MG survival, significant differences were only noted for 2 and 4 Gy C-12 ion irradiations ($p = 0.0442$ and 0.0296, respectively; **Figure 3D**).

SER values for the three HDACi and four radiation qualities used in this study are shown in **Figure 5**. Significant levels of HDACi-mediated γ-ray radiosensitization were observed for NFF28 fibroblasts ($p = 0.024$ for 10 μM SAHA and 0.0075 for 5 μM PTACH by two-way ANOVA), A549 cells ($p = 0.0123$ for 10 μM SAHA), and U87MG cells ($p = 0.0064$ for 10 μM M344). Unlike the nearly uniform radiosensitization observed for γ-rays with all four cell types, pretreatment with the optimal HDACi γ-ray radiosensitizing concentrations yielded mixed results in terms of charged particle radiosensitization or radioprotection depending on the cell strain/line and ion species. For 200 MeV protons, levels of radiosensitization similar to γ-rays were observed for quiescent NFF28 fibroblasts and U87MG cells only (**Figures 2A, D**; $p = 0.0096$ for U87MG cells pretreated with 5 μM PTACH). For A549 lung carcinoma cells (**Figure 2B**), pretreatment with 10 μM SAHA radiosensitized cells to protons; however, pretreatment with 10 μM M344 and 5 μM PTACH conversely provided radioprotection. For U2OS osteosarcoma cells (**Figure 2C**), only pretreatment with 10 μM SAHA showed slight radiosensitization for protons, while the other two HDACi provided mild radioprotection. Results for the intermediate LET C-12 and O-16 ion irradiations were even more surprising, with all three HDACi providing radioprotection for quiescent G0/G1-phase NFF28 fibroblasts (significantly so for O-16 ions, $p = 0.0054$–0.023; **Figures 3A**, **4A**, **5A**). For the three tumor cell lines, patterns of HDACi-mediated radiosensitization and radioprotection varied for C-12 and O-16 ions. A549 cells showed mild HDACi-mediated radiosensitization for C-12 ions and radioprotection for O-16 ions (**Figures 3B**, **4B**). U2OS cells showed the reverse pattern whereby the inhibitors provided mild radioprotection for C-12 ions and radiosensitization for O-16 ions (**Figures 3C**, **4C**). For U87MG cells, HDACi pretreatment generally resulted in radiosensitization for both ions (**Figures 3D**, **4D**), although pretreatment with 10 μM SAHA resulted in C-12 ion radioprotection.

In order to compare responses to the different radiation types alone (without HDACi treatments), survival curves for DMSO-treated vehicle controls are shown in **Figure 6**. Per **Figure 6A**, there is a direct correlation of cell killing with particle LET in G0/G1-phase NFF28 fibroblasts, with exposures to cesium-137 γ-rays and 200 MeV Bragg plateau protons yielding approximately equivalent survival. Both C-12 and O-16 ion irradiations resulted in significantly increased NFF28 cell killing compared to γ-rays ($p = 0.015$–0.0268 for C-12 ions and 0.0008–0067 for O-16 ions by one-way ANOVA). Significantly increased tumor cell killing following C-12 and O-16 ion irradiations was also observed for A549 cells ($p = 0.0002$–0.0385 for C-12 ion and 0.0011–0.0146 for O-16 ions), U2OS cells ($p = 0.0032$–0.0137 for C-12 ions and 0.0084–0.0429 for O-16 ions), and U87MG cells ($p = 0.0104$–0.0303 for C-12 ions and 0.0179–0.0438 for O-16 ions). Interestingly, in all three tumor lines, cell killing was greater for 290 MeV/n Bragg plateau C-12 ions (LET = 13.02 keV/μm) compared to higher LET 350 MeV/n Bragg plateau O-16 ions (LET = 20.90 keV/μm; **Figures 6B–D**). For proton irradiations, only A549 cells showed increased cell killing compared to γ-rays ($p = 0.0094$ at 50 cGy).

To summarize the charged particle clonogenic survival results from DMSO and HDACi-treated cells in **Figures 2–4**, RBE values for the three radiation types compared to reference cesium-137 γ-rays (**Figure 1** and **Supplementary Figures 2**, **3**) are reported in

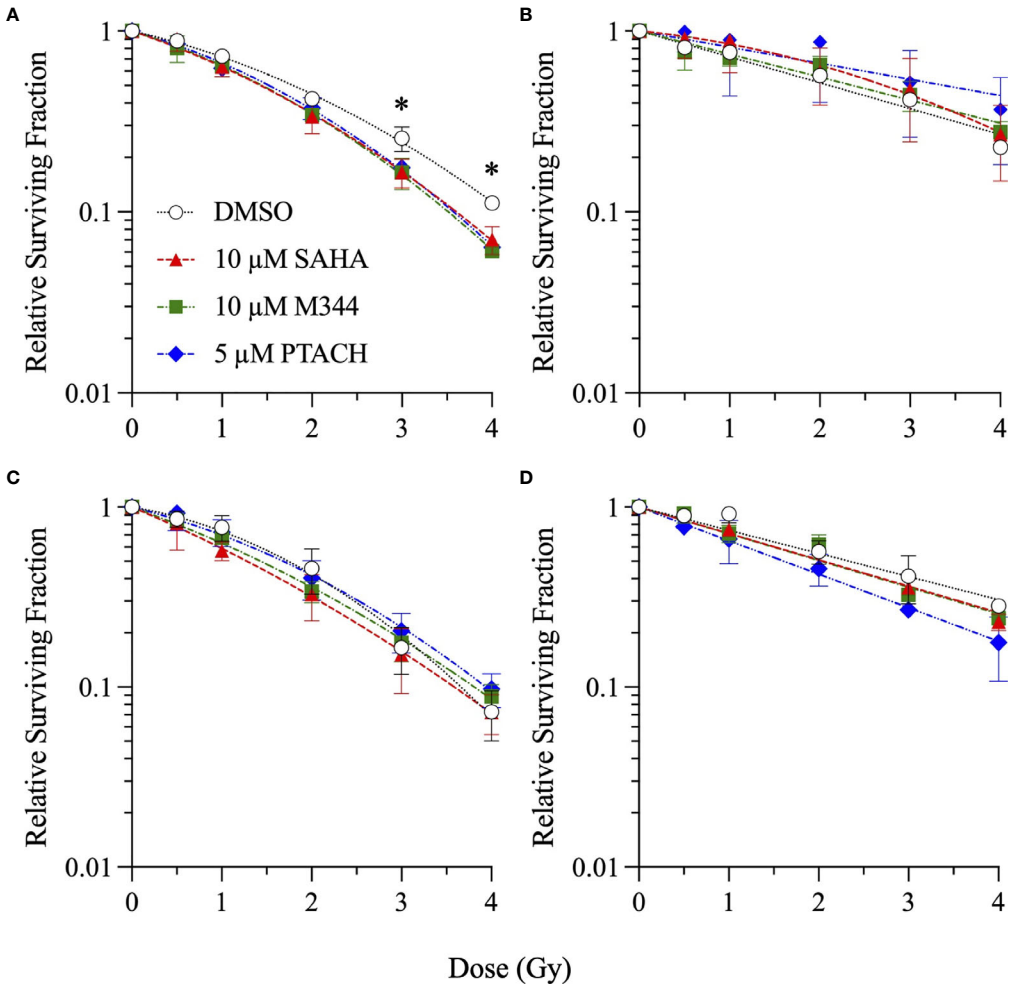

FIGURE 2 | Clonogenic survival of G0/G1-phase normal NFF28 primary fibroblasts **(A)** and asynchronously growing A549 lung carcinoma **(B)**, U2OS osteosarcoma **(C)**, and U87MG malignant glioma cells **(D)** pretreated for 18 h with 10 μM SAHA, 10 μM M344, or 5 μM PTACH and exposed to 0.5–4 Gy 200 MeV protons in the Bragg plateau region (LET = 0.45 keV/μm). Data reported as mean ± SD; where error bars are not visible, they are smaller than the data point. Asterisks mark significant differences compared to DMSO controls at *p*-values of ≤0.05 (*) by one-way ANOVA.

Figure 7 with RBE values for HDACi-treated cells calculated from corresponding γ-ray survival D_{10} values of cells pretreated with the identical HDACi concentrations. In this case, RBE values <1 would imply that the particular combination of charged particle and HDACi was less effective for cell killing than the corresponding γ-ray/HDACi combination. For protons, HDACi pretreatment provided no added advantage compared to exposing pretreated cultures to γ-rays and often was less effective (significantly so for U87MG cells pretreated with 10 μM M344, $p = 0.0365$). For C-12 ions, DMSO and HDACi-pretreated cells yielded significantly higher RBE values by ANOVA analyses in all three tumor cell lines (p = <0.0001–0.0057 for A549 cells, 0.0002–0.0241 for U2OS cells, and <0.0001–0.0003 for U87MG cells), and the HDACi treatments nearly uniformly resulted in tumor cell radioprotection compared to vehicle controls. Significantly increased cell killing was observed in NFF28 fibroblasts following O-16 ion irradiation (p = 0.0002), but this effect was lost in the HDACi-pretreated cultures. Significantly increased U2OS and U87MG tumor cell killing was also observed for O-16 ion irradiations (p = 0.0048–0.0197 and <0.0001–0.0225, respectively), with little added effect seen following HDACi pretreatments. In NFF28 fibroblasts and A549 cells, HDACi pretreatments resulted in radioprotection for O-16 ion exposures. **Supplementary Table 2** summarizes the various D_{10}, HDACi SER, and charged particle RBE values for the four cell types.

DSB-Associated Foci Assays

Results of γ-H2AX/53BP1 foci analyses conducted in quiescent G0/G1-phase cultures of NFF28 fibroblasts pretreated for 18 h with 10 μM SAHA and subsequently irradiated with 5–25 cGy doses of cesium-137 γ-rays, 200 MeV protons, and 290 MeV/n C-12 ions are shown in **Figures 8A–C**, respectively, reported as numbers of mean (± SEM) IR-induced foci per unit dose.

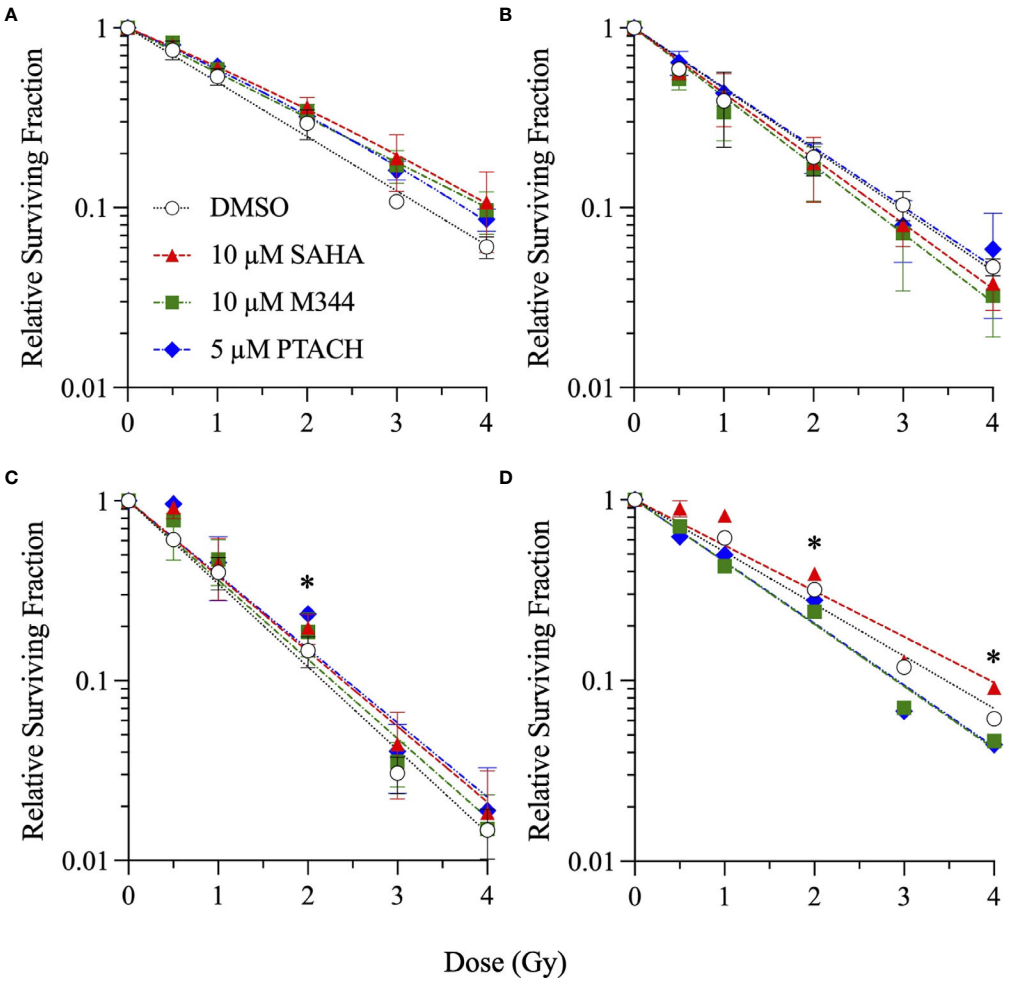

FIGURE 3 | Clonogenic survival of G0/G1-phase normal NFF28 primary fibroblasts **(A)** and asynchronously growing A549 lung carcinoma **(B)**, U2OS osteosarcoma **(C)**, and U87MG malignant glioma cells **(D)** pretreated for 18 h with 10 μM SAHA, 10 μM M344, or 5 μM PTACH and exposed to 0.5–4 Gy 290 MeV/n C-12 ions in the Bragg plateau region (LET = 13.02 keV/μm). Data reported as mean ± SD; where error bars are not visible, they are smaller than the data point. Asterisks mark significant differences compared to DMSO controls at *p*-values of ≤0.05 (*) by one-way ANOVA.

Multiple post-translational modifications of histone H2AX and 53BP1 occur after the initial recognition of IR-induced DSBs, including the phosphorylation of H2AX on serine 139 (γ-H2AX pS139) by the DDR kinases ATM and DNA-PK (54–56) and 53BP1 recruitment and binding to post-translationally modified histones (57–61). The formation and colocalization of these cytogenetically visible DSB-associated foci permit their more efficient detection and enumeration at low IR doses (50, 62, 63). Peak DSB-associated foci induction was observed 30 min post-irradiation for all three radiation types, followed by similar rates of NHEJ-mediated DSB repair and foci resolution to at or near background levels by 24 h, similar to the low dose responses of other normal primary fibroblast strains reported in (50). Mean background levels of foci measured in sham-irradiated cultures were 1.02 foci/cell for DMSO-pretreated cultures and 0.99 foci/cell for 10 μM SAHA-pretreated cultures. The greatest amount of radiosensitization, measured as ~1.4-fold increased levels of peak induced foci formation, was observed following cesium-137 γ-ray irradiation (**Figure 8A**). Significant differences in γ-ray-induced foci levels between DMSO vehicle and 10 μM SAHA pretreatments were observed 10 min post-IR (p = 0.0216), as well as at the 6 and 24 h timepoints (p = 0.0208 and 0.0144, respectively). Low-dose proton-induced foci levels were similar in control and SAHA-pretreated cultures (**Figure 8B**), and foci levels were reduced ~1.4-fold in 10 μM SAHA-pretreated cells following low dose C-12 ion irradiation (**Figure 8C**). These patterns reflect the results of the clonogenic assay results whereby the greatest degree of low dose radiosensitization is observed for cesium-137 γ-rays, followed by similar survival of control and SAHA-pretreated cells following low-dose proton irradiation, and radioprotection observed for C-12 ion-irradiated NFF28 fibroblasts pretreated with SAHA.

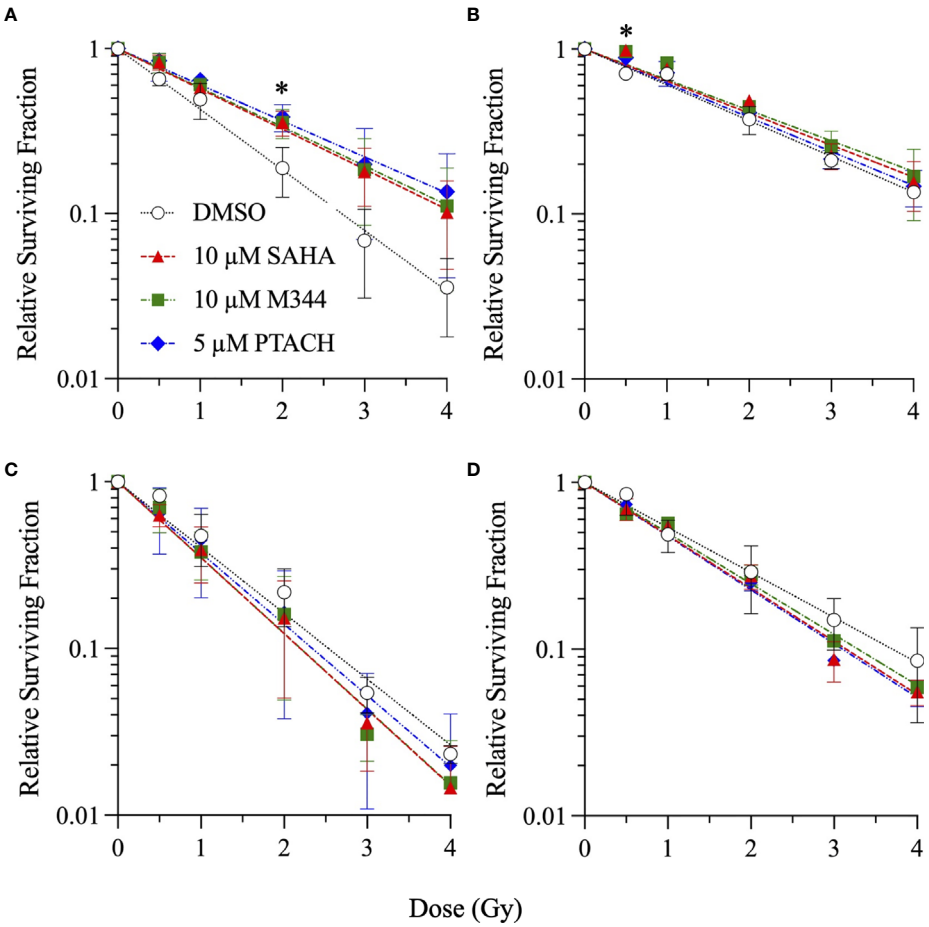

FIGURE 4 | Clonogenic survival of G0/G1-phase normal NFF28 primary fibroblasts **(A)** and asynchronously growing A549 lung carcinoma **(B)**, U2OS osteosarcoma **(C)**, and U87MG malignant glioma cells **(D)** pretreated for 18 h with 10 μM SAHA, 10 μM M344, or 5 μM PTACH and exposed to 0.5–4 Gy 350 MeV/n O-16 ions in the Bragg plateau region (LET = 20.90 keV/μm). Data reported as mean ± SD; where error bars are not visible, they are smaller than the data point. Asterisks mark significant differences compared to DMSO controls at *p*-values of ≤0.05 (*) by one-way ANOVA.

NFF28 Asynchronous Cell Survival and Transformation Assays

Finally, the clonogenic survival of asynchronously growing NFF28 fibroblasts and frequencies of *in vitro* cellular transformation, measured as the acquisition of anchorage-independent (A-I) growth in soft agar, following HDACi pretreatment and irradiation with cesium-137 γ-rays, 200 MeV protons, 290 MeV/n C-12 ions, and 350 MeV/n O-16 ions are shown in **Figures 9**, **10**, respectively. These assays were conducted using protocols devised by Dr. Betsy Sutherland and colleagues that utilize asynchronously growing log-phase human fibroblast cultures rather than quiescent G0/G1-phase cultures. Following a 7-day culture recovery period to allow clearance of dead cells, surviving irradiated NFF28 fibroblasts were subcultured, plated at low density in soft agar, and incubated for a 20-day colony formation period after which the dishes were rinsed and evaluated for A-I colonies. In contrast to the G0/G1-phase survival assay results reported in previous figures whereby HDACi pretreatment was radiosensitizing for γ-ray and proton irradiations but radioprotective for C-12 and O-16 ion irradiations, 18 h HDACi pretreatment of asynchronously growing log-phase NFF28 cultures resulted in sensitization for *all* radiation types as shown in **Figure 9** (suggesting that the higher proportion of S and G2-phase cells in these cultures are more sensitive to HDAC inhibition and subsequent charged particle irradiation than G0/G1-phase cells). Of the three HDACi tested, pretreatments with 10 μM SAHA consistently yielded the best radiosensitization; however, neither 10 μM M344 nor 5 μM PTACH was effective at radiosensitizing asynchronously growing NFF28 cells to γ-rays. Significant differences in clonogenic survival between HDACi and DMSO vehicle-pretreated cells were observed primarily for C-12 ions (**Figure 9C**; *p*-values ranging from ≤0.0001 to 0.0334 by one-way ANOVA), while only SAHA and PTACH were able to significantly radiosensitize cells to higher doses of O-16 ions (p = 0.0127 and 0.0304 at 3 Gy, respectively).

Frequencies of IR-induced NFF28 cellular transformation, measured as the yields of A-I colonies per 10^5 surviving cells, are

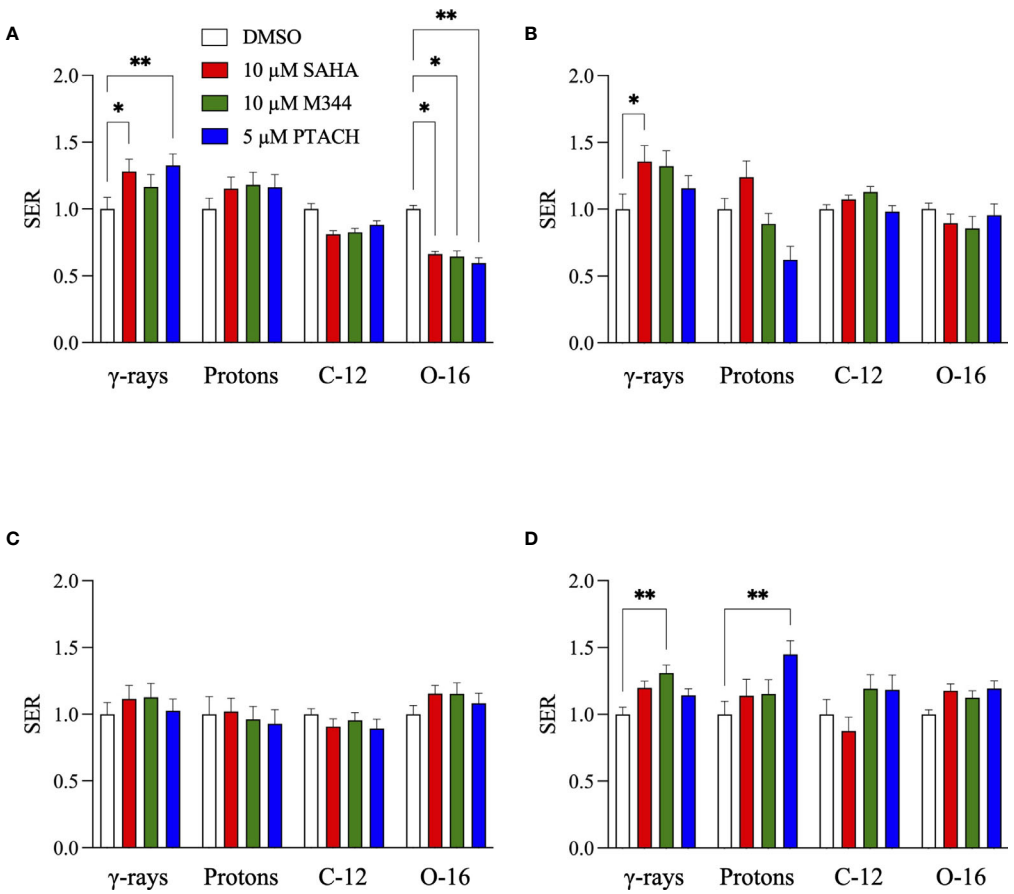

FIGURE 5 | HDACi sensitizer enhancement ratio (SER) values ± SEM for G0/G1-phase normal NFF28 primary fibroblasts **(A)** and asynchronously growing A549 lung carcinoma **(B)**, U2OS osteosarcoma **(C)**, and U87MG malignant glioma cells **(D)** pretreated for 18 h with 10 μM SAHA, 10 μM M344, and 5 μM PTACH and irradiated with cesium-137 γ-rays, 200 MeV protons, 290 MeV/n C-12 ions, or 350 MeV/n O-16 ions [calculated using D_{10} survival values; asterisks mark significant differences at *p*-values of ≤0.05 (*) and ≤0.01 (**) by two-way ANOVA].

plotted in **Figure 10**. The lowest overall induction occurred following 200 MeV proton irradiation (~0.74-fold that of cesium-137 γ-rays) with C-12 and O-16 ion irradiations producing ~1.7-fold and ~3.2-fold higher maximal yields of transformants per unit dose compared to cesium-137 γ-rays, respectively. All four radiation qualities demonstrate a rapid increase in transformation induction for doses ≤50 cGy (significantly so for γ-ray and proton exposures), a plateauing at 1 Gy, and in the case of protons and C-12 ions, decreasing yields at higher doses. Both cesium-137 γ-rays and O-16 ions also showed a general plateau at higher doses up to 2 Gy; however, yields of transformants were further increased at 3 Gy for both radiation types. Yields of γ-ray and proton-induced transformants per unit dose measured at low doses (≤25 cGy) were ~1.8 and 2.8-fold higher, respectively, than yields measured at higher doses (>50 cGy), with ratios of ~1.3 and ~1 calculated for C-12 and O-16 ions, respectively. HDACi pretreatment in the majority of cases resulted in decreased yields of transformants at low doses (≤25 cGy) and increased yields of transformants for all radiation types at higher doses (>50 cGy). The only exceptions were M344 pretreatment followed by proton irradiation and SAHA pretreatment followed by O-16 ion irradiation. Although per **Figure 9**, HDACi pretreatments were radiosensitizing for asynchronously NFF28 fibroblast survival, the fact that yields of transformants are weighted and reported per number of *surviving* cells implies that HDACi treatments generally increased both γ-ray and charged particle-induced normal fibroblast transformation overall (although the differences were not statistically significant).

Given the steep increase in yield of transformants at low doses, the frequencies of IR-induced NFF28 fibroblast transformation per unit dose at low doses (≤25 cGy) and higher doses (>50 cGy) following SAHA, M344, or PTACH pretreatment are comparatively plotted in **Figure 11**. Low dose transformation frequencies were calculated as the slope of induction from 5–25 cGy, and the higher dose transformation frequencies were obtained from the mean transformation frequencies at 1 Gy, the dose where peak (maximal) transformation occurs for both 200 MeV protons and 290 MeV/n C-12 ions (**Figures 10B, C**). As per **Figures 11A, B**,

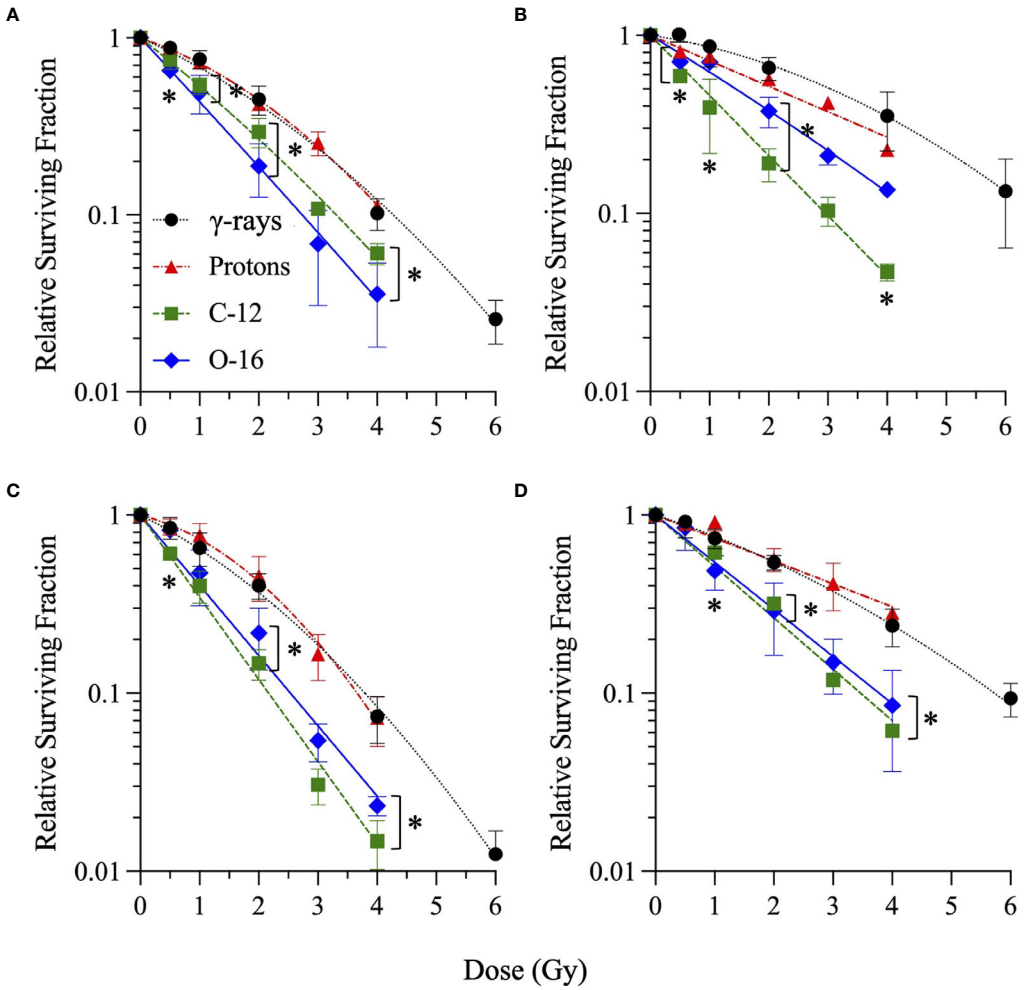

FIGURE 6 | Clonogenic survival of DMSO-treated (vehicle control) G0/G1-phase normal NFF28 primary fibroblasts **(A)** and asynchronously growing A549 lung carcinoma **(B)**, U2OS osteosarcoma **(C)**, and U87MG malignant glioma cells **(D)** irradiated with cesium-137 γ-rays, 200 MeV protons, 290 MeV/n C-12 ions, or 350 MeV/n O-16 ions. Data reported as mean ± SD; where error bars are not visible, they are smaller than the data point. A LET-dependent increase in cell killing is observed for NFF28 fibroblasts; however 290 MeV/n C-12 ions (LET = 13.02 keV/μm) were more effective than 350 MeV/n O-16 ions (LET = 20.90 keV/μm) for cell killing in all three tumor cell lines. Asterisks mark significant differences compared to cesium-137 γ-rays at *p*-values of ≤0.05 (*) by one-way ANOVA.

both cesium-137 γ-rays and protons showed significantly higher yields of transformants per unit dose at low doses compared to higher doses (p = 0.0477 and <0.0001–0.003, respectively, by two-way ANOVA), with HDACi pretreatment reducing the yields of low dose transformants for both radiation types compared to DMSO-treated controls. This pattern of low dose transformation sparing is likewise observed for 18 h PTACH pretreatment preceding C-12 ion irradiation and SAHA pretreatment prior to O-16 ion irradiation. Pretreatment with either SAHA or M344 followed by C-12 ions resulted in equivalent yields of transformants at both low and high doses, and pretreatment with M344 or PTACH prior to O-16 ion irradiation increased transformation at higher doses. Low-dose hyper-radiosensitivity for NFF28 fibroblast transformation was generally not observed for C-12 or O-16 ions, suggesting it may be a phenomenon particular to low LET radiations. Results of the clonogenic survival and transformation experiments conducted with asynchronously growing NFF28 fibroblasts are summarized in **Supplementary Tables 3, 4** (D_{10} values and yields of transformants per unit dose, respectively, along with associated HDACi SER and charged particle RBE values).

DISCUSSION

In light of previous reports of promising levels of SAHA and other HDACi-induced X- and γ-ray radiosensitization, we sought to determine if these agents would be likewise useful for radiosensitizing tumor cells to charge particle-based radiotherapy modalities (without likewise doing so to surrounding normal tissues) using normal diploid human fibroblasts and three tumor cell lines as *in vitro* models. Few

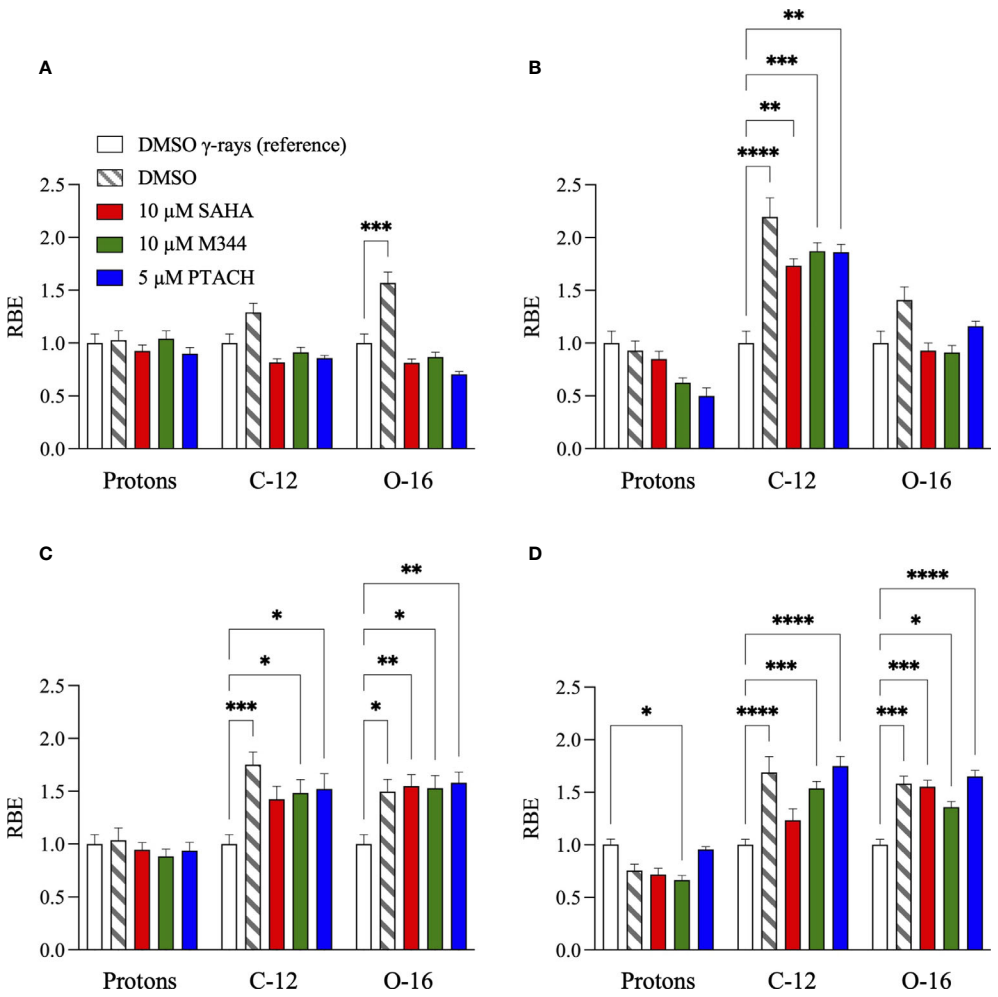

FIGURE 7 | Relative biological effectiveness (RBE) values ± SEM for G0/G1-phase normal NFF28 primary fibroblasts **(A)** and asynchronously growing A549 lung carcinoma **(B)**, U2OS osteosarcoma **(C)**, and U87MG malignant glioma cells **(D)** pretreated for 18 h with 10 μM SAHA, 10 μM M344, and 5 μM PTACH and irradiated 200 MeV protons, 290 MeV/n C-12 ions, or 350 MeV/n O-16 ions compared to respective DMSO control or HDACi-pretreated cultures exposed to reference cesium-137 γ-rays [calculated using D_{10} survival values; asterisks mark significant differences at *p*-values of ≤0.05 (*), ≤0.01 (**), ≤0.001 (***), and ≤10^{-4} (****) by two-way ANOVA].

reports exist on the utility of using HDACi as adjuvants for proton or carbon ion radiotherapies, with available studies generally showing increased tumor cell killing *in vitro via* clonogenic survival assays and increased levels of IR-induced DSBs measured by DSB-associated foci assays, often with delayed foci repair kinetics in HDACi-treated cells compared to vehicle-treated controls. In this study, we validated that the clinically approved HDACi SAHA and two related hydroxamate analogues M344 and PTACH were effective for radiosensitizing normal human fibroblasts and tumor cells to cesium-137 γ-rays and 200 MeV protons (**Figures 1**, **2**). However, the three HDACi tested provided comparatively less radiosensitization (and in some case radioprotection) to pretreated tumor cells prior to C-12 or O-16 ion irradiation (**Figures 3**, **4**). Effects of HDACi pretreatment in NFF28 fibroblasts depended on whether cultures were quiescent or cycling, with radioprotection afforded to stationary G0/G1-phase cultures exposed to C-12 and O-16 ions. HDACi pretreatment radiosensitized log-phase NFF28 cells to these ions (**Figure 9**) and generally increased the frequencies of IR-induced transformation following exposure to all four radiation types (**Figure 10**). These studies therefore provide mixed results on the utility of HDACi for increasing the effectiveness of light ion-based hadron radiotherapies.

The clonogenic survival of A549 lung carcinoma and diploid normal fibroblasts reported herein are very similar to those reported in (38) who used 24 h pretreatments of 0.2 or 2 μM SAHA concentrations prior to irradiation (compared to 18 h pretreatments in our study). We both report cesium-137 γ-ray D_{10} values of 6.5 Gy for control (DMSO-treated) A549 cells and very similar D_{10} values of 4.31 and 4.27 Gy for two low-passage G0/G1-phase primary fibroblast strains (AG01522 and NFF28, respectively; **Supplementary Table 1**). From their report,

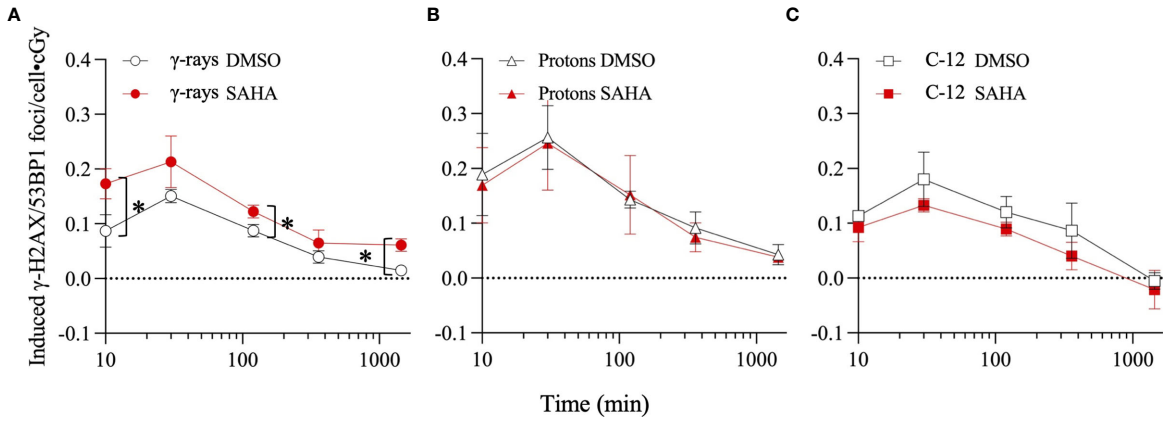

FIGURE 8 | Dose-corrected γ-H2AX pS139/53BP1 foci levels in quiescent G0/G1-phase normal NFF28 primary fibroblasts pretreated for 18 h with 0.1% DMSO (vehicle control) or 10 μM SAHA measured by immunocytochemistry/image analysis in samples fixed 10 min to 24 h post-irradiation following low dose (5–25 cGy) exposures of cesium-137 γ-rays **(A)**, 200 MeV protons **(B)**, and 290 MeV/n C-12 ions **(C)**. Peak foci formation occurs at 30 min post-IR for all three radiation qualities. Data reported as IR-induced means ± SD, background-subtracted for foci levels measured in sham-irradiated cultures (indicated by dashed line). Asterisks mark significant differences compared to DMSO controls at *p*-values of ≤0.05 (*) by two-tailed Student's *t*-tests.

pretreatment with 2 μM SAHA results in increased γ-ray radiosensitization in both cell types (D_{10} values of 4.67 Gy for A549 cells and 4.21 Gy for AG01522 fibroblasts) similar to the 1 and 5 μM SAHA pretreatment D_{10} values of 4.27–4.78 Gy for A549 cells and 3.43–4.34 Gy for NFF28 fibroblasts reported in **Supplementary Table 1**. For survival following 200 MeV SOBP proton irradiations (LET = 2.2 keV/μm), this group also documented that SAHA pretreatment radiosensitized both cell types. However, per **Figure 2B**, pretreatment of A549 cells with SAHA and the other two HDACi used in our studies resulted in radioprotection following proton irradiation (**Figure 2** and **Supplementary Table 2**). This group likewise observed radiosensitization in SAHA-pretreated A549 cells exposed to 290 MeV/n SOBP C-12 ions (LET = 55 keV/μm), as we did in **Figure 3B**, but did not observe any differences in the survival of DMSO *versus* SAHA-treated AG01522 cells. Since we used a 5-fold higher SAHA concentration, it is possible that the 2 μM concentration used in their experiments may not have been sufficient to provide the radioprotection we observed for NFF28 cells exposed to C-12 or O-16 ions (**Figures 3A**, **4A**). It should again also be noted that our experiments employed 200 MeV proton and 290 MeV/n C-12 ion irradiations delivered in the lower LET Bragg plateau/entrance region (LET values of 0.45 and 13 keV/μm, respectively) to mimic normal tissue entrance exposures. As such, we report slightly higher corresponding D_{10} values for experiments presented herein—though the patterns and relative degree of SAHA-mediated radiosensitization or radioprotection are similar (**Supplementary Table 2**). Levels of C-12 ion-induced cell killing in DMSO-treated NFF28 fibroblasts and U87MG cells in this report are consistent with entrance region (13 keV/μm) C-12 ion exposures of NB1RBG fibroblasts reported in (64) and U87MG cells in (65) delivered at the HIMAC facility in Chiba, Japan.

As seen in **Figures 3**, **4**, HDACi-mediated C-12 and O-16 ion radiosensitization was cell line/strain- and HDACi-specific. Along with NFF28 fibroblasts (**Figure 3A**), HDACi pretreatment of U2OS osteosarcoma cells was also radioprotective for C-12 ion exposures (**Figure 3C**), as was PTACH pretreatment in A549 cells and SAHA pretreatment in U87MG cells (**Figures 3B, D**). Conversely, M344 and SAHA pretreatment radiosensitized A549 cells and M344 and PTACH radiosensitized U87MG cells to C-12 ion irradiation. For O-16 ion irradiations, pretreatment of quiescent G0/G1-phase NFF28 fibroblasts with each of the three HDACi was strongly radioprotective (**Figure 4A**) and likewise conferred mild radioprotection to A549 cells (**Figure 4B**). Only HDACi pretreatments of U2OS and U87MG cells were effective in moderately radiosensitizing them to subsequent O-16 ion exposures (**Figures 4C, D**). Another interesting result is seen in **Figure 6** in which cell survival is plotted for DMSO vehicle-treated controls only. While the canonical pattern of increased LET-dependent cell killing is seen for NFF28 fibroblasts, whereby 350 MeV/n O-16 ion (20.9 keV/μm) exposures are more effective at cell killing than 290 MeV/n C-12 ion (13 keV/μm) exposures (**Figure 6A**), for all three tumor lines, the lower LET C-12 ions are more effective for cell killing compared to O-16 ions (**Figures 6B–D**). It remains to be determined if this would be repeated using higher LET SOBP C-12 and O-16 ion irradiations.

Unlike the report by (38) and other groups that have also examined the effects of SAHA pretreatment on post-irradiation γ-H2AX and 53BP1 foci induction and repair kinetics, we did not identify any significant effects of inhibitor pretreatment on the *rates* of DSB repair and accompanying foci resolution, rather only observed differences in the overall foci induction *levels* post-IR. It should also be noted that many of the studies that describe HDACi-induced delayed γ-H2AX foci repair kinetics report results from human tumor cell lines (36, 66). We observed increased colocalized γ-H2AX pS139/53BP1 foci induction in SAHA-pretreated NFF28 fibroblasts following cesium-137 γ-irradiation, which, unlike DMSO-treated vehicle controls, did

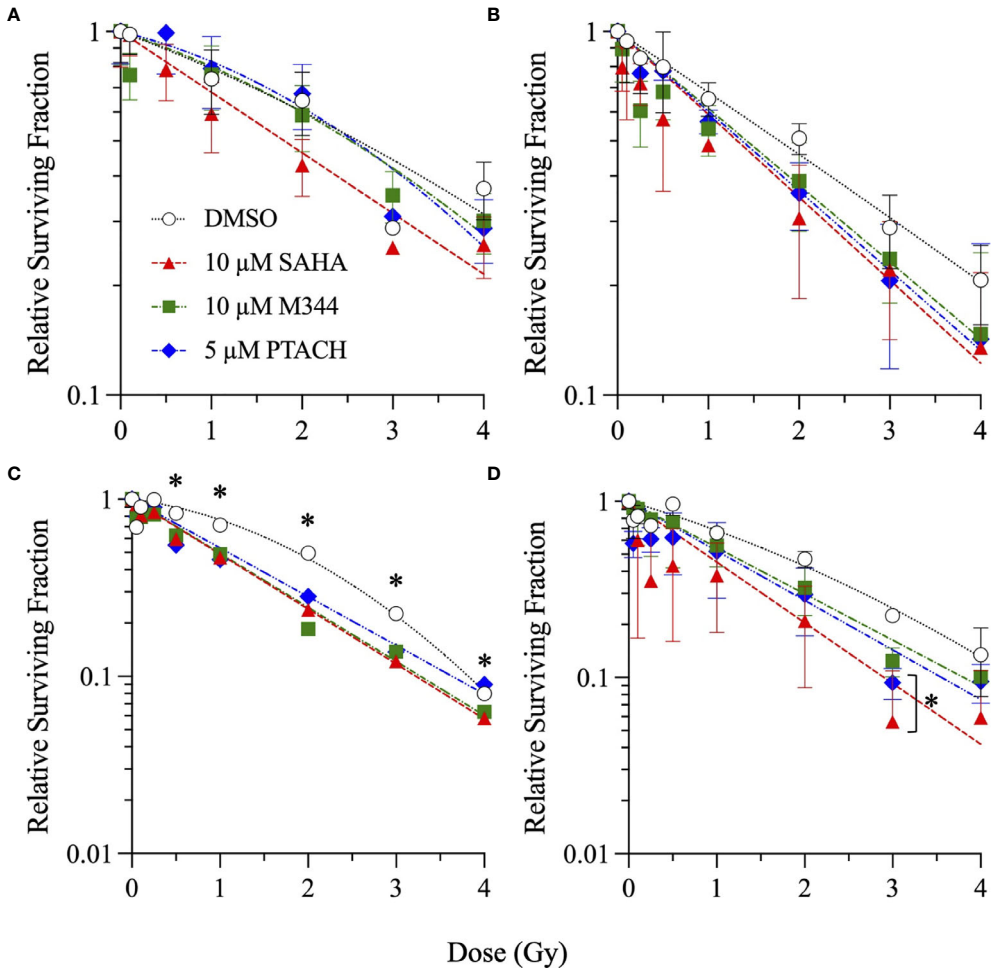

FIGURE 9 | Clonogenic survival of asynchronously growing normal NFF28 primary fibroblasts pretreated for 18 h with 10 μM SAHA, 10 μM M344, and 5 μM PTACH and irradiated cesium-137 γ-rays **(A)**, 200 MeV protons **(B)**, 290 MeV/n C-12 ions **(C)**, or 350 MeV/n O-16 ions **(D)**. Data reported as mean ± SD; where error bars are not visible, they are smaller than the data point. Unlike the radioprotection observed following HDACi pretreatment in G0/G1-phase cultures irradiated with C-12 or O-16 ions, 18 h HDACi pretreatment of asynchronously growing NFF28 fibroblast cultures resulted in radiosensitization. Asterisks mark significant differences compared to DMSO controls at *p*-values of ≤0.05 (*) by one-way ANOVA.

not return to baseline levels by 24 h (**Figure 8A**). Similar results were documented in (67) demonstrating radiosensitization for γ-H2AX foci induction in G0/G1-phase HSF1 fibroblasts pretreated for 12 h with 10 μM SAHA prior to irradiation with 0.5 Gy of 90 kV X-rays. This significant increase in γ-ray-induced foci levels following 10 μM SAHA pretreatment shown in **Figure 8A** coincides with the increased radiosensitivity for clonogenic survival in **Figure 1A**. No differences in γ-H2AX/53BP1 foci induction levels were noted in DMSO *versus* SAHA-pretreated NFF28 cells exposed to 200 MeV protons in this study (**Figure 8B**), similar to results reported in (38), and levels of residual foci at 24 h remained above background in these cultures. Similarly, little difference in clonogenic survival was seen between DMSO control and SAHA-treated NFF28 fibroblasts irradiated with low-dose 200 MeV protons per **Figure 2A**. However, unlike the Gerelchuluun et al. report, we identified SAHA pretreatment as radioprotective (rather than radiosensitizing) for C-12 ion-induced peak DSB-associated foci induction with *lower* levels of DSB-associated foci induced per unit dose in irradiated cultures, as well as levels of IR-induced foci falling below background levels by 24 h (**Figure 8C**). The lower induction of foci following C-12 ion irradiation coincides with our finding of increased survival (radioprotection) in C-12 ion-irradiated G0/G1-phase NFF28 fibroblasts pretreated with 10 μM SAHA in **Figure 3A** [a finding likewise reported for confluent AG01522 fibroblast survival in (38)]. Lower levels of γ-H2AX expression measured by flow cytometry along with increased cell survival were also observed in 1 μM SAHA-treated hFOB 1.19 osteoblast cells irradiated with C-12 ions at the HIT facility in Heidelberg, Germany, as reported by (35). Thus, for the three radiation types used in **Figure 8**, effects of 10 μM SAHA pretreatment on the relative induction of DSB-

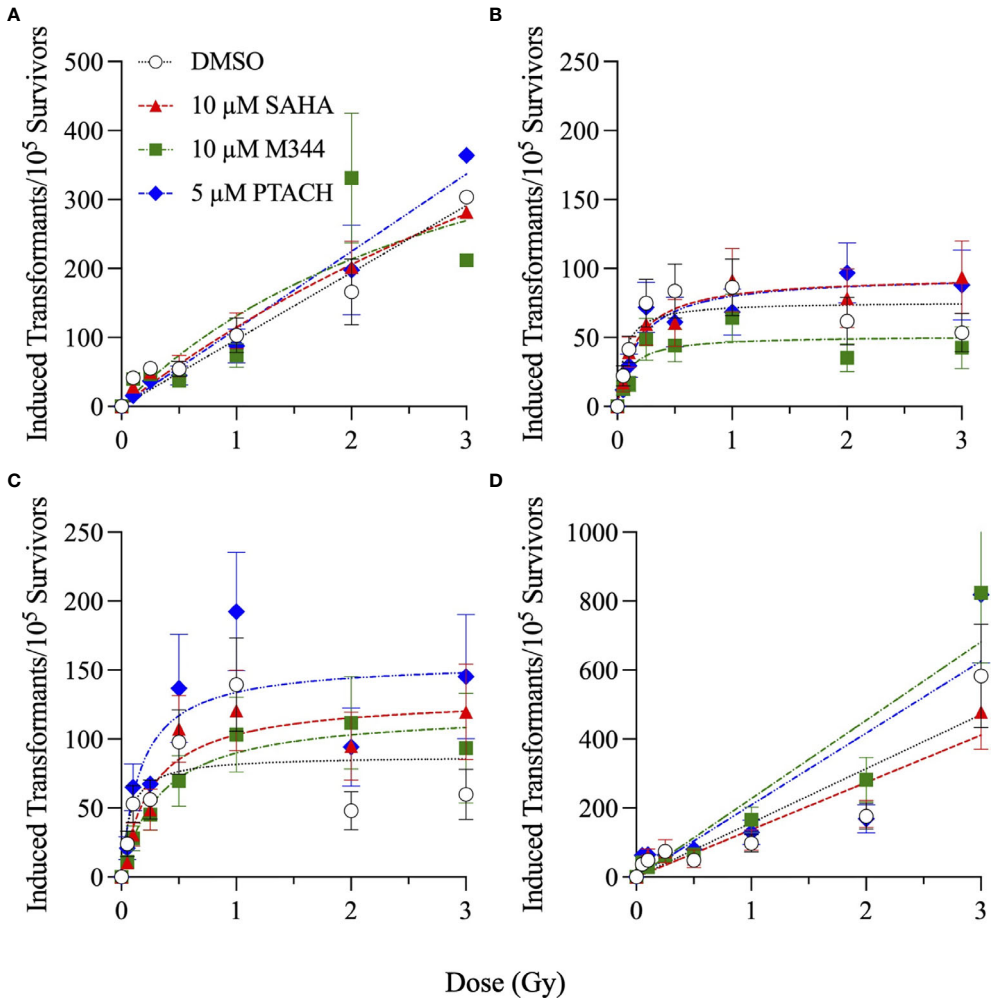

FIGURE 10 | Cellular transformation of asynchronously growing normal NFF28 primary fibroblasts pretreated for 18 h with 10 μM SAHA, 10 μM M344, and 5 μM PTACH and irradiated cesium-137 γ-rays **(A)**, 200 MeV protons **(B)**, 290 MeV/n C-12 ions **(C)**, or 350 MeV/n O-16 ions **(D)** measured as the acquisition of anchorage-independent colony formation in soft agar per 10^5 surviving cells. Data reported as mean ± SEM; where error bars are not visible, they are smaller than the data point. A hyperlinear response is observed for low-dose exposures with transformation frequencies peaking at 1 Gy and then declining at higher doses following proton and C-12 ion irradiation.

associated foci directly matched the respective patterns of radiosensitization or radioprotection observed for NFF28 clonogenic survival (**Figures 1**–**3**).

Irradiation with 200 MeV protons produced the greatest number of induced colocalized γ-H2AX/53BP1 foci per unit dose (0.26 foci/cGy), followed by 290 MeV/n C-12 ions (0.18 foci/cGy) and cesium-137 γ-rays (0.15 foci/cGy; **Figure 8**). A recent study by (68) likewise documented lower γ-H2AX and 53BP1 foci induction per Gy in human TIG-3-20 fibroblasts irradiated with 190 MeV C-12 ions compared to 20 MeV protons and 63-MeV He-4 ions, noting that it is likely multiple DSBs would be contained with a single C-12 ion-induced focus given the higher density of ionizations along individual particle trajectories of these higher LET-charged particles. Assuming a mean G0/G1-phase human fibroblast cell nucleus surface area of ~200 μm^2 (69, 70), exposure to entrance region 290 MeV C-12 ions (LET = 13.02 keV/μm) in our experiments results in ~1 C-12 ion traversal/nucleus per cGy compared to ~29.2 entrance region 200 MeV proton (LET = 0.45 keV/μm) traversals/nucleus per cGy and ~14.5 cesium-137 γ-ray-induced photoelectron [LET = 0.91 keV/μm at full buildup (71),] traversals/nucleus per cGy. This equates to ~0.009 induced foci/proton, 0.01 induced foci/photoelectron, and ~0.18 induced foci/C-12 ion: relative ratios of ~20:1 for 290 MeV/n C-12 ions and 1.15:1 for γ-rays compared to 200 MeV protons in this case. Since the relative ratios of their respective LET values are ~33.4 for 290 MeV/n C-12 ions and ~2.3 for cesium-137 γ-rays compared to 200 MeV protons, respectively, there is a correlation between particle LET and DSB-associated foci induction levels when reported per particle fluence (rather than per unit dose).

To our knowledge, this is the first study to report frequencies of IR-induced normal cell transformation *in vitro* following

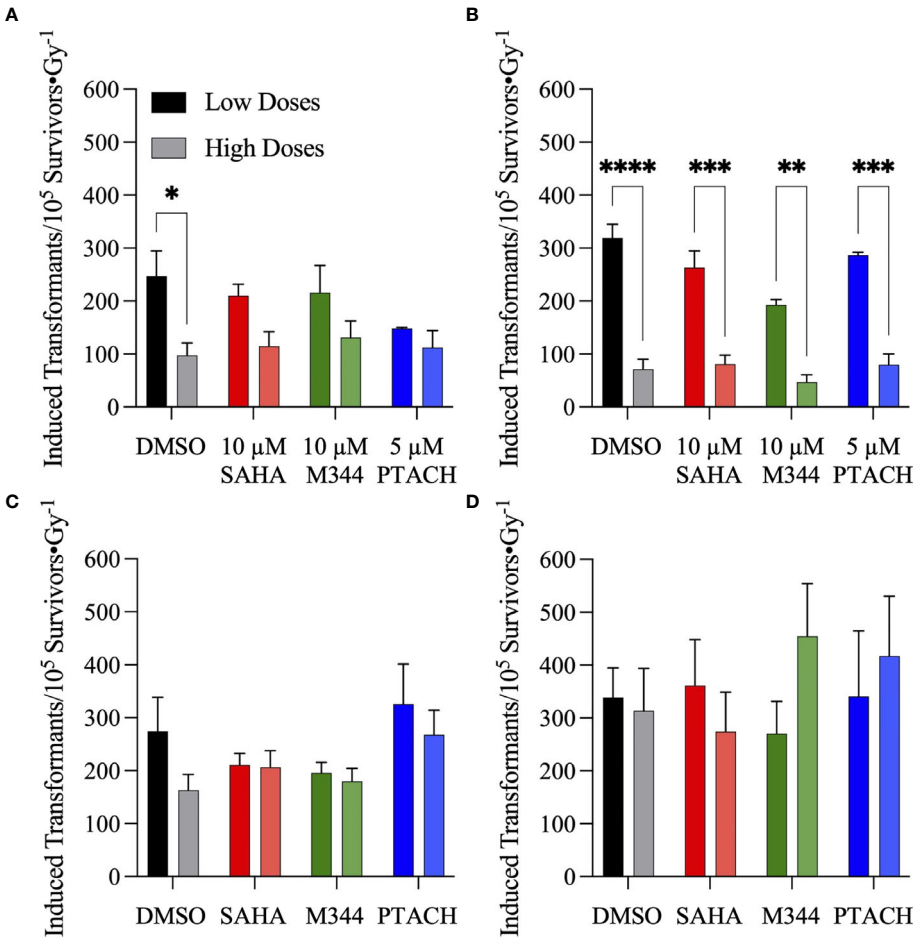

FIGURE 11 | Frequencies of normal NFF28 primary fibroblast anchorage-independent (A–I) colony formation in soft agar per unit dose ± SEM at low (≤25 cGy) and higher doses (>50 cGy) of cesium-137 γ-rays **(A)**, 200 MeV protons **(B)**, 290 MeV/n C-12 ions **(C)** and 350 MeV/n O-16 ions **(D)**. IR-induced yields of transformants are background-corrected for levels of transformants measured in DMSO and HDACi-treated/sham-irradiated cultures (~6.1–7.2). Low dose transformation frequencies are calculated from the slope of induction from 5 to 25 cGy and the higher dose transformation frequencies obtained from the mean transformation frequencies at 1 Gy, the dose where peak (maximal) transformation occurs for both protons and C-12 ions. Both cesium-137 γ-rays and protons show a pronounced hyper-radiosensitivity for NFF28 fibroblast *in vitro* transformation at low doses. Asterisks mark significant differences at *p*-values of ≤0.05 (*), ≤0.01 (**), ≤0.001 (***), and ≤10^{-4} (****) by two-way ANOVA.

HDACi pretreatment. Cellular transformation assays assessing anchorage-independent growth in soft agar of irradiated primary human fibroblasts or CGL1 HeLa/fibroblast hybrid cells (72) have been employed in radiobiology for decades as a surrogate *in vitro* model capable of recapitulating some of the essential features of *in vivo* human carcinogenesis (73). The frequencies of NFF28 fibroblast transformation following cesium-137 γ-rays, 200 MeV protons, 290 MeV/n C-12 ions, and 350 MeV/n O-16 ions we measured in this study (**Figures 10**, **11**) are similar to those reported previously by the Sutherland group for low-passage NFF28 fibroblasts exposed to other proton energies, 250 kVp X-rays and intermediate to high LET Si-28, Ti-48, and Fe-56 ions (45–48). Overall, the HDACi pretreatments did not significantly affect NFF28 fibroblast transformation induction for any of the four radiation types tested (**Figure 10**), although 10 μM SAHA pretreatment resulted in increased proton and C-12 ion-induced transformation at higher doses. The hyperlinear increase in cellular transformation we observed at low doses (≤25 cGy) of protons and C-12 ions documented in these figures is concerning when considering exposures to normal tissues in irradiated entrance regions prior to the targeted tumor volume that may accrue over the course of a typical radiotherapy treatment regimen. It is also relevant for the radiation protection of astronauts exposed to the complex, chronic mixed-field space radiation environment during long-duration missions to the Moon and Mars, and potentially high doses they may receive during solar particle events (SPE) (74, 75). However, at higher (clinically relevant) doses used in this study, protons do appear to be less capable of inducing normal fibroblast transformation than cesium-137 γ-rays. This is reflected in a recent pooled cohort analysis of secondary cancer induction following clinical megavoltage photon- and electron-based IMRT or proton-based PBRT that shows incidence is approximately threefold higher for IMRT compared to

PBRT (76). While our results show higher transformation following C-12 or O-16 ions compared to γ-rays, there are no clinical reports demonstrating C-12 ion-induced second cancer induction in CIRT patients given the low numbers of patients treated to date with this modality and long latency periods associated with solid cancer development (4, 77). Risk projections for CIRT-induced second cancer induction suggest comparable overall incidence compared to PBRT (78).

Overall, unlike the promising levels of HDACi-mediated radiosensitization observed for cesium-137 γ-rays (**Figures 1**, **5**), HDACi pretreatments resulted in generally more modest levels of radiosensitization for protons (and radioprotection in the case of A549 and U2OS cells pretreated with either M344 or PTACH; **Figures 2**, **5**). For C-12 ion irradiations, HDACi pretreatments had more minimal effects on the post-irradiation survival of the three tumor cell lines tested (**Figure 3**), while slight radiosensitization was observed for U2OS and U87MG cells exposed to O-16 ions (**Figure 4**). Survival assays using NFF28 fibroblasts showed the HDACi were effective for radiosensitizing both quiescent G0/G1-phase and log-phase cultures to γ-rays and protons, but were radioprotective when quiescent cultures were irradiated with C-12 and O-16 ions (**Figures 1**, **2**, **9**). This radioprotective effect was recapitulated in the DSB-associated foci assay results shown in **Figure 8** whereby lower levels of foci were observed in 10 μM SAHA-pretreated quiescent NFF28 cultures. Finally, while HDACi pretreatments were radiosensitizing to cycling NFF28 cells exposed to all three charged particle types, the increased yields of transformants measured in HDACi-treated cultures at higher doses in many cases (**Figures 10**, **11**) suggest they may possibly be associated with higher incidence of secondary cancer induction if utilized as PBRT or CIRT adjuvants.

DATA AVAILABILITY STATEMENT

The original contributions presented in the study are included in the article/**Supplementary Material**. Further inquiries can be directed to the corresponding author.

AUTHOR CONTRIBUTIONS

PW, DK, and PB conceived and designed the experiments. AJ, KS, AH, PB, JJ, DK, and PW performed the experiments. PW, AJ, DK, and PB summarized and analyzed the data. PW, AJ, DK, and PB wrote the paper. All authors contributed to the article and approved the submitted version.

ACKNOWLEDGMENTS

The authors acknowledge the invaluable assistance of BNL's NSRL and Biology Department support staff without whom none of this work could be completed. We would also like to kindly acknowledge support for KS and AH from the U.S. Department of Energy Science Undergraduate Laboratory Internships (SULI) program. Portions of this article were authored by Brookhaven Science Associates, LLC, under contract number DE-AC02-98CH10886 with the U.S. Department of Energy and supported by BNL Laboratory-Directed Research and Development (LDRD) grant 12-012 (PW). The United States Government retains and the publisher, by accepting the article for publication, acknowledges that the United States Government retains a non-exclusive, paid-up, irrevocable, worldwide license to publish or reproduce the published form of this manuscript, or allow others to do so, for United States Government purposes.

SUPPLEMENTARY MATERIAL

The Supplementary Material for this article can be found online at: https://www.frontiersin.org/articles/10.3389/fonc.2021.735940/full#supplementary-material

Supplementary Figure 1 | Sham-irradiated plating efficiencies (PE) ± SEM for G0/G1-phase normal NFF28 primary fibroblasts **(A)** and asynchronously growing A549 lung carcinoma **(B)**, U2OS osteosarcoma **(C)**, and U87MG malignant glioma cells **(D)** pretreated for 18 h with 0.1% DMSO (vehicle control) or 1–20 μM concentrations of SAHA, M344, and PTACH. Asterisks mark significant differences at p-values of ≤0.05 (*), ≤0.01 (**), ≤0.001 (***), and ≤10^{-4} (****).

Supplementary Figure 2 | Clonogenic survival of G0/G1-phase normal NFF28 primary fibroblasts **(A)** and asynchronously growing A549 lung carcinoma **(B)**, U2OS osteosarcoma **(C)**, and U87MG malignant glioma cells **(D)** pretreated for 18 h with 1–20 μM concentrations of M344 and exposed to 0.5–6 Gy cesium-137 γ-rays. Data reported as mean ± SD; where error bars are not visible, they are smaller than the data point. Asterisks mark significant differences at p-values of ≤0.05 (*).

Supplementary Figure 3 | Clonogenic survival of G0/G1-phase normal NFF28 primary fibroblasts **(A)** and asynchronously growing A549 lung carcinoma **(B)**, U2OS osteosarcoma **(C),** and U87MG malignant glioma cells **(D)** pretreated for 18 h with 1–20 μM concentrations of PTACH and exposed to 0.5–6 Gy cesium-137 γ-rays. Data reported as mean ± SD; where error bars are not visible, they are smaller than the data point. Asterisks mark significant differences at p-values of ≤0.05 (*).

Supplementary Figure 4 | HDACi sensitizer enhancement ratio (SER) values ± SEM for G0/G1-phase normal NFF28 primary fibroblasts **(A)** and asynchronously growing A549 lung carcinoma **(B)**, U2OS osteosarcoma **(C)**, and U87MG malignant glioma cells **(D)** pretreated for 18 h with 1–20 μM concentrations of SAHA, M344, and PTACH and irradiated with cesium-137 γ-rays [calculated using D_{10} survival values; asterisks mark significant differences at p-values of ≤0.05 (*) and ≤0.01 (**)].

REFERENCES

1. Schardt D, Elsässer T, Schulz-Ertner D. Heavy-Ion Tumor Therapy: Physical and Radiobiological Benefits. *Rev Mod Phys* (2010) 82(1):383–425. doi: 10.1103/RevModPhys.82.383
2. Sutherland BM, Bennett PV, Schenk H, Sidorkina O, Laval J, Trunk J, et al. Clustered DNA Damages Induced by High and Low LET Radiation, Including Heavy Ions. *Phys Med* (2001) 17 Suppl 1:202–4.
3. Sutherland BM, Bennett PV, Sidorkina O, Laval J. Clustered DNA Damages Induced in Isolated DNA and in Human Cells by Low Doses of Ionizing Radiation. *Proc Natl Acad Sci USA* (2000) 97(1):103–8. doi: 10.1073/pnas.97.1.103
4. Malouff TD, Mahajan A, Krishnan S, Beltran C, Seneviratne DS, Trifiletti DM. Carbon Ion Therapy: A Modern Review of an Emerging Technology. *Front Oncol* (2020) 10:82. doi: 10.3389/fonc.2020.00082
5. Nagasawa H, Peng Y, Wilson PF, Lio YC, Chen DJ, Bedford JS, et al. Role of Homologous Recombination in the Alpha-Particle-Induced Bystander Effect

for Sister Chromatid Exchanges and Chromosomal Aberrations. *Radiat Res* (2005) 164(2):141–7 doi: 10.1667/RR3420

6. Lin YF, Nagasawa H, Little JB, Kato TA, Shih HY, Xie XJ, et al. Differential Radiosensitivity Phenotypes of DNA-PKcs Mutations Affecting NHEJ and HRR Systems Following Irradiation With Gamma-Rays or Very Low Fluences of Alpha Particles. *PloS One* (2014) 9(4):e93579. doi: 10.1371/journal.pone.0093579
7. Thompson LH. Recognition, Signaling, and Repair of DNA Double-Strand Breaks Produced by Ionizing Radiation in Mammalian Cells: The Molecular Choreography. *Mutat Res* (2012) 751(2):158–246. doi: 10.1016/j.mrrev.2012.06.002
8. Saha J, Wilson P, Thieberger P, Lowenstein D, Wang M, Cucinotta FA. Biological Characterization of Low-Energy Ions With High-Energy Deposition on Human Cells. *Radiat Res* (2014) 182(3):282–91. doi: 10.1667/RR13747.1
9. Rall M, Kraft D, Volcic M, Cucu A, Nasonova E, Taucher-Scholz G, et al. Impact of Charged Particle Exposure on Homologous DNA Double-Strand Break Repair in Human Blood-Derived Cells. *Front Oncol* (2015) 5:250. doi: 10.3389/fonc.2015.00250
10. Zafar F, Seidler SB, Kronenberg A, Schild D, Wiese C. Homologous Recombination Contributes to the Repair of DNA Double-Strand Breaks Induced by High-Energy Iron Ions. *Radiat Res* (2010) 173(1):27–39. doi: 10.1667/RR1910.1
11. Jakob B, Dubiak-Szepietowska M, Janiel E, Schmidt A, Durante M, Taucher-Scholz G. Differential Repair Protein Recruitment at Sites of Clustered and Isolated DNA Double-Strand Breaks Produced by High-Energy Heavy Ions. *Sci Rep* (2020) 10(1):1443. doi: 10.1038/s41598-020-58084-6
12. Kawata T, Ito H, Furusawa Y, Durante M, George K, Wu H, et al. Heavy-Ion Induced Chromatid Break and Repair Kinetics in Normal Human Fibroblasts. *Biol Sci Space* (2001) 15(3):276–7
13. Durante M, George K, Wu H, Cucinotta FA. Karyotypes of Human Lymphocytes Exposed to High-Energy Iron Ions. *Radiat Res* (2002) 158(5):581–90. doi: 10.1667/0033-7587(2002)158[0581:KOHLET]2.0.CO;2
14. Lee R, Sommer S, Hartel C, Nasonova E, Durante M, Ritter S. Complex Exchanges Are Responsible for the Increased Effectiveness of C-Ions Compared to X-Rays at the First Post-Irradiation Mitosis. *Mutat Res* (2010) 701(1):52–9. doi: 10.1016/j.mrgentox.2010.03.004
15. George KA, Hada M, Cucinotta FA. Biological Effectiveness of Accelerated Protons for Chromosome Exchanges. *Front Oncol* (2015) 5:226. doi: 10.3389/fonc.2015.00226
16. Lee Y, Okayasu R. Strategies to Enhance Radiosensitivity to Heavy Ion Radiation Therapy. *Int J Part Ther* (2018) 5(1):114–21. doi: 10.14338/IJPT-18-00014.1
17. Tsuboi K. Advantages and Limitations in the Use of Combination Therapies With Charged Particle Radiation Therapy. *Int J Part Ther* (2018) 5(1):122–32. doi: 10.14338/IJPT-18-00019.1
18. Marks PA, Richon VM, Miller T, Kelly WK. Histone Deacetylase Inhibitors. *Adv Cancer Res* (2004) 91:137–68. doi: 10.1016/S0065-230X(04)91004-4
19. Gui CY, Ngo L, Xu WS, Richon VM, Marks PA. Histone Deacetylase (HDAC) Inhibitor Activation of P21waf1 Involves Changes in Promoter-Associated Proteins, Including HDAC1. *Proc Natl Acad Sci USA* (2004) 101(5):1241–6. doi: 10.1073/pnas.0307708100
20. Karagiannis TC, El-Osta A. Modulation of Cellular Radiation Responses by Histone Deacetylase Inhibitors. *Oncogene* (2006) 25(28):3885–93. doi: 10.1038/sj.onc.1209417
21. Richon VM, Garcia-Vargas J, Hardwick JS. Development of Vorinostat: Current Applications and Future Perspectives for Cancer Therapy. *Cancer Lett* (2009) 280(2):201–10. doi: 10.1016/j.canlet.2009.01.002
22. Mann BS, Johnson JR, Cohen MH, Justice R, Pazdur R. FDA Approval Summary: Vorinostat for Treatment of Advanced Primary Cutaneous T-Cell Lymphoma. *Oncologist* (2007) 12(10):1247–52. doi: 10.1634/theoncologist.12-10-1247
23. Garcia-Manero G, Yang H, Bueso-Ramos C, Ferrajoli A, Cortes J, Wierda WG, et al. Phase 1 Study of the Histone Deacetylase Inhibitor Vorinostat (Suberoylanilide Hydroxamic Acid [SAHA]) in Patients With Advanced Leukemias and Myelodysplastic Syndromes. *Blood* (2008) 111(3):1060–6. doi: 10.1182/blood-2007-06-098061
24. Suraweera A, O'Byrne KJ, Richard DJ. Combination Therapy With Histone Deacetylase Inhibitors (HDACi) for the Treatment of Cancer: Achieving the Full Therapeutic Potential of HDACi. *Front Oncol* (2018) 8:92. doi: 10.3389/fonc.2018.00092
25. Ramalingam SS, Parise RA, Ramanathan RK, Lagattuta TF, Musguire LA, Stoller RG, et al. Phase I and Pharmacokinetic Study of Vorinostat, a Histone Deacetylase Inhibitor, in Combination With Carboplatin and Paclitaxel for Advanced Solid Malignancies. *Clin Cancer Res* (2007) 13(12):3605–10. doi: 10.1158/1078-0432.CCR-07-0162
26. Kelly WK, Richon VM, O'Connor O, Curley T, MacGregor-Curtelli B, Tong W, et al. Phase I Clinical Trial of Histone Deacetylase Inhibitor: Suberoylanilide Hydroxamic Acid Administered Intravenously. *Clin Cancer Res* (2003) 9(10 Pt 1):3578–88.
27. Kelly WK, O'Connor OA, Krug LM, Chiao JH, Heaney M, Curley T, et al. Phase I Study of an Oral Histone Deacetylase Inhibitor, Suberoylanilide Hydroxamic Acid, in Patients With Advanced Cancer. *J Clin Oncol* (2005) 23(17):3923–31. doi: 10.1200/JCO.2005.14.167
28. Lee JH, Choy ML, Ngo L, Foster SS, Marks PA. Histone Deacetylase Inhibitor Induces DNA Damage, Which Normal But Not Transformed Cells can Repair. *Proc Natl Acad Sci USA* (2010) 107(33):14639–44. doi: 10.1073/pnas.1008522107
29. Yasuda T, Kagawa W, Ogi T, Kato TA, Suzuki T, Dohmae N, et al. Novel Function of HATs and HDACs in Homologous Recombination Through Acetylation of Human RAD52 at Double-Strand Break Sites. *PloS Genet* (2018) 14(3):e1007277. doi: 10.1371/journal.pgen.1007277
30. Ladd B, Ackroyd JJ, Hicks JK, Canman CE, Flanagan SA, Shewach DS. Inhibition of Homologous Recombination With Vorinostat Synergistically Enhances Ganciclovir Cytotoxicity. *DNA Repair (Amst)* (2013) 12(12):1114–21. doi: 10.1016/j.dnarep.2013.10.008
31. Blattmann C, Oertel S, Ehemann V, Thiemann M, Huber PE, Bischof M, et al. Enhancement of Radiation Response in Osteosarcoma and Rhabdomyosarcoma Cell Lines by Histone Deacetylase Inhibition. *Int J Radiat Oncol Biol Phys* (2010) 78(1):237–45. doi: 10.1016/j.ijrobp.2010.03.010
32. Zhang Y, Jung M, Dritschilo A, Jung M. Enhancement of Radiation Sensitivity of Human Squamous Carcinoma Cells by Histone Deacetylase Inhibitors. *Radiat Res* (2004) 161(6):667–74. doi: 10.1667/rr3192
33. Groselj B, Sharma NL, Hamdy FC, Kerr M, Kiltie AE. Histone Deacetylase Inhibitors as Radiosensitisers: Effects on DNA Damage Signalling and Repair. *Br J Cancer* (2013) 108(4):748–54. doi: 10.1038/bjc.2013.21
34. Chinnaiyan P, Vallabhaneni G, Armstrong E, Huang SM, Harari PM. Modulation of Radiation Response by Histone Deacetylase Inhibition. *Int J Radiat Oncol Biol Phys* (2005) 62(1):223–9. doi: 10.1016/j.ijrobp.2004.12.088
35. Oertel S, Thiemann M, Richter K, Weber KJ, Huber PE, Perez RL, et al. Combination of Suberoylanilide Hydroxamic Acid With Heavy Ion Therapy Shows Promising Effects in Infantile Sarcoma Cell Lines. *Radiat Oncol* (2011) 6:119. doi: 10.1186/1748-717X-6-119
36. Barazzuol L, Jeynes JC, Merchant MJ, Wera AC, Barry MA, Kirkby KJ, et al. Radiosensitization of Glioblastoma Cells Using a Histone Deacetylase Inhibitor (SAHA) Comparing Carbon Ions With X-Rays. *Int J Radiat Biol* (2015) 91(1):90–8. doi: 10.3109/09553002.2014.946111
37. Yu JI, Choi C, Shin SW, Son A, Lee GH, Kim SY, et al. Valproic Acid Sensitizes Hepatocellular Carcinoma Cells to Proton Therapy by Suppressing NRF2 Activation. *Sci Rep* (2017) 7(1):14986. doi: 10.1038/s41598-017-15165-3
38. Gerelchuluun A, Maeda J, Manabe E, Brents CA, Sakae T, Fujimori A, et al. Histone Deacetylase Inhibitor Induced Radiation Sensitization Effects on Human Cancer Cells After Photon and Hadron Radiation Exposure. *Int J Mol Sci* (2018) 19(2):496. doi: 10.3390/ijms19020496
39. Krisnawan VE, Stanley JA, Schwarz JK, DeNardo DG. Tumor Microenvironment as a Regulator of Radiation Therapy: New Insights Into Stromal-Mediated Radioresistance. *Cancers (Basel)* (2020) 12(10):2916. doi: 10.3390/cancers12102916
40. Chaudhary P, Marshall TI, Perozziello FM, Manti L, Currell FJ, Hanton F, et al. Relative Biological Effectiveness Variation Along Monoenergetic and Modulated Bragg Peaks of a 62-MeV Therapeutic Proton Beam: A Preclinical Assessment. *Int J Radiat Oncol Biol Phys* (2014) 90(1):27–35. doi: 10.1016/j.ijrobp.2014.05.010
41. Horendeck D, Walsh KD, Hirakawa H, Fujimori A, Kitamura H, Kato TA. High LET-Like Radiation Tracks at the Distal Side of Accelerated

Proton Bragg Peak. *Front Oncol* (2021) 11:690042. doi: 10.3389/fonc.2021.690042
42. Averbeck NB, Topsch J, Scholz M, Kraft-Weyrather W, Durante M, Taucher-Scholz G. Efficient Rejoining of DNA Double-Strand Breaks Despite Increased Cell-Killing Effectiveness Following Spread-Out Bragg Peak Carbon-Ion Irradiation. *Front Oncol* (2016) 6:28. doi: 10.3389/fonc.2016.00028
43. Bronk L, Guan F, Patel D, Ma D, Kroger B, Wang X, et al. Mapping the Relative Biological Effectiveness of Proton, Helium and Carbon Ions With High-Throughput Techniques. *Cancers (Basel)* (2020) 12(12):3658. doi: 10.3390/cancers12123658
44. Bennett PV, Cuomo NL, Paul S, Tafrov ST, Sutherland BM. Endogenous DNA Damage Clusters in Human Skin, 3-D Model, and Cultured Skin Cells. *Free Radic Biol Med* (2005) 39(6):832–9. doi: 10.1016/j.freeradbiomed.2005.05.008
45. Sutherland BM, Cuomo NC, Bennett PV. Induction of Anchorage-Independent Growth in Primary Human Cells Exposed to Protons or HZE Ions Separately or in Dual Exposures. *Radiat Res* (2005) 164(4 Pt 2):493–6. doi: 10.1667/rr3357.1
46. Zhou G, Bennett PV, Cutter NC, Sutherland BM. Proton-HZE-Particle Sequential Dual-Beam Exposures Increase Anchorage-Independent Growth Frequencies in Primary Human Fibroblasts. *Radiat Res* (2006) 166(3):488–94. doi: 10.1667/RR0596.1
47. Bennett PV, Cutter NC, Sutherland BM. Split-Dose Exposures *Versus* Dual Ion Exposure in Human Cell Neoplastic Transformation. *Radiat Environ Biophys* (2007) 46(2):119–23. doi: 10.1007/s00411-006-0091-y
48. Stisova V, Abele WH, Thompson KH, Bennett PV, Sutherland BM. Response of Primary Human Fibroblasts Exposed to Solar Particle Event Protons. *Radiat Res* (2011) 176(2):217–25. doi: 10.1667/rr2490.1
49. Kim MH, Rusek A, Cucinotta FA. Issues for Simulation of Galactic Cosmic Ray Exposures for Radiobiological Research at Ground-Based Accelerators. *Front Oncol* (2015) 5:122. doi: 10.3389/fonc.2015.00122
50. Wilson PF, Nham PB, Urbin SS, Hinz JM, Jones IM, Thompson LH. Inter-Individual Variation in DNA Double-Strand Break Repair in Human Fibroblasts Before and After Exposure to Low Doses of Ionizing Radiation. *Mutat Res* (2010) 683(1-2):91–7. doi: 10.1016/j.mrfmmm.2009.10.013
51. Kato TA, Wilson PF, Nagasawa H, Fitzek MM, Weil MM, Little JB, et al. A Defect in DNA Double Strand Break Processing in Cells From Unaffected Parents of Retinoblastoma Patients and Other Apparently Normal Humans. *DNA Repair (Amst)* (2007) 6(6):818–29. doi: 10.1016/j.dnarep.2007.01.008
52. Wilson PF, Nagasawa H, Warner CL, Fitzek MM, Little JB, Bedford JS. Radiation Sensitivity of Primary Fibroblasts From Hereditary Retinoblastoma Family Members and Some Apparently Normal Controls: Colony Formation Ability During Continuous Low-Dose-Rate Gamma Irradiation. *Radiat Res* (2008) 169(5):483–94. doi: 10.1667/RR1333.1
53. Sutherland BM, Freeman AG, Bennett PV. Human Cell Transformation in the Study of Sunlight-Induced Cancers in the Skin of Man. *Mutat Res* (1988) 199 (2):425–36. doi: 10.1016/0027-5107(88)90219-9
54. Rogakou EP, Pilch DR, Orr AH, Ivanova VS, Bonner WM. DNA Double-Stranded Breaks Induce Histone H2AX Phosphorylation on Serine 139. *J Biol Chem* (1998) 273(10):5858–68. doi: 10.1074/jbc.273.10.5858
55. Burma S, Chen BP, Murphy M, Kurimasa A, Chen DJ. ATM Phosphorylates Histone H2AX in Response to DNA Double-Strand Breaks. *J Biol Chem* (2001) 276(45):42462–7. doi: 10.1074/jbc.C100466200C100466200
56. Stiff T, O'Driscoll M, Rief N, Iwabuchi K, Lobrich M, Jeggo PA. ATM and DNA-PK Function Redundantly to Phosphorylate H2AX After Exposure to Ionizing Radiation. *Cancer Res* (2004) 64(7):2390–6. doi: 10.1158/0008-5472.CAN-03-3207
57. Schultz LB, Chehab NH, Malikzay A, Halazonetis TD. P53 Binding Protein 1 (53BP1) Is an Early Participant in the Cellular Response to DNA Double-Strand Breaks. *J Cell Biol* (2000) 151(7):1381–90. doi: 10.1083/jcb.151.7.1381
58. Huyen Y, Zgheib O, Ditullio RA Jr, Gorgoulis VG, Zacharatos P, Petty TJ, et al. Methylated Lysine 79 of Histone H3 Targets 53BP1 to DNA Double-Strand Breaks. *Nature* (2004) 432(7015):406–11. doi: 10.1038/nature03114
59. Botuyan MV, Lee J, Ward IM, Kim JE, Thompson JR, Chen J, et al. Structural Basis for the Methylation State-Specific Recognition of Histone H4-K20 by 53BP1 and Crb2 in DNA Repair. *Cell* (2006) 127(7):1361–73. doi: 10.1016/j.cell.2006.10.043
60. Bohgaki M, Bohgaki T, El Ghamrasni S, Srikumar T, Maire G, Panier S, et al. RNF168 Ubiquitylates 53BP1 and Controls its Response to DNA Double-Strand Breaks. *Proc Natl Acad Sci USA* (2013) 110(52):20982–7. doi: 10.1073/pnas.1320302111
61. Fradet-Turcotte A, Canny MD, Escribano-Diaz C, Orthwein A, Leung CC, Huang H, et al. 53BP1 Is a Reader of the DNA-Damage-Induced H2A Lys 15 Ubiquitin Mark. *Nature* (2013) 499(7456):50–4. doi: 10.1038/nature12318
62. Markova E, Schultz N, Belyaev IY. Kinetics and Dose-Response of Residual 53BP1/Gamma-H2AX Foci: Co-Localization, Relationship With DSB Repair and Clonogenic Survival. *Int J Radiat Biol* (2007) 83(5):319–29. doi: 10.1080/09553000601170469
63. Costes SV, Chiolo I, Pluth JM, Barcellos-Hoff MH, Jakob B. Spatiotemporal Characterization of Ionizing Radiation Induced DNA Damage Foci and Their Relation to Chromatin Organization. *Mutat Res* (2010) 704(1-3):78–87. doi: 10.1016/j.mrrev.2009.12.006
64. Tsuruoka C, Suzuki M, Kanai T, Fujitaka K. LET and Ion Species Dependence for Cell Killing in Normal Human Skin Fibroblasts. *Radiat Res* (2005) 163 (5):494–500. doi: 10.1667/rr3360
65. Kato TA, Tsuda A, Uesaka M, Fujimori A, Kamada T, Tsujii H, et al. *In Vitro* Characterization of Cells Derived From Chordoma Cell Line U-CH1 Following Treatment With X-Rays, Heavy Ions and Chemotherapeutic Drugs. *Radiat Oncol* (2011) 6:116. doi: 10.1186/1748-717X-6-116
66. Munshi A, Tanaka T, Hobbs ML, Tucker SL, Richon VM, Meyn RE. Vorinostat, a Histone Deacetylase Inhibitor, Enhances the Response of Human Tumor Cells to Ionizing Radiation Through Prolongation of Gamma-H2AX Foci. *Mol Cancer Ther* (2006) 5(8):1967–74. doi: 10.1158/1535-7163.MCT-06-0022
67. Purrucker JC, Fricke A, Ong MF, Rube C, Rube CE, Mahlknecht U. HDAC Inhibition Radiosensitizes Human Normal Tissue Cells and Reduces DNA Double-Strand Break Repair Capacity. *Oncol Rep* (2010) 23(1):263–9. doi: 10.3892/or_00000632
68. Oizumi T, Ohno R, Yamabe S, Funayama T, Nakamura AJ. Repair Kinetics of DNA Double Strand Breaks Induced by Simulated Space Radiation. *Life (Basel)* (2020) 10(12):341. doi: 10.3390/life10120341
69. Jakob B, Scholz M, Taucher-Scholz G. Biological Imaging of Heavy Charged-Particle Tracks. *Radiat Res* (2003) 159(5):676–84. doi: 10.1667/0033-7587(2003)159[0676:biohct]2.0.co;2
70. Antonelli F, Campa A, Esposito G, Giardullo P, Belli M, Dini V, et al. Induction and Repair of DNA DSB as Revealed by H2AX Phosphorylation Foci in Human Fibroblasts Exposed to Low- and High-LET Radiation: Relationship With Early and Delayed Reproductive Cell Death. *Radiat Res* (2015) 183(4):417–31. doi: 10.1667/RR13855.1
71. ICRP. Relative Biological Effectiveness, Radiation Weighting and Quality Factor. ICRP Publication 92. *Ann ICRP* (2003) 33(4). doi: 10.1016/S0146-6453(03)00024-1
72. Pirkkanen JS, Boreham DR, Mendonca MS. The CGL1 (HeLa X Normal Skin Fibroblast) Human Hybrid Cell Line: A History of Ionizing Radiation Induced Effects on Neoplastic Transformation and Novel Future Directions in SNOLAB. *Radiat Res* (2017) 188(4.2):512–24. doi: 10.1667/RR14911.1
73. Hanahan D, Weinberg RA. Hallmarks of Cancer: The Next Generation. *Cell* (2011) 144(5):646–74. doi: 10.1016/j.cell.2011.02.013
74. Durante M, Cucinotta FA. Physical Basis of Radiation Protection in Space Travel. *Rev Mod Phys* (2011) 83:1245–81. doi: 10.1103/RevModPhys.83.1245
75. Townsend LW, Adams JH, Blattnig SR, Clowdsley MS, Fry DJ, Jun I, et al. Solar Particle Event Storm Shelter Requirements for Missions Beyond Low Earth Orbit. *Life Sci Space Res (Amst)* (2018) 17:32–9. doi: 10.1016/j.lssr.2018.02.002
76. Xiang M, Chang DT, Pollom EL. Second Cancer Risk After Primary Cancer Treatment With Three-Dimensional Conformal, Intensity-Modulated, or Proton Beam Radiation Therapy. *Cancer* (2020) 126(15):3560–8. doi: 10.1002/cncr.32938
77. Mohamad O, Sishc BJ, Saha J, Pompos A, Rahimi A, Story MD, et al. Carbon Ion Radiotherapy: A Review of Clinical Experiences and Preclinical Research, With an Emphasis on DNA Damage/Repair. *Cancers (Basel)* (2017) 9(6):66. doi: 10.3390/cancers9060066
78. Eley JG, Friedrich T, Homann KL, Howell RM, Scholz M, Durante M, et al. Comparative Risk Predictions of Second Cancers After Carbon-Ion Therapy

Versus Proton Therapy. *Int J Radiat Oncol Biol Phys* (2016) 95(1):279–86. doi: 10.1016/j.ijrobp.2016.02.032

Conflict of Interest: The authors declare that the research was conducted in the absence of any commercial or financial relationships that could be construed as a potential conflict of interest.

Publisher's Note: All claims expressed in this article are solely those of the authors and do not necessarily represent those of their affiliated organizations, or those of the publisher, the editors and the reviewers. Any product that may be evaluated in this article, or claim that may be made by its manufacturer, is not guaranteed or endorsed by the publisher.

frontiers in Oncology

REVIEW
published: 18 October 2021
doi: 10.3389/fonc.2021.749496

Clinical and Preclinical Outcomes of Combining Targeted Therapy With Radiotherapy

May Elbanna[1,2], *Nayela N. Chowdhury*[3], *Ryan Rhome*[1,2] *and Melissa L. Fishel*[2,3,4*]

[1] Department of Radiation Oncology, Indiana University School of Medicine, Indianapolis, IN, United States, [2] Indiana University Simon Comprehensive Cancer Center, Indiana University School of Medicine, Indianapolis, IN, United States, [3] Department of Pharmacology and Toxicology, Indiana University School of Medicine, Indianapolis, IN, United States, [4] Department of Pediatrics and Herman B Wells Center for Pediatric Research, Indiana University School of Medicine, Indianapolis, IN, United States

In the era of precision medicine, radiation medicine is currently focused on the precise delivery of highly conformal radiation treatments. However, the tremendous developments in targeted therapy are yet to fulfill their full promise and arguably have the potential to dramatically enhance the radiation therapeutic ratio. The increased ability to molecularly profile tumors both at diagnosis and at relapse and the co-incident progress in the field of radiogenomics could potentially pave the way for a more personalized approach to radiation treatment in contrast to the current ''one size fits all'' paradigm. Few clinical trials to date have shown an improved clinical outcome when combining targeted agents with radiation therapy, however, most have failed to show benefit, which is arguably due to limited preclinical data. Several key molecular pathways could theoretically enhance therapeutic effect of radiation when rationally targeted either by directly enhancing tumor cell kill or indirectly through the abscopal effect of radiation when combined with novel immunotherapies. The timing of combining molecular targeted therapy with radiation is also important to determine and could greatly affect the outcome depending on which pathway is being inhibited.

Keywords: cancer, DNA damage, combination (combined) therapy, radiation therapy, radiosenisitizing agent, targeted therapy

OPEN ACCESS

Edited by:
Shubhankar Suman, Georgetown University, United States

Reviewed by:
Christopher Paul Cifarelli, West Virginia University Hospitals, United States
John E Mignano, Tufts University School of Medicine, United States

***Correspondence:**
Melissa L. Fishel
mfishel@iu.edu

Specialty section:
This article was submitted to Radiation Oncology, a section of the journal Frontiers in Oncology

Received: *29 July 2021*
Accepted: *30 September 2021*
Published: *18 October 2021*

Citation:
Elbanna M, Chowdhury NN, Rhome R and Fishel ML (2021) Clinical and Preclinical Outcomes of Combining Targeted Therapy With Radiotherapy. Front. Oncol. 11:749496. doi: 10.3389/fonc.2021.749496

INTRODUCTION

A plethora of factors are involved in the development and progression of cancer in individuals such as family history, age, sex, primary site of origin and driver mutations; thus, treatment depends upon the goal of therapy - curative or palliative. Treatment for cancer involves multiple approaches including surgery, chemotherapy, immunotherapy, small molecules that target certain cancer signaling pathways, and radiation depending on cancer type or status. The use of multiple treatments concurrently is referred to as multi-modality treatment. Radiation therapy plays a crucial role in the management of cancer. Also known as radiotherapy (RT), it is a method of impeding cancer cell division by using high-energy ionizing radiation to induce DNA damage and disrupt cell cycle progression. In the treatment of cancer, RT can be given alone or coupled with

chemotherapy or surgery and is aimed at reducing local tumor burden. The primary advantage, however, that RT confers over chemotherapy is the ability to precisely target the tumor and reduce systemic side effects. Epidemiological studies have reported that almost 54% of breast cancer survivors were treated with radiation therapy in 2016 and this is projected to become 60% by 2030 (1). Treatment mode is usually determined by stage and type of cancer, genetic mutations, age, and overall health of patient.

RT can be delivered in several ways; the most commonly used modality is broadly defined as External Beam Radiation Therapy (EBRT), which includes Stereotactic Body Radiation therapy (SBRT) and Stereotactic Radiosurgery (SRS). EBRT most typically uses a linear accelerator to deliver radiation directly into the cancer site in the form of photons. Depending on the location of the tumor, this radiation can be of high or low energy. For instance, high energy EBRT is used in the treatment of head and neck cancer, breast, lung, and eye cancer (2–5) while lower energy photons are used for more superficial cancers such as melanoma (6). Another modality of delivery is brachytherapy, which utilizes a radioactive source placed as close to the tumor as possible and can be given in conjunction with EBRT (5, 7, 8). Some examples of cancers where brachytherapy is frequently administered are cervical, vaginal, and prostate cancer (8–11). Ideally, RT will preferentially or more frequently damage DNA of cancer cells, with less or reparable damage to surrounding healthy cells. Similar to the brachytherapy concept, IntraOperative Radiation Therapy (IORT) constitutes the precise delivery of radiation to the tumor/tumor bed during surgery while minimizing exposure to the surrounding healthy tissues. IORT can be done utilizing electrons, low-kV X-rays, and high dose rate (HDR) brachytherapy. TARGIT, an international randomized clinical trial designed to test the hypothesis that delivering a single dose of targeted IORT in patients eligible for breast conserving surgery (+ EBRT in patients at high risk for local recurrence) is equivalent to a conventional course of post-operative EBRT showed that there was no statistically significant difference between EBRT and the IORT approach with respect to local recurrence-free survival, invasive local recurrence-free survival, mastectomy-free survival, distant disease-free survival or breast cancer mortality (12). In a study looking at brain metastases, retrospective data suggests that IORT is a safe and effective tool in the adjuvant setting following surgical resection of brain metastases; an area that continues to be under debate (13). IORT is currently under investigation in the adjuvant setting following the maximal safe resection of recurrent glioblastoma multiforme (GBM) (NCT04763031, NCT04681677).

Conventional fractionated EBRT was traditionally based off the classical "four R's" of radiation biology: reassortment, repair, reoxygenation, and repopulation (14), to which radiosensitivity was later added (15). IORT on the other hand is generally performed with either low energy X-rays or electrons; both of which are considered low linear energy transfer (LET) radiation compared to high energy X-rays used in conventional EBRT. Unlike high LET radiation where the linear quadratic model (L-Q) model predicts that radiobiological effectiveness (RBE) should decrease as the dose per fraction increases (16), evidence suggests that this may not be true for low-LET radiation. With a predicted higher RBE, emerging evidence suggests that IORT can be effective by overwhelming the repair system leading to increased genomic instability and thus more cancer cell killing. Additionally, IORT performed during surgery eliminates repopulation of residual tumor cells in the tumor bed, which could theoretically happen during wound healing (17). The ability of IORT to eliminate repopulation could also be attributed to the radiation-induced bystander effect (RIBE) which is thought to be more common with high dose/fraction as is the case with IORT. Abscopal effect in normal non-irradiated cells in the vicinity of tumor could reduce tumor recurrence, modifying the wound microenvironment, and eradicating residual tumor cells when applied immediately after surgical procedure (18).

Additionally, SBRT or SRS is used to deliver very high doses of radiation to the primary sites or metastatic sites in few treatments (1–5), with extraordinary precision made possible by real-time monitoring of the patient under CT scan throughout the duration of therapy. Together they can be combined into a term Stereotactic Ablative Radiotherapy (SABR). Unlike IORT, which arguably does not fit the current L-Q model, current data suggests that this is not the case for SABR, which behaves biologically similar to conventionally fractionated EBRT. However, the higher tumor control that is achievable with SABR when compared to conventional EBRT is attributed to a more geometrically precise technique of dose delivery that allows for prescribing high biological effective doses (BED), which were simply unachievable with conventional dose delivery techniques (19). Additionally, ablative effect on the surrounding tumor endothelium provides additional mechanism of death that is not as prominent in conventionally fractionated EBRT. Emerging data suggest that better tumor control with SABR could also partly be attributable to the abscopal effect brought about by high dose radiation in non-irradiated cells such as enhanced endothelial cell damage and/or enhanced tumor immunity similar to what was suggested in the setting of IORT (20).

HOW DOES RADIATION WORK: THE BIOLOGIC EFFECTS OF RADIATION

Effects of Radiation Therapy: DNA Damage

Ionizing radiation introduces energy into molecular structures which then releases electrons creating ions that are capable of breaking covalent bonds. The breakdown of these covalent bonds within DNA produces DNA breaks, including double-stranded breaks. Radiation also leads to the generation of reactive oxygen species (ROS) which oxidize lipids and proteins and are capable of damaging DNA in many ways, including single-strand breaks. This damage leads to cell death and failure of mitosis.

Consequently, highly proliferating cells are most susceptible to damage due to radiation. DNA damage is not an uncommon phenomenon, with as many as 50,000 lesions, or instances of

DNA damage, in each cell, every day. Cellular mechanisms of DNA repair are able to fix this continuous damage and maintain functional DNA. Endogenously induced lesions are generally isolated and more evenly distributed throughout DNA. Damage resulting from radiation is far less dispersed. When two or more lesions are found within two helical turns, this is referred to as a clustered damage site, and these are far more difficult to repair than isolated lesions (21, 22). The most highly damaging effect of ionizing radiation is considered to be the double-stranded DNA breaks where both phosphodiester backbones of the two strands of DNA are broken within 10 base pairs (23–28). Double-stranded DNA breaks are likely particularly cytotoxic as they are not regularly induced endogenously (28–30). The linear energy transfer (LET) ratio of the radiation determines the type of damage it induces in the DNA. Particles with a higher LET (e.g., protons, neutrons, alpha particles) results in roughly 90% of the damage occurring in the form of clustered damage sites, while low LET radiation (e.g., gamma rays, x-rays, and electrons) produces roughly 70% of its damage as isolated lesions and the remaining 30% in the form of clustered damage sites (23, 31).

Radiation kills cancer cells either by damaging the DNA directly or generating excessive ROS which damages the DNA (**Figure 1**). However, cancer cells can become resistant to RT *via* several mechanisms which enhance their DNA repair capacity or suppress the functions of tumor suppressors (32). Therefore, strategies that disrupt the DNA repair machinery or the detection of DNA damage has largely been explored to enhance radiosensitization of tumors. Inhibitors of DNA repair proteins have widely been studied alone or in conjunction with radiotherapy to enhance tumor suppression. For instance, the inhibition of the DNA base excision repair (BER) protein apurinic/apyrimidinic endonuclease, APE1, has been shown to suppress growth of several cancers (33, 34). Similarly, overexpression of APE1 has been linked to radioresistance (35, 36), and suppression has been shown to enhance cancer cells to RT (37). Inhibition of several other DNA repair proteins such as Poly (ADP-ribose) polymerase (PARP) and ataxia telangiectasia mutated (ATM) have demonstrated similar effects (38, 39). The quantity and characteristics of DNA damage are also impacted by the tumor microenvironment, with the oxygen levels of the tumor being of particular importance. Hypoxic tumors do not respond as well to radiation therapy compared to tumors that are well oxygenated. This is because oxygen reacts very quickly with DNA radicals that result from radiation to produce DNA lesions when it is present. Molecules that will react with the DNA radicals can be introduced and function in a similar capacity to oxygen, such as nitroaromatic compounds (e.g., nimorazole, nitrotriazole or sanazole) (40, 41). Nitric oxide is another molecule that is of interest in this regard, though some of its effect may be due to increased oxygen tension of the tumor microenvironment (TME) (42). Due to the potential clinical impact, many preclinical studies have investigated the use of radiosensitizing agents to increase tumor cells' susceptibility to RT which will be discussed in the sections below (43–46).

Effects of Radiation Therapy: Cellular Damage

Traditionally, RT has been reported to arrest cancer cell proliferation by inducing DNA damage through stimulation of cell death mechanisms such as apoptosis, necrosis, and senescence. However, radiation can also inhibit cell proliferation by disrupting the neoplastic cells physically through damage to the cell membrane and organelles, and thereby interfering with signal transduction (47–49). Damage to several organelles including the endoplasmic reticulum, ribosome, lysosome, and mitochondria have been implicated in the effects of RT-induced tumor cell death (50–59).

The mitochondria, in particular, is an important target of RT as it regulates cellular respiration and metabolism, and altered

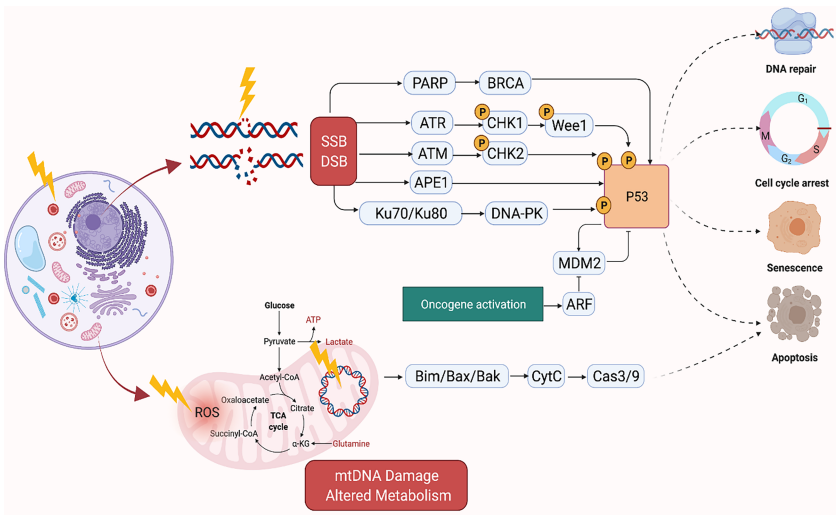

FIGURE 1 | Mechanism of DNA Damage Induced by Ionizing Radiation. Created in BioRender.com.

metabolism is considered a hallmark of cancer (**Figure 1**) (60). RT-induced damage within the mitochondrial DNA can induce programmed cell death in cancer cells (61). The mitochondrial respiratory chain generates ROS as a byproduct of cellular respiration in normal cells. On the other hand, excess ROS production can potentiate tumor growth. Together, this suggests that cellular response to ROS varies according to levels of ROS generated in the cells. For instance, tumorigenic events such as hypoxia or oncogene activation can induce tumor growth by generating abundant ROS to drive cell cycle progression, metastasis, angiogenesis, etc. However, RT can generate an ROS overload which can arrest the cell cycle and induce apoptosis through mitochondrial collapse in cancer cells (62, 63). For example, FLASH radiation is a novel radiotherapy technology, defined as a single ultra-high dose-rate (≥40 Gy/s) radiotherapy, which unlike conventional dose-rate radiation (described above) leads to strikingly differential responses between healthy and tumor tissues. This differential effect has been attributed to multiple theoretical mechanisms such as distinct mechanisms of DNA damage and the significantly higher ability of FLASH to produce ROS at a rate that can't be scavenged by tumor cells compared to healthy cells which have a lower oxidant load and higher catalase reduction reserve capacity. More future studies are needed to better understand the mechanism of FLASH and its clinical implications (64).

Several strategies targeting the mitochondria to sensitize cancer cells to RT have been investigated (65–67). The mitochondrial respiratory chain generates ROS as a byproduct of cellular respiration, and RT also generates an ROS overload which can induce apoptosis through mitochondrial collapse in cancer cells (62). LKB1 (also known as serine-threonine kinase 11, STK11) is a tumor suppressor and functions in the AMPK (adenosine monophosphate-activated protein kinase) pathway necessary for cell metabolism, homeostasis, and autophagy (68). In esophageal cancer, overexpressed LKB1 has been reported to confer resistance to radiation therapy, activate autophagy, and inhibit apoptosis (69). One of the metabolic changes that cancer cells initiate during low glucose conditions is the switch from glycolysis to oxidative phosphorylation (OXPHOS) to adjust to fluctuating microenvironmental conditions (70, 71). Irradiated human esophageal adenocarcinoma cells had a higher number of mitochondria with additional mitochondrial mutations compared to their non-irradiated counterparts. Analysis of patient tumors of esophageal adenocarcinoma showed an increase of ATP5B, a marker of OXPHOS, in patients who had poor response to neoadjuvant chemoradiation therapy, suggesting that changes in mitochondrial metabolism can potentially play a role in radioresistance (71).

RADIOGENOMICS AND RATIONAL DESIGN FOR RADIATION-TARGETED THERAPY COMBINATIONS

The combination of radiation therapy and traditional cytotoxic chemotherapy is a clinically well-established approach to improve overall survival of cancer patients (72). However, to date, despite the significant advancements in developing molecularly targeted therapy, little progress has been made in identifying and defining optimal targeted therapy and radiotherapy combinations to improve the efficacy of cancer treatment (73). The rapidly growing arsenal of targeted therapies can be categorized according to their respective effects on one or more of the hallmarks of carcinogenesis which were coined by Hanahan and Weinberg (74, 75). Importantly, the clinical success of these agents was largely based on the identification of predictive biomarkers of response, which enabled the selection of patients and/or tumors that would benefit from these novel agents. This subsequently led to the rise of precision medicine and simultaneously sparked interest in the concept of 'precision radiation medicine', yet that concept remains in its infancy.

Precision radiation medicine proposes to leverage genomic information derived from human cancers or preclinical tumor models to identify subsets that are sensitive to specific radiation/drug combinations, radiation alone at tailored doses or predict those at high risk for radiation-related normal tissue side effects (76, 77). As our knowledge of how radiation works evolved over time (as outlined above), several groups have attempted to characterize preclinical models, particularly cell lines to identify genomic signatures that are predictive of radiation sensitivity. The largest effort to date was done by Yard et al., who underwent large-scale profiling of cellular survival after exposure to radiation in a diverse collection of 533 genetically annotated human tumor cell lines and were able to demonstrate the wide range of radiation susceptibility and the novel genetic features driving that diversity (78). Currently, there are several genomic signatures that have been clinically validated for guiding radiation treatment. For example, OncotypeDX®, a 21 gene classifier that was initially validated to predict the benefit of adjuvant chemotherapy in hormone receptor positive breast cancer, is currently used to estimate the risk of locoregional recurrence after radiation for invasive breast cancer and therefore guide addition or omission of radiation in the adjuvant setting (79). Similarly, for ductal carcinoma *in situ* (DCIS), DCISionRT® is a multigene assay (80) that has been prospectively validated in 327 patients with DCIS that participated in the E5194 trial (81) to help inform decision-making regarding the addition of radiation in the adjuvant setting in conjunction with clinic-pathologic criteria (82, 83). Decipher® is a 22 gene classifier that was developed as a prognostic tool for men with high-risk prostate cancer and was prospectively validated to guide that addition of post-prostatectomy radiation in that risk group whether in the adjuvant or salvage setting (84, 85). In the 2019, the American Society of Clinical Oncology (ASCO) guideline on molecular markers in localized prostate cancer, only Decipher was recommended to guide the decision between salvage and adjuvant radiation and Decipher® PORTOS was the only predictive signature of radiation response (86). Nonetheless, salvage radiation is generally preferred based on randomized data (87) and so far genetic testing is not part of the standard of care to guide radiation timing until validated in the randomized

setting (NCT02783950) (88). In a collaborative novel effort to personalize radiation dose based on genetics and transcend the 'one size fits all' paradigm, a novel algorithm that uses genomic adjusted radiation dose (GARD) was proposed to independently quantify differences in clinical outcomes across different cancers that are not attributed to the physical radiation dose alone. This effort aims to guide the integration of genomics into radiation dose decisions (89–92).

While several genomic signatures have been studied in the preclinical setting and a few have been clinically validated to better tailor radiation therapy, limited clinical trials with RT were designed to prospectively test whether specific patient subpopulations with distinct genomic signatures would benefit from radiation or not. For example, HN002 is a phase II study that evaluated radiation dose de-escalation in patients with human papilloma virus (HPV) positive oropharyngeal cancers who are thought to have improved survival outcomes due to impaired DNA repair (93–95). In that study, radiation dose de-escalation was found to be non-inferior to standard dose, which justifies hypothesis testing in the phase III setting. Another eloquent example is in pediatric medulloblastoma where several trials are investigating tailoring radiation dose and technique based on distinct molecular subgroups rather than clinic-pathologic characteristics per say (96). Recently, the ACNS0331 trial demonstrated that reduction of boost volume but not craniospinal radiation dose is safe in average risk medulloblastoma patients and this may occur in a genetic subgroup-dependent manner (97).

The equally important aspect of radiation therapy, which is crucial for an optimal therapeutic ratio, is better understanding and prediction of normal tissue toxicity, particularly late side effects, which are usually irreversible and can severely impact quality of life. While demographic and clinical factors are well-recognized culprits of late tissue toxicity, the evolving field of radiogenomics proposed genetic factors as key players as well. Kerns et al. proposed two arching goals for the field: first, identifying key molecular pathways that can predict radiation-induced normal tissue toxicity and second, developing an assay to identify the patients who are more likely to develop late tissue toxicities and therefore require tailored treatment (98). Several genome-wide association studies have identified associations between specific single nucleotide polymorphisms (SNPs) and radiation toxicity (99–101). The REQUITE international prospective toxicity profiling effort, initiated by The Radiogenomics Consortium, represents the largest study to date in that regard and has led to the creation of a centralized database of relevant clinical information including treatment, dosimetry, toxicity, and genome-wide SNP genotyping data in an effort to prospectively validate these findings for clinical use (102, 103).

Despite the efforts outlined above, the radiation oncology field significantly lags behind in designing clinical trials that are poised to prospectively test whether specific combinations of radiation and targeted therapy can particularly benefit a genomically distinct patient population. To that end, several collaborative efforts aimed to outline guidelines to usher the field toward optimizing the clinical development of novel drug-radiotherapy combinations. Two key points were proposed: 1) reconsidering novel endpoints in clinical trial design such as local control, organ preservation, and patient reported outcomes, and 2) prioritizing the development of promising therapeutics that target relevant pathways to radiation such as DNA repair inhibitors and immunotherapies (104–106).

Traditional radiosensitizing agents (such as cisplatin and 5-fluorouracil) typically exert their effect by augmenting DNA damage (72). As large genomic studies continue to unravel the landscape of DNA repair pathway deficiencies across different tumor types, it will be critical to propose novel rationally designed combinations of radiation and targeted therapy that fit specific genomic contexts (77). PARP1, WEE1, DNA-PK, ATM, ATR, and CHK1 are among the most critical mediators of DNA damage response (DDR) (**Figure 1**). DDR inhibitors (such as PARP inhibitors) were initially developed as monotherapy to target DDR defects that are present in tumor cells, but not in normal cells. This selectivity gave rise to the concept of synthetic lethality (107). Theoretically radiation is an attractive DNA-damaging agent that can be combined with novel DDR inhibitors to promote cell-selective radio-sensitization by three mechanisms: firstly, by increasing the amount of DNA damage to levels that induce apoptosis or cell death mechanisms rather than DNA repair or cell cycle arrest, secondly by exploiting synthetic lethality, and thirdly, by augmenting DNA damage and thus increasing the tumor mutation burden which in turn enhances tumor antigenicity and thus T-cell mediated killing (108).

Preclinical evidence suggests that DDR inhibitors can act as potent radiosensitizers and potentially have greater cytotoxic effects in cancer cells compared to normal cells (**Figure 2**). This also brought about the idea of synthetic lethality in which cancer cells, unlike their healthy counterparts, carry DNA repair defects, making them particularly vulnerable to DDR inhibitors, especially when simultaneously targeted with a DNA damaging agent such as radiation (109, 110). For example, PARP inhibitors have been shown to be potent radiosensitizers, irrespective of the tumor's homologous recombination (HR) status (111), albeit at lower doses in HR-deficient tumors (112). Similarly, Adavosertib, a WEE1 inhibitor is also an effective radiosensitizer (113, 114). Inhibition of WEE1 abrogates the G2/M checkpoint which is crucial for P53 mutant cancer cells, which also lack the G1 checkpoint. Therefore, WEE1 inhibition represents another form of tumor-selective radiosensitization (115). Induction of replication stress is another appealing mechanism that can selectively enhance radiation sensitivity in cancer cells particularly in the context of cMyc and KRAS mutations (116, 117). Several DDR inhibitors including PARP, WEE1, and ATR inhibitors have been implicated in the induction of replication stress either as monotherapy or in combination with other DDR inhibitors together with RT (118). Several clinical trials are currently testing the premise of combining radiation with DDR inhibitors in various disease sites.

In the era of immunotherapy, modulation of the host and the tumor microenvironment holds a lot of promise when combined with radiation as demonstrated in a plethora of eloquent

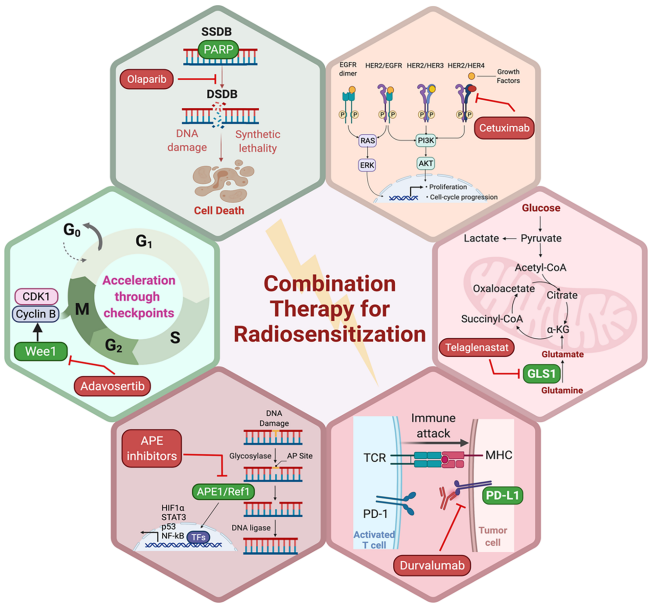

FIGURE 2 | Potential pathways and representative small molecule inhibitors of the key proteins in those pathways with potential to enhance the sensitivity of tumor cells to RT. Created in BioRender.com.

preclinical studies. Radiation and immunotherapy agents are thought to interact through five distinct mechanisms based of the modified Steel hypothesis (119): (1) spatial cooperation, (2) temporal modulation, (3) biological cooperation, (4) cytotoxic enhancement, and (5) normal tissue protection (120). Radiation has immunostimulatory and immunosuppressive effects. Radiation can induce immunogenic cell death and increase expression of tumor specific antigens and thus sensitize tumors to the effects of immunotherapy (121, 122). In the preclinical setting, Twyman-Saint Victor et al. demonstrated synergy between radiation therapy and combined anti-PD-1/PD-L1 and anti-CTLA4 blockade. In this study, the combination led to an increased response within the tumor as the radiation induced the diversification of the T-cell repertoire in tumor-associated lymphocytes and the immune checkpoint inhibitors inhibited T-regulatory cells (Tregs), which resulted in an increase in the CD8/Treg ratio and subsequently led to improved outcomes compared to either modality alone in a variety of tumor models (123). The abscopal effect of radiation refers to another form of RT-immunotherapy synergy where anecdotal studies (mostly in patients with melanoma) have shown tumor response in non-irradiated lesions presumably due to an incited systemic immune response resulting from local radiation treatment (20, 124–127). Conversely, radiation can promote tumor infiltration by suppressive regulatory T cells, inhibitory macrophage and myeloid-derived suppressor cell lineages (128, 129), therefore combination with immunotherapy in that context is crucial to maintain the anticipated cytotoxic effect of RT. The optimal dose, fractionation, volume, and sequencing of RT with immunotherapy remain to be elucidated to strike the balance between the immunostimulatory and immunosuppressive effects of radiation and to fulfill the modified Steel criteria (76, 77, 120).

Thus far, the failure to predict treatment efficacy using genetic variables represents one of the most significant obstacles to the personalization of radiation-based treatment regimens. The potential success of radiosensitizing-targeted therapy is contingent upon our better understanding of radiogenomics, which pertain to defining biomarkers of response and genetic determinants of late tissue toxicity (106, 130, 131). Moving forward, two key concepts need to be considered in order to facilitate rational design of novel radiation-targeted therapy combinations that are effective: redefining end points of interest and efficacy and identifying and validating biomarkers that can enable the early identification of ineffective or toxic compounds. These two key concepts will require the optimization of preclinical models that can accurately recapitulate the complexity of human tumors and thus faithfully predict promising combinations and subsequently re-thinking clinical trial design in a way that is relevant to radiation and its paradigm.

BUILDING PREDICTIVE EXPERIMENTAL MODELS IN THE VALIDATION OF COMBINATION THERAPY THAT INCLUDES RADIATION

For a small molecule to be maximally effective as radiosensitizer, it must be highly specific and directly toxic to the tumor. Tumor cells depend more heavily on certain signaling pathways over

normal tissues, therefore combination of RT with small molecule inhibitors of these pathways offers an alternative strategy to chemoradiation that is potentially less toxic to surrounding healthy tissues. A general limitation to this is the lack of preclinical models that mimic the human cancer to a molecular level which provides information regarding predictive biomarkers that differentiate between radioresistance and radiosensitivity.

Preclinical models for studying cancer radiogenomics as well as cancer efficacy studies require recapitulation of human cancer on an anatomical and histological level in a manner that closely mimics the human tumor characteristics. The driver or passenger mutations, microenvironment, hypoxia, angiogenesis, immune components, and therapeutic response are all important factors to consider. Therefore, several approaches are being used to build multi-cellular *in vitro* models as well as *in vivo* models with appropriate genetic manipulations to capture the aforementioned characteristics in response to RT. Methods include genetic knockdown, knock-in, activation, tissue-specific expression, inducible expression, and sequential expression in traditional cell culture, 3-dimensional (3D), organoid, and xenograft models. My laboratory has focused on generating 3D mono- and co-cultures using various cancers such as pancreatic, colon, and bladder (132–135). The use of both tumor cells and CAFs with distinct fluorescent markers allows us to monitor the effects of both cell populations following selective pathway inhibition. For example, we demonstrated the enhancement of tumor cell killing with dual inhibition of APE1/Ref-1 as well as CA9 (carbonic anhydrase 9), a HIF-1α target. Through blocking the full activation of HIF-1α through APE1/Ref-1 and the cells ability to respond to changes in pH through CA9, the spheroid growth was dramatically reduced (135). This model is now being interrogated to understand the effects of RT on growth of the spheroids and the impact on the cells of the TME as well as RT in combination with targeted agents that would impact hypoxia as well as metabolic signaling.

In vitro models often use a panel of radiosensitive and radioresistant cell lines and compare the effects of select small molecule inhibitors or the effects of knocking down potentially important signaling molecules. Other approaches include generation of radioresistant lines and determining which molecular factors play a role in their resistance. 3D models can aid in recapitulating the cell-cell interactions within tumor and stroma, cytokine signaling, hypoxia response, and combination therapy involving RT and allow us to quantitate the effects on the tumor as well as cells from the TME such as CAFs (136–138). A study comparing radiosensitive and radioresistant non-small cell lung cancer (NSCLC) demonstrated that pathways previously implicated including DNA repair, apoptosis, and NFκB activation in NSCLC were involved in the cellular response to RT (54). Prostate cancer cell lines and the transgenic mouse model TRAMP (Transgenic adenocarcinoma of mouse prostate) used natural product, Nexrutine (Nx), to sensitize the prostate cancer cells to RT both *in vivo* and *in vitro*. Downregulation of ribosomal and cell cycle proteins as well as HIF-1α were implicated in the sensitization of the tumors to Nx (56). These are just two examples of preclinical studies that utilize various models to test the radioresistance and sensitivity of various cancer types. The predictability of the model and the complexity of the 3D or monolayer system in response to RT will enable the preclinical studies to have a greater impact on the rationale design of combination therapy which will ultimately lead to translational impact.

RATIONAL COMBINATIONS OF RADIATION AND TARGETED THERAPY IN THE PRECLINICAL SETTING

PARP proteins are involved in DDR and inhibitors of PARP have been widely studied for radiosensitization both preclinically and in the clinic (discussed below and **Figure 2**). Currently, there are four PARP inhibitors in the clinic: Olaparib, Rucaparib, Niraparib, and Talazoparib (**Table 1**). The efficacy of this combination therapy has also been studied in preclinical models of human non-small cell lung cancer (NSCLC): Calu-3 and Calu-6 cell lines. Even though both cell lines exhibited increased radiosensitization following Olaparib treatment *in vitro*, only xenografts of Clau-6 showed increased response to combination RT *in vivo*. Difference in response between Clau-3 and Clau-6 were most likely due to microenvironmental factors that contributed to the sensitivity of cells, indicating that preclinical modeling must be approached unbiased and carefully with the appropriate TME (139). Talazoparib and Niraparib have also been studied for their sensitizing effects. Primary melanoma cultures treated with combination therapy of Talazoparib, Niraparib and radiation, demonstrate that both PARP inhibitors sensitize melanoma cells to IR (162). A short-term phase 1 clinical trial looking at the efficacy of combination therapy of radiation and Olaparib has determined the safety of the combination regimen in doses up to 200 mg/day without any side effects (163).

Apurinic/apyrimidinic endonuclease 1/Redox factor-1 (APE1/Ref-1) possesses multiple functions that could affect the cellular response to RT (**Figure 2**). APE1/Ref-1 is key in the base excision repair (BER) pathway of DNA lesions, acting as the major AP endonuclease in both the nucleus and mitochondria and in eukaryotic transcriptional regulation of gene expression as a reduction-oxidation (redox) factor (164–166). APE1 contributes to the repair of ionizing radiation through its ability to repair a 3'-phosphoglycolate end within a DNA strand break that is generated following ionizing radiation (IR) (167). A decrease in expression of APE1/Ref-1 in cancer cells results in apoptosis, cell cycle arrest, a decrease in proliferative capacity, a blockade of mitochondrial metabolism, and sensitization to various anti-cancer agents including RT (166, 168–170). Biochemical studies using oligonucleotides with clustered damage sites as would be encountered in a cell following RT demonstrate that APE1/Ref-1 can repair these types of DNA lesions (171). An inhibitor of the DNA repair activity of APE1/Ref-1 has been difficult to identify and develop preclinically, therefore two recent studies in pediatric and adult

TABLE 1 | List of radiosensitizers, respective mechanism of actions and preclinical models used to study them.

Radiosensitizer	Mechanism	Cell models studied	References
Olaparib	Blocks DNA repair by inhibiting PARP	Breast cancer: MCF-7, MDA-MB-231, MDA-MB-231, T47D, BT-549, HCC-1954 NSCLC: Clau-3, Clau-6	(139, 140)
Rucaparib	Blocks DNA repair by inhibiting PARP	Cervical cancer: HeLa Prostate cancer: PC3, LNCaP, DU145, VCaP Neuroblastoma SK-N-BE(2c), UVW	(141–143)
Cetuximab	Inhibits epidermal growth factor (EGF) from binding to its receptor	HNSCC: HN30, HPV-negative HTB-43, UM-SCC1, UM-SCC2, UM-SCC6, HPV-positive UM-SCC47, UPCI : SCC090 cells	(144, 145)
Telaglenastat	Interferes with mitochondrial metabolism by inhibiting the conversion of glutamine into glutamate	HNSCC: FaDu, HN5, CAL-27 Lung Cancer: H460, A427, A549	(146, 147)
Tirapazamine	Selective for hypoxic cells; Generates reactive oxygen species which cause DNA damage	Human Nasopharyngeal Carcinoma: HNE-1 Cervical cancer: HeLa	(148, 149)
Everolimus	Inhibits mTOR kinase	NSCLC: NCI-H460, NCI-H661 Glioblastoma: GS-2	(150, 151)
Nimorazole	Generates reactive oxygen species which cause DNA damage	HNSC: HPV-negative FaDu, UTSCC5, UTSCC33 and HPV positive: UMSCC47, UDSCC2 UPCISCC90	(152)
Trametinib	Inhibits MEK	NSCLC: A549, H460 Melanoma: A375, D04, WM1631, WM1791c	(153, 154)
Adavosertib	Inhibits Wee1 and impairs the G2 DNA damage checkpoint	Esophageal Cancer: OE33, FLO1	(155)
Peposertib	Inhibits DNA-PK and impairs DNA repair	Leukemia: Molm-13, Molt-4 HNSCC: FaDu Colon Cancer: HCT116	(156, 157)
Silver NP	Deposit high levels of energy in cells when exposed to ionizing radiation; ROS generation and DNA damage	Glioma: C6 Colon cancer: HCT116, HT29	(158, 159)
Gold NP	Deposit high levels of energy in cells when exposed to ionizing radiation; ROS generation and DNA damage	Breast Cancer: SK-BR-3	(160)
Bismuth NP	Not fully understood; Possibly by depositing high levels of energy in cells when exposed to ionizing radiation; ROS generation and DNA damage	Breast cancer: MCF-7, 4T1	(161)

brain tumors utilized nanoparticle delivery of APE1/Ref-1 siRNA to achieve sensitivity to RT (168, 169). One of APE1/Ref-1's interacting protein partners is nucleophosmin 1 (NPM1) and perturbation of the APE1/Ref-1 – NPM1 interaction can lead to decreased DNA repair activity of APE1/Ref-1 and increase in sensitivity to chemotherapeutic agents such as bleomycin (172, 173). Recently in NSCLC cells, radiosensitizing agent YTR107 was shown to bind to NPM1, disrupt RAD51 foci formation, and synergize with PARP inhibition (174). These findings highlight the complex interplay between radiation-induced DNA damage and repair and the potential proteins that can be exploited as drug targets to sensitize cancer cells to RT. Due to APE1/Ref-1's role in the repair of DNA lesions induced by RT, the blockade of APE1/Ref-1 DNA repair activity could be highly effective in combination with RT. The caveat of course would be toxicity to normal tissues, and therefore development of tumor targeting strategies would be of paramount importance.

In addition to DNA repair activity, APE1/Ref-1 also plays an important role in signaling within the tumor and TME through the transcription factors (TFs) it regulates, and many of these TFs also play a role in inflammation (166). Functioning as a redox factor, APE1/Ref-1 stimulates the DNA binding activity of TFs by reducing cysteine residues within the TF (175). APE1/Ref-1 activates TFs including HIF1a, STAT3, p53, NF-kB and others that directly govern critical cellular functions, including hypoxia, DNA repair, inflammation, and angiogenesis (166). Cells, both tumor and normal, possess reduction-oxidation systems such as NRF2, thioredoxin, peroxiredoxins, and glutathione. In contrast, APE1/Ref-1 functions as a signaling molecule rather than a general redox system (176, 177). Our team has extensively characterized APE1/Ref-1 redox signaling inhibitors in several indications including cancer as well as chemotherapy- or IR-induced neuropathy (165, 178, 179). Vasko et al. demonstrated that the DNA repair function of APE1/Ref-1 was protective against the neurotoxicity induced by IR and APE1/Ref-1 redox inhibitor, APX3330 could protect dorsal root ganglia against IR-induced cytotoxicity (179). Blockade of APE1/Ref-1's redox activity could also sensitize radioresistant cancer cells or remodel the TME to affect the tumor's response to RT as HIF, STAT3, NF-kB, and others have been strongly implicated in the cellular response to RT (180–183).

Finally, inhibition of DDR signals by enhancing p53 function has also proven to be effective for radiosensitization in preclinical models. Several strategies employed for this revolve around suppressing the functions of proteins that inhibit p53. For instance, mouse double minute 2 homolog (MDM2) inhibitors have widely been studied for combination radiotherapy in several different cancers which enhance anti-tumor effects *in vitro* and *in vivo* (184–188).

Moving on from DNA damage, the traditional culprit in radiation medicine, now significant interest exists in developing radiosensitizers that more selectively radiosensitize tumors, but not normal tissues, by targeting signal transduction pathways that are more commonly activated in tumors, such as the EGFR

pathway (189, 190). Growth factors are essential for cancer cell proliferation and inhibition of apoptosis, and therefore, can contribute to radioresistance *via* several mechanisms, including activating proteins or pathways involved in repairing radiation-induced DNA damage (191, 192). Preclinical evidence has supported a radiosensitizing role for EGFR inhibition (193) and indeed, the addition of cetuximab to RT in patients with head and neck squamous cell cancer was shown to improve tumor control and overall survival compared with radiation alone (189). However, understanding the impact of the spectrum of EGFR alterations on radiosensitivity remains to be understood (194, 195). Similarly, the blockage of ERBB2 (human epidermal growth factor receptor2 [HER2]), which is commonly amplified in a subset of breast cancer (196), can reverse ERBB2-mediated radioresistance (197). These findings were translatable into the clinic which was evident from a recent analysis of the HERA trial which demonstrated the potential of combining radiotherapy with trastuzumab in reducing loco-regional recurrence rates in breast cancer patients with 1 to 3 positive lymph nodes (198). In the prostate cancer field, the combination of androgen deprivation therapy (ADT) and radiation in patients with intermediate and high risk prostate cancer is a well-established approach to prolonging survival in that subset of patients (199). Despite being one of the earliest examples of combining radiation with targeted therapy, the mechanism of synergy between ADT and radiation remains controversial. Initially much of the benefit was thought to be derived by the orchestrated effect of radiation controlling disease locally in the prostate and ADT treating micrometastatic disease elsewhere (200). Newer preclinical data suggests that ADT has direct effects in the prostate that result in radiosensitization *via* several mechanisms including relieving hypoxia (201), suppressing DNA repair (202) and deactivating androgen receptor (AR). The blockade of AR signaling is thought to regulate the transcription of DNA repair genes and thus mediate radioresistance (203). The modulation of several other oncogenic pathways could provide another approach to enhance radiation sensitivity such as intracellular signaling (i.e. PI3K/AKT pathway) (204) and tumor-associated epigenetic changes (205).

As mentioned previously, the rationale for targeting tumor metabolism to sensitize cancer cells to RT is well-established. Mitochondrial metabolism is crucial to cancer cell survival and RT-induced mitochondrial DNA damage as well as excess ROS generation provides an attractive target to suppress cancer cell proliferation and induce apoptosis (146, 147, 206). Glutamine metabolism facilitates cancer cell survival, and breakdown of glutamine is mediated by glutaminases, making them the focus for development of small molecule inhibitors. Indeed, preclinical data supports the combination of the glutaminase inhibitor, Telaglenastat (CB-839), in radiosensitization of cancer cells (**Figure 2**). Telaglenastat suppresses cancer cell proliferation alone and in combination with 5-FU or EGFR in several colorectal and lung cell lines (207, 208). Combination therapy of radiation and Telaglenastat diminishes cancer progression in cell culture and mouse models of head and neck squamous cell carcinoma. Clonogenic cell survival assays with FaDu (pharynx), HN5 (tongue), and CAL-27 (tongue) cell lines treated with radiation and Telaglenastat demonstrated significantly diminished proliferation compared to radiation or Telaglenastat treatment alone. These findings were confirmed using xenograft models in which combination therapy was superior to monotherapy (147). Similar results have been reported in lung cancer radiosensitization where treatment with Telaglenastat increased efficacy of RT by 30% in multiple cell lines and in H460-derived tumor xenografts (146).

Tumor hypoxia is another well-established mediator of radioresistance (209) and typically indicative of aggressive and treatment-resistant disease. Targeting tumor hypoxia by traditional cytotoxic chemotherapy has served as a cornerstone for concurrent chemoradiation regimens for decades. However, the validation of biomarkers of tumor hypoxia in patients that could guide the implementation of novel rationally designed combinations of radiation and hypoxia-targeting agents remains underexplored (105). Historically, several methods have been investigated in order to override hypoxia-mediated radioresistance. Such methods included: hyperbaric oxygen (210), oxygen mimetics which belong to the nitroimidazole class of agents (211), and hypoxia activated cytotoxic prodrugs such as tirapazamine (212). More recently, with the advent of the concept of normalizing tumor blood flow using anti-angiogenic therapy (AAT), several studies proposed RT-AAT combinations to alter oxygenation and improve therapeutic response. In xenograft mouse models, PI3K targeted inhibition led to improved tumor local control following radiation, which was associated with normalization of vasculature and increasing intrinsic radiosensitivity (213). In patients with NSCLC, PI3K inhibition led to reduction in tumor hypoxia as measured by FMISO PET in patients and was well tolerated in combination with palliative thoracic radiation (214). In GBM where angiogenesis is thought to be the hallmark of pathogenesis and VEGF its main driver (215), combining VEGF/EGFR with RT has been shown to halt the growth of glioma cells preclinically (216) and to have a significant synergistic anti-tumor effect with RT (217, 218).

The role of the tumor microenvironment on response to RT alone and in combination with chemotherapy or targeted agents is an important and understudied area. Stromal normalization is one approach to modulating the tumor microenvironment and reducing tumor hypoxia particularly with respect to radiation. Cancer-associated fibroblasts (CAFs) are naturally radioresistant, and data suggests that radiation can induce their pro-tumorigenic capabilities. However, the concept of combining RT with CAF targeting has not been investigated to date (219). Alternatively, another novel paradigm of targeting tumor hypoxia is the modulation of the tumor microenvironment by altering tumor metabolism through the inhibition of oxidative phosphorylation and thus decreasing tumor oxygen consumption rate and relieving hypoxia (220). Atovaquone, an FDA approved anti-malarial that functions through inhibition of mitochondrial complex III has been shown in pre-clinical models to alleviate tumor hypoxia and in turn results in tumor radiosensitization (221).

Finally, owing to rapid advances in nanotechnology, nanomaterials have attracted particular attention to enhance the anticancer efficacy of radiotherapy (158, 161, 222, 223). Nanoparticle delivery enhances tumor targeting while simultaneously improving effectiveness of radiotherapy by increasing local deposition of ionizing radiation dose or by augmenting production of ROS, DNA damage and cell cycle arrest (224). Silver nanoparticles were reported to sensitize both hypoxic and normoxic glioma U251 cells and C6 cells to radiotherapy (222). In additional studies, silver nanoparticles surface modified with polyethyleneglycol (PEG) and aptamer improved nanoparticle penetration and targeting in 3D glioma models, and conjugation with PEG/aptamer further enhanced radiosensitization in C6 xenograft models as well (158). The development of theragnostics further expand the scope of nanoparticles for multifunctional use (161). For instance, PEG conjugated bismuth gadolinium oxide nanoparticles (BiGdO3) not only sensitized breast cancer MCF-7 and 4T1 lines and 4T1 xenograft models to radiation, but the bismuth and gadolinium also allowed for MRI and CT imaging (161).

Even with the multitude of preclinical studies looking at combining RT with targeted therapy, chemotherapy, or immunotherapy, there are still very few examples of combinations that have translated into success clinically. We will now highlight some examples as well as future directions (**Table 1** and **Figure 2**).

RADIATION-TARGETED THERAPY COMBINATIONS IN THE CLINIC: STORIES OF SUCCESS AND FAILURE

A large body of preclinical evidence exists to support novel radiation-targeted therapy combinations. However, to date the EGFR inhibitor cetuximab remains to be the only molecular targeted agent approved by the U.S. Food and Drug Administration (FDA) for use with radiation therapy in head and neck cancer (189). Interestingly however the equivalence of cetuximab and cisplatin as radiosensitizers in head and neck cancer has been a crucial point of contention in the field. A small randomized trial by Margini et al. suggested that cetuximab was inferior to cisplatin when combined with radiation in patients with locoregionally advanced head and neck cancer (225). Two recent large, randomized trials have provided more conclusive evidence that cetuximab is indeed inferior. In the De-ESCALaTE Human Papilloma Virus (HPV trial), patients with low-risk HPV-positive oropharyngeal cancer had higher rates of local recurrence and lower overall survival when treated with cetuximab-RT compared to when treated with cisplatin-RT (226). That was also the case in the RTOG 1016 trial (227).

Although cetuximab was relatively successful as a radiosensitizer in the setting of head and neck cancer, it failed to show promising results in other cancers where EGFR signaling is relevant (**Figure 2**) (228–230). There is also a multitude of phase I/II data that demonstrated similarly disappointing results for other EGFR inhibitors. For example, EGFR is amplified in around 40% of GBM cases and its overexpression is associated with poor prognosis (231–233). Three phase II studies have examined the role of erlotinib, an oral tyrosine kinase inhibitor of the human EGF receptor that is FDA approved for the treatment of non–small cell lung and pancreatic cancers, given concurrently with RT plus temozolomide and have demonstrated widely contrasting results with respect to survival and toxicity. The overall trend however pointed towards increased toxicity with no substantial survival benefit. Phase I and II clinical trials have also been developed to study the combination of RT with erlotinib in pancreatic cancer in both the adjuvant and unresectable, locally advanced settings. Although toxicity profile was acceptable, only modest increases in efficacy have been observed (234–238). Alternative strategies for EGFR targeting have also been attempted in the early clinical settings. For instance, m-TOR targeting which is downstream of the EGFR/PI3K pathway have been trialed in the GBM setting. Two multi-institutional phase II studies have investigated the use of m-TOR inhibitor, Everolimus, in combination with standard RT plus TMZ, The North Central Cancer Treatment Group (NCCTG) N057K trial (239) and The Radiation Therapy Oncology Group (RTOG) 0913 trial (240). Despite having distinct designs, both trials showed no improvement in survival and increased toxicity. The rationale for the combination of EGFR inhibitors with RT is mainly based on the role of EGFR in driving the disease rather than on how the two modalities might work together to kill the tumor. Perhaps in future studies, combinations of RT with targeted agents need to be more rationally designed in order to see greater success clinically.

Another targeted radiosensitizer that has been relatively successful in the clinical setting is nimorazole. Nimorazole is a targeted radiosensitizer which selectively targets hypoxic tumor cells and has been shown in a phase III trial to significantly improve locoregional control by 16% in patients with cancer of the supraglottic larynx and pharynx when combined with radiation compared to radiation alone (241). However, nimorazole is currently only used in Denmark and has failed to become adopted as standard of care in the United States and elsewhere (242). In order to overcome hypoxia to sensitize tumors to radiation, Accelerated Radiation, Carbogen, and Nicotinamide, also known as the ARCON regimen, has demonstrated promising locoregional control rates and yet toxicity in a two large phase II studies in patients with head and neck cancer (243) and bladder cancer, respectively (244). This led to the phase III BCON trial which showed improved locoregional control and overall survival in bladder cancer patients who were treated using that regimen compared to patients treated with conventionally fractionated radiation alone (245). However, in a phase III study testing this regimen in laryngeal cancer patients, there was no significant improvement in either local control nor organ preservation rates in ARCON treated patients albeit with benefit in patients with hypoxic tumors (246). Taken together, this regimen has not been widely adopted due to practical difficulties in delivering this regimen, proper patient selection due difficulties in accurately determining highly hypoxic tumors, and inconclusive results from phase III data (247). Tirapazamine, the most clinically developed drug among hypoxia-activated cytotoxic prodrugs, which represent another class of hypoxia-targeted

radiosensitizers (212), have failed in phase III trials to demonstrate improved outcomes when combined with chemoradiation compared to conventional chemoradiation alone in both cervical (248) and head and neck cancers (249). Similarly, VEGF targeting which theoretically represents another attractive way of normalizing tumor vasculature and overcoming hypoxia, failed to improve OS in GBM patients where VEGF targeting was particularly alluring given its centrality to the disease pathogenesis (250–252). Interestingly however, another study showed that GBM patients that have increased tumor oxygenation following anti-angiogenic therapy when combined with conventional chemoradiation live significantly longer (253). Alternatively, targeting the stroma has been clinically attempted for radiosensitization with the goal of modulating RT-induced inflammatory responses (247). Recently, a phase II trial in patients with locally advanced pancreatic cancer has shown that addition of losartan to chemoradiation enhanced tumor shrinkage and enabled more margin negative resections likely due to interfering with TGF-β signaling in CAFs which are characteristic of the desmoplastic tumor microenvironment in pancreatic cancer (254).

Predictive biomarkers of response, which served as the premise of the systemic targeted therapy revolution, are needed in the radiation oncology field to improve trial design and success rates. To that goal, several early-stage clinical trials are currently underway; testing radiation resistance pathways that have been validated in the preclinical setting. For example, KRas, a proto-oncogene that is frequently mutated in a wide range of cancers (255) is a well-known driver of resistance to cancer therapy including radiation (256–258). Several exploratory clinical trials have demonstrated a link between KRas mutation status and decreased likelihood of locoregional control following radiation treatment (259–261). Midostaurin, a multikinase inhibitor that is FDA approved for treatment of FLT3 mutant acute myeloid leukemia (262) is currently being tested in phase Ib trial to be given concurrently with conventional chemoradiation in rectal cancer patients (263). This was based on an *in vitro* screen of 32 cell lines that represented lung, colorectal, head and neck, and genitourinary cell lines and identified Midostaurin as a potential radiosensitizer for KRas mutant cancers (264). Trametinib, a MEK inhibitor that is FDA approved for treatment of metastatic melanoma, is also being tested in a phase I trial in combination with chemoradiation for locally advanced KRas mutant NSCLC (265). Importantly, KRas has been so far inaccessible for direct inhibition until the recent FDA approval of sotorasib for the management of KRas mutated NSCLC based of the CodeBreaK 100 trial (266). It will be interesting to see how this could change the landscape of radiosensitization in the setting of KRas mutated cancer in the near future.

As discussed previously, DNA damage response is central to radiation response. However, so far there are many perceived challenges to clinically implementing this combination such as optimal sequencing, ideal genetic background, and importantly therapeutic window to avoid increased toxicity (267). There are numerous ongoing phase I/II trials combining radiation or conventional chemoradiation with novel targeted DDR inhibitors. Among DDR inhibitors, PARP inhibitors are the most clinically developed followed by WEE1 inhibitor, Adavosertib (**Figure 2**). In inflammatory or locally recurrent breast cancer, a phase I multicenter study evaluated veliparib, a PARP inhibitor, and concurrent RT for 30 patients. The study showed overall acceptable toxicity with only five (16.7%) patients experiencing a dose limiting toxicity (DLT) within 10 weeks from RT initiation. Although severe acute toxicity did not exceed 30% at even the highest dose, nearly half of the surviving patients demonstrated G3 adverse events at 3 years. Of the 30 patients, 15 experienced disease control failures during the 3 years of follow-up and 13 died which highlights the importance of long-term monitoring of toxicity in trials of radiosensitizing agents (268). A phase II trial comparing radiation with or without Olaparib in patients with inflammatory breast cancer, which is known to be particularly aggressive with dismal prognosis (269), is currently recruiting (NCT03598257). In pancreatic cancer, if the patient is homology recombination repair deficient (HRD), this may render the tumor particularly vulnerable to PARPi (270). Velaparib concurrent with chemo-RT was tested in a phase I study of 30 patients with locally advanced disease. Sixteen DLTs were detected in 12 patients (40%). Interestingly, median OS for DDR pathway gene-altered- and DDR-intact patients was 19 and 14 months, respectively. The most commonly mutated DDR gene was ARID1A (n = 4). Loss of ARID1A impairs both checkpoint activation and the repair of DSBs, which sensitizes cells to DSB-inducing treatments such as RT and PARP inhibitors (271). PARP inhibitors are also being tested in conjunction with other forms of targeted therapy such as EGFR inhibitors. A recent phase I study showed that Olaparib may be safely combined with concurrent cetuximab and radiation for patients with locally advanced head and neck squamous cell carcinoma who have a long smoking history. That combination has also demonstrated improved 2 year OS in that subset of patients compared to historical controls (72% *vs* 60% 2 year OS) (272). Other classes of DDR inhibitors such as WEE1 (Adavosertib), ATM, and DNA-PK inhibitors are currently being tested in phase I trials either in conjunction with radiation alone or chemoradiation in multiple disease sites. A recently completed phase I study evaluated Adavosertib in combination with RT and full-dose gemcitabine for 34 patients with locally advanced pancreatic cancer (273). In that study, median OS was 21.7 months which compares favorably with that of patients treated in the LAP07 trial (11.9–13.6 months), which had similar eligibility criteria and used gemcitabine (274). This sets Adavosertib as a promising drug in terms of clinical development compared to PARP inhibitors. The DNA-PKc inhibitor M3814 (Peposertib) has demonstrated promising anti-tumor activity in a recently published phase Ia study and is currently being tested concurrent with radiation in at least four phase I clinical trials covering different disease sites and different radiation fractionation regimens (275). ATM, ATR, and CHK1 inhibitors are also currently in several early phase clinical trials. Taken together, validating biomarkers of response for these novel agents to identify the subset of patients who will derive

the most benefit and the most acceptable toxicity in return remains to be a challenge (276).

Nanotechnology offers a new area of exciting research where nanoparticles can be used for targeted radiotherapy, either as sensitizers of external beams or as delivery vehicles for therapeutic radionuclides (277). In a phase II/III study, NBTXR3, a first-in-class radiosensitizer hafnium oxide nanoparticle, which is activated by radiation therapy, a significantly higher pathologic complete response was observed in the patients whose soft tissue sarcomas were injected with NBTXR3 prior to radiation compared to those who were not. There was no significant difference in toxicity between the two groups and no treatment-related death occurred (278). Although this is very promising data in the sarcoma field where very few patients achieve pathologic complete response with preoperative radiation and possibly in other cancers as well, a lot of challenges lie ahead for the clinical implementation of this technology and overcoming its limitations, particularly optimization of delivery (279).

The PACIFIC trial has revolutionized the management and therefore the outcomes of patients with locally advanced NSCLC. It has also set unprecedented clinical evidence supporting the interplay of chemoradiation and immunotherapy (280, 281). Importantly however it has posed many pressing questions regarding the optimal dosing, sequencing, and safety of combining radiation with immunotherapy. Currently, a plethora of clinical trials are attempting to answer those questions. Recently, the DETERRED trial demonstrated the safety and efficacy of adding Atezolizumab (anti-PD-L1) concurrently with chemoradiation (282) as well as the Phase 2 KEYNOTE-799 with concurrent delivery of Pembrolizumab (anti-PD-1) and radiation in locally advanced NSCLC (283). It will therefore be important to compare that regimen with the PACIFIC regimen where Durvalumab (anti-PD-L1) was given after chemoradiation in the consolidation setting. In head and neck cancer, a number of phase I/II clinical trials are testing the feasibility of combining chemoradiation with immunotherapy in the definitive setting. Collectively, those early studies have demonstrated the safety of the combination (284–287). A recent report by Weiss et al. showed that concurrent definitive immunoradiotherapy for patients with stage III-IV head and neck cancer who are ineligible for cisplatin had 24-month PFS and overall survival rates were 71% which exceeded their primary hypothesis (288). However, a substantial clinical benefit is yet to be proven in the phase III setting.

In the metastatic setting, several prospective trials have been conducted to test the abscopal effect of radiation, which stems from many anecdotal reports and arguably stimulated much of the hype regarding the combination of radiation and immunotherapy (289). The abscopal effect of radiation refers to the shrinkage or disappearance of sites of metastasis that were not directly treated with radiation. Although the mechanisms of this observation are still being elucidated, it is believed that the addition of immunotherapy to radiation regimens allows the immune system to mount a more systemic response against the tumor. PEMBRO-RT is a phase II study which asked the question whether stereotactic body radiotherapy (SBRT) enhances the effect of immune checkpoint inhibition in nonirradiated lung cancer lesions in metastatic NSCLC. In that study, patients with metastatic NSCLC were randomized to receiving pembrolizumab either alone or after SBRT, which was delivered to a single tumor site. There was a trend towards better overall response (ORR) and improved PFS in the combination arm but did not reach statistical significance. Interestingly, the benefit was more evident in patients with PD-L1 negative tumors and in subgroup analysis, improved ORR and PFS reached statistical significance in that group of patients (290). This again highlights the importance of discovering and understanding what molecular markers are important in the response to RT alone and in combination with targeted agents. In metastatic head and neck cancer, a similar phase II study randomized patients to either Nivolumab (anti-PD-1) alone or after SBRT to one metastatic site. Unfortunately the study did not find improvement in response, PFS, or OS between the two arms and there was no evidence of an abscopal effect with the addition of SBRT to Nivolumab in unselected patients with metastatic HNSCC (291). Interestingly however, in the neoadjuvant setting in early stage resectable NSCLC, concurrent SBRT and Durvalumab was safe and associated with significantly better pathological response compared to neoadjuvant Durvalumab alone demonstrating a robust evidence of abscopal immune-modulatory effect of radiation (292). These contrasting results could probably be attributed to the hypothesis that immunotherapy is generally more effective with less disease burden and therefore the abscopal effect could be captured in that setting (293). Taken together, phase III data is needed to validate the combinatorial benefit of radiation and immunotherapy in the metastatic setting and also better defining correlates of response based on biomarkers.

As outlined above there are many clinical trials testing different radiosensitization paradigms. That is not meant to be a comprehensive list but rather to paint a picture for the diverse nature of signaling mechanisms that could potentially be targeted to improve the therapeutic ratio of radiation. Importantly, while there are examples of successful radiation-targeted therapy combination in clinic, failures certainly outweigh those few successes. Therefore, a lot remains to be done in to decrease attrition rates of novel radiosensitizers in the clinic.

THE CHALLENGES AHEAD FOR CLINICAL IMPLEMENTATION

Oncology drug development has witnessed a significant growth over the last decade that was coupled with improved cancer outcomes and unprecedented drop in cancer related death rates (294). However, the development of novel radiosensitizers lagged behind reflecting lack of incentive by pharmaceutical industry to invest in this pipeline. This huge gap led to holding a collaborative workshop by the FDA-AACR-ASTRO in 2018 to bring together various stakeholders including representatives of academia, industry, patient advocacy groups and the FDA to identify key challenges and design a roadmap for bridging this gap (104). This effort was also preceded by similar efforts in the UK highlighting the

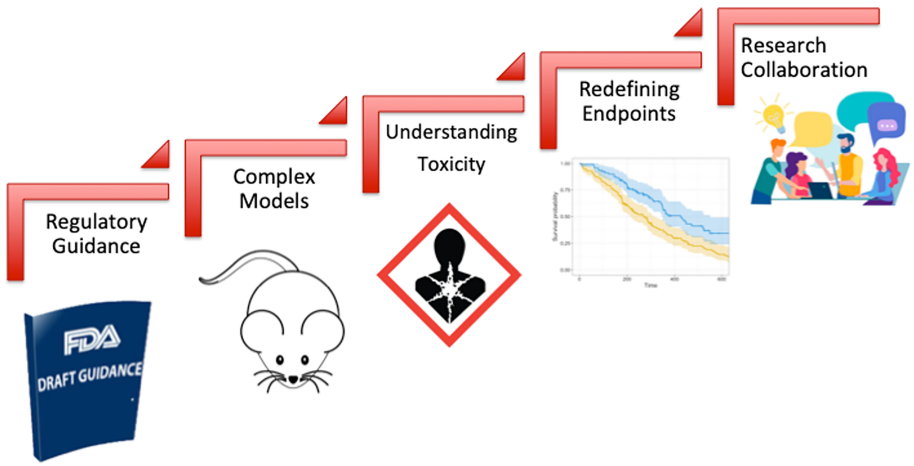

FIGURE 3 | Challenges of clinical development of novel drug-radiotherapy combinations.

importance of this issue in the overall goal of improving cancer control rates where radiation therapy plays a central role as a curative and palliative treatment (105). As highlighted in **Figure 3**, the main challenges identified were: (1) lack of regulatory guidance by the FDA detailing the approval pathway for drug-radiotherapy combination particularly with regard to the extent of required preclinical data, (2) choice of adequate model systems that can reflect tumor complexity and heterogeneity and enable testing various radiation techniques and schedules, (3) complexity of the definition of 'safety' in the radiation setting as it should take into account normal tissue toxicity and long term toxicity which are not traditionally considered in drug only studies, (4) perceived impracticality of traditional clinical trial regulatory endpoints (such as OS and PFS) when testing novel drug-radiotherapy combinations particularly in the curative setting and finally (5) historically limited collaboration among medical and radiation oncologists particularly in the United states which is crucial for aligning research perspectives and goals. Moving forward, overcoming these hurdles and prioritizing communication among key stakeholders in the field will be crucial to propel the radiosensitizer pipeline. The year 2020 was arguably a landmark year for drug-radiotherapy combinations, with two novel radiosensitizers getting fast track and breakthrough designations: NBTXR3 and Debio 1143 respectively (294). However, the field is yet to witness new market approvals as we strive to overcome challenges and improve patient outcomes.

AUTHOR CONTRIBUTIONS

ME and NC contributed equally to the writing and planning of the content of the review. RR provided clinical input and expertise to the review and MF edited and directed the writing and content within the review. All authors contributed to the article and approved the submitted version.

FUNDING

MF was supported by grants from the National Institute of Health and National Cancer Institute R01CA167291, R01CA211098, R01 CA254110. NC and MF were also supported by NIH/NCI grant U01HL143403. MF was additionally supported by the Riley Children's Foundation.

REFERENCES

1. Bryant AK, Banegas MP, Martinez ME, Mell LK, Murphy JD. Trends in Radiation Therapy Among Cancer Survivors in the United States, 2000–2030. *Cancer Epidemiol Prev Biomarkers* (2017) 26(6):963–70. doi: 10.1158/1055-9965.EPI-16-1023
2. Dupin C, Lang P, Dessard-Diana B, Simon J-M, Cuenca X, Mazeron J-J, et al. Treatment of Head and Neck Paragangliomas With External Beam Radiation Therapy. *Int J Radiat Oncol Biol Phys* (2014) 89(2):353–9. doi: 10.1016/j.ijrobp.2014.02.010
3. Mondal D, Sharma DN. External Beam Radiation Techniques for Breast Cancer in the New Millennium: New Challenging Perspectives. *J Egyptian Natl Cancer Institute* (2016) 28(4):211–8. doi: 10.1016/j.jnci.2016.08.001
4. Higgins KA, O'Connell K, Liu Y, Gillespie TW, McDonald MW, Pillai RN, et al. National Cancer Database Analysis of Proton *Versus* Photon Radiation Therapy in Non-Small Cell Lung Cancer. *Int J Radiat Oncol Biol Phys* (2017) 97(1):128–37. doi: 10.1016/j.ijrobp.2016.10.001
5. Kim J-Y, Park Y. Treatment of Retinoblastoma: The Role of External Beam Radiotherapy. *Yonsei Med J* (2015) 56(6):1478. doi: 10.3349/ymj.2015.56.6.1478
6. Magnuson WJ, Halligan JB. Successful Treatment of Melanoma Metastatic to the Left Atrium Using External Beam Radiation Therapy. *Oncology* (2010) 24(7):650.
7. Wang T-H, Huang P-I, Hu Y-W, Lin K-H, Liu C-S, Lin Y-Y, et al. Combined Yttrium-90 Microsphere Selective Internal Radiation Therapy and External Beam Radiotherapy in Patients With Hepatocellular

Carcinoma: From Clinical Aspects to Dosimetry. *PloS One* (2018) 13(1): e0190098. doi: 10.1371/journal.pone.0190098
8. Yang J, Cai H, Xiao ZX, Wang H, Yang P. Effect of Radiotherapy on the Survival of Cervical Cancer Patients: An Analysis Based on SEER Database. *Medicine* (2019) 98(30):e16421. doi: 10.1097/MD.0000000000016421
9. Glaser SM, Beriwal S. Brachytherapy for Malignancies of the Vagina in the 3D Era. *J Contemp Brachytherapy* (2015) 7(4):312. doi: 10.5114/jcb.2015.54053
10. Falk AT, Claren A, Benezery K, François E, Gautier M, Gerard J-P, et al. Interstitial High-Dose Rate Brachytherapy as Boost for Anal Canal Cancer. *Radiat Oncol* (2014) 9(1):1–9. doi: 10.1186/s13014-014-0240-4
11. Zaorsky NG, Davis BJ, Nguyen PL, Showalter TN, Hoskin PJ, Yoshioka Y, et al. The Evolution of Brachytherapy for Prostate Cancer. *Nat Rev Urol* (2017) 14(7):415. doi: 10.1038/nrurol.2017.76
12. Vaidya JS, Bulsara M, Baum M, Wenz F, Massarut S, Pigorsch S, et al. New Clinical and Biological Insights From the International TARGIT-A Randomised Trial of Targeted Intraoperative Radiotherapy During Lumpectomy for Breast Cancer. *Br J Cancer* (2021) 125(3):380–9. doi: 10.14324/000.wp.10121050
13. Cifarelli CP, Brehmer S, Vargo JA, Hack JD, Kahl KH, Sarria-Vargas G, et al. Intraoperative Radiotherapy (IORT) for Surgically Resected Brain Metastases: Outcome Analysis of an International Cooperative Study. *J Neuro-Oncology* (2019) 145(2):391–7. doi: 10.1007/s11060-019-03309-6
14. Withers HR. The Four R's of Radiotherapy. *Adv Radiat Biol 5: Elsevier;* (1975) 241–71. doi: 10.1016/B978-0-12-035405-4.50012-8
15. Steel GG, McMillan TJ, Peacock J. The 5Rs of Radiobiology. *Int J Radiat Biol* (1989) 56(6):1045–8. doi: 10.1080/09553008914552491
16. Joiner MC, Burmeister JW, Dörr W. Linear Energy Transfer and Relative Biological Effectiveness. In: *Basic Clinical Radiobiology*. CRC Press (2018). p. 54–60. doi: 10.1201/9780429490606-6
17. Herskind C, Ma L, Liu Q, Zhang B, Schneider F, Veldwijk MR, et al. Biology of High Single Doses of IORT: RBE, 5 R's, and Other Biological Aspects. *Radiat Oncol* (2017) 12(1):1–14. doi: 10.1186/s13014-016-0750-3
18. Sologuren I, Rodríguez-Gallego C, Lara PC. Immune Effects of High Dose Radiation Treatment: Implications of Ionizing Radiation on the Development of Bystander and Abscopal Effects. *Trans Cancer Res* (2014) 3:18–31. doi: 10.3390/ijms15010927
19. Brown JM, Carlson DJ, Brenner DJ. The Tumor Radiobiology of SRS and SBRT: Are More Than the 5 Rs Involved? *Int J Radiat Oncol Biol Phys* (2014) 88(2):254–62. doi: 10.1016/j.ijrobp.2013.07.022
20. Marconi R, Strolin S, Bossi G, Strigari L. A Meta-Analysis of the Abscopal Effect in Preclinical Models: Is the Biologically Effective Dose a Relevant Physical Trigger? *PloS One* (2017) 12(2):e0171559. doi: 10.1371/journal.pone.0171559
21. Riballo E, Kühne M, Rief N, Doherty A, Smith GC, Recio M-J, et al. A Pathway of Double-Strand Break Rejoining Dependent Upon ATM, Artemis, and Proteins Locating to γ-H2AX Foci. *Mol Cell* (2004) 16 (5):715–24. doi: 10.1016/j.molcel.2004.10.029
22. Eccles LJ, O'Neill P, Lomax ME. Delayed Repair of Radiation Induced Clustered DNA Damage: Friend or Foe? *Mutat Research/Fundamental Mol Mech Mutagenesis* (2011) 711(1-2):134–41. doi: 10.1016/j.mrfmmm.2010.11.003
23. Gulston M, Fulford J, Jenner T, de Lara C, O'Neill P. Clustered DNA Damage Induced by γ Radiation in Human Fibroblasts (HF19), Hamster (V79-4) Cells and Plasmid DNA Is Revealed as Fpg and Nth Sensitive Sites. *Nucleic Acids Res* (2002) 30(15):3464–72. doi: 10.1093/nar/gkf467
24. Asaithamby A, Chen DJ. Mechanism of Cluster DNA Damage Repair in Response to High-Atomic Number and Energy Particles Radiation. *Mutat Research/Fundamental Mol Mech Mutagenesis* (2011) 711(1-2):87–99. doi: 10.1016/j.mrfmmm.2010.11.002
25. Nickoloff JA, Sharma N, Taylor L. Clustered DNA Double-Strand Breaks: Biological Effects and Relevance to Cancer Radiotherapy. *Genes* (2020) 11 (1):99. doi: 10.3390/genes11010099
26. Hanai M, Yazu K, Hieda R. On the Experimental Distinction Between Ssbs and Dsbs in Circular DNA. *Int J Radiat Biol* (1998) 73(5):475–9. doi: 10.1080/095530098142013
27. Van Der Schans G. Gamma-Ray Induced Double-Strand Breaks in DNA Resulting From Randomly-Inflicted Single-Strand Breaks: Temporal Local Denaturation, a New Radiation Phenomenon? *Int J Radiat Biol Related Stud Physics Chem Med* (1978) 33(2):105–20. doi: 10.1080/09553007814550011
28. Zheng Y, Sanche L. Clustered DNA Damages Induced by 0.5 to 30 eV Electrons. *Int J Mol Sci* (2019) 20(15):3749.
29. Sutherland BM, Bennett PV, Cintron NS, Guida P, Laval J. Low Levels of Endogenous Oxidative Damage Cluster Levels in Unirradiated Viral and Human DNAs. *Free Radical Biol Med* (2003) 35(5):495–503. doi: 10.1016/S0891-5849(03)00327-7
30. Bennett PV, Cintron NS, Gros L, Laval J, Sutherland BM. Are Endogenous Clustered DNA Damages Induced in Human Cells? *Free Radical Biol Med* (2004) 37(4):488–99. doi: 10.1016/j.freeradbiomed.2004.05.004
31. Nikjoo H, O'Neill P, Terrissol M, Goodhead D. Quantitative Modelling of DNA Damage Using Monte Carlo Track Structure Method. *Radiat Environ biophysics* (1999) 38(1):31–8. doi: 10.1007/s004110050135
32. Pavlopoulou A, Bagos PG, Koutsandrea V, Georgakilas AG. Molecular Determinants of Radiosensitivity in Normal and Tumor Tissue: A Bioinformatic Approach. *Cancer Lett* (2017) 403:37–47. doi: 10.1016/j.canlet.2017.05.023
33. Fishel ML, Jiang Y, Rajeshkumar N, Scandura G, Sinn AL, He Y, et al. Impact of APE1/Ref-1 Redox Inhibition on Pancreatic Tumor Growth. *Mol Cancer Ther* (2011) 10(9):1698–708. doi: 10.1158/1535-7163.MCT-11-0107
34. Gampala S, Shah F, Zhang C, Rhodes SD, Babb O, Grimard M, et al. Exploring Transcriptional Regulators Ref-1 and STAT3 as Therapeutic Targets in Malignant Peripheral Nerve Sheath Tumours. *Br J Cancer* (2021) 124(9):1566–80. doi: 10.1038/s41416-021-01270-8
35. Robertson KA, Bullock HA, Xu Y, Tritt R, Zimmerman E, Ulbright TM, et al. Altered Expression of Ape1/ref-1 in Germ Cell Tumors and Overexpression in NT2 Cells Confers Resistance to Bleomycin and Radiation. *Cancer Res* (2001) 61(5):2220–5.
36. Naidu MD, Mason JM, Pica RV, Fung H, Peña LA. Radiation Resistance in Glioma Cells Determined by DNA Damage Repair Activity of Ape1/Ref-1. *J Radiat Res* (2010) 51(4):393–404. doi: 10.1269/jrr.09077
37. Cun Y, Dai N, Xiong C, Li M, Sui J, Qian C, et al. Silencing of APE1 Enhances Sensitivity of Human Hepatocellular Carcinoma Cells to Radiotherapy *In Vitro* and in a Xenograft Model. *PloS One* (2013) 8(2): e55313. doi: 10.1371/journal.pone.0055313
38. Zhao W, Hu H, Mo Q, Guan Y, Li Y, Du Y, et al. Function and Mechanism of Combined PARP-1 and BRCA Genes in Regulating the Radiosensitivity of Breast Cancer Cells. *Int J Clin Exp Pathol* (2019) 12(10):3915.
39. Teng P-N, Bateman NW, Darcy KM, Hamilton CA, Maxwell GL, Bakkenist CJ, et al. Pharmacologic Inhibition of ATR and ATM Offers Clinically Important Distinctions to Enhancing Platinum or Radiation Response in Ovarian, Endometrial, and Cervical Cancer Cells. *Gynecologic Oncol* (2015) 136(3):554–61. doi: 10.1016/j.ygyno.2014.12.035
40. Metwally MAH, Frederiksen KD, Overgaard J. Compliance and Toxicity of the Hypoxic Radiosensitizer Nimorazole in the Treatment of Patients With Head and Neck Squamous Cell Carcinoma (HNSCC). *Acta Oncol* (2014) 53 (5):654–61. doi: 10.3109/0284186X.2013.864050
41. Wardman P. Nitroimidazoles as Hypoxic Cell Radiosensitizers and Hypoxia Probes: Misonidazole, Myths and Mistakes. *Br J Radiol* (2018) 92 (1093):20170915. doi: 10.1259/bjr.20170915
42. Somasundaram V, Basudhar D, Bharadwaj G, No JH, Ridnour LA, Cheng RY, et al. Molecular Mechanisms of Nitric Oxide in Cancer Progression, Signal Transduction, and Metabolism. *Antioxidants Redox Signaling* (2019) 30(8):1124–43. doi: 10.1089/ars.2018.7527
43. Fokas E, Prevo R, Pollard J, Reaper P, Charlton P, Cornelissen B, et al. Targeting ATR *In Vivo* Using the Novel Inhibitor VE-822 Results in Selective Sensitization of Pancreatic Tumors to Radiation. *Cell Death Dis* (2012) 3(12):e441–e. doi: 10.1038/cddis.2012.181
44. Riaz MA, Sak A, Erol YB, Groneberg M, Thomale J, Stuschke M. Metformin Enhances the Radiosensitizing Effect of Cisplatin in Non-Small Cell Lung Cancer Cell Lines With Different Cisplatin Sensitivities. *Sci Rep* (2019) 9 (1):1–16. doi: 10.1038/s41598-018-38004-5
45. Wu C-H, Chen C-Y, Yeh C-T, Lin K-H. Radiosensitization of Hepatocellular Carcinoma Through Targeting Radio-Associated Microrna. *Int J Mol Sci* (2020) 21(5):1859. doi: 10.3390/ijms21051859
46. Masoudi-Khoram N, Abdolmaleki P, Hosseinkhan N, Nikoofar A, Mowla SJ, Monfared H, et al. Differential miRNAs Expression Pattern of Irradiated

Breast Cancer Cell Lines is Correlated With Radiation Sensitivity. *Sci Rep* (2020) 10(1):1–12. doi: 10.1038/s41598-020-65680-z
47. Shimura T, Sasatani M, Kawai H, Kamiya K, Kobayashi J, Komatsu K, et al. A Comparison of Radiation-Induced Mitochondrial Damage Between Neural Progenitor Stem Cells and Differentiated Cells. *Cell Cycle* (2017) 16 (6):565–73. doi: 10.1080/15384101.2017.1284716
48. Lei G, Zhang Y, Koppula P, Liu X, Zhang J, Lin SH, et al. The Role of Ferroptosis in Ionizing Radiation-Induced Cell Death and Tumor Suppression. *Cell Res* (2020) 30(2):146–62. doi: 10.1038/s41422-019-0263-3
49. Corre I, Niaudet C, Paris F. Plasma Membrane Signaling Induced by Ionizing Radiation. *Mutat Research/Reviews Mutat Res* (2010) 704(1-3):61–7. doi: 10.1016/j.mrrev.2010.01.014
50. Zhang S-R, Zhang X-C, Liang J-F, Fang H-M, Huang H-X, Zhao Y-Y, et al. Chalcomoracin Inhibits Cell Proliferation and Increases Sensitivity to Radiotherapy in Human Non-Small Cell Lung Cancer Cells *via* Inducing Endoplasmic Reticulum Stress-Mediated Paraptosis. *Acta Pharmacologica Sin* (2020) 41(6):825–34. doi: 10.1038/s41401-019-0351-4
51. Qiao Q, Sun C, Han C, Han N, Zhang M, Li G. Endoplasmic Reticulum Stress Pathway PERK-eIF 2α Confers Radioresistance in Oropharyngeal Carcinoma by Activating NF-κb. *Cancer Sci* (2017) 108(7):1421–31. doi: 10.1111/cas.13260
52. Gong C, Yang Z, Zhang L, Wang Y, Gong W, Liu Y. Quercetin Suppresses DNA Double-Strand Break Repair and Enhances the Radiosensitivity of Human Ovarian Cancer Cells *via* P53-Dependent Endoplasmic Reticulum Stress Pathway. *OncoTargets Ther* (2018) 11:17. doi: 10.2147/OTT.S147316
53. Yasui H, Takeuchi R, Nagane M, Meike S, Nakamura Y, Yamamori T, et al. Radiosensitization of Tumor Cells Through Endoplasmic Reticulum Stress Induced by PEGylated Nanogel Containing Gold Nanoparticles. *Cancer Lett* (2014) 347(1):151–8. doi: 10.1016/j.canlet.2014.02.005
54. Yang HJ, Youn H, Seong KM, Jin Y-W, Kim J, Youn B. Phosphorylation of Ribosomal Protein S3 and Antiapoptotic TRAF2 Protein Mediates Radioresistance in Non-Small Cell Lung Cancer Cells. *J Biol Chem* (2013) 288(5):2965–75. doi: 10.1074/jbc.M112.385989
55. Zhao Y, Tan M, Liu X, Xiong X, Sun Y. Inactivation of Ribosomal Protein S27-Like Confers Radiosensitivity *via* the Mdm2-P53 and Mdm2–MRN–ATM Axes. *Cell Death Dis* (2018) 9(2):1–11. doi: 10.1038/s41419-017-0192-3
56. Hussain SS, Huang S-B, Bedolla RG, Rivas P, Basler JW, Swanson GP, et al. Suppression of Ribosomal Protein RPS6KB1 by Nexrutine Increases Sensitivity of Prostate Tumors to Radiation. *Cancer Lett* (2018) 433:232–41. doi: 10.1016/j.canlet.2018.07.009
57. Wu P-H, Onodera Y, Giaccia AJ, Le Q-T, Shimizu S, Shirato H, et al. Lysosomal Trafficking Mediated by Arl8b and BORC Promotes Invasion of Cancer Cells That Survive Radiation. *Commun Biol* (2020) 3(1):1–15. doi: 10.1038/s42003-020-01339-9
58. Bagshaw RD, Callahan JW, Mahuran DJ. The Arf-Family Protein, Arl8b, is Involved in the Spatial Distribution of Lysosomes. *Biochem Biophys Res Commun* (2006) 344(4):1186–91. doi: 10.1016/j.bbrc.2006.03.221
59. Cho YH, Lee S-H, Lee S-J, Kim HN, Koh J-Y. A Role of Metallothionein-3 in Radiation-Induced Autophagy in Glioma Cells. *Sci Rep* (2020) 10(1):1–11. doi: 10.1038/s41598-020-58237-7
60. Tang L, Wei F, Wu Y, He Y, Shi L, Xiong F, et al. Role of Metabolism in Cancer Cell Radioresistance and Radiosensitization Methods. *J Exp Clin Cancer Res* (2018) 37(1):1–15. doi: 10.1186/s13046-018-0758-7
61. Tann AW, Boldogh I, Meiss G, Qian W, Van Houten B, Mitra S, et al. Apoptosis Induced by Persistent Single-Strand Breaks in Mitochondrial Genome: Critical Role of EXOG (5′-EXO/endonuclease) in Their Repair. *J Biol Chem* (2011) 286(37):31975–83. doi: 10.1074/jbc.M110.215715
62. Li N, Yu L, Wang J, Gao X, Chen Y, Pan W, et al. A Mitochondria-Targeted Nanoradiosensitizer Activating Reactive Oxygen Species Burst for Enhanced Radiation Therapy. *Chem Sci* (2018) 9(12):3159–64. doi: 10.1039/C7SC04458E
63. Liou G-Y, Storz P. Reactive Oxygen Species in Cancer. *Free Radical Res* (2010) 44(5):479–96. doi: 10.3109/10715761003667554
64. Lin B, Gao F, Yang Y, Wu D, Zhang Y, Feng G, et al. FLASH Radiotherapy: History and Future. *Front Oncol* (2021) 11:1890. doi: 10.3389/fonc.2021.644400
65. Ni K, Lan G, Veroneau SS, Duan X, Song Y, Lin W. Nanoscale Metal-Organic Frameworks for Mitochondria-Targeted Radiotherapy-Radiodynamic Therapy. *Nat Commun* (2018) 9(1):1–13. doi: 10.1038/s41467-018-06655-7
66. Yamazaki T, Kirchmair A, Sato A, Buqué A, Rybstein M, Petroni G, et al. Mitochondrial DNA Drives Abscopal Responses to Radiation That are Inhibited by Autophagy. *Nat Immunol* (2020) 21(10):1160–71. doi: 10.1038/s41590-020-0751-0
67. Atkinson J, Kapralov AA, Yanamala N, Tyurina YY, Amoscato AA, Pearce L, et al. A Mitochondria-Targeted Inhibitor of Cytochrome C Peroxidase Mitigates Radiation-Induced Death. *Nat Commun* (2011) 2(1):1–9. doi: 10.1038/ncomms1499
68. Momcilovic M, Shackelford D. Targeting LKB1 in Cancer–Exposing and Exploiting Vulnerabilities. *Br J Cancer* (2015) 113(4):574–84. doi: 10.1038/bjc.2015.261
69. He Q, Li J, Dong F, Cai C, Zou X. LKB1 Promotes Radioresistance in Esophageal Cancer Cells Exposed to Radiation, by Suppression of Apoptosis and Activation of Autophagy *via* the AMPK Pathway. *Mol Med Rep* (2017) 16(2):2205–10. doi: 10.3892/mmr.2017.6852
70. Porporato PE, Filigheddu N, Bravo-San Pedro JM, Kroemer G, Galluzzi L. Mitochondrial Metabolism and Cancer. *Cell Res* (2018) 28(3):265–80. doi: 10.1038/cr.2017.155
71. Lynam-Lennon N, Maher SG, Maguire A, Phelan J, Muldoon C, Reynolds JV, et al. Altered Mitochondrial Function and Energy Metabolism is Associated With a Radioresistant Phenotype in Oesophageal Adenocarcinoma. *PloS One* (2014) 9(6):e100738. doi: 10.1371/journal.pone.0100738
72. Lawrence YR, Vikram B, Dignam JJ, Chakravarti A, Machtay M, Freidlin B, et al. NCI–RTOG Translational Program Strategic Guidelines for the Early-Stage Development of Radiosensitizers. *J Natl Cancer Institute* (2013) 105 (1):11–24. doi: 10.1093/jnci/djs472
73. Ataman OU, Sambrook SJ, Wilks C, Lloyd A, Taylor AE, Wedge SR. The Clinical Development of Molecularly Targeted Agents in Combination With Radiation Therapy: A Pharmaceutical Perspective. *Int J Radiat Oncol Biol Phys* (2012) 84(4):e447–e54. doi: 10.1016/j.ijrobp.2012.05.019
74. Hanahan D, Weinberg RA. The Hallmarks of Cancer. *Cell* (2000) 100(1):57–70. doi: 10.1016/S0092-8674(00)81683-9
75. Hanahan D, Weinberg RA. Hallmarks of Cancer: The Next Generation. *cell* (2011) 144(5):646–74. doi: 10.1016/j.cell.2011.02.013
76. Willers H, Keane FK, Kamran SC. Toward a New Framework for Clinical Radiation Biology. *Hematology/Oncology Clinics* (2019) 33(6):929–45. doi: 10.1016/j.hoc.2019.07.001
77. Kamran SC, Mouw KW. Applying Precision Oncology Principles in Radiation Oncology. *JCO Precis Oncol* (2018) 2:1–23. doi: 10.1200/PO.18.00034
78. Yard BD, Adams DJ, Chie EK, Tamayo P, Battaglia JS, Gopal P, et al. A Genetic Basis for the Variation in the Vulnerability of Cancer to DNA Damage. *Nat Commun* (2016) 7(1):1–14. doi: 10.1038/ncomms11428
79. Mamounas EP, Tang G, Fisher B, Paik S, Shak S, Costantino JP, et al. Association Between the 21-Gene Recurrence Score Assay and Risk of Locoregional Recurrence in Node-Negative, Estrogen Receptor–Positive Breast Cancer: Results From NSABP B-14 and NSABP B-20. *J Clin Oncol* (2010) 28(10):1677. doi: 10.1200/JCO.2009.23.7610
80. Solin LJ, Gray R, Baehner FL, Butler SM, Hughes LL, Yoshizawa C, et al. A Multigene Expression Assay to Predict Local Recurrence Risk for Ductal Carcinoma *in Situ* of the Breast. *J Natl Cancer Institute* (2013) 105(10):701–10. doi: 10.1093/jnci/djt067
81. Solin LJ, Gray R, Hughes LL, Wood WC, Lowen MA, Badve SS, et al. Surgical Excision Without Radiation for Ductal Carcinoma *in Situ* of the Breast: 12-Year Results From the ECOG-ACRIN E5194 Study. *J Clin Oncol* (2015) 33 (33):3938. doi: 10.1200/JCO.2015.60.8588
82. Rakovitch E, Baehner R, Shak S, Miller D, Cherbavaz D, Anderson J, et al. A Large Prospectively Designed Study of the DCIS Score: Recurrence Risk After Local Excision for Ductal Carcinoma *in Situ* Patients With and Without Irradiation. *Int J Radiat Oncology• Biology• Phys* (2015) 93(3): S135–S6. doi: 10.1016/j.ijrobp.2015.07.323
83. Rakovitch E, Sutradhar R, Nofech-Mozes S, Gu S, Fong C, Hanna W, et al. 21-Gene Assay and Breast Cancer Mortality in Ductal Carcinoma *in Situ*. *JNCI: J Natl Cancer Institute* (2021) 113(5):572–9. doi: 10.1093/jnci/djaa179
84. Den RB, Yousefi K, Trabulsi EJ, Abdollah F, Choeurng V, Feng FY, et al. Genomic Classifier Identifies Men With Adverse Pathology After Radical

Prostatectomy Who Benefit From Adjuvant Radiation Therapy. *J Clin Oncol* (2015) 33(8):944. doi: 10.1200/JCO.2014.59.0026
85. Gore JL, du Plessis M, Santiago-Jiménez M, Yousefi K, Thompson DJ, Karsh L, et al. Decipher Test Impacts Decision Making Among Patients Considering Adjuvant and Salvage Treatment After Radical Prostatectomy: Interim Results From the Multicenter Prospective PRO-IMPACT Study. *Cancer* (2017) 123(15):2850–9. doi: 10.1002/cncr.30665
86. Eggener SE, Rumble RB, Armstrong AJ, Morgan TM, Crispino T, Cornford P, et al. Molecular Biomarkers in Localized Prostate Cancer: ASCO Guideline. *J Clin Oncol* (2020) 38(13):1474–94. doi: 10.1200/JCO.19.02768
87. Vale CL, Fisher D, Kneebone A, Parker C, Pearse M, Richaud P, et al. Adjuvant or Early Salvage Radiotherapy for the Treatment of Localised and Locally Advanced Prostate Cancer: A Prospectively Planned Systematic Review and Meta-Analysis of Aggregate Data. *Lancet* (2020) 396 (10260):1422–31. doi: 10.1016/S0140-6736(20)31952-8
88. Morgan TM, Miller DC, Dunn R, Susan L, Okoth L, Johnson A, et al. Prospective Randomized Trial of Genomic Classifier Impact on Treatment Decisions in Patients at High Risk of Recurrence Following Radical Prostatectomy (G-MINOR). *Am Soc Clin Oncol* (2018). doi: 10.1200/JCO.2018.36.6_suppl.TPS154
89. Scott JG, Berglund A, Schell MJ, Mihaylov I, Fulp WJ, Yue B, et al. A Genome-Based Model for Adjusting Radiotherapy Dose (GARD): A Retrospective, Cohort-Based Study. *Lancet Oncol* (2017) 18(2):202–11. doi: 10.1016/S1470-2045(16)30648-9
90. Scott JG, Sedor G, Ellsworth P, Scarborough JA, Ahmed K, Eschrich SA, et al. Pan-Cancer Prediction of Radiotherapy Benefit using Genomic-Adjusted Radiation Dose (GARD): A Cohort-based Pooled Analysis. *Lancet Oncol* (2021) 22(9):1221–9. doi: 10.1016/S1470-2045(21)00347-8
91. Ahmed KA, Liveringhouse CL, Mills MN, Figura NB, Grass GD, Washington IR, et al. Utilizing the Genomically Adjusted Radiation Dose (GARD) to Personalize Adjuvant Radiotherapy in Triple Negative Breast Cancer Management. *EBioMedicine* (2019) 47:163–9. doi: 10.1016/j.ebiom.2019.08.019
92. Ahmed KA, Scott JG, Arrington JA, Naghavi AO, Grass GD, Perez BA, et al. Radiosensitivity of Lung Metastases by Primary Histology and Implications for Stereotactic Body Radiation Therapy Using the Genomically Adjusted Radiation Dose. *J Thorac Oncol* (2018) 13(8):1121–7. doi: 10.1016/j.jtho.2018.04.027
93. Rieckmann T, Tribius S, Grob TJ, Meyer F, Busch C-J, Petersen C, et al. HNSCC Cell Lines Positive for HPV and P16 Possess Higher Cellular Radiosensitivity Due to an Impaired DSB Repair Capacity. *Radiotherapy Oncol* (2013) 107(2):242–6. doi: 10.1016/j.radonc.2013.03.013
94. Kimple RJ, Smith MA, Blitzer GC, Torres AD, Martin JA, Yang RZ, et al. Enhanced Radiation Sensitivity in HPV-Positive Head and Neck Cancer. *Cancer Res* (2013) 73(15):4791–800. doi: 10.1158/0008-5472.CAN-13-0587
95. Tinhofer I, Stenzinger A, Eder T, Konschak R, Niehr F, Endris V, et al. Targeted Next-Generation Sequencing Identifies Molecular Subgroups in Squamous Cell Carcinoma of the Head and Neck With Distinct Outcome After Concurrent Chemoradiation. *Ann Oncol* (2016) 27(12):2262–8. doi: 10.1093/annonc/mdw426
96. Northcott PA, Korshunov A, Witt H, Hielscher T, Eberhart CG, Mack S, et al. Medulloblastoma Comprises Four Distinct Molecular Variants. *J Clin Oncol* (2011) 29(11):1408. doi: 10.1200/JCO.2009.27.4324
97. Michalski JM, Janss AJ, Vezina LG, Smith KS, Billups CA, Burger PC, et al. Children's Oncology Group Phase III Trial of Reduced-Dose and Reduced-Volume Radiotherapy With Chemotherapy for Newly Diagnosed Average-Risk Medulloblastoma. *J Clin Oncol* (2021) 39(24):2685–97. doi: 10.1200/JCO.20.02730
98. Kerns SL, Ostrer H, Rosenstein BS. Radiogenomics: Using Genetics to Identify Cancer Patients at Risk for Development of Adverse Effects Following Radiotherapy. *Cancer Discov* (2014) 4(2):155–65. doi: 10.1158/2159-8290.CD-13-0197
99. Kerns SL, Stock R, Stone N, Buckstein M, Shao Y, Campbell C, et al. A 2-Stage Genome-Wide Association Study to Identify Single Nucleotide Polymorphisms Associated With Development of Erectile Dysfunction Following Radiation Therapy for Prostate Cancer. *Int J Radiat Oncol Biol Phys* (2013) 85(1):e21–e8. doi: 10.1016/j.ijrobp.2012.08.003
100. Kerns SL, Stone NN, Stock RG, Rath L, Ostrer H, Rosenstein BS. A 2-Stage Genome-Wide Association Study to Identify Single Nucleotide Polymorphisms Associated With Development of Urinary Symptoms After Radiotherapy for Prostate Cancer. *J Urol* (2013) 190(1):102–8. doi: 10.1016/j.juro.2013.01.096
101. Barnett GC, Thompson D, Fachal L, Kerns S, Talbot C, Elliott RM, et al. A Genome Wide Association Study (GWAS) Providing Evidence of an Association Between Common Genetic Variants and Late Radiotherapy Toxicity. *Radiotherapy Oncol* (2014) 111(2):178–85. doi: 10.1016/j.radonc.2014.02.012
102. West C, Azria D, Chang-Claude J, Davidson S, Lambin P, Rosenstein B, et al. The REQUITE Project: Validating Predictive Models and Biomarkers of Radiotherapy Toxicity to Reduce Side-Effects and Improve Quality of Life in Cancer Survivors. *Clin Oncol* (2014) 26(12):739–42. doi: 10.1016/j.clon.2014.09.008
103. Kerns SL, Fachal L, Dorling L, Barnett GC, Baran A, Peterson DR, et al. Radiogenomics Consortium Genome-Wide Association Study Meta-Analysis of Late Toxicity After Prostate Cancer Radiotherapy. *JNCI: J Natl Cancer Institute* (2020) 112(2):179–90. doi: 10.1093/jnci/djz075
104. Ahmad SS, Crittenden MR, Tran PT, Kluetz PG, Blumenthal GM, Bulbeck H, et al. Clinical Development of Novel Drug–Radiotherapy Combinations. *Clin Cancer Res* (2019) 25(5):1455–61. doi: 10.1158/1078-0432.CCR-18-2466
105. Sharma RA, Plummer R, Stock JK, Greenhalgh TA, Ataman O, Kelly S, et al. Clinical Development of New Drug–Radiotherapy Combinations. *Nat Rev Clin Oncol* (2016) 13(10):627. doi: 10.1038/nrclinonc.2016.79
106. Hall WA, Bergom C, Thompson RF, Baschnagel AM, Vijayakumar S, Willers H, et al. Precision Oncology and Genomically Guided Radiation Therapy: A Report From the American Society for Radiation Oncology/American Association of Physicists in Medicine/National Cancer Institute Precision Medicine Conference. *Int J Radiat Oncol Biol Phys* (2018) 101(2):274–84. doi: 10.1016/j.ijrobp.2017.05.044
107. Pilié PG, Tang C, Mills GB, Yap TA. State-Of-the-Art Strategies for Targeting the DNA Damage Response in Cancer. *Nat Rev Clin Oncol* (2019) 16(2):81–104. doi: 10.1038/s41571-018-0114-z
108. Samstein RM, Riaz N. The DNA Damage Response in Immunotherapy and Radiation. *Adv Radiat Oncol* (2018) 3(4):527–33. doi: 10.1016/j.adro.2018.08.017
109. Topatana W, Juengpanich S, Li S, Cao J, Hu J, Lee J, et al. Advances in Synthetic Lethality for Cancer Therapy: Cellular Mechanism and Clinical Translation. *J Hematol Oncol* (2020) 13(1):1–22. doi: 10.1186/s13045-020-00956-5
110. Morgan MA, Lawrence TS. Molecular Pathways: Overcoming Radiation Resistance by Targeting DNA Damage Response Pathways. *Clin Cancer Res* (2015) 21(13):2898–904. doi: 10.1158/1078-0432.CCR-13-3229
111. Wéra A-C, Lobbens A, Stoyanov M, Lucas S, Michiels C. Radiation-Induced Synthetic Lethality: Combination of Poly (ADP-Ribose) Polymerase and RAD51 Inhibitors to Sensitize Cells to Proton Irradiation. *Cell Cycle* (2019) 18(15):1770–83. doi: 10.1080/15384101.2019.1632640
112. Lesueur P, Chevalier F, Austry J-B, Waissi W, Burckel H, Noël G, et al. Poly-(ADP-Ribose)-Polymerase Inhibitors as Radiosensitizers: A Systematic Review of Pre-Clinical and Clinical Human Studies. *Oncotarget* (2017) 8 (40):69105. doi: 10.18632/oncotarget.19079
113. Karnak D, Engelke CG, Parsels LA, Kausar T, Wei D, Robertson JR, et al. Combined Inhibition of Wee1 and PARP1/2 for Radiosensitization in Pancreatic Cancer. *Clin Cancer Res* (2014) 20(19):5085–96. doi: 10.1158/1078-0432.CCR-14-1038
114. Kausar T, Schreiber JS, Karnak D, Parsels LA, Parsels JD, Davis MA, et al. Sensitization of Pancreatic Cancers to Gemcitabine Chemoradiation by WEE1 Kinase Inhibition Depends on Homologous Recombination Repair. *Neoplasia* (2015) 17(10):757–66. doi: 10.1016/j.neo.2015.09.006
115. Cuneo KC, Morgan MA, Davis MA, Parcels LA, Parcels J, Karnak D, et al. Wee1 Kinase Inhibitor AZD1775 Radiosensitizes Hepatocellular Carcinoma Regardless of TP53 Mutational Status Through Induction of Replication Stress. *Int J Radiat Oncol Biol Phys* (2016) 95(2):782–90. doi: 10.1016/j.ijrobp.2016.01.028
116. Al Zubaidi T, Gehrisch OF, Genois M-M, Liu Q, Lu S, Kung J, et al. Targeting the DNA Replication Stress Phenotype of KRAS Mutant Cancer Cells. *Sci Rep* (2021) 11(1):1–12. doi: 10.1038/s41598-021-83142-y

117. Ubhi T, Brown GW. Exploiting DNA Replication Stress for Cancer Treatment. *Cancer Res* (2019) 79(8):1730–9. doi: 10.1158/0008-5472.CAN-18-3631
118. Parsels LA, Karnak D, Parsels JD, Zhang Q, Vélez-Padilla J, Reichert ZR, et al. PARP1 Trapping and DNA Replication Stress Enhance Radiosensitization With Combined WEE1 and PARP Inhibitors. *Mol Cancer Res* (2018) 16(2):222–32. doi: 10.1158/1541-7786.MCR-17-0455
119. Bentzen SM, Harari PM, Bernier J. Exploitable Mechanisms for Combining Drugs With Radiation: Concepts, Achievements and Future Directions. *Nat Clin Pract Oncol* (2007) 4(3):172–80. doi: 10.1038/ncponc0744
120. Jagodinsky JC, Harari PM, Morris ZS. The Promise of Combining Radiation Therapy With Immunotherapy. *Int J Radiat Oncol Biol Phys* (2020) 108 (1):6–16. doi: 10.1016/j.ijrobp.2020.04.023
121. Golden EB, Frances D, Pellicciotta I, Demaria S, Helen Barcellos-Hoff M, Formenti SC. Radiation Fosters Dose-Dependent and Chemotherapy-Induced Immunogenic Cell Death. *Oncoimmunology* (2014) 3(4):e28518. doi: 10.4161/onci.28518
122. Ngwa W, Irabor OC, Schoenfeld JD, Hesser J, Demaria S, Formenti SC. Using Immunotherapy to Boost the Abscopal Effect. *Nat Rev Cancer* (2018) 18(5):313–22. doi: 10.1038/nrc.2018.6
123. Twyman-Saint Victor C, Rech AJ, Maity A, Rengan R, Pauken KE, Stelekati E, et al. Radiation and Dual Checkpoint Blockade Activate Non-Redundant Immune Mechanisms in Cancer. *Nature* (2015) 520(7547):373–7. doi: 10.1038/nature14292
124. Stamell EF, Wolchok JD, Gnjatic S, Lee NY, Brownell I. The Abscopal Effect Associated With a Systemic Anti-Melanoma Immune Response. *Int J Radiat Oncol Biol Phys* (2013) 85(2):293–5. doi: 10.1016/j.ijrobp.2012.03.017
125. Postow MA, Callahan MK, Barker CA, Yamada Y, Yuan J, Kitano S, et al. Immunologic Correlates of the Abscopal Effect in a Patient With Melanoma. *New Engl J Med* (2012) 366(10):925–31. doi: 10.1056/NEJMoa1112824
126. Golden EB, Demaria S, Schiff PB, Chachoua A, Formenti SC. An Abscopal Response to Radiation and Ipilimumab in a Patient With Metastatic Non–Small Cell Lung Cancer. *Cancer Immunol Res* (2013) 1(6):365–72. doi: 10.1158/2326-6066.CIR-13-0115
127. Golden EB, Chhabra A, Chachoua A, Adams S, Donach M, Fenton-Kerimian M, et al. Local Radiotherapy and Granulocyte-Macrophage Colony-Stimulating Factor to Generate Abscopal Responses in Patients With Metastatic Solid Tumours: A Proof-of-Principle Trial. *Lancet Oncol* (2015) 16(7):795–803. doi: 10.1016/S1470-2045(15)00054-6
128. Merrick A, Errington F, Milward K, O'Donnell D, Harrington K, Bateman A, et al. Immunosuppressive Effects of Radiation on Human Dendritic Cells: Reduced IL-12 Production on Activation and Impairment of Naive T-Cell Priming. *Br J Cancer* (2005) 92(8):1450–8. doi: 10.1038/sj.bjc.6602518
129. Chiang C-S, Fu S-Y, Wang S-C, Yu C-F, Chen F-H, Lin C-M, et al. Irradiation Promotes an M2 Macrophage Phenotype in Tumor Hypoxia. *Front Oncol* (2012) 2:89. doi: 10.3389/fonc.2012.00089
130. Quon H, McNutt T, Lee J, Bowers M, Jiang W, Lakshminarayanan P, et al. Needs and Challenges for Radiation Oncology in the Era of Precision Medicine. *Int J Radiat Oncol Biol Phys* (2019) 103(4):809–17. doi: 10.1016/j.ijrobp.2018.11.017
131. Baumann M, Krause M, Overgaard J, Debus J, Bentzen SM, Daartz J, et al. Radiation Oncology in the Era of Precision Medicine. *Nat Rev Cancer* (2016) 16(4):234. doi: 10.1038/nrc.2016.18
132. Caston RA, Shah F, Starcher CL, Wireman R, Babb O, Grimard M, et al. Combined Inhibition of Ref-1 and STAT3 Leads to Synergistic Tumour Inhibition in Multiple Cancers Using 3D and *In Vivo* Tumour Co-Culture Models. *J Cell Mol Med* (2020) 25(2):784–800. doi: 10.1111/jcmm.16132
133. Fishel ML, Xia H, McGeown J, McIlwain DW, Elbanna M, Craft AA, et al. Antitumor Activity and Mechanistic Characterization of APE1/Ref-1 Inhibitors in Bladder Cancer. *Mol Cancer Ther* (2019) 18(11):1947–60. doi: 10.1158/1535-7163.MCT-18-1166
134. Prabhu L, Wei H, Chen L, Demir O, Sandusky G, Sun E, et al. Adapting AlphaLISA High Throughput Screen to Discover a Novel Small-Molecule Inhibitor Targeting Protein Arginine Methyltransferase 5 in Pancreatic and Colorectal Cancers. *Oncotarget* (2017) 8(25):39963–77. doi: 10.18632/oncotarget.18102
135. Logsdon DP, Shah F, Carta F, Supuran CT, Kamocka M, Jacobsen MH, et al. Blocking HIF Signaling *via* Novel Inhibitors of CA9 and APE1/Ref-1 Dramatically Affects Pancreatic Cancer Cell Survival. *Sci Rep* (2018) 8 (1):13759. doi: 10.1038/s41598-018-32034-9
136. Logsdon DP, Grimard M, Luo M, Shahda S, Jiang Y, Tong Y, et al. Regulation of HIF1alpha Under Hypoxia by APE1/Ref-1 Impacts CA9 Expression: Dual Targeting in Patient-Derived 3d Pancreatic Cancer Models. *Mol Cancer Ther* (2016) 15(11):2722–32. doi: 10.1158/1535-7163.MCT-16-0253
137. Selby M, Delosh R, Laudeman J, Ogle C, Reinhart R, Silvers T, et al. 3d Models of the NCI60 Cell Lines for Screening Oncology Compounds. *SLAS Discovery* (2017) 22(5):473–83. doi: 10.1177/2472555217697434
138. Chen O, Michlíková S, Eckhardt L, Wondrak M, De Mendoza AM, Krause M, et al. Efficient Heat Shock Response Affects Hyperthermia-Induced Radiosensitization in a Tumor Spheroid Control Probability Assay. *Cancers (Basel)* (2021) 13(13):3168. doi: 10.3390/cancers13133168
139. Jiang Y, Verbiest T, Devery AM, Bokobza SM, Weber AM, Leszczynska KB, et al. Hypoxia Potentiates the Radiation-Sensitizing Effect of Olaparib in Human Non-Small Cell Lung Cancer Xenografts by Contextual Synthetic Lethality. *Int J Radiat Oncol Biol Phys* (2016) 95(2):772–81. doi: 10.1016/j.ijrobp.2016.01.035
140. Lafontaine J, Boisvert J-S, Glory A, Coulombe S, Wong P. Synergy Between Non-Thermal Plasma With Radiation Therapy and Olaparib in a Panel of Breast Cancer Cell Lines. *Cancers* (2020) 12(2):348. doi: 10.3390/cancers12020348
141. Saha S, Howarth R, Pappworth I, Marchbank K, Curtin N. Potential Use of the PARP Inhibitor Rucaparib to Enhance Cervical Cancer Treatment. *Eur J Cancer* (2020) 138:S37. doi: 10.1016/S0959-8049(20)31169-2
142. Chatterjee P, Choudhary GS, Sharma A, Singh K, Heston WD, Ciezki J, et al. PARP Inhibition Sensitizes to Low Dose-Rate Radiation TMPRSS2-ERG Fusion Gene-Expressing and PTEN-Deficient Prostate Cancer Cells. *PloS One* (2013) 8(4):e60408. doi: 10.1371/journal.pone.0060408
143. Nile DL, Rae C, Hyndman IJ, Gaze MN, Mairs RJ. An Evaluation *In Vitro* of PARP-1 Inhibitors, Rucaparib and Olaparib, as Radiosensitisers for the Treatment of Neuroblastoma. *BMC Cancer* (2016) 16(1):1–13. doi: 10.1186/s12885-016-2656-8
144. McDaniel NK, Iida M, Nickel KP, Longhurst CA, Fischbach SR, Rodems TS, et al. AXL Mediates Cetuximab and Radiation Resistance Through Tyrosine 821 and the C-ABL Kinase Pathway in Head and Neck Cancer. *Clin Cancer Res* (2020) 26(16):4349–59. doi: 10.1158/1078-0432.CCR-19-3142
145. Zeng L, Beggs RR, Cooper TS, Weaver AN, Yang ES. Combining Chk1/2 Inhibition With Cetuximab and Radiation Enhances *In Vitro* and *In Vivo* Cytotoxicity in Head and Neck Squamous Cell Carcinoma. *Mol Cancer Ther* (2017) 16(4):591–600. doi: 10.1158/1535-7163.MCT-16-0352
146. Boysen G, Jamshidi-Parsian A, Davis MA, Siegel ER, Simecka CM, Kore RA, et al. Glutaminase Inhibitor CB-839 Increases Radiation Sensitivity of Lung Tumor Cells and Human Lung Tumor Xenografts in Mice. *Int J Radiat Biol* (2019) 95(4):436–42. doi: 10.1080/09553002.2018.1558299
147. Wicker CA, Hunt BG, Krishnan S, Aziz K, Parajuli S, Palackdharry S, et al. Glutaminase Inhibition With Telaglenastat (CB-839) Improves Treatment Response in Combination With Ionizing Radiation in Head and Neck Squamous Cell Carcinoma Models. *Cancer Lett* (2021) 502:180–8. doi: 10.1016/j.canlet.2020.12.038
148. Xu P, Huang J-M, Ren Y, Zha X, Deng B-F, Wu J-H, et al. Regulation of Hypoxia-Induced mRNA Expressions of HIF-1alpha and Osteopontin and *In Vitro* Radiosensitization by Tirapazamine in Human Nasopharyngeal Carcinoma HNE-1 and CNE-1 Cells. *Chin J Cancer* (2010) 29(2):126–30. doi: 10.5732/cjc.009.10500
149. Liu Y, Liu Y, Bu W, Xiao Q, Sun Y, Zhao K, et al. Radiation-/Hypoxia-Induced Solid Tumor Metastasis and Regrowth Inhibited by Hypoxia-Specific Upconversion Nanoradiosensitizer. *Biomaterials* (2015) 49:1–8. doi: 10.1016/j.biomaterials.2015.01.028
150. Chen Y, Li W-W, Peng P, Zhao W-H, Tian Y-J, Huang Y, et al. Mtorc1 Inhibitor RAD001 (Everolimus) Enhances Non-Small Cell Lung Cancer Cell Radiosensitivity *In Vitro via* Suppressing Epithelial–Mesenchymal Transition. *Acta Pharmacologica Sin* (2019) 40(8):1085–94. doi: 10.1038/s41401-019-0215-y
151. Chaumeil MM, Ozawa T, Park I, Scott K, James CD, Nelson SJ, et al. Hyperpolarized 13c MR Spectroscopic Imaging can be Used to Monitor Everolimus Treatment *In Vivo* in an Orthotopic Rodent Model of Glioblastoma. *Neuroimage* (2012) 59(1):193–201. doi: 10.1016/j.neuroimage.2011.07.034

152. Sørensen BS, Busk M, Olthof N, Speel E-J, Horsman MR, Alsner J, et al. Radiosensitivity and Effect of Hypoxia in HPV Positive Head and Neck Cancer Cells. *Radiotherapy Oncol* (2013) 108(3):500–5. doi: 10.1016/j.radonc.2013.06.011
153. Tao Z, Le Blanc JM, Wang C, Zhan T, Zhuang H, Wang P, et al. Coadministration of Trametinib and Palbociclib Radiosensitizes KRAS-Mutant Non–Small Cell Lung Cancers *In Vitro* and *In Vivo*. *Clin Cancer Res* (2016) 22(1):122–33. doi: 10.1158/1078-0432.CCR-15-0589
154. Schick U, Kyula J, Barker H, Patel R, Zaidi S, Gregory C, et al. Trametinib Radiosensitises RAS-And BRAF-Mutated Melanoma by Perturbing Cell Cycle and Inducing Senescence. *Radiotherapy Oncol* (2015) 117(2):364–75. doi: 10.1016/j.radonc.2015.06.026
155. Yang L, Shen C, Pettit CJ, Li T, Hu AJ, Miller ED, et al. Wee1 Kinase Inhibitor AZD1775 Effectively Sensitizes Esophageal Cancer to Radiotherapy. *Clin Cancer Res* (2020) 26(14):3740–50. doi: 10.1158/1078-0432.CCR-19-3373
156. Haines E, Nishida Y, Carr MI, Montoya RH, Ostermann LB, Zhang W, et al. DNA-PK Inhibitor Peposertib Enhances P53-Dependent Cytotoxicity of DNA Double-Strand Break Inducing Therapy in Acute Leukemia. *Sci Rep* (2021) 11(1):1–14. doi: 10.1038/s41598-021-90500-3
157. Zenke FT, Zimmermann A, Sirrenberg C, Dahmen H, Kirkin V, Pehl U, et al. Pharmacologic Inhibitor of DNA-PK, M3814, Potentiates Radiotherapy and Regresses Human Tumors in Mouse Models. *Mol Cancer Ther* (2020) 19(5):1091–101. doi: 10.1158/1535-7163.MCT-19-0734
158. Zhao J, Liu P, Ma J, Li D, Yang H, Chen W, et al. Enhancement of Radiosensitization by Silver Nanoparticles Functionalized With Polyethylene Glycol and Aptamer As1411 for Glioma Irradiation Therapy. *Int J nanomedicine* (2019) 14:9483. doi: 10.2147/IJN.S224160
159. Habiba K, Aziz K, Sanders K, Santiago CM, Mahadevan LSK, Makarov V, et al. Enhancing Colorectal Cancer Radiation Therapy Efficacy Using Silver Nanoprisms Decorated With Graphene as Radiosensitizers. *Sci Rep* (2019) 9(1):1–9. doi: 10.1038/s41598-019-53706-0
160. Cala PG, Chambrier I, Cook MJ, Haines AH, Field RA, Russell DA. Targeted Photodynamic Therapy of Breast Cancer Cells Using Lactose-Phthalocyanine Functionalized Gold Nanoparticles. *J colloid Interface Sci* (2018) 512:249–59. doi: 10.1016/j.jcis.2017.10.030
161. Rajaee A, Wang S, Zhao L, Wang D, Liu Y, Wang J, et al. Multifunction Bismuth Gadolinium Oxide Nanoparticles as Radiosensitizer in Radiation Therapy and Imaging. *Phys Med Biol* (2019) 64(19):195007. doi: 10.1088/1361-6560/ab2154
162. Jonuscheit S, Jost T, Gajdošová F, Wrobel M, Hecht M, Fietkau R, et al. PARP Inhibitors Talazoparib and Niraparib Sensitize Melanoma Cells to Ionizing Radiation. *Genes* (2021) 12(6):849. doi: 10.3390/genes12060849
163. Loap P, Loirat D, Berger F, Ricci F, Vincent-Salomon A, Ezzili C, et al. Combination of Olaparib and Radiation Therapy for Triple Negative Breast Cancer: Preliminary Results of the RADIOPARP Phase 1 Trial. *Int J Radiat Oncol Biol Phys* (2021) 109(2):436–40. doi: 10.1016/j.ijrobp.2020.09.032
164. Malfatti MC, Antoniali G, Codrich M, Burra S, Mangiapane G, Dalla E, et al. New Perspectives in Cancer Biology From a Study of Canonical and Non-Canonical Functions of Base Excision Repair Proteins With a Focus on Early Steps. *Mutagenesis* (2019) 35(1):129–49. doi: 10.1093/mutage/gez051
165. Shah F, Logsdon D, Messmann RA, Fehrenbacher JC, Fishel ML, Kelley MR. Exploiting the Ref-1-APE1 Node in Cancer Signaling and Other Diseases: From Bench to Clinic. *NPJ Precis Oncol* (2017) 1:19. doi: 10.1038/s41698-017-0023-0
166. Caston RA, Gampala S, Armstrong L, Messmann RA, Fishel ML, Kelley MR. The Multifunctional APE1 DNA Repair-Redox Signaling Protein as a Drug Target in Human Disease. *Drug Discov Today* (2021) 26(1):218–28. doi: 10.1016/j.drudis.2020.10.015
167. Parsons JL, Dianova II, Dianov GL. APE1 Is the Major 3'-Phosphoglycolate Activity in Human Cell Extracts. *Nucleic Acids Res* (2004) 32(12):3531–6. doi: 10.1093/nar/gkh676
168. Kievit FM, Wang K, Ozawa T, Tarudji AW, Silber JR, Holland EC, et al. Nanoparticle-Mediated Knockdown of DNA Repair Sensitizes Cells to Radiotherapy and Extends Survival in a Genetic Mouse Model of Glioblastoma. *Nanomedicine* (2017) 13(7):2131–9. doi: 10.1016/j.nano.2017.06.004
169. Liu Z, Yan H, Li H. Silencing of DNA Repair Sensitizes Pediatric Brain Tumor Cells to Gamma-Irradiation Using Gold Nanoparticles. *Environ Toxicol Pharmacol* (2017) 53:40–5. doi: 10.1016/j.etap.2017.04.017
170. Gampala S, Shah F, Lu X, Moon H, Sandusky G, Hulsey E, et al. Ref-1 Redox Activity Alters Cancer Cell Metabolism in Pancreatic Cancer: Exploiting This Novel Finding as a Potential Target. *J Exp Clin Can Res* (2021) 40(1):251. doi: 10.21203/rs.3.rs-125304/v1
171. Bignon E, Gattuso H, Morell C, Dehez F, Georgakilas AG, Monari A, et al. Correlation of Bistranded Clustered Abasic DNA Lesion Processing With Structural and Dynamic DNA Helix Distortion. *Nucleic Acids Res* (2016) 44(18):8588–99. doi: 10.1093/nar/gkw773
172. Vascotto C, Fantini D, Romanello M, Cesaratto L, Deganuto M, Leonardi A, et al. APE1/Ref-1 Interacts With NPM1 Within Nucleoli and Plays a Role in the rRNA Quality Control Process. *Mol Cell Biol* (2009) 29(7):1834–54. doi: 10.1128/MCB.01337-08
173. Poletto M, Malfatti MC, Dorjsuren D, Scognamiglio PL, Marasco D, Vascotto C, et al. Inhibitors of the Apurinic/Apyrimidinic Endonuclease 1 (APE1)/nucleophosmin (NPM1) Interaction That Display Anti-Tumor Properties. *Mol Carcinog* (2016) 55(5):688–704. doi: 10.1002/mc.22313
174. Traver G, Sekhar KR, Crooks PA, Keeney DS, Freeman ML. Targeting NPM1 in Irradiated Cells Inhibits NPM1 Binding to RAD51, RAD51 Foci Formation and Radiosensitizes NSCLC. *Cancer Lett* (2021) 500:220–7. doi: 10.1016/j.canlet.2020.12.023
175. Kelley MR, Georgiadis MM, Fishel ML. APE1/Ref-1Role in Redox Signaling: Translational Applications of Targeting the Redox Function of the DNA Repair/Redox Protein APE1/Ref-1. *Curr Mol Pharmacol* (2012) 5(1):36–53. doi: 10.2174/1874467211205010036
176. Hawkes HJ, Karlenius TC, Tonissen KF. Regulation of the Human Thioredoxin Gene Promoter and Its Key Substrates: A Study of Functional and Putative Regulatory Elements. *Biochim Biophys Acta* (2014) 1840(1):303–14. doi: 10.1016/j.bbagen.2013.09.013
177. Tell G, Damante G, Caldwell D, Kelley MR. The Intracellular Localization of APE1/Ref-1: More Than a Passive Phenomenon? *Antioxid Redox Signal* (2005) 7(3-4):367–84. doi: 10.1089/ars.2005.7.367
178. Kelley MR, Wikel JH, Guo C, Pollok KE, Bailey BJ, Wireman R, et al. Identification and Characterization of New Chemical Entities Targeting Apurinic/Apyrimidinic Endonuclease 1 for the Prevention of Chemotherapy-Induced Peripheral Neuropathy. *J Pharmacol Exp Ther* (2016) 359(2):300–9. doi: 10.1124/jpet.116.235283
179. Vasko MR, Guo C, Thompson EL, Kelley MR. The Repair Function of the Multifunctional DNA Repair/Redox Protein APE1 Is Neuroprotective After Ionizing Radiation. *DNA Repair (Amst)* (2011) 10(9):942–52. doi: 10.1016/j.dnarep.2011.06.004
180. Galeaz C, Totis C, Bisio A. Radiation Resistance: A Matter of Transcription Factors. *Front Oncol* (2021) 662840. doi: 10.3389/fonc.2021.662840
181. Wang X, Zhang X, Qiu C, Yang N. STAT3 Contributes to Radioresistance in Cancer. *Front Oncol* (2020) 10:1120. doi: 10.3389/fonc.2020.01120
182. Mortezaee K, Najafi M, Farhood B, Ahmadi A, Shabeeb D, Musa AE. NF-kappaB Targeting for Overcoming Tumor Resistance and Normal Tissues Toxicity. *J Cell Physiol* (2019) 234(10):17187–204. doi: 10.1002/jcp.28504
183. Pordanjani SM, Hosseinimehr SJ. The Role of NF-kB Inhibitors in Cell Response to Radiation. *Curr Med Chem* (2016) 23(34):3951–63. doi: 10.2174/0929867323666160824162718
184. Yi H, Yan X, Luo Q, Yuan L, Li B, Pan W, et al. A Novel Small Molecule Inhibitor of MDM2-P53 (APG-115) Enhances Radiosensitivity of Gastric Adenocarcinoma. *J Exp Clin Cancer Res* (2018) 37(1):1–10. doi: 10.1186/s13046-018-0765-8
185. Feng FY, Zhang Y, Kothari V, Evans JR, Jackson WC, Chen W, et al. MDM2 Inhibition Sensitizes Prostate Cancer Cells to Androgen Ablation and Radiotherapy in a P53-Dependent Manner. *Neoplasia* (2016) 18(4):213–22. doi: 10.1016/j.neo.2016.01.006
186. Werner LR, Huang S, Francis DM, Armstrong EA, Ma F, Li C, et al. Small Molecule Inhibition of MDM2–p53 Interaction Augments Radiation Response in Human Tumors. *Mol Cancer Ther* (2015) 14(9):1994–2003. doi: 10.1158/1535-7163.MCT-14-1056-T
187. Phelps D, Bondra K, Seum S, Chronowski C, Leasure J, Kurmasheva RT, et al. Inhibition of MDM2 by RG7388 Confers Hypersensitivity to X-

Radiation in Xenograft Models of Childhood Sarcoma. *Pediatr Blood Cancer* (2015) 62(8):1345–52. doi: 10.1002/pbc.25465
188. Rew Y, Sun D. Discovery of a Small Molecule MDM2 Inhibitor (AMG 232) for Treating Cancer. *J medicinal Chem* (2014) 57(15):6332–41. doi: 10.1021/jm500627s
189. Bonner JA, Harari PM, Giralt J, Azarnia N, Shin DM, Cohen RB, et al. Radiotherapy Plus Cetuximab for Squamous-Cell Carcinoma of the Head and Neck. *New Engl J Med* (2006) 354(6):567–78. doi: 10.1056/NEJMoa053422
190. Nieder C, Pawinski A, Dalhaug A, Andratschke N. A Review of Clinical Trials of Cetuximab Combined With Radiotherapy for Non-Small Cell Lung Cancer. *Radiat Oncol* (2012) 7(1):1–7. doi: 10.1186/1748-717X-7-3
191. Toulany M. Targeting DNA Double-Strand Break Repair Pathways to Improve Radiotherapy Response. *Genes* (2019) 10(1):25. doi: 10.3390/genes10010025
192. Das AK, Chen BP, Story MD, Sato M, Minna JD, Chen DJ, et al. Somatic Mutations in the Tyrosine Kinase Domain of Epidermal Growth Factor Receptor (EGFR) Abrogate EGFR-Mediated Radioprotection in Non–Small Cell Lung Carcinoma. *Cancer Res* (2007) 67(11):5267–74. doi: 10.1158/0008-5472.CAN-07-0242
193. Huang S-M, Bock JM, Harari PM. Epidermal Growth Factor Receptor Blockade With C225 Modulates Proliferation, Apoptosis, and Radiosensitivity in Squamous Cell Carcinomas of the Head and Neck. *Cancer Res* (1999) 59(8):1935–40.
194. Pfäffle HN, Wang M, Gheorghiu L, Ferraiolo N, Greninger P, Borgmann K, et al. EGFR-Activating Mutations Correlate With a Fanconi Anemia–like Cellular Phenotype That Includes PARP Inhibitor Sensitivity. *Cancer Res* (2013) 73(20):6254–63. doi: 10.1158/0008-5472.CAN-13-0044
195. Johung KL, Yao X, Li F, James BY, Gettinger SN, Goldberg S, et al. A Clinical Model for Identifying Radiosensitive Tumor Genotypes in Non–Small Cell Lung Cancer. *Clin Cancer Res* (2013) 19(19):5523–32. doi: 10.1158/1078-0432.CCR-13-0836
196. Braunstein LZ, Taghian AG, Niemierko A, Salama L, Capuco A, Bellon JR, et al. Breast-Cancer Subtype, Age, and Lymph Node Status as Predictors of Local Recurrence Following Breast-Conserving Therapy. *Breast Cancer Res Treat* (2017) 161(1):173–9. doi: 10.1007/s10549-016-4031-5
197. Liang K, Lu Y, Jin W, Ang KK, Milas L, Fan Z. Sensitization of Breast Cancer Cells to Radiation by Trastuzumab. *Mol Cancer Ther* (2003) 2(11):1113–20.
198. Abi Jaoude J, de Azambuja E, Makki M, Tamim H, Tfayli A, Geara F, et al. Post-Mastectomy Radiation Therapy in Human Epidermal Growth Factor Receptor 2 Positive Breast Cancer Patients: Analysis of the HERA Trial. *Int J Radiat Oncol Biol Phys* (2020) 106(3):503–10. doi: 10.1016/j.ijrobp.2019.10.022
199. Wolff RF, Ryder S, Bossi A, Briganti A, Crook J, Henry A, et al. A Systematic Review of Randomised Controlled Trials of Radiotherapy for Localised Prostate Cancer. *Eur J Cancer* (2015) 51(16):2345–67. doi: 10.1016/j.ejca.2015.07.019
200. Messing EM, Manola J, Yao J, Kiernan M, Crawford D, Wilding G, et al. Immediate *Versus* Deferred Androgen Deprivation Treatment in Patients With Node-Positive Prostate Cancer After Radical Prostatectomy and Pelvic Lymphadenectomy. *Lancet Oncol* (2006) 7(6):472–9. doi: 10.1016/S1470-2045(06)70700-8
201. Milosevic M, Chung P, Parker C, Bristow R, Toi A, Panzarella T, et al. Androgen Withdrawal in Patients Reduces Prostate Cancer Hypoxia: Implications for Disease Progression and Radiation Response. *Cancer Res* (2007) 67(13):6022–5. doi: 10.1158/0008-5472.CAN-07-0561
202. Wo JY, Zietman AL. Why does androgen deprivation enhance the results of radiation therapy? *Urol Oncol* (2008) 26(5):522–9. doi: 10.1016/j.urolonc.2008.03.008
203. Polkinghorn WR, Parker JS, Lee MX, Kass EM, Spratt DE, Iaquinta PJ, et al. Androgen Receptor Signaling Regulates DNA Repair in Prostate Cancers. *Cancer Discov* (2013) 3(11):1245–53. doi: 10.1158/2159-8290.CD-13-0172
204. Zumsteg ZS, Morse N, Krigsfeld G, Gupta G, Higginson DS, Lee NY, et al. Taselisib (GDC-0032), a Potent β-Sparing Small Molecule Inhibitor of PI3K, Radiosensitizes Head and Neck Squamous Carcinomas Containing Activating PIK3CA Alterations. *Clin Cancer Res* (2016) 22(8):2009–19. doi: 10.1158/1078-0432.CCR-15-2245
205. Chinnaiyan P, Vallabhaneni G, Armstrong E, Huang S-M, Harari PM. Modulation of Radiation Response by Histone Deacetylase Inhibition. *Int J Radiat Oncol Biol Phys* (2005) 62(1):223–9. doi: 10.1016/j.ijrobp.2004.12.088
206. Gampala S, Shah F, Lu X, Moon H-R, Sandusky G, Hulsey E, et al. Ref-1 Redox Activity Alters Cancer Cell Metabolism in Pancreatic Cancer: Exploiting This Novel Finding as a Potential Target. (2020) 40(1):251. doi: 10.21203/rs.3.rs-125304/v1
207. Zhao Y, Feng X, Chen Y, Selfridge JE, Gorityala S, Du Z, et al. 5-Fluorouracil Enhances the Antitumor Activity of the Glutaminase Inhibitor CB-839 Against PIK3CA-Mutant Colorectal Cancers. *Cancer Res* (2020) 80 (21):4815–27. doi: 10.1158/0008-5472.CAN-20-0600
208. Momcilovic M, Bailey ST, Lee JT, Fishbein MC, Magyar C, Braas D, et al. Targeted Inhibition of EGFR and Glutaminase Induces Metabolic Crisis in EGFR Mutant Lung Cancer. *Cell Rep* (2017) 18(3):601–10. doi: 10.1016/j.celrep.2016.12.061
209. Gray LH, Conger AD, Ebert M, Hornsey S, Scott O. The Concentration of Oxygen Dissolved in Tissues at the Time of Irradiation as a Factor in Radiotherapy. *Br J Radiol* (1953) 26(312):638–48. doi: 10.1259/0007-1285-26-312-638
210. Overgaard J. Hypoxic Modification of Radiotherapy in Squamous Cell Carcinoma of the Head and Neck–A Systematic Review and Meta-Analysis. *Radiotherapy Oncol* (2011) 100(1):22–32. doi: 10.1016/j.radonc.2011.03.004
211. Bentzen J, Toustrup K, Eriksen JG, Primdahl H, Andersen LJ, Overgaard J. Locally Advanced Head and Neck Cancer Treated With Accelerated Radiotherapy, the Hypoxic Modifier Nimorazole and Weekly Cisplatin. Results From the DAHANCA 18 Phase II Study. *Acta Oncol* (2015) 54 (7):1001–7. doi: 10.3109/0284186X.2014.992547
212. Mistry IN, Thomas M, Calder ED, Conway SJ, Hammond EM. Clinical Advances of Hypoxia-Activated Prodrugs in Combination With Radiation Therapy. *Int J Radiat Oncol Biol Phys* (2017) 98(5):1183–96. doi: 10.1016/j.ijrobp.2017.03.024
213. Fokas E, Im JH, Hill S, Yameen S, Stratford M, Beech J, et al. Dual Inhibition of the PI3K/mTOR Pathway Increases Tumor Radiosensitivity by Normalizing Tumor Vasculature. *Cancer Res* (2012) 72(1):239–48. doi: 10.1158/0008-5472.CAN-11-2263
214. McGowan DR, Skwarski M, Bradley KM, Campo L, Fenwick JD, Gleeson FV, et al. Buparlisib With Thoracic Radiotherapy and Its Effect on Tumour Hypoxia: A Phase I Study in Patients With Advanced Non-Small Cell Lung Carcinoma. *Eur J Cancer* (2019) 113:87–95. doi: 10.1016/j.ejca.2019.03.015
215. Jain RK, Di Tomaso E, Duda DG, Loeffler JS, Sorensen AG, Batchelor TT. Angiogenesis in Brain Tumours. *Nat Rev Neurosci* (2007) 8(8):610–22. doi: 10.1038/nrn2175
216. Rich JN, Sathornsumetee S, Keir ST, Kieran MW, Laforme A, Kaipainen A, et al. ZD6474, a Novel Tyrosine Kinase Inhibitor of Vascular Endothelial Growth Factor Receptor and Epidermal Growth Factor Receptor, Inhibits Tumor Growth of Multiple Nervous System Tumors. *Clin Cancer Res* (2005) 11(22):8145–57. doi: 10.1158/1078-0432.CCR-05-0319
217. Sandström M, Johansson M, Bergström P, Bergenheim AT, Henriksson R. Effects of the VEGFR Inhibitor ZD6474 in Combination With Radiotherapy and Temozolomide in an Orthotopic Glioma Model. *J Neuro-Oncology* (2008) 88(1):1–9. doi: 10.1007/s11060-008-9527-3
218. Damiano V, Melisi D, Bianco C, Raben D, Caputo R, Fontanini G, et al. Cooperative Antitumor Effect of Multitargeted Kinase Inhibitor ZD6474 and Ionizing Radiation in Glioblastoma. *Clin Cancer Res* (2005) 11(15):5639–44. doi: 10.1158/1078-0432.CCR-05-0174
219. Wang Z, Tang Y, Tan Y, Wei Q, Yu W. Cancer-Associated Fibroblasts in Radiotherapy: Challenges and New Opportunities. *Cell Communication Signaling* (2019) 17(1):1–12. doi: 10.1186/s12964-019-0362-2
220. Ashton TM, McKenna WG, Kunz-Schughart LA, Higgins GS. Oxidative Phosphorylation as an Emerging Target in Cancer Therapy. *Clin Cancer Res* (2018) 24(11):2482–90. doi: 10.1158/1078-0432.CCR-17-3070
221. Ashton TM, Fokas E, Kunz-Schughart LA, Folkes LK, Anbalagan S, Huether M, et al. The Anti-Malarial Atovaquone Increases Radiosensitivity by Alleviating Tumour Hypoxia. *Nat Commun* (2016) 7(1):1–13. doi: 10.1038/ncomms12308
222. Liu Z, Tan H, Zhang X, Chen F, Zhou Z, Hu X, et al. Enhancement of Radiotherapy Efficacy by Silver Nanoparticles in Hypoxic Glioma Cells. *Artif*

Cells Nanomedicine Biotechnol (2018) 46(sup3):S922–30. doi: 10.1080/21691401.2018.1518912

223. Song G, Chao Y, Chen Y, Liang C, Yi X, Yang G, et al. All-In-One Theranostic Nanoplatform Based on Hollow TaOx for Chelator-Free Labeling Imaging, Drug Delivery, and Synergistically Enhanced Radiotherapy. *Advanced Funct Materials* (2016) 26(45):8243–54. doi: 10.1002/adfm.201603845
224. Kempson I. Mechanisms of Nanoparticle Radiosensitization. *Wiley Interdiscip Reviews: Nanomedicine Nanobiotechnology* (2021) 13(1):e1656. doi: 10.1002/wnan.1656
225. Magrini SM, Buglione M, Corvò R, Pirtoli L, Paiar F, Ponticelli P, et al. Cetuximab and Radiotherapy *Versus* Cisplatin and Radiotherapy for Locally Advanced Head and Neck Cancer: A Randomized Phase II Trial. *J Clin Oncol* (2016) 34(5):427–35. doi: 10.1200/JCO.2015.63.1671
226. Mehanna H, Robinson M, Hartley A, Kong A, Foran B, Fulton-Lieuw T, et al. Radiotherapy Plus Cisplatin or Cetuximab in Low-Risk Human Papillomavirus-Positive Oropharyngeal Cancer (De-ESCALaTE HPV): An Open-Label Randomised Controlled Phase 3 Trial. *Lancet* (2019) 393 (10166):51–60. doi: 10.1016/S0140-6736(18)32752-1
227. Gillison ML, Trotti AM, Harris J, Eisbruch A, Harari PM, Adelstein DJ, et al. Radiotherapy Plus Cetuximab or Cisplatin in Human Papillomavirus-Positive Oropharyngeal Cancer (NRG Oncology RTOG 1016): A Randomised, Multicentre, Non-Inferiority Trial. *Lancet* (2019) 393 (10166):40–50. doi: 10.1016/S0140-6736(18)32779-X
228. Bradley JD, Paulus R, Komaki R, Masters G, Blumenschein G, Schild S, et al. Standard-Dose *Versus* High-Dose Conformal Radiotherapy With Concurrent and Consolidation Carboplatin Plus Paclitaxel With or Without Cetuximab for Patients With Stage IIIA or IIIB Non-Small-Cell Lung Cancer (RTOG 0617): A Randomised, Two-by-Two Factorial Phase 3 Study. *Lancet Oncol* (2015) 16 (2):187–99. doi: 10.1016/S1470-2045(14)71207-0
229. Garg MK, Zhao F, Sparano JA, Palefsky J, Whittington R, Mitchell EP, et al. Cetuximab Plus Chemoradiotherapy in Immunocompetent Patients With Anal Carcinoma: A Phase II Eastern Cooperative Oncology Group–American College of Radiology Imaging Network Cancer Research Group Trial (E3205). *J Clin Oncol* (2017) 35(7):718. doi: 10.1200/JCO.2016.69.1667
230. Sparano JA, Lee JY, Palefsky J, Henry DH, Wachsman W, Rajdev L, et al. Cetuximab Plus Chemoradiotherapy for HIV-Associated Anal Carcinoma: A Phase II AIDS Malignancy Consortium Trial. *J Clin Oncol* (2017) 35(7):727. doi: 10.1200/JCO.2016.69.1642
231. Libermann TA, Nusbaum HR, Razon N, Kris R, Lax I, Soreq H, et al. Amplification, Enhanced Expression and Possible Rearrangement of EGF Receptor Gene in Primary Human Brain Tumours of Glial Origin. *Nature* (1985) 313(5998):144–7. doi: 10.1038/313144a0
232. Chakravarti A, Chakladar A, Delaney MA, Latham DE, Loeffler JS. The Epidermal Growth Factor Receptor Pathway Mediates Resistance to Sequential Administration of Radiation and Chemotherapy in Primary Human Glioblastoma Cells in a RAS-Dependent Manner. *Cancer Res* (2002) 62(15):4307–15.
233. Barker FGII, Simmons ML, Chang SM, Prados MD, Larson DA, Sneed PK, et al. EGFR Overexpression and Radiation Response in Glioblastoma Multiforme. *Int J Radiat Oncol Biol Phys* (2001) 51(2):410–8. doi: 10.1016/S0360-3016(01)01609-1
234. Iannitti D, Dipetrillo T, Akerman P, Barnett JM, Maia-Acuna C, Cruff D, et al. Erlotinib and Chemoradiation Followed by Maintenance Erlotinib for Locally Advanced Pancreatic Cancer: A Phase I Study. *Am J Clin Oncol* (2005) 28(6):570–5. doi: 10.1097/01.coc.0000184682.51193.00
235. Duffy A, Kortmansky J, Schwartz G, Capanu M, Puleio S, Minsky B, et al. A Phase I Study of Erlotinib in Combination With Gemcitabine and Radiation in Locally Advanced, Non-Operable Pancreatic Adenocarcinoma. *Ann Oncol* (2008) 19(1):86–91. doi: 10.1093/annonc/mdm441
236. Ma WW, Herman JM, Jimeno A, Laheru D, Messersmith WA, Wolfgang CL, et al. A Tolerability and Pharmacokinetic Study of Adjuvant Erlotinib and Capecitabine With Concurrent Radiation in Resected Pancreatic Cancer. *Trans Oncol* (2010) 3(6):373–9. doi: 10.1593/tlo.10196
237. Bao PQ, Ramanathan RK, Krasinkas A, Bahary N, Lembersky BC, Bartlett DL, et al. Phase II Study of Gemcitabine and Erlotinib as Adjuvant Therapy for Patients With Resected Pancreatic Cancer. *Ann Surg Oncol* (2011) 18 (4):1122–9. doi: 10.1245/s10434-010-1401-9
238. Herman JM, Fan KY, Wild AT, Hacker-Prietz A, Wood LD, Blackford AL, et al. Phase 2 Study of Erlotinib Combined With Adjuvant Chemoradiation and Chemotherapy in Patients With Resectable Pancreatic Cancer. *Int J Radiat Oncol Biol Phys* (2013) 86(4):678–85. doi: 10.1016/j.ijrobp.2013.03.032
239. Ma DJ, Galanis E, Anderson SK, Schiff D, Kaufmann TJ, Peller PJ, et al. A Phase II Trial of Everolimus, Temozolomide, and Radiotherapy in Patients With Newly Diagnosed Glioblastoma: NCCTG N057K. *Neuro-Oncology* (2015) 17(9):1261–9. doi: 10.1093/neuonc/nou328
240. Chinnaiyan P, Won M, Wen PY, Rojiani AM, Werner-Wasik M, Shih HA, et al. A Randomized Phase II Study of Everolimus in Combination With Chemoradiation in Newly Diagnosed Glioblastoma: Results of NRG Oncology RTOG 0913. *Neuro-Oncology* (2018) 20(5):666–73. doi: 10.1093/neuonc/nox209
241. Overgaard J, Hansen HS, Overgaard M, Bastholt L, Berthelsen A, Specht L, et al. A Randomized Double-Blind Phase III Study of Nimorazole as a Hypoxic Radiosensitizer of Primary Radiotherapy in Supraglottic Larynx and Pharynx Carcinoma. Results of the Danish Head and Neck Cancer Study (DAHANCA) Protocol 5-85. *Radiotherapy Oncol* (1998) 46(2):135–46. doi: 10.1016/s0167-8140(97)00220-x
242. Overgaard J. Hypoxic Radiosensitization: Adored and Ignored. *J Clin Oncol* (2007) 25(26):4066–74. doi: 10.1200/JCO.2007.12.7878
243. Kaanders JH, Pop LA, Marres HA, Bruaset I, van den Hoogen FJ, Merkx MA, et al. ARCON: Experience in 215 Patients With Advanced Head-and-Neck Cancer. *Int J Radiat Oncol Biol Phys* (2002) 52(3):769–78. doi: 10.1016/S0360-3016(01)02678-5
244. Hoskin P, Rojas A, Saunders M. Accelerated Radiotherapy, Carbogen, and Nicotinamide (ARCON) in the Treatment of Advanced Bladder Cancer: Mature Results of a Phase II Nonrandomized Study. *Int J Radiat Oncol Biol Phys* (2009) 73(5):1425–31. doi: 10.1016/j.ijrobp.2008.06.1950
245. Hoskin PJ, Rojas AM, Bentzen SM, Saunders MI. Radiotherapy With Concurrent Carbogen and Nicotinamide in Bladder Carcinoma. *J Clin Oncol* (2010) 28(33):4912–8. doi: 10.1200/JCO.2010.28.4950
246. Janssens GO, Rademakers SE, Terhaard CH, Doornaert PA, Bijl HP, van den Ende P, et al. Accelerated Radiotherapy With Carbogen and Nicotinamide for Laryngeal Cancer: Results of a Phase III Randomized Trial. *J Clin Oncol* (2012) 30(15):1777–83. doi: 10.1200/JCO.2011.35.9315
247. Barker HE, Paget JT, Khan AA, Harrington KJ. The Tumour Microenvironment After Radiotherapy: Mechanisms of Resistance and Recurrence. *Nat Rev Cancer* (2015) 15(7):409–25. doi: 10.1038/nrc3958
248. DiSilvestro PA, Ali S, Craighead PS, Lucci JA, Lee Y-C, Cohn DE, et al. Phase III Randomized Trial of Weekly Cisplatin and Irradiation *Versus* Cisplatin and Tirapazamine and Irradiation in Stages IB2, IIA, IIB, IIIB, and IVA Cervical Carcinoma Limited to the Pelvis: A Gynecologic Oncology Group Study. *J Clin Oncol* (2014) 32(5):458. doi: 10.1200/JCO.2013.51.4265
249. Rischin D, Peters LJ, O'Sullivan B, Giralt J, Fisher R, Yuen K, et al. Tirapazamine, Cisplatin, and Radiation *Versus* Cisplatin and Radiation for Advanced Squamous Cell Carcinoma of the Head and Neck (TROG 02.02, HeadSTART): A Phase III Trial of the Trans-Tasman Radiation Oncology Group. *Oncology* (2008) 28(18):2989–95. doi: 10.1200/jco.2008.26.15_suppl.lba6008
250. Gilbert MR, Dignam JJ, Armstrong TS, Wefel JS, Blumenthal DT, Vogelbaum MA, et al. A Randomized Trial of Bevacizumab for Newly Diagnosed Glioblastoma. *New Engl J Med* (2014) 370(8):699–708. doi: 10.1056/NEJMoa1308573
251. Chinot OL, Wick W, Mason W, Henriksson R, Saran F, Nishikawa R, et al. Bevacizumab Plus Radiotherapy–Temozolomide for Newly Diagnosed Glioblastoma. *New Engl J Med* (2014) 370(8):709–22. doi: 10.1056/NEJMoa1308345
252. Lai A, Tran A, Nghiemphu PL, Pope WB, Solis OE, Selch M, et al. Phase II Study of Bevacizumab Plus Temozolomide During and After Radiation Therapy for Patients With Newly Diagnosed Glioblastoma Multiforme. *J Clin Oncol* (2011) 29(2):142. doi: 10.1200/JCO.2010.30.2729
253. Batchelor TT, Gerstner ER, Emblem KE, Duda DG, Kalpathy-Cramer J, Snuderl M, et al. Improved Tumor Oxygenation and Survival in Glioblastoma Patients Who Show Increased Blood Perfusion After Cediranib and Chemoradiation. *Proc Natl Acad Sci* (2013) 110(47):19059–64. doi: 10.1073/pnas.1318022110

254. Murphy JE, Wo JY, Ryan DP, Clark JW, Jiang W, Yeap BY, et al. Total Neoadjuvant Therapy With FOLFIRINOX in Combination With Losartan Followed by Chemoradiotherapy for Locally Advanced Pancreatic Cancer: A Phase 2 Clinical Trial. *JAMA Oncol* (2019) 5(7):1020–7. doi: 10.1001/jamaoncol.2019.0892
255. Prior IA, Lewis PD, Mattos C. A Comprehensive Survey of Ras Mutations in Cancer. *Cancer Res* (2012) 72(10):2457–67. doi: 10.1158/0008-5472.CAN-11-2612
256. Bernhard EJ, Stanbridge EJ, Gupta S, Gupta AK, Soto D, Bakanauskas VJ, et al. Direct Evidence for the Contribution of Activated N-Ras and K-Ras Oncogenes to Increased Intrinsic Radiation Resistance in Human Tumor Cell Lines. *Cancer Res* (2000) 60(23):6597–600.
257. Cengel KA, Voong KR, Chandrasekaran S, Maggiorella L, Brunner TB, Stanbridge E, et al. Oncogenic K-Ras Signals Through Epidermal Growth Factor Receptor and Wild-Type H-Ras to Promote Radiation Survival in Pancreatic and Colorectal Carcinoma Cells. *Neoplasia* (2007) 9(4):341–8. doi: 10.1593/neo.06823
258. Kim I-A, Bae S-S, Fernandes A, Wu J, Muschel RJ, McKenna WG, et al. Selective Inhibition of Ras, Phosphoinositide 3 Kinase, and Akt Isoforms Increases the Radiosensitivity of Human Carcinoma Cell Lines. *Cancer Res* (2005) 65(17):7902–10. doi: 10.1158/0008-5472.CAN-05-0513
259. Mak RH, Hermann G, Lewis JH, Aerts HJ, Baldini EH, Chen AB, et al. Outcomes by Tumor Histology and KRAS Mutation Status After Lung Stereotactic Body Radiation Therapy for Early-Stage Non–Small-Cell Lung Cancer. *Clin Lung Cancer* (2015) 16(1):24–32. doi: 10.1016/j.cllc.2014.09.005
260. Hong TS, Wo JY, Borger DR, Yeap BY, McDonnell EI, Willers H, et al. Phase II Study of Proton-Based Stereotactic Body Radiation Therapy for Liver Metastases: Importance of Tumor Genotype. *JNCI: J Natl Cancer Institute* (2017) 109(9):djx031. doi: 10.1093/jnci/djx031
261. Jethwa KR, Jang S, Mullikin TC, Harmsen WS, Petersen MM, Olivier KR, et al. Association of Tumor Genomic Factors and Efficacy for Metastasis-Directed Stereotactic Body Radiotherapy for Oligometastatic Colorectal Cancer. *Radiotherapy Oncol* (2020) 146:29–36. doi: 10.1016/j.radonc.2020.02.008
262. Gallogly MM, Lazarus HM, Cooper BW. Midostaurin: A Novel Therapeutic Agent for Patients With FLT3-Mutated Acute Myeloid Leukemia and Systemic Mastocytosis. *Ther Adv Hematol* (2017) 8(9):245–61. doi: 10.1177/2040620717721459
263. Hong TS, Wo JY-L, Ryan DP, Zheng H, Borger DR, Kwak EL, et al. Phase Ib Study of Neoadjuvant Chemoradiation (CRT) With Midostaurin, 5-Fluorouracil (5-FU) and Radiation (XRT) for Locally Advanced Rectal Cancer: Sensitization of RAS Mutant Tumors. *Am Soc Clin Oncol* (2018) 36(15_suppl):e15674–e15674. doi: 10.1200/JCO.2018.36.15_suppl.e15674
264. Liu Q, Wang M, Kern AM, Khaled S, Han J, Yeap BY, et al. Adapting a Drug Screening Platform to Discover Associations of Molecular Targeted Radiosensitizers With Genomic Biomarkers. *Mol Cancer Res* (2015) 13 (4):713–20. doi: 10.1158/1541-7786.MCR-14-0570
265. Lin SH, Mok I, Leos D, Pasia MG, Thall PF, Lin HY, et al. NCI 9448: Phase I Study of Trametinib in Combination With Chemoradiation for KRAS-Mutant Non-Small Cell Lung Cancer. *Am Soc Clin Oncol* (2015) 33 (15_suppl):TPS7585-TPS7585. doi: 10.1200/jco.2015.33.15_suppl.tps7585
266. Hong DS, Fakih MG, Strickler JH, Desai J, Durm GA, Shapiro GI, et al. KRASG12C Inhibition With Sotorasib in Advanced Solid Tumors. *New Engl J Med* (2020) 383(13):1207–17. doi: 10.1056/NEJMoa1917239
267. O'Connor MJ. Targeting the DNA Damage Response in Cancer. *Mol Cell* (2015) 60(4):547–60. doi: 10.1016/j.molcel.2015.10.040
268. Jagsi R, Griffith KA, Bellon JR, Woodward WA, Horton JK, Ho A, et al. Concurrent Veliparib With Chest Wall and Nodal Radiotherapy in Patients With Inflammatory or Locoregionally Recurrent Breast Cancer: The TBCRC 024 Phase I Multicenter Study. *J Clin Oncol* (2018) 36(13):1317. doi: 10.1200/JCO.2017.77.2665
269. Connolly E, Silvera D, Badura M, Braunstein S, Formenti S, Schneider R. Inflammatory Breast Cancer Radio-Resistance and Its Cancer Stem Cell Population are Oppositely Controlled by Translation Factor Eif4g. *Int J Radiat Oncol Biol Phys* (2010) 78(3):S221. doi: 10.1016/j.ijrobp.2010.07.531
270. Hu Y, Guo M. Synthetic Lethality Strategies: Beyond BRCA1/2 Mutations in Pancreatic Cancer. *Cancer Sci* (2020) 111(9):3111–21. doi: 10.1111/cas.14565
271. Tuli R, Shiao SL, Nissen N, Tighiouart M, Kim S, Osipov A, et al. A Phase 1 Study of Veliparib, a PARP-1/2 Inhibitor, With Gemcitabine and Radiotherapy in Locally Advanced Pancreatic Cancer. *EBioMedicine* (2019) 40:375–81. doi: 10.1016/j.ebiom.2018.12.060
272. Karam SD, Reddy K, Blatchford PJ, Waxweiler T, DeLouize AM, Oweida A, et al. Final Report of a Phase I Trial of Olaparib With Cetuximab and Radiation for Heavy Smoker Patients With Locally Advanced Head and Neck Cancer. *Clin Cancer Res* (2018) 24(20):4949–59. doi: 10.1158/1078-0432.CCR-18-0467
273. Cuneo KC, Morgan MA, Sahai V, Schipper MJ, Parsels LA, Parsels JD, et al. Dose Escalation Trial of the Wee1 Inhibitor Adavosertib (AZD1775) in Combination With Gemcitabine and Radiation for Patients With Locally Advanced Pancreatic Cancer. *J Clin Oncol* (2019) 37(29):2643. doi: 10.1200/JCO.19.00730
274. Hammel P, Huguet F, van Laethem J-L, Goldstein D, Glimelius B, Artru P, et al. Effect of Chemoradiotherapy *vs* Chemotherapy on Survival in Patients With Locally Advanced Pancreatic Cancer Controlled After 4 Months of Gemcitabine With or Without Erlotinib: The LAP07 Randomized Clinical Trial. *Jama* (2016) 315(17):1844–53. doi: 10.1001/jama.2016.4324
275. Van Triest B, Damstrup L, Falkenius J, Budach V, Troost E, Samuels M, et al. A Phase Ia/Ib Trial of the DNA-PK Inhibitor M3814 in Combination With Radiotherapy (RT) in Patients (Pts) With Advanced Solid Tumors: Dose-Escalation Results. *Am Soc Clin Oncol* (2018) 36(15_suppl):2518. doi: 10.1200/JCO.2018.36.15_suppl.2518
276. Huang R-X, Zhou P-K. DNA Damage Response Signaling Pathways and Targets for Radiotherapy Sensitization in Cancer. *Signal Transduction Targeted Ther* (2020) 5(1):1–27. doi: 10.1038/s41392-020-0150-x
277. Kwatra D, Venugopal A, Anant S. Nanoparticles in Radiation Therapy: A Summary of Various Approaches to Enhance Radiosensitization in Cancer. *Transl Cancer Res* (2013) 2(4):330–42. doi: 10.3978/j.issn.2218-676X.2013.08.06
278. Bonvalot S, Rutkowski PL, Thariat J, Carrère S, Ducassou A, Sunyach M-P, et al. NBTXR3, a First-in-Class Radioenhancer Hafnium Oxide Nanoparticle, Plus Radiotherapy *Versus* Radiotherapy Alone in Patients With Locally Advanced Soft-Tissue Sarcoma (Act. In. Sarc): A Multicentre, Phase 2–3, Randomised, Controlled Trial. *Lancet Oncol* (2019) 20(8):1148–59. doi: 10.1016/S1470-2045(19)30326-2
279. Pallares RM, Abergel RJ. Nanoparticles for Targeted Cancer Radiotherapy. *Nano Res* (2020) 1–11. doi: 10.1007/s12274-020-2957-8
280. Antonia SJ, Villegas A, Daniel D, Vicente D, Murakami S, Hui R, et al. Durvalumab After Chemoradiotherapy in Stage III Non–Small-Cell Lung Cancer. *New Engl J Med* (2017) 377(20):1919–29. doi: 10.1056/NEJMoa1709937
281. Antonia SJ, Villegas A, Daniel D, Vicente D, Murakami S, Hui R, et al. Overall Survival With Durvalumab After Chemoradiotherapy in Stage III NSCLC. *New Engl J Med* (2018) 379(24):2342–50. doi: 10.1056/NEJMoa1809697
282. Lin SH, Lin Y, Yao L, Kalhor N, Carter BW, Altan M, et al. Phase II Trial of Concurrent Atezolizumab With Chemoradiation for Unresectable NSCLC. *J Thorac Oncol* (2020) 15(2):248–57. doi: 10.1016/j.jtho.2019.10.024
283. Jabbour SK, Berman AT, Decker RH, Lin Y, Feigenberg SJ, Gettinger SN, et al. Phase 1 Trial of Pembrolizumab Administered Concurrently With Chemoradiotherapy for Locally Advanced Non–Small Cell Lung Cancer: A Nonrandomized Controlled Trial. *JAMA Oncol* (2020) 6(6):848–55. doi: 10.1001/jamaoncol.2019.6731
284. Weiss J, Bauman JR, Deal AM, Sheth S, Chera BS, Shen C, et al. Preliminary Toxicity Data From the Combination of Pembrolizumab and Definitive-Dose Radiotherapy for Locally Advanced Head and Neck Cancer With Contraindication to Cisplatin Therapy. *Am Soc Clin Oncol* (2018) 36 (15_suppl):6069. doi: 10.1200/JCO.2018.36.15_suppl.6069
285. Sun XS, Sire C, Tao Y, Martin L, Alfonsi M, Prevost JB, et al. A Phase II Randomized Trial of Pembrolizumab *Versus* Cetuximab, Concomitant With Radiotherapy (RT) in Locally Advanced (LA) Squamous Cell Carcinoma of the Head and Neck (SCCHN): First Results of the GORTEC 2015-01 "PembroRad" Trial. *J Clin Oncol* (2018) 36(15_suppl):6018. doi: 10.1200/JCO.2018.36.15_suppl.6018
286. Powell SF, Gitau MM, Sumey CJ, Reynolds JT, Lohr M, McGraw S, et al. Safety of Pembrolizumab With Chemoradiation (CRT) in Locally Advanced Squamous Cell Carcinoma of the Head and Neck (LA-SCCHN). *Am Soc Clin Oncol* (2017) 35(15_suppl):6011. doi: 10.1200/JCO.2017.35.15_suppl.6011
287. Tao Y, Aupérin A, Sun X, Sire C, Martin L, Coutte A, et al. Avelumab–cetuximab–radiotherapy *Versus* Standards of Care in Locally Advanced Squamous-Cell Carcinoma of the Head and Neck: The Safety Phase of a

Randomised Phase III Trial GORTEC 2017-01 (REACH). *Eur J Cancer* (2020) 141:21–9. doi: 10.1016/j.ejca.2020.09.008
288. Weiss J, Sheth S, Deal AM, Olson JEG, Patel S, Hackman TG, et al. Concurrent Definitive Immunoradiotherapy for Patients With Stage III–IV Head and Neck Cancer and Cisplatin Contraindication. *Clin Cancer Res* (2020) 26(16):4260–7. doi: 10.1158/1078-0432.CCR-20-0230
289. Rodríguez-Ruiz ME, Vanpouille-Box C, Melero I, Formenti SC, Demaria S. Immunological Mechanisms Responsible for Radiation-Induced Abscopal Effect. *Trends Immunol* (2018) 39(8):644–55. doi: 10.1016/j.it.2018.06.001
290. Theelen WS, Peulen HM, Lalezari F, van der Noort V, De Vries JF, Aerts JG, et al. Effect of Pembrolizumab After Stereotactic Body Radiotherapy *vs* Pembrolizumab Alone on Tumor Response in Patients With Advanced Non–Small Cell Lung Cancer: Results of the PEMBRO-RT Phase 2 Randomized Clinical Trial. *JAMA Oncol* (2019) 5(9):1276–82. doi: 10.1001/jamaoncol.2019.1478
291. McBride S, Sherman E, Tsai CJ, Baxi S, Aghalar J, Eng J, et al. Randomized Phase II Trial of Nivolumab With Stereotactic Body Radiotherapy *Versus* Nivolumab Alone in Metastatic Head and Neck Squamous Cell Carcinoma. *J Clin Oncol* (2021) 39(1):30–7. doi: 10.1200/JCO.20.00290
292. Altorki NK, McGraw TE, Borczuk AC, Saxena A, Port JL, Stiles BM, et al. Neoadjuvant Durvalumab With or Without Stereotactic Body Radiotherapy in Patients With Early-Stage Non-Small-Cell Lung Cancer: A Single-Centre, Randomised Phase 2 Trial. *Lancet Oncol* (2021) 22(6):824–35. doi: 10.1016/S1470-2045(21)00149-2
293. Alexander BM, Schoenfeld JD, Trippa L. Hazards of Hazard Ratios-Deviations From Model Assumptions in Immunotherapy. *New Engl J Med* (2018) 378(12):1158–9. doi: 10.1056/NEJMc1716612
294. Walker AJ, DeWeese TL, Viswanathan AN. Drug-Radiotherapy Combinations in 2020—A Landmark Year? *JAMA Oncol* (2021) 7(3):349–50. doi: 10.1001/jamaoncol.2020.6139

Conflict of Interest: The authors declare that the research was conducted in the absence of any commercial or financial relationships that could be construed as a potential conflict of interest.

Publisher's Note: All claims expressed in this article are solely those of the authors and do not necessarily represent those of their affiliated organizations, or those of the publisher, the editors and the reviewers. Any product that may be evaluated in this article, or claim that may be made by its manufacturer, is not guaranteed or endorsed by the publisher.

frontiers in Oncology

ORIGINAL RESEARCH
published: 26 October 2021
doi: 10.3389/fonc.2021.730607

Silencing of Fused Toes Homolog (FTS) Increases Radiosensitivity to Carbon-Ion Through Downregulation of Notch Signaling in Cervical Cancer Cells

Prabakaran D.S.[1†], *Pankaj Kumar Chaturvedi*[1†], *Takashi Shimokawa*[2], *Ki-Hwan Kim*[3] *and Woo-Yoon Park*[1*]

[1] Department of Radiation Oncology, Chungbuk National University Hospital, Chungbuk National University College of Medicine, Cheongju, South Korea, [2] Department of Accelerator and Medical Physics, Institute for Quantum Medical Science, QST, Chiba, Japan, [3] Department of Radiation Oncology, Chungnam National University Hospital, Daejeon, South Korea

OPEN ACCESS

Edited by:
Pankaj Chaudhary,
Queen's University Belfast,
United Kingdom

Reviewed by:
Janapriya Saha,
Leidos, United States
Haritha Kunhiraman,
Emory University, United States

***Correspondence:**
Woo-Yoon Park
wynpark@chungbuk.ac.kr

[†]These authors have contributed equally to this work

Specialty section:
This article was submitted to Radiation Oncology, a section of the journal Frontiers in Oncology

Received: 25 June 2021
Accepted: 07 October 2021
Published: 26 October 2021

Citation:
D.S. P, Chaturvedi PK, Shimokawa T, Kim K-H and Park W-Y (2021) Silencing of Fused Toes Homolog (FTS) Increases Radiosensitivity to Carbon-Ion Through Downregulation of Notch Signaling in Cervical Cancer Cells. Front. Oncol. 11:730607. doi: 10.3389/fonc.2021.730607

The effects of Carbon ion radiation (C-ion) alone or in combination with fused toes homolog (FTS) silencing on Notch signaling were investigated in uterine cervical cancer cell lines (ME180 and CaSki). In both cell lines, upon irradiation with C-ion, the expression of Notch signaling molecules (Notch1, 2, 3 and cleaved Notch1), γ-secretase complex molecules and FTS was upregulated dose-dependently (1, 2 and 4 Gy) except Notch1 in ME180 cells where the change in expression was not significant. However, overexpression of these molecules was attenuated upon silencing of FTS. The spheroid formation, expression of stem cell markers (OCT4A, Sox2 and Nanog) and clonogenic cell survival were reduced by the combination as compared to FTS silencing or C-ion irradiation alone. Additionally, immunoprecipitation and immunofluorescence assay revealed interaction and co-localization of FTS with Notch signaling molecules. In conclusion, FTS silencing enhances the radio-sensitivity of the cervical cancer cells to C-ion by downregulating Notch signaling molecules and decreasing the survival of cancer stem cells.

Keywords: cervical cancer, fused toes homolog, notch, spheroid, carbon-ion beam

Abbreviations: CCRT, concurrent chemo-radiotherapy; C-ion, Carbon ion; CSCs, cancer stem cells; DAPI, 4′,6-diamidino-2-phenylindole; DMF, dose modifying factor; ECL, enhanced chemiluminescence; EGF, epidermal growth factor; FTS, fused toes homolog; GSI, γ-secretase inhibitors; Gy, Gray; h, hour; HES1, hairy and enhancer of split-1; HEY, HES related with YRPW motif; HIMAC, Heavy Ion Medical Accelerator in Chiba; HNSCC, head and neck squamous cell carcinoma; HPV, Human papillomavirus; IF, immunofluorescence; IP, immunoprecipitation; LET, linear energy transfer; NICD, Notch intracellular domain; OCT4A, Octamer-binding transcription factor 4A; PBS, phosphate-buffered saline; *PEN-2*, presenilin enhancer 2; RT, radiation therapy; SF, surviving fraction; SOX2, SRY-Box Transcription Factor 2.

INTRODUCTION

Uterine cervical cancer is the fourth most commonly diagnosed cancer with the fourth leading cause of death due to cancer in women worldwide. There were estimates of 604,000 new cases and 342,000 deaths in 2020. Nevertheless, it is the leading cause of malignancies related death in sub-Saharan Africa, South America and South-Eastern Asia (1). The human papillomavirus (HPV), most frequently HPV 16, is the predominant risk factor of cervical cancer (2). Notch signaling has been reported to play a crucial role in cervical cancer development (3) in which E6 and E7 oncoproteins of HPV regulate the Notch expression and conjoin to induce cellular transformation (4).

Notch signaling is a conserved pathway that determines mammalian cell fate (5). The transmembrane receptors of Notch communicate with the neighboring cells which express membrane-bound ligands. The interaction of Notch ligands with its receptors triggers proteolytic cleavage leading to the release and translocation of the Notch intracellular domain (NICD) to the nucleus where NICD activates the target genes transcription. Constitutive Notch signaling targets comprise not only the transcriptional regulators of the hairy enhancer split (HES) and HES related with YRPW motif-family (HEY), but also the oncogenes like Myc or Ras (6). Thus, the Notch pathway plays a central role in the maintenance of cancer stem-like properties and its persistent activation may lead to cancer progression and metastasis (7, 8).

Even though some tumors relapse, radiation therapy (RT) is considered as one of the main modalities for cancer treatment (9). Recently, Notch pathway has been demonstrated to mediate resistance for RT in tumor cells (10). A thorough understanding of Notch regulation and its interactions with other relevant therapeutic pathways is essential for its successful targeting (11).

Carbon ion (C-ion) RT offers more advantages than conventional RT as it enables efficient cell killing, attributable to a more accurate dose distribution (12). Furthermore, C-ion allows high energy deposition and high linear energy transfer (LET) to its target compared with photon and proton beams. In addition, the upsurge of energy deposition along the path of ion beam in the body results in less toxicity to the neighboring normal tissues (13). More than 27,000 patients with various types of tumors, including adenoid cystic carcinoma, adenocarcinoma, malignant melanoma and sarcomas, which are very often x-rays resistant, have been treated with C-ion worldwide during 1994-2018 (14, 15).

A favorable local control with minimal radiation toxicity by C-ion RT alone has been reported for locally advanced cervical cancer (16). However, despite favorable local control rates, distant metastasis was high, disease-free survival and overall survival rates were not too satisfactory compared to concurrent chemoradiotherapy (CCRT) (17), therefore, efforts to improve the efficacy of C-ion therapy are highly desirable.

Cancer stem cells (CSCs) can self-renew, differentiate and repair DNA damage, which renders them resistant to various therapies, including RT (18). The dose-response curves comparison for the CSCs and non-CSCs indicated that CSCs are resistant to x-rays and C-ion beam (19). Therefore, eradication of all CSCs is a prerequisite for ultimate cancer treatment. Some researchers have reported that cisplatin or gemcitabine in combination with C-ion RT in pancreatic, mesothelioma and breast cancer improved the efficacy of C-ion and overcame CSC resistance (20–22). The invasive and migratory potential of CSCs in head and neck squamous cell carcinoma (HNSCC) enhance their radioresistance. CSC invasion process was significantly inhibited by the combination of cetuximab and C-ion (23). In uterine cervical cancer C-ion therapy overcame the radiation resistance origination from hypoxia (24). The radioresistance in CSCs has been often linked with Notch signaling. Thus inhibition of Notch pathway could be used to develop an adjuvant approach to RT (25).

Our previous findings have shown FTS as a potential target for Notch-mediated resistance upon x-ray irradiation in cervical cancer (10). In this study, effects of the C-ion beam on the Notch signaling and spheroid formation were investigated in FTS intact and silenced cells with an objective to evaluate whether targeting FTS can be a Notch-mediated adjuvant approach in improving the efficacy of C-ion therapy in cervical cancer.

MATERIALS AND METHODS

Cell Culture and Antibiotics

Two human cervical cancer cell lines, ME180 and CaSki cells, were procured from RIKEN BioResource Center (Japan) and cultured in RPMI 1640 and DMEM (Invitrogen, Carlsbad, CA, USA) supplemented with 10% fetal bovine serum (FBS), penicillin (100 units/mL) and streptomycin (100 mg/mL). The cells were grown in a humidified incubator at 37°C and 5% CO_2. Cell harvesting and passaging was done with the help of Trypsin-EDTA. All standard cell culture reagents were procured from Invitrogen. Antibodies for FTS and Actin were purchased from Santa Cruz Biotechnology, Inc. (Dallas, TX, USA). All other primary and secondary antibodies were purchased from Cell Signaling Technologies (Beverly, MA, USA).

C-Ion and X-Ray Beam Irradiation

Cells grown in T-25 flasks were irradiated at room temperature with C-ions accelerated by the Heavy Ion Medical Accelerator in Chiba (HIMAC) at the National Institute of Radiological Sciences (NIRS) (Chiba, Japan). The 290 MeV/n carbon-ion beams were adjusted to be about 70 KeV/μm at the cell surface using a scatterer (Ta = 0.2 mm, Pb = 1.6 mm), air: 11.8 m, the flask and PMMA range shifters: 140 mm water-equivalent. The flasks were positioned in vertical position with the cell adhesion surface facing the beam source. The particulars regarding the beam characteristics of C-ion, dosimetry and irradiation procedures have been explained previously (26–28). To compare the radiation effects of C-ion and x-ray by FTS silencing, cells were also irradiated with various doses of x-ray in a field size of 20 cm x 20 cm at room temperature using a 6 MV medical linear accelerator (Oncor, Siemens, Concord, CA, USA) at Chungbuk National University Hospital, Department of

Radiation Oncology. QA of the medical linear accelerator is performed in compliance to IAEA-TRS-398.

Colony Formation Assay

The cell survival by irradiation was evaluated using colony formation assay. After C-ion/x-ray irradiation, cells were washed with 1X PBS pH 7.5 and single-cell suspension was prepared by trypsinization. The cells were counted and re-seeded in triplicates into 60 mm cell culture dishes at appropriate cell densities for colony formation. The cells were cultured for 7-9 days to make colonies, fixed with 20% ethanol and stained with 0.2% crystal violet (Sigma, St. Louis, Missouri, USA). The colonies comprising 50 or more cells were considered as survivors and counted using a microscope (Olympus Optical, Shinjuku, Tokyo, Japan). Surviving fractions were calculated on the basis of the plating efficiencies of corresponding non-irradiated cells. Three independent experiments were performed with each cervical cancer cell line. The graphs were plotted for surviving fractions by C-ion and x-ray in the FTS intact and silenced cells. Dose modifying factor (DMF) was calculated as the ratio between FTS intact and silenced group for the radiation doses of C-ion or x-ray with 10% surviving fraction (SF_{10}).

Western Blotting

After irradiation, the cells were washed in cold PBS and lysed with 200 µl of cell lysis buffer (Cell Signaling Technology, Danvers, MA, USA) supplemented with complete protease inhibitor cocktail and phosphatase inhibitors (Roche, Mannheim, Germany) for 30 min on ice. Protein concentration of each sample was determined using Bradford reagent (Bio-Rad, Hercules, CA, USA). 30 µg of total protein from each sample was resolved on SDS-PAGE gels and transferred onto PVDF membranes (Millipore, Billerica, MA, USA). The membranes were then probed with appropriate primary and secondary antibodies. Finally, the membranes were exposed to the ECL substrate solution (Thermo Scientific, Rockford, IL, USA) and images were recorded with the help of chemidoc (Fujifilm, Tokyo, Japan). Expression of each protein was calculated by densitometric measurement using the Multi-Gauge ver. 3.1 Software (Fujifilm, Tokyo, Japan). Band densities of target proteins were normalized to actin expression to plot the bar graphs (**Supplementary Figures S2–S5**).

Spheroid Formation Assay

After transfection with scrambled siRNA or FTS siRNA for 24 h, the cells were irradiated with C-ion beam. Post-irradiation, the cells were trypsinized, harvested and single-cell suspension was prepared. The single-cell suspension was cultured in 60 mm ultralow attachment plates (Corning, Lowell, MA, USA), in a serum-free DMEM/F12 growth medium supplemented with 10 ng/mL EGF (Sigma, St. Louis, MO, USA), 10 ng/mL bFGF (Invitrogen) and 2% B27 (Invitrogen). The images of spheroids were taken using the Olympus IX71 microscope (Tokyo, Japan).

Cell Viability Assay in Spheroids

To analyze the number of viable cells constituting the spheroids, 7 days after spheroid culture 50 µl of WST-1 solution (DoGenBio, Seoul, South Korea) was added to each well. After 4 h, absorbance at 450 nm was recorded with the help of a microplate reader (BIO-RAD, CA, USA).

FTS Silencing

Cells were seeded in T-25 or T-75 flask in antibiotic-free RPMI and allowed to attach overnight. Next morning, the medium was replaced with transfection medium containing 50 nM of either scrambled siRNA (sc-37007, Santa Cruz) or FTS siRNA (sc-93013, Santa Cruz) and incubated at 37°C. After 6 h, the medium was replaced with complete growth medium supplemented with 10% FBS and 1% antibiotics, and the cells were incubated for another 24 h.

Immunoprecipitation (IP) Assay

The cells were lysed 24 h after C-ion irradiation using cell lysis buffer (Cell Signaling Technology) for 30 min on ice and scraped using cell scraper (SPL Life Sciences, South Korea). The cell lysates were centrifuged at 12,000 g for 10 min at 4°C and the supernatants were collected. 200 µg of total protein from each sample was incubated overnight with the anti-FTS antibody at 4°C, followed by incubation with protein A/G agarose (Santa Cruz) for 1 h. Immunoprecipitates were washed twice for 5 min with cell lysis buffer at 4°C. Bead bound proteins were eluted with non-reducing sample buffer (Thermo Scientific) at 95°C for 3 min and then subjected to SDS-PAGE and western blot analyses.

Immunofluorescence (IF) Assay

Cells were grown on chamber slides (154526, Thermo Fisher, MA, USA), transfected using scrambled or FTS siRNA, irradiated with 1 Gy C-ion and incubated for 24 h at 37°C in a CO_2 incubator. After incubation, the cells were fixed with 4% formaldehyde (Thermo Scientific), permeabilized with 0.1% Triton X-100 (Amresco, Ohio, US) and blocked with 10% FBS for 30 min followed by overnight incubation at 4°C with respective primary antibody (1:100 dilution). Cells were further incubated in the dark at room temperature with Alexa-488/Alexa 594-conjugated secondary antibody for 1 h. Nuclei were counter stained with DAPI at a concentration of 1 µg/mL (Sigma). After staining with DAPI the chambers were removed and mounted using cover slips with anti-fade mounting solution (Dako, CA, US). The slides were dried overnight in the dark and stored at -20°C until imaging. Z-stack images were captured with the help of confocal microscope (Leica DM-IRB, Mannheim, Germany). For spheroids immunofluorescence, the cells were irradiated with 1 Gy C-ion after transfection with scrambled or FTS siRNA. The cells were cultured further in an ultra-low attachment plate and allowed to form spheroids. The spheroids were then carefully transferred onto chamber slides and allowed to adhere overnight. Next morning immunofluorescence protocol was followed as mentioned above for adherent cells.

Statistical Analysis

All analytical data are presented as the means ± SD of three independent experiments. Differences among the groups were

calculated by GraphPad Prism (GraphPad Software, version 9.1.0 (221), La Jolla, CA, USA, www.graphpad.com) using two way analysis of variance (ANOVA) module followed by Dunnett's/Tukey multiple comparison post-hoc test; $p \leq 0.05$, was considered to be statistically significant.

RESULTS

C-Ion Upregulates FTS, the Notch Signaling and γ-Secretase Complex Molecules

To determine the effect of C-ion on the Notch signaling, first, we investigated the change in the expression level of the Notch signaling molecules at three different doses of C-ion (0, 1, 2 and 4 Gy). In CaSki, the expression of Notch1, 2, 3, cleaved Notch1, Hes1 and FTS was increased dose-dependently in response to C-ion irradiation. In ME180, cleaved Notch1 and FTS expression increased dose-dependently, while other molecules expression didn't change much in response to increased radiation doses (**Figure 1**). Similarly, the protein expression level of γ-secretase complex molecules (presenilin1, presenilin2, nicastrin and PEN2) was also elevated, in a dose and time-dependent manner in both cell lines (**Figures 2A, B**). Changes in the expression level of FTS, Notch and γ-secretase complex molecules in response to radiation doses were highly significant when compared with unirradiated group (**Supplementary Figures S2, S3**).

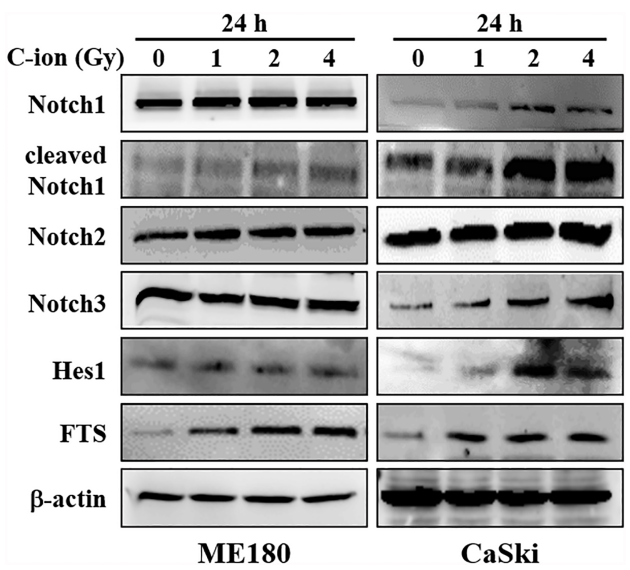

FIGURE 1 | The expression of Notch signaling molecules (Notch1, 2, 3, cleaved Notch1, Hes1) and FTS were increased by C-ion beam in cervical cancer cells (ME180, CaSki). The cells were irradiated with 0, 1, 2 and 4 Gy of C-ion and the protein expression was measured with immunoblot 24 h post-irradiation. The images shown in this figure are the representatives of at least three independent experiments.

FTS-Silencing Attenuates the Expression of Notch Signaling Molecules

To study the role of FTS on Notch signaling, the FTS gene was silenced using siRNA. Silencing of FTS reduced C-ion induced upregulation of Notch1, 2, 3, cleaved Notch1 and Hes1 significantly (**Figure 3A** and **Supplementary Figure S4**), in addition to γ-secretase complex proteins (presenilin1, presenilin2, nicastrin and PEN2) (**Figure 3B** and **Supplementary Figure S4**) in both cell lines. Downregulation of these molecules was further augmented when FTS silencing was combined with C-ion irradiation (**Figures 3A, B**, and **Supplementary Figure S4**).

Interaction Between FTS and the Notch Molecules Increases Upon C-Ion

Immunoprecipitation and immunofluorescence assay were performed to demonstrate the interaction between FTS and the Notch signaling molecules. Immunoprecipitation demonstrated the physical interaction between FTS and Notch1/cleaved Notch1/Hes1 (**Figure 4A**). Immunofluorescence showed the increased co-localization of FTS with Notch1/cleaved Notch1/Hes1 by C-ion irradiation, but the interaction and co-localization were reduced substantially by FTS-silencing (**Figures 4B–D**).

The Combination of FTS-Silencing and C-Ion Decreases Spheroid Formation, Cancer Stem Cell Markers and Clonogenic Cell Survival

The spheroid formation and the expression of stem cell marker proteins (OCT4A, SOX2 and Nanog) in the two cell lines were not changed by C-ion alone. However, they were decreased dramatically when combined with FTS-silencing (**Figures 5A–C** and **Supplementary Figure S5**). The number of spheroids and the viable cells in the spheroids were also reduced significantly by the combination of FTS-silencing and C-ion (**Figures 5D, E**). The RBE value of C-ion to x-rays has been generally considered to be about 2.5, hence we chose 1, 2 and 4 Gy of C-ion to compare the radiation effects with 2.5, 5 and 10 Gy doses of x-ray. The survival curves by C-ion or x-rays were significantly lowered when combined with FTS silencing (**Figure 6**). Silencing of FTS was seen to reduce the radiation dose by approximately 9.3% (x-rays) and 11.8% (C-ion) in ME180 cells, whereas 17.2% (x-rays) and 9.5% (C-ion) in CaSki cells (**Supplementary Table T1**). Therefore, the DMF at SF_{10} for ME180 cells was 1.093 (x-ray) and 1.118 (C-ion), whereas it was 1.172 (x-rays) and 1.095 (C-ion) for CaSki cells. We also calculated the RBE at SF10 for both the cell lines which were 2.58 for ME180 and 2.66 for CaSki in FTS intact group, while in the FTS silenced group it was 2.64 for ME180 and 2.49 for CaSki. We observed changes in the RBE value of C-ion by approximately 15.52% in ME180 cells and 16.72% in CaSki cells under the influence of FTS silencing (**Supplementary Table T1**).

DISCUSSION

In the current study, the expression of FTS and Notch signaling molecules (Notch 1 2, 3, cleaved Notch1 and Hes1) was

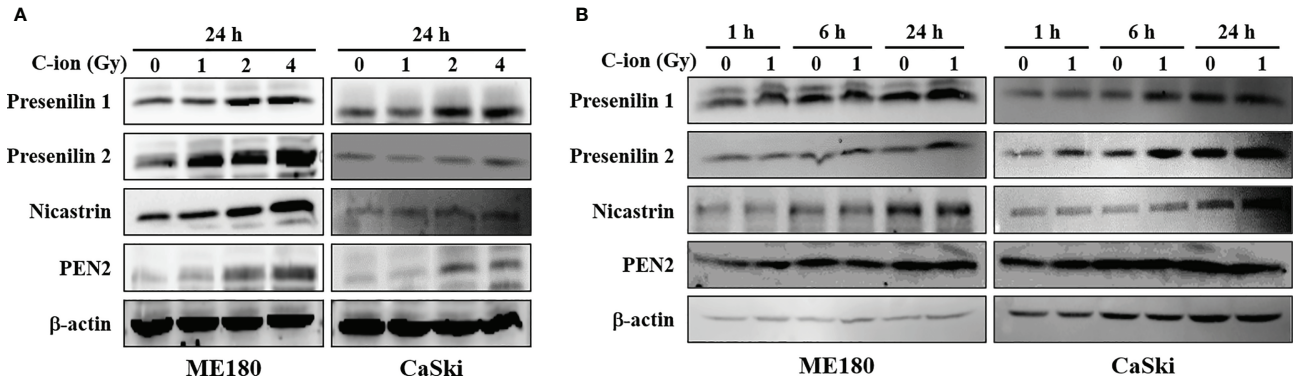

FIGURE 2 | The expression of γ-secretase complex proteins was upregulated by C-ion. The cells were irradiated with 0, 1, 2 and 4 Gy of C-ion and the protein expression was detected by western blotting 24 h post-irradiation **(A)** or the cells were irradiated with 0 and 1 Gy C-ion and the protein expression was measured after 1, 6 and 24 h post-irradiation **(B)**. The images shown are the representatives of at least three independent experiments.

upregulated, dose dependently, in response to C-ion in CaSki cells (**Figure 1** and **Supplementary Figure S2**). Additionally, upregulation of γ-secretase complex molecules (presenilin1, presenilin2, nicastrin and PEN2) was also observed in a radiation dose and time dependent manner (**Figure 2** and **Supplementary Figure S3**). The notch signaling pathway is well-known for its vital role in regulating cell division, differentiation, survival and maintenance of the CSC population in many human cancers, including cervical cancer (25, 29–32). RT awakens CSCs to lead tumor relapse and subsequent metastasis, although little is known about the underlying mechanism (33). The radioresistance of CSCs is governed by a few extrinsic factors (hypoxia, tumor microenvironment, etc.) and intrinsic factors (reactive oxygen species, DNA repair, apoptosis, autophagy, cell cycle status, etc.). Activation of Notch signaling leads to treatment failure after RT. Theys et al. reported that radiation induces upregulation of Notch signaling in non-small cell lung cancer (NSCLC) *in vitro* (34). Higher Notch signaling has been shown to accelerate tumor growth and increased radioresistance in NSCLC *in vivo* (35). Therefore, targeting the Notch signaling pathway could be an effective therapeutic approach to overcome radioresistance (11). The γ-secretase complex is a multi-subunit enzyme that plays an important role in the cleavage of intramembrane substrates of Notch receptors. The cleaved Notch1 is accountable for inducing the genomic functions of

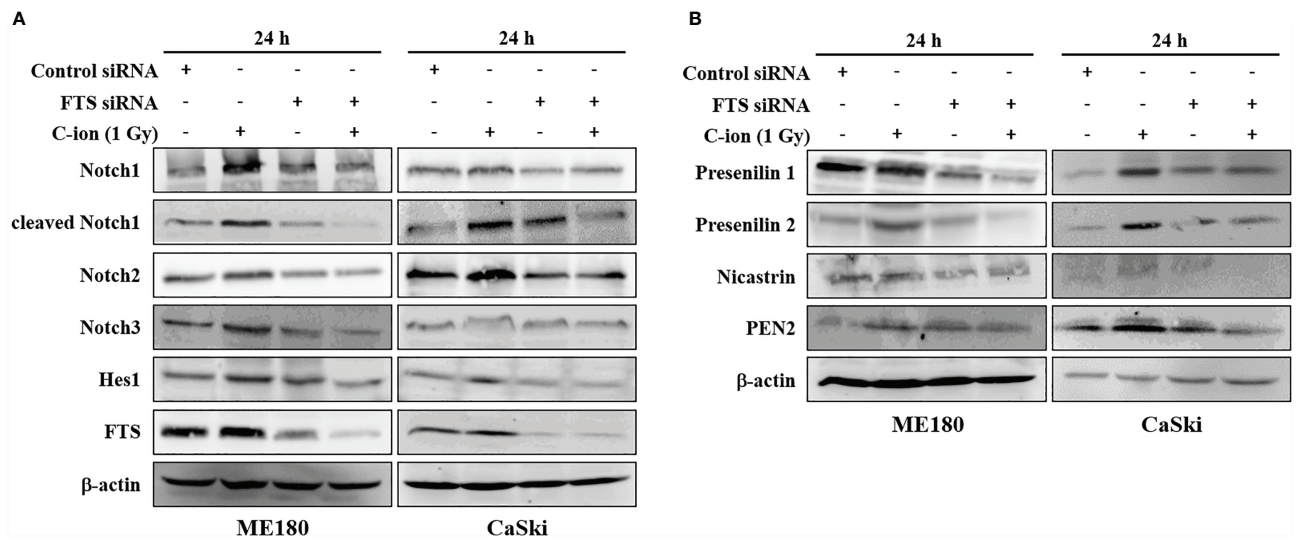

FIGURE 3 | FTS-silencing combined C-ion radiation targets the protein expression of Notch molecules **(A)** and γ-secretase complex **(B)**. ME180 and CaSki cells were transfected with scrambled siRNA or FTS siRNA. Cells were irradiated with C-ion 1 Gy and the protein expression was measured with immunoblot 24 h post-irradiation. The images shown in this figure are the representatives of at least three independent experiments.

Notch signaling. Inhibition of γ-secretase has been reported to enhance radiosensitivity *via* blocking the Notch signaling pathway (36). γ-Secretase inhibitors (GSIs) in combination with radiation may prevent up-regulation of the Notch receptor, ligand and other family members and consequently diminish the number of surviving CSCs (37). Therefore γ-secretase inhibitors are now being studied in many clinical trials against colorectal cancer, breast cancer, melanoma, glioma and lung cancer (37). This study observed that silencing of FTS alone or in combination with C-ion attenuated overexpression of Notch and γ-secretase complex molecules (**Figure 3** and **Supplementary Figure S4**).

In adherent cervical cancer cells FTS co-precipitated with Notch1/cleaved Notch1/Hes1, suggesting FTS molecular interaction with Notch molecules (**Figure 4A**). IF assay demonstrated FTS co-localization with Notch1/cleaved Notch1/Hes1 in both the cell lines. FTS silencing not only diminished their expression but also prominently reduced the co-localization (**Figures 4B–D**). The co-localization of Notch1/cleaved Notch/Hes1 and FTS spectacles the importance of FTS in mediating the Notch signaling in cervical cancer cells. We have previously identified putative residues involved in the interaction between FTS and Notch by *in silico* molecular docking (10), which further strengthens our IP and IF findings. CSCs are in a quiescent state in most of the established tumors. Their innate radioresistance helps them survive the radiation exposure more easily as compared to differentiated cancer cells. Recent evidences show that CSCs play a crucial role in recurrence and metastasis in many cancers after radiotherapy (33). It has been reported that following radiation, CSCs are enriched both *in vitro* and *in vivo*, indicating towards the possibility of radiation-induced generation of CSCs (38). Formation of spheroids is a hallmark of cancer stem cells, therefore in the present study, we evaluated spheroid formation in the cervical cancer cells and compared expression levels of Notch and its target protein Hes1, in addition to cancer stem cell markers. In this study, we report that 1 Gy C-ion does not affect the spheroid formation ability of ME180 and CaSki cells. Our finding is consistent with other reports, where sphere-type cells were found to be resistant to both x-rays and C-ion beams (39). Interestingly, FTS silencing alone or in combination with 1 Gy C-ion inhibited spheroid formation in both the cell lines; however, spheroid inhibition was more remarkable in ME180 cells (**Figures 5A, D**). Similarly, the cell viability of spheroids was unchanged with 1 Gy C-ion, but it was reduced by FTS silencing alone or in combination with C-ion (**Figure 5E**). Upregulation of SOX2 and OCT4A indicates radiation resistance in cervical cancer cells (40). The stem cell signaling molecules (Notch related) were overexpressed in cervical cancer adherent cells as a result of 1 Gy C-ion (**Figure 1**), but there was no change in the expression level of these molecules along with other cancer stem cell markers (Nanog, SOX2 and OCT4A) in the spheroid populations

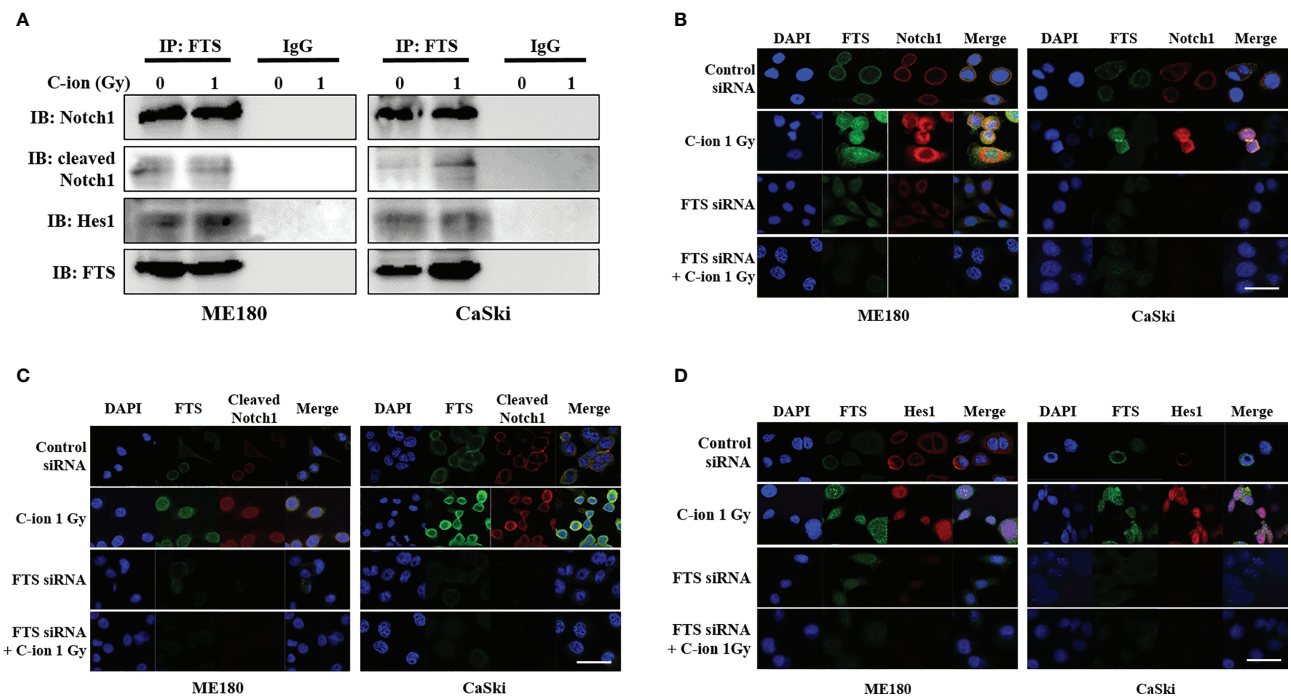

FIGURE 4 | Immunoprecipitation assay and immunofluorescence show the interaction between FTS and Notch1/cleaved Notch1/Hes1 in ME180 and CaSki cells. Cells were irradiated with 0 or 1 Gy C-ion and lysed after 24 h. Immunoprecipitation was performed with whole cell lysates using FTS antibody. IgG was used as negative control **(A)**. For immunofluorescence, the cells were grown in chamber slides. Cells were irradiated with 0 or 1 Gy C-ion. FTS was detected with Alexa Fluor 488 (green), whereas Notch1, cleaved Notch1 and Hes1 were detected using Alexa Fluor 594 (red), 24 h post-irradiation **(B–D)**. The images shown in this figure are the representatives of at least three independent experiments. White bar in each panel corresponds to 10 μm.

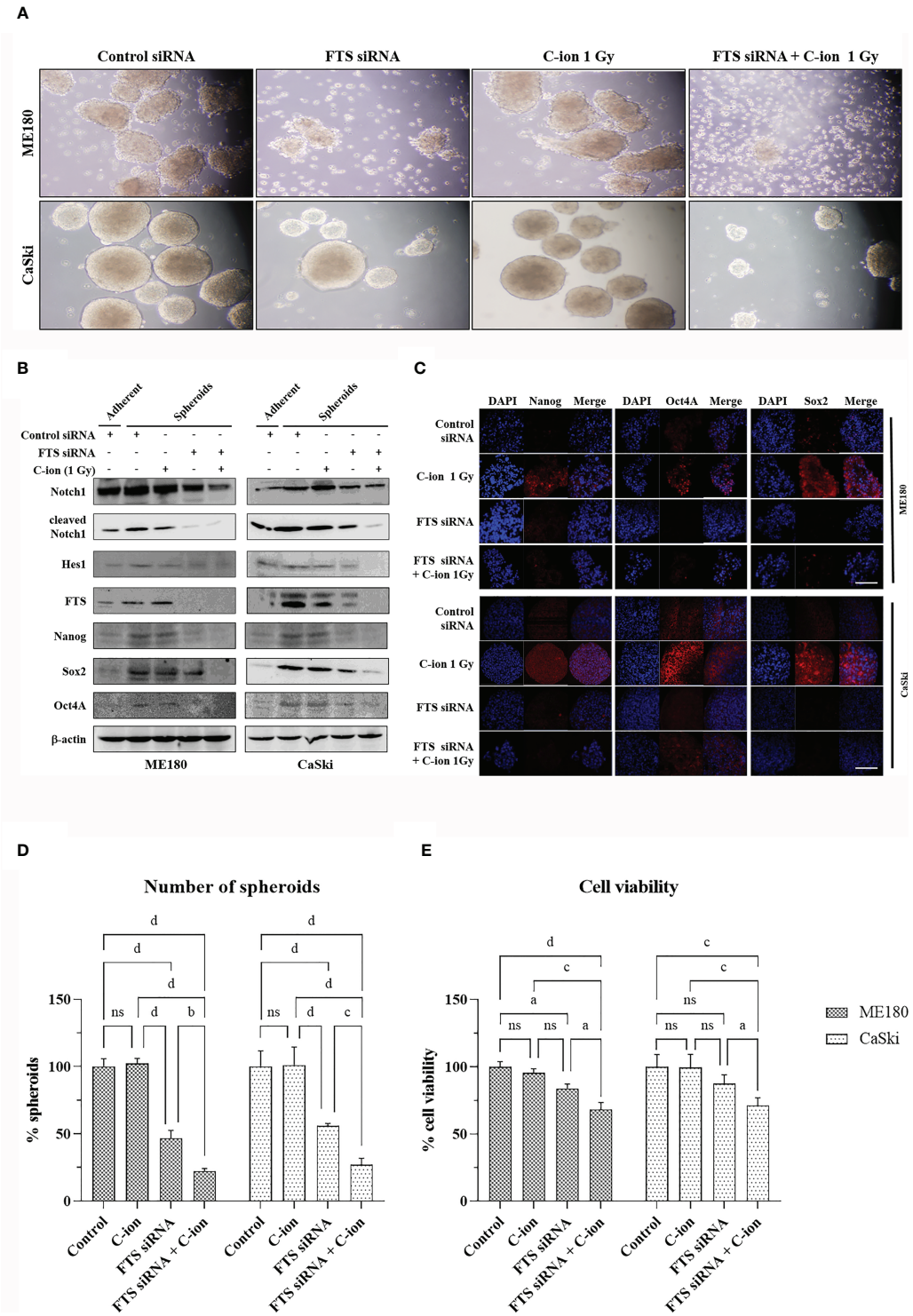

FIGURE 5 | FTS silencing combined with C-ion reduces spheroid formation and cancer stem cell markers in cervical cancer cells. FTS intact or silenced ME180 and CaSki cells were irradiated with 0 or 1 Gy of C-ion. Following irradiation, the cells were harvested and cultured in ultra-low attachment plates for seven days. Spheroid formation assay **(A)**. Western blots and immunofluorescence performed with the spheroids displaying the reduced expression of stem cell markers in the FTS silenced group **(B, C)**, white bar in each panel corresponds to 50 μm. **(D)** shows the mean number of spheroids from five randomly selected fields under the microscope in each treatment group. Bars represent normalized values against control group, error bars represent ± SD. **(E)** shows the viability of the spheroid forming cells in each treatment group. Bars represent normalized values against control group, error bars represent ± SD. P values of < 0.05 were considered statistically significant. a $p < 0.05$; b $p < 0.005$; c $p < 0.001$; d $p < 0.0001$; ns, not significant.

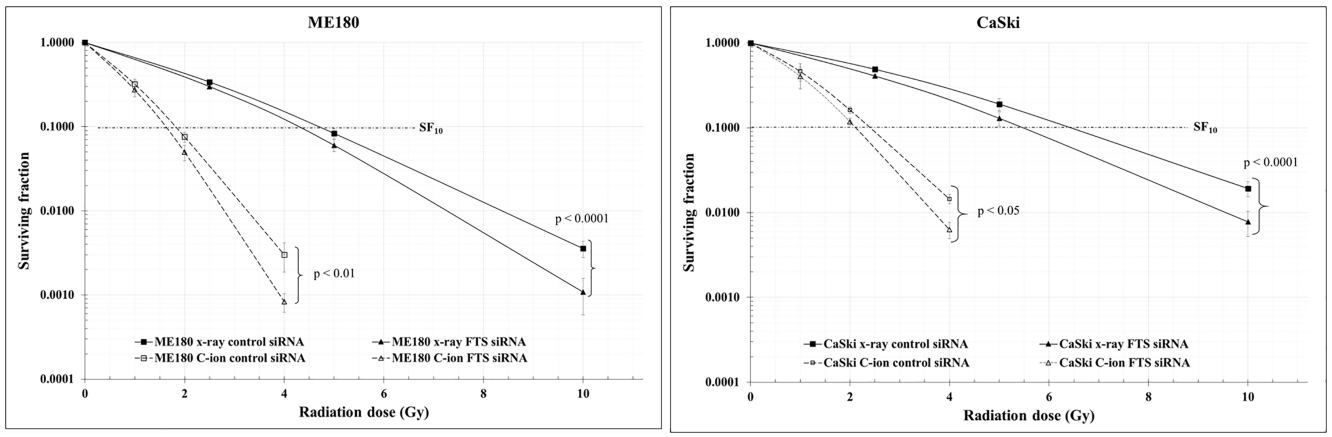

FIGURE 6 | Clonogenic cell survival was reduced by the combination of radiation with FTS silencing. Cells treated with scrambled siRNA or FTS siRNA were irradiated with C-ion (0, 1, 2 and 4 Gy) or x-rays (0, 2.5, 5 and 10 Gy). Following irradiation, the cells were trypsinized, harvested and seeded in triplicates, in appropriate cell densities in 60 mm dishes. The cells were allowed to grow for 7-8 days. Colonies with 50 or more cells were considered as survivors. The survival curves represent the mean of three independent experiments ± SD.

(**Figures 5B, C** and **Supplementary Figure S5**). Nonetheless, a significant attenuation of Notch molecules and cancer stem cell markers was observed upon FTS silencing, indicating a potential role of FTS in the cancer stem cell signaling pathway (**Figures 5B, C** and **Supplementary Figure S5**). We finally compared DMF at SF_{10} after irradiation with C-ion and x-ray in FTS intact and silenced cells. Both the cell lines exhibit significantly increased radiation sensitivity upon FTS silencing (ME180-x-ray: p value <0.0001, C-ion: p value <0.01; CaSki – x-ray: p value <0.0001; C-ion: p value <0.05). At SF_{10} doses of C-ion and x-ray (**Figure 6** and **Supplementary Figure S6, Supplementary Table T1**) a reduction of approximately 10% radiation dose was observed in the FTS silenced group. These findings suggest radiosensitization can be achieved both in C-ion and x-ray by FTS-silencing.

Although few reports on C-ion therapy show eradication of CSC in glioma/cancer (41), data pertaining to the Notch signaling pathway by C-ion therapy are not available. This is the first report to show that FTS silencing combined with C-ion targets the Notch signaling and reduces the spheroid formation, cancer stem cell markers and clonogenic survival in cervical cancer cells.

AUTHOR'S NOTE

PDS, PKC and W-YP performed the experiments described in this manuscript at NIRS, Japan, as visiting researchers.

DATA AVAILABILITY STATEMENT

The raw data supporting the conclusions of this article will be made available by the authors, without undue reservation.

AUTHOR CONTRIBUTIONS

PDS: conceptualization, methodology, investigation, writing - original draft. PKC: methodology, investigation, writing - review and editing. TS: project administration, resources, supervision. K-HK: writing - review and editing. W-YP: visualization, supervision, writing - review and editing, project administration, resources and funding acquisition. All authors contributed to the article and approved the submitted version.

FUNDING

This work was supported by the National Research Foundation of Korea (NRF-2016K1A3A7A09005582, 2018M7A1A1072274, 202011B36-04).

ACKNOWLEDGMENTS

We would like to thank Dr. Tsuyoshi Hamano and AEC support team for their technical support and the "Research Project with Heavy Ions at NIRS-HIMAC" for allowing us to use the HIMAC facility at NIRS, Japan.

SUPPLEMENTARY MATERIAL

The Supplementary Material for this article can be found online at: https://www.frontiersin.org/articles/10.3389/fonc.2021.730607/full#supplementary-material

REFERENCES

1. Sung H, Ferlay J, Siegel RL, Laversanne M, Soerjomataram I, Jemal A, et al. Global Cancer Statistics 2020: GLOBOCAN Estimates of Incidence and Mortality Worldwide for 36 Cancers in 185 Countries. *CA Cancer J Clin* (2021) 71(3):209–49. doi: 10.3322/caac.21660
2. Walboomers JM, Jacobs MV, Manos MM, Bosch FX, Kummer JA, Shah KV, et al. Human Papillomavirus Is a Necessary Cause of Invasive Cervical Cancer Worldwide. *J Pathol* (1999) 189(1):12–9. doi: 10.1002/(SICI)1096-9896(199909)189:1<12::AID-PATH431>3.0.CO;2-F
3. Yousif NG, Sadiq AM, Yousif MG, Al-Mudhafar RH, Al-Baghdadi JJ, Hadi N. Notch1 Ligand Signaling Pathway Activated in Cervical Cancer: Poor Prognosis With High-Level JAG1/Notch1. *Arch Gynecol Obstet* (2015) 292(4):899–904. doi: 10.1007/s00404-015-3694-1
4. Weijzen S, Zlobin A, Braid M, Miele L, Kast WM. HPV16 E6 and E7 Oncoproteins Regulate Notch-1 Expression and Cooperate to Induce Transformation. *J Cell Physiol* (2003) 194(3):356–62. doi: 10.1002/jcp.10217
5. Artavanis-Tsakonas S, Muskavitch MA. Notch: The Past, the Present, and the Future. *Curr Top Dev Biol* (2010) 92:1–29. doi: 10.1016/S0070-2153(10)92001-2
6. Miele L, Golde T, Osborne B. Notch Signaling in Cancer. *Curr Mol Med* (2006) 6(8):905–18. doi: 10.2174/156652406779010830
7. Blaumueller CM, Qi H, Zagouras P, Artavanis-Tsakonas S. Intracellular Cleavage of Notch Leads to a Heterodimeric Receptor on the Plasma Membrane. *Cell* (1997) 90(2):281–91. doi: 10.1016/S0092-8674(00)80336-0
8. Zhao Q, Mao A, Guo R, Zhang L, Yan J, Sun C, et al. Suppression of Radiation-Induced Migration of Non-Small Cell Lung Cancer Through Inhibition of Nrf2-Notch Axis. *Oncotarget* (2017) 8(22):36603–13. doi: 10.18632/oncotarget.16622
9. Koch U, Krause M, Baumann M. Cancer Stem Cells at the Crossroads of Current Cancer Therapy Failures–Radiation Oncology Perspective. *Semin Cancer Biol* (2010) 20(2):116–24. doi: 10.1016/j.semcancer.2010.02.003
10. Prabakaran DS, Muthusami S, Sivaraman T, Yu JR, Park WY. Silencing of FTS Increases Radiosensitivity by Blocking Radiation-Induced Notch1 Activation and Spheroid Formation in Cervical Cancer Cells. *Int J Biol Macromol* (2019) 126:1318–25. doi: 10.1016/j.ijbiomac.2018.09.114
11. Yahyanejad S, Theys J, Vooijs M. Targeting Notch to Overcome Radiation Resistance. *Oncotarget* (2016) 7(7):7610–28. doi: 10.18632/oncotarget.6714
12. Aggarwal G, Aggarwal SK. Evolution and Progress in the Application of Radiation in Cancer Diagnosis and Therapy. *Curr Sci* (2017) 113(3):413–21. doi: 10.18520/cs/v113/i03/413-421
13. Durante M, Orecchia R, Loeffler JS. Charged-Particle Therapy in Cancer: Clinical Uses and Future Perspectives. *Nat Rev Clin Oncol* (2017) 14(8):483–95. doi: 10.1038/nrclinonc.2017.30
14. Kamada T, Tsujii H, Blakely EA, Debus J, De Neve W, Durante M, et al. Carbon Ion Radiotherapy in Japan: An Assessment of 20 Years of Clinical Experience. *Lancet Oncol* (2015) 16(2):e93–e100. doi: 10.1016/S1470-2045(14)70412-7
15. Particle Therapy Co-Operative Group. *Statistics of Patients Treated in Particle Therapy 361 Facilities Worldwide*. Villigen (CH): PTCOG (2019). Available from: https://ptcog.ch/index.php/patient-statistics
16. Okonogi N, Wakatsuki M, Kato S, Shiba S, Kobayashi D, Kiyohara H, et al. Long-Term Outcomes of Carbon-Ion Radiotherapy for Locally Advanced Squamous Cell Carcinoma of the Uterine Cervix. *Anticancer Res* (2018) 38(1):457–63. doi: 10.21873/anticanres.12244
17. Sturdza A, Potter R, Fokdal LU, Haie-Meder C, Tan LT, Mazeron R, et al. Image Guided Brachytherapy in Locally Advanced Cervical Cancer: Improved Pelvic Control and Survival in RetroEMBRACE, a Multicenter Cohort Study. *Radiother Oncol* (2016) 120(3):428–33. doi: 10.1016/j.radonc.2016.03.011
18. Arnold CR, Mangesius J, Skvortsova II, Ganswindt U. The Role of Cancer Stem Cells in Radiation Resistance. *Front Oncol* (2020) 10:164. doi: 10.3389/fonc.2020.00164
19. Cui X, Oonishi K, Tsujii H, Yasuda T, Matsumoto Y, Furusawa Y, et al. Effects of Carbon Ion Beam on Putative Colon Cancer Stem Cells and Its Comparison With X-Rays. *Cancer Res* (2011) 71(10):3676–87. doi: 10.1158/0008-5472.CAN-10-2926
20. Sai S, Wakai T, Vares G, Yamada S, Kamijo T, Kamada T, et al. Combination of Carbon Ion Beam and Gemcitabine Causes Irreparable DNA Damage and Death of Radioresistant Pancreatic Cancer Stem-Like Cells *In Vitro* and In Vivo. *Oncotarget* (2015) 6(8):5517–35. doi: 10.18632/oncotarget.3584
21. Sai S, Vares G, Kim EH, Karasawa K, Wang B, Nenoi M, et al. Carbon Ion Beam Combined With Cisplatin Effectively Disrupts Triple Negative Breast Cancer Stem-Like Cells In Vitro. *Mol Cancer* (2015) 14:166. doi: 10.1186/s12943-015-0429-7
22. Sai S, Suzuki M, Kim EH, Hayashi M, Vares G, Yamamoto N, et al. Effects of Carbon Ion Beam Alone or in Combination With Cisplatin on Malignant Mesothelioma Cells In Vitro. *Oncotarget* (2018) 9(19):14849–61. doi: 10.18632/oncotarget.23756
23. Moncharmont C, Guy JB, Wozny AS, Gilormini M, Battiston-Montagne P, Ardail D, et al. Carbon Ion Irradiation Withstands Cancer Stem Cells' Migration/Invasion Process in Head and Neck Squamous Cell Carcinoma (HNSCC). *Oncotarget* (2016) 7(30):47738–49. doi: 10.18632/oncotarget.10281
24. Nakano T, Suzuki Y, Ohno T, Kato S, Suzuki M, Morita S, et al. Carbon Beam Therapy Overcomes the Radiation Resistance of Uterine Cervical Cancer Originating From Hypoxia. *Clin Cancer Res* (2006) 12(7 Pt 1):2185–90. doi: 10.1158/1078-0432.CCR-05-1907
25. Chang L, Graham P, Hao J, Ni J, Deng J, Bucci J, et al. Cancer Stem Cells and Signaling Pathways in Radioresistance. *Oncotarget* (2016) 7(10):11002–17. doi: 10.18632/oncotarget.6760
26. Bolst D, Tran LT, Guatelli S, Matsufuji N, Rosenfeld AB. Modelling the Biological Beamline at HIMAC Using Geant4. *J Physics: Conf Ser* (2019) 1154:012003. doi: 10.1088/1742-6596/1154/1/012003
27. Kanai T, Endo M, Minohara S, Miyahara N, Koyama-ito H, Tomura H, et al. Biophysical Characteristics of HIMAC Clinical Irradiation System for Heavy-Ion Radiation Therapy. *Int J Radiat Oncol Biol Phys* (1999) 44(1):201–10. doi: 10.1016/S0360-3016(98)00544-6
28. Kanai T, Kohno T, Minohara S, Sudou M, Takada E, Soga F, et al. Dosimetry and Measured Differential W Values of Air for Heavy Ions. *Radiat Res* (1993) 135(3):293–301. doi: 10.2307/3578867
29. Takebe N, Miele L, Harris PJ, Jeong W, Bando H, Kahn M, et al. Targeting Notch, Hedgehog, and Wnt Pathways in Cancer Stem Cells: Clinical Update. *Nat Rev Clin Oncol* (2015) 12(8):445–64. doi: 10.1038/nrclinonc.2015.61
30. Weng AP, Ferrando AA, Lee W, Morris J, Silverman LB, Sanchez-Irizarry C, et al. Activating Mutations of NOTCH1 in Human T Cell Acute Lymphoblastic Leukemia. *Science* (2004) 306(5694):269–71. doi: 10.1126/science.1102160
31. Pece S, Serresi M, Santolini E, Capra M, Hulleman E, Galimberti V, et al. Loss of Negative Regulation by Numb Over Notch Is Relevant to Human Breast Carcinogenesis. *J Cell Biol* (2004) 167(2):215–21. doi: 10.1083/jcb.200406140
32. Rodrigues C, Joy LR, Sachithanandan SP, Krishna S. Notch Signalling in Cervical Cancer. *Exp Cell Res* (2019) 385(2):111682. doi: 10.1016/j.yexcr.2019.111682
33. Liu Y, Yang M, Luo J, Zhou H. Radiotherapy Targeting Cancer Stem Cells "Awakens" Them to Induce Tumour Relapse and Metastasis in Oral Cancer. *Int J Oral Sci* (2020) 12(1):19. doi: 10.1038/s41368-020-00087-0
34. Theys J, Yahyanejad S, Habets R, Span P, Dubois L, Paesmans K, et al. High NOTCH Activity Induces Radiation Resistance in Non Small Cell Lung Cancer. *Radiother Oncol* (2013) 108(3):440–5. doi: 10.1016/j.radonc.2013.06.020
35. Kang J, Kim E, Kim W, Seong KM, Youn H, Kim JW, et al. Rhamnetin and Cirsiliol Induce Radiosensitization and Inhibition of Epithelial-Mesenchymal Transition (EMT) by miR-34a-Mediated Suppression of Notch-1 Expression in Non-Small Cell Lung Cancer Cell Lines. *J Biol Chem* (2013) 288(38):27343–57. doi: 10.1074/jbc.M113.490482
36. Lin J, Zhang XM, Yang JC, Ye YB, Luo SQ. Gamma-Secretase Inhibitor-I Enhances Radiosensitivity of Glioblastoma Cell Lines by Depleting CD133+ Tumor Cells. *Arch Med Res* (2010) 41(7):519–29. doi: 10.1016/j.arcmed.2010.10.006
37. Lagadec C, Vlashi E, Alhiyari Y, Phillips TM, Bochkur Dratver M, Pajonk F. Radiation-Induced Notch Signaling in Breast Cancer Stem Cells. *Int J Radiat Oncol Biol Phys* (2013) 87(3):609–18. doi: 10.1016/j.ijrobp.2013.06.2064
38. Wang L, Huang X, Zheng X, Wang X, Li S, Zhang L, et al. Enrichment of Prostate Cancer Stem-Like Cells From Human Prostate Cancer Cell Lines by Culture in Serum-Free Medium and Chemoradiotherapy. *Int J Biol Sci* (2013) 9(5):472–9. doi: 10.7150/ijbs.5855
39. Bertrand G, Maalouf M, Boivin A, Battiston-Montagne P, Beuve M, Levy A, et al. Targeting Head and Neck Cancer Stem Cells to Overcome Resistance to Photon and Carbon Ion Radiation. *Stem Cell Rev Rep* (2014) 10(1):114–26. doi: 10.1007/s12015-013-9467-y

40. Shen L, Huang X, Xie X, Su J, Yuan J, Chen X. High Expression of SOX2 and OCT4 Indicates Radiation Resistance and an Independent Negative Prognosis in Cervical Squamous Cell Carcinoma. *J Histochem Cytochem* (2014) 62 (7):499–509. doi: 10.1369/0022155414532654
41. Chiblak S, Tang Z, Lemke D, Knoll M, Dokic I, Warta R, et al. Carbon Irradiation Overcomes Glioma Radioresistance by Eradicating Stem Cells and Forming an Antiangiogenic and Immunopermissive Niche. *JCI Insight* (2019) 4(2):123837. doi: 10.1172/jci.insight.123837

Conflict of Interest: The authors declare that the research was conducted in the absence of any commercial or financial relationships that could be construed as a potential conflict of interest.

Publisher's Note: All claims expressed in this article are solely those of the authors and do not necessarily represent those of their affiliated organizations, or those of the publisher, the editors and the reviewers. Any product that may be evaluated in this article, or claim that may be made by its manufacturer, is not guaranteed or endorsed by the publisher.

frontiers in Oncology

ORIGINAL RESEARCH
published: 23 November 2021
doi: 10.3389/fonc.2021.768493

High-LET Carbon and Iron Ions Elicit a Prolonged and Amplified p53 Signaling and Inflammatory Response Compared to low-LET X-Rays in Human Peripheral Blood Mononuclear Cells

Ellina Macaeva[1,2,3], *Kevin Tabury*[1,4], *Arlette Michaux*[1], *Ann Janssen*[1], *Nicole Averbeck*[5], *Marjan Moreels*[1], *Winnok H. De Vos*[6], *Sarah Baatout*[1,2] *and Roel Quintens*[1]*

[1] Radiobiology Unit, Studiecentrum voor kernenergie - Centre d'étude de l'énergie nucléaire (SCK CEN), Mol, Belgium, [2] Department of Molecular Biotechnology, Ghent University, Ghent, Belgium, [3] Department of Oncology, KU Leuven, Leuven, Belgium, [4] Department of Biomedical Engineering, University of South Carolina, Columbia, SC, United States, [5] Department of Biophysics, GSI Helmholtzzentrum für Schwerionenforschung, Darmstadt, Germany, [6] Department of Veterinary Sciences, University of Antwerp, Antwerp, Belgium

OPEN ACCESS

Edited by:
Pankaj Chaudhary, Queen's University Belfast, United Kingdom

Reviewed by:
Giuseppe Schettino, National Physical Laboratory, United Kingdom
Orla Linda Howe, Technological University Dublin, Ireland

***Correspondence:**
Roel Quintens
roel.quintens@sckcen.be

Specialty section:
This article was submitted to Radiation Oncology, a section of the journal Frontiers in Oncology

Received: *31 August 2021*
Accepted: *01 November 2021*
Published: *23 November 2021*

Citation:
Macaeva E, Tabury K, Michaux A, Janssen A, Averbeck N, Moreels M, De Vos WH, Baatout S and Quintens R (2021) High-LET Carbon and Iron Ions Elicit a Prolonged and Amplified p53 Signaling and Inflammatory Response Compared to low-LET X-Rays in Human Peripheral Blood Mononuclear Cells. Front. Oncol. 11:768493. doi: 10.3389/fonc.2021.768493

Understanding the differences in biological response to photon and particle radiation is important for optimal exploitation of particle therapy for cancer patients, as well as for the adequate application of radiation protection measures for astronauts. To address this need, we compared the transcriptional profiles of isolated peripheral blood mononuclear cells 8 h after exposure to 1 Gy of X-rays, carbon ions or iron ions with those of non-irradiated cells using microarray technology. All genes that were found differentially expressed in response to either radiation type were up-regulated and predominantly controlled by p53. Quantitative PCR of selected genes revealed a significantly higher up-regulation 24 h after exposure to heavy ions as compared to X-rays, indicating their prolonged activation. This coincided with increased residual DNA damage as evidenced by quantitative γH2AX foci analysis. Furthermore, despite the converging p53 signature between radiation types, specific gene sets related to the immune response were significantly enriched in up-regulated genes following irradiation with heavy ions. In addition, irradiation, and in particular exposure to carbon ions, promoted transcript variation. Differences in basal and iron ion exposure-induced expression of DNA repair genes allowed the identification of a donor with distinct DNA repair profile. This suggests that gene signatures may serve as a sensitive indicator of individual DNA damage repair capacity. In conclusion, we have shown that photon and particle irradiation induce similar transcriptional pathways, albeit with variable amplitude and timing, but also elicit radiation type-specific responses that may have implications for cancer progression and treatment

Keywords: ionizing radiation, gene expression, DNA damage, X-rays, heavy ions, p53, alternative splicing, immunity

INTRODUCTION

The use of charged particles is a promising modality in cancer therapy. Particle therapy, which uses focused beams of charged particles such as protons and carbon ions, has become the treatment of choice for targeting specific solid tumors (1, 2), which plays an important role in tumor management particularly in pediatric patients (3). The main advantage of charged particle beams is the possibility to target the tumor more precisely, while the surrounding healthy tissues receive a lower dose as compared to conventional photon radiotherapy (4). This reduces the chance of secondary cancer development (5) and impairment of the immune system (6). However, high linear energy transfer (LET) radiation, like for instance carbon ions, has a higher relative biological effectiveness (RBE) compared to conventional low-LET photon therapy (7), as particles deposit their energy in a more focused manner and therefore result in more complex clustered DNA damage which is more lethal to the tumor cells (8) but may also affect the healthy tissue. Moreover, high-LET radiation is also characterized by higher RBE in terms of other endpoints, such as chromosome aberrations, genetic alterations and normal tissue damage (9). Normal tissue damage is a complex process, which is not solely caused by cell death (10). Radiation-induced DNA damage also triggers changes in chemokine and cytokine production, cell-cell interactions, influx of inflammatory cells and the induction of restorative processes in healthy tissues (11). Genes involved in DNA damage repair, apoptosis, proliferation and inflammatory processes therefore also play a role in the normal tissue response to irradiation (12).

A second important field where charged particles are of relevance is human space exploration. The more feasible and realistic long-term and interplanetary space missions and commercial space flights will become, the more concern they will raise about possible health risks due to exposure to cosmic radiation (13). Astronauts in deep space are subjected to galactic cosmic rays (GCR) and solar particle events (SPE), which result in levels of radiation hundreds of times higher than on Earth. The GCR spectrum is composed of about 87% high energy protons, 12% alpha-particles and 1% of heavier ions up to iron (HZE particles) (14) which are extremely penetrating and difficult to shield (15). Though the HZE particles are less abundant, they possess significantly higher ionizing power with a greater potential for radiation induced damage and, consequently, health effects (16). SPE consist of low to medium energy protons and alpha-particles. Up to now, the assessment of radiation risk for astronauts is almost completely based on extrapolation from epidemiological data on low-LET exposures. Therefore, comprehensive models and radiobiological studies comparing the biological response to different radiation types are needed to validate this approach (17).

The particles and energies which are most often used for particle therapy partially overlap with the lower range of charge and energies (Z=1-26 and approximately 100-1000 MeV/nucleon) of the ions that constitute cosmic radiation. Although the exposure conditions (low *vs*. high doses, low *vs*. high dose rates, whole body *vs*. partial body exposure) and relevant biological endpoints (cancer induction *vs*. tumor cell killing) are different in space and during particle therapy treatment, it is well accepted that a substantial overlap exists in several research topics, e.g. individual radiosensitivity, late stochastic effects such as cancer induction (18, 19) and modulation of the immune system (20). Understanding the cellular radiation response and the processes governing individual sensitivity to high-LET radiation is of pivotal importance in rational choice of radiotherapy treatment schemes. The same holds true for the risk assessment of astronauts and the development of effective protection measures.

Radiobiological transcriptional studies can offer valuable insight in this regard, revealing the biological basis of the cellular response to different radiation types (21, 22). Peripheral blood is an easily-accessible biological sample which allows minimally invasive testing. Furthermore, blood cells are continuously exposed to radiation during radiotherapy and are often used as a surrogate tissue for damage-based radiation biodosimentry and normal tissue radiation sensitivity assessment (23). However, to date, there have been only a limited number of studies comparing gene expression profiles following exposure to low- and high-LET radiation in human peripheral blood cells exposed *in vitro* to α-particles and X-rays (24), neutrons and X-rays (25), mixed-field neutron/X-rays (26, 27), or mouse blood cells exposed *in vivo* to neutrons and X-rays (28).

To add to the knowledge of the cellular response to low- and high-LET radiation, we compared in this study the transcriptional profiles of peripheral blood mononuclear cells (PBMCs) from healthy donors after the cells had been exposed to X-rays, carbon ions or iron ions. We identified specific biological processes that were induced by exposure to heavy ions or X-rays, as well as processes shared by both types of radiation. Our results provide an important basis for further detailed investigation of the differential cellular and tissue response to high- and low-LET radiation.

MATERIALS AND METHODS

In the present study two aspects of biological response to radiation exposure were assessed: gene expression changes (using microarray technology with further qRT-PCR validation) and DNA damage repair (using γH2AX immunofluorescent staining). Irradiations were performed at SCK CEN, Belgium (X-rays) and at GSI Helmholtzzentrum für Schwerionenforschung (abbreviated GSI), Germany (X-rays, iron and carbon ions). Blood samples were collected on three different days, corresponding to three microarray experiments: X-rays (10 donors), carbon (7 donors) and iron ion irradiation (6 donors). The exact number of samples used for every assay is indicated in **Figure 1**, not all the samples could be used for all the assays due to insufficient RNA quality or insufficient number of cells to run all the assays. Matched samples were used for iron ion experiment only. **Figure 1** gives an overview of experimental conditions and number of samples used for every assay. Detailed description of all experimental procedures is given below.

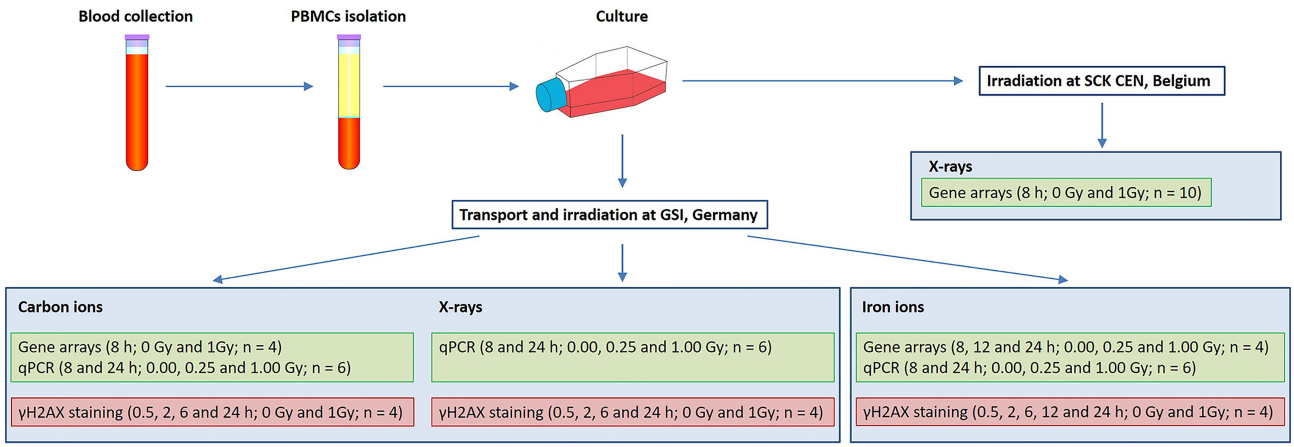

FIGURE 1 | Experimental setup. Samples listed in the same blue box were irradiated in parallel.

Blood Collection and PBMCs Isolation

Peripheral blood samples were collected from healthy donors in 9 ml EDTA vacutainer tubes. Blood collection was approved by the local SCK CEN Ethics Committee and was carried out in accordance with the ethical standards of the Helsinki Declaration of 1975, as revised in 2000. Prior to blood donation all the donors involved in the present study signed an informed consent form. Within 30-60 min of blood drawing, PBMCs were isolated by centrifugation on Histopaque-1077 density gradient (Sigma-Aldrich, Bornem, Belgium) according to the manufacturer's instructions. Isolated cells were suspended at a density of 10^6 cells/ml in LGM-3 culture medium (Lonza, Walkersville, MD, USA) and were allowed to equilibrate to culture conditions at 37°C in a humidified 5% CO_2 atmosphere.

Cell Cultures

Three human lymphoblastoid cell lines TK6, WTK1 and NH32 were used in this study. TK6 cell line was purchased from DSMZ, Leibniz-Institute, Braunschweig, Germany, while WTK1 and NH32 cells were a generous gift from the laboratory of Prof Schwartz, University of Washington. All three cell lines have the same progenitor, WIL2 cell line (29). The TK6 cells express wild-type p53, while WTK1 cells overexpress a mutant form of p53 due to methionine to isoleucine substitution at codon 237 and no wild-type p53 protein (30). The NH32 cell line is genetically homologous to TK6, but its *TP53* gene has been genetically inactivated by a homozygous knockout (31). Cell lines were maintained as exponentially growing stationary cultures in RPMI-1640 medium supplemented with 10% heat-inactivated foetal bovine serum at 37°C in 5% CO_2 at densities of 4–10 × 10^5 cells/ml. Cell line irradiations were performed in three replicates (1 × 10^6 cells per sample) as described below. Following irradiations cells were incubated at standard conditions for 24 h prior to RNA extraction.

In Vitro Irradiation

X-ray, carbon and iron ion irradiations were performed independently, on different days. X-ray irradiation experiments were performed at the irradiation facility at SCK CEN, Belgian Nuclear Research Centre, Mol, Belgium (for microarrays) and at GSI, Darmstadt, Germany (for qRT-PCR validation and γH2AX staining). At SCK CEN, PBMCs were exposed to 1.00 Gy of X-rays, using a Pantak HF420RX machine (250 kV, 15 mA, dose rate of 0.26 Gy/min). Cells were irradiated "free-in-air" at 21°C in a horizontal position with single doses of 0.1 and 1.0 Gy of X-rays from a Pantak HF420 RX generator at an air kerma (K_{air}) rate of 0.26 Gy/min or were sham-irradiated. The beam quality can be approximated to H-250 (ISO4037): 250 kV, 15 mA, 1.2 mm Al equivalent inherent filtration and 1 mm Cu additional filtration. First HVL was 2.43 mm Cu and the second HVL was 3.52 mm Cu. The K_{air} at the reference position was measured using a NE2571 ionization chamber (SN309) connected to a Farmer 2500 electrometer. The chamber, together with the electrometer, was calibrated in terms of K_{air} and the traceability to the international standards was assured. The reference point of the ionization chamber was placed at the same distance with the reference position of the samples. The ionization chamber was always placed in the beam, next to the samples, for a precise measurement of the time integrated K_{air}. The stability of the X-ray generator during the irradiation was verified in this way using a monitor chamber. Cell line samples were exposed to 1.00 and 3.00 Gy at SCK CEN following the same procedures. For samples that were irradiated at GSI, freshly isolated PBMCs were transported for 4 h by car to GSI using a transportable incubator. X-ray exposures at GSI were performed using an IV320-13 X-ray tube (250 keV, 16 mA, dose rate of 0.5 Gy/min; Seifert, Germany) at 0.25 and 1.00 Gy. Irradiation with heavy ions was performed at GSI on the heavy-ion synchrotron SIS. Carbon ion exposure (0.25 and 1.00 Gy) was performed in the middle of a 25 mm spread-out Bragg peak (center depth 42.5 mm, realized with a PMMA bolus), obtained by active energy variation of the beam in the range of 114.6 – 158.4 MeV/nucleon. Accordingly, the dose averaged LET at the proximal and distal part of the samples (5-ml plastic tube, inside diameter 10 mm) was 60-80 keV/μm. Irradiation with iron ions (0.25 and 1.00 Gy) was performed with a monoenergetic beam (1 GeV/nucleon;

LET 155 keV/μm). The beam monitor calibration was performed according to the procedure described by Luoni et al. (32). For verification of the applied dose, additional absolute dosimetry was performed by measuring the absorbed dose to water using a PTW TM30013 Farmer ionization chamber positioned at the sample depth. The dose-averaged LET was calculated using the TRiP98 treatment planning system (33). Sham-irradiated samples were always subjected to the same procedures as the irradiated ones, except for the radiation exposure itself. After *in vitro* irradiation, cells were incubated at 37°C in a humidified 5% CO_2 atmosphere for the indicated time until further processing.

RNA Extraction

For RNA isolation, a combination of the TRIzol® reagent (Invitrogen, Carlsbad, CA, USA) extraction method and the clean-up on Qiagen RNeasy columns (Qiagen, Venlo, The Netherlands) was used. Briefly, 5 x 10^6 cells were lysed in 1 ml of TRIzol® reagent and further processed following the manufacturer's recommendations. Following the RNA precipitation with isopropanol, the obtained pellet was re-suspended in 1 ml of ethanol and transferred to the RNeasy column. Further purification was done according to the manufacturer's instructions. RNA concentration was measured on a NanoDrop-2000 spectrophotometer (Thermo Scientific, Erembodegem, Belgium) and the quality of total RNA samples was assessed using Agilent 2100 Bioanalyzer (Agilent Technologies, Santa Clara, CA, USA). Only samples with an RNA integrity number >7 were considered as suitable for further microarray hybridization. RNA extraction from cell line samples was performed following the same procedures.

Microarray Hybridization

Gene expression profiling was performed using the GeneChip® Human Gene 1.0 ST Array (Affymetrix, Santa Clara, CA, USA) which interrogates 28,536 well-annotated genes with 253,002 distinct probe sets, allowing expression analysis at both gene and exon level. Ten μg of cRNA, synthesized and purified from 0.25 μg of total RNA using the Ambion® WT Expression kit (Ambion, USA) was used for cDNA synthesis, followed by cDNA fragmentation and labeling with the GeneChip® Terminal Labeling kit (Affymetrix). Fragmented and labeled cDNA was hybridized to Human Gene 1.0 ST arrays (Affymetrix) using the GeneChip® Hybridization, Wash and Stain kit (Affymetrix) (hybridization module) and hybridization controls (Affymetrix) with rotation at 45°C for 16 hours. After hybridization, arrays were washed and stained using the GeneChip® Hybridization, Wash and Stain kit (stain module) after which the arrays were immediately scanned using an Affymetrix GeneChip® Scanner. Raw data of X-ray and heavy ion experiments have been submitted to the ArrayExpress database under accession numbers E-MTAB-3463 and E-MTAB-5761, respectively.

Microarray Data Analysis

The obtained microarray data were imported into Partek Genomics Suite, version 6.6 (Partek Inc., St Louis, MO, USA) as.CEL-files. The probe summarization and probe set normalization were done using the Robust Multichip Analysis (RMA) algorithm (34) which includes background correction, quantile normalization and $\log_2$ transformation. Microarray data were analyzed using ANOVA with dose, donor and time point (whenever applicable) as factors. To correct for multiple testing, we used the false discovery rate (FDR) as described by Benjamini and Hochberg (35) to adjust *p*-values (FDR < 0.05). Genes were considered significantly differentially expressed between the two groups if adjusted *p*-values were < 0.05. In some cases, a more stringent additional cut-off of fold-change ≥| 2| was used, as explained in the text.

We also performed Alternative Splicing ANOVA in Partek to detect genes which were alternatively spliced in response to different radiation types. An FDR-corrected *p*-value of < 0.05 was considered significant for alternative splicing events. To further reduce the number of false positives, the probe sets with $\log_2$ values below the noise level in all samples were excluded from analysis, except for the cases where there was a significant difference in expression of a single exon between the groups ($p < 0.05$).

The Venny on-line tool (36) was used to compare gene lists and create Venn diagrams: http://bioinfogp.cnb.csic.es/tools/venny/index.html.

Reverse Transcription and qRT-PCR

The following genes were selected for qRT-PCR validation: *PCNA, GADD45A, RPS27L, ASTN2, NDUFAF6, FDXR, MAMDC4*. The same RNA samples as those used for microarray hybridization plus two additional samples irradiated on the same day but not selected for microarray hybridization (n=6), were used for cDNA synthesis with the GoScript™ Reverse Transcription System (Promega, Leiden, The Netherlands) with random hexamer primers. For each gene, qRT-PCR reactions were run in duplicate using the MESA GREEN® qRT-PCR kit (Eurogentec, Seraing, Belgium) on an Applied Biosystems® 7500 Real-Time PCR instrument following the manufacturer's instructions. To determine the efficiency and specificity of the designed primers, a standard curve experiment with melt curve was run for every primer pair. qRT-PCR data were analyzed by 7500 Software v2.0.6 and Microsoft Excel using the Pfaffl method (37). The relative amount of transcript of the selected genes was normalized to *PGK1* and *HPRT1* using the geometric mean of these reference genes (38). cDNA synthesis and qRT-PCR of the cell line samples was performed following identical procedures for the following genes: *EDA2R*, *NDUFAF6*, *PTPN14* and *VWCE*. All primer sequences can be found in **Supplementary Table 1**.

Rank-Rank Hypergeometric Overlap (RRHO) Analysis

The RRHO algorithm allows for the comparison of two microarray datasets. Each dataset is processed as a ranked list based on expression differences between two classes of samples (0 Gy and 1 Gy, in our case). RRHO analysis (39) was performed using the online tool (http://systems.crump.ucla.edu/rankrank/index.php). As this algorithm only allows the comparison of two gene lists at a time, the following comparisons were performed: X-rays *vs* carbon ions, X-rays *vs* iron ions and carbon ions *vs* iron ions using a step size of 100.

Transcription Factor and Gene Ontology Terms Enrichment Analysis

Transcription factor and Gene Ontology terms enrichment analysis was performed using the Enrichr online tool (http://amp.pharm.mssm.edu/Enrichr/) (40, 41) which uses input gene lists to calculate enrichment of genes based on different databases of chromatin immunoprecipitation experiments and Ontologies. We used the "ENCODE and ChEA Consensus TFs from ChIP-X" and "GO Biological Process 2015" databases to calculate enrichment of transcription factor binding and biological processes, respectively, in significantly differentially expressed genes. The same tool was used to calculate enrichment of GO biological processes terms in significantly alternatively spliced genes.

Gene Set Enrichment Analysis (GSEA)

Gene set enrichment analysis (42) was performed using default settings: the significance of the normalized enrichment score for each gene set was assessed through 1000 gene set permutations. Gene sets with an FDR q-value < 0.25 were considered significant, as suggested by the GSEA tutorial. For each radiation type, 1-Gy and sham-irradiated samples analyzed at 8 h after exposure were used for comparison. To have a general view of response to each radiation type, Hallmark Gene Sets collection of the Molecular Signatures Database was used. This collection consists of 50 gene sets representing specific well-defined biological states and processes, which helps to reduce noise and redundancy in different available databases and provides a better delineated biological space for GSEA.

γH2AX Foci Detection Using Fluorescent Microscopy

PBMCs from four donors were fixed in 4% paraformaldehyde (Merck KGaA, Darmstadt, Germany) at several time points (see **Figure 1**). Following the fixation step, cells were cytospun on glass slides using Shandon™ EZ Double Cytofunnels™ and permeabilized with 0.25% Triton X 100 (Sigma Aldrich, Belgium) for 5 min, blocked with 3% bovine serum albumin (Sigma Aldrich, Belgium) for 30 min and incubated overnight at room temperature with monoclonal mouse anti-γH2AX (phospho S139) antibody [3F2] (ab22551, Abcam, Cambridge, MA, USA) at 4°C. Cells were then incubated for 1 h with polyclonal goat anti-mouse secondary antibody coupled to FITC (F2012, Sigma Aldrich, Belgium) at 37°C and then mounted in Vectashield mounting medium containing DAPI (Vector Laboratories, Burlingame, CA, USA). Between each of the previous steps, the slides were washed with phosphate-buffered saline.

An automated inverted fluorescence microscope (Eclipse Ti, Nikon, Tokyo, Japan), equipped with a motorized XYZ stage was used for image acquisition of immunostained slides. Images were acquired with a 40X Plan Fluor oil objective (Numerical aperture 1.3) and an Andor iXon3 camera (Andor Technology, South Windsor, CT, USA), providing images with a lateral resolution of 0.2 μm/pixel. For each sample, 25 fields were acquired on 7 Z-planes (separated by 1 μm). The obtained images were analyzed with the CellBlocks.ijm script (43), written for FIJI image analysis freeware (44), essentially as described before (45). In brief, the image analysis workflow starts by segmenting each nucleus in the DAPI channel, using an automatic thresholding algorithm, after noise reduction and flat field correction. Subsequently, γH2AX foci signals are selectively enhanced by means of a multiscale Laplacian and segmented by means of automatic thresholding. Within each nucleus, the intensity of the γH2AX channel is measured along with the number of γH2AX foci and the foci occupancy, *i.e.*, the total projected area of the nucleus that is occupied by spots (total spot area divided by the nucleus area). On average, 500 nuclei were analyzed per sample.

RESULTS

Gene Level Transcriptome Analysis Shows a Common p53-Regulated Gene Expression Signature After Low- and High-LET Irradiation

To compare the effects of high- and low-LET radiation exposure on gene expression in human PBMCs, microarray analysis was performed at 8 h after exposure to 1 Gy of X-rays, carbon ions or iron ions. This time point was chosen because we observed a prominent gene expression response after 8 h in our previous studies (46, 47), moreover we found that prolonged culturing times trigger activation of apoptosis-related genes also in control samples, which might complicate data interpretation (48). We also observed dose-dependent gene expression up-regulation for doses ranging from 0.025 to 2.00 Gy, however, following 2.00 Gy exposure a clear saturation of the effect was observed (48), therefore in this study we opted for using 1 Gy for all PBMCs exposures. Following the exposure to X-rays, carbon ions or iron ions, 69, 95 and 78 genes, respectively, were detected as differentially expressed (FDR-corrected $p < 0.05$) compared to control samples (**Figures 2A–E** and **Supplementary Tables 2–4**). The majority of these genes were induced after irradiation (**Figures 2A–E**), including 30 genes that were differentially expressed in response to all radiation types. Of these, 14 genes were up-regulated more than 2-fold (**Figure 2E**). The lists of genes differentially expressed exclusively following the exposure to X-rays, carbon or iron ions can be found in **Supplementary Tables 2–4**, respectively.

When comparing two independent high-throughput gene expression experiments with different sample numbers, threshold-free methods outperform threshold-based ones in providing reliable results (39). Thus, to obtain a better impression of the similarity in gene expression after exposure to different radiation types, the Rank-rank Hypergeometric Overlap algorithm was used. This revealed a very significant degree of overlap among the genes up-regulated in both conditions (shown in the top right corner of the heatmap) for the comparisons between X-rays and carbon ions (47 overlapping genes, lowest $p \approx 10^{-56}$) (**Figure 2F**) as well as X-rays and iron ions (59 overlapping genes, lowest $p \approx 10^{-65}$) (**Figure 2G**). However, for the comparison between the two high-LET ions (**Figure 2H**) the degree of overlap was much more significant (1715 overlapping genes, lowest $p \approx 10^{-146}$). Together, our data show that irrespective of the radiation type, the majority of the affected genes are up-regulated after exposure, and that the identity of these genes is highly similar, although some radiation type-specific genes do seem to exist.

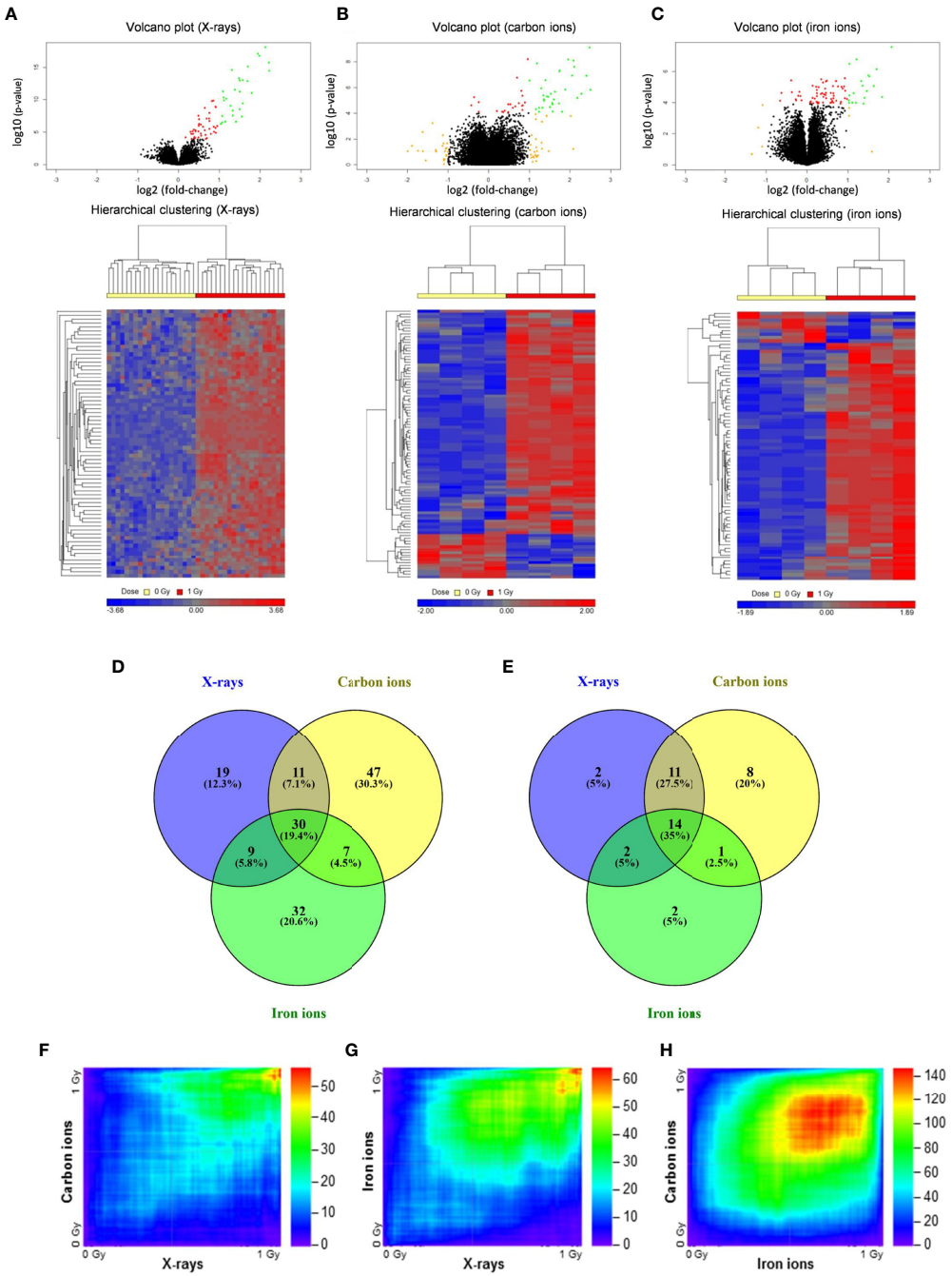

FIGURE 2 | Changes in gene expression in PBMCs after exposure to X-rays, carbon ions and iron ions. **(A–C)** Volcano plots and heatmaps of gene expression changes between controls and cells irradiated with X-rays **(A)**, carbon ions **(B)** or iron ions **(C)** at 8 h after exposure. Red points on volcano plots indicate genes with FDR <0.05, orange points indicate genes with |FC| >2 and green points indicate genes with FDR <0.05 and |FC| >2. Heatmaps show expression profiles of differentially expressed genes with an FDR <0.05. **(D, E)** Venn diagrams showing overlap in differentially expressed genes with FDR <0.05 **(D)** or FDR <0.05 and |FC| >2 **(E)** between the different radiation types. **(F–H)** Rank-rank hypergeometric overlap heatmaps indicating overlap in gene expression changes between X-rays and carbon ions **(F)**, between X-rays and iron ions **(G)**, and between carbon ions and iron ions **(H)**. Color scale bars indicate the $\log_{10}$-transformed hypergeometric *p*-values.

Transcription factor enrichment analysis suggested that, for all radiation types, the affected genes were transcriptionally regulated by p53 (**Figure 3**, left panel), and they were enriched in functions related to canonical p53-dependent pathways such as response to (ultra violet) radiation, negative regulation of the cell cycle, DNA repair and apoptosis (**Figure 3**, right panel).

The list of p53 targets is constantly growing and it remains probably the most studied transcription factor. There are at least

350 confirmed p53 targets and over 3500 potential targets (49). To confirm the p53-dependent activation of some of the significantly up-regulated genes, three lymphoblastoid cell lines with different p53 status were irradiated with different doses of X-rays (0 Gy, 1 Gy and 3 Gy). qRT-PCR was performed to measure gene expression of selected hits *EDA2R*, *NDUFAF6*, *PTPN14* and *VWCE*, all of which were induced after X-ray, carbon and iron irradiation. *EDA2R* is a well-known *bona fide* p53 target (50), while PTPN14 has been recently identified as such (51). *VWCE* is often found in genome-wide data sets of activated p53 targets (49). *NDUFAF6* has not yet been validated as a direct p53 target gene, but was identified to be radiation-responsive in our previous study (47). In TK6 cells, which have wild-type p53, we observed a significant, dose-dependent induction of all four genes. In contrast, none of these genes were induced after irradiation of WTK1 (p53 mutated) or NH32 (p53 null) cells (**Figure S1**).

Gene Set Enrichment Analysis (GSEA) Reveals Stronger Enrichment of Immune Response and Inflammation-Related Gene Sets by High-LET Radiation

Next, to detect modest but coordinated changes, we performed GSEA (52). A classical DNA damage response, with p53-pathway, apoptosis and DNA damage repair-related gene sets being very significantly enriched in up-regulated genes was observed after exposure to 1 Gy of all radiation types (**Figures 4** and **5A**). Interestingly, especially after exposure to heavy ions, also several immune response and inflammation-related gene sets were identified as significantly enriched in irradiated samples (**Figures 4** and **5B, C**). For instance, genes related to the inflammatory response showed no preferential enrichment in either sham- or X-irradiated PBMCs. In contrast, exposure to heavy ions, especially iron ions, resulted in a significant up-regulation of these genes (**Figure 5B**). Similarly, the radiation

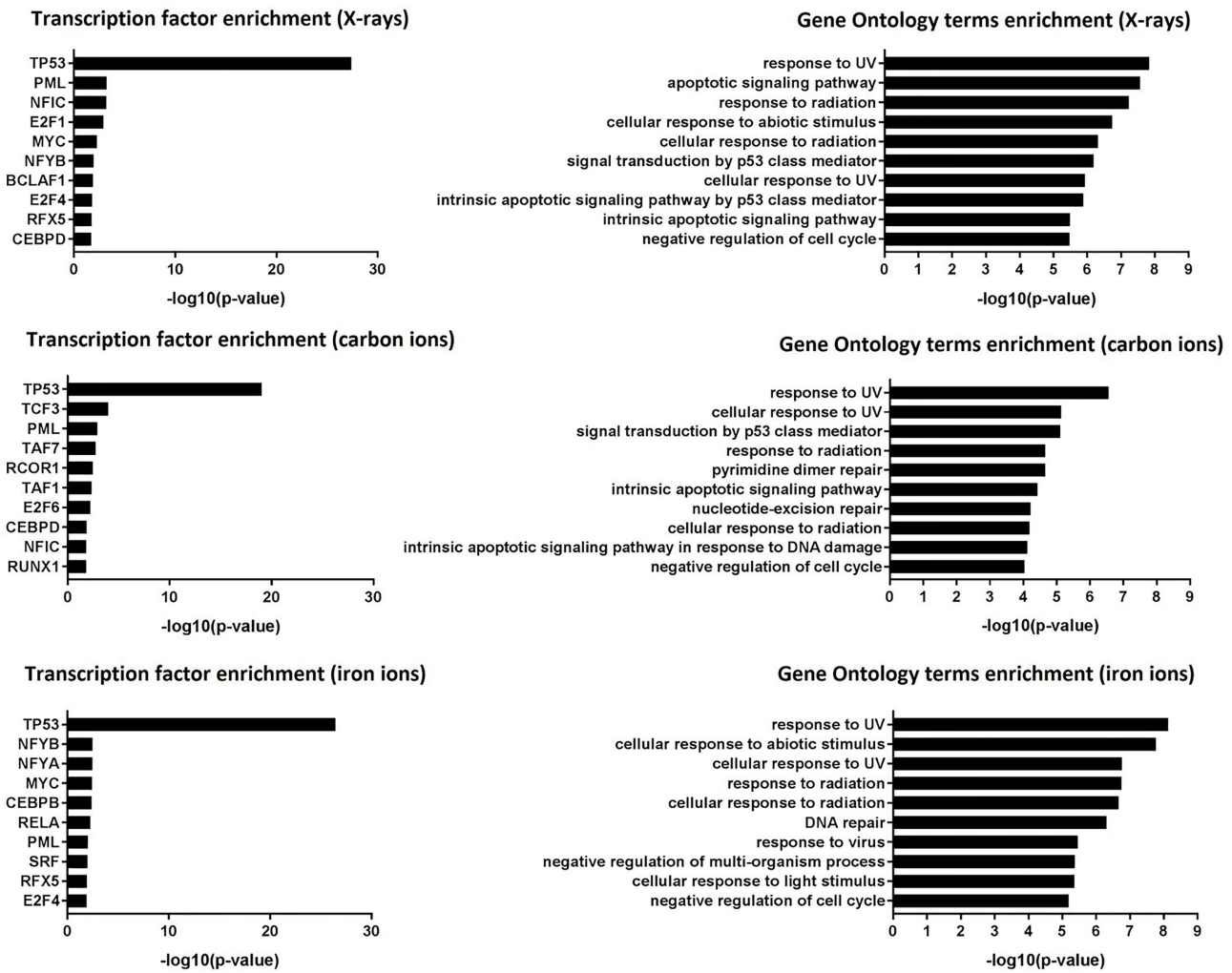

FIGURE 3 | Transcription factor enrichment and GO term enrichment. Left panel: transcription factor enrichment results following exposure to X-rays, carbon ions or iron ions. Right panel: Biological processes that are mostly affected following exposure to X-rays, carbon ions or iron ions, based on gene level analysis.

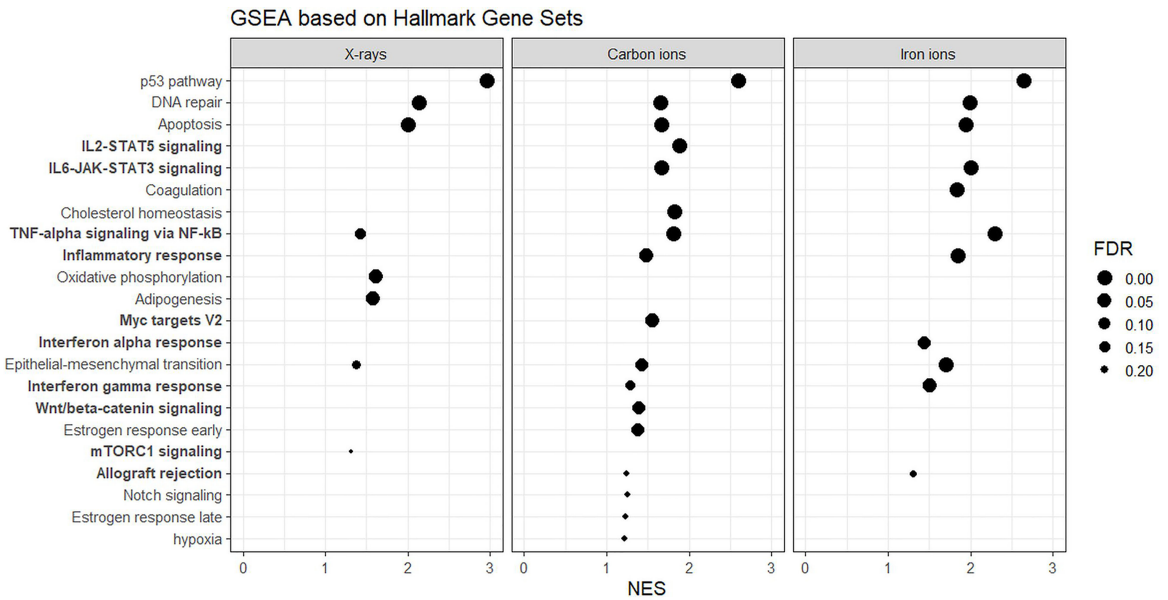

FIGURE 4 | GSEA based on Hallmark Gene Sets. Gene sets related to the immune system and inflammation are in bold. NES, normalized enrichment score; FDR, false discovery rate q-value.

effect on genes involved in TNFα signaling *via* NF-κB was more pronounced after heavy ion irradiation as compared to X-irradiation (**Figure 5C**). Together, these results corroborate the observation that exposure of PBMCs to heavy ion irradiation induces similar pathways but with more pronounced changes in gene expression when compared to X-rays, while certain pathways, especially those related to inflammation are particularly triggered by heavy ions.

qRT-PCR Analysis Shows Radiation Type- and Time-Dependent Gene Expression Response

Seven genes (*PCNA*, *GADD45A*, *RPS27L*, *ASTN2*, *NDUFAF6*, *FDXR*, *MAMDC4)* were selected for qRT-PCR validation of microarray data and temporal follow-up. The rationale of gene selection for qRT-PCR validation is explained below. *PCNA*, *FDXR*, *GADD45A* and *RPS27L* were significantly up-regulated 8 h after exposure to all radiation types, while *ASTN2* showed significant up-regulation after exposure to X-rays and iron ions, but not to carbon ions according to the microarray data. *NDUFAF6* and *MAMDC4* were alternatively spliced (see next section for detailed description) in response to exposure to all radiation types. To obtain better insight in the dose- and time-dependence of expression of these genes, a lower dose (0.25 Gy) as well as an additional time point (24 h) were included (**Figure 6**). All selected genes showed significant up-regulation at 8 h after exposure to 1 Gy of all radiation types. In many cases their induction was significant even at a lower dose of 0.25 Gy. *FDXR* showed the highest degree of induction following the exposure to all radiation types. The expression of *ASTN2*, in contrast to microarray results, was also significantly induced by carbon ions. Importantly, while all genes, except *MAMDC4*, reduced in expression with time in X-irradiated cells, their up-regulation was in general retained, or often even further induced in cells exposed to heavy ions, especially in the case of carbon ions.

Transcript Variation Is Induced by Low- and High-LET Radiation

Exposure to low-LET radiation not only changes gene expression but also triggers the production of alternative transcripts (due to alternative splicing or transcription) (47, 53–55). A core signature of genes that become alternatively spliced in response to all radiation types was identified (**Figure 7A**). The majority of these genes were also differentially expressed at the gene level (36 out of 46), which aligned well with our previous results (47). More overlap was observed between the iron- and carbon-ion irradiated groups – 33% of the genes were in common, while between the X-ray irradiated cells and heavy-ion irradiated cells the overlap was only about 15%. We also compared the number of differentially expressed exons between different radiation types to assess the levels of induction of transcript variants. Exposure to 1 Gy of X-rays resulted in significant (FDR < 0.05) up-regulation of 724 exons, to carbon ions – of 511 exons and to iron ions – of 708 exons (**Supplementary Table 6**). In this case, more overlap was observed between iron ions and X-rays – 32.8% of exons were in common (**Figure 7B**). When comparing the fold-changes in expression of the overlapping 246 exons (**Supplementary Table 6**), the highest induction levels were shown by carbon ions (**Figure 7C**). In addition, changes in expression of the 20-exon signature identified earlier (47) were compared between different radiation types (**Supplementary Table 6**). These 20 exons are particularly responsive to X-rays and important for the sample classification according to the

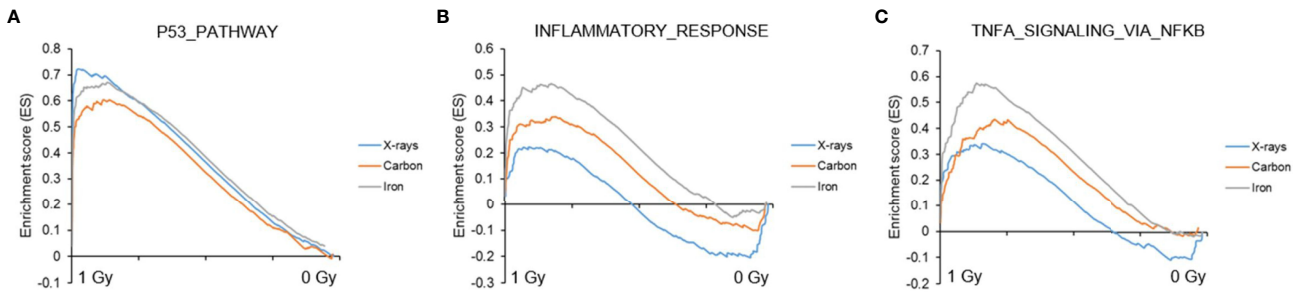

FIGURE 5 | GSEA analysis. GSEA enrichment plots for three gene sets following exposure to X-rays, carbon or iron ions: **(A)** p53 pathway, **(B)** Inflammatory response, **(C)** TNFα signaling via NF-κB. Gene sets with a distinct peak at the beginning or the end of the ranked list are generally the most relevant, indicating that this specific gene set is enriched in up- or down-regulated genes, respectively.

exposure dose. The comparison revealed that most of the above-mentioned 20 exons are in general less responsive to heavy ions compared to X-irradiation (**Figure 7D**). The detailed results for four genes overlapping for all radiation types (*PCNA*, *VWCE*, *FDXR* and *MAMDC4*) are shown in **Figures 7E–H**. In this case, the most pronounced alternative splicing response was observed after carbon ions exposure. This was especially the case for *MAMDC4* and *VWCE*. The Gene Ontology Biological Processes terms enriched in alternatively spliced genes common for all radiation types were predominantly related to apoptosis and DNA damage repair (**Supplementary Table 5**). Carbon ion exposure resulted in alternative splicing of several genes coding for classical HLA class I molecules (HLA-A, HLA-B, and HLA-H) and class II molecules (HLA-DMB) and histone-coding genes (HIST2H3A, HIST2H3PS2, HIST2H3C, and HIST2H3D), which was not observed following the exposure to iron ions or X-rays.

Heavy Ion Exposure Results in Clustered DNA Damage and Slower DNA Damage Repair as Compared to X-Rays

Next to a transcriptional profiling, we evaluated the genotoxic impact of radiation exposure in the PBMCs over time for all radiation types. While quantification of DNA damage is commonly performed by counting the number of nuclear γH2AX foci (56, 57), high-LET radiation induces strongly clustered breaks along the track of the beam that may result in few microscopic foci, but with large relative size when a cell is visualized perpendicular to the orientation of the beam track (**Figure 8A**). γH2AX foci nuclear occupancy may therefore be a better measure for damage severity (45). Indeed, when calculated as the number of foci per nucleus, the absolute number of unrepaired breaks after 24 h was similar for all radiation types (**Figure 8B**). However, when considering foci occupancy, the amount of unrepaired DNA double-strand breaks (DSBs) 24 h after irradiation was 23% for X-rays, 42% for carbon ions and 31% for iron ions. When considering the foci occupancy per nucleus, the amount of damage still present 24 h after exposure to iron ions was comparable to the amount of damage observed in X-irradiated cells at 0.5 h (**Figure 8C**). For X-rays and iron ions the maximal foci occupancy was detected at 0.5 h post-irradiation, while for carbon ions this peak was observed at 2 h post-irradiation. The severity of DNA damage and kinetics of the repair were therefore clearly LET-dependent.

Gene Expression May Serve as a Proxy for DNA Damage Repair Efficiency

To compare the changes in gene expression with DNA repair kinetics at the level of individual donors, samples of four individuals that were irradiated with iron ions were used. All four individuals showed a clear reduction in the number of DSBs with time (**Figure 9A**). However, for Donor 1 the percentage of unrepaired DNA DSBs after 24 h was 43.6% and the difference between the damage detected at 0.5 h and 24 h time point was not statistically significant. In contrast, for the other donors this difference was significant, and the percentages of unrepaired damage were lower, ranging between 25.2-28.7%.

Hierarchical clustering of the gene expression profiles of DNA repair-related genes showed time- and subject-dependent expression. This resulted in two major clusters of samples depending on the time point, with 24-h samples segregating from 8-h and 12-h samples (**Figure 9B**). Within each time cluster, expression profiles of Donor 1 clustered separately from those of the other three subjects (**Figure 9B**). Several radiation-induced DNA repair genes (e.g., *PCNA*, *DDB2*, *RBM14*) showed an enhanced radiation response in Donor 1 compared to other donors, especially after a high dose (**Figures 9C–E**). This donor also showed elevated levels of expression of several DNA damage response-related genes, (e.g., *ATM, ATR, RAD51D, MRE11A*) independent of the irradiation dose and time point (**Figures 9F–I**). This indicates that individual differences in the overall and radiation-induced expression levels of DNA repair genes exist, which may possibly explain individual differences in DNA repair kinetics.

DISCUSSION

In the present study, we compared the genome-wide transcriptional response of human PBMCs after acute exposure

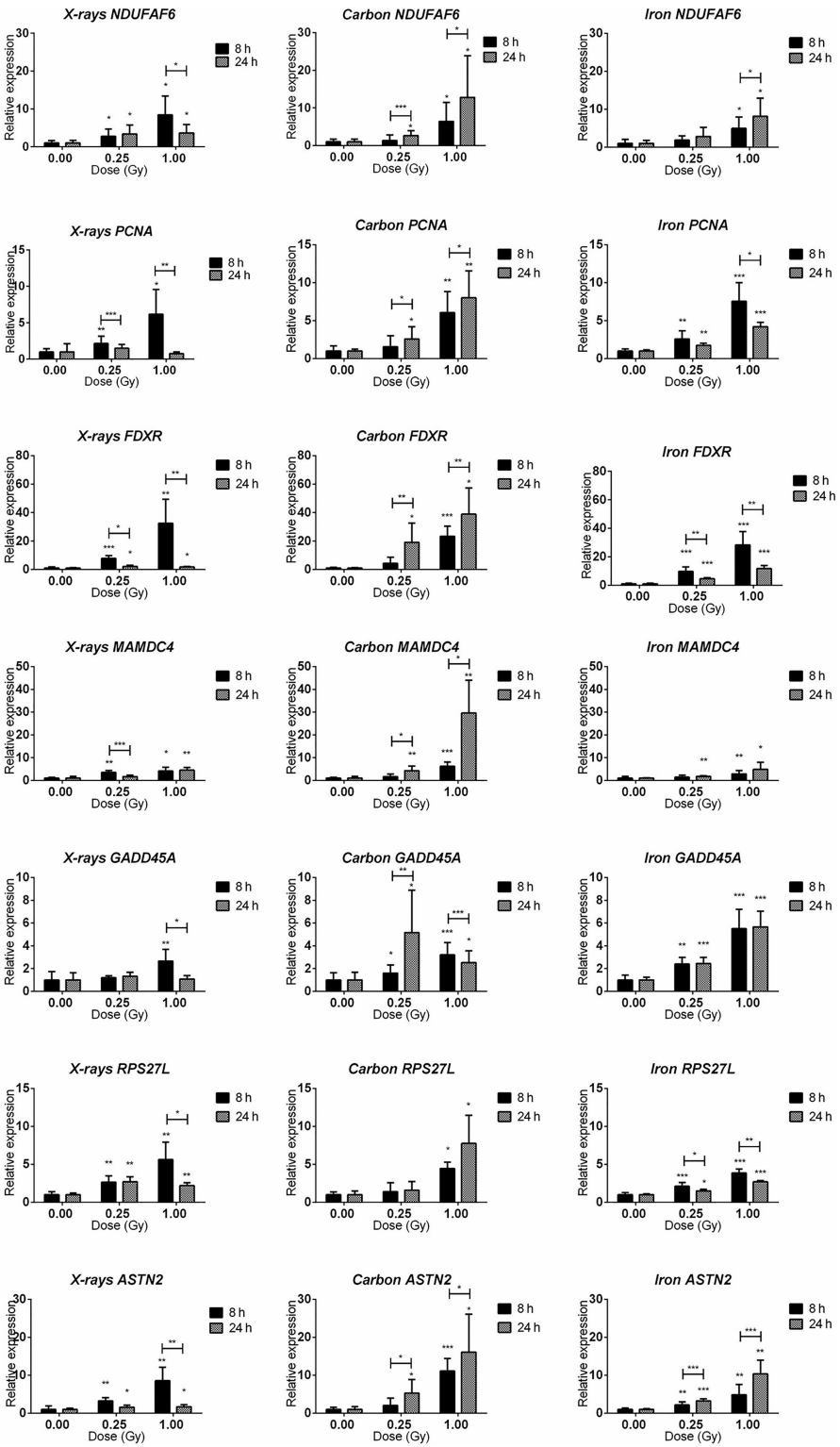

FIGURE 6 | qRT-PCR validation of the microarray results. qRT-PCR results for *NDUFAF6, PCNA, FDXR, MAMDC4, GADD45A, RPS27L*, and *ASTN2* genes (shown in rows) at 8 and 24 h after irradiation with 0.25 and 1.00 Gy of X-rays, carbon or iron ions (shown in columns). Graphs represent mean of six biological replicates + standard deviation. Statistical comparison between samples irradiated with different doses at two different time points was performed using 2-way ANOVA with Bonferroni *post-hoc* test (*$p < 0.05$, **$p < 0.005$, ***$p < 0.0001$).

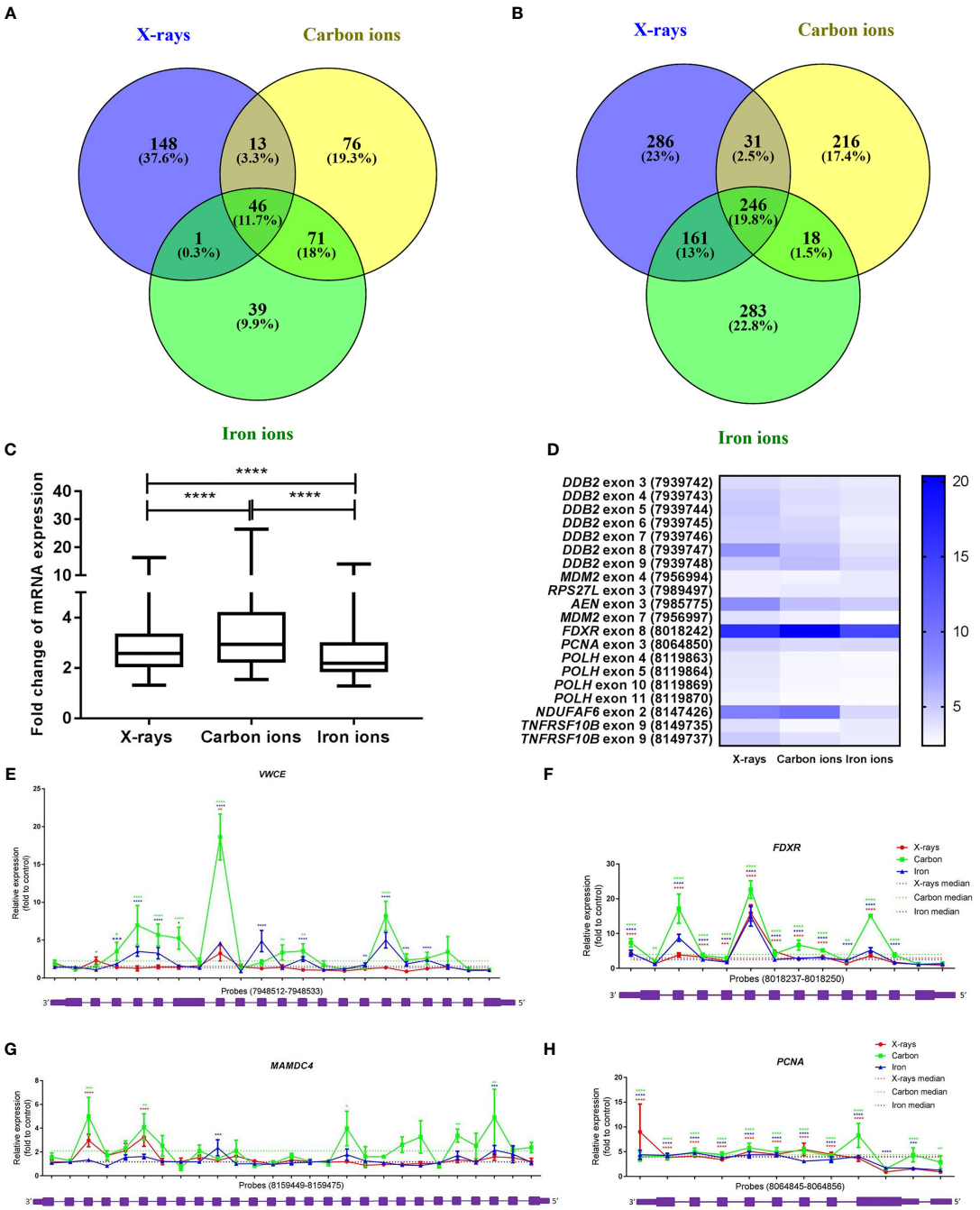

FIGURE 7 | Radiation-induced alternative splicing. **(A)** Venn diagram showing the number of alternatively spliced genes with FDR-corrected p-value < 0.05 at 8 h after exposure to 1 Gy of X-rays, carbon or iron ions. **(B)** Venn diagram showing the number of differentially expressed exons with FDR-corrected p-value < 0.05 at 8 h after exposure to 1 Gy of X-rays, carbon or iron ions. **(C)** Changes in exon expression induced at 8 hours after exposure to 1 Gy of different radiation types. Centerlines show the median, boxes represent the range between the first and third quartiles and whiskers represent the highest and lowest values. Statistical comparison was performed using Wilcoxon matched-pairs signed rank test (****p-value < 0.0001). **(D)** Heatmap showing fold-changes in the expression of the 20-exon signature (probe set numbers are shown in brackets) 8 hours after exposure to 1 Gy of different radiation types. This 20-exon signature was identified as particularly responsive to X-ray exposure (47). **(E–H)** Alternative transcription/splicing of *VWCE*, *FDXR*, *MAMDC4* and *PCNA* genes at 8 h after exposure to 1 Gy of X-rays, carbon or iron ions. Genomic organization of each gene is shown below the graph in purple; every box represents an exon of the gene, schematic representation of the exons does not correspond to their actual size. Fold-changes to control values are shown for every probe set specific to each exon of the gene. Median fold-change to control value for each radiation type is shown with the dotted line. Error bars represent SEM (n = 10 for X-rays, n = 4 for carbon and iron ions). Statistical comparison between irradiated and non-irradiated samples was performed using repeated measures 2-way ANOVA with Sidak's *post-hoc* test (*p < 0.05, **p < 0.005, ***p < 0.001, ****p < 0.0001).

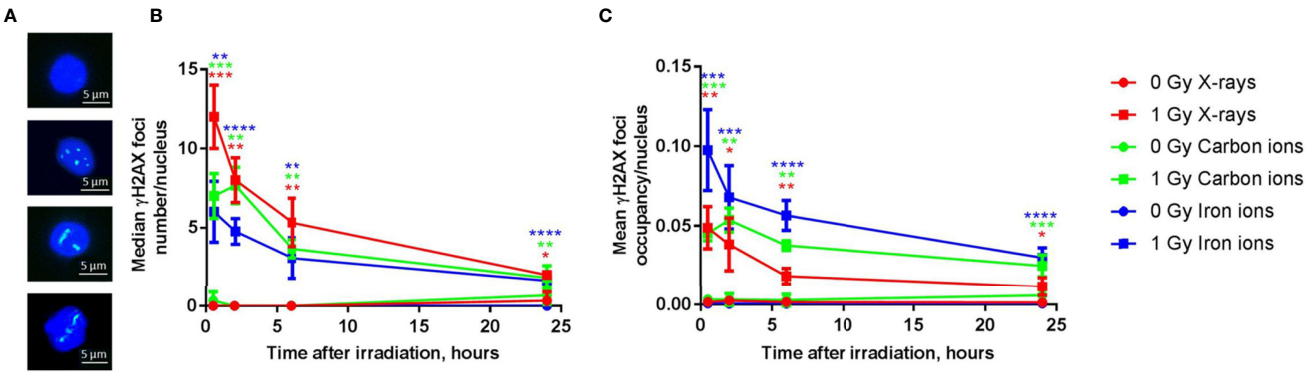

FIGURE 8 | DNA repair kinetics after exposure to different types of radiation. **(A)** Representative examples of immunostained γH2AX foci in PBMCs 6 h following (from top to bottom) sham-irradiation, exposure to 1 Gy of X-rays, iron ions or carbon ions. **(B)** The number of γH2AX foci per nucleus after exposure to 1 Gy of X-rays, carbon and iron ions at different time points (median of three biological replicates for X-rays and carbon ions and four biological replicates for iron ions, error bars represent standard deviations). **(C)** The occupancy of γH2AX foci per nucleus (average of three biological replicates for X-rays and carbon ions and four biological replicates for iron ions, error bars represent standard deviations) after exposure to 1 Gy of X-rays, carbon and iron ions at different time points. Statistical comparison between irradiated and sham-irradiated samples was performed using unpaired *t*-test (*$p < 0.05$, **$p < 0.005$, ***$p < 0.001$, ****$p < 0.0001$).

to three radiation types with different LET characteristics: X-rays, carbon and iron ions. An equal dose of 1 Gy was used, as our main goal was to identify the differences in response caused by high- and low-LET radiation rather than to compare RBE-weighted doses. It was also previously suggested to compare equal rather than equitoxic doses of high- and low-LET radiation in the context of gene expression analysis (58). In addition, we analyzed the DNA repair kinetics after exposure to the above-mentioned radiation types.

In our study, we found a very similar primary p53-dependent response to all radiation types at 8 h after exposure. The identity of differentially expressed genes was in good accordance with other transcriptional radiobiological studies performed on human blood samples (59). A similar result was obtained by Sokolov and co-authors who showed that gene expression profiles in normal human fibroblasts following γ-radiation and decays of high-LET-like ^{125}I share the majority of genes, indicating activation of similar pathways (60). A study by Kurpinski and co-authors showed that most of the differentially expressed genes which were in common after exposure to 1 Gy of X-rays and iron ions in human mesenchymal stem cells were involved in cell cycle and DNA damage response and repair, which is in accordance with our observations (61). Study by Ding et al. on human bronchial epithelial cells exposed to 0.5 and 1 Gy of γ-rays, 1000 MeV/nucleon iron and silicon ions (LET of 150 and 44 keV/µm respectively) showed induction of common gene sets related to cell death, cell cycle regulation, DNA repair and cellular growth and proliferation as well as activation of several p53-regulated genes for all radiation types (62). However, the expression profiles were LET-dependent and distinct enough to classify the samples according to radiation type with very high accuracy (62).

Even though we also found several genes "unique" to a specific radiation type, it is likely that many of them would also respond to the other radiation types in a different experimental set-up (i.e. time-dose combination) due to the differences in RBE and\or gene expression kinetics, but what is already clear from our and other studies is that the magnitude of gene expression changes and the number of differentially expressed genes are consistently higher for high-LET particles (22). Some of the observed differences may be explained by the different nature of X-rays (photons) and heavy ions (particles). The DNA damage caused by particles is more complex and difficult to repair compared to X-rays, as confirmed by slower DNA repair kinetics shown in our study, which may result in different signaling responses. A similar observation was made after exposure to accelerated nickel ions, which induced a persistent DNA damage response in endothelial cells up to 24 h after treatment (63). Even though the LET of iron ions was higher than that of carbon ions we observed a more pronounced response after exposure to the latter, for example, in case of gene expression induction, alternative splicing and slower DNA repair kinetics. This observation might possibly be explained by the higher fluence used for the carbon irradiation resulting in cells being hit by more ions, thus other factors and not just the LET value alone should be considered when interpreting the results.

Interestingly, GSEA identified several immune response-related gene sets as significantly enriched specifically in samples irradiated with heavy ions. Paradoxically, radiation was reported to modulate immune responses in a complex dose-dependent manner with possible pro- and anti-inflammatory responses (64). NF-kB is the key transcription factor which plays a central role in regulation of the expression of pro-inflammatory cytokines and chemokines such as TNF-α, IL-1, IL-2, IL-6 and MCP-1 (20, 65). Low-dose radiation is well known to treat benign inflammatory or hypoproliferative conditions (66), and this is thought to be due to inhibition of NF-κB at doses below 2 Gy (67), however, different cell types show different sensitivity toward NF-κB inhibition/activation by ionizing radiation. The possible mechanisms responsible for NF-κB inhibition are the decrease in p38 (an up-stream molecule of

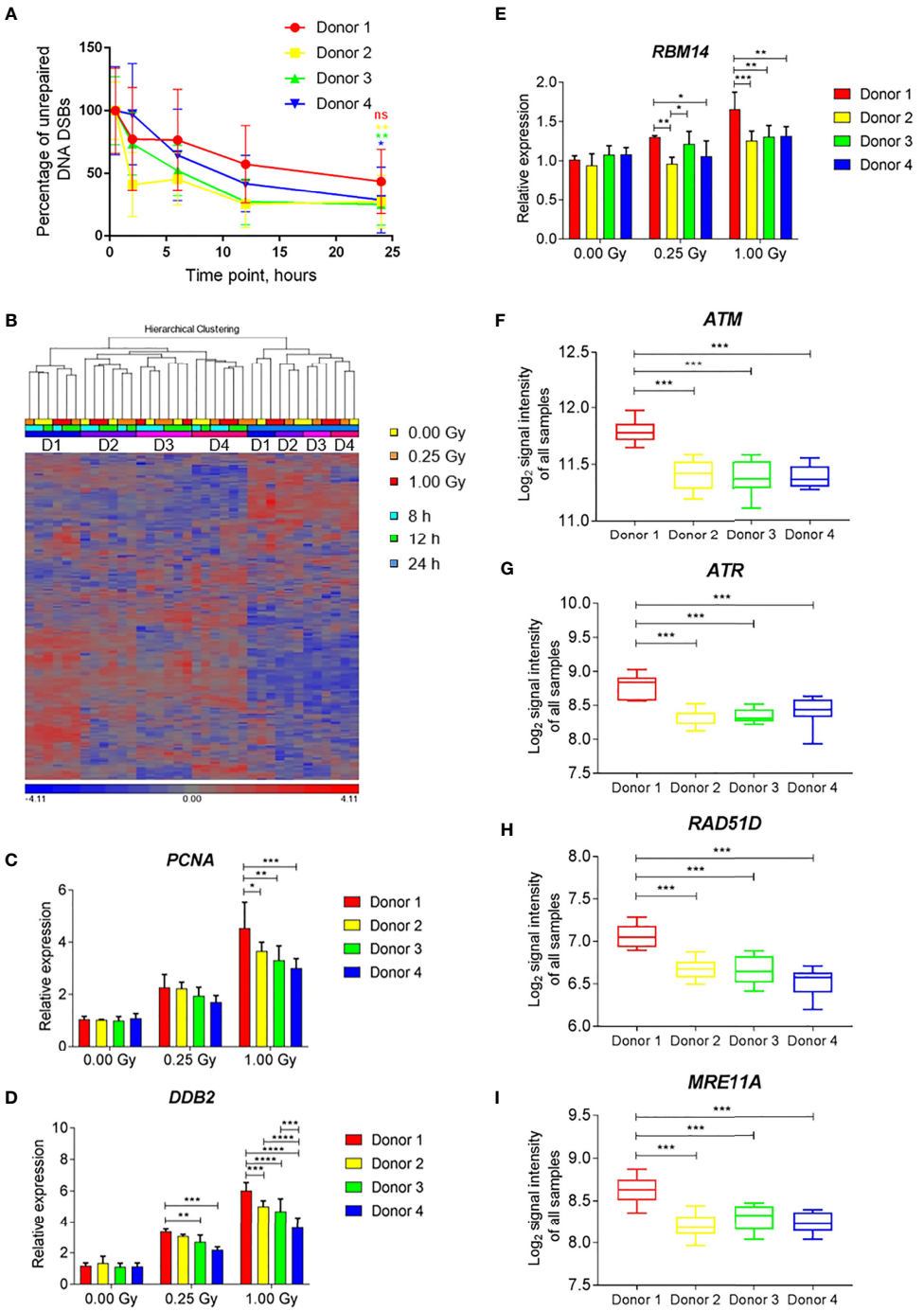

FIGURE 9 | Individual differences in DNA damage repair kinetics and gene expression induced by exposure to iron ions. **(A)** Individual DNA repair kinetics of four donors shown as percentage of gH2AX foci occupancy compared to 1 Gy-irradiated sample at 0.5 h time point (baseline damage subtracted). Error bars represent SEM of 2 technical replicates. Statistical comparison between the amount of damage per donor detected at 0.5 h and 24 h following irradiation was performed using repeated measures 2-way ANOVA with Sidak's post hoc test (*$p < 0.05$, **$p < 0.005$, ns-not significant). **(B)** Hierarchical clustering of DNA repair genes (MsigDB gene set DNA Repair) shows time- and subject-dependent expression. **(C–E)** Dose-dependent expression of selected DNA repair genes shows higher induction in Donor 1 compared to other donors. Bars show the mean of three time points, error bars show SD. Statistical comparison was performed using repeated measures 2-way ANOVA with Tukey's post-hoc test (*$p < 0.05$, **$p < 0.005$, ***$p < 0.001$, ****$p < 0.0001$). **(F–I)** Expression levels of selected DNA repair genes shows overall higher expression in Donor 1 compared to other donors. Box plots show the mean of all samples (all doses and time points), whiskers show minimal and maximal values. Statistical comparison was performed using unpaired t-test (***$p < 0.001$) ns - not significant.

NF-κB) (68) and decrease in 26S proteasome activity resulting in prevention of the IκB regulatory complex degradation leading to reduced translocation of NF-κB complex to the nucleus (69). Radiation doses above 2 Gy have conversely been demonstrated to increase the activity of NF-κB (64). In a study by Baumstark-Khan and co-authors high-LET argon ions (272 keV/μm, 95 MeV/nucleon) induced a stronger NF-kB-dependent reporter gene expression compared to X-rays (70). A later study from the same group showed that carbon ions (33 and 73 keV/μm) and X-rays activate NF-kB-dependent gene expression in HEK293 cells 4 h after exposure. However, activation by carbon ions was induced by 1.3 Gy while activation by X-rays required a higher dose of 16 Gy (71). A further group reported NF-κB activation in normal human monocytes exposed to 0.7 Gy of iron ions (72). Ding and co-authors found more significant expression changes in the pro-inflammatory acute phase response pathway in bronchial epithelial cells following the exposure to iron and silicon ions compared to low-LET γ-rays when using equal doses of 0.5 and 1 Gy, which is in accordance with our results (62). We hypothesize that the activation of immune response and inflammation-related gene sets particularly by heavy ions observed in our study is mainly due to the use of equal doses of different radiation types. This observation suggesting overall increase of carcinogenic potential related to NF-kB activation (73, 74) by heavy ions at doses as low as 1 Gy might have implications for both radiotherapy patients and astronauts on long-term space missions.

However, there are two sides of the coin. Currently, it is accepted that radiotherapy not only stimulates but can also activate the immune system turning the tumor into an *in situ* personalized vaccine (75). Diegeler and Hellweg emphasize the intercellular communication between tumor cells and immune cells after exposure to different radiation types and sustain our observation that the level of expression of cytokines, which modulate the immune cell behavior, is LET dependent (76). Carbon ions were also shown to induce anti-tumor immune response in a murine model (77). Another study examining five human cancer cell lines showed that comparable levels of high mobility group box 1, which plays an important role in activating anti-tumor immunity, were detected after irradiation with equitoxic doses of X-rays and carbon ions, meaning that a lower dose of carbon ions was needed to achieve the same effect (78). These results suggest that carbon ion therapy might activate the immune system to a greater extent than conventional radiotherapy, even when equivalent doses are used. Accumulating evidence demonstrates positive modulation of immune cells by radiation increasing their anti-tumor activity, however, there have also been reports of opposite effect of radiation inhibiting effective anti-tumor responses of immune cells (67). Therefore, further understanding of the effect of different radiation types on cytokine production by the immune cells is crucial for designing new therapeutic approaches combining radiation and immunotherapies.

Another important aspect of the transcriptional response to ionizing radiation (47, 54, 79) and other genotoxic agents (80–84) is alternative splicing and transcription. Exposure to low and moderate doses of low-LET ionizing radiation initiates alternative splicing and transcription of a large number of genes (47, 54, 79). In the present study, we also assessed the induction of alternative transcription and splicing by high- and low-LET radiation and observed a more pronounced response after exposure to heavy ions, especially carbon ions. A proteome-wide study in mouse embryonic fibroblasts exposed to carbon ions revealed significant changes in RNA metabolic processes, including RNA splicing (85). The exons most extensively regulated in response to X-ray exposure were not the most regulated after heavy ions exposure, suggesting specificity in response. Although it is not possible to draw any definite conclusions on the biological relevance of this observation from the microarray data, it is tempting to further study the role of alternatively transcribed/spliced genes in response to different radiation types. In a recent study exposure to UV was shown to trigger a shift from protein-coding mRNA of the *ASCC3* gene, which was alternatively spliced in response to heavy ions exposure in our set up, to a shorter non-coding isoform incorporating an alternative last exon. This RNA isoform, rather than the encoded protein, is critical for the eventual recovery of transcription (86). The non-coding ASCC3 isoform, in fact, counteracts the function of the protein-coding isoform and has an opposite effect on transcription recovery after UV-induced DNA damage (86).

Defects in DNA repair mechanisms often result in increased radiosensitivity of cells (87–91). Studies aiming at establishing an assay for predicting radiosensitivity focused on colony-forming assays (92, 93) or the measurement of DNA DSBs repair efficiency by means of the comet assay (94–96) or the γH2AX assay (96, 97). However, no single DNA damage-based assay proved to be capable of discriminating the full range of cellular radiosensitivity (98). A possible explanation is that radiosensitivity can also be associated with differences in cell cycle and apoptosis pathways regulation (99, 100). In this regard, transcriptional changes, which allow focusing on several instead of isolated cellular aspects, were suggested to be a promising predictive parameter for radiosensitivity (96, 101). Greve and co-authors identified a set of 67 differentially expressed genes in peripheral blood lymphocytes exposed to 5 Gy of γ-rays, which allowed distinguishing between the group of severely radiosensitive and non-radiosensitive breast, head and neck carcinoma patients (96). Rieger and co-workers used microarray gene expression profiling in lymphoblastoid cells derived from a diverse group of cancer patients with acute radiation toxicity. A set of 24 genes predicted radiation toxicity in 9 of 14 patients with no false positives among 43 controls (102).

In our study, we integrated the two approaches mentioned above, DNA DSB repair efficiency and transcriptional changes, based on the data of four donors after exposure of PBMCs to iron ions. It is important to mention that all the subjects involved in this study were apparently healthy, without any known abnormal variations in radiosensitivity. We aimed at exploring whether differences in gene expression can reflect the efficiency and kinetics of DSB repair measured by γH2AX assay. Although we did not find any significant differences in the repair efficiency between the four donors, the donor that showed the lowest repair

rate, also displayed a distinct DNA damage repair gene expression profile after radiation exposure. This might imply that this individual is more radiosensitive compared to the other three donors. Interestingly, a recent study comparing transcriptional response of radiosensitive and radioresistant immortalized B-lymphocytes also showed a greater and prolonged response of p53-regulated genes in radiosensitive cells after exposure to 2 Gy of γ-rays (103). A similar approach of combining γH2AX with transcriptomics data was used for biodosimetry purposes in mice injected with ^{137}Cs and proved to be more efficient than any of these methods alone (104).

Our study has limitations. First, the number of samples used for microarray experiments is limited to 4 to 10 per experimental condition, which might not be sufficient to draw definite conclusions at this stage. Moreover, gene expression changes in response to irradiation are very dynamic, thus the choice of the dose and time point is critically important for correct interpretation of the results. Our microarray study included only one time point and one dose, therefore direct translation of our results to radiotherapy, where higher doses are used, or space flights, during which the total doses and dose rates are lower, should be done cautiously. Nevertheless, several studies addressing the effect of dose rate on gene expression were previously performed in total body irradiated mice (105) and *ex vivo* irradiated human blood (3.1 mGy/min *vs* 1.03 Gy/min) (106). Overall, these studies showed that a significant number of genes responded similarly to low dose rate and acute exposures. Transcriptional response observed in blood samples obtained from radiotherapy patients undergoing total body irradiation was also in good accordance with the results obtained in *in vitro* studies (107, 108). Therefore, we believe that as our findings are in line with previously published results in other experimental models, they can serve as a solid basis for further studies. Second, at this stage our study describes the response to different radiation types only at transcriptional level, therefore the biological importance of our observations remains to be investigated. Finally, only 4 donors were considered. Although this study is small in scale, our results could be of interest for assessing the DNA repair efficiency and overall response to radiation in long-term space missions crew members and, potentially, radiotherapy patients. Moreover, gene expression measurements are more straight-forward and are technically less affected by such factors as radiation type compared to the γH2AX assay. At the same time, measuring gene expression for radiosensitivity assessment allows having a broader look at the cause of radiosensitivity as virtually any gene can be included in the assay. In conclusion, we have shown that both low- and high-LET irradiation induce similar transcriptional pathways, albeit with variable amplitude and timing, but that high-LET radiation also elicits specific and more persistent transcriptional events that may exacerbate the carcinogenic potential or, on the other hand, induce immune response against tumor cells. Our results imply that more detailed investigations of transcriptional response could bring new insight into differential normal tissue responses to high- and low-LET radiation and might have implications for the development of particle therapy treatment and radiation protection.

DATA AVAILABILITY STATEMENT

The original contributions presented in the study are included in the article/**Supplementary Material**. Further inquiries can be directed to the corresponding author.

ETHICS STATEMENT

The studies involving human participants were reviewed and approved by SCK CEN Ethics Committee. The patients/participants provided their written informed consent to participate in this study.

AUTHOR CONTRIBUTIONS

EM, KT, AJ, and AM performed experiments. NA directed heavy ion irradiations at GSI. EM and RQ analyzed data. EM, KT, MM, SB, and RQ designed the study. MM, WV, SB, and RQ directed the work. EM and RQ wrote the manuscript. All authors contributed to the article and approved the submitted version.

FUNDING

This work was supported by ESA PRODEX contracts (PEA 4000130301 and PEA 4000109861), the University of Antwerp (BOF/29267), by the ESA IBER-10 program project "GYMBRASS" (AO-10-IBER-26) and a grant from the Belgian FPS Economy, S.M.E.s, Self-employed and Energy (Belgian Royal Decree of February 23 2018, Article. 3. §4. 3° Project 19). EM is the recipient of a joint SCK CEN/UGent PhD scholarship. WV is member of the Research Excellence Consortium μNEURO at the University of Antwerp.

ACKNOWLEDGMENTS

The authors wish to thank the GSI physicists involved in dosimetry, as well as the beam operator team for their help during numerous night shifts. We would also like to thank the SCK CEN medical service staff for the help with blood drawing and all the blood donors involved in this study for their invaluable contribution.

SUPPLEMENTARY MATERIAL

The Supplementary Material for this article can be found online at: https://www.frontiersin.org/articles/10.3389/fonc.2021.768493/full#supplementary-material

REFERENCES

1. Kim PJ, Shih HA. The Place of Ion Beams in Clinical Applications. In: Linz U, editor. *Ion Beam Therapy. Biological and Medical Physics, Biomedical Engineering, vol 320*. Springer, Berlin, Heidelberg (2012). doi: 10.1007/978-3-642-21414-1_2
2. LaRiviere MJ, Santos PMG, Hill-Kayser CE, Metz JM. Proton Therapy. *Hematol Oncol Clin North Am* (2019) 33(6):989–1009. doi: 10.1016/j.hoc.2019.08.006
3. Thomas H, Timmermann B. Paediatric Proton Therapy. *Br J Radiol* (2020) 93(1107):20190601. doi: 10.1259/bjr.20190601
4. Baumann M, Krause M, Overgaard J, Debus J, Bentzen SM, Daartz J, et al. Radiation Oncology in the Era of Precision Medicine. *Nat Rev Cancer* (2016) 16(4):234–49. doi: 10.1038/nrc.2016.18
5. Moteabbed M, Yock TI, Paganetti H. The Risk of Radiation-Induced Second Cancers in the High to Medium Dose Region: A Comparison Between Passive and Scanned Proton Therapy, IMRT and VMAT for Pediatric Patients With Brain Tumors. *Phys Med Biol* (2014) 59(12):2883–99. doi: 10.1088/0031-9155/59/12/2883
6. Durante M, Orecchia R, Loeffler JS. Charged-Particle Therapy in Cancer: Clinical Uses and Future Perspectives. *Nat Rev Clin Oncol* (2017) 14(8):483–95. doi: 10.1038/nrclinonc.2017.30
7. Kramer M, Weyrather WK, Scholz M. The Increased Biological Effectiveness of Heavy Charged Particles: From Radiobiology to Treatment Planning. *Technol Cancer Res Treat* (2003) 2(5):427–36. doi: 10.1177/153303460300200507
8. Held KD, Kawamura H, Kaminuma T, Paz AE, Yoshida Y, Liu Q, et al. Effects of Charged Particles on Human Tumor Cells. *Front Oncol* (2016) 6:23. doi: 10.3389/fonc.2016.00023
9. Ando K, Kase Y. Biological Characteristics of Carbon-Ion Therapy. *Int J Radiat Biol* (2009) 85(9):715–28. doi: 10.1080/09553000903072470
10. De Ruysscher D, Niedermann G, Burnet NG, Siva S, Lee AWM, Hegi-Johnson F. Radiotherapy Toxicity. *Nat Rev Dis Primers* (2019) 5(1):13. doi: 10.1038/s41572-019-0064-5
11. Bentzen SM. Preventing or Reducing Late Side Effects of Radiation Therapy: Radiobiology Meets Molecular Pathology. *Nat Rev: Cancer* (2006) 6(9):702–13. doi: 10.1038/nrc1950
12. Barnett GC, West CM, Dunning AM, Elliott RM, Coles CE, Pharoah PD, et al. Normal Tissue Reactions to Radiotherapy: Towards Tailoring Treatment Dose by Genotype. *Nat Rev: Cancer* (2009) 9(2):134–42. doi: 10.1038/nrc2587
13. Chancellor JC, Scott GB, Sutton JP. Space Radiation: The Number One Risk to Astronaut Health Beyond Low Earth Orbit. *Life (Basel)* (2014) 4(3):491–510. doi: 10.3390/life4030491
14. Simpson JA. Elemental and Isotopic Composition of the Galactic Cosmic-Rays. *Annu Rev Nucl Particle Sci* (1983) 33:323–81. doi: 10.1146/annurev.ns.33.120183.001543
15. Kim M, Cucinotta F, Chappell L. Evaluating Shielding Approaches to Reduce Space Radiation Cancer Risks. In: *Nasa*. Houston: NASA (2012).
16. Durante M, Cucinotta FA. Heavy Ion Carcinogenesis and Human Space Exploration. *Nat Rev Cancer* (2008) 8(6):465–72. doi: 10.1038/nrc2391
17. Cucinotta FK, M, Chappell L. *Space Radiation Cancer Risk Projections and Uncertainties - 2012. NASA Technical Publication, 2013-217375*. Houston: NASA (2013).
18. Blakely EA. New Measurements for Hadrontherapy and Space Radiation: Biology. *Phys Med* (2001) 17 Suppl 1:50–8.
19. Durante M. Heavy Ion Radiobiology for Hadrontherapy and Space Radiation Protection. *Radiother Oncol* (2004) 73(Suppl 2):S158–60. doi: 10.1016/S0167-8140(04)80040-9
20. Fernandez-Gonzalo R, Baatout S, Moreels M. Impact of Particle Irradiation on the Immune System: From the Clinic to Mars. *Front Immunol* (2017) 8:177. doi: 10.3389/fimmu.2017.00177
21. Amundson SA, Bittner M, Fornace AJ Jr. Functional Genomics as a Window on Radiation Stress Signaling. *Oncogene* (2003) 22(37):5828–33. doi: 10.1038/sj.onc.1206681
22. Amundson SA. Gene Expression Studies for the Development of Particle Therapy. *Int J Part Ther* (2018) 5(1):49–59. doi: 10.14338/IJPT-18-00010.1
23. Moertl S, Buschmann D, Azimzadeh O, Schneider M, Kell R, Winkler K, et al. Radiation Exposure of Peripheral Mononuclear Blood Cells Alters the Composition and Function of Secreted Extracellular Vesicles. *Int J Mol Sci* (2020) 21(7):2336. doi: 10.3390/ijms21072336
24. Chauhan V, Howland M, Wilkins R. Identification of Gene-Based Responses in Human Blood Cells Exposed to Alpha Particle Radiation. *BMC Med Genomics* (2014) 7:43. doi: 10.1186/1755-8794-7-43
25. Broustas CG, Xu Y, Harken AD, Chowdhury M, Garty G, Amundson SA. Impact of Neutron Exposure on Global Gene Expression in a Human Peripheral Blood Model. *Radiat Res* (2017) 187(4):433–40. doi: 10.1667/RR0005.1
26. Mukherjee S, Grilj V, Broustas CG, Ghandhi SA, Harken AD, Garty G, et al. Human Transcriptomic Response to Mixed Neutron-Photon Exposures Relevant to an Improvised Nuclear Device. *Radiat Res* (2019) 192(2):189–99. doi: 10.1667/RR15281.1
27. Broustas CG, Andrew D. Harken AD, Garty G, Amundson SA. Identification of Differentially Expressed Genes and Pathways in Mice Exposed to Mixed Field Neutron/Photon Radiation. *BMC Genomics* (2018) 19(504). doi: 10.1186/s12864-018-4884-6
28. Broustas CG, Xu Y, Harken AD, Garty G, Amundson SA. Comparison of Gene Expression Response to Neutron and X-Ray Irradiation Using Mouse Blood. *BMC Genomics* (2017) 18(1):2. doi: 10.1186/s12864-016-3436-1
29. Skopek TR, Liber HL, Penman BW, Thilly WG. Isolation of a Human Lymphoblastoid Line Heterozygous at the Thymidine Kinase Locus: Possibility for a Rapid Human Cell Mutation Assay. *Biochem Biophys Res Commun* (1978) 84(2):411–6. doi: 10.1016/0006-291x(78)90185-7
30. Xia F, Wang X, Wang YH, Tsang NM, Yandell DW, Kelsey KT, et al. Altered P53 Status Correlates With Differences in Sensitivity to Radiation-Induced Mutation and Apoptosis in Two Closely Related Human Lymphoblast Lines. *Cancer Res* (1995) 55(1):12–5.
31. Chuang YY, Chen Q, Brown JP, Sedivy JM, Liber HL. Radiation-Induced Mutations at the Autosomal Thymidine Kinase Locus Are Not Elevated in P53-Null Cells. *Cancer Res* (1999) 59(13):3073–6.
32. Luoni F, Weber U, Boscolo D, Durante M, Reidel C-A, Schuy C, et al. Beam Monitor Calibration for Radiobiological Experiments With Scanned High Energy Heavy Ion Beams at FAIR. *Front Phys* (2020) 8(397). doi: 10.3389/fphy.2020.568145
33. Krämer M, Jäkel O, Haberer T, Kraft G, Schardt D, Weber U. Treatment Planning for Heavy-Ion Radiotherapy: Physical Beam Model and Dose Optimization. *Phys Med Biol* (2000) 45(11):3299–317. doi: 10.1088/0031-9155/45/11/313
34. Wu Z, Irizarry RA. Preprocessing of Oligonucleotide Array Data. *Nat Biotechnol* (2004) 22(6):656–8; author reply 658. doi: 10.1038/nbt0604-656b
35. Benjamini Y, Hochberg Y. Controlling the False Discovery Rate: A Practical and Powerful Approach to Multiple Testing. *J R Stat Soc* (1995) 57(1):289–300. doi: 10.1111/j.2517-6161.1995.tb02031.x
36. Oliveros JC. Venny. An Interactive Tool for Comparing Lists With Venn's Diagrams. (2007–2015).
37. Pfaffl MW. A New Mathematical Model for Relative Quantification in Real-Time RT-PCR. *Nucleic Acids Res* (2001) 29(9):e45. doi: 10.1093/nar/29.9.e45
38. Vandesompele J, De Preter K, Pattyn F, Poppe B, Van Roy N, De Paepe A, et al. Accurate Normalization of Real-Time Quantitative RT-PCR Data by Geometric Averaging of Multiple Internal Control Genes. *Genome Biol* (2002) 3(7):RESEARCH0034. doi: 10.1186/gb-2002-3-7-research0034
39. Plaisier SB, Taschereau R, Wong JA, Graeber TG. Rank-Rank Hypergeometric Overlap: Identification of Statistically Significant Overlap Between Gene-Expression Signatures. *Nucleic Acids Res* (2010) 38(17):e169. doi: 10.1093/nar/gkq636
40. Chen EY, Tan CM, Kou Y, Duan Q, Wang Z, Meirelles GV, et al. Enrichr: Interactive and Collaborative HTML5 Gene List Enrichment Analysis Tool. *BMC Bioinf* (2013) 14:128. doi: 10.1186/1471-2105-14-128
41. Kuleshov MV, Jones MR, Rouillard AD, Fernandez NF, Duan Q, Wang Z, et al. Enrichr: A Comprehensive Gene Set Enrichment Analysis Web Server 2016 Update. *Nucleic Acids Res* (2016) 44(W1):W90–7. doi: 10.1093/nar/gkw377
42. Subramanian A, Tamayo P, Mootha VK, Mukherjee S, Ebert BL, Gillette MA, et al. Gene Set Enrichment Analysis: A Knowledge-Based Approach for Interpreting Genome-Wide Expression Profiles. *Proc Natl Acad Sci USA* (2005) 102(43):15545–50. doi: 10.1073/pnas.0506580102

43. De Vos WH, Van Neste L, Dieriks B, Joss GH, Van Oostveldt P. High Content Image Cytometry in the Context of Subnuclear Organization. *Cytomet A* (2010) 77(1):64–75. doi: 10.1002/cyto.a.20807
44. Schindelin J, Arganda-Carreras I, Frise E, Kaynig V, Longair M, Pietzsch T, et al. Fiji: An Open-Source Platform for Biological-Image Analysis. *Nat Methods* (2012) 9(7):676–82. doi: 10.1038/nmeth.2019
45. Dieriks B, De Vos W, Meesen G, Van Oostveldt K, De Meyer T, Ghardi M, et al. High Content Analysis of Human Fibroblast Cell Cultures After Exposure to Space Radiation. *Radiat Res* (2009) 172(4):423–36. doi: 10.1667/RR1682.1
46. El-Saghire H, Thierens H, Monsieurs P, Michaux A, Vandevoorde C, Baatout S. Gene Set Enrichment Analysis Highlights Different Gene Expression Profiles in Whole Blood Samples X-Irradiated With Low and High Doses. *Int J Radiat Biol* (2013) 89(8):628–38. doi: 10.3109/09553002.2013.782448
47. Macaeva E, Saeys Y, Tabury K, Janssen A, Michaux A, Benotmane MA, et al. Radiation-Induced Alternative Transcription and Splicing Events and Their Applicability to Practical Biodosimetry. *Sci Rep* (2016) 6:19251. doi: 10.1038/srep19251
48. Macaeva E, Mysara M, De Vos W, Baatout S, Quintens R. Gene Expression-Based Biodosimetry for Radiological Incidents: Assessment of Dose and Time After Radiation Exposure. *Int J Radiat Biol* (2019) 95(1):64–75. doi: 10.1080/09553002.2018.1511926
49. Fischer M. Census and Evaluation of P53 Target Genes. *Oncogene* (2017) 36 (28):3943–56. doi: 10.1038/onc.2016.502
50. Tanikawa C, Furukawa Y, Yoshida N, Arakawa H, Nakamura Y, Matsuda K. XEDAR as a Putative Colorectal Tumor Suppressor That Mediates P53-Regulated Anoikis Pathway. *Oncogene* (2009) 28(34):3081–92. doi: 10.1038/onc.2009.154
51. Mello SS, Valente LJ, Raj N, Seoane JA, Flowers BM, McClendon J, et al. A P53 Super-Tumor Suppressor Reveals a Tumor Suppressive P53-Ptpn14-Yap Axis in Pancreatic Cancer. *Cancer Cell* (2017) 32(4):460–73. doi: 10.1016/j.ccell.2017.09.007
52. Mootha VK, Lindgren CM, Eriksson KF, Subramanian A, Sihag S, Lehar J, et al. PGC-1alpha-Responsive Genes Involved in Oxidative Phosphorylation Are Coordinately Downregulated in Human Diabetes. *Nat Genet* (2003) 34 (3):267–73. doi: 10.1038/ng1180
53. Forrester HB, Li J, Hovan D, Ivashkevich AN, Sprung CN. DNA Repair Genes: Alternative Transcription and Gene Expression at the Exon Level in Response to the DNA Damaging Agent, Ionizing Radiation. *PloS One* (2012) 7(12):e53358. doi: 10.1371/journal.pone.0053358
54. Sprung CN, Li J, Hovan D, McKay MJ, Forrester HB. Alternative Transcript Initiation and Splicing as a Response to DNA Damage. *PloS One* (2011) 6 (10):e25758. doi: 10.1371/journal.pone.0025758
55. Wahba A, Ryan MC, Shankavaram UT, Camphausen K, Tofilon PJ. Radiation-Induced Alternative Transcripts as Detected in Total and Polysome-Bound Mrna. *Oncotarget* (2018) 9(1):691–705. doi: 10.18632/oncotarget.21672
56. Dieriks B, De Vos W, Baatout S, Van Oostveldt P. Repeated Exposure of Human Fibroblasts to Ionizing Radiation Reveals an Adaptive Response That Is Not Mediated by Interleukin-6 or TGF-Beta. *Mutat Research-Fundamental Mol Mech Mutagene* (2011) 715(1-2):19–24. doi: 10.1016/j.mrfmmm.2011.07.002
57. Rombouts C, Aerts A, Beck M, De Vos WH, Van Oostveldt P, Benotmane MA, et al. Differential Response to Acute Low Dose Radiation in Primary and Immortalized Endothelial Cells. *Int J Radiat Biol* (2013) 89(10):841–50. doi: 10.3109/09553002.2013.806831
58. Suetens A, Moreels M, Quintens R, Soors E, Buset J, Chiriotti S, et al. Dose- and Time-Dependent Gene Expression Alterations in Prostate and Colon Cancer Cells After *In Vitro* Exposure to Carbon Ion and X-Irradiation. *J Radiat Res* (2015) 56(1):11–21. doi: 10.1093/jrr/rru070
59. Lacombe J, Sima C, Amundson SA, Zenhausern F. Candidate Gene Biodosimetry Markers of Exposure to External Ionizing Radiation in Human Blood: A Systematic Review. *PloS One* (2018) 13(6):e0198851. doi: 10.1371/journal.pone.0198851
60. Sokolov M, Panyutin IG, Neumann R. Genome-Wide Gene Expression Changes in Normal Human Fibroblasts in Response to Low-LET Gamma-Radiation and High-LET-Like 125iudr Exposures. *Radiat Prot Dosimet* (2006) 122(1-4):195–201. doi: 10.1093/rpd/ncl423
61. Kurpinski K, Jang DJ, Bhattacharya S, Rydberg B, Chu J, So J, et al. Differential Effects of X-Rays and High-Energy Fe-56 Ions on Human Mesenchymal Stem Cells. *Int J Radiat Oncol Biol Phys* (2009) 73(3):869–77. doi: 10.1016/j.ijrobp.2008.10.002
62. Ding LH, Park S, Peyton M, Girard L, Xie Y, Minna JD, et al. Distinct Transcriptome Profiles Identified in Normal Human Bronchial Epithelial Cells After Exposure to Gamma-Rays and Different Elemental Particles of High Z and Energy. *BMC Genomics* (2013) 14:372. doi: 10.1186/1471-2164-14-372
63. Beck M, Rombouts C, Moreels M, Aerts A, Quintens R, Tabury K, et al. Modulation of Gene Expression in Endothelial Cells in Response to High LET Nickel Ion Irradiation. *Int J Mol Med* (2014) 34(4):1124–32. doi: 10.3892/ijmm.2014.1893
64. Hellweg CE. The Nuclear Factor Kappab Pathway: A Link to the Immune System in the Radiation Response. *Cancer Lett* (2015) 368(2):275–89. doi: 10.1016/j.canlet.2015.02.019
65. Lin Y, Bai L, Chen WJ, Xu SL. The NF-Kappa B Activation Pathways, Emerging Molecular Targets for Cancer Prevention and Therapy. *Expert Opin Ther Targets* (2010) 14(1):45–55. doi: 10.1517/14728220903431069
66. Hildebrandt G, Seed MP, Freemantle CN, Alam CA, Colville-Nash PR, Trott KR. Mechanisms of the Anti-Inflammatory Activity of Low-Dose Radiation Therapy. *Int J Radiat Biol* (1998) 74(3):367–78. doi: 10.1080/095530098141500
67. Kumari A, Simon SS, Moody TD, Garnett-Benson C. Immunomodulatory Effects of Radiation: What Is Next for Cancer Therapy? *Future Oncol (London England)* (2016) 12(2):239–56. doi: 10.2217/fon.15.300
68. Lodermann B, Wunderlich R, Frey S, Schorn C, Stangl S, Rodel F, et al. Low Dose Ionising Radiation Leads to a NF-Kappab Dependent Decreased Secretion of Active IL-1beta by Activated Macrophages With a Discontinuous Dose-Dependency. *Int J Radiat Biol* (2012) 88(10):727–34. doi: 10.3109/09553002.2012.689464
69. Pajonk F, McBride WH. Ionizing Radiation Affects 26s Proteasome Function and Associated Molecular Responses, Even at Low Doses. *Radiother Oncol* (2001) 59(2):203–12. doi: 10.1016/S0167-8140(01)00311-5
70. Baumstark-Khan C, Hellweg CE, Arenz A, Meier MM. Cellular Monitoring of the Nuclear Factor Kappa B Pathway for Assessment of Space Environmental Radiation. *Radiat Res* (2005) 164(4):527–30. doi: 10.1667/Rr3397.1
71. Hellweg CE, Baumstark-Khan C, Schmitz C, Lau P, Meier MM, Testard I, et al. Carbon-Ion-Induced Activation of the NF-Kappa B Pathway. *Radiat Res* (2011) 175(4):424–31. doi: 10.1667/Rr2423.1
72. Natarajan M, Aravindan N, Meltz ML, Herman TS. Post-Translational Modification of I-Kappa B Alpha Activates NF-Kappa B in Human Monocytes Exposed to 56Fe Ions. *Radiat Environ Biophys* (2002) 41 (2):139–44. doi: 10.1007/s00411-002-0143-x
73. Karin M. NF-Kappab as a Critical Link Between Inflammation and Cancer. *Cold Spring Harbor Perspect Biol* (2009) 1(5):a000141. doi: 10.1101/cshperspect.a000141
74. Multhoff G, Radons J. Radiation, Inflammation, and Immune Responses in Cancer. *Front Oncol* (2012) 2:58. doi: 10.3389/fonc.2012.00058
75. Golden EB, Marciscano AE, Formenti SC. Radiation Therapy and the *in Situ* Vaccination Approach. *Int J Radiat Oncol Biol Phys* (2020) 108(4):891–8. doi: 10.1016/j.ijrobp.2020.08.023
76. Diegeler S, Hellweg CE. Intercellular Communication of Tumor Cells and Immune Cells After Exposure to Different Ionizing Radiation Qualities. *Front Immunol* (2017) 8:664. doi: 10.3389/fimmu.2017.00664
77. Matsunaga A, Ueda Y, Yamada S, Harada Y, Shimada H, Hasegawa M, et al. Carbon-Ion Beam Treatment Induces Systemic Antitumor Immunity Against Murine Squamous Cell Carcinoma. *Cancer* (2010) 116(15):3740–8. doi: 10.1002/cncr.25134
78. Yoshimoto Y, Oike T, Okonogi N, Suzuki Y, Ando K, Sato H, et al. Carbon-Ion Beams Induce Production of an Immune Mediator Protein, High Mobility Group Box 1, at Levels Comparable With X-Ray Irradiation. *J Radiat Res* (2015) 56(3):509–14. doi: 10.1093/jrr/rrv007
79. Quintens R, Verreet T, Janssen A, Neefs M, Leysen L, Michaux A, et al. Identification of Novel Radiation-Induced P53-Dependent Transcripts Extensively Regulated During Mouse Brain Development. *Biol Open* (2015) 4(3):331–44. doi: 10.1242/bio.20149969

80. Munoz MJ, Perez Santangelo MS, Paronetto MP, de la Mata M, Pelisch F, Boireau S, et al. DNA Damage Regulates Alternative Splicing Through Inhibition of RNA Polymerase II Elongation. *Cell* (2009) 137(4):708–20. doi: 10.1016/j.cell.2009.03.010
81. Dutertre M, Sanchez G, De Cian MC, Barbier J, Dardenne E, Gratadou L, et al. Cotranscriptional Exon Skipping in the Genotoxic Stress Response. *Nat Struct Mol Biol* (2010) 17(11):1358–66. doi: 10.1038/nsmb.1912
82. Paronetto MP, Minana B, Valcarcel J. The Ewing Sarcoma Protein Regulates DNA Damage-Induced Alternative Splicing. *Mol Cell* (2011) 43(3):353–68. doi: 10.1016/j.molcel.2011.05.035
83. Tresini M, Warmerdam DO, Kolovos P, Snijder L, Vrouwe MG, Demmers JAA, et al. The Core Spliceosome as Target and Effector of Non-Canonical ATM Signalling. *Nature* (2015) 523(7558):53. doi: 10.1038/nature14512
84. Shkreta L, Toutant J, Durand M, Manley JL, Chabot B. SRSF10 Connects DNA Damage to the Alternative Splicing of Transcripts Encoding Apoptosis, Cell-Cycle Control, and DNA Repair Factors. *Cell Rep* (2016) 17(8):1990–2003. doi: 10.1016/j.celrep.2016.10.071
85. Wang Y, Guan H, Xie DF, Xie Y, Liu XD, Wang Q, et al. Proteomic Analysis Implicates Dominant Alterations of RNA Metabolism and the Proteasome Pathway in the Cellular Response to Carbon-Ion Irradiation. *PloS One* (2016) 11(10):e0163896. doi: 10.1371/journal.pone.0163896
86. Williamson L, Saponaro M, Boeing S, East P, Mitter R, Kantidakis T, et al. UV Irradiation Induces a Non-Coding RNA That Functionally Opposes the Protein Encoded by the Same Gene. *Cell* (2017) 168(5):843–55.e13. doi: 10.1016/j.cell.2017.01.019
87. Lavin LF, Khanna KK. Review: ATM: The Protein Encoded by the Gene Mutated in the Radiosensitive Syndrome Ataxia-Telangiectasia. *Int J Radiat Biol* (1999) 75(10):1201–14. doi: 10.1080/095530099139359
88. Taylor AMR, Groom A, Byrd PJ. Ataxia-Telangiectasia-Like Disorder (ATLD) - Its Clinical Presentation and Molecular Basis. *DNA Repair* (2004) 3(8-9):1219–25. doi: 10.1016/j.dnarep.2004.04.009
89. Dvorak CC, Cowan MJ. Radiosensitive Severe Combined Immunodeficiency Disease. *Immunol Allergy Clin N Am* (2010) 30(1):125. doi: 10.1016/j.iac.2009.10.004
90. Riballo E, Critchlow SE, Teo SH, Doherty AJ, Priestley A, Broughton B, et al. Identification of a Defect in DNA Ligase IV in a Radiosensitive Leukaemia Patient. *Curr Biol* (1999) 9(13):699–702. doi: 10.1016/S0960-9822(99)80311-X
91. Digweed M, Sperling K. Nijmegen Breakage Syndrome: Clinical Manifestation of Defective Response to DNA Double-Strand Breaks. *DNA Repair* (2004) 3(8-9):1207–17. doi: 10.1016/j.dnarep.2004.03.004
92. Burnet NG, Nyman J, Turesson I, Wurm R, Yarnold JR, Peacock JH. Prediction of Normal-Tissue Tolerance to Radiotherapy From *in-Vitro* Cellular Radiation Sensitivity. *Lancet* (1992) 339(8809):1570–1. doi: 10.1016/0140-6736(92)91833-T
93. Geara FB, Peters LJ, Ang KK, Wike JL, Brock WA. Prospective Comparison of *In Vitro* Normal Cell Radiosensitivity and Normal Tissue Reactions in Radiotherapy Patients. *Int J Radiat Oncol Biol Phys* (1993) 27(5):1173–9. doi: 10.1016/0360-3016(93)90540-C
94. Joubert A, Zimmerman KM, Bencokova Z, Gastaldo J, Chavaudra N, Favaudon V, et al. DNA Double-Strand Break Repair Defects in Syndromes Associated With Acute Radiation Response: At Least Two Different Assays to Predict Intrinsic Radiosensitivity? *Int J Radiat Biol* (2008) 84(2):107–25. doi: 10.1080/09553000701797039
95. Strasser H, Grabenbauer GG, Sprung CN, Sauer R, Distel LVR. DNA Double-Strand Break Induction and Repair in Irradiated Lymphoblastoid, Fibroblast Cell Lines and White Blood Cells From ATM, NBS and Radiosensitive Patients. *Strahlenther und Onkologie* (2007) 183(8):447–53. doi: 10.1007/s00066-007-1683-4
96. Greve B, Bolling T, Amler S, Rossler U, Gomolka M, Mayer C, et al. Evaluation of Different Biomarkers to Predict Individual Radiosensitivity in an Inter-Laboratory Comparison-Lessons for Future Studies. *PloS One* (2012) 7(10). doi: 10.1371/journal.pone.0047185
97. Martin NT, Nahas SA, Tunuguntla R, Fike F, Gatti RA. Assessing 'Radiosensitivity' With Kinetic Profiles of Gamma-H2AX, 53BP1 and BRCA1 Foci. *Radiother Oncol* (2011) 101(1):35–8. doi: 10.1016/j.radonc.2011.05.065
98. Chua MLK, Rothkamm K. Biomarkers of Radiation Exposure: Can They Predict Normal Tissue Radiosensitivity? *Clin Oncol* (2013) 25(10):610–6. doi: 10.1016/j.clon.2013.06.010
99. Hornhardt S, Rossler U, Sauter W, Rosenberger A, Illig T, Bickeboller H, et al. Genetic Factors in Individual Radiation Sensitivity. *DNA Repair (Amst)* (2014) 16:54–65. doi: 10.1016/j.dnarep.2014.02.001
100. Snyder AR, Morgan WF. Gene Expression Profiling After Irradiation: Clues to Understanding Acute and Persistent Responses? *Cancer Metastasis Rev* (2004) 23(3-4):259–68. doi: 10.1023/B:CANC.0000031765.17886.fa
101. Svensson JP, Stalpers LJA, Esveldt-van Lange REE, Franken NAP, Haveman J, Klein B, et al. Analysis of Gene Expression Using Gene Sets Discriminates Cancer Patients With and Without Late Radiation Toxicity. *PloS Med* (2006) 3(10):1904–14. doi: 10.1371/journal.pmed.0030422
102. Rieger KE, Hong WJ, Tusher VG, Tang J, Tibshirani R, Chu G. Toxicity From Radiation Therapy Associated With Abnormal Transcriptional Responses to DNA Damage. *Proc Natl Acad Sci USA* (2004) 101(17):6635–40. doi: 10.1073/pnas.0307761101
103. Borras-Fresneda M, Barquinero JF, Gomolka M, Hornhardt S, Rossler U, Armengol G, et al. Differences in DNA Repair Capacity, Cell Death and Transcriptional Response After Irradiation Between a Radiosensitive and a Radioresistant Cell Line. *Sci Rep* (2016) 6:27043. doi: 10.1038/srep27043
104. Shuryak I, Ghandhi SA, Turner HC, Weber W, Melo D, Amundson SA, et al. Dose and Dose-Rate Effects in a Mouse Model of Internal Exposure From 137Cs. Part 2: Integration of Gamma-H2AX and Gene Expression Biomarkers for Retrospective Radiation Biodosimetry. *Radiat Res* (2020) 196(5):491–500. doi: 10.1667/RADE-20-00042.1
105. Paul S, Smilenov LB, Elliston CD, Amundson SA. Radiation Dose-Rate Effects on Gene Expression in a Mouse Biodosimetry Model. *Radiat Res* (2015) 184(1):24–32. doi: 10.1667/RR14044.1
106. Ghandhi SA, Smilenov LB, Elliston CD, Chowdhury M, Amundson SA. Radiation Dose-Rate Effects on Gene Expression for Human Biodosimetry. *BMC Med Genomics* (2015) 8(22). doi: 10.1186/s12920-015-0097-x
107. Paul S, Barker CA, Turner HC, McLane A, Wolden SL, Amundson SA. Prediction of *In Vivo* Radiation Dose Status in Radiotherapy Patients Using *Ex Vivo* and *In Vivo* Gene Expression Signatures. *Radiat Res* (2011) 175(3):257–65. doi: 10.1667/RR2420.1
108. Abend M, Badie C, Quintens R, Kriehuber R, Manning G, Macaeva E, et al. Examining Radiation-Induced *In Vivo* and *In Vitro* Gene Expression Changes of the Peripheral Blood in Different Laboratories for Biodosimetry Purposes: First RENEB Gene Expression Study. *Radiat Res* (2016) 185(2):109–23. doi: 10.1667/RR14221.1

Conflict of Interest: The authors declare that the research was conducted in the absence of any commercial or financial relationships that could be construed as a potential conflict of interest.

GLOSSARY

ASCC3	activating signal cointegrator 1 complex subunit 3
ASTN2	astrotactin 2
ATM	ataxia telangiectasia mutated
ATR	ataxia telangiectasia and Rad3-related
cDNA	complementary deoxyribonucleic acid
cRNA	complementary ribonucleic acid
DDB2	DNA damage binding protein 2
DNA	deoxyribonucleic acid
DSB	double-strand break
EDTA	ethylenediaminetetraacetic acid
FC	fold-change
FDR	false discovery rate
FDXR	ferredoxin reductase
FITC	fluorescein isothiocyanate
GADD45A	growth arrest and DNA damage inducible alpha
GCR	galactic cosmic rays
GO	gene ontology
GSEA	gene set enrichment analysis
HIST2H3A	histone cluster 2 H3a
HIST2H3PS2	histone cluster 2 H3 pseudogene 2
HIST2H3C	histone cluster 2 H3c
HIST2H3D	histone cluster 2 H3d
HLA-A	major histocompatibility complex class I A
HLA-B	major histocompatibility complex class I B
HLA-H	major histocompatibility complex class I H (pseudogene)
HLA-DMB	major histocompatibility complex class II DM beta
HPRT1	hypoxanthine phosphoribosyltransferase 1
HZE	high (Z) atomic number and energy
IL-1	interleukin-1
IL-2	interleukin-2
IL-6	interleukin-6
JAK	Janus kinase
LET	linear energy transfer
MAMDC4	MAM domain containing 4
MCP-1	monocyte chemoattractant protein-1
MRE11A	meiotic recombination 11 homolog A
mRNA	messenger ribonucleic acid
mTORC1	mammalian target of rapamycin complex 1
NDUFAF6	NADH : Ubiquinone oxidoreductase complex assembly factor 6
NES	normalized enrichment score
NF-κB	nuclear factor κB
PBMC	peripheral blood mononuclear cell
PCNA	proliferating cell nuclear antigen
PGK1	phosphoglycerate kinase 1
qRT-PCR	quantitative reverse transcription polymerase chain reaction
RAD51D	DNA repair protein RAD51 homolog D
RBE	relative biological effectiveness
RBM14	RNA binding motif protein 14
RMA	robust multichip analysis
RNA	ribonucleic acid
RPS27L	ribosomal protein S27 like
RRHO	rank-rank hypergeometric overlap
SPE	solar particle event
STAT3	signal transducer and activator of transcription 3
STAT5	signal transducer and activator of transcription 5
TNF-α	tumor necrosis factor alpha
TP53	tumor protein 53
UV	ultra violet
VWCE	Von Willebrand factor C and EGF domains
γH2AX	phosphorylated histone subtype H2A isoform X.

frontiers in Oncology

REVIEW
published: 24 November 2021
doi: 10.3389/fonc.2021.766407

Recent Advances in Brachytherapy Using Radioactive Nanoparticles: An Alternative to Seed-Based Brachytherapy

Baljeet Seniwal[1], *Velaphi C. Thipe*[2,3], *Sukhvir Singh*[4]*, *Telma C. F. Fonseca*[5] *and Lucas Freitas de Freitas*[2]

[1] Centre de Recherche du Centre Hospitalier Universitaire de Québec-Université Laval (CR-CHU de Québec), Axe Médecine Régénératrice, Québec, QC, Canada, [2] Instituto de Pesquisas Energéticas e Nucleares, Comissão Nacional de Energia Nuclear (IPEN-CNEN), Cidade Universitária, São Paulo, Brazil, [3] Department of Radiology, Institute of Green Nanotechnology, School of Medicine, University of Missouri, Columbia, MO, United States, [4] Institute of Nuclear Medicine and Allied Sciences, Defence Research and Development Organisation, Delhi, India, [5] Departamento de Engenharia Nuclear—Universidade Federal de Minas Gerais, Belo Horizonte, Brazil

OPEN ACCESS

Edited by:
Shubhankar Suman, Georgetown University, United States

Reviewed by:
Alessandro Grattoni, Houston Methodist Research Institute, United States
Zhilei Shen, University of Southern California, United States

***Correspondence:**
Sukhvir Singh
sukhvir.phy@gmail.com

Specialty section:
This article was submitted to Radiation Oncology, a section of the journal Frontiers in Oncology

Received: *29 August 2021*
Accepted: *29 October 2021*
Published: *24 November 2021*

Citation:
Seniwal B, Thipe VC, Singh S, Fonseca TCF and Freitas de Freitas L (2021) Recent Advances in Brachytherapy Using Radioactive Nanoparticles: An Alternative to Seed-Based Brachytherapy. Front. Oncol. 11:766407. doi: 10.3389/fonc.2021.766407

Interstitial brachytherapy (BT) is generally used for the treatment of well-confined solid tumors. One example of this is in the treatment of prostate tumors by permanent placement of radioactive seeds within the prostate gland, where low doses of radiation are delivered for several months. However, successful implementation of this technique is hampered due to several posttreatment adverse effects or symptoms and operational and logistical complications associated with it. Recently, with the advancements in nanotechnology, radioactive nanoparticles (radio-NPs) functionalized with tumor-specific biomolecules, injected intratumorally, have been reported as an alternative to seed-based BT. Successful treatment of solid tumors using radio-NPs has been reported in several preclinical studies, on both mice and canine models. In this article, we review the recent advancements in the synthesis and use of radio-NPs as a substitute to seed-based BT. Here, we discuss the limitations of current seed-based BT and advantages of radio-NPs for BT applications. Recent progress on the types of radio-NPs, their features, synthesis methods, and delivery techniques are discussed. The last part of the review focuses on the currently used dosimetry protocols and studies on the dosimetry of nanobrachytherapy applications using radio-NPs. The current challenges and future research directions on the role of radio-NPs in BT treatments are also discussed.

Keywords: interstitial brachytherapy, nanobrachytherapy, radioactive nanoparticles, intratumoral injection, solid tumors

1 INTRODUCTION

Cancer is one of the main causes of human death worldwide (1). Along with chemotherapy and surgery, radiotherapy (RT), also termed as radiation therapy, is a well-established method of treating non-metastatic cancers (2–4). In current practice, more than half of the cancer patients receive RT as primary mode of cancer therapy or adjuvant mode of treatment along with

chemotherapy, immunotherapy, or surgery (5). In RT, high doses of ionizing radiation are delivered to ablate cancer cells and suppress recurrence and progression of cancer cells. RT can be broadly categorized into three types: external beam RT (EBRT), systemic RT, and internal RT (6, 7). In EBRT, high-energy photon or electron or ion beams are employed to deliver radiation to the tumor volume by placing radiation source outside the patient's body (2). Systemic radiation therapies such as targeted RT deliver radioisotopes labeled with carrier molecules with high affinity towards receptors overexpressed by the cancer cells, e.g., monoclonal antibodies (mAb), through ingestion, infusion using catheter, or intravenous injection. In internal RT, also known as brachytherapy (BT), minimal invasive methods are used to place the radiation sources either inside or in close proximity to the tumor volume. BT allows delivery of high doses of radiation precisely to the tumor volume, while minimizing radiation exposure to the healthy tissues and organs at risk. Due to the precise and targeted dose delivery characteristics of BT, it can be employed to effectively treat solid tumors with minimum side effects and short treatment time at low cost.

Clinical trials and preclinical studies using BT have reported promising outcomes. However, the logistical and operational difficulties associated with BT seed placement have impeded its successful application. For instance, in patients with prostate tumor, the transrectal ultrasound (TRUS)-based implantation approach is used to implant radioactive seeds within the tumor (8, 9). The seed implantation causes trauma and edema in the prostate gland. This may consequently result in inaccurate or off-target placement of the seeds. The placement of radioactive seeds outside the tumor volume may result in undesired radiation exposure to the organs at risk, e.g., urinary bladder and rectum. Further, inaccurate seed placement may produce non-uniform dose distribution and may consequently result in mild to severe clinical side effects. Additionally, post-implantation migration of seeds to the lungs has also been reported and may require seed removal (8, 10).

Recently, several preclinical studies on localized delivery of radioactive nanoparticles (radio-NPs) into the tumor, similar to BT, have been reported in the literature, and this technique is termed as nanobrachytherapy (11–13). In nanobrachytherapy, radio-NPs are injected intratumorally as an alternative to the implantation of radioactive seeds. One recent example of this mode of treatment is the work by Salvanou et al. (14), who reported the use of gold nanoparticles (AuNPs) radiolabeled with ^{225}Ac (alpha emitter) as an unconventional BT procedure, involving intratumoral injection of these radiolabeled AuNPs. Such nanoparticle-based systems i) conserve the characteristics of BT, i.e., precise and targeted dose delivery; ii) can be administered through injection; and iii) have the ability to provide patient-specific treatment, as radiation dose can be divided into several fractions. Additionally, these radiopharmaceuticals do not need seed removal; hence, they can be handled easily and can be extremely useful. The nanometer size of these radiopharmaceuticals allows local diffusion from the site of injection and may result in homogeneous dose distribution within the tumor volume. Lastly, these nanomaterials (particularly high Z nanoparticles) can be used as multifunctional carriers to deliver radioisotopes to provide imaging and RT capabilities. Such radioactive high-Z nanoparticles may also enhance radiation dose through self-sensitization and may require less radioactivity in comparison with conventional BT.

In this article, we review the recent advancements in the synthesis and use of radio-NPs as nanobrachytherapeutic agents. The subsequent section presents a review and discussion on different techniques involved in radiosynthesis of nanoparticles. The particles emitted by radionuclides, present in the obtained radionuclide–nanoparticle complex, must deposit their energy locally and spare the surrounding normal tissues. Hence, in the succeeding section, the essential characteristics of radionuclide–nanoparticle complexes, which are vital to qualifying them as nanobrachytherapeutic agents, are discussed. After intratumoral injection, these radio-NPs diffuse 1–2 mm within the extracellular medium, from the site of injection (15), and are internalized by the tumor cells. Thus, different mechanisms involved in the internalization of radio-NPs by tumor cells are reviewed in the next section. Thereafter, we summarize and review the most recently published preclinical studies on nanobrachytherapy. Additionally, for any RT-based treatment, dosimetry and treatment planning are the two crucial steps to ensure and quantify its accuracy and efficacy. Hence, the subsequent section reviews the recent dosimetric studies on use of radio-NPs as nanobrachytherapeutic agents. Lastly, current challenges and future research directions on the role of radio-NPs in BT treatments are discussed.

2 METHODS OF RADIOSYNTHESIS OF NANOPARTICLES

Although several advances in cancer treatment have been made throughout the years, it is paramount to develop more precise diagnostic and therapeutic regimens essential to achieve better diagnostic and therapeutic outcomes. Tumor presents a multifactorial etiology, which makes it an extremely complex and heterogeneous disease, attributed to an almost unique expression of biomarkers from patient to patient. To circumvent this complexity, the development of so-called precision and personalized medicine is pivotal towards the battle against cancer (16). One of the major strategies is through the combination of nuclear medicine modalities and nanotechnology to offer unique opportunities to develop an effective single chemical entity with diagnostic and therapeutic capabilities for clinical applications in theranostic nanoradiopharmaceuticals. This is achieved by designing architectural radiolabeled nanoconstructs based on the amalgamation of four major components for the intended *in vivo* pharmacokinetics (17):

1. Appropriate nanoparticles including inorganic, organic polymers, and metallics
2. Targeting ligand (e.g., biomolecule, antibody, and peptide)—allows for specific targeting of receptors overexpressed on tumor cells or within the tumor microenvironment

3. Radionuclide selection (imaging and/or therapeutic)—emission mode, decay half-life, and chemical properties, availability, and radiolabeling reaction
4. Radiolabeling strategy to achieve the maximal radiochemical purity and yield, which reflects specific activity of nanoradiopharmaceuticals

Among the different types of nanoparticles, AuNPs and iron oxide nanoparticles (IONPs) have gained more prominence due to their superior biocompatibility, low toxicity, ease in surface versatile functionalization and radiolabeling with a plethora of imaging, and therapeutic radionuclides towards the development of nanoradiopharmaceuticals for imaging and therapy of cancer. Translational medicine that makes use of nanoradiopharmaceutical agents demonstrates excellent pharmacokinetics in terms of radiochemical production, purity and stability (nanoradioformulation integrity), biodistribution, dosimetry, low off-target localization, and favorable renal clearance profiles, which represent a versatile theranostic tool in cancer management, ranging from nuclear medicine imaging and image-guided surgery to alpha/beta-particle targeted therapy, and most recently targeted nanobrachytherapy (18–21). The use of targeted nanobrachytherapy through radiolabeled nanoparticles affords intra- or peritumoral administration, thus allowing less invasiveness and homogenizing the radiation dose deposition in the tumor as compared with conventional BT (22).

2.1 Radiolabeling Nanoparticles

A plethora of orthogonal (radio)labeling strategies for nanoparticles are available for the development of multimodal nanoradiotherapeutics (23) as shown in **Figure 1**. The radiolabeling of nanoparticles for medical imaging and therapy has been discussed in-depth in reviews, which are highly recommended for further reading (20). The most pertinent consideration for radiolabeling nanoparticles is the functionalization with suitable molecular entities to allow for the coordination/conjugation of the radioisotopes achieved through the use of chelators *via* coordination chemistry approaches (19, 20, 24):

1. Bifunctional moieties that provide capping/stabilizing capabilities with subsequent binding affinity to the radioisotopes
2. Direct surface conjugation of amino/thiolated molecules followed by ligand exchange

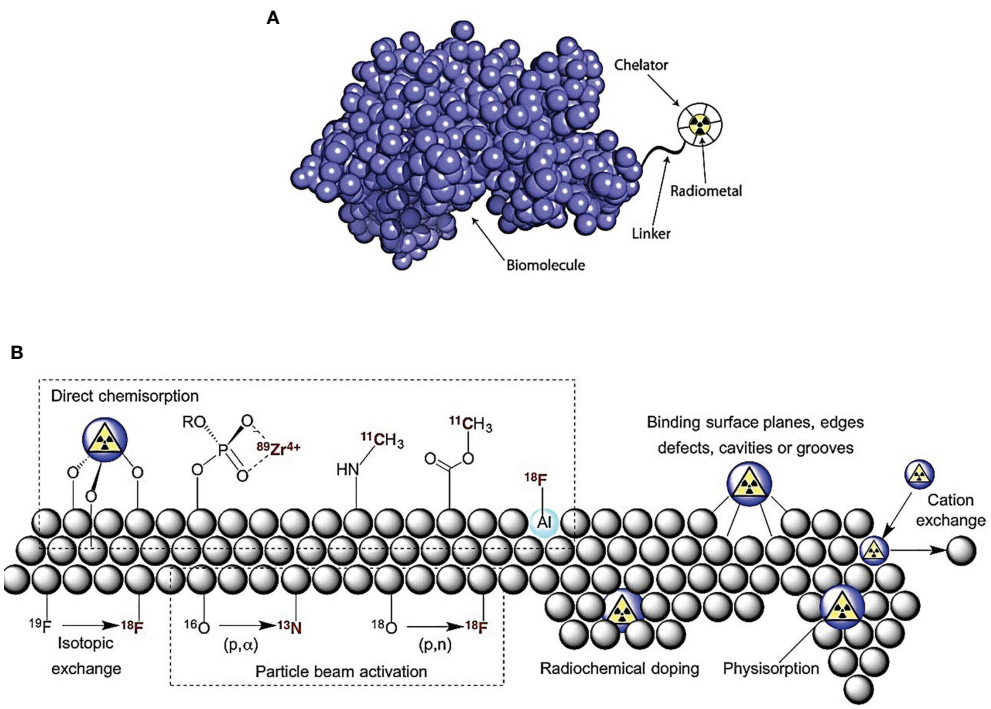

FIGURE 1 | Radiolabeling nanoparticle strategies include the following: **(A)** indirect radiolabeling by bifunctional chelator—compounds having reactive functional groups that enable them to be covalently linked (conjugated) to biologically relevant vectors (e.g., protein and peptide). **(B)** Direct radiolabeling *via* i) chemisorption, high binding affinity chemical bonding between nanoparticles and radionuclides; ii) cavity entrapment, entrapment of radionuclides in native cavities or core-shell/layered nanoparticles; iii) isotopic exchange, exchanging stable and radioactive isotopes of an element in different chemical states; iv) particle beam activation, hadronic bombardment to initiate a nuclear reaction that converts stable isotopes in the nanoparticle lattice into radioactive nanoparticles; v) radiochemical doping, using a radionuclide as a surrogate during the synthesis, yielding inherently radioactive nanoparticles; vi) physisorption, physical bonding to the surface of nanoparticles by Van der Waals forces; vii) cation exchange, cation exchange between the nanoparticle's cation and a different cationic radionuclide [adapted with permission from Lamb et al. (23)].

3. Chemical modification of molecules already attached on the surface of the nanoparticles

2.1.1 Indirect Radiolabeling

Indirect radiolabeling is attainable *via* exogenous coordination chemistry moieties [bifunctional chelators (BFCs) and prosthetic groups] through chemical linkers to aid complexation (25).

2.1.1.1 Bifunctional Chelators

BFCs are molecules consisting of a metal chelating unit that binds to metallic radionuclides and a reactive functionality for conjugation with surface of the nanoparticles. BFCs are highly preferred due to *in vivo* radiolabel stability strongly dependent on the coordination chemistry between the radionuclide and the BFC. However, the drawback of radionuclide–BFC coordination complexes is *in vivo* dissociation due to enzymatic and/or trans-chelating interactions with proteins such as transferrin and ferritin. A successful BFC allows for minimal *in vivo* dissociation of the radionuclide from the chelator, dependent on the kinetic inertness and thermodynamic stability of the BFC, where polydentate ligands form stable complexes over their monodentate ligands due to the "chelate effect" (19, 20). The bioconjugation of BFC to nanoparticles is usually facilitated by functional groups present on the surface of nanoparticles that include amine conjugation (e.g., anhydride, NHS ester, and isothiocyanate), carboxylic acid conjugation (e.g., carbodiimide couplings), thiol conjugation (e.g., maleimide coupling), and click chemistry conjugation (e.g., Cu-catalyzed azide-alkyne cycloaddition and inverse electron demand Diels–Alder cycloaddition) to ensure the *in vivo* inertness of the resulting radiometal complex (20). The chelator selection is dependent on the radionuclide and desired physicochemical properties and pharmacokinetics of the radiolabeled nanoparticles.

Categories of BFCs (**Figure 2**):

1. Macrocyclic chelators—relatively rigid and pre-organized structure allowing for high complexation stability due to macrocyclic effect but suffer from slow complexation kinetics
2. Acyclic/linear chelators—offer rapid radiometal complexation due to their lack of rigidity

2.1.1.1.1 Radiolabeling via Dodecane Tetraacetic Acid-Based Chelators. Macrocyclic multidentate chelator, dodecane tetraacetic acid (DOTA), is the most commonly utilized BFC owing to its high affinity to most metal radionuclides (^{64}Cu, ^{177}Lu, ^{68}Ga, and ^{111}In). Among the radionuclides, ^{177}Lu ($t_{1/2}$ = 6.734 days) with both β emissions and γ rays is of interest for theranostics. ^{177}Lu entrapping AuNPs inside the dendritic cavity of a generation 4 (G4) polyamidoamine (PAMAM) dendrimer, which had been pre-conjugated with *p*-SCN-benzyl-DOTA as well as folate/bombesin for cancer targeting (26). Cancer immunotherapy with mAb such as atezolizumab, pembrolizumab, and trastuzumab has been conjugated to DOTA and radiolabeled with ^{64}Cu (^{64}Cu-DOTA-mAb) for positron emission tomography (PET) imaging utilized to estimate tumor density, perfusion, and distribution in mice bearing MDA-MB231 anti-programmed death-ligand 1 (PD-L1-positive) xenograft and HER2-targeted antibodies for patients with metastatic HER2-positive breast cancer (BC) (27, 28). Poly-(isobutylene-alt-maleic anhydride)-graft-dodecyl (PMA) is a polymer shell, which was integrated with DOTA for ^{111}In loading, thus resulting in ^{111}In-DOTA/^{198}Au nanoparticles being classified as a

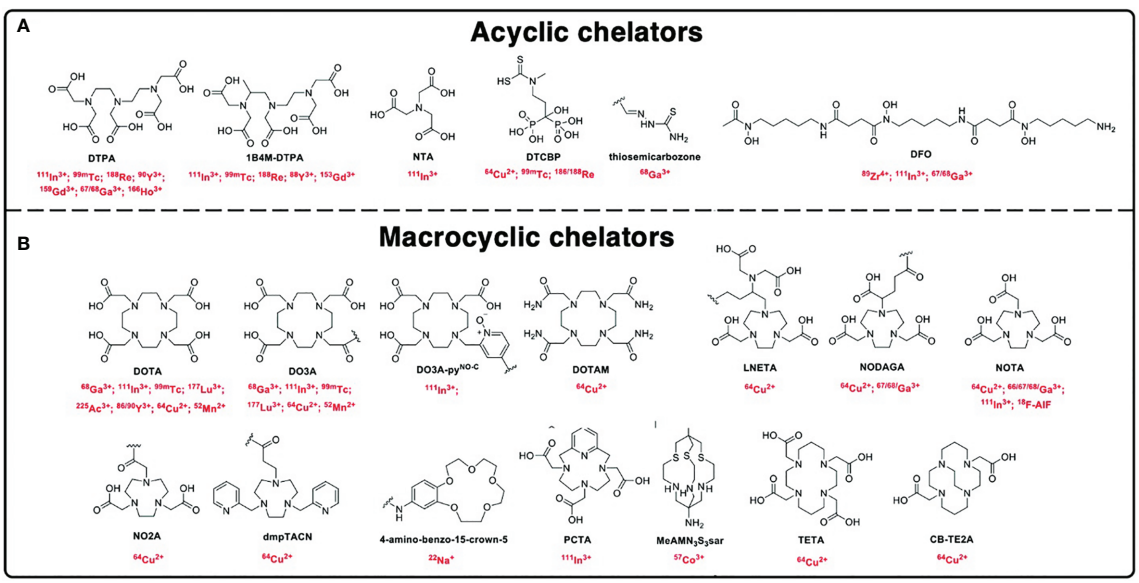

FIGURE 2 | Chemical structures of the chelators. **(A)** Acyclic chelators and **(B)** macrocyclic chelators and their respective radionuclides used for radiolabeling nanomaterials [adapted from Pellico et al. (20)].

post-formulation chelation (21). Hajiramezanali et al. (29) developed ^{68}GA-radiolabeled bombesin conjugated to trimethyl chitosan-coated superparamagnetic nanoparticles (^{68}Ga-DOTA-BN-TMC-MNPs) with radiochemical purity >98%. Most recently, AGuIX® represents gadolinium (^{67}Gd)-DOTAGA cyclic chelates covalently grafted to polysiloxane matrix to produce AGuIX nanoparticles (30, 31).

2.1.1.1.2 Radiolabeling via 1,4,7-Triazacyclononane-N,N′,N″-Triacetic Acid-Based Chelators. A hexadentate N_3O_3 chelator, 1,4,7-triazacyclononane-*N*,*N*′,*N*″-triacetic acid (NOTA), and its derivative are commonly used for gallium and copper radiopharmaceuticals (^{67}Ga/^{68}Ga and ^{64}Cu) for radiolabeling nanoparticles. The general approach for conjugating nanoparticles with NOTA moiety for ^{67}/^{68}Ga and ^{64}Cu labeling is through thiol-functionalized NOTA (NOTA-SH) for radiolabeling and conjugation, additionally linkers/spacers such as polyethylene glycol (PEG) and PEI to optimize *in vivo* pharmacokinetics. NOTA-SH can be achieved by reacting *p*-SCN-Bn-NOTA with 2-aminoethanethiol hydrochloride in the presence of triethanolamine.

2.1.1.1.3 Radiolabeling via Diethylenetriaminepentaacetic Acid-Based Chelators. A polydentate acyclic chelator, diethylenetriaminepentaacetic acid (DTPA), is commonly used in the construction of MRI and nuclear imaging agents (^{99m}Tc, ^{111}In, and ^{67}/^{68}Ga). However, the DTPA complex exhibits low *in vivo* kinetic stability characterized by fast dissociation kinetics and radiometal complexation, and the functionalization of nanoparticles with polymers such as PAMAM and PEI improved stability.

2.1.1.2 Prosthetic Groups

Indirect radiolabeling *via* chelators is susceptible to *in vivo* radiometal trans-chelation with native biological chelators and ions as well as metalloenzymes, transport, and storage proteins in the body. This problem is evaded by radiolabeling with non-metallic radionuclides covalently bound to nanoparticles through prosthetic groups (^{11}C, ^{14}C, ^{18}F, ^{123}I, ^{124}I, ^{125}I, and ^{131}I) (25). [^{18}F]-Fluoro-2-deoxy-D-glucose (^{18}F-FDG) is used for the assessment of glycolysis as a non-invasive PET imaging agent. In an archetypical example, radiolabeling nanoparticles with ^{18}F has been reported by first conjugating cysteamine to mannose triflate (Man-CA) and then ^{18}F labeling resulting to a cysteamine-linked radiotracer (^{18}F-FDG-CA). The ^{18}F-FDG-CA is mixed with gold chloride ($HAuCl_4$) to obtain AuNPs (^{18}F-FDG-CA-AuNPs) (32).

2.1.1.3 Ionophore-Based

Ionophore-based radiolabeling is divided into subclasses: i) ionophore-chelate binding and ii) remote loading radiolabeling. Both ionophore-chelate binding and remote loading radiolabeling use lipophilic radiotracers with passive lipid membrane permeability properties (20). Radiolabeling based on ionophore ligand binding to radionuclide metal ion through lipophilic radio-ionophore complexation allows for transport across lipid bilayers. Once internalized in the vesicle, the radiometal dissociates from the radio-ionophore complex and binds to chelating molecules (e.g., proteins/nucleic acids or drugs) within the vesicle, which is preferentially relevant for vesicle-based nanoparticles such as liposomes and exosomes/extracellular vesicles containing lipid bilayer membranes. Remote loading is similar to ionophore-based chelator with the addition that the complex contains functional groups that can be charged within the vesicle core. Aranda-Lara et al. (33) reviewed the radiolabeling of liposomes and lipoproteins as lipidic nanoparticles.

2.1.2 Direct Radiolabeling

Indirect radiolabeling using chelator-based (bifunctional and prosthetic group) has gained prevalence in nuclear medicine. The negative impact on the biological activity of the overall radiolabeled nanoparticles is attributed to changes in the size, surface charge, and hydrophilicity of the nanoparticles. This problem can be overcome through direct and chelator-free radiolabeling strategies while maintaining the nanoparticle's native pharmacokinetic characteristics.

2.1.2.1 Chemisorption and Physisorption

Chemisorption is facilitated by mixing the radionuclides with nanoparticles that exhibit high binding affinity towards the radionuclides for direct chemical bond formation between the surface of the nanoparticles and the radionuclide. This is achieved through the oppositely charged moieties on the surface of the nanoparticles and the radionuclide, thus allowing for chemical adsorption. Likewise, physisorption occurs when charged radionuclide ions interact with the molecular surface of the nanoparticles *via* electrostatic attraction or van der Waals interactions (23). Pei et al. (34) designed a simple chelation between glutathione-modified gold nanoclusters (AuNCs) and radionuclides (^{99m}Tc and ^{177}Lu) to produce ^{99m}Tc@AuNCs and ^{177}Lu@AuNCs, respectively, as a novel approach for tumor radio-immunotherapy.

2.1.2.2 Radiochemical Doping (Hot-Plus-Cold Precursors)

Radiochemical labeling involves incorporation of the radionuclide as a surrogate during the synthesis of the nanoparticles resulting in intrinsically radioactive nanoparticles often carried out in automated closed lead-shielded unit due to the increased radiation exposure (21, 32). This type of radiolabeling is divided into two subcategories: hetero-radionuclides, where nanoparticle core cation and the radionuclide are different (e.g., doping AuNPs with ^{64}Cu or ^{111}In), and homo-radionuclides, where a radioisotope of the metal element to form the nanoparticle core is used (e.g., premixture of $H^{198}AuCl_4$ to $HAuCl_4$ precursor for the production of ^{198}AuNPS) (10, 35, 36). Similar studies by Laprise-Pelletier et al. (15) produced ^{103}Pd : Pd@^{198}Au : Au-PEG nanoparticles by premixing $^{103}PdCl_2/PdCl_2$ and $H^{198}AuCl_4/HAuCl_4$; and Chakravarty et al. (37) produced ^{199}Au nanoparticles conjugated with cyclic arginine-glycine-aspartate peptide (^{199}AuNP-RGD) by intrinsically radiolabeling during synthesis of AuNPs through the use of $H^{199}AuCl_4$ precursor. Fach et al. (38) doped [^{103}Pd]$PdCl_2$ in a solution of $HAuCl_4$ for co-reduction to produce AuPdNPs intrinsically

labeled with ^{103}Pd ([^{103}Pd]AuPdNPs) with ≈20 nm, and then ethylenediaminetetraacetic acid (EDTA) was used to scavenge free Pd^{2+} to avoid unspecific labeling of the nanoparticle surface resulting in radiolabeling efficiencies of 79% to >99%.

2.1.2.3 Hadronic Bombardment (Particle Beam Transmutation/Activation)

Formulated nanoparticles/nanocarriers contain stable precursors of the desired radionuclide (21). Radiolabeling *via* hadronic bombardment is performed by irradiating prefabricated nanoparticles *via* bombardment with accelerated particles (i.e., neutrons, protons, or deuterons) using a high-energy particle accelerator or nuclear reactor to induce a nuclear reaction to convert the stable isotope in the nanoparticle lattice to radioisotopes, resulting in radio-NPs. This radiolabeling is controlled by the bombardment time, current, and beam-line energy; the latter energies are often >10 MeV higher than for nanoparticle stability. To overcome this, an effective heat dissipation technique is a prerequisite for this method. Pérez-Campaña et al. (39) produced [^{13}N]Al_2O_3NPs by 16-MeV proton irradiation of Al_2O_3NPs *via* the 16O(p,α) ^{13}N nuclear reaction.

2.1.2.4 Encapsulation (Cavity Entrapment)

Encapsulation is through entrapping the radionuclide inside the native cavity within the nanoparticles or within core-shell/layered structured nanoparticles. Lee et al. (40) demonstrated the encapsulation of ^{124}I or ^{125}I to produce ^{124}/^{125}I embedded AuNPs. This was achieved by modifying the amine groups of the adenine-rich oligonucleotides on the surface of the AuNPs with sulfosuccimidyl-3-[4-hydroxyphenyl]propionate for ^{124}I or ^{125}I radiolabeling, followed by reacting the nanoparticles with $HAuCl_4$ to form a Au shell to shield radionuclide dissociation, thus resulting in ^{124}/^{125}I-Au@AuNPs this approach was further used to produce ^{124}I-labeled tannic acid gold core-shell nanoparticles (^{124}I-TA-Au@AuNPs) exhibiting 98% radiochemical yield. Laan et al. (41) reported a facile method for ^{111}In-labeling polystyrene-*b*-poly (ethylene oxide) diblock copolymer micelles without the necessity of any chemical modification.

2.2 Heterogeneous/Homogeneous Radioisotopic Exchange or Cation Exchange

2.2.1 Heterogeneous/Homogeneous Radioisotopic Exchange

Isotope exchange is facilitated through chemical equivalent exchange between the stable and radioactive isotopes of an element in different chemical states resulting only in low specific activity. For example, Freund et al. (42) produced ^{59}Fe-labeled IONPs by oleic acid-functionalized IONPs in chloroform, and then the IONPs were incubated with $^{59}FeCl_3$ which led to approximately 0.01%–0.5% ^{59}Fe exchange with Fe^{3+} (homogenous) in the IONPs. The low isotope exchange of ^{59}Fe/Fe is attributed to Fe surface availability of the IONPs. Heterogeneous radioisotopic exchange was demonstrated by Tang et al. (43) chelator-free radiolabeling of zinc sulfide (ZnS) quantum dots (QDs) with ^{68}Ga or ^{64}Cu through cation exchange.

2.2.2 Cation Exchange (Radio-Halogenation)

Similar to isotope exchange approach, cation exchange is a relatively new alternative that is more effective but still needs some improvements. It is carried out by a cation exchange between the cation within the nanoparticle and a different cationic radionuclide. Gaikwad et al. (44) intrinsically radiolabeled chitosan nanoparticles with ^{177}Lu *via* ionic gelation technique to produce ^{177}Lu-labeled chitosan nanoparticles (^{177}Lu-CH NP) with >98% radiochemical purity. Zhang et al. (45) developed PEGylated covalent organic frameworks (COFs) with strong affinity for Ag^+ ions, followed by ^{125}I radiolabeling at the Ag site to produce nanoscale ^{125}I-labeled PEG-COF-Ag with 94% radiolabeling yield in 30 s for BT.

In conclusion, beta emitters are preferred radionuclides over their alpha counterparts during radiolabeling owing to the large recoil energy (in the order of 100 keV) during decay of the latter (46). However, targeted alpha therapy (TAT) has received sufficient attention; therefore, effective radiolabeling strategies have been developed. Recently, Yi et al. (47) developed X-ray-optimized delivery of radiolabeled albumin for cancer theranostics. The authors utilized the abundant tyrosine existing in human serum albumin (HSA) nanoparticles for ^{125}I/^{131}I radiolabeling forming iodotyrosine for the production of ^{125}I/^{131}I-HSANPs.

3 RADIONUCLIDES FOR NANOBRACHYTHERAPY

The radionuclides to be used for internal RT must deliver high doses of radiation locally and spare the surrounding normal tissues (5, 13). Hence, radionuclides emitting radiation with higher linear energy transfer (LET) are generally preferred. LET is the amount of energy transferred, by the emitted particles, to the medium traversed per unit distance. These radionuclides are categorized into three groups based on the emitted particle type (48). It includes α, β, and Auger particle-emitting radionuclides, as reported in **Table 1**.

It is important to evaluate the suitability of these radionuclides for nanobrachytherapy applications. The must-have features for radionuclides can be classified into two main groups: i) physical and ii) biochemical characteristics. The physical characteristics to be considered are a) physical half-life; b) emitted particle type—α, β, and Auger electrons or photons; c) energy of the emitted particles; d) daughter product(s) and their stability; e) radionuclide purity and length of purification step; f) penetration depth of the emitted particles in the biological tissues; g) LET of the emitted particle; and h) size of the tumor to be treated (5, 13). Additionally, the biochemical characteristics to be evaluated are a) approach used to target tumor cells/tissues; b) retention of radio-NPs within the tumor; c) *in vivo* stability of the radionuclide–nanoparticle complex; and d) toxicity caused by the complex (53–55).

The physical half-life of the radionuclide should match with the *in vivo* pharmacokinetics of the radionuclide–nanoparticle complex (55). The life span (T) of the radionuclide can be

TABLE 1 | Summary of radionuclides and radioactive nanocarriers investigated in preclinical studies on nanobrachytherapy.

Radioisotopes	Half-life [days]	Decay mode	Emissions	Energy [keV]	Range max	References
			β	961 (99%), 285 (1%)	4 mm	
Au-198	22.7	β (100%)	γ	412 (96%), 676 (<1%), 1088 (<1%)	–	(49)
			β	462 (6.0%), 296 (71.6%), 250 (22.4%)	–	
Au-199	23.1	β (100%)	γ	159 (37%)	–	(37)
			β	497 (79%), 385 (9%)	1.6 mm	
Lu-177	26.7	β (100%)	γ	208 (11%), 113 (6%)	–	(50)
			β	248 (2%), 334 (7%), 606 (90%)	0.6 mm	
I-131	28	β (100%)	γ	284 (6%), 365 (82%), 637 (7%)	–	(17)
Ac-225	10	α (100%)	α	5800 (100%)	100 um	(14)
At-211	0.3	α (100%)	α	5870 (100%)	–	(51)
Pd-103	17	EC (100%)	γ	20 (64%), 23 (13%)	–	(38)
I-125	59.9	EC (100%)	γ	27 (114%), 31 (26%), 36 (7%)	–	(45)
In-111	2.8	EC (100%)	γ	245 (94%), 171 (90%)	–	(52)

EC, electron capture.

estimated from the physical half-life (Tp) of the radionuclide and half-clearance time, also known as biological half-life (T_b), of the radionuclide–nanoparticle complex using the relation $1/T = 1/T_p + 1/T_b$ (56). The physical half-life of the radionuclide can be known from the published radionuclide data; and to estimate the biological half-life of the radionuclide–nanoparticle complex, knowledge on the spatial and temporal distribution of the complex within the tumor and body is required. T_b depends on the mode of delivery, uptake, and metabolism of the radionuclide–nanoparticle complex by the tumor cells and its excretion from the patient's body (48, 53, 54).

The radionuclides with physical half-life of between 6 h and 7 days are preferred for therapeutic purposes. An extremely short physical half-life hampers the flexibility in administration of the radiotherapeutic agent and is impractical for clinical use. On the contrary, the use of long-lived radionuclides may result in retention of radiation dose in the patient for a longer period of time. Furthermore, patients may be required to be isolated and admitted in the hospital, in order to minimize the risk of radiation exposure to the general public. Additionally, the biological half-life of the radionuclide–nanoparticle complex is dependent on the properties of the nanocarrier used. The nanocarriers with long biological half-life should be used with radionuclides having short physical half-life (13, 48). The radio-NPs must be efficiently retained within the tumor volume so that higher doses of radiation can be delivered to the tumor tissues. The use of nanocarriers with short biological half-life may result in excretion of radio-NPs with high activity and may need extensive management of radioactive waste. Hence, for efficient delivery of radiation dose, the radionuclide–nanoparticle complex with optimal physical and biological half-life must be selected (48, 54, 55).

α-Particle emitters such as ^{225}Ac and ^{211}At emit positively charged helium nuclei, having high higher LET and short penetration depths in biological tissues (5). For instance, ^{225}Ac emits alpha particles in an energy range of 5–9 MeV and has LET value between 80 and 100 keV/μm and spatial penetration range between 40 and 100 μm. Hence, it has a probability of depositing most of the radiation within the tumor volume and can ablate tumor cells efficiently. Thus, α-emitting radionuclides are suitable in treating small or residual microscopic-size tumors. The main limitation of α-emitting radionuclides is that they have multiple daughter products with variable half-lives. Hence, migration of these nanocarriers labeled with α emitters can lead to significant damage to normal tissues (13, 14, 51, 57).

β-Emitting radionuclides are the most widely used radionuclides for internal RT purposes. The emitted electrons have lower LET and longer range (several millimeters) in comparison with the α emitters (58, 59). For example, ^{90}Y emits electrons with LET of 0.2 keV/μm and mean range of 3,960 μm. Hence, it may result in less cytotoxicity in comparison with the α-emitting radionuclides and radiation damage caused by these long-range β-particles, far from its origin, which is termed as "crossfire effect." Thus, due to the long penetration depth of the emitted electrons (≈0.05–12 mm), β emitters are regarded as the most suitable for the treatment of large or bulky tumors (7). β-Emitting radionuclides ^{198}Au, ^{199}Au, ^{131}I, and ^{177}Lu have been investigated as potential nanobrachytherapeutic agents (17, 37, 49, 50). ^{198}Au was used in the initial works of radioactive collidal gold (60). It is because ^{198}Au can be easily integrated with AuNPs. Some β-emitting radionuclides also decay with γ-radiation. For nanocarriers composed of high-Z materials, AuNP in particular, gamma radiation on interaction with the material of the nanoparticles may result in the enhancement of radiation dose deposition by the mechanism of radiosensitization (13, 15). Photoelectric effect plays a vital role in radiosensitization, and for Au, it is the strongest for gamma radiation of energy below or equal to 200 keV. ^{198}Au, ^{131}I, and ^{177}Lu emit gamma radiation with energy >200 keV. Hence, the photoelectric effect for gold is the strongest for photons with energy lower than 200 keV. The gamma radiation emitted by these radionuclides does not provide maximum radiosensitization effect (5). However, ^{199}Au emits gamma radiations with maximum energy ≈158 keV. Thus, dose enhancement *via* radiosensitization effect can be expected. In this regard, gold was used as a nanomaterial in preclinical studies,

using AuNPs radiolabeled with β-emitting radionuclides, due to its biocompatibility. Additionally, this gamma emission associated with β-emitting radionuclides can be advantageous in visualizing the spatial and temporal distribution of radio-NPs within the patient with the help of gamma scintigraphy techniques. Lastly, it should be considered that the long range of emitted electrons may result in non-specific cytotoxicity by depositing radiation dose to the surrounding normal cells/tissues (48, 54, 55).

Radionuclides emitting Auger electrons are considered to be beneficial in the treatment of small tumors or a cluster of tumor cells. This is attributed to higher cytotoxicity caused by these low-energy electrons (less than 500 eV or a few keV) with short range in the biological tissues (a few nanometers) (5, 54, 55). ^{103}Pd, ^{111}In, and ^{125}I have been used as nanobrachytherapeutic agents in preclinical studies involving tumor-bearing xenograft models (38, 45, 52). These radionuclides decay by internal conversion (IC) and electron capture (EC) mode and emit Auger electrons. The energy of the emitted Auger electrons range from ≈500 eV to a few keV with a spatial penetration depth of 2–500 nm. For effective ablation of tumor cells, these radionuclides must be internalized as close as possible to the cell nucleus. These radionuclides, ^{103}Pd, ^{111}In, and ^{125}I, also emit gamma radiation. ^{125}I and ^{103}Pd emit low-energy (30 keV) photons and have been used for low-dose-rate BT applications since the 1970s. The emitted photons deposit up to 98% of their energy within ≈5–8 cm of soft tissue and can be used to treat large and bulky tumors. ^{111}In also emits photons with energy greater than 200 keV and is not suitable for internal RT purposes or radiation dose enhancement through radiosensitization (13). In case of preclinical studies using xenograft models, the energy deposited to the tumor models is mainly due to these emitted Auger electrons and photoelectrons generated due to the interaction of low-energy photons and gold (7, 61).

Hence, the choice of the radionuclide also depends on the size of the tumor to be treated. It is because bulky tumors, micrometastases, and a small cluster of tumor cells require particles of specific energy for effective ablation of cancer cells. Further, the mode of radiosynthesis of nanoparticles and the length of the purification step (of radionuclides) must be selected according to the half-life of the radionuclide (54, 55). In terms of the spatial penetration depth and energy of the emitted particles, Auger and β-emitting radionuclides are most suitable for the treatment of solid tumors such as brain, breast, and prostate tumors by using nanobrachytherapy procedures (5, 13, 61).

Considering biochemical properties, a clinically acceptable radionuclide–nanoparticle complex must selectively concentrate within the tumor and have a prolonged retention. Also, it should have minimum or no uptake in the normal tissues or organs. Furthermore, the ratio of retention of a nanobrachytherapy agent should be high in the tumor volume in comparison with the normal tissues (10), so that high radiation doses can be delivered to the tumor volume and minimum or no radiation dose is delivered to the normal tissues or organs. Additionally, the radionuclide–nanoparticle complex should be stable enough at the time of injection and should have prolonged retention *in vivo* before it is excreted or metabolized (5, 13). Other biochemical features to be taken care of are low toxicity, appropriate pH, and optimal biological half-life. Furthermore, the radionuclide and nanoparticle (to which a radionuclide is attached) must have a high complexation yield and must form a stable complex in the biological environment (48, 53).

4 MECHANISMS FOR NANOPARTICLE INTERNALIZATION

The four main mechanisms of nanomaterial internalization by cells are micropinocytosis, caveolae-mediated endocytosis, clathrin-mediated endocytosis, and a mechanism independent of caveolae or clathrin (**Figure 3**) (62). The differential profile of AuNP internalization by different cell types depends on a large extent to the differences in their biophysical mechanisms, especially the cell membrane characteristics. Regarding the nanoparticle characteristics, the uptake is influenced significantly by the surface chemistry and the morphology of different nanomaterials. Additionally, one should be aware of the size of nanoparticle clusters that might be formed by aggregated particles in contact with cells, and the consequence of this aggregation in the internalization efficiency, as well as the location of nanoparticles and nanoaggregates in terms of organelles and intracellular vesicles (63, 64).

In 2008, Douglas and colleagues investigated the internalization and cytotoxicity of alginate–chitosan nanoparticles in 293T, COS7, and CHO cells. It was demonstrated that trypsinization can prevent alginate–chitosan nanoparticle internalization depending on the cell type. After trypsinization in 293T and COS7 cells, 75–85% of the binding efficiency to plasma membrane was lost, indicating that the interaction of those nanoparticles with the cells was mediated by chitosan and trypsin-sensitive proteins, but the same was not observed in CHO cells (65).

In the same study, it was observed that the vectors were not localized in lysosomes once they enter the cells, and the endocytic mechanism is different among the studied cell lines. For instance, clathrin-dependent endocytosis is important in 293T and COS7 cell lines, while caveolin-dependent internalization is significant for COS7 and CHO cells. Macropinocytosis was not relevant for any of the cell lines, but another mechanism dependent on actin microfilaments plays an important role for the internalization in 293T cells. This study supported the assumption that many factors are important for cell internalization and for the fate of nanomaterials in the cells, i.e., cell physiology, complex size, composition, and endocytosis mechanism. These parameters must be fully indicated in order to increase the success rate in the designed treatment (65).

The mechanism of internalization of 200-nm-diameter nanoparticles seems to be a combination of energy-dependent phagocytosis and clathrin-mediated endocytosis. But in all cases, the endocytoses were proven to be energy-dependent, while for smaller particles, an actin-dependent mechanism seems to play an important role. Caveolae-mediated endocytosis is the most

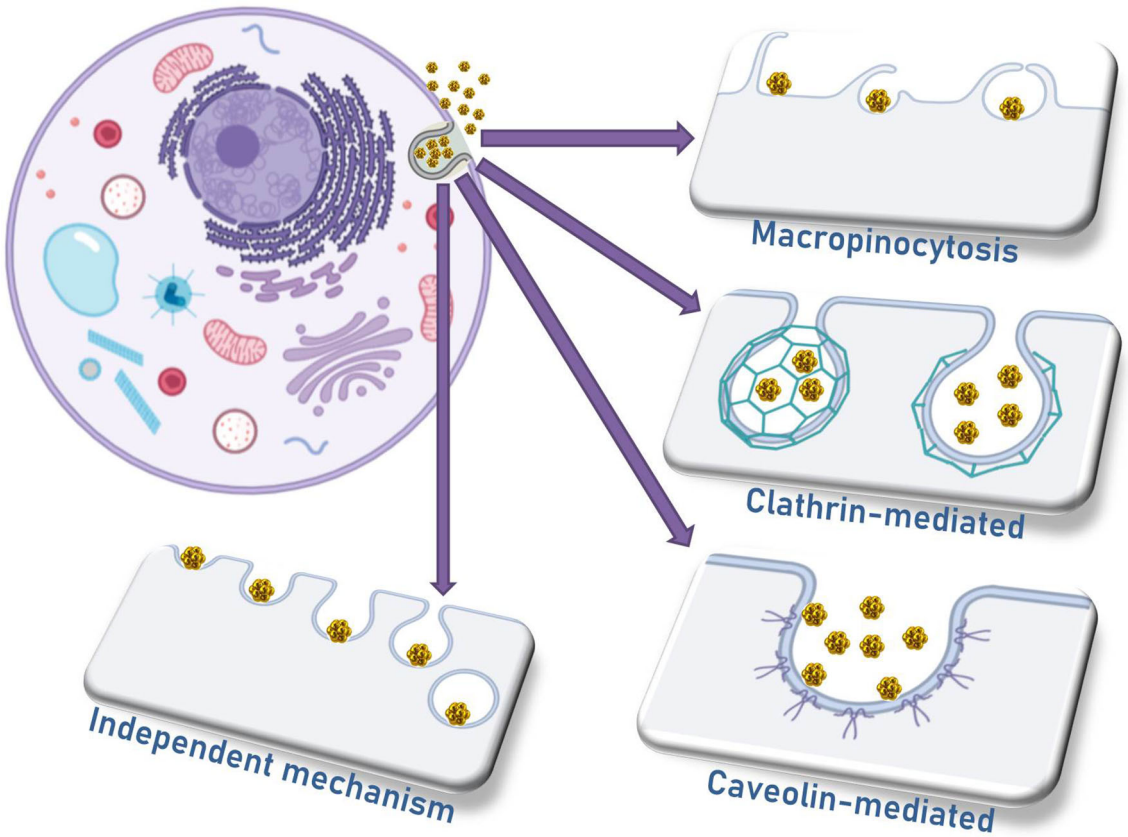

FIGURE 3 | The four main mechanisms responsible for the cell internalization of nanoparticles.

important mechanism for 150- and 200-nm nanoparticles, but it is worthy to mention that all internalization pathways contribute to the internalization of 150-nm nanoparticles, and this might explain the higher efficiency of endocytosis for those particles (66). Positively charged nanoparticles were observed to be significantly more internalized than negatively charged ones (84% against 5%, respectively). It is clear that negatively charged particles must rely on surface functionalization so that receptor-mediated endocytosis can compensate for the lower internalization rates.

Bannunah and collaborators published a thorough study comparing negatively and positively charged particles, of different sizes, in terms of their epithelial and cell uptake efficiency, as well as their toxicity to CaCo-2 (human intestinal adenocarcinoma) and Calu-3 (human airway epithelial) cells. According to their study, positively charged nanoparticles cause higher levels of cytotoxicity as compared with negatively charged ones, and it might be due to the oxidative stress, mitochondrial damage, and cellular overall toxicity observed for those kinds of particles. Negatively charged particles are known to be less cytotoxic to epithelial cells, and this might be explained by the fact that those cells present a net negative charge in their extracellular portion of plasma membrane, enabling a better interaction with positively charged nanoparticles. The results obtained for other cell types are sometimes conflicting; therefore, more studies might be necessary in order to understand the mechanisms for each tissue (67).

When inhibitors of dynamin-dependent and clathrin-dependent endocytoses are used, it seems that both negatively and positively charged nanoparticles are not significantly internalized *via* a dynamin-dependent mechanism, but the inhibition of clathrin-mediated transport likely caused an increase in the transport of negatively charged particles, though with no effect on their cell uptake. Regarding positively charged particles, clathrin inhibition reduced by 46% their cell uptake and by 38% their transcellular transport, whereas micropinocytosis inhibition reduced the internalization of the same particles by 42%, and the transcellular transport by 38%, similarly to micropinocytosis inhibition by methyl-β-cyclodextrin (67). No effect on negatively charged nanoparticles was observed after micropinocytosis inhibition.

The disruption of microtubules with nocodazole had no effect on the internalization of any of the nanoparticles, but the transport across the cells was significantly impaired. Genistein, a tyrosine-kinase inhibitor, impaired both the internalization (50%) and the intracellular transport (48%) of negatively charged nanoparticles, leading to the assumption that caveolae-dependent endocytosis plays an important role for those nanoparticles (67).

The protein corona is another key factor to be considered when developing any nanomaterial with biomedical applications. The protein corona is formed whenever a nanomaterial is introduced into a complex protein aqueous system and consists in the rapid adsorption of the most abundant proteins onto the surface of the nanomaterial, followed by the exchange of at least part of these proteins for others with higher affinity for the nanomaterial. The result is a nanoparticle with a completely different surface coating than that predicted in the design phase, sometimes with tendency for aggregation or with higher stability, with different internalization rates (enhanced or impaired), and different pharmacokinetics (68, 69).

The composition of the protein corona is not universal, as it depends on the nanomaterial and on the previous coating. It was demonstrated, for instance, that citrate-coated IONPs were not stable while in contact with fetal calf serum proteins but were efficiently internalized by lymphoblastoid cells, while poly(acrylic acid)-coated IONPs were quite stable, although were poorly taken up, which can be a barrier to be faced by the nanomaterials inside the blood (68).

Another barrier that the nanoparticles must overcome is the reticuloendothelial system (RES), responsible for a rapid clearance of the nanomaterials once they enter in the bloodstream, decreasing their pharmacological action. Strategies to avoid the clearance by RES include surface modification with molecules that prevent opsonization and increase the half-life in blood, such as PEG. However, as described previously, many variables must be added, such as surface charge. Harush-Frenkel and collaborators verified once more the preferential internalization of positively charged nanoparticles (twice the endocytosis of their negatively charged counterparts) in HeLa cells, and after 45 min, the cells tend to decrease the uptake rate, characterizing a saturation phase (70).

Another factor that contributes to the decreased circulating time of nanoparticles in blood is the mononuclear phagocytic system, in which the macrophages quickly scavenge nanoparticles that are agglomerated or covered with the protein corona, preventing their arrival at the target site. Zhang and coworkers used the advantage of folic acid as a functionalizing agent in PEGylated superparamagnetic magnetite nanoparticles (circa 10 nm in diameter) in the internalization efficiency by mouse macrophages (RAW 264.7 cells) and human breast tumor (BT-20 cells). PEG was responsible in partially inhibiting the formation of the protein corona in order to decrease the recognition of nanoparticles by macrophages, whereas folic acid was added to the surface of nanoparticles to specifically target cancer cells overexpressing folate receptors in order to increase their uptake (71).

5 PRECLINICAL STUDIES ON NANOBRACHYTHERAPY

The alpha-, beta-, and Auger-emitting radionuclides have been investigated for nanobrachytherapy applications. A few preclinical studies on nanobrachytherapy applications using alpha, beta, and Auger emitters have been published in literature. The most recent ones are briefly discussed in this section, and a brief summary of these studies is also presented in **Table 2**.

5.1 Alpha Emitters

Dziawer et al. (51) synthesized AuNPs at diameters of 5 and 15 nm. The nanoparticles were functionalized with Substance P(5-11) [SP(5-11)] peptide fragment to actively target the NK1 receptors overexpressed by T98G glioma cells. The AuNP-S-PEG-SP(5-11) bioconjugate was radiolabeled by adsorbing ^{211}At on the surface of AuNPs. The *in vitro* cytotoxicity of the obtained ^{211}At-AuNP-S-PEG-SP (5-11) radiobioconjugate was evaluated in human serum and cerebrospinal fluid. No study on therapeutic efficacy and *in vivo* biodistribution of radiobioconjugate has been reported. However, the authors recommended the intratumoral injection of ^{211}At-AuNP-S-PEG-SP (5-11) radiopharmaceutical, instead of intravenous injection due to its large size.

Recently, the same group synthesized 5-nm-sized AuNPs, with ^{211}At chemically adsorbed on its surface for nanobrachytherapy purposes using alpha emitters [56]. The nanoparticles were activated with PEG and trastuzumab (antibody) to actively target HER-2 proteins overexpressed on the surface of ovarian cancer-derived SKOV-3 cells. In the *in vitro* study, the authors demonstrated that AuNP-S-PEG-trastuzumab bioconjugate was effectively internalized by SKOV-3 cells. Furthermore, an *in vitro* cell viability test demonstrated that ^{211}At-AuNP-trastuzumab radiobioconjugate effectively reduced the metabolic activity of ovarian cancer cells with a median lethal dose of 0.5 MBq/mL. In this case as well, no biodistribution or therapeutic evaluation was reported.

Salvanou et al. (14) synthesized AuNPs radiolabeled with ^{225}Ac *via* DOTA-derivative (TADOTAGA) chelator. The chelator TADOTAGA formed a strong bond with the AuNPs resulting in the formation of a highly stable colloid in aqueous medium, and the chelating characteristics of DOTA-derived macrocyclic compound were exploited to radiolabel the Au@TADOTAGA nanocarriers. The [^{225}Ac]^{225}Ac-Au@TADOTAGA nanoparticles (5–9 nm) were synthesized with radiochemical yield of 86% and radiochemical purity greater than 93%. The aim of the study was to evaluate [^{225}Ac]^{225}Ac-Au@TADOTAGA nanoparticles as a nanobrachytherapy agent. The radiolabeled nanoparticles were evaluated in terms of i) its stability and *in vitro* cytotoxicity in U-87 MG (human glioblastoma–astrocytoma) cancer cells and ii) *in vivo* biodistribution by intravenous (i.v.) and intratumoral injection of [^{225}Ac]^{225}Ac-Au@TADOTAGA nanoparticles to the mice bearing U-87 tumor. Additionally, the tumor regression studies were performed over a period of 22 days to evaluate the therapeutic efficacy of intratumorally injected ^{225}Ac radiolabeled nanoparticles. For *in vivo* biodistribution studies, the mice (tumor volume = 200–400 mm^3) were divided into two groups, with three to five mice in each group. The [^{225}Ac]^{225}Ac-Au@TADOTAGA (100 μ, ≈1 kBq per mouse) nanoparticles were injected intravenously to the first group and intratumorally to the second group. The mice were euthanized at 2, 4, 24, 72, 120, and 288 h after injection; all the major tissues and organs were

TABLE 2 | Summary of nanobrachytherapy-based preclinical studies.

Main type of emission	Nanoparticle	Study (tumor model) type	Target	Main results	Reference
α	AuNPs (5 and 15 nm) functionalized with a peptide from Substance P(5-11) and labeled with ^{211}At.	*In vitro* (-).	NK1 receptors overexpressed in T98G glioma cells.	The authors recommended the intratumoral injection of the NPs instead of intravenous injection due to the their large size.	(51)
α	AuNPs (5 nm) with chemically adsorbed ^{211}At and activated with PEG and trastuzumab.	*In vitro* (-).	HER-2 proteins overexpressed in SKOV-3 cell ovarian cancer cells.	AuNP-S-PEG-trastuzumab bioconjugate was effectively internalized by SKOV-3 cells and reduced the metabolic activity of ovarian cancer cells with a median lethal dose of 0.5 MBq/mL.	(57)
α	AuNPs (5–9 nm) radiolabeled with ^{225}Ac using TADOTAGA chelator.	*In vivo* (U-87 MG tumor xenograft).	Nanobrachytherapy for xenograft bearing U-87 MG human glioblastoma–astrocytoma cells.	For mice (therapy group) injected with 100 μL/5 kBq of [^{225}Ac]^{225}Ac-Au@TADOTAGA per mouse (on days 1, 3, and 5), the tumor volume was reported to be ≈2.4 times lower after 8 days of radioactive injection and ≈4 times lower after 22 days of injection, in comparison with the control group.	(14)
Auger electrons	AuNPs coated with a layer of ^{103}Pd (120 nm).	*In vivo* (PC-3 tumor xenograft).	Nanobrachytherapy for prostate cancer.	After 5 weeks of radioactive injection (1.5 mCi per mouse), the decrease in tumor volume by about 75% for the ^{103}Pd@Au-treated group was reported, and over 95% of NPs still remained in the tumor.	(72)
Auger electrons	AuNPs radiolabeled with ^{111}In (30 nm) using DTPA chelator and functionalized with PEG and trastuzumab.	*In vivo* (subcutaneous HER2-overexpressing breast cancer (BC) xenografts).	HER-2-positive BC cells.	Therapeutic effectiveness of trastuzumab-AuNP-^{111}In was assessed by intratumorally injecting 10 MBq of radiopharmaceutical to the BC murine model. Inhibition in growth of tumor was reported for the treated group, whereas in the case of an untreated group, the tumors grew to eightfold of the initial tumor size.	(52)
Auger electrons	^{103}Pd core coated with Au or ^{198}Au (5–30 nm) functionalized with PEG.	*In vivo* (PC-3 tumor xenograft).	PC-3 prostate cancer cells.	4 weeks post radioactive injection (single dose of 1.6–1.7 mCi per mouse), a delay in tumor growth by 56% and 75% was reported for ^{103}Pd@AuNPs and ^{103}Pd@^{198}AuNPs, respectively, with respect to the controls. 75% of the injected dose was detected in the tumor.	(15)
Auger electrons	Covalent organic frameworks (COF)-Ag particles conjugated with PEG and radiolabeled with ^{125}I.	*In vivo* (PC-3 tumor xenograft).	PC-3 prostate cancer cells.	For the ^{125}I-COF-treated group (injected with 1 mCi of PEG-COF-Ag-^{125}I per mouse), reduction in tumor volume by about 63% in comparison with the initial size was reported.	(45)
Auger electrons	Nanogel with ^{103}Pd-AuNPs coated with poly(*N*-isopropylacrylamide) (37.3 nm).	*In vivo* (CT26 colorectal tumor xenograft).	CT26 colorectal cancers.	The delay in the tumor growth for treated group (injected with 25 MBq of radioactive LOIB : EtOH-[^{103}Pd]AuPd nanogel) after day 10 p.i. was reported in comparison with the control and cold nanogel groups. Further, the *ex vivo* biodistribution studies elucidated that up to 95%ID/g of injected radioactive nanogel was retained in the tumor post day 20 of injection.	(38)
β	^{198}Au-poly (amidoamine) dendrimer nanoparticles (10–50 nm)	*In vivo* (B16F10 melanoma tumor model).	B16F10 tumor cells.	Reduction in tumor growth by more than 45% was observed for Group B mice (injected with 74 μ of poly{^{198}Au}) in comparison with the control and Group A mice (injected with 35 μCi of poly{^{198}Au}).	(11)
β	^{198}AuNPs stabilized with gum arabic (4–10 nm).	*In vitro* (PC-3 tumor cell lines) and *in vivo* (PC-3 tumor xenograft)	PC-3 prostate cancer cells.	*In vitro* stability studies demonstrated excellent stability of GA-^{198}AuNPs for periods of over 6 months. The biodistribution studies performed in a murine model demonstrated that more than 85% of GA-^{198}AuNPs were contained in the liver.	(73)
β	^{198}AuNPs stabilized with gum arabic (12–18 nm).	*In vivo* (PC-3 tumor xenograft).	PC-3 prostate cancer cells.	After 3 weeks of radioactive injection (408 μCi of GA-^{198}AuNP per mouse), the tumor volumes of treated groups were found to be 82% smaller than those of the control group. Furthermore, even after 30 days of injection, on *ex vivo* analysis, radioactive nanoparticles were found in the tumor (20% ID), the liver (1% ID), and the carcass (18.5% ID).	(35)

(Continued)

TABLE 2 | Continued

Main type of emission	Nanoparticle	Study (tumor model) type	Target	Main results	Reference
β	^{198}Au-EGCg nanoparticles	*In vivo* (PC-3 tumor xenograft).	Lam 67R receptors in prostate cancer cells.	After 24 h of radioactive injection (136 μCi of ^{198}Au-EGCg nanoparticles per mouse), approximately 72% of nanoparticles were retained in the tumor. After 28 days of injection, the tumor size of the treated group was found to be 80% smaller than that of the control group.	(36)
β	^{198}AuNPs stabilized with gum arabic (12–15 nm).	*In vivo* (dogs diagnosed with prostate cancer).	Spontaneous prostate cancer in dogs.	The dogs were injected with activity in the range of 3 to 13.8 mCi of ^{198}Au. A decrease in tumor volume by 30%–50% was observed in two specimens; an increase in tumor size by 12%–26% was observed in 2 dogs; and for the remaining specimens, there was an increase or decrease of 3% in tumor volume (probably due to limited retention in the tumor volume).	(74)
β	Mangiferin-^{198}Au nanoparticles (35 nm)	*In vivo* (PC-3 tumor xenograft).	PC-3 prostate cancer cells.	Mice bearing prostate cancer were divided into three groups: Group A and Group B were injected with 160 μCi/30 μL of MGF-^{198}AuNPs, and Group C was injected with 30 μL of saline. After 2 weeks of injection, a decrease in tumor volume by 2 fold with respect to control was reported for the treated groups. Three weeks post radioactive injection, there was an increase in tumor volume by fivefold for Group C; Group A = 0.18 ± 0.17 cm^3 and Group B = 0.22 ± 0.02 cm^3 were reported. Furthermore, after 3 weeks, 69.70 ± 14.40% ID was found to be retained in the tumor, 6.80 ± 5.9%ID in the carcass, and 1.44 ± 2.97%ID in the liver.	(10)
β	^{198}AuNPs stabilized with gum arabic (~2 nm).	*In vivo* (H460 tumor xenograft).	H460 non-small cell lung cancer cells.	Post 7 days of injection (103 μCi of ^{198}AuNPs@GA per mouse), a decrease in tumor volume by more than 90% was observed in the ^{198}AuNPs@GA-treated group in comparison with the controls and mice injected with non-radioactive nanoparticles. Even after 2 weeks of radioactive injection, 50% of the nanoparticles were found to be accumulated in the tumor and 8.9% in the liver.	(49)
β	AuNPs radiolabeled with ^{177}Lu *via* DOTA chelator, functionalized with PEG and panitumumab.	*In vivo* (MDA-MB-468 human breast cancer mice model)	MDA-MB-468 human breast cancer cells.	A single dose of 4.5 MBq of ^{177}Lu-AuNP was intratumorally administered to the mice carrying subcutaneous BC cells. No significant impact of active targeting of ^{177}Lu-AuNP was observed in retaining the AuNPs within the tumors. Less than 3%ID/g radioactivity migrated to the liver and spleen, and its value increased by two to fivefold post 48 h of injection, whereas the radioactivity found in other organs was less than 0.5%ID/g. In the treated groups, inhibition of tumor growth by a factor of ≈30 in comparison with the untreated groups was reported.	(50)
β	AuNPs radiolabeled with ^{177}Lu *via* DOTA chelator, functionalized with PEG and trastuzumab (30 nm).	*In vivo* (breast cancer xenografts).	BC tumor cells.	3 MBq of ^{177}LuAuNPs was injected intratumorally to each mouse. The targeted nanoparticles (trastuzumab-AuNP-^{177}Lu) were reported to be 1.8 times more efficient in inhibiting tumor growth in comparison with the non-targeted (AuNP-^{177}Lu) and 2.2 times in comparison with the untreated group.	(75)
β	^{199}AuNPs stabilized with [f(RGDfK)] peptide (11 nm).	*In vivo* (melanoma tumor xenograft).	Integrin $\alpha_v\beta_3$ receptors in melanoma cells.	Significant delay in tumor growth was observed in mice injected with 2, 5, or 10 MBq of ^{199}Au-c(RGDfK) nanoparticles in comparison with the control.	(37)
β	Melanin-silver nanoparticles radiolabeled with ^{131}I cyan (6 nm).	*In vivo* (PC-3 tumor xenograft).	PC-3 prostate cancer cells.	The MNP-Ag-^{131}I-treated group (injected with 500 mCi of ^{131}I) had tumor volume equal to initial volume, whereas the control and ^{131}I-treated group had tumor size 1.5 times larger in comparison with the initial volume.	(17)
β	Mesoporous silica nanoparticles radiolabeled with ^{131}I and activated with anti-VEGFR2 antibodies and bovine serum albumin.	*In vivo* (thyroid cancer-bearing mice).	VEGFR2 in human thyroid carcinoma FRO cells.	The mice were intratumorally administered with a single dose of 74 MBq of radioactive nanoparticles. Gradual increase in tumor volume was reported for all the groups except ^{131}I-BSA-MSNPs-anti-VEGFR2-treated group.	(76)
β	AuNPs radiolabeled with ^{131}I and activated with twin arginine translocation (TAT) peptide (~8.36 nm).	*In vivo* (HCT-116 colon cancer xenografts).	Human colon cancer (HCT-116) cells *in vivo*.	After 18 days of radioactive injection (500 μCi/mL per mouse), reduction in tumor size by 79.95% was reported for the ^{131}I-AuNPs-TAT-treated group, whereas in the untreated group, the tumor grew to 8.08 times the original tumor size.	(77)

removed and weighted; and radioactivity was counted in terms of % injected dose per gram (%ID/g). For the first group (i.v. injection) at 2 h post injection (p.i.), the uptake of radiopharmaceuticals in the kidney ≈28%ID/g decreased to ≈9% ID/g at 120 h p.i., which showed the renal clearance of AuNPs, whereas the uptake in the liver and spleen increased from 9.5%ID/g and 7.2%ID/g at 2 h p.i. to 21.5%ID/g and 13.3%ID/g at 120 h p.i. The maximum uptake in tumors (4%ID/g) occurred at 2 h p.i. and decreased to 1%ID/g at 120 h p.i. On the other hand, for the second group (intratumoral injection), the reported tumor uptake was 60.67%ID at 2 h p.i. and decreased to 5.2%ID/g at 228 h p.i. For therapeutic efficacy evaluation, mice with ≈300 mm^3 of U-87 MG tumor xenograft were again divided into two groups. The first group (control) was injected intratumorally with 100 µL of saline, and the second group (therapy group) was injected with 100 µL/5 kBq of [^{225}Ac]^{225}Ac-Au@TADOTAGA on days 1, 3, and 5; and the tumor volume was tracked over 22 days. The tumor volume of therapy group was reported ≈2.4 times lower after 8 days of radioactive injection and ≈4 times lower after 22 days of injection, in comparison with the control group.

5.2 Auger Emitters

Moeendarbari et al. (72) reported the synthesis of nanoparticles radiolabeled with ^{103}Pd for nanobrachytherapy applications. A monodispersed layer of ^{103}Pd was coated on gold spherical shells, hence synthesizing ^{103}Pd@Au nanoseeds with a diameter of approximately 120 nm. These nanoseeds were injected intratumorally to mice bearing prostate cancer tumors to evaluate their *in vivo* therapeutic efficacy and biodistribution. The mice were randomized into three groups (n = 6), treated with phosphate-buffered saline (PBS) solution, non-radioactive (cold) Pd@Au nanoparticles in PBS suspension, and radioactive ^{103}Pd@Au nanoparticles in PBS suspension. In order to achieve uniform distribution of radiation dose in the whole tumor mass (181.7 ± 62.1 mm^3), the intratumoral injection was injected at six to nine locations, and radioactivity of 1.5 mCi per tumor was injected. The total injected volume of PBS, cold Pd@AuNPs, and ^{103}Pd@AuNPs was kept below 40 µL. The evaluation of retention of nanoseeds within the tumor volume and their migration to other organs was performed *ex vivo* and with single-photon-emission CT (SPECT)/CT. Upon SPECT/CT imaging, it was reported that after day 1 of radioactive injection, 101.50 ± 23.72% ID/g was retained within the tumor volume, and a negligible amount of radioactivity (≈0.1%ID/g) was observed in the liver and spleen. Furthermore, after 5 weeks of radioactive injection, 274.5 ± 77.6%ID/g was detected in the tumor volume, as the tumor volume decreased over the course of the treatment. This indicated the expected radiotherapeutic effect of the ^{103}Pd@Au nanoseeds. Furthermore, the *ex vivo* biodistribution investigation (5 weeks p.i.) results showed that ≈95% of nanoseeds were retained within the tumor, ≈3% migrated to the liver, and approximately 0.5% were found in the spleen. In terms of therapeutic efficacy, after 5 weeks of radioactive injection, the decrease in the tumor volume by about 75% for the ^{103}Pd@Au treated group was reported, whereas the increase in the tumor volume for groups treated with PBS and cold nanoparticles was reported.

Cai et al. (52) synthesized AuNPs radiolabeled with ^{111}In of 30-nm diameter. The radionuclides (^{111}In) were attached to the AuNPs using DTPA. The nanoparticles were also functionalized with PEG chains linked to antibody trastuzumab. Consequently, trastuzumab-AuNP-^{111}In radiopharmaceutical was obtained. Trastuzumab was used to actively target HER2-positive BC cells. The authors evaluated the *in vitro* cytotoxicity of synthesized radiolabeled nanoparticles on HER2-positive BC cells. Additionally, *in vivo* therapeutic effectiveness of trastuzumab-AuNP-^{111}In was also assessed by intratumorally injecting 10 MBq (≈270 µCi) of radiopharmaceutical into subcutaneous HER2-overexpressing BC xenografts. Tumor growth in the BC murine model was monitored for more than 70 days post radioactive injection. Inhibition in growth of tumor was reported for the treated group, whereas in the case of the untreated group, the tumors grew up to eightfold of the initial size. Tissue toxicity was not observed. No information regarding the migration of radiolabeled AuNPs to the liver and spleen was provided, as the authors did not perform biodistribution evaluation.

Laprise-Pelletier et al. (15) synthesized two types of radio-NPs composed of a nanoscopic core of radioactive palladium (^{103}Pd : Pd) coated with gold (Au)-^{103}Pd : Pd@Au and ^{103}Pd : Pd@^{198}Au : Au. These nanoparticles were synthesized using chemical reduction technique, one-pot method. In ^{103}Pd-Au nanoparticles, the ^{103}Pd : Pd radioactive core served the purpose of low-energy photon source, and the outer gold (Au) shell provided biocompatibility and protection and enhanced the radiation dose delivered by the process of radiosensitization. Additionally, ^{103}Pd-Au nanoparticles were labeled with ^{198}Au (high-energy beta emitter). In order to minimize the absorption of Auger and delta electrons by gold, the core size was kept at the range of 5–30 nm. The nanoparticles were synthesized with radiochemical yield of 87%. These nanoparticles were further functionalized with PEG; ^{103}Pd : Pd@Au-PEG and ^{103}Pd : Pd@^{198}Au : Au-PEG nanoparticles were synthesized. In order to assess the therapeutic efficacy of both types of nanoparticles, a single dose of 1.6–1.7 mCi (2–4 µL) was intratumorally injected to the mice with prostate cancer tumors (PC-3 cell lines). Four weeks post radioactive injection, a delay in tumor growth by 56% and 75% was reported for ^{103}Pd : Pd@Au-PEG NPs and ^{103}Pd : Pd@^{198}Au : Au-PEG NPs, respectively, with respect to the controls. Through biodistribution evaluation, the authors demonstrated that most of the nanoparticles were retained within the tumor, as more than 75% of the total radioactivity measured in the mice at the time of euthanasia was found there. Additionally, up to 16% of nanoparticles were found in the liver, 3% in the spleen, and less than 1% in other organs.

Zhang et al. (45) used COFs to synthesize nanoparticles radiolabeled with ^{125}I. Initially, Ag^+ ion was attached to the N atom of the bipyridine group present on 2,2′-bipyridine-based COF, and COF-Ag bioconjugate was formed. This bioconjugate was functionalized with PEG and radiolabeled with ^{125}I, consequently resulting in the formation of PEG-COF-Ag-^{125}I nanoparticles with radiolabeling yield of 94% and stability of more than 90% (after 7 days) in PBS and serum. The authors also evaluated the *in vitro* radiotoxicity of PEG-COF-Ag-^{125}I

nanoparticles on PC-3 cell lines with variable activity (0–200 Ci/mL). The decrease in the survival of PC-3 cells by 25.8% was reported. Furthermore, the therapeutic efficacy of the ^{125}I radiolabeled nanoparticles was also evaluated. To evaluate the therapeutic efficacy, the mice were divided into three groups: i) control, injected with 50 μL of PBS; ii) ^{125}I group, injected with 1 mCi of ^{125}I in 50 μL of PBS; and iii) ^{125}I-COF group, treated with 1 mCi of PEG-COF-Ag-^{125}I radiobioconjugate. The radiopharmaceutical and PBS were injected intratumorally to the mice. The activity retention time was studied through SPECT/CT at 0.5, 10, 24, and 36 h p.i. The authors demonstrated that at 0.5 h p.i., signal intensity was 3.2 times higher at tumor site for ^{125}I-COF group in comparison with ^{125}I group. On average, 61.67% of PEG-COF-Ag-^{125}I nanoparticles were retained in the tumor volume. Based on the data of time of retention of nanoparticles in the tumor volume, all three groups were reinjected with PBS, 1 mCi of ^{125}I, and 1 mCi of PEG-COF-Ag-^{125}I after 4 days; and the mice were euthanized 9 days after the first day of radioactive injection. For the ^{125}I-COF group, the reduction in the tumor volume by about 63% in comparison with the initial size was reported. Additionally, an increase in the tumor size by factor of 2 for control and ^{125}I group with respect to the initial tumor size was reported. The authors did not perform the biodistribution evaluation of the radio-NPs.

Fach et al. (38) synthesized [^{103}Pd]AuPd radio-NPs using chelator-free radiolabeling technique. The [^{103}Pd]Pd^{2+} was reduced in the presence of Au^{3+} and citric acid to form [^{103}Pd]AuPd radio-NPs of 15-nm size and 23.5-nm hydrodynamic diameter. The radio-NPs were coated with a biocompatible polymer, poly (*N*-isopropylacrylamide) (PNIPAAm), resulting in the formation of hydrophobic [^{103}Pd]AuPd radio-NPs of 37.3-nm diameter. The PNIPAAm-coated radio-NPs were further mixed with sucrose acetate isobutyrate (SAIB) or lactose octaisobutyrate (LOIB) in the presence of ethanol. A biocompatible, low-viscosity, injectable LOIB : EtOH radioactive "nanogel" containing [^{103}Pd]AuPd was synthesized. The therapeutic efficacy of the radioactive nanogel was assessed on mice with syngeneic CT26 colorectal cancers. The mice were divided into three groups: i) control group: the intratumoral injection was mimicked by inserting a syringe needle into the tumor, and nothing was injected. ii) "Cold nanogel" group: 50 μL of LOIB : OH bioconjugate was injected into the tumor through intratumoral injection. iii) Treated group: 0.675 μCi (25 MBq) was injected into 50 μL of radioactive LOIB : EtOH-[^{103}Pd]AuPd nanogel. The delay in the tumor growth after day 10 p.i. was reported in comparison with the control and cold nanogel groups. Further, the *ex vivo* biodistribution studies elucidated that up to 95%ID/g of injected radioactive nanogel was retained in the tumor post day 20 of injection and less than 0.01%ID/g of nanogel was found in the kidney, liver, spleen, and muscles of the mice. Additionally, the authors found no evidence of release of radioactivity from the LOIB : EtOH gel.

5.3 Beta Emitters

Khan et al. (11) synthesized radioactive polymerized gold-dendrimer (poly{^{198}Au}) nanoparticles using poly(amidoamine) (PAMAM) dendrimers and chloroauric ($HAuCl_4$) acid for nanobrachytherapy applications. The steps involved in the synthesis of gold-dendrimer nanoparticles were formation and decomposition of dendrimer-amine[AuCl4] complex, followed by reduction of Au^{3+} to Au. Consequently, positively charged poly{^{197}Au} nanoparticles of 10- to 50-nm size range were fabricated. The positive charge of these nanocarriers was expected to enhance the internalization of nanoparticles within the tumor cells. Furthermore, the 10- to 50-nm size range was used to take advantage of enhanced permeability and retention (EPR) effect. EPR effect is increased in accumulation of nanoparticles within the tumor due to the porosity and irregularity in the tumor microvasculature. The aqueous solution of poly{^{197}Au} nanoparticles was irradiated with neutron beam, and poly{^{198}Au} was obtained. The therapeutic efficacy studies of poly{^{198}Au} were performed on C57BL/6J mice having B16F10 melanoma tumor model. At the time of treatment, mice were approximately 8 weeks old and had tumor size of 440 to 530 mm^3. For therapeutic evaluation, the mice were divided into three groups, with each group having seven mice: i) Group A was administered 35 μCi of poly{^{198}Au}, in PBS, intratumorally; ii) Group B received 74 μCi of poly{^{198}Au} in PBS through intratumoral injection; and (iii) Group C was injected with 75 μL of PBS per mouse. The tumor size was monitored for 8 days post radioactive injection. Group A mice (treated with 35 μCi of poly{^{198}Au}) showed a delay in tumor growth in comparison with the control (Group C). However, the difference was not statistically significant. Reduction in tumor growth by more than 45% was observed for Group B mice (injected with 74 μCi of poly{^{198}Au}) in comparison with the control and Group A. The authors did not perform biodistribution studies.

A research group from the University of Missouri used phytochemicals to synthesize radioactive AuNPs through chemical reduction techniques (35, 73). In their first research work, they reported the production of AuNPs using gum arabic (GA) solution. The GA-coated radioactive AuNPs (GA-^{198}AuNPs), with a diameter of 4–10 nm, were synthesized by adding tris hydroxymethyl phosphine-aniline ($P(CH_2NHCH(CH_3)\text{-}COOH)_3$ (a reducing agent) and GA to $H^{198}AuCl4$ (73). Here, GA was used as a stabilizing agent. *In vitro* stability studies demonstrated excellent stability of GA-^{198}AuNPs for periods of over 6 months. The biodistribution studies performed in a murine model demonstrated that more than 85% of GA-^{198}AuNPs were contained in the liver. Additionally, the authors performed detailed *in vivo* therapeutic assessments, where GA-^{198}AuNPs (diameter 12–18 nm) were injected intratumorally to the severely compromised immunodeficient (SCID) mice bearing prostate tumor (PC3 cells) xenografts. Each mouse was given an intratumoral injection of 408 μCi of GA-^{198}AuNPs (30 μL). The tumor volume was monitored over a period of 30 days, and retardation in tumor growth for the treated group in comparison with the untreated group was reported. After 3 weeks of radioactive injection, the tumor volumes of treated groups were found to be 82% smaller than in the control group. Furthermore, even after 30 days of injection, on *ex vivo* analysis, radio-NPs were found in the

tumor (20%ID), the liver (1%ID), and the carcass (18.5%ID) (78). In recent years, the researchers from the University of Missouri have developed similar products and tested the radio-NPs *in vivo* as potential nanobrachytherapeutic agents.

Shukla et al. (36) synthesized radioactive AuNPs functionalized with epigallocatechin gallate (EGCg)-^{198}Au-EGCg. EGCg is a phytochemical extracted from green tea leaves and can be used to actively target laminin receptors (Lam 67R), which are overexpressed by the prostate cancer cells. In this study, i) the synthesis and characterization of ^{198}Au-EGCg nanoparticles were reported; ii) the affinity of EGCg for laminin receptors and internalization of ^{198}Au-EGCg through endocytosis was demonstrated; (iii) *in vivo* therapeutic assessment of ^{198}Au-EGCg nanoparticles was performed. For *in vivo* therapeutic assessment, 136 μCi (30 μL) of ^{198}Au-EGCg nanoparticles, with a diameter of 40–55 nm, were injected intratumorally to the mice bearing prostate tumor. The pharmacokinetic study results demonstrated that after 24 h of injection, approximately 72% of ^{198}Au-EGCg nanoparticles were retained in the tumor. After 28 days of injection, the tumor size of the treated group was found to be 80% smaller than of the control group. The results of end-of-study biodistribution, conducted on day 42 post radioactive injection, showed that radio-NPs were retained in the tumor (34.7%ID), liver (2.5%ID), and carcass (18%ID).

The therapeutic effectiveness of GA-coated AuNPs (GA-^{198}AuNPs) was also assessed in the canine model (74). Nine dogs diagnosed with prostate cancer were injected with GA-^{198}AuNPs (diameter 12–15 nm) intratumorally. In order to obtain homogeneous distribution of a radiotherapeutic agent within the tumor volume, two to eight needles were inserted, and several injections of 100–200 μL were administered. Activity to be administered was selected as a function of tumor volume. The dogs were injected with activity in the range of 3 to 13.8 mCi of ^{198}Au. This activity range corresponded to the biological effective dose of 50 (n = 2) and 150 Gy (n = 7). After 30 min of radioactive injection, scintigraphy scans were performed. In six dogs, the migration of nanoparticles to the bladder, urethra, and prostatic extra region from the prostate was observed. After 30 min of injection, only 53% of injected radio-NPs were retained in the prostate. Four weeks posttreatment, CT scan was performed to measure the tumor volume. The authors expressed the effectiveness of the treatment in terms of decrease in the tumor volume. A decrease in the tumor volume by 30%–50% was observed in two specimens, an increase in tumor size by 12%–26% was observed in two dogs, and for the remaining specimens, there was an increase or decrease of 3% in the tumor volume. The nanoparticles did not induce any sign of toxicity. The authors concluded that the therapeutic effectiveness of GA-^{198}AuNPs in the canine model was compromised due to the limited retention of radio-NPs within the tumor volume. Hence, the influence of tumor vasculature and the lymphatic drainage on retention or leakage of nanoparticles need to be investigated before conducting clinical trials.

In the most recent publication from this group (10), they used mangiferin (MGF), a phytochemical extracted from mango, to fabricate ^{198}Au nanoparticles. Mangiferin is a glucose-functionalized xanthonoid and is capable of reducing ^{198}Au precursors to ^{198}Au nanoparticles. The sugar-polyphenolic groups present in mangiferin are capable of encapsulating and binding on the surface of AuNPs and provide optimum stability both *in vitro* and *in vivo*. Hence, MGF-encapsulated ^{198}AuNP-MGF-^{198}AuNPs with 35 ± 2 nm of core size and 55 ± 0.9 nm of hydrodynamics size were fabricated. Furthermore, due to the presence of glucose functionality, MGF was used to effectively target laminin receptors overexpressed by the prostate cancer (PC-3) tumor cells. Hence, selective accumulation of MGF-^{198}AuNPs within the tumor volume was achieved. The authors reported the following: i) the fabrication and characterization of MGF-^{198}AuNPs; (ii) studies on stability of MGF-^{198}AuNPs *in vitro* and *in vivo* and biodistribution studies; and (iii) studies on the evaluation of therapeutic efficacy of MGF-^{198}AuNPs on mice bearing prostate tumors. In order to evaluate the *in vivo* stability, normal mice (N = 25) were given intravenous injection of 8.0 μCi/100 μL of MGF-^{198}AuNPs and were euthanized at 30 min, 1 h, 2 h, 4 h, and 24 h post radioactive injection. All the important organs (liver, spleen, lungs, bladder, etc.) were collected, and radioactivity accumulation in these organs was estimated. MGF-^{198}AuNPs predominantly accumulated in the spleen and liver clearance through hepatobiliary pathway, and almost no uptake occurred in the blood and lungs. In order to evaluate the selective accumulation of MGF-^{198}AuNPs, due to the glucose functionality of MGF, the authors performed a study on the retention of radiopharmaceuticals within the tumor. Mice bearing PC-3 tumor (N = 5) were administered with a single dose of 4 μCi/30 μL of MGF-^{198}AuNPs for each tumor through intratumoral injection. The mice were euthanized at an interval of 30 min, 1 h, 2 h, 4 h, and 24 h post radioactive injection; and tumors and the organs of interest (liver, spleen, etc.) were excised. Radioactivity accumulation in tumor and different organs was estimated in terms of %ID/organ. At 30 min and 24 h p.i., 80.98% ± 13.39% and 79.82% ± 10.55% of MGF-^{198}AuNPs were respectively found to be accumulated in the tumor, whereas liver increase from 4.05% ± 5.27% (at 30 min) to 10.65% ± 8.31% (at 24 h) was reported. Additionally, low uptake of radio-NPs was also found in feces (0% at 30 min and 2.2% ± 4.5% at 24 h) and the stomach (0.10% at 30 min and 0.02% at 24 h), and no noticeable uptake was found in the lungs, blood, and other organs. Lastly, the authors also performed a detailed study to evaluate the therapeutic efficacy of MGF-^{198}AuNPs. Mice bearing PC-3 tumors were divided into three groups: i) Group A, tumor volume ranging from 0.15 to 0.2 cm^3; ii) Group B, mice with tumor volume about 0.43 cm^3 were injected with a single dose of 160 μCi/30 μL of MGF-^{198}AuNPs per tumor through intratumoral injection; and iii) Group C, mice with 0.15 to 0.2 cm^3 of tumor size were injected with 30 μL of saline intratumorally and served as control. The tumor volume was monitored for 3 weeks. Post 7 days of injection, a decrease in the tumor volume for Groups A and B was observed. After 2 weeks of injection, a decrease in the tumor volume by twofold with respect to control was reported for the treated groups. Three

weeks post radioactive injection, there was an increase in the tumor volume by fivefold for Group C; Group A = 0.18 ± 0.17 cm^3 and Group B = 0.22 ± 0.02 were reported. Furthermore, after 3 weeks, 69.70 ± 14.40%ID was found to be retained in the tumor, 6.80 ± 5.9%ID in the carcass, and 1.44 ± 2.97%ID in the liver.

Lin et al. (49) fabricated AuNPs stabilized with GA-AuNPs@GA of ≈2-nm size for nanobrachytherapy applications. The X-ray irradiation of $HAuCl_4$ and GA resulted in the formation of AuNPs@GA. AuNPs@GA nanocarriers were made radioactive through neutron activation, and ^{198}AuNPs@GA were obtained. Radiotherapeutic efficacy, biodistribution, and toxicity studies were performed on mice bearing H460 tumor. Suspension of 103 μCi (injection volume = 100 μL) of ^{198}AuNPs@GA nanoparticles per mouse was administered intratumorally to the mice bearing H460 tumors, and the tumor volume was monitored for 2 weeks. Toxicity caused by administration of ^{198}AuNPs@GA nanocarriers was evaluated in terms of loss in body weight. Less than 20% decrease in body weight was found post 4 days of radioactive injection; and post 7 days of injection, the body weight was recovered. Hence, the authors effectively showed that ^{198}AuNPs@GA are safe for treatment. In order to perform biodistribution studies, mice were euthanized, and important organs (liver, spleen, kidney, carcass, etc.) were collected. The authors also collected urine and feces. Post 7 days of injection, a decrease in the tumor volume by more than 90% was observed in the ^{198}AuNPs@GA-treated group in comparison with the controls and mice injected with non-radioactive nanoparticles. Even after 2 weeks of radioactive injection, 50% of the nanoparticles were found to be accumulated in the tumor and 8.9% in the liver. Furthermore, clearance of ^{198}AuNPs@GA was observed in urine and feces.

Yook et al. (50) evaluated the therapeutic efficacy of radioactive AuNPs in a MDA-MB-468 human BC model. The AuNPs were radiolabeled with ^{177}Lu using a macrocyclic complex: 1,4,7,10-Tetraazacyclododecane-1,4,7,10-tetraacetic acid (DOTA) and NPs)were functionalized with PEG and panitumumab (an antibody) to target the epidermal growth factor receptors (EGFRs). The EGFRs are overexpressed by the BC tumor cells. Radio-NPs were divided into two categories: i) targeted—functionalized with PEG and panitumumab-^{177}Lu-T-AuNP; and ii) non-targeted—functionalized with PEG but not panitumumab-^{177}Lu-NT-AuNP. A single dose of 4.5 MBq of both targeted and non-targeted nanoparticles in 30 μL of saline was administered through intratumoral injection into the mice carrying subcutaneous human BC cells. Both targeted and non-targeted ^{177}Lu radiolabeled AuNPs were found to be capable of delaying tumor growth for more than 90 days, and no organ toxicity caused by these nanoparticles was reported. In the treated groups, inhibition of tumor growth by a factor of ≈30 in comparison with the untreated groups was reported. The amount of nanoparticles that was retained within the tumor was evaluated by performing SPECT/CT imaging at 1 and 48 h post radioactive injection. *Ex vivo* analysis was also done to assess the distribution of ^{177}Lu-T-AuNP and ^{177}Lu-NT-AuNP in different organs. Post 1 h of injection, most of the radio-NPs were confined within the tumors, and migration of this radioactive out of tumors was observed at 48 h. Furthermore, the authors reported that high concentrations of both targeted and non-targeted nanoparticles, >300%–400%ID/g, accumulated within the tumors after 1 h of intratumoral administration. Hence, no significant impact of active targeting of ^{177}Lu-AuNP was observed in retaining the AuNPs within the tumors. Less than 3%ID/g radioactivity migrated to the liver and spleen, and its value increased by two- to fivefold post 48 h of injection, whereas the radioactivity found in other organs was less than 0.5%ID/g.

Cai et al. (75) radiolabeled AuNPs with ^{177}Lu-DOTA to synthesize ^{177}Lu-AuNPs. These nanoparticles were further functionalized with trastuzumab antibodies using PEG. Initially, the PEG chains were linked on the AuNPs, and the trastuzumab molecules were attached on these chains. The nanoparticles were categorized into two groups: i) targeted—nanoparticles functionalized with trastuzumab (trastuzumab-AuNP-^{177}Lu); and ii) non-targeted—nanoparticles not functionalized with trastuzumab (AuNP-^{177}Lu). In order to assess therapeutic effectiveness of these nanoparticles, 3 MBq (≈81 μCi) was administered intratumorally in mice bearing BC tumors. The tumor growth was monitored for 16 days. The targeted nanoparticles (trastuzumab-AuNP-^{177}Lu) were reported to be 1.8 times more efficient in inhibiting tumor growth in comparison with the non-targeted nanoparticles (AuNP-^{177}Lu) and 2.2 times in comparison with the untreated group. No significant tissue toxicity was reported by the authors for both targeted and non-targeted treatments. Additionally, the authors provided no information on the amount of nanoparticles that migrated to the liver and spleen.

Chakravarty et al. (37) synthesized neutron-activated ^{199}Au radio-NPs with an average particle size 11 nm and hydrodynamic size of about 30.2 nm. Cyclic (arginine-glycine-aspartate-phenylalanine-lysine) [f(RGDfK)] peptide was used as both a stabilizing agent and a reducing agent for the synthesis of ^{199}Au-c(RGDfK) nanoparticles to target integrin $\alpha_v\beta_3$ receptors for nanobrachytherapy applications. Additionally, non-targeted ^{199}Au nanoparticles were also synthesized by labeling ^{199}Au nanoparticles with scrambled sequence of RGD cyclic (arginine-glycine-lysine-phenylalanine aspartic acid [c(RGKfD)]. The non-targeted ^{199}Au-c(RGKfD) nanoparticles were used as control. The authors characterized the nanoparticles using numerous analytical techniques to evaluate the particle identity, size, *in vitro* stability, compatibility to biological medium, and suitability for clinical use. The biodistribution studies were conducted in C57BL/6 mice bearing melanoma tumors after intratumoral administration of ^{199}Au-c(RGDfK) nanoparticles. The non-targeted ^{199}Au-c(RGKfD) nanoparticles were also injected intratumorally to another group of C57L/6 mice having melanoma tumors and were used as control. The mice were euthanized at 24, 72, and 192 h post radioactive injection, and samples of normal tissues and tumor were collected. At 24 h p.i., a high percentage of administered radioactive ^{199}Au nanoparticles (both targeted and non-targeted) were retained within the tumor volume. The uptake of targeted ^{199}Au-c(RGDfK) nanoparticles (497 ± 56%

ID/g) was reported to be higher than that of non-targeted (400 ± 67%ID/g). Between 24 and 192 h post intratumoral injection, a gradual decrease in radioactivity, accumulated in the tumor, was observed for both targeted and non-targeted ^{199}Au nanoparticles. Additionally, at 192 h p.i., twofold higher retention of the targeted ^{199}Au-c(RGDfK) nanoparticles (375 ± 78%ID/g) in comparison with non-targeted ^{199}Au-c(RGDfK) nanoparticles (182 ± 23%ID/g) was observed. Consequently, higher radioactivity was found in the blood for non-targeted nanoparticles in comparison with the targeted nanoparticles, indicating their leakage from the tumor. Post 120 h of injection, the uptake of targeted ^{199}Au-c(RGDfK) (≈4%ID/g) in the liver and kidney was found to be three times lower than of non-targeted ^{199}Au-c(RGKfD) (≈12%ID/g) nanoparticles. The uptake in the spleen (≈2%ID/g) was nearly equal for both targeted and non-targeted ^{199}Au nanoparticles. The uptake of radio-NPs in the remaining organs was less than 1%ID/g. The therapeutic efficacy of these targeted and non-targeted ^{199}Au nanoparticles was evaluated on melanoma-bearing C57BL/6 mice. The mice with tumor size approximately 150 mm^3 were divided into five sets (five mice per set). Each group was given a single intratumoral injection of saline, non-radioactive Au-c(RGDfK), 2 MBq of ^{199}Au-c(RGDfK), 5 MBq of ^{199}Au-c(RGDfK) nanoparticles, or 10 MBq of ^{199}Au-c(RGDfK) nanoparticles. The first two groups were used as control. Furthermore, the tumor volume and body weight of the mice were monitored for 15 days. A significant delay in tumor growth was observed in mice injected with 2, 5, or 10 MBq of ^{199}Au-c(RGDfK) nanoparticles in comparison with the control.

Sheng et al. (17) synthesized melanin nanoparticles (MNPs) radiolabeled with ^{131}I. The MNPs were radiolabeled with Ag-I two-step method. First, Ag^+ ions were chelated by MNPs, and ^{131}I ions were attached to Ag^+ ions to form MNP-Ag-^{131}I nanoparticles (diameter = 6 nm, and hydrodynamic diameter = 11 nm) with 99% radiolabeling yield. The authors further evaluated the solubility and/or stability of MNP-Ag-^{131}I in demineralized water (DI water), PBS, and serum. Additionally, the *in vitro* biocompatibility was tested in PC-3 prostate cancer cells, and no cytotoxicity was observed. In order to evaluate the *in vivo* therapeutic efficacy of MNP-Ag-^{131}I nanoparticles, the mice were divided into three groups: i) control, ii) ^{131}I group, and iii) MNP-Ag-^{131}I-treated group. On day 1, the ^{131}I group and MNP-Ag-^{131}I-treated group were injected with 1 mCi of ^{131}I and MNP-Ag-^{131}I through intratumoral injection; and radiopharmaceutical retention within the tumor was observed through SPECT and Cherenkov radiation. On day 3, through intratumoral injections, control, ^{131}I group, and MNP-Ag-^{131}I-treated group were injected with 20 mL of PBS, 500 mCi of ^{131}I in 20 mL of DI, and 500 mCi of MNP-Ag-^{131}I in 20 mL of PBS. The mice were euthanized after 7 days of radioactive injection, and tumor and other important organs were collected. The MNP-Ag-^{131}I-treated group had a tumor volume equal to the initial volume, whereas the control and ^{131}I-treated group had tumor size 1.5 times larger in comparison with the initial volume.

Zhang et al. (76) synthesized mesoporous silica nanoparticles (MSNPs), radiolabeled with ^{131}I and activated with anti-vascular endothelial growth factor receptor 2 (anti-VEGFR2) antibodies and bovine serum albumin (BSA) for the treatment of anaplastic thyroid cancers (APCs). The radiolabeling of the MSNPs was performed using Chloramine-T method, resulting in the formation of ^{131}I-BSA-MSNPs-anti-VEGFR2 radioactive nanocarriers. *In vitro* cellular uptake of ^{131}I-BSA-MSNPs-anti-VEGFR2 in human thyroid carcinoma FRO cell lines was evaluated through confocal imaging, and time-dependent cellular uptake was evaluated by measuring radioactivity using gamma counter. The therapeutic efficacy of radioactive ^{131}I-BSA-MSNPs-anti-VEGFR2 was tested on mice bearing FRO tumor cells. The radiopharmaceutical retention within the tumor was measured through SPECT/CT imaging. The mice were divided into four groups: control, injected with PBS; and ^{131}I-BSA-MSNPs, Na^{131}I, and ^{131}I-BSA-MSNPs-anti-VEGFR2-treated groups (n = 3). Each group was administered with radioactivity of 74 MBq (50 μL) through intratumoral injection. A gradual increase in the tumor volume was reported for all the groups except ^{131}I-BSA-MSNPs-anti-VEGFR2-treated group.

Su et al. (77) synthesized AuNPs radiolabeled with ^{131}I and activated with twin arginine translocation (TAT) peptide. In order to construct ^{131}I-AuNPs-TAT radiopharmaceuticals, first, AuNPs (diameter = ≈8.36 nm) were prepared. Later, AuNPs were functionalized with amino-poly(ethylene glycol)-thiol (HS-PEG2000-NH2) to prepare AuNPs-PEG, and they were conjugated with TAT peptide to prepare AuNPs-TAT. Lastly, through iodogen-catalyzed procedure, AuNPs-TAT was radiolabeled with ^{131}I to synthesize ^{131}I-AuNPsTAT radiopharmaceutical with radiolabeling yield of 96.5% and radiochemical purity above 78%. *In vitro* experiments on radiocytotoxicity, estimating the rate of apoptosis and suppression of tumor cell proliferation, were performed using cell counting kit-8 (CCK-8) assay by exposing human colon cancer (HCT-116) cells to ^{131}I-AuNPs-TAT radiopharmaceutical. The authors concluded that, after the addition of TAT peptide and AuNPs, ^{131}I-AuNPs-TAT was internalized by the cell nuclei and caused short-term and long-term damage to the tumor cells. From the results of *in vitro* studies, the authors concluded that 500 μCi/mL of ^{131}I-AuNPs-TAT (composed of AuNPs = 100 μg/mL and TAT = 10 g/mL) is appropriate for therapeutic studies. Mice bearing HCT166 tumors were used to evaluate the therapeutic efficacy of ^{131}I-AuNPs-TAT. Prior to treatment, SPECT/CT imaging was used to monitor the metabolic distribution of intratumorally administered ^{131}I-AuNPs-TAT. The authors reported that about 20.09% of ^{131}I-AuNPs-TAT was retained at the site of injection after 36 h. Post SPECT/CT imaging, mice were administered with 500 μCi/mL (per mouse) of ^{131}I-AuNPs-TAT through intratumoral injection. After 18 days of radioactive injection, reduction in tumor size by 79.95% was reported for the ^{131}I-AuNPs-TAT-treated group, whereas in the untreated group, the tumor grew to 8.08 times the original tumor size. The authors concluded that the presence of TAT and AuNPs i) internalized the radiopharmaceutical to the nuclei of the tumor cells, which elevated the DNA damage; and ii) the high-energy beta particles emitted from ^{131}I on interaction with Au produced low-energy X-rays—this further reduced the cold spots and induced a strong immune response.

From the data collected regarding alpha emitters in preclinical studies, it is possible to observe that the most commonly used radioisotope is ^{211}At followed by ^{225}Ac, mostly radiolabeling AuNPs with small diameter (from 5 to 15 nm). The most interesting finding among the collected studies was the fact that intratumoral injection likely leads to a better outcome in terms of cancer ablation compared with intravenous injection. When it comes to Auger emitters, palladium comes into the scene more often, either cold palladium combined with gold in the core of nanoparticles or ^{103}Pd as a radionuclide. Other Auger emitters that are also used are ^{111}In and ^{125}I, and the intratumoral injection was the chosen route for administering the nanoparticles in all studies recruited for this paper. Interestingly, the tumor ablation appears to be higher than alpha emitters, with tumors decreasing in size from 56% to 75% among the recruited studies. Finally, beta emitters are likely the most effective in ablating solid tumors, with tumor size decreasing more than 80% in various preclinical studies. The most commonly used radionuclides are ^{198}Au and ^{199}Au followed by ^{131}I and ^{177}Lu. Again, the administration route for the nanoparticles was the intratumoral injection.

Among the studies recruited for this paper, most of the authors synthesize the nanomaterials, making use of some sort of targeting strategy in order to enhance the tumor localization of the nanoparticles, apart from the intratumoral injection, which also contributes in this regard. However, targeting strategies are more utilized when the authors use beta emitters. Biodistribution studies were performed more often with beta emitters than alpha- or Auger-emitting radionuclides. In this matter, it is of utmost importance to carefully follow the pharmacokinetics of radioactive nanomaterials in order to avoid side effects and non-specific radioactive damage to healthy cells; therefore, researchers should work with novel strategies related to theranostic radioactive nanomaterials. Targeting strategies, i.e., mAb and tissue-specific receptor ligands, are very useful for concentrating therapeutic agents inside the tumor tissues; thus, they should be taken into consideration by those working with this kind of biomaterials. **Figure 4** summarizes the main findings from the preclinical studies.

6 NANOBRACHYTHERAPY WITH INTRATUMORAL IMMUNOTHERAPY

Cancer treatment is a multipronged approach wherein the combination of treatment regimens such as surgery, chemotherapy, RT, and more recently immunotherapy is adopted to achieve better therapeutic index. For example, immunotherapy alone has occasional responses, and benefits are limited to a minority of patients in limited disease sites due to immune evasion properties of tumor cells (79). A rare phenomenon called "abscopal effect" is observed with the local radiation treatments where tumors outside the treatment fields have been observed to shrink as a result of immune response provoked by RT (80–82). The abscopal effect is rare with radiation alone but profoundly observed in patients undergoing immune checkpoint blockade therapy (83–86). Similarly, immunotherapy can enhance the efficacy of RT *via* activation of the innate and adaptive immune system (79, 87). With the development of tumor-specific antibodies, immune checkpoint inhibitor antibodies, and chimeric antigen receptor T-cell therapies, immunotherapy has revolutionized the treatment of metastatic disease including melanoma, non-small cell lung cancer, and renal cell carcinoma (88, 89). The unique synergistic relationship between radiation and immunotherapy provides the benefit of controlling systemic disease with local delivery of treatment. Many clinical trials are ongoing, testing the outcomes (safety, tumor response, immune response, and toxicities) of the combination of immune checkpoint inhibitor therapeutics and RT for prostate cancer (castrate resistant), soft tissue sarcoma, BC, glioma, pancreatic cancer, and melanoma (79, 88, 89). The RT techniques employed are mostly EBRT, including highly conformal intensity modulated RT and stereotactic body RT (SBRT) combined with high-precision image guidance (IGRT). In many studies, immunotherapy was administered intratumorally to envisage lesser immune-related adverse events, better local immune response, and control of systemic metastatic disease (90–96).

In one of the studies, Moreau et al. investigated the use of multifunctional smart RT biomaterial (SRB) loaded with immunoadjuvants to study the abscopal effect of local RT (93). Lewis lung carcinoma (LLC) tumors were generated on both the right and left flanks of the mice, and one tumor was implanted with an SRB device loaded with CD40 antibody in PLGA matrix followed by RT. The SRB device releases immunotherapeutic drug intratumorally and provides image guidance for EBRT using small animal radiation research platform (SARRP). The treatment response was observed in both irradiated and un-irradiated tumors owing to the radiation-mediated systemic antitumor immune response.

There was one attempt to administer both radiation and an immune stimulator directly to the tumor. Sodium alginate formulation containing catalase was labeled with ^{131}I and injected intratumorally. This creates *in situ* gelation to confine ^{131}I within the tumor and alleviates tumor hypoxia (97). They also showed that when ^{131}I was added with CpG oligonucleotide (immunostimulator) administered intratumorally and combined with systemic checkpoint blockade therapy (CTLA-4 antibodies), it leads to local tumor eradication as well as increased systemic immune response to inhibit distal metastasis and tumor recurrence.

Radiation in the form of nanoparticles is being investigated for intratumoral administration to reduce the side effects to normal tissues, and similarly, immunotherapeutic drugs are being administered intratumorally to avoid immune-related adverse events. The therapeutic combination of nanobrachytherapy and intratumoral immunotherapy has great potential to achieve higher therapeutic index in a synergistic manner. They may deliver larger doses of therapeutics to the tumor, reduce normal tissue toxicities of systemic delivery, eradicate distal malignant cells owing to the enhanced abscopal effect, and enhance the efficacy of immunotherapy as well as RT for multiple disease sites and larger patient base.

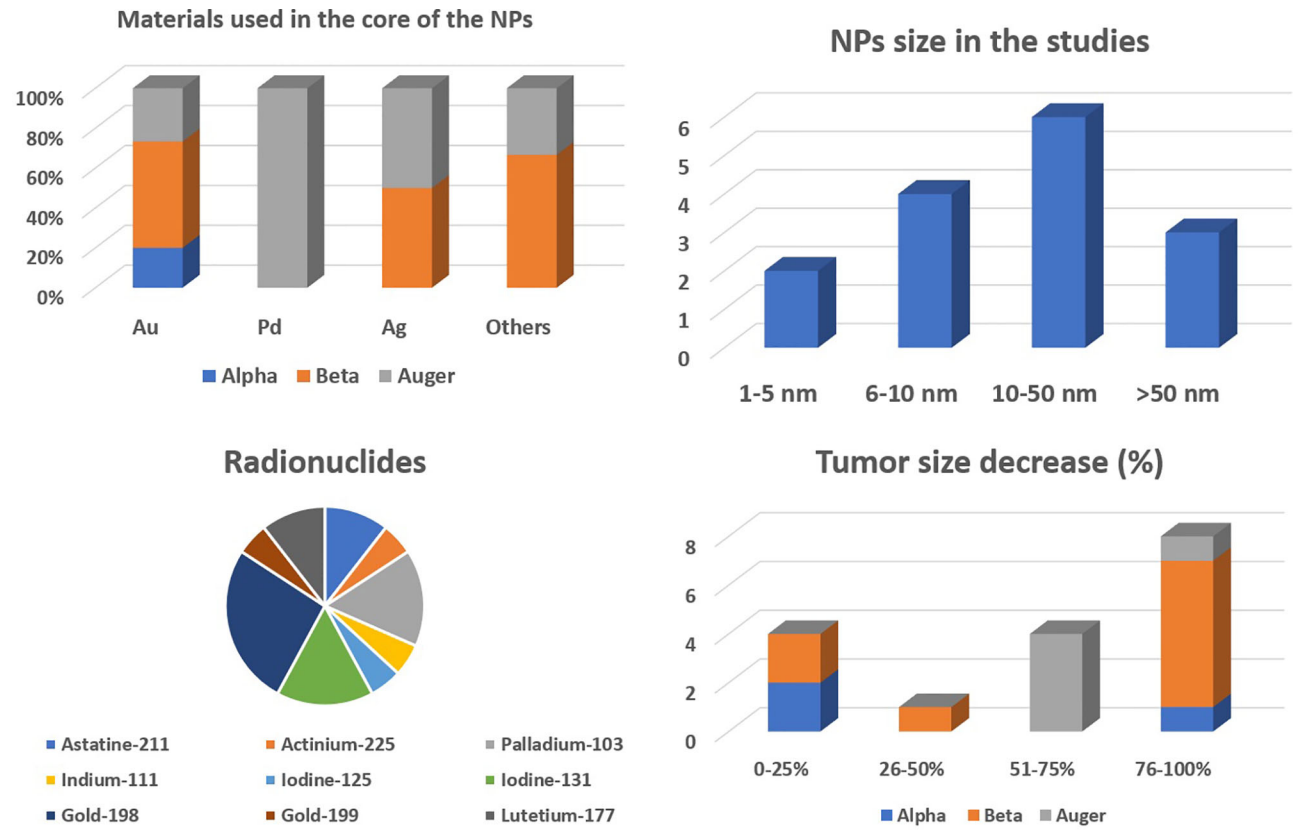

FIGURE 4 | Summary of the main findings from the preclinical studies.

7 DOSIMETRIC STUDIES ON NANOBRACHYTHERAPY APPLICATIONS USING MONTE CARLO METHODS

Radio-NPs are emerging as promising radiotherapeutic agents for cancer treatment and are being probed as a replacement to seed-based BT. Prior to using radio-NPs for RT applications, accurate dosimetric simulations are needed in order to determine the dose distribution within the tumor volume and the surrounding normal tissues. Monte Carlo simulation techniques can be used efficiently to determine the energy or dose distribution within the region of interest. As per our knowledge, only three studies addressing the problem of dosimetry for nanobrachytherapy using radio-NPs have been published so far. The main highlights of these three studies are briefly discussed below.

Laprise-Pelletier et al. (98) used both experimental and theoretical approaches to estimate the dose distribution maps in the tumor tissues. Initially, radio-NPs ^{103}Pd : Pd@Au were synthesized (15) and administered intratumorally to the mice bearing prostate cancer tumors. At different time points (2 h, 24 h, and 8 days), tumors were harvested and analyzed through optical and transmission electron microscopy (TEM). A comprehensive biodistribution study confirmed that more than 80% of radio-NPs were retained in the tumor volume and that a small percentage of NPs migrated to the liver and spleen. The intracellular distribution of ^{103}Pd : Pd@AuNPs was quantified through optical and TEM images. Maps and profiles of energy deposition at microscopic and macroscopic levels were estimated using these data. At the macroscopic level, the dose distribution, in terms of isodose curves, obtained for ^{103}Pd : Pd@AuNPs (also termed as "cloud" of radio-NPs) was compared with the dose distribution obtained for the conventional millimeter-sized, low-dose BT: ^{103}Pd seed. A sharper dose fall in the isodose curves estimated for a single injection of radio-NPs was reported in comparison with the conventional BT seed. This sharper dose fall was attributed to the attenuation of photons by the gold atoms present in the "cloud" of NPs. The authors stressed that this feature can be useful in effectively sparing organs at risk and delivering high doses of radiation to the tumor tissues, as NPs deposit very high doses of radiation in their immediate vicinity. The TEM images of the xenograft tumor cells were used to simulate the energy deposited by ^{103}Pd : Pd@AuNPs at the microscopic level. The Monte Carlo simulation was conducted in three steps: i) the TEM images representative of microdistribution of NPs were selected and digitized. These digitized images were virtually placed in the middle of 50-μm^3 cubical phantom. ii) Nanoconstructs (r = 25 nm) with Pd core (r = 5 nm) coated with a thick layer of gold

(r = 20 nm) were simulated. These nanoconstructs were positioned in the resampled TEM images, placed in the cubical phantom. iii) Emitted photons and electrons produced in the interactions were simulated, and energy deposition maps were computed. From the computed dose distribution, it was found that the highest dose deposition occurred in the immediate vicinity of the NPs. That is, the electrons escaping from the NPs lost most of their energy in a very short range, and almost no NPs were found in the nuclei. The same microdosimetric approach was used to quantify the radiosensitization effect induced by gold. In this case, two simulations were performed, considering i) ^{103}Pd : Pd core coated with gold and ii) ^{103}Pd : Pd not coated with gold. The estimated energy deposition map was reported as a ratio of energy-deposited values (energy deposited by radio-NPs coated with gold/energy deposited by radio-NPs not coated with gold). The ratio of energy-deposited value quantified the dose enhancement effect due to the presence of gold. Enhancement in dose by factor of 25, in the immediate vicinity of the NPs coated with gold, was observed, whereas for regions 2 μm further from the radio-NPs, no radiosensitization effect was observed. Hence, the radiosensitization effect was found to be extremely localized around the gold-coated radio-NPs. Based on the microdosimetric results, the authors concluded that reactive oxygen species (ROS) can be the main factor responsible for cell killing and observed strong tumor control effect (15).

Al-Yasiri et al. (99) used MCNP6.1.1 Monte Carlo (MC) code to construct a simple geometrical replica of a human prostate, containing a tumor inside it, and estimated the dose distribution due to the gold radio-NPs (^{198}AuNPs or ^{199}AuNPs) homogeneously distributed within the tumor. This simple model consisted of spheres representing the following: tumor (radius (r) = 0.4 cm) located within the prostate (r = 2 cm), prostate, bladder (r = 3.5 cm), and rectum (r = 1.5 cm). Dose distribution was estimated for tumor and other organs at risk (healthy prostate, bladder, and rectum), assuming that 10 mCi of ^{198}AuNPs/^{199}AuNPs was homogeneously distributed within the tumor volume. The authors reported that for both ^{198}AuNPs and ^{199}AuNPs, the maximum dose was deposited at the center of the tumor and decreased rapidly towards the tumor prostate interface and other surrounding organs. Owing to the high-energy beta emissions from ^{198}Au, high dose rates were reported for ^{198}Au at a) center of the tumor, 12 Gy/h; b) prostate tumor periphery, 1.46 Gy/h; c) prostate periphery, 0.1 Gy/h; d) center of the bladder, 0.013 Gy; and e) center of the rectum, 0.026 Gy/h. On the other hand, due to low-energy beta emissions for ^{199}Au, for the same locations, the dose rates were 1.6, 0.53, 0.26, 0.0013, and 0.004 Gy/h. Based on these findings, the authors concluded that ^{198}AuNPs are suitable for the treatment of solid tumors and that ^{199}Au can be used for imaging purposes.

In one of our recent *in silico* dosimetry study (61), we replicated the cell survival curves for three preclinical studies (10, 15, 100), published in literature, on the use of radioactive nanocarriers as nanobrachytherapeutic agents using a mathematical model (101) and EGSnrc (102) MC code. The mathematical model used took into account the doubling rate of tumor cells, complete repair of sublethal damage, uptake rate, and washout rate of nanocarriers to and from tumor cell monoexponential function of time. Furthermore, this study anticipated several possibilities and evaluated the dosimetric characteristics and therapeutic efficacy of nanoparticles radiolabeled with ^{103}Pd (Auger emitter), ^{153}Sm (medium energy beta emitter), and ^{198}Au (high-energy beta emitter). Initially, the dosimetric characteristics of ^{103}Pd, ^{153}Sm, and ^{198}Au were evaluated using single cell dosimetry (7). It was found that at the cellular level, ^{153}Sm deposited maximum dose, followed by ^{103}Pd and ^{198}Au. The least energy deposition for ^{198}Au was attributed to the emitted highly energetic beta particles. These beta particles exit the cell volume (radius = 5 μm) without depositing enough energy. Second, the estimated cell survival curves were found to be in good agreement with the experimental results published in literature. Lastly, we evaluated the impact of i) tumor size, ii) tumor type, and iii) amount of injected activity on the cell survival curves. We found that ^{153}Sm and ^{198}Au effectively ablated tumor cells for all three cases with minimum injected activity (≤20 MBq), whereas for ^{103}Pd, higher radioactivity was required to achieve a similar effect. Hence, we concluded that for radioresistant, large size (≈1 cm^3) and rapidly growing tumors, ^{153}Sm and ^{198}Au can be conclusively used as nanobrachytherapeutic agents, whereas ^{103}Pd is only suitable for small-size (≈0.3 cm^3) tumors that have injected activity ≥60 MBq.

8 CONCLUSION, CURRENT CHALLENGES, AND FUTURE PROSPECTS

The application of interstitial BT is impeded by several posttreatment adverse effects or symptoms and the associated operational and logistical complications. The emerging nano-platforms can be used to efficiently deliver radiopharmaceuticals to the tumor. In comparison with free radioisotopes or radioisotopes functionalized with single tumor-specific biomolecules, nanoparticles can be loaded with higher doses of radioactivity, and multiple radioisotopes can be accommodated within a single nanoparticle. Moreover, these nanocarriers can also provide several additional functions, for instance: i) photothermal effect, ii) load chemotherapeutic drug, iii) radiosensitization in case of high-Z nanoparticles, and iv) real-time tumor imaging. Hence, they can be helpful in improving the efficacy or optimizing the therapeutic planning of internal RT or systemic therapy. Radio-NPs, injected intratumorally, can directly deliver radiation dose to the tumor like BT; and this technique is termed as nanobrachytherapy.

In this article, we review the recent progress in the radiosynthesis of the nanoparticles and their use for nanobrachytherapy applications. Recent progress on the i) radiosynthesis methods, ii) selection of a radionuclide for nanobrachytherapy application, iii) modes of internalization of nanocarriers, and iv) the most recent preclinical and dosimetric studies on BT are discussed.

The intratumoral (i.t.) injection of radio-NPs for nanobrachytherapy applications is associated with several challenges and shortcomings. The two main obstacles that

have impeded the clinical translation of radio-NPs are i) leakage of fraction of injected radio-NPs from the tumor and ii) inhomogeneous distribution of radioactivity within the tumor post i.t. injection.

Intratumoral retention of radio-NPs is crucial for the therapeutic effectiveness of nanobrachytherapy application and must be maximized. It also reduces the risk of irradiating normal tissues or healthy organs (especially the liver and spleen). Both inhomogeneous intratumoral radioactivity distribution and leakage of radio-NPs from the tumor post injection are caused by irregular tumor vasculature, variable blood and lymph flow, and pressure gradients. Since tumors are unique, the radio-NP leakage ratio and distribution of NPs within the tumor may vary from patient to patient. This will probably make treatment planning and dosimetric computations complicated and challenging. The tumor retention of radio-NPs can be improved by i) functionalizing surface of radio-NPs with tumor-specific biomolecules or ii) co-injecting biocompatible polymers that sequester NPs within the tumor, along with radio-NPs. The delivery systems, injected intratumorally, that can homogeneously distribute radioactivity throughout the tumor volume with minimal leakage have not been developed yet.

Consequently, for clinical translation of intratumorally injected radio-NPs for nanobrachytherapy applications, the injected radio-NPs should i) have high intratumoral retention and ii) homogeneously distribute radioactivity throughout the tumor volume.

Hence, more comprehensive biodistribution studies are required to understand and control the excretion routes of radio-NPs. Furthermore, intratumoral distribution and diffusion of NPs depend on i) tumor architecture and its density; ii) interstitial fluid pressure; iii) tumor vasculature, blood flow, and lymph flow; and iv) specifics of extracellular matrix of the tumor. These factors must be investigated in a wide range of tumors in order to reduce the inhomogeneity in the intratumoral radioactivity distribution. Lastly, for accurate computation of dose distribution at the cellular and subcellular levels within a tumor injected with radio-NPs, the computational model should consider i) *in vivo* microscopic distribution of radio-NPs, ii) complex cell geometry, and iii) distribution of radio-NPs near and within the nucleus. The computational model should also include all possible physics processes that are susceptible to participate in radiation dose distribution at the microscopic scale.

AUTHOR CONTRIBUTIONS

BS: initial idea, conceptualization, data collection, and manuscript preparation. LF: manuscript preparation. VT: manuscript preparation. SS: initial idea, basic framework, review of the manuscript, and supervision. TF: supervision and manuscript review. All authors contributed to the article and approved the submitted version.

ACKNOWLEDGMENTS

LF would like to thank FAPESP for the financial support on the project 2018/15598-2. Additionally, VT would also like to thank FAPESP for the financial support on the project (Grant Nos. 2018/15598-2 and 2019/15154-0).

REFERENCES

1. Bray F, Ferlay J, Soerjomataram I, Siegel R, Torre L, Jemal A. Erratum: Global Cancer Statistics 2018: Globocan Estimates of Incidence and Mortality Worldwide for 36 Cancers in 185 Countries. *CA Cancer J Clin* (2020) 70:313. doi: 10.3322/caac.21609
2. Seniwal B, Bhatt C, Fonseca TC. Comparison of Dosimetric Accuracy of Acuros Xb and Analytical Anisotropic Algorithm Against Monte Carlo Technique. *Biomed Phys Eng Express* (2020) 6:015035. doi: 10.1088/2057-1976/ab6e1b
3. Seniwal B, Mendes BM, Malano F, Pérez P, Valente M, Fonseca TC. Monte Carlo Assessment of Low Energy Electron Range in Liquid Water and Dosimetry Effects. *Phys Med* (2020) 80:363–72. doi: 10.1016/j.ejmp.2020.11.013
4. Fonseca T, Antunes P, Belo M, Bastos F, Campos T, Geraldo J, et al. Mcmeg: Intercomparison Exercise on Prostate Radiotherapy Dose Assessment. *Radiat Phys Chem* (2020) 167:108295. doi: 10.1016/j.radphyschem.2019.04.045
5. Song G, Cheng L, Chao Y, Yang K, Liu Z. Emerging Nanotechnology and Advanced Materials for Cancer Radiation Therapy. *Adv Mater* (2017) 29:1700996. doi: 10.1002/adma.201700996
6. Mendes BM, Antunes PCG, Branco ISL, do Nascimento E, Seniwal B, Fonseca TCF, et al. Calculation of Dose Point Kernel Values for Monoenergetic Electrons and Beta Emitting Radionuclides: Intercomparison of Monte Carlo Codes. *Radiat Phys Chem* (2021) 181:109327. doi: 10.1016/j.radphyschem.2020.109327
7. Seniwal B, Bernal MA, Fonseca TC. Microdosimetric Calculations for Radionuclides Emitting β and α Particles and Auger Electrons. *Appl Radiat Isot* (2020) 166:109302. doi: 10.1016/j.apradiso.2020.109302
8. Park DS. Current Status of Brachytherapy for Prostate Cancer. *Korean J Urol* (2012) 53:743. doi: 10.4111/kju.2012.53.11.743
9. De La Puente P, Azab AK. Delivery Systems for Brachytherapy. *J Control Release* (2014) 192:19–28. doi: 10.1016/j.jconrel.2014.06.057
10. Al–Yasiri A, Khoobchandani M, Cutler C, Watkinson L, Carmack T, Smith C, et al. Mangiferin Functionalized Radioactive Gold Nanoparticles (Mgf–198 Aunps) in Prostate Tumor Therapy: Green Nanotechnology for Production, *In Vivo* Tumor Retention and Evaluation of Therapeutic Efficacy. *Dalton Trans* (2017) 46:14561–71. doi: 10.1039/C7DT00383H
11. Khan MK, Minc LD, Nigavekar SS, Kariapper MS, Nair BM, Schipper M, et al. Fabrication of {198au0}4 Radioactive Composite Nanodevices and Their Use for Nanobrachytherapy. *Nanomedicine: Nanotechnol Biol Med* (2008) 4:57–69. doi: 10.1016/j.nano.2007.11.005
12. Ehlerding EB, Cai W. Smaller Agents for Larger Therapeutic Indices: Nanoscale Brachytherapy With 177lu–Labeled Gold Nanoparticles. *J Nucl Med* (2016) 57:834–5. doi: 10.2967/jnumed.116.173278
13. Laprise–Pelletier M, Simão T, Fortin MA. Gold Nanoparticles in Radiotherapy and Recent Progress in Nanobrachytherapy. *Adv Healthc Mater* (2018) 7:1701460. doi: 10.1002/adhm.201701460
14. Salvanou EA, Stellas D, Tsoukalas C, Mavroidi B, Paravatou–Petsotas M, Kalogeropoulos N, et al. A Proof–of–Concept Study on the Therapeutic Potential of Au Nanoparticles Radiolabeled With the Alpha–Emitter Actinium–225. *Pharmaceutics* (2020) 12:188. doi: 10.3390/pharmaceutics12020188
15. Laprise–Pelletier M, Lagueux J, Côté MF, LaGrange T, Fortin MA. Low–dose Prostate Cancer Brachytherapy With Radioactive Palladium–Gold Nanoparticles. *Adv Healthc Mater* (2017) 6:1601120. doi: 10.1002/adhm.201601120

16. Silva F, Cabral Campello MP, Paulo A. Radiolabeled Gold Nanoparticles for Imaging and Therapy of Cancer. *Materials* (2021) 14:4. doi: 10.3390/ma14010004
17. Sheng J, Wang X, Yan J, Pan D, Yang R, Wang L, et al. Theranostic Radioiodine–Labelled Melanin Nanoparticles Inspired by Clinical Brachytherapy Seeds. *J Mater Chem B* (2018) 6:8163–9. doi: 10.1039/C8TB02817F
18. Filippi L, Frantellizzi V, Chiaravalloti A, Pontico M, De Feo MS, Corica F, et al. Prognostic and Theranostic Applications of Positron Emission Tomography for a Personalized Approach to Metastatic Castration–Resistant Prostate Cancer. *Int J Mol Sci* (2021) 22:3036. doi: 10.3390/ijms22063036
19. Daems N, Michiels C, Lucas S, Baatout S, Aerts A. Gold Nanoparticles Meet Medical Radionuclides. *Nucl Med Biol* (2021) 101-101:61–90. doi: 10.1016/j.nucmedbio.2021.06.001
20. Pellico J, Gawne PJ, de Rosales RT. Radiolabelling of Nanomaterials for Medical Imaging and Therapy. *Chem Soc Rev* (2021) 50:3355–423. doi: 10.1039/D0CS00384K
21. Perez–Medina C, Teunissen AJ, Kluza E, Mulder WJ, van der Meel R. Nuclear Imaging Approaches Facilitating Nanomedicine Translation. *Adv Drug Deliv Rev* (2020) 154-155:1230–41. doi: 10.1016/j.addr.2020.07.017
22. Majkowska–Pilip A, Gawęda W, Żelechowska–Matysiak K, Wawrowicz K, Bilewicz A. Nanoparticles in Targeted Alpha Therapy. *Nanomaterials* (2020) 10:1366. doi: 10.3390/nano10071366
23. Lamb J, Holland JP. Advanced Methods for Radiolabeling Multimodality Nanomedicines for Spect/Mri and Pet/Mri. *J Nucl Med* (2018) 59:382–9. doi: 10.2967/jnumed.116.187419
24. Datta P, Ray S. Nanoparticulate Formulations of Radiopharmaceuticals: Strategy to Improve Targeting and Biodistribution Properties. *J Labelled Comp Radiopharm* (2020) 63:333–55. doi: 10.1002/jlcr.3839
25. Shen W, Zhou H, Liu T, Pei P, Huang J, Yi X, et al. The Potential Clinical Applications of Radionuclide Labeled/Doped Gold–Based Nanomaterials. *Radiat Med Prot* (2020) 1(4):186–95. doi: 10.1016/j.radmp.2020.11.001
26. de Maria R, Mendoza-Nava H, Ferro-Flores G, Raírez FD, Ocampo-García B, Santos-Cuevas C, et al. 177lu–Dendrimer Conjugated to Folate and Bombesin With Gold Nanoparticles in the Dendritic Cavity. *J Nanomater* (2016) 2016:1039258. doi: 10.1155/2016/1039258
27. Jarrett AM, Hormuth DA, Adhikarla V, Sahoo P, Abler D, Tumyan L, et al. Towards Integration of 64 Cu–Dota–Trastuzumab Pet–Ct and Mri With Mathematical Modeling to Predict Response to Neoadjuvant Therapy in Her2+ Breast Cancer. *Sci Rep* (2020) 10:1–14. doi: 10.1038/s41598-020-77397-0
28. Nagarajan V, Park S, Kim DI, Woo SK, Lim I. Pet Imaging and Biodistribution of 64cu–Dota–Atezolizumab in Mice Bearing Mda–Mb231 Xenograft. *Nucl Med* (2021) 62:1490.
29. Hajiramezanali M, Atyabi F, Mosayebnia M, Akhlaghi M, Geramifar P, Jalilian AR, et al. 68ga–Radiolabeled Bombesin–Conjugated to Trimethyl Chitosan–Coated Superparamagnetic Nanoparticles for Molecular Imaging: Preparation, Characterization and Biological Evaluation. *Int J Nanomed* (2019) 14:2591. doi: 10.2147/IJN.S195223
30. Huclier–Markai S, Ntsiba E, Thomas E, Alliot C, Cutler C, Lux F, et al. Multimodal Aguix® Nanoparticles: Size Characterization by Hf5 and Optimization of the Radiolabeling With Various Spect/Pet/Theranostic Tracers. *Int J Med Nano Res* (2019) 6:1–30. doi: 10.23937/2378-3664.1410027
31. Lux F, Tran VL, Thomas E, Dufort S, Rossetti F, Martini M, et al. Aguix® From Bench to Bedside—Transfer of an Ultrasmall Theranostic Gadolinium–Based Nanoparticle to Clinical Medicine. *Br J Radiol* (2019) 92:20180365. doi: 10.1259/bjr.20180365
32. Ranjbar Bahadori S, Mulgaonkar A, Hart R, Wu CY, Zhang D, Pillai A, et al. Radiolabeling Strategies and Pharmacokinetic Studies for Metal Based Nanotheranostics. *Wiley Interdiscip Rev Nanomed Nanobiotechnol* (2021) 13:e1671. doi: 10.1002/wnan.1671
33. Aranda–Lara L, Morales–Avila E, Luna–Gutiérrez MA, Olivé–Alvarez E, Isaac–Olivé K. Radiolabeled Liposomes and Lipoproteins as Lipidic Nanoparticles for Imaging and Therapy. *Chem Phys Lipids* (2020) 230:104934. doi: 10.1016/j.chemphyslip.2020.104934
34. Pei P, Shen W, Zhou H, Sun Y, Zhong J, Liu T, et al. Radionuclide Labeled Gold Nanoclusters Boost Effective Anti–Tumor Immunity for Augmented Radio–Immunotherapy of Cancer. *Nano Today* (2021) 38:101144. doi: 10.1016/j.nantod.2021.101144
35. Chanda N, Kattumuri V, Shukla R, Zambre A, Katti K, Upendran A, et al. Bombesin Functionalized Gold Nanoparticles Show *In Vitro* and *In Vivo* Cancer Receptor Specificity. *Proc Natl Acad Sci* (2010) 107:8760–5. doi: 10.1073/pnas.1002143107
36. Shukla R, Chanda N, Zambre A, Upendran A, Katti K, Kulkarni RR, et al. Laminin Receptor Specific Therapeutic Gold Nanoparticles (198aunp–Egcg) Show Efficacy in Treating Prostate Cancer. *Proc Natl Acad Sci* (2012) 109:12426–31. doi: 10.1073/pnas.1121174109
37. Chakravarty R, Chakraborty S, Guleria A, Shukla R, Kumar C, Vimalnath Nair K, et al. Facile One–Pot Synthesis of Intrinsically Radiolabeled and Cyclic Rgd Conjugated 199au Nanoparticles for Potential Use in Nanoscale Brachytherapy. *Ind Eng Chem Res* (2018) 57:14337–46. doi: 10.1021/acs.iecr.8b02526
38. Fach M, Fliedner FP, Kempen PJ, Melander F, Hansen AE, Bruun LM, et al. Effective Intratumoral Retention of [103pd] Aupd Alloy Nanoparticles Embedded in Gel–Forming Liquids Paves the Way for New Nanobrachytherapy. *Adv Healthc Mater* (2021) 10:2002009. doi: 10.1002/adhm.202002009
39. Pérez–Campaña C, Gómez–Vallejo V, Puigivila M, Martín A, Calvo–Fernández T, Moya SE, et al. Biodistribution of Different Sized Nanoparticles Assessed by Positron Emission Tomography: A General Strategy for Direct Activation of Metal Oxide Particles. *ACS nano* (2013) 7:3498–505. doi: 10.1021/nn400450p
40. Lee SB, Kumar D, Li Y, Lee IK, Cho SJ, Kim SK, et al. Pegylated Crushed Gold Shell–Radiolabeled Core Nanoballs for *In Vivo* Tumor Imaging With Dual Positron Emission Tomography and Cerenkov Luminescent Imaging. *J Nanobiotechnology* (2018) 16:1–12. doi: 10.1186/s12951-018-0366-x
41. Laan AC, Santini C, Jennings L, de Jong M, Bernsen MR, Denkova AG. Radiolabeling Polymeric Micelles for *In Vivo* Evaluation: A Novel, Fast, and Facile Method. *EJNMMI Res* (2016) 6:1–10. doi: 10.1186/s13550-016-0167-x
42. Freund B, Tromsdorf UI, Bruns UI, Heine M, Giemsa A, Bartelt A, et al. A Simple and Widely Applicable Method to 59Fe-radiolabel Monodisperse Superparamagnetic Iron Oxide Nanoparticles for *In Vivo* Quantification Studies. *ACS Nano* (2012) 6(8):7318–25. doi: 10.1021/nn3024267
43. Tang T, Wei Y, Yang Q, Yang Y, Sailor MJ, Pang HB. Rapid Chelator–Free Radiolabeling of Quantum Dots for *In Vivo* Imaging. *Nanoscale* (2019) 11:22248–54. doi: 10.1039/C9NR08508D
44. Gaikwad G, Rohra N, Kumar C, Jadhav S, Sarma HD, Borade L, et al. A Facile Strategy for Synthesis of a Broad Palette of Intrinsically Radiolabeled Chitosan Nanoparticles for Potential Use in Cancer Theranostics. *J Drug Deliv Sci Technol* (2021) 63:102485. doi: 10.1016/j.jddst.2021.102485
45. Zhang Y, Sheng J, Zhai F, Wang X, Chen L, Shi C, et al. Pioneering Iodine–125–Labeled Nanoscale Covalent Organic Frameworks for Brachytherapy. *Bioconjug Chem* (2021) 32:755–62. doi: 10.1021/acs.bioconjchem.1c00040
46. Pallares RM, Abergel RJ. Nanoparticles for Targeted Cancer Radiotherapy. *Nano Res* (2020) 13:2887–97. doi: 10.1007/s12274-020-2957-8
47. Yi X, Zhou H, Zhang Z, Xiong S, Yang K. X–rays–optimized Delivery of Radiolabeled Albumin for Cancer Theranostics. *Biomaterials* (2020) 233:119764. doi: 10.1016/j.biomaterials.2020.119764
48. Yeong CH, Mh C, Ng KH. Therapeutic Radionuclides in Nuclear Medicine: Current and Future Prospects. *J Zhejiang Univ Sci B* (2014) 15:845–63. doi: 10.1631/jzus.B1400131
49. Lin FS, Chen CH, Tseng FG, Hwu Y, Chen JK, Lin SY, et al. Radiotherapy of the Excretable Radioactive Gold Nanocomposite With Intratumoral Injection. *IJMMM* (2013) 1:265–8. doi: 10.7763/IJMMM.2013.V1.56
50. Yook S, Cai Z, Lu Y, Winnik MA, Pignol JP, Reilly RM. Intratumorally Injected 177lu–Labeled Gold Nanoparticles: Gold Nanoseed Brachytherapy With Application for Neoadjuvant Treatment of Locally Advanced Breast Cancer. *J Nucl Med* (2016) 57:936–42. doi: 10.2967/jnumed.115.168906
51. Dziawer L, Koźmiński P, Męczyńska–Wielgosz S, Pruszyński M, Łyczko M, Wąs B, et al. Gold Nanoparticle Bioconjugates Labelled With 211 at for Targeted Alpha Therapy. *RSC Adv* (2017) 7:41024–32. doi: 10.1039/C7RA06376H

52. Cai Z, Chattopadhyay N, Yang K, Kwon YL, Yook S, Pignol JP, et al. 111in–Labeled Trastuzumab–Modified Gold Nanoparticles Are Cytotoxic *In Vitro* to Her2–Positive Breast Cancer Cells and Arrest Tumor Growth *In Vivo* in Athymic Mice After Intratumoral Injection. *Nucl Med Biol* (2016) 43:818–26. doi: 10.1016/j.nucmedbio.2016.08.009
53. Farzin L, Sheibani S, Moassesi ME, Shamsipur M. An Overview of Nanoscale Radionuclides and Radiolabeled Nanomaterials Commonly Used for Nuclear Molecular Imaging and Therapeutic Functions. *J Biomed Mater Res Part A* (2019) 107:251–85. doi: 10.1002/jbm.a.36550
54. Peltek OO, Muslimov AR, Zyuzin MV, Timin AS. Current Outlook on Radionuclide Delivery Systems: From Design Consideration to Translation Into Clinics. *J Nanobiotechnology* (2019) 17:1–34. doi: 10.1186/s12951-019-0524-9
55. Czerwińska M, Bilewicz A, Kruszewski M, Wegierek–Ciuk A, Lankoff A. Targeted Radionuclide Therapy of Prostate Cancer—From Basic Research to Clinical Perspectives. *Molecules* (2020) 25:1743. doi: 10.3390/molecules25071743
56. Toohey RE, Stabin MG, Watson EE. The Aapm/Rsna Physics Tutorial for Residents: Internal Radiation Dosimetry: Principles and Applications 1 (Cme Available in Print Version and on Rsna Link). *Radiographics* (2000) 20:533–46. doi: 10.1148/radiographics.20.2.g00mc33533
57. Dziawer Ł, Majkowska–Pilip A, Gaweł D, Godlewska M, Pruszyński M, Jastrzębski J, et al. Trastuzumab–modified Gold Nanoparticles Labeled With 211at as a Prospective Tool for Local Treatment of Her2–Positive Breast Cancer. *Nanomaterials* (2019) 9:632. doi: 10.3390/nano9040632
58. Mancini–Terracciano C, Donnarumma R, Bencivenga G, Bocci V, Cartoni A, Collamati F, et al. Feasibility of Beta–Particle Radioguided Surgery for a Variety of "Nuclear Medicine" Radionuclides. *Phys Med* (2017) 43:127–33. doi: 10.1016/j.ejmp.2017.10.012
59. Ahmadzadehfar H. Targeted Therapy for Metastatic Prostate Cancer With Radionuclides. In: *Prostate Cancer–Leading–Edge Diagnostic Procedures and Treatments*. Croatia: InTech (2016). p. 60–4.
60. Flocks R, Kerr H, Elkins H, Culp D. Treatment of Carcinoma of the Prostate by Interstitial Radiation With Radio–Active Gold (Au198): A Preliminary Report. *J Urol* (1952) 68:510–22. doi: 10.1016/S0022-5347(17)68230-2
61. Seniwal B, Freitas LF, Mendes BM, Lugão AB, Katti KV, Fonseca TC. *In Silico* Dosimetry of Low–Dose Rate Brachytherapy Using Radioactive Nanoparticles. *Phys Med Biol* (2021) 66:045016. doi: 10.1088/1361-6560/abd671
62. Mann SK, Czuba E, Selby LI, Such GK, Johnston AP. Quantifying Nanoparticle Internalization Using a High Throughput Internalization Assay. *Pharm Res* (2016) 33:2421–32. doi: 10.1007/s11095-016-1984-3
63. Chen HH, Chien CC, Petibois C, Wang CL, Chu YS, Lai SF, et al. Quantitative Analysis of Nanoparticle Internalization in Mammalian Cells by High Resolution X–Ray Microscopy. *J Nanobiotechnol* (2011) 9:1–15. doi: 10.1186/1477-3155-9-14
64. Zhao F, Zhao Y, Liu Y, Chang X, Chen C, Zhao Y. Cellular Uptake, Intracellular Trafficking, and Cytotoxicity of Nanomaterials. *Small* (2011) 7:1322–37. doi: 10.1002/smll.201100001
65. Douglas KL, Piccirillo CA, Tabrizian M. Cell Line–Dependent Internalization Pathways and Intracellular Trafficking Determine Transfection Efficiency of Nanoparticle Vectors. *Eur J Pharm Biopharm* (2008) 68:676–87. doi: 10.1016/j.ejpb.2007.09.002
66. Grainger A. Difficulties in Tracking the Long–Term Global Trend in Tropical Forest Area. *Proc Natl Acad Sci* (2008) 105:818–23. doi: 10.1073/pnas.0703015105
67. Bannunah AM, Vllasaliu D, Lord J, Stolnik S. Mechanisms of Nanoparticle Internalization and Transport Across an Intestinal Epithelial Cell Model: Effect of Size and Surface Charge. *Mol Pharm* (2014) 11:4363–73. doi: 10.1021/mp500439c
68. Gottstein C, Wu G, Wong BJ, Zasadzinski JA. Precise Quantification of Nanoparticle Internalization. *ACS nano* (2013) 7:4933–45. doi: 10.1021/nn400243d
69. Santi M, Maccari G, Mereghetti P, Voliani V, Rocchiccioli S, Ucciferri N, et al. Rational Design of a Transferrin–Binding Peptide Sequence Tailored to Targeted Nanoparticle Internalization. *Bioconjug Chem* (2017) 28:471–80. doi: 10.1021/acs.bioconjchem.6b00611
70. Harush–Frenkel O, Debotton N, Benita S, Altschuler Y. Targeting of Nanoparticles to the Clathrin–Mediated Endocytic Pathway. *Biochem Biophys Res Commun* (2007) 353:26–32. doi: 10.1016/j.bbrc.2006.11.135
71. Zhang Y, Kohler N, Zhang M. Surface Modification of Superparamagnetic Magnetite Nanoparticles and Their Intracellular Uptake. *Biomaterials* (2002) 23:1553–61. doi: 10.1016/S0142-9612(01)00267-8
72. Moeendarbari S, Tekade R, Mulgaonkar A, Christensen P, Ramezani S, Hassan G, et al. Theranostic Nanoseeds for Efficacious Internal Radiation Therapy of Unresectable Solid Tumors. *Sci Rep* (2016) 6:1–9. doi: 10.1038/srep20614
73. Kannan R, Rahing V, Cutler C, Pandrapragada R, Katti KK, Kattumuri V, et al. Nanocompatible Chemistry Toward Fabrication of Target–Specific Gold Nanoparticles. *J Am Chem Soc* (2006) 128:11342–3. doi: 10.1021/ja063280c
74. Axiak–Bechtel SM, Upendran A, Lattimer JC, Kelsey J, Cutler CS, Selting KA, et al. Gum Arabic–Coated Radioactive Gold Nanoparticles Cause No Short–Term Local or Systemic Toxicity in the Clinically Relevant Canine Model of Prostate Cancer. *Int J Nanomed* (2014) 9:5001. doi: 10.2147/IJN.S67333
75. Cai Z, Yook S, Lu Y, Bergstrom D, Winnik MA, Pignol JP, et al. Local Radiation Treatment of Her2–Positive Breast Cancer Using Trastuzumab–Modified Gold Nanoparticles Labeled With 177 Lu. *Pharm Res* (2017) 34:579–90. doi: 10.1007/s11095-016-2082-2
76. Zhang R, Zhang Y, Tan J, Wang H, Zhang G, Li N, et al. Antitumor Effect of 131 I–Labeled Anti–Vegfr2 Targeted Mesoporous Silica Nanoparticles in Anaplastic Thyroid Cancer. *Nanoscale Res Lett* (2019) 14:1–11. doi: 10.1186/s11671-019-2924-z
77. Su W, Chen C, Wang T, Li X, Liu Y, Wang H, et al. Radionuclide–labeled Gold Nanoparticles for Nuclei–Targeting Internal Radio–Immunity Therapy. *Mater Horiz* (2020) 7:1115–25. doi: 10.1039/C9MH01725A
78. Chanda N, Kan P, Watkinson LD, Shukla R, Zambre A, Carmack TL, et al. Radioactive Gold Nanoparticles in Cancer Therapy: Therapeutic Efficacy Studies of Ga–198aunp Nanoconstruct in Prostate Tumor–Bearing Mice. *Nanomedicine: Nanotechnol Biol Med* (2010) 6:201–9. doi: 10.1016/j.nano.2009.11.001
79. Kalbasi A, June CH, Haas N, Vapiwala N. Radiation and Immunotherapy: A Synergistic Combination. *J Clin Invest* (2013) 123:2756–63. doi: 10.1172/JCI69219
80. Ehlers G, Fridman M. Abscopal Effect of Radiation in Papillary Adenocarcinoma. *Br J Radiol* (1973) 46:220–2. doi: 10.1259/0007-1285-46-543-220
81. Ohba K, Omagari K, Nakamura T, Ikuno N, Saeki S, Matsuo I, et al. Abscopal Regression of Hepatocellular Carcinoma After Radiotherapy for Bone Metastasis. *Gut* (1998) 43:575–7. doi: 10.1136/gut.43.4.575
82. Wersäll PJ, Blomgren H, Pisa P, Lax I, Kälkner KM, Svedman C. Regression of non–Irradiated Metastases After Extracranial Stereotactic Radiotherapy in Metastatic Renal Cell Carcinoma. *Acta Oncol* (2006) 45:493–7. doi: 10.1080/02841860600604611
83. Demaria S, Ng B, Devitt ML, Babb JS, Kawashima N, Liebes L, et al. Ionizing Radiation Inhibition of Distant Untreated Tumors (Abscopal Effect) Is Immune Mediated. *Int J Radiat Oncol Biol Phys* (2004) 58:862–70. doi: 10.1016/j.ijrobp.2003.09.012
84. Formenti SC, Demaria S. Combining Radiotherapy and Cancer Immunotherapy: A Paradigm Shift. *J Natl Cancer Inst* (2013) 105:256–65. doi: 10.1093/jnci/djs629
85. Kang J, Demaria S, Formenti S. Current Clinical Trials Testing the Combination of Immunotherapy With Radiotherapy. *J Immunother Cancer* (2016) 4:1–20. doi: 10.1186/s40425-016-0156-7
86. Ngwa W, Irabor OC, Schoenfeld JD, Hesser J, Demaria S, Formenti SC. Using Immunotherapy to Boost the Abscopal Effect. *Nat Rev Cancer* (2018) 18:313–22. doi: 10.1038/nrc.2018.6
87. Apetoh L, Ghiringhelli F, Tesniere A, Obeid M, Ortiz C, Criollo A, et al. Toll–like Receptor 4–Dependent Contribution of the Immune System to Anticancer Chemotherapy and Radiotherapy. *Nat Med* (2007) 13:1050–9. doi: 10.1038/nm1622
88. Jagodinsky JC, Harari PM, Morris ZS. The Promise of Combining Radiation Therapy With Immunotherapy. *Int J Radiat Oncol Biol Phys* (2020) 108:6–16. doi: 10.1016/j.ijrobp.2020.04.023
89. Mondini M, Levy A, Meziani L, Milliat F, Deutsch E. Radiotherapy–immunotherapy Combinations–Perspectives and Challenges. *Mol Oncol* (2020) 14:1529–37. doi: 10.1002/1878-0261.12658

90. Chao Y, Liang C, Tao H, Du Y, Wu D, Dong Z, et al. Localized Cocktail Chemoimmunotherapy After *In Situ* Gelation to Trigger Robust Systemic Antitumor Immune Responses. *Sci Adv* (2020) 6:eaaz4204. doi: 10.1126/sciadv.aaz4204
91. Chua CYX, Jain P, Susnjar A, Rhudy J, Folci M, Ballerini A, et al. Nanofluidic Drug–Eluting Seed for Sustained Intratumoral Immunotherapy in Triple Negative Breast Cancer. *J Control Release* (2018) 285:23–34. doi: 10.1016/j.jconrel.2018.06.035
92. Chua CYX, Ho J, Demaria S, Ferrari M, Grattoni A. Emerging Technologies for Local Cancer Treatment. *Adv Ther* (2020) 3:2000027. doi: 10.1002/adtp.202000027
93. Moreau M, Yasmin–Karim S, Kunjachan S, Sinha N, Gremse F, Kumar R, et al. Priming the Abscopal Effect Using Multifunctional Smart Radiotherapy Biomaterials Loaded With Immunoadjuvants. *Front Oncol* (2018) 8:56. doi: 10.3389/fonc.2018.00056
94. Rahimian S, Fransen MF, Kleinovink JW, Amidi M, Ossendorp F, Hennink WE. Polymeric Microparticles for Sustained and Local Delivery of Anticd40 and Antictla–4 in Immunotherapy of Cancer. *Biomaterials* (2015) 61:33–40. doi: 10.1016/j.biomaterials.2015.04.043
95. Wang Y, Deng W, Li N, Neri S, Sharma A, Jiang W, et al. Combining Immunotherapy and Radiotherapy for Cancer Treatment: Current Challenges and Future Directions. *Front Pharmacol* (2018) 9:185. doi: 10.3389/fphar.2018.00185
96. Yu S, Wang C, Yu J, Wang J, Lu Y, Zhang Y, et al. Injectable Bioresponsive Gel Depot for Enhanced Immune Checkpoint Blockade. *Adv Mater* (2018) 30:1801527. doi: 10.1002/adma.201801527
97. Chao Y, Xu L, Liang C, Feng L, Xu J, Dong Z, et al. Combined Local Immunostimulatory Radioisotope Therapy and Systemic Immune Checkpoint Blockade Imparts Potent Antitumour Responses. *Nat Biomed Eng* (2018) 2:611–21. doi: 10.1038/s41551-018-0262-6
98. Laprise–Pelletier M, Ma Y, Lagueux J, Cote MF, Beaulieu L, Fortin MA. Intratumoral Injection of Low–Energy Photon–Emitting Gold Nanoparticles: A Microdosimetric Monte Carlo–Based Model. *ACS nano* (2018) 12:2482–97. doi: 10.1021/acsnano.7b08242
99. Al–Yasiri AY, White NE, Katti KV, Loyalka SK. Estimation of Tumor and Local Tissue Dose in Gold Nanoparticles Radiotherapy for Prostate Cancer. *Rep Pract Oncol Radiother* (2019) 24:288–93. doi: 10.1016/j.rpor.2019.02.006
100. Wang JTW, Spinato C, Klippstein R, Costa PM, Martincic M, Pach E, et al. Neutron–irradiated Antibody–Functionalised Carbon Nanocapsules for Targeted Cancer Radiotherapy. *Carbon* (2020) 162:410–22. doi: 10.1016/j.carbon.2020.02.060
101. Šefl M, Kyriakou I, Emfietzoglou D. Impact of Cell Repopulation and Radionuclide Uptake Phase on Cell Survival. *Med Phys* (2016) 43:2715–20. doi: 10.1118/1.4948504
102. Kawrakow I. Accurate Condensed History Monte Carlo Simulation of Electron Transport. I. Egsnrc, the New Egs4 Version. *Med Phys* (2000) 27:485–98. doi: 10.1118/1.598917

Conflict of Interest: The authors declare that the research was conducted in the absence of any commercial or financial relationships that could be construed as a potential conflict of interest.

Publisher's Note: All claims expressed in this article are solely those of the authors and do not necessarily represent those of their affiliated organizations, or those of the publisher, the editors and the reviewers. Any product that may be evaluated in this article, or claim that may be made by its manufacturer, is not guaranteed or endorsed by the publisher.

frontiers in Oncology

ORIGINAL RESEARCH
published: 25 November 2021
doi: 10.3389/fonc.2021.769385

HIF2 Regulates Intestinal Wnt5a Expression

*Carolina J. García García[1,2,3,4], Ariana C. Acevedo Diaz[5], Neeraj Kumari[2,3], Suman Govindaraju[3], Marimar de la Cruz Bonilla[1,3,4], F. Anthony San Lucas[6], Nicholas D. Nguyen[2,3], Iancarlos Jiménez Sacarello[4], Helen Piwnica-Worms[3], Anirban Maitra[6] and Cullen M. Taniguchi[2,3]**

[1] The University of Texas MD Anderson Cancer Center UTHealth Graduate School of Biomedical Sciences, Houston, TX, United States, [2] Department of Radiation Oncology, The University of Texas MD Anderson Cancer Center, Houston, TX, United States, [3] Department of Experimental Radiation Oncology, The University of Texas MD Anderson Cancer Center, Houston, TX, United States, [4] School of Medicine, University of Puerto Rico, Rio Piedras, PR, United States, [5] Department of Biology, University of Puerto Rico, Bayamon, PR, United States, [6] Department of Pathology, The University of Texas MD Anderson Cancer Center, Houston, TX, United States

OPEN ACCESS

Edited by:
Shubhankar Suman, Georgetown University, United States

Reviewed by:
Zachary Scott Morris, University of Wisconsin-Madison, United States
Subhrajit Saha, University of Kansas Medical Center, United States

***Correspondence:**
Cullen M. Taniguchi
CTaniguchi@mdanderson.org

Specialty section:
This article was submitted to Radiation Oncology, a section of the journal Frontiers in Oncology

Received: *01 September 2021*
Accepted: *29 October 2021*
Published: *25 November 2021*

Citation:
García García CJ, Acevedo Diaz AC, Kumari N, Govindaraju S, de la Cruz Bonilla M, San Lucas FA, Nguyen ND, Jimenez Sacarello I, Piwnica-Worms H, Maitra A and Taniguchi CM (2021) HIF2 Regulates Intestinal Wnt5a Expression. Front. Oncol. 11:769385. doi: 10.3389/fonc.2021.769385

Radiation therapy for abdominal tumors is challenging because the small intestine is exquisitely radiosensitive. Unfortunately, there are no FDA-approved therapies to prevent or mitigate GI radiotoxicity. The EGLN protein family are oxygen sensors that regulate cell survival and metabolism through the degradation of hypoxia-inducible factors (HIFs). Our group has previously shown that stabilization of HIF2 through genetic deletion or pharmacologic inhibition of the EGLNs mitigates and protects against GI radiotoxicity in mice by improving intestinal crypt stem cell survival. Here we aimed to elucidate the molecular mechanisms by which HIF2 confers GI radioprotection. We developed duodenal organoids from mice, transiently overexpressed non-degradable HIF2, and performed bulk RNA sequencing. Interestingly, HIF2 upregulated known radiation modulators and genes involved in GI homeostasis, including *Wnt5a*. Non-canonical Wnt5a signaling has been shown by other groups to improve intestinal crypt regeneration in response to injury. Here we show that HIF2 drives *Wnt5a* expression in multiple duodenal organoid models. Luciferase reporter assays performed in human cells showed that HIF2 directly activates the *WNT5A* promoter *via* a hypoxia response element. We then evaluated crypt regeneration using spheroid formation assays. Duodenal organoids that were pre-treated with recombinant Wnt5a had a higher cryptogenic capacity after irradiation, compared to vehicle-treated organoids. Conversely, we found that *Wnt5a* knockout decreased the cryptogenic potential of intestinal stem cells following irradiation. Treatment with recombinant Wnt5a prior to irradiation rescued the cryptogenic capacity of *Wnt5a* knockout organoids, indicating that Wnt5a is necessary and sufficient for duodenal radioprotection. Taken together, our results suggest that HIF2 radioprotects the GI tract by inducing Wnt5a expression.

Keywords: radiotherapy, intestinal stem cells, GI radiotoxicity, hypoxia, HIF2, Wnt5a

INTRODUCTION

Radiation is one of the four pillars of cancer care, with approximately half of cancer patients receiving radiotherapy at some point of their treatment regimen (1). Similar to chemotherapy, the efficacy of radiotherapy is limited by normal tissue toxicity. This toxicity is especially limiting in the case of abdominal and pelvic cancers, which are surrounded by the exquisitely radiosensitive gastrointestinal (GI) tract, and they require high doses of radiation to achieve tumoricidal effects (2). Multiple studies have highlighted how common GI radiotoxicity is among cancer patients (3–5). Results from a Phase 3 clinical trial showed that over a third of patients treated with 45 Gy or 50.4 Gy four-field pelvic radiotherapy or pelvic intensity-modulated radiotherapy reported GI symptoms following radiation treatment (6). Consequently, abdominal radiotherapy for cancers of the hepatobiliary tract and pancreas are administered at sub-curative doses to avoid GI radiotoxicity. Recent clinical trials have shown that dose-escalated radiotherapy using highly precise 3D conformal radiation techniques, such as stereotactic body radiotherapy and intensity-modulated radiotherapy, can improve outcomes (7–9), but these techniques still cannot fully avoid the small intestines (10). Furthermore, these sophisticated techniques are not widely accessible, as they require specialized expertise that is limited to some academic centers. Thus, an alternative to reduce GI radiotoxicity in cancer patients is to use a radioprotector to prevent radiation-induced damage and/or to improve GI repair following radiotherapy (9).

There are currently no FDA-approved radioprotectors of the GI tract. The intestine has a physiological hypoxia gradient that arises due to its vascular anatomy, and the hypoxia-inducible factors (HIFs) regulate various genes required for intestinal barrier function (11). The HIFs are transcription factors which are hydroxylated by the EGLN family of prolyl hydroxylases in the presence of oxygen, iron, and 2-oxoglutarate, allowing the von Hippel-Lindau E3 ubiquitin ligase complex to bind and tag HIFs for proteasomal degradation (12–19). The stabilization of HIFs through hypoxia or EGLN inhibition allows them to regulate cell metabolism and survival (12), induce tissue remodeling (20), increase epithelial integrity (21), and promote stem cell survival (13). There are two main HIF isoforms: HIF1 and HIF2. Our group has previously shown that stabilization of HIF2, but not HIF1, significantly reduces GI radiotoxicity without sparing hypoxic pancreatic tumors (22, 23). However, the mechanisms by which HIF2 confers radioprotection to the small intestine remain unclear.

In the current study, we generated a 3D murine small intestinal organoid model system (24), transiently overexpressed a non-degradable *HIF2* allele (25), and performed whole transcriptomic analysis to gain insight in this regard. We found that HIF2 directly induces Wnt5a expression, a non-canonical Wnt family glycoprotein, in both murine and human cell lines, by activating its promoter. Like other Wnt family members, Wnt5a plays an important role in the in the embryonic development and subsequent homeostasis GI tract, and enhances regeneration following injury (26, 27). Here, we show that Wnt5a is necessary for small intestinal crypt regeneration following radiation and that addition of exogenous Wnt5a to duodenal 3D organoid cultures improves their cryptogenic capacity. Together, our data indicate that HIF2 radioprotects the small intestine, at least in part, by inducing Wnt5a expression.

MATERIALS AND METHODS

Cell Lines and Reagents

L-WRN cells were obtained from the ATCC (CRL-3276). HEK293-derived Adherent-293 (AD-293) cells were obtained from Stratagene (240085). CBRLuc-mCherry reporter murine duodenal organoids were a gift from Dr. Helen Piwnica-Worms (28). Murine duodenal organoids were cultured at 37°C in 5% CO_2 and 5% O_2, while all other cell lines were cultured at 37°C in standard 5% CO_2 incubators. All cell lines were authenticated by short tandem repeat profiling and were confirmed to be *Mycoplasma* free. Recombinant human/mouse Wnt5a was purchased from R&D Biosystems (645-WN-010-CF).

Mice

All experimental mouse work adhered to the standards articulated in the Animal Research: Reporting of *In Vivo* Experiments guidelines. Additionally, all mouse work was approved by the Institutional Animal Care and Use Committee of The University of Texas MD Anderson Cancer Center. Mice were maintained on a 12-hour light/dark cycle and were provided with sterilized water and standard rodent chow (Prolab Isopro RMH 3000 irradiated feed) *ad libitum*. C57BL/6 mice (RRID : IMSR_JAX:000664), *Wnt5a*$^{fl/fl}$ mice (RRID : IMSR_JAX:026626) (29), and *R26-LSL-hHIF2a*^{dPA} mice (RRID : IMSR_JAX:009674) (25) were obtained from Jackson Laboratories.

Generation of 3D Small Intestinal Organoids

L-WRN conditioned media was prepared as previously described (24, 28). Briefly, L-WRN cells were maintained in DMEM high glucose media (Sigma, D6429) supplemented with 10% (v/v) FBS (Sigma, F4135, 1% (v/v) Penicillin/Streptomycin (Sigma, P4333), 500 µg/ml Hygromycin B Gold (*In vivo*Gen, ant-hg-1), and 500 µg/ml G418 (Sigma, G8168). Once cells were confluent, the media was replaced with Advanced DMEM/F12 media (Gibco, 12634010) supplemented with 10% (v/v) FBS, 1% (v/v) Penicillin/Streptomycin, and 2 mM L-glutamine (Sigma, G7513). Conditioned media was collected for six days, centrifuged at 3,000 rpm for 5 minutes, vacuum filtered through a 20 µM PES membrane (Thermo Scientific, 567-0020), and stored at -80°C.

Duodenal crypts were isolated from C57BL/6 mice, *R26-LSL-hHIF2a*^{dPA} mice, and *Wnt5a*$^{fl/fl}$ mice, and 3D organoid cultures were established as previously described (24, 28). For all steps in this protocol, EDTA (Sigma-Aldrich, E7889) was added fresh to both PBS (Cytiva, SH30256.LS) and HBSS without calcium and magnesium (Gibco, 14025092) to a final concentration of 2 mM,

and kept on ice. Mice were humanely euthanized by CO_2 inhalation followed by cervical dislocation. The duodenum was measured 1 cm below the pylorus, and 4 cm were resected and flushed with PBS/EDTA, then incubated on fresh PBS/EDTA for 10 min on ice, and finally transferred to ice-cold HBSS/EDTA. Duodenal samples were then serially vortexed at 1,600 rpm at 4°C, in fresh HBSS each time, for 5 min, 3 min, and 8 min. Supernatants from the second and third vortexes were combined and passed through 70-μm strainers (Corning, 431751) to isolate crypts and remove any villi that might remain after the washes. Duodenal crypts were pelleted at 1,000 rpm at 4°C, then washed in Advanced DMEM/F12 supplemented with 10% (v/v) FBS, 1% (v/v) Penicillin/Streptomycin, and 2 mM L-glutamine, and re-centrifuged as before. The pelleted crypts were resuspended in 50% (v/v) Matrigel (Corning, 354234) diluted with the crypt washing media, and then were seeded as domes into 24-well plates (Corning, 3524). After Matrigel solidification at 37°C, the duodenal organoids were cultured in 50% (v/v) L-WRN conditioned media supplemented with 10 mM Y27632 (ROCK inhibitor; Sigma-Aldrich, Y0503) and 10 μM SB431542 (TGF-β RI Kinase Inhibitor VI; Sigma-Aldrich, 616461). The culture media was refreshed every other day and the organoids were passaged every third day.

Adenoviral Transduction

Ad-GFP (VVC-U of Iowa-4, Ad5CMVeGFP), Ad-Cre (VVC-U of Iowa-5, Ad5CMVCre), and Ad-Cre-GFP (VVC-U of Iowa-1174, Ad5CMVCre-eGFP) viral vectors were provided by the University of Iowa Viral Vector Core (http://www.medicine.uiowa.edu/vectorcore). Ad-human HIF1 and Ad-human HIF2 viral vectors were previously produced (30) using hHIF1 (Addgene #18955) and hHIF2 plasmids (Addgene #18956) that contain double proline-to-alanine substitutions which render them nondegradable by VHL (31). Duodenal organoids were transduced after at least three passages. First, organoids were harvested by incubation with Cell Recovery Solution (Corning, 354253) for 30 min on ice, then centrifuged at 1,000 rpm for 5 min at 4°C, and then washed with cold PBS. Organoids were then digested into single intestinal stem cells (ISCs) *via* mechanical digestion while incubating in TrypLE (Gibco, 12605010) supplemented with 10 μM Y27632 and 500 μM N-acetylcysteine (Sigma-Aldrich, A0737) for 5 min at 37°C. To neutralize TrypLE, cold Advanced DMEM/F12 media supplemented with 10% (v/v) FBS, 1% (v/v) Penicillin/Streptomycin, 2 mM L-glutamine, 10 μM Y27632, and 10 μM SB431542 was added and the ISC suspension was centrifuged at 1,500 rpm for 5 min at 4°C. Single ISCs were resuspended in Advanced DMEM/F12 supplemented as described above and passed through a 35-μM strainer (Corning, 352235). Single ISCs were stained with Trypan Blue (Bio-Rad, 1450021) and counted on a TC20 Automated Cell Counter (Bio-Rad). Duodenal ISCs were transduced with adenoviral particles at MOI rates of 50 particles per cell for 1.5 h at 37°C. Afterwards, transduced ISCs and leftover adenoviral particles were resuspended in 50% (v/v) Matrigel, seeded into 24-well plates, and cultured in 50% (v/v) L-WRN conditioned media supplemented with 10 μM Y27632, 10 μM SB431542, and 10 mM Nicotinamide (Sigma-Aldrich, N3376). RNA purification of duodenal organoids was done approximately 72 hours post-transduction.

Western Blotting

Duodenal organoids were released from Matrigel by incubation with Cell Recovery Solution for 30 min on ice, then centrifugation at 1,000 rpm for 5 min at 4°C, followed by washing with cold PBS. Organoids were then lysed in M-PER mammalian protein extraction reagent (Thermo Fisher Scientific, 78501) supplemented with protease inhibitor (Roche Life Science, 11836170001) and phosphatase inhibitor (Roche Life Science, 4906837001), and then denatured with 4x Laemmli sample buffer (Bio-Rad, 1610747). Equal cell protein lysate amounts were resolved on SDS-PAGE gel (Bio-Rad, 4568034) and transferred onto a nitrocellulose membrane (Bio-Rad, 1620215) using a Trans-Blot Turbo transfer system (Bio-Rad). After blocking with 5% (w/v) skim milk powder (Bio-Rad, 1706404XTU) in TBS-T for 1h at room temperature, the membrane was probed with primary antibodies diluted in Superblock T20 (ThermoFisher Scientific, 37536) at 4°C overnight. Anti-HIF2α rabbit (Novus Biologicals, NB100-122) was used at 1:500 and anti-β-actin rabbit (Cell Signaling Technology, 4970S) was used at 1:1,000. The membrane was then washed and incubated with HRP-conjugated secondary antibody for 1h. The membrane was developed with Clarity Western ECL Substrate kit (Bio-Rad, 1705061) and visualized using a ChemiDoc imaging system (Bio-Rad). Relative protein expression was quantified based on band intensity using ImageJ software (RRID : SCR_003070) and normalized to control group.

RNA Purification and Quantitative Real Time-PCR Analysis

Duodenal organoids were released from Matrigel as indicated above, then homogenized by vortexing and vigorously pipetting, and then RNA was purified using an RNeasy mini kit following the manufacturer's handbook (Qiagen, 74106). Reverse transcription was performed with a mix of random primers and oligos using an iScript cDNA Synthesis kit (Bio-Rad, 1708891). Next, qRT-PCR was performed using SYBR Green Master mix (Bio-Rad, 1725124) and the primer assays listed on **Supplementary Table 1**, on a CFX384 Real-time system (Bio-Rad). Relative gene expression and fold change was calculated using *Hprt* and *Tbp* as reference genes.

RNA Sequencing and Analysis

Duodenal organoids from C57BL/6 mice transduced with either Ad-GFP, Ad-hHIF1, or Ad-hHIF2 were harvested and RNA was purified using an RNeasy mini kit. RNA purity and concentration were measured using an Epoch Microplate Spectrophotometer with a Take3 Micro-Volume Plate, and Gen5 software (v2), all from BioTek Instruments, Inc. Library preparation and sequencing were performed in the Sequencing and Microarray Facility at MD Anderson Cancer Center. The raw sequencing data was downloaded from the core server and low-quality reads were removed and Q20 and GC contents were calculated. Transcript abundance was quantified using the RSEM software package (RRID : SCR_013027) (32). Differential

expression analysis was performed using EBSeq software package (RRID : SCR_003526) (33). **Supplementary Tables 2** and **3** show the output differential expression gene matrix for Ad-HIF2 and Ad-HIF1, respectively, compared to Ad-GFP.

WNT5A Promoter Analysis and Dual Luciferase Assays

The human WNT5a promoter from −2000 to +200 nucleotides from the +1 transcriptional start site (34) was synthesized directly into the KpnI- and XhoI-flanked region of the pUC57 vector (Genscript, SD1176). All mutant promoters were synthesized in a similar fashion. The specific sequences of the mutations can be found in **Supplementary Figure 2**. The KpnI- and XhoI-flanked fragments of each of the promoter constructs were excised and then ligated into the compatible BglII- and HindIII-flanked sites in the pGL4.10[*luc2*] vector (Promega, E6651). AD-293 cells were cultured in DMEM supplemented with 10% FBS and 2 mM L-Glutamine. Cells were transfected using Xfect Transfection Reagent (TakaraBio, 631318) using the manufacturer's standard protocol. For instance, a 96-well opaque plate was seeded with 9.5 x 10^3 cells/well and transfected with 0.08 μg of hHIF1 plasmid, hHIF2 plasmid, or control GFP plasmid (Addgene #26822), 0.09 μg of *WNT5A*-luciferase construct, and 9 ng of *Renilla* luciferase, along with Xfect polymer. The transfected cells were incubated for 48 h in Opti-MEM media (Gibco, 31985070). Dual luciferase assays were performed using the Dual-Glo® Reagent (Promega, E2940) kit according to manufacturer's instructions. The luminescence data was measured on a Cytation 3 luminometer (Biotek Instruments, Inc.). Luciferase signal was normalized to Renilla signal, and then *WNT5A* promotor transactivation was calculated as a fold change over control GFP plasmid transfection.

Spheroid Formation Assays

Spheroid Formation Assays were performed as previously described (28), using a murine duodenal Click Beetle Red Luciferase-mCherry (CBRLuc-mCherry) reporter organoid line and *Wnt5a*$^{fl/fl}$ duodenal organoids. Briefly, duodenal organoid cultures were exposed to the indicated pre-radiation treatments and then irradiated using an X-Rad 320 cell irradiator (Precision X-Ray). Immediately after irradiation, the duodenal organoids were harvested using Cell Recovery Solution and then digested into single ISCs using TrypLE supplemented with Y27632 and N-Acetylcysteine, followed by filtering through a cell strainer as detailed above for Adenoviral Transduction. Live cells were quantified using ViaStain™ AO/PI Staining Solution (Nexcelom, CS2-0106) in a Cellometer® Vision CBA Image Cytometer (Nexcelom). Live duodenal ISCs were seeded in Matrigel in 24-well culture plates at a density of 5,000 cells/well. Organoids were maintained in 50% L-WRN conditioned media supplemented with 10 μM Y27632 and 10 μM SB431542 for six days, then surviving cells were assessed *via* bioluminescence or z-stack imaging. For quantification of bioluminescence, organoids were incubated with 300 μg/ml of D-Luciferin Firefly (Gold Biotechnology, L-123) in the media for 20 min at 37°C, and measurements were taken using a CLARIOstar plate reader (BMG Labtech). Sample wells were first normalized to blank Matrigel wells, and then to unirradiated controls. Z-stack images covering the entire Matrigel dome area were taken using a Cytation 3 Cell Imaging Multi-Mode Reader (Biotek Instruments, Inc.). Z-stack images were stitched using Photoshop version 19.1.7 (RRID : SCR_014199) and viable organoids measuring at least 150 μm were manually quantified using ImageJ version 1.52q (RRID : SCR_003070). For organoids analyzed *via* z-stack imaging, the surviving fraction was calculated as described previously (35).

Statistical Methods

All statistical analyses were performed using GraphPad Prism® V.8 (San Diego, CA; RRID : SCR_002798), with a significance level of $\alpha = 0.05$. Dunnett's multiple comparisons test was used to analyze Dual Luciferase Assays.

RESULTS

Transcriptomic Analysis of HIF2 Overexpression in Small Intestinal Organoids by RNA Sequencing

To gain insight into how the HIFs regulate GI biology and to understand the mechanisms by which HIF2 confers radioprotection to the small intestine, we generated a 3D murine small intestinal organoid model system. We harvested duodenum crypts of wild-type C57BL/6 mice, seeded them in basement membrane matrix (Matrigel), and cultured them in conditioned media containing Wnt3a, R-spondin 3, and noggin (**Figure 1A**) (24). These conditions enrich for intestinal stem cells (ISCs), which self-assemble into crypt-like 3D structures that are able to recapitulate the small intestinal crypt *ex vivo* (36). We then transiently overexpressed a non-degradable *HIF1* or *HIF2* allele (25), which contain mutations in the two key prolyl residues that are hydroxylated by the EGLN proteins, rendering them stable even under normoxic conditions, using adenoviral particles (**Figure 1A**). We confirmed adenoviral-mediated HIF overexpression by both western blot and qRT-PCR, and then performed RNA sequencing (**Figures 1A–C**).

Among thousands of coding transcripts assessed, 1,113 genes exhibited significant differential expression between control GFP- and HIF2-overexpressing duodenal organoids (**Figure 2A** and **Supplementary Table 2**). All the differentially expressed genes with statistical significance were selected with $p < 0.05$, False Discovery Rate (FDR) < 0.05, and at least 2-fold change. Hierarchical clustering analysis revealed a total of 461 upregulated genes and 652 downregulated genes (**Supplementary Table 2**). The entire set of differentially expressed genes can be visualized in a volcano plot in **Figure 2B**. To validate our RNA sequencing results, we independently assessed the expression of 5 genes by qRT-PCR. Our results confirmed that *Stat6*, *Aqp8*, and *Nos2* were upregulated and that *Wnt4* and *Egr1* were downregulated in HIF2-overexpressing duodenal organoids compared to wild-type

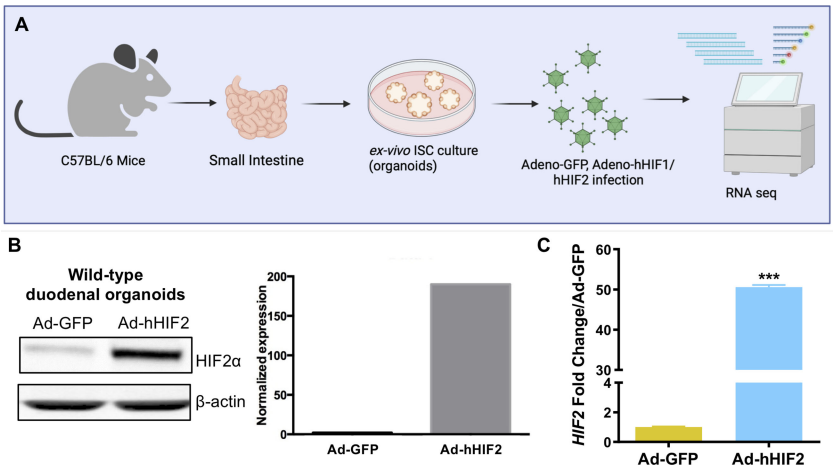

FIGURE 1 | HIF2 overexpression in ISC-enriched duodenal organoid cultures. **(A)** Experimental design to generate 3D murine small intestinal organoid model system. Duodenal organoids were transduced with Adenovirus-human HIF1 (Ad-hHIF1), Ad-hHIF2, or Ad-GFP as control, and then RNA sequencing was performed. **(B)** Validation of adenovirus-mediated gene transfer by Western blot (*left*) and its quantification (*right*). **(C)** Validation of adenovirus-mediated gene transfer by qRT-PCR. All error bars represent mean ± SEM. ***$P < 0.001$, by Student's *t* test.

duodenal organoids, indicating that the RNA sequencing dataset is reliable (**Figure 2C**).

We also examined the transcriptome of HIF1-overexpressing organoids to gain more insight into how the HIFs regulate overall ISC biology. Among the thousands of coding transcripts assessed, only 55 genes exhibited significant differential expression between control GFP- and HIF1-overexpressing duodenal organoids, in which 25 genes were upregulated and 30 genes were downregulated (**Supplementary Figure 1** and **Supplementary Table 3**). Interestingly, the only genes commonly upregulated by HIF1 and HIF2 in our dataset were *Nanp*, *Ppp1r3c*, *Rasgrf1*, *Klhl3*, *Mical2*, and *Nos2*, and the only

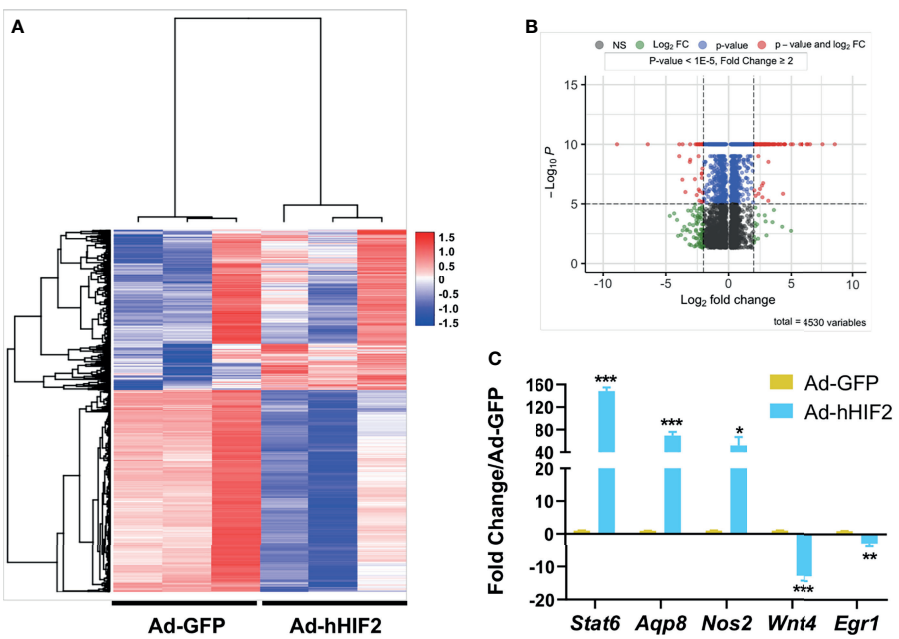

FIGURE 2 | Differentially expressed gene profile in HIF2-overexpressing duodenal organoids. **(A)** Heatmap shows all the differentially expressed genes in duodenal organoids infected with Ad-hHIF2 or control Ad-GFP evaluated *via* RNA sequencing (n = 3 biological replicates/group). **(B)** Volcano plot of the differentially expressed genes. **(C)** qRT-PCR validation of the sequencing data in **(A)**. All error bars represent mean ± SEM. *$P < 0.05$, **$P < 0.01$, ***$P < 0.001$, by Student's *t* test.

transcripts commonly downregulated by both HIFs were *Slc18a1*, *Gm37069*, *Hr*, *Gm12480*, *Gm13151*, *Gm21981*, *Klhl30*, *Vcp-rs*, *Gm4204*, *AY512931*, and *Gm28037* (**Supplementary Tables 2** and **3**). We then focused our attention on the HIF2 dataset, as HIF2 and not HIF1, has been shown to be the main HIF isoform driving GI radioprotection (22).

HIF2 Induces Intestinal Non-Canonical *Wnt5a* Expression

Interestingly, the HIF2-induced transcriptome included known radiation modulators as well as genes involved in GI healing and homeostasis, as highlighted in **Figure 3A** in blue and red, respectively. We identified *Wnt5a* as a transcriptional target of HIF2, but not HIF1 (**Figure 3A** and **Supplementary Tables 2** and **3**), and interestingly, Wnt5a has a known connection to non-canonical intestinal crypt regeneration (26). Thus, we took a candidate approach to further investigate its transcriptional regulation by HIF2. We verified that *Wnt5a* was upregulated by HIF2 using two approaches. First, we performed qRT-PCR to independently evaluate duodenal organoids that transiently overexpressed non-degradable *HIF2 via* Adeno-hHIF2 transduction (25), and found significantly increased *Wnt5a* expression by almost 50-fold compared to organoids transduced with Adeno-GFP (**Figure 3B**). Second, we generated duodenal organoids from mice that conditionally overexpressed non-degradable human *HIF2* by knock-in into the *Rosa* 26 *locus* (R26-LSL-hHIF2) (25), transduced them with either Adeno-Cre or control Adeno-GFP vectors, and assessed *Wnt5a* expression using qRT-PCR. Stable *HIF2* overexpression also resulted in significant upregulation of *Wnt5a* by 6-fold (**Figure 3C**). Together, these results suggest that HIF2 induces intestinal *Wnt5a* expression.

HIF2 Directly Activates the WNT5A Promoter

The HIFs are transcription factors that recognize and bind hypoxia response elements (HREs) in promoter or enhancer regions to induce gene transcription (13). Thus, we analyzed the *WNT5A* promoter sequence to determine whether it contained putative HRE motifs and identified multiple low- and high-stringency HRE consensus sequences (**Figure 4A** and **Supplemental Figure 2**). To determine whether induction by HIF2 occurs directly or indirectly, we designed luciferase reporter constructs of the human *WNT5A* promoter spanning from 2,000 nucleotides upstream of the transcriptional start site (34) to 200 nucleotides downstream, containing five HRE consensus sequences that are closely associated with HIF ancillary sequences (HAS) and E-box motifs (**Figure 4A** and **Supplemental Figure 2**). HAS and E-box motifs are cis-element that are required for an HRE to be functionally active. Both motifs play a role in the recruitment of transcriptional machinery that together with HIF2 induce promoter activation (37–39).We transfected this construct into human embryonic kidney-derived Adherent 293 (AD-293) cells along with an expression vector

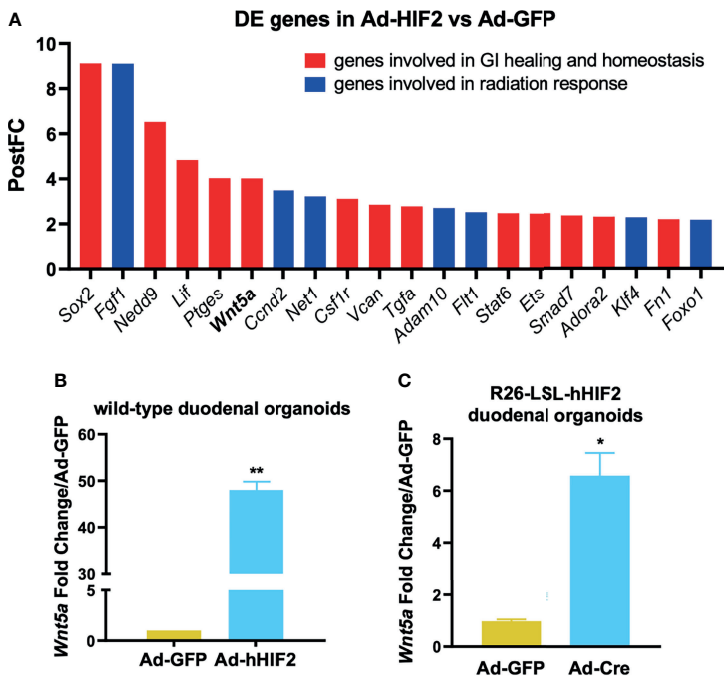

FIGURE 3 | Candidate approach identifies Wnt5a as direct HIF2 target. **(A)** Post-Fold Change (PostFC) of 20 differentially expressed (DE) genes identified from the RNA sequencing analysis. **(B)** qRT-PCR validation of HIF2-induced *Wnt5a* upregulation in wild-type duodenal organoids infected with Ad-GFP or Ad-hHIF2. Data represents 3 biological replicates (3 technical replicates/mouse). **(C)** qRT-PCR showing HIF2-induced upregulation of *Wnt5a* in *LSL-hHIF2* duodenal organoids infected with Ad-GFP or Ad-Cre. Data represents 3 biological replicates (3 technical replicates/mouse). All error bars represent mean ± SEM. *$P < 0.05$, **$P < 0.01$, by Student's *t* test.

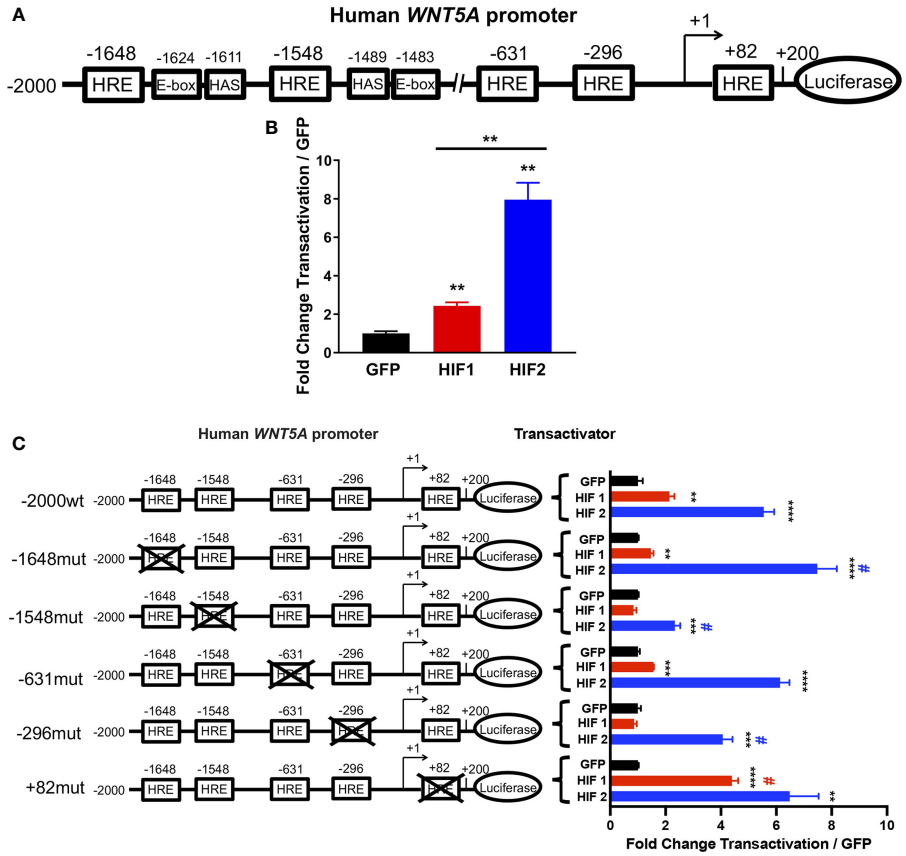

FIGURE 4 | HIF2 directly activates the *WNT5A* promoter *via* HREs. **(A)** Human *WNT5A* promoter scheme showing distal (-1648, -1548, and -631) and proximal (-296 and +82) HREs identified by sequence analysis. **(B)** Dual luciferase reporter assay in AD-293 cells with wild-type human *WNT5A* promoter-luciferase construct and transactivation by HIF1, HIF2, or GFP control plasmids (n = 4 transfections/group). **(C)** Dual luciferase reporter assay in AD-293 cells with human *WNT5A* promoter-luciferase construct containing wild-type sequence (-2000wt) or mutations of distal (-1648mut, -1548mut, -631mut) and proximal (-296mut and +82mut) HREs with transactivation by HIF1, HIF2, or GFP control plasmids (n = 4 transfections/group). All error bars represent mean ± SEM. Asterisks indicate comparison of HIF1 or HIF2 to their respective GFP controls. **P < 0.01, ***P < 0.001, ****P < 0.0001, by Student's t test with False Discovery Rate two-stage step-up approach. # indicates comparison of construct transactivation in wild-type sequence to mutated sequences by HIF1 (red #) or by HIF2 (blue #); P < 0.05, by two-way ANOVA.

encoding GFP or constitutively active human HIF1 or HIF2 (11) and performed dual luciferase reporter assays (25). We found that HIF2 significantly increased *WNT5A* promoter transactivation by eight-fold over GFP controls (**Figure 4B**). HIF1 only modestly affected promoter activity (**Figure 4B**).

To understand if any specific HRE motif of the *WNT5A* promoter is required for its activation by HIF2, we performed mutational analyses. We engineered transversion point mutations on the guanine and cytosine nucleotides of three distal and two proximal putative HRE sites within the promoter, and transfected AD-293 cells with these constructs to perform promoter activation studies (**Figure 4C** and **Supplementary Figure 2**). We found that independently mutating the two most distal HREs in the *WNT5A* promoter had the most impact on HIF2-induced transactivation, and that these two HREs are differentially regulated by HIF2. The point mutation at the HRE in position -1548 significantly diminished the previously observed HIF2-induced promoter activation, suggesting that the -1548HRE is necessary for HIF2's ability to bind and positively regulate the *WNT5A* promoter (**Figure 4C**). Importantly, this -1548HRE resides upstream of a HAS, which is also in close proximity to an E-box (**Figure 4A** and **Supplementary Figure 2**). Conversely, mutating the -1648HRE resulted in an increased ability of HIF2 to transactivate the *WNT5A* promoter, suggesting that it might be a repressive HRE. Although the HRE at -1648 resides nearby E-box and HAS motifs, HRE sites that are preceded by cytosine nucleotides on 5' form E-box binding sites of other basic helix-loop-helix transcription factor families, and HIFs rarely recognize these (38). Moreover, while HIF2-induced gene upregulation is largely mediated by direct HIF2 binding to DNA motifs, HIF2-induced gene repression tends to occur indirectly through transcriptional co-repressors (37). Thus, we posit that direct binding of HIF2 to the -1548HRE promotes *WNT5A* transcription, whereas HIF2 interaction with the -1648HRE promotes the recruitment of repressive transcriptional machinery. The point mutations of the HREs at positions -631, -296, and +82 did not alter the activation of the WNT5A promoter by HIF2 (**Figure 4C**).

Takenall together, our results indicate that HIF2 directly activates the *WNT5A* promoter, possibly by binding the -1548HRE.

Wnt5a Increases ISC Survival and Cryptogenic Potential Following Radiation

Wnt5a is a non-canonical Wnt ligand that has been shown to promote the formation of new intestinal crypts in order to re-establish homeostasis after intestinal mucosal injury (26). To evaluate whether Wnt5a mediates HIF2-afforded GI radioprotection, we performed a spheroid formation assay, which is an *ex vivo* microcolony assay that allows us to evaluate potential radiation modulators in small intestinal organoid cultures (28). We treated CBRLuc-mCherry, a murine duodenal mCherry reporter organoid line (28), with recombinant Wnt5a (rWnt5a) 10 hours prior to irradiation, then exposed them to 0-8Gy of Xrays, and re-seeded single cells in Matrigel (**Figures 5A, B**). CBRLuc-mCherry organoids that were pre-treated with rWnt5a produced significantly higher relative bioluminescence levels six days after irradiation, compared to vehicle-treated organoids, indicating that rWnt5a increased the number of regenerating crypts (**Figure 5B**). Pre-treatment with rWnt5a significantly increased the cryptogenic capacity of CBRLuc-mCherry organoids exposed to 2 Gy and 4 Gy by 2-fold and 6-fold, respectively, and also increased the cryptogenic capacity of organoids exposed to 6 Gy by 2.8-fold, but this was not statistically significant (**Figure 5B**). Interestingly, CBRLuc-mCherry organoids that continued receiving rWnt5a treatment after irradiation did not display improved cryptogenic capacity (**Supplementary Figure 3A**). Moreover, initiating rWnt5a treatments only after irradiation also did not improve the cryptogenic capacity of CBRLuc-mCherry organoids (**Supplementary Figure 3B**). These results suggest that Wnt5a could be radioprotective to small intestinal crypts but does not mitigate radiation damage after it has occurred. A possible explanation for these results is that Wnt5a suppresses intestinal organoid proliferation by inducing TGF-β signaling (26), which would protect cycling ISCs from radiation, but would dampen their capacity to regenerate crypts if Wnt5a treatment was continued after the radiation injury was incited.

To understand whether Wnt5a is necessary for intestinal crypt regeneration following radiation injury, we generated conditional *Wnt5a* knockout ($Wnt5a^{CKO}$) duodenal organoids from $Wnt5a^{fl/fl}$ mice and transduced them with Adeno-Cre-GFP or control Adeno-GFP vectors. In agreeance with published work demonstrating that Wnt5a is dispensable for homeostasis in the gut postnatally (40), deletion of Wnt5a did not affect organoid growth or morphology (**Figure 5C**). We then performed a modified spheroid formation assay using the $Wnt5a^{CKO}$ duodenal organoids and z-stack imaging, rather than bioluminescence, to quantify regenerating organoids (**Figure 5D**). Loss of Wnt5a did not affect the cryptogenic capacity of unirradiated duodenal organoids (**Figure 5E** and **Supplementary Figure 4**), again confirming that *Wnt5a* is dispensable for crypt homeostasis (**Figure 5C**) (40). On the other hand, deletion of *Wnt5a* significantly reduced the fraction of surviving duodenal organoids after 6 Gy of radiation (**Figure 5E** and **Supplementary Figure 4**), indicating that Wnt5a is necessary for crypt regeneration following radiation. Furthermore, treatment with recombinant Wnt5a (rWnt5a) rescued Wnt5a-depleted duodenal organoids from radiation-induced ISC death (**Figure 6**). Taken together, these results suggest that Wnt5a increases ISC survival and is both necessary and sufficient for ISC radioprotection.

DISCUSSION

Radiation therapy for abdominal and pelvic tumors is challenging because the small intestine is exquisitely

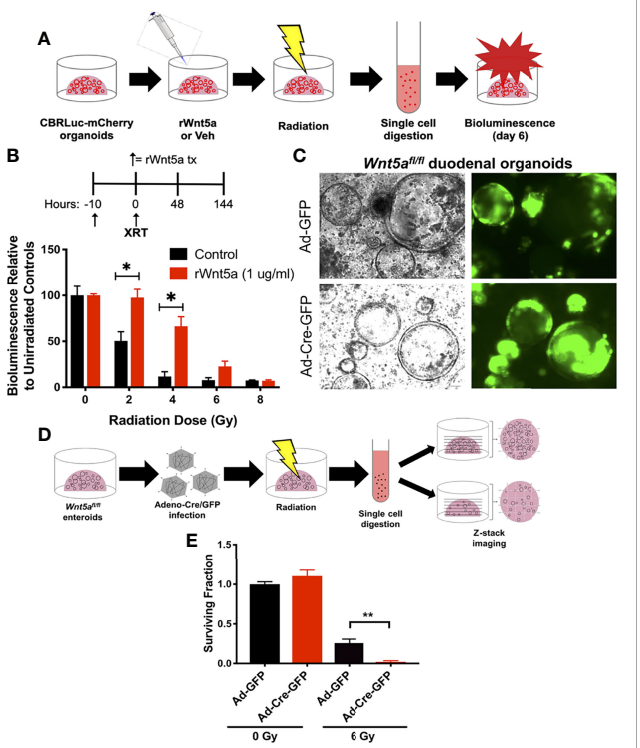

FIGURE 5 | Wnt5a mediates HIF2-associated radioprotection of the small intestine. **(A)** Schematic representation illustrating how spheroid formation assays were performed using murine duodenal CBRLuc-mCherry reporter organoids to test whether rWnt5a radioprotects. **(B)** CBRLuc-mCherry organoids treated with vehicle (PBS) or 1 μg/ml rWnt5a for 10h were exposed to the indicated doses of ionizing radiation. Bioluminescence was measured 6 days post-radiation (n = 3 per group). **(C)** $Wnt5a^{fl/fl}$ duodenal organoids were transduced with Adeno-Cre-GFP or control Adeno-GFP to generate Wnt5a knockouts. Representative bright field and GFP images are shown. **(D)** Schematic representation illustrating how spheroid formation assays were performed using $Wnt5a^{fl/fl}$ duodenal organoids to test whether Wnt5a is necessary for crypt regeneration following radiation. **(E)** $Wnt5a^{fl/fl}$ duodenal organoids infected with Adeno-Cre-GFP or Adeno-GFP were exposed to the indicated doses of ionizing radiation. Z-stack images were stitched and organoids larger than 150 μm in diameter were quantified 6 days post-radiation and mean surviving fraction is plotted (n = 3 per group). All error bars represent mean ± SEM. *$P < 0.05$, **$P < 0.01$, by Student's t test.

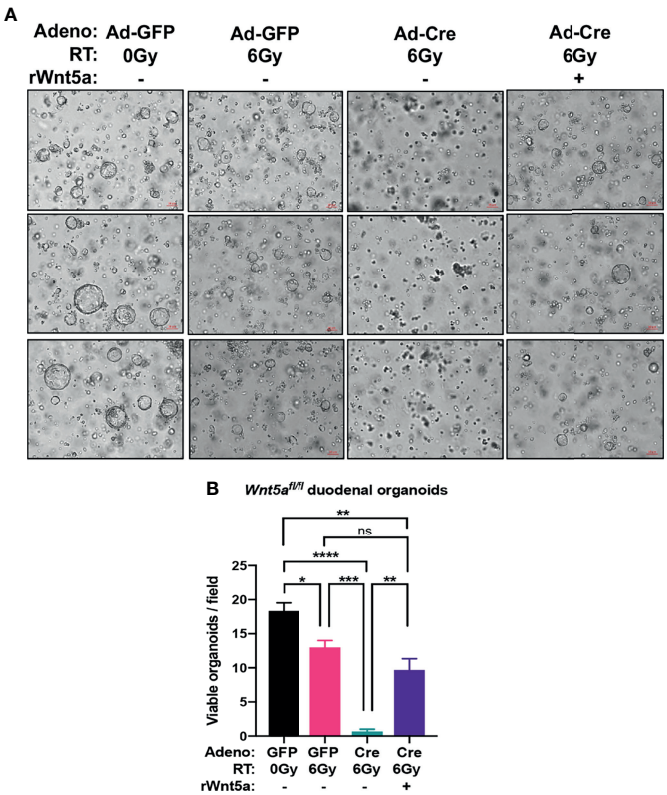

FIGURE 6 | rWnt5a treatment rescues crypt regeneration in irradiated *Wnt5a*^{CKO} duodenal organoids. *Wnt5a*$^{fl/fl}$ organoids were infected with Adeno-Cre-GFP or control Adeno-GFP, treated with vehicle or rWnt5a (600 ng/ml), and then treated with the indicated doses of ionizing radiation. **(A)** Representative bright field images with **(B)** quantification of viable organoids are shown 6 days after irradiation (n = 3 per group). All error bars represent mean ± SEM. *P < 0.05, **P < 0.01, ***P < 0.001, ****P < 0.0001, and ns = not significant, by Tukey's multiple comparisons test" instead of "*P < 0.05, **P < 0.01, ***P < 0.001, ****P < 0.0001, and ns, not significant, by Tukey's multiple comparisons test.

radiosensitive, which limits the dose that can be delivered to tumors without major GI toxicity (2–6). Unfortunately, there are no FDA-approved therapies to prevent GI radiotoxicities. Multiple groups, including our own, have shown that HIF2 stabilization by pharmacological EGLN inhibition protects the small intestine against radiation (22, 23, 41, 42). However, the mechanism by which HIF2 radioprotects ISC and prevents GI radiotoxicity remains unclear. The current study provides mechanistic insight into how HIF2 reduces the radiosensitivity of the intestinal crypt. Moreover, to the best of our knowledge, this is the first study that evidences a convergence between non-canonical Wnt signaling and hypoxia signaling.

Here we used ISC-enriched 3D duodenal organoid cultures to mimic the small intestinal crypt and studied the mechanism of HIF2 radioprotecion by both transient and stable HIF2 overexpression. Unsurprisingly, the HIF2-induced intestinal transcriptome included many genes that are essential for normal GI homeostasis and barrier function, and interestingly, some of these genes have been implicated in cellular response to radiation. We took a candidate approach and focused our attention on Wnt5a, which has been shown to play roles in the development of the intestinal tract, the proliferation of ISCs, and their capacity to regenerate upon GI injury (26, 40, 43). In zebrafish embryos, Wnt5a has also been shown to regulate gastrulation and to ameliorate radiation-induced toxicity (43). Here we provide evidence that Wnt5a is a direct HIF2 target. We identified five major HRE sites within the human *WNT5A* promoter and our experiments in human cells confirmed that HIF2 directly activates the *WNT5A* promoter through a functional HRE motif located 1548 nucleotides upstream of the transcriptional start site. This -1548HRE site resides near HAS and E-box sequences, which help recruit transcriptional co-activators (38). Nevertheless, our promoter studies were focused on 2,2000 nucleotides surrounding the *WNT5A* transcriptional start site, thus, there could be additional distal HRE sites that are regulated by HIF2.

Our study is the first to show that Wnt5a could be a potential target to prevent GI radiotoxicity. We showed that Wnt5a is both necessary and sufficient for ISC survival and crypt regeneration after exposure to radiation. Deletion of *Wnt5a* completely impaired the ability of ISCs to form crypt spheres after being irradiated, and addition of rWnt5a rescued ISCs from radiation-induced cell death. Importantly, our phenotype was only reproducible when rWnt5a was administered before radiation

treatments. Wnt5a signaling has been shown to inhibit both intestinal and hematopoietic stem cell proliferation (26, 44). Because radiation is more toxic to rapidly proliferating cells, suppression of cell proliferation prior to radiation would allow ISCs to sustain the effects of radiation. Wnt5a binds to the Frizzled (Fzd) family of cell surface receptors, including Fzd-1/2/4/5/7/8 (45), and its canonical co-receptors Lrp5/6 or its non-canonical co-receptors Ror1/2 and Ryk, and activates either the canonical Wnt/Beta-catenin pathway, the non-canonical planar cell polarity pathway, or the non-canonical Wnt/Ca^{2+} pathways (34). In intestinal organoids, non-canonical Wnt5a signaling through Ror2 induces TGF-β signaling and Smad3 phosphorylation with subsequent nuclear translocation, leading to increased expression of multiple cyclin-dependent kinase inhibitors, and ultimately arrest of cell proliferation (26). Thus, activation of these downstream signaling pathways could be a possible explanation for the relative success of Wnt5a as a radioprotector while failing to mitigate radiation injury post-exposure. It is important to note that our studies were limited to *ex vivo* duodenal organoid models and that our observations should be validated using *in vivo* GI radiation models.

Wnt5a has been implicated in tumor progression, raising concerns about its potential use as a GI radioprotective agent in cancer patients (46, 47). While this concern is warranted, HIF2 would only be activated for a short period only during radiation to reduce normal tissue toxicity, which may reduce the potential oncogenic effects of this molecule. Additional pre-clinical studies using cancer models to assess this relative risk are warranted before Wnt5a can be considered for clinical translation. Furthermore, we note that our radiation model employs conventional single fractions, whereas many GI radiation oncology regimens employ fractionated radiation. Accordingly, the extent of Wnt5a-afforded ISC radioprotection would need to be evaluated in the setting of fractionated regimens.

We note that HIF2 may have additional molecular mechanisms by which it promotes ISC survival and intestinal radioprotection. Prior studies have shown that HIF2 both protects and mitigates GI radiation injury (22), yet our results here suggest that Wnt5a does not mitigate intestinal crypt radiation injury. Thus, future studies should assess which HIF2 targets are potential GI radiation mitigators. For example, the *Neuroepithelial cell transforming 1* (*Net1*) gene, which was significantly upregulated in our HIF2 dataset, has been shown to play a role in DNA damage repair after ionizing radiation (48, 49). Similarly, *Ets1* and *Klf4* are transcription factors that are essential for stem cell self-renewal and can regulate DNA damage repair (50, 51), and both were significantly upregulated by HIF2.

Moreover, our study was limited to the ISC compartment of the small intestine. However, other cellular compartments, such as the intestinal stromal niche, gut macrophages and the endothelial compartment have established roles in the intestinal response to injury (52, 53). Further investigation into these cellular compartments is required to fully dissect the role of HIF2 in the radiation responses of the intestinal tract.

DATA AVAILABILITY STATEMENT

The data presented in this study are deposited in the GEO repository, accession number GSE186927.

ETHICS STATEMENT

The animal study was reviewed and approved by the Institutional Animal Care and Use Committee of The University of Texas MD Anderson Cancer Center.

AUTHOR CONTRIBUTIONS

Conceptualization, CG and CT. Data Curation, CG and SG. Formal Analysis, CG, AA, NK, SG, MD, and FL. Funding Acquisition, CG and CT. Investigation, CG, AA, and SG. Methodology, CG, SG, MD, HP-W, and CT. Project Administration, CG, SG, and CT. Resources, HP-W, AM, and CT. Software, FL and NN. Supervision, CT. Validation, CG, AA, NK, NN, and CT. Visualization, CG, AA, SG, NK, MD, and FL. Writing – Original Draft, CG, AA, NK, IJ, and CT. Writing – Review and Editing, CG, IJ, and CT. All authors contributed to the article and approved the submitted version.

FUNDING

CT was supported by funding from the National Institutes of Health (NIH) under award number R01CA227517-01A1 and GI SPORE grant (P50CA221707), by the Cancer Prevention & Research Institute of Texas (CPRIT) under grant RR140012, by the V Foundation (V2015-22), by the Sidney Kimmel Foundation, by a Sabin Family Foundation Fellowship, by the Reaumond Family Foundation, by the Mark Foundation, by the Childress Family Foundation, by the McNair Family Foundation, and by generous philanthropic contributions to The University of Texas MD Anderson Moon Shots Program. CG was supported by the National Institute of Diabetes, Digestive and Kidney Diseases (NIDDK) of the NIH under award number F31DK121384. MD was supported by the National Cancer Institute (NCI) of the NIH under award number F31CA210631. CG, MD, AA, and IS were also supported by the NIH/NCI under award number U54CA096300/297. This work was also supported in part by NIH/NIDDK grant DK056338, which supports the Texas Medical Center Digestive Diseases Center, and by NIH/NCI Cancer Center Support Grants (CCSG) P30CA016672, which supports MDACC's Sequencing and Microarray Facility.

ACKNOWLEDGMENTS

We thank all the members and alumni of the Taniguchi Lab for input throughout the course of this study. Experimental design figures were made using BioRender.com.

SUPPLEMENTARY MATERIAL

The Supplementary Material for this article can be found online at: https://www.frontiersin.org/articles/10.3389/fonc.2021.769385/full#supplementary-material

Supplementary Table 1 | Primer Assays used for qRT-PCR.

Supplementary Table 2 | Differentially Expressed Genes in HIF2-overexpessing duodenal organoids versus wild-type duodenal organoids.

Supplementary Table 3 | Differentially Expressed Genes in HIF1-overexpessing duodenal organoids versus wild-type duodenal organoids.

Supplemental Figure 1 | Differentially expressed gene profile in HIF1-overexpressing duodenal organoids. **(A)** Heatmap shows all the differentially expressed genes in duodenal organoids infected with Adeno-hHIF1 or control Adeno-GFP evaluated via RNA sequencing (n = 3 biological replicates/group). **(B)** Volcano plot of the differentially expressed genes.

Supplementary Figure 2 | Sequences of the Human WNT5A promoter WT and HRE mutant constructs used for this study.

Supplementary Figure 3 | Wnt5a does not a mitigate radiation-induced intestinal crypt cell death. **(A)** (CBRLuc-mCherry duodenal reporter organoids treated with vehicle (PBS) or 1 μg/ml rWnt5a for 10h were exposed to the indicated doses of ionizing radiation, and then were treated with rWnt5a again immediately after the spheroid formation assay was seeded, and 48h later. Bioluminescence was measured 6 days post-radiation (n = 3 per group). Continuous rWnt5a treatment does not improve clonogenic capacity of CBRLuc-mCherry organoids exposed to radiation. **(B)** CBRLuc-mCherry duodenal reporter organoids were exposed to the indicated doses of ionizing radiation, and then were treated with vehicle (PBS) or 1 μg/ml rWnt5a for 5h and 48h after irradiation. Bioluminescence was measured 6 days post-radiation (n = 3 per group). Post-radiation rWnt5a treatment does not improve clonogenic capacity of CBRLuc-mCherry organoids. All error bars represent mean ± SEM. *P < 0.05, by Student's t test.

Supplementary Figure 4 | Wnt5a is necessary for crypt regeneration in response to radiation. Wnt5afl/fl duodenal organoids infected with Adeno-Cre-GFP or Adeno-GFP and were then exposed to the indicated doses of ionizing radiation. Z-stack images were stitched and organoids larger than 150 μm in diameter were quantified 6 days post-radiation (see Figure 5E for mean surviving fraction values; n = 3 per group). Representative bright field Z-stack images are shown.

REFERENCES

1. Begg AC, Stewart FA, Vens C. Strategies to Improve Radiotherapy With Targeted Drugs. *Nat Rev Cancer* (2011) 11(4):239–53. doi: 10.1038/nrc3007
2. Kelly P, Das P, Pinnix CC, Beddar S, Briere T, Pham M, et al. Duodenal Toxicity After Fractionated Chemoradiation for Unresectable Pancreatic Cancer. *Int J Radiat Oncol Biol Physics* (2013) 85(3):e143–e9. doi: 10.1016/j.ijrobp.2012.09.035
3. Elhammali A, Patel M, Weinberg B, Verma V, Liu J, Olsen JR, et al. Late Gastrointestinal Tissue Effects After Hypofractionated Radiation Therapy of the Pancreas. *Radiat Oncol* (2015) 10(1):186. doi: 10.1186/s13014-015-0489-2
4. Lee KJ, Yoon HI, Chung MJ, Park JY, Bang S, Park S, et al. A Comparison of Gastrointestinal Toxicities Between Intensity-Modulated Radiotherapy and Three-Dimensional Conformal Radiotherapy for Pancreatic Cancer. *J Chest Surg* (2016) 10(2):303–9. doi: 10.5009/gnl15186
5. Raturi VP, Tochinai T, Hojo H, Rachi T, Hotta K, Nakamura N, et al. Dose-Volume and Radiobiological Model-Based Comparative Evaluation of the Gastrointestinal Toxicity Risk of Photon and Proton Irradiation Plans in Localized Pancreatic Cancer Without Distant Metastasis. *Front Oncol* (2020) 10:517061. doi: 10.3389/fonc.2020.517061
6. Klopp AH, Yeung AR, Deshmukh S, Gil KM, Wenzel L, Westin SN, et al. Patient-Reported Toxicity During Pelvic Intensity-Modulated Radiation Therapy: NRG Oncology–RTOG 1203. *J Clin Oncol* (2018) 36(24):2538–44. doi: 10.1200/JCO.2017.77.4273
7. Krishnan S, Chadha AS, Suh Y, Chen H-C, Rao A, Das P, et al. Focal Radiation Therapy Dose Escalation Improves Overall Survival in Locally Advanced Pancreatic Cancer Patients Receiving Induction Chemotherapy and Consolidative Chemoradiation. *Int J Radiat Oncol Biol Physics* (2016) 94(4):755–65. doi: 10.1016/j.ijrobp.2015.12.003
8. Kim SK, Wu C-C, Horowitz DP. Stereotactic Body Radiotherapy for the Pancreas: A Critical Review for the Medical Oncologist. *J Gastrointest Oncol* (2016) 7(3):479–86. doi: 10.21037/jgo.2015.10.01
9. Hoffe S, Frakes JM, Aguilera TA, Czito B, Palta M, Brookes M, et al. Randomized, Double-Blinded, Placebo-Controlled Multicenter Adaptive Phase 1-2 Trial of GC 4419, a Dismutase Mimetic, in Combination With High Dose Stereotactic Body Radiation Therapy (SBRT) in Locally Advanced Pancreatic Cancer (Pc). *Int J Radiat Oncol Biol Phys* (2020) 108(5):1399–400. doi: 10.1016/j.ijrobp.2020.09.022
10. Yan KS, Chia LA, Li X, Ootani A, Su J, Lee JY, et al. The Intestinal Stem Cell Markers Bmi1 and Lgr5 Identify Two Functionally Distinct Populations. *Proc Natl Acad Sci* (2012) 109(2):466. doi: 10.1073/pnas.1118857109
11. Taylor CT, Colgan SP. Hypoxia and Gastrointestinal Disease. *J Mol Med* (2007) 85(12):1295–300. doi: 10.1007/s00109-007-0277-z
12. Kaelin WG, Ratcliffe PJ. Oxygen Sensing by Metazoans: The Central Role of the HIF Hydroxylase Pathway. *Mol Cell* (2008) 30(4):393–402. doi: 10.1016/j.molcel.2008.04.009
13. Keith B, Simon MC. Hypoxia-Inducible Factors, Stem Cells, and Cancer. *Cell* (2007) 129(3):465–72. doi: 10.1016/j.cell.2007.04.019
14. Ivan M, Kondo K, Yang H, Kim W, Valiando J, Ohh M, et al. Hifα Targeted for VHL-Mediated Destruction by Proline Hydroxylation: Implications for O2 Sensing. *Science* (2001) 292(5516):464. doi: 10.1126/science.1059817
15. Jaakkola P, Mole DR, Tian Y-M, Wilson MI, Gielbert J, Gaskell SJ, et al. Targeting of HIF-α to the Von Hippel-Lindau Ubiquitylation Complex by O2-Regulated Prolyl Hydroxylation. *Science* (2001) 292(5516):468. doi: 10.1126/science.1059796
16. Yu F, White SB, Zhao Q, Lee FS. HIF-1α Binding to VHL is Regulated by Stimulus-Sensitive Proline Hydroxylation. *Proc Natl Acad Sci* (2001) 98(17):9630. doi: 10.1073/pnas.181341498
17. Masson N, Willam C, Maxwell PH, Pugh CW, Ratcliffe PJ. Independent Function of Two Destruction Domains in Hypoxia-Inducible Factor-α Chains Activated by Prolyl Hydroxylation. *EMBO J* (2001) 20(18):5197–206. doi: 10.1093/emboj/20.18.5197
18. Epstein ACR, Gleadle JM, McNeill LA, Hewitson KS, O'Rourke J, Mole DR, et al. C. Elegans EGL-9 and Mammalian Homologs Define a Family of Dioxygenases That Regulate HIF by Prolyl Hydroxylation. *Cell* (2001) 107(1):43–54. doi: 10.1016/S0092-8674(01)00507-4
19. Bruick RK, McKnight SL. A Conserved Family of Prolyl-4-Hydroxylases That Modify HIF. *Science* (2001) 294(5545):1337. doi: 10.1126/science.1066373
20. Graham CH, Forsdike J, Fitzgerald CJ, Macdonald-Goodfellow S. Hypoxia-Mediated Stimulation of Carcinoma Cell Invasiveness via Upregulation of Urokinase Receptor Expression. *Int J Cancer* (1999) 80(4):617–23. doi: 10.1002/(SICI)1097-0215(19990209)80:4<617::AID-IJC22>3.0.CO;2-C
21. Synnestvedt K, Furuta GT, Comerford KM, Louis N, Karhausen J, Eltzschig HK, et al. Ecto-5′-Nucleotidase (CD73) Regulation by Hypoxia-Inducible Factor-1 Mediates Permeability Changes in Intestinal Epithelia. *J Clin Invest* (2002) 110(7):993–1002. doi: 10.1172/JCI15337

22. Taniguchi CM, Miao YR, Diep AN, Wu C, Rankin EB, Atwood TF, et al. PHD Inhibition Mitigates and Protects Against Radiation-Induced Gastrointestinal Toxicity *via* HIF2. *Sci Trans Med* (2014) 6(236):236ra64. doi: 10.1126/scitranslmed.3008523
23. Fujimoto TN, Colbert LE, Huang Y, Molkentine JM, Deorukhkar A, Baseler L, et al. Selective EGLN Inhibition Enables Ablative Radiotherapy and Improves Survival in Unresectable Pancreatic Cancer. *Cancer Res* (2019) 79(9):2327. doi: 10.1158/0008-5472.CAN-18-1785
24. Miyoshi H, Stappenbeck TS. *In Vitro* Expansion and Genetic Modification of Gastrointestinal Stem Cells in Spheroid Culture. *Nat Protoc* (2013) 8 (12):2471–82. doi: 10.1038/nprot.2013.153
25. Kim WY, Safran M, Buckley MRM, Ebert BL, Glickman J, Bosenberg M, et al. Failure to Prolyl Hydroxylate Hypoxia-Inducible Factor α Phenocopies VHL Inactivation *In Vivo*. *EMBO J* (2006) 25(19):4650–62. doi: 10.1038/sj.emboj.7601300
26. Miyoshi H, Ajima R, Luo CT, Yamaguchi TP, Stappenbeck TS. Wnt5a Potentiates TGF-β Signaling to Promote Colonic Crypt Regeneration After Tissue Injury. *Science* (2012) 338(6103):108. doi: 10.1126/science.1223821
27. Flanagan DJ, Austin CR, Vincan E, Phesse TJ. Wnt Signalling in Gastrointestinal Epithelial Stem Cells. *Genes* (2018) 9(4):178. doi: 10.3390/genes9040178
28. de la Cruz Bonilla M, Stemler KM, Taniguchi CM, Piwnica-Worms H. Stem Cell Enriched-Epithelial Spheroid Cultures for Rapidly Assaying Small Intestinal Radioprotectors and Radiosensitizers *In Vitro*. *Sci Rep* (2018) 8 (1):15410. doi: 10.1038/s41598-018-33747-7
29. Ryu YK, Collins SE, Ho H-YH, Zhao H, Kuruvilla R. An Autocrine Wnt5a-Ror Signaling Loop Mediates Sympathetic Target Innervation. *Dev Biol* (2013) 377(1):79–89. doi: 10.1016/j.ydbio.2013.02.013
30. Taniguchi CM, Finger EC, Krieg AJ, Wu C, Diep AN, LaGory EL, et al. Cross-Talk Between Hypoxia and Insulin Signaling Through Phd3 Regulates Hepatic Glucose and Lipid Metabolism and Ameliorates Diabetes. *Nat Med* (2013) 19(10):1325–30. doi: 10.1038/nm.3294
31. Yan Q, Bartz S, Mao M, Li L, Kaelin William G. The Hypoxia-Inducible Factor 2α N-Terminal and C-Terminal Transactivation Domains Cooperate To Promote Renal Tumorigenesis *In Vivo*. *Mol Cell Biol* (2007) 27(6):2092–102. doi: 10.1128/MCB.01514-06
32. Li B, Dewey CN. RSEM: Accurate Transcript Quantification From RNA-Seq Data With or Without a Reference Genome. *BMC Bioinf* (2011) 12:323. doi: 10.1186/1471-2105-12-323
33. Leng N, Dawson JA, Thomson JA, Ruotti V, Rissman AI, Smits BMG, et al. EBSeq: An Empirical Bayes Hierarchical Model for Inference in RNA-Seq Experiments. *Bioinformatics* (2013) 29(8):1035–43. doi: 10.1093/bioinformatics/btt087
34. Katula KS, Joyner-Powell NB, Hsu C-C, Kuk A. Differential Regulation of the Mouse and Human Wnt5a Alternative Promoters A and B. *DNA Cell Biol* (2012) 31(11):1585–97. doi: 10.1089/dna.2012.1698
35. Franken NAP, Rodermond HM, Stap J, Haveman J, van Bree C. Clonogenic Assay of Cells *In Vitro*. *Nat Protoc* (2006) 1(5):2315–9. doi: 10.1038/nprot.2006.339
36. Sato T, Vries RG, Snippert HJ, van de Wetering M, Barker N, Stange DE, et al. Single Lgr5 Stem Cells Build Crypt-Villus Structures *In Vitro* Without a Mesenchymal Niche. *Nature* (2009) 459(7244):262–5. doi: 10.1038/nature07935
37. Schödel J, Mole DR, Ratcliffe PJ. Pan-Genomic Binding of Hypoxia-Inducible Transcription Factors. *Biol Chem* (2013) 394(4):507–17. doi: 10.1515/hsz-2012-0351
38. Rashid I, Pathak AK, Kumar R, Srivastava P, Singh M, Murali S, et al. Genome-Wide Comparative Analysis of HIF Binding Sites in Cyprinus Carpio for In Silico Identification of Functional Hypoxia Response Elements. *Front Genet* (2019) 10:659. doi: 10.3389/fgene.2019.00659
39. Kimura H, Weisz A, Ogura T, Hitomi Y, Kurashima Y, Hashimoto K, et al. Identification of Hypoxia-Inducible Factor 1 Ancillary Sequence and Its Function in Vascular Endothelial Growth Factor Gene Induction by Hypoxia and Nitric Oxide *. *J Biol Chem* (2001) 276(3):2292–8. doi: 10.1074/jbc.M008398200
40. Bakker ERM, Raghoebir L, Franken PF, Helvensteijn W, van Gurp L, Meijlink F, et al. Induced Wnt5a Expression Perturbs Embryonic Outgrowth and Intestinal Elongation, But is Well-Tolerated in Adult Mice. *Dev Biol* (2012) 369(1):91–100. doi: 10.1016/j.ydbio.2012.06.007
41. Jalili-Firoozinezhad S, Prantil-Baun R, Jiang A, Potla R, Mammoto T, Weaver JC, et al. Modeling Radiation Injury-Induced Cell Death and Countermeasure Drug Responses in a Human Gut-On-a-Chip. *Cell Death Dis* (2018) 9(2):223. doi: 10.1038/s41419-018-0304-8
42. Ayrapetov MK, Xu C, Sun Y, Zhu K, Parmar K, D'Andrea AD, et al. Activation of Hif1α by the Prolylhydroxylase Inhibitor Dimethyoxalyglycine Decreases Radiosensitivity. *PloS One* (2011) 6(10): e26064. doi: 10.1371/journal.pone.0026064
43. Si J, Zhou R, Zhao B, Xie Y, Gan L, Zhang J, et al. Effects of Ionizing Radiation and HLY78 on the Zebrafish Embryonic Developmental Toxicity. *Toxicology* (2019) 411:143–53. doi: 10.1016/j.tox.2018.10.004
44. Murdoch B, Chadwick K, Martin M, Shojaei F, Shah KV, Gallacher L, et al. Wnt-5A Augments Repopulating Capacity and Primitive Hematopoietic Development of Human Blood Stem Cells *In Vivo*. *Proc Natl Acad Sci* (2003) 100(6):3422. doi: 10.1073/pnas.0130233100
45. Masckauchán TNH, Agalliu D, Vorontchikhina M, Ahn A, Parmalee NL, Li C-M, et al. Wnt5a Signaling Induces Proliferation and Survival of Endothelial Cells *In Vitro* and Expression of MMP-1 and Tie-2. *Mol Biol Cell* (2006) 17 (12):5163–72. doi: 10.1091/mbc.e06-04-0320
46. Zhou Y, Kipps TJ, Zhang S. Wnt5a Signaling in Normal and Cancer Stem Cells. *Stem Cells Int* (2017) 2017:5295286. doi: 10.1155/2017/5295286
47. Douglass SM, Fane ME, Sanseviero E, Ecker BL, Kugel CH, Behera R, et al. Myeloid-Derived Suppressor Cells Are a Major Source of Wnt5A in the Melanoma Microenvironment and Depend on Wnt5A for Full Suppressive Activity. *Cancer Res* (2021) 81(3):658. doi: 10.1158/0008-5472.CAN-20-1238
48. Oh W, Frost JA. Rho GTPase Independent Regulation of ATM Activation and Cell Survival by the RhoGEF Net1A. *Cell Cycle* (2014) 13(17):2765–72. doi: 10.4161/15384101.2015.945865
49. Cheng C, Seen D, Zheng C, Zeng R, Li E. Role of Small GTPase RhoA in DNA Damage Response. *Biomolecules* (2021) 11(2):212. doi: 10.3390/biom11020212
50. Zhou Z, Huang F, Shrivastava I, Zhu R, Luo A, Hottiger M, et al. New Insight Into the Significance of KLF4 PARylation in Genome Stability, Carcinogenesis, and Therapy. *EMBO Mol Med* (2020) 12(12):e12391. doi: 10.15252/emmm.202012391
51. Legrand AJ, Choul-Li S, Spriet C, Idziorek T, Vicogne D, Drobecq H, et al. The Level of Ets-1 Protein Is Regulated by Poly(ADP-Ribose) Polymerase-1 (PARP-1) in Cancer Cells to Prevent DNA Damage. *PloS One* (2013) 8(2): e55883. doi: 10.1371/journal.pone.0055883
52. Gazit VA, Swietlicki EA, Liang MU, Surti A, McDaniel R, Geisman M, et al. Stem Cell and Niche Regulation in Human Short Bowel Syndrome. *JCI Insight* (2020) 5(23):e137905. doi: 10.1172/jci.insight.137905
53. Wu N, Sun H, Zhao X, Zhang Y, Tan J, Qi Y, et al. MAP3K2-Regulated Intestinal Stromal Cells Define a Distinct Stem Cell Niche. *Nature* (2021) 592 (7855):606–10. doi: 10.1038/s41586-021-03283-y

Conflict of Interest: CT is on the clinical advisory board of Accuray, as well as has a patent for oral amifostine as a radioprotectant of the upper GI tract issued, licensed, and with royalties paid from Xerient Pharmaceuticals and PHD inhibitors as a radioprotectant of the GI tract pending, and was the lead principal investigator of a multicenter trial testing the effects of high-dose SBRT with the radiomodulator, GC4419. CT is also a paid consultant for Phebra Pty, Ltd.

The remaining authors declare that the research was conducted in the absence of any commercial or financial relationships that could be construed as a potential conflict of interest.

Publisher's Note: All claims expressed in this article are solely those of the authors and do not necessarily represent those of their affiliated organizations, or those of the publisher, the editors and the reviewers. Any product that may be evaluated in this article, or claim that may be made by its manufacturer, is not guaranteed or endorsed by the publisher.

frontiers in Oncology

ORIGINAL RESEARCH
published: 08 December 2021
doi: 10.3389/fonc.2021.788182

A Combination of Cabozantinib and Radiation Does Not Lead to an Improved Growth Control of Tumors in a Preclinical 4T1 Breast Cancer Model

Norman Reppingen[1†], *Alexander Helm*[1†], *Laura Doleschal*[2], *Marco Durante*[1,3*] *and Claudia Fournier*[1]

[1] Department of Biophysics, GSI Helmholtz Center for Heavy Ion Research, Darmstadt, Germany, [2] Department of Biology, Technische Universität Darmstadt, Darmstadt, Germany, [3] Department of Condensed Matter Physics, Technische Universität Darmstadt, Darmstadt, Germany

OPEN ACCESS

Edited by:
Shubhankar Suman, Georgetown University, United States

Reviewed by:
Gabriele Multhoff, Technical University of Munich, Germany
Michael Wayne Epperly, University of Pittsburgh, United States
Asit Kumar Manna, Henry M. Jackson Foundation for the Advancement of Military Medicine (HJF), United States

***Correspondence:**
Marco Durante
M.Durante@gsi.de

[†]*These authors have contributed equally to this work*

Specialty section:
This article was submitted to Radiation Oncology, a section of the journal Frontiers in Oncology

Received: *01 October 2021*
Accepted: *19 November 2021*
Published: *08 December 2021*

Citation:
Reppingen N, Helm A, Doleschal L, Durante M and Fournier C (2021) A Combination of Cabozantinib and Radiation Does Not Lead to an Improved Growth Control of Tumors in a Preclinical 4T1 Breast Cancer Model. Front. Oncol. 11:788182. doi: 10.3389/fonc.2021.788182

The tyrosine kinase inhibitor Cabozantinib has been applied in clinical studies in combination with radiotherapy. We investigated the effect of such combination on triple-negative 4T1 cells as a metastatic breast cancer model *in vitro* and *in vivo* upon inoculation in BALB/c mice. *In vitro* assays indicated a potential for improved effects using the combination. Both Cabozantinib (2.5 μM) and 10 Gy of 250 kV x-rays were able to cease the growth of 4T1 cells as revealed by growth curves. In a clonogenic survival assay, the effect of Cabozantinib added on the effects of irradiation and the effectiveness of inhibiting the clonogenic survival was found to be 2 (RBE_{10}). Additionally, cell death measurements of apoptosis plus necrosis revealed a synergistic effect when combining irradiation with Cabozantinib. Surprisingly, however, *in vivo* tumor growth kinetics showed no additional effect in growth control when irradiation was used together with Cabozantinib. Since both ionizing radiation and Cabozantinib are acknowledged to feature immunogenic effects, we additionally investigated the effect of the treatments on lung metastases. No difference to the control groups was found here, neither for irradiation nor Cabozantinib alone nor in combination. Yet, upon analysis of the mice' livers, CD11b-positive cells, indicating immune suppressive myeloid derived suppressor cells were found diminished following treatment with Cabozantinib. In conclusion, despite promising *in vitro* controls of the combination of Cabozantinib and irradiation, tumor growth control was not increased by the combination, which was true also for the occurrence of lung metastases.

Keywords: Cabozantinib, radiotherapy, SBRT, triple-negative breast cancer, 4T1 cells

INTRODUCTION

The combination of treatments including immunotherapy (1), small molecule pharmacology (2, 3) and radiotherapy (4, 5) is a rapidly growing and promising field. Radiotherapy (RT) may induce immunologically relevant molecular and cellular effects, including abscopal effects with shrinking or vanishing tumors outside the radiation field (6) and is hence a match for combination therapies

featuring immune responses. Cabozantinib, a tyrosine kinase inhibitor, was shown to optimize anti tumor immunity, reducing the prevalence of regulatory T cells (7) and myeloid-derived suppressor cells (MDSCs) in mouse models (7, 8). Clinical trials combining both have been set up for treatment of glioblastoma (in combination with temozolomide) (9) or sarcomas of the extremities (NCT04220229).

Triple-negative breast cancer (TNBC) represents a challenging therapeutic target due to the highly invasive nature and relatively low response to therapeutics. TNBC is managed with conventional therapeutics, including RT, often leading to systemic relapse since there is an absence of specific treatment strategies for this tumor subgroup (10). In a Phase II study in TNBC patients, Cabozantinib increased the number of circulating CD8+ T-Cells and decreased the presence of CD14+ myeloid cells (11). RT administered in stereotactic body radiation therapy (SBRT) character is held to trigger a powerful immune activation (12). Combination of RT in a SBRT-like character and Cabozantinib may be beneficial in the treatment of TNBC. We investigated the potential of such a combined therapy using the murine 4T1 model of metastatic breast cancer.

Both Cabozantinib (2.5 μM) and 10 Gy of 250 kV x-rays were able to cease the growth of 4T1 cells *in vitro* as measured by reduced growth and reduced clonogenic survival. We observed that the effect of Cabozantinib added on the effects of irradiation. Additionally, cell death measurements revealed a slightly synergistic effect. In contrast, *in vivo* tumor growth kinetics showed, compared to Cabozantinib treatment alone, no additional effect in growth control for combined treatment. With respect to the occurrence of lung metastases, no difference to the untreated control groups was found here. Yet, upon analysis of the mice' livers, CD11b-positive cells, indicating immune suppressive myeloid derived suppressor cells (MDSC) were found diminished following treatment with Cabozantinib. In conclusion, despite promising *in vitro* results of the combination of Cabozantinib and irradiation, tumor growth controls was not increased by the combination, which was true also for the occurrence of lung metastases.

MATERIAL AND METHODS

Animal and Cell Models

4T1 cells were from ATCC and maintained in RPMI culture medium from Merck with 9.6% of fetal bovine serum (Biochrom AG) and 1% penicillin/streptomycin solution from Invitrogen. For *in vitro* experiments, Cabozantinib was used at 2.5 μM as in Kwilas et al. (7) in the supplemented medium. Irradiation of cells was furnished with 250 kV x-rays from the IV320-13 from Seifert using a filter consisting of 7 mm Be, 1 mm Cu and 1 mm Al, using a SN4 dosimeter from PTW at a dose rate of 2.5 Gy/min.

BALB/c mice were kept in accordance with federal policies on animal research. The corresponding ethical approval code is 23 177-07/G 15-8-058. After a week of adapation, $1*10^5$ 4T1 cells in 20 μl PBS were injected into the second mammary fat pad under ketamine/xylazine narcosis. Tumor size was measured every three days using vernier calipers. Tumor volume was calculated using the formula $V = (A*B^2)/2$, with A as the largest and B as the smallest diameter of the tumor. Mice were sacrificed 26 days post tumor inoculation, corresponding to 12 days after radiation exposure. For the count of lung metastases, the lungs were infused with blue ink upon resection, counting the superficially visible metastases.

Irradiation was performed with a 320 kV x-ray tube from X-RAD at a dose rate of 0.47 Gy/min at day 14 after tumor cell inoculation, using lead collimation to shield non-tumor areas under ketamine/xylazine narcosis, which was also applied to the unexposed groups. Drugging with Cabozantinib started on day 5 after tumor inoculation and lasted 21 days, until the end of the study. The drug was applied *via* mouse chow as a purified ingredient diet prepared by Research Diets, New Brunswick, NJ, containing 66.7 mg/kg Cabozantinib malate salt (LC Labs), which was established to correspond to a daily dose of 10 mg/kg (7). An untreated control group did not receive neither irradiation nor Cabozantinib. The number if mice assigned to the experimental groups were 8 (negative controls and 14 Gy) and 12 (Cabozantinib and 14 Gy + Cabozantinib), respectively.

Masson Goldner Staining and CD11b Staining

The liver samples were fixed in Histofix (Carl Roth) and stored in 70% Ethanol, transferred into paraffin blocks *via* ethanol/xylene stages, and cut with a rotary microtome from Leica in slices of about 5 μm. After deparaffination in xylene and rehydration, the samples were stained according to the method of Masson and Goldner. For immunohistological staining of CD11b, following deparaffination and antigen retrieval in citrate buffer in a household microwave oven for 20 minutes and washing in PBS buffer, the samples were blocked with goat serum (Sigma) diluted in PBS, supplemented with 1% of Triton X-100 for 30 minutes. The rabbit primary antibody directed against CD11b (abcam 133357, clone EPR1344), was applied at a concentration of 1:4000 in PBS and incubated over night at 4°C in the dark. After washing with PBS, the slides were incubated with blocking reagent for 30 min. followed by 2 h of incubation with a HRP-conjugated anti rabbit secondary antibody (abcam 6721, polyclonal) at a dilution of 1:100 (also in PBS). The staining was developed using the ImmPACT VIP substrate according to manufacturer specifications, dehydrated over alcohol and xylene stages and embedded in Eukitt (Sigma). Samples were captured using a BX61 microsope from Olympus equipped with plan - apochromatically corrected lenses.

Assessment of Cell Growth

Petri dishes were seeded with $1*10^4$ 4T1 cells one day prior to treatment with irradiation and/or Cabozantinib as described above. Cells were harvested and counted 24, 48, 72 and 96h following treatment using an automated cell counter (Coulter).

Assessment of Clonogenic Survival

Clonogenic cell survival was assessed using the standard colony forming assay as described elsewhere (13). Briefly, directly after

exposure cells were trypsinized, counted and plated in triplicate into 25 cm^2 tissue culture flasks. The numbers of cells seeded were estimated to result in a statistically significant formation of at least 100 colonies. After seven days of incubation, cells were fixed and stained with a methylene blue solution. Cell clusters consisting of at least 50 cells were counted as a colony.

Assessment of Cell Death

In order to assess cell death, the supernatant of cells was collected by decanting in 15 ml falcon tubes. The cells remaining in the T25 culture flask were washed with PBS, and the PBS added to the supernatant in the tube. 2 ml of Accumax cell dissociation solution from PAN-Biotech was added and the T25 flask incubated for 10 min. at 37 C. The liquid in the Falcon of the respective tube was unified with the Accumax solution and centrifuged at 300 g. The remaining pellet was stained using 100 µl of a staining solution consisting of propidium iodide (1 µg/ml), and Annexin-V Pacific Blue (ThermoFisher) according to manufacturer instructions (5 µl per sample) in a Buffer supplemented with Ca2+. After incubation for 20 min. at 4 C in the dark, 700 µl staining buffer was added, following by centrifugation for 5 minutes at 300 g. Using 300 µl of staining buffer, the pellet was transferred to 5 ml polystyrene tubes and subjected to flow cytometry analysis with a FACSCanto II instrument. The data was analyzed using FlowJo Software, version 10.5.3.

Gene Expression Analysis

At least 1.5 Million cells growing in T75 culture flasks were deprived of medium and treated with 1 ml of TRIZol (Thermofisher). Further workup occurred as per manufacturer description, using 400 µl of chloroform (Alfa Aesar, Molecular Biology Reagent, stabilized with 50 ppm amylene), Iso-Propanol (Sigma, HPLC grade) and Ethanol (Roth, p.A.). The resulting RNA was characterized with a colibri-nanodrop device from Titertek Berthold and used for cDNA synthesis using the RevertAid kit (Thermofisher). For the Q-PCR runs on a StepOnePlus instrument from Applied Biosystems, 100 ng of the resulting cDNA were used per sample using vinculin as a housekeeping gene. The resulting probe volume was 25 µl, using the Quantitect primer system from QIAGEN and evaGreen 5x Q-PCR Mastermix with ROX dye from Solis Biodyne. PCR plates were from Saarstedt. The sample data was evaluated according to the Ct method with the StepOne Software version 2.3.

Assessment of GM-CSF Release

GM-CSF release was quantified by ELISA (Thermofisher), according to manufacturer specifications, and the obtained values normalized to the cell number.

Statistical Analysis

Data are displayed as the mean values of independent experiments plus/minus the standard error of the mean (SEM) or the standard deviation (SD) unless indicated elsewise. Significance tests were performed using GraphPad Prism version 6, GraphPad Software, La Jolla California USA.

RESULTS

Cabozantinib Adds on the Effects of X-Rays in Terms of Cell Inactivation and Growth Control *In Vitro*, but This Is Not Reflected *In Vivo*

To determine the concentration of Cabozantinib and the radiation dose resulting in cell growth control, we investigated the growth of cells *in vitro* following different treatments. We tested a concentration of 2.5 µM as applied by Kwilas and colleagues (7), which resulted in control of the cell growth up to 96h after beginning of treatment, while concentrations of 0.5 or 1 µM Cabozantinib were not sufficient to do so (**Figure 1A**). As for x-rays alone, 10 Gy were found sufficient to control the growth, whereas 2 and 5 Gy failed (**Figure 1B**). Consequently, a combination of 10 Gy and 2.5 µM of Cabozantinib resulted in a total growth control up to 96h after treatment (**Figures 1B, C**), which significantly differed only partly, but not at 96h. Next, we investigated clonogenic cell survival. When Cabozantinib (2.5 µM) was added, the clonogenic survival decreased and the relative biological effectiveness (RBE) was found to be about 2 at an iso-survival level of 10% (**Figure 2**). The α/β-ratios resulting from linear-quadratic fits for the curves were 1.4 (x-rays) and 7.4 (x-rays + Cabozantinib, **Supplementary Table 1**). Comparing σ values of α, the curves were found to differ significantly ($p<0.001$, t-test). Additionally, cell death measurements 72h after treatment revealed a significant reduction in the amount of living cells (i.e. negative both for propidium iodide and Annexin-V) following exposure to irradiation from 91.9% for negative controls to 62.3% ($p<0.0001$). Cabozantinib alone reduced, yet not significantly the amount of living cells to 84.7%. This was found also when Cabozantinib was added to irradiaton (56.5%, **Figure 3**).

These results prompted to investigate in a pilot-experiment the effects in a syngeneic *in vivo* model (BALB/c mice), in which tumors were injected in the flanks of the mice. Mice were irradiated with 10 Gy and Cabozantinib was administered as described above. However, the results revealed no differences between the group administered with Cabozantinib only versus combination with 10 Gy x-rays with respect to tumor growth control and amount of superficial lung metastases (data not shown). To account for the differences for tumor cell inactivation *in vivo* as compared to our *in vitro* studies, we increased the dose given to tumors to 14 Gy in a further experiment.

When tumors were irradiated with 14 Gy but mice were not treated with Cabozantinib, tumor growth was only slightly delayed and not significantly different from the untreated controls (**Figure 4**). In contrast, the administration of Cabozantinib to the mice starting from day 5 after tumor inoculation resulted in a significantly reduced tumor volume ($p=0.002$ and 0.006, Mann-Whitney U Test, without and with irradiation, respectively), as compared to the untreated controls. However, when the tumors of mice were treated with Cabozantinib and additionally irradiated with 14 Gy, no differences were found as compared to tumors in mice only administered with Cabozantinib. In summary, while

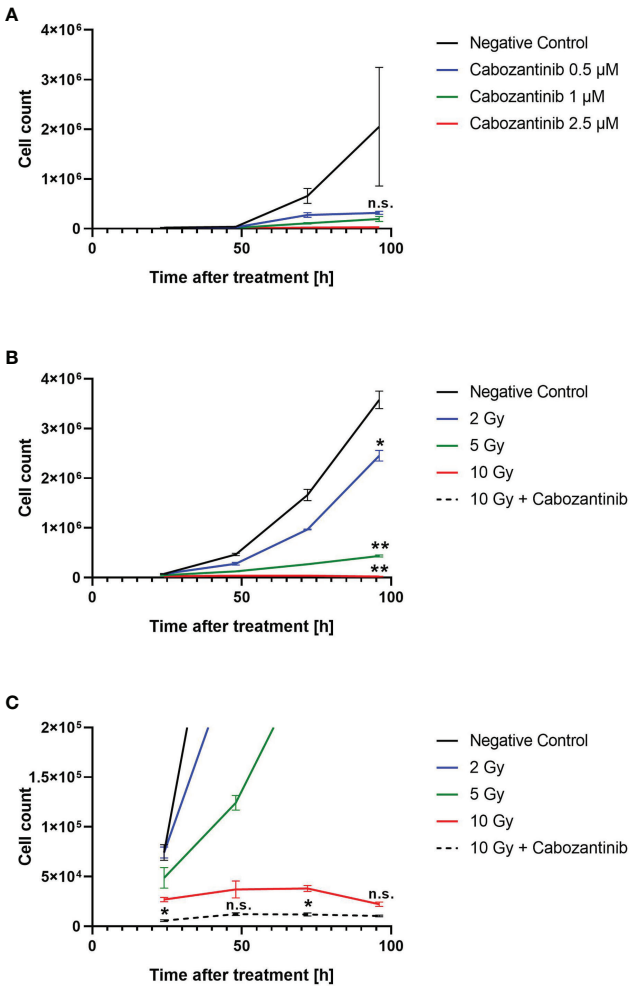

FIGURE 1 | *In vitro* cell growth following treatment with Cabozantinib **(A)** or x-rays and Cabozantinib **(B)**. Cells were counted 24, 48, 72 and 96h following treatment and results are derived from experiments carried out in triplicates (mean value ± SEM). Please note that curves for 10 Gy and 10 Gy + Cabozantinib cannot be distinguished due to the scale in **(B)**. Therefore, in **(C)**, the same data as in **(B)** are displayed in a different scale. A Two-way ANOVA (at 96h, negative controls vs. each other group) revealed significant differences to the negative controls only following irradiation (**B**, *p<0.05, **p<0.01). A comparison between 10 Gy and 10 Gy + Cabozantinib revealed no significant differences at 96h **(C)**.

Cabozantinib added on the effects of tumor cell inactivation *in vitro*, this was not reflected by the combined treatment *in vivo* with respect to tumor growth control, since the combined treatment regime did not show significant differences to the group administered with Cabozantinib only. In order to screen for systemic effects, we additionally investigated lungs and livers of the mice.

Systemic Responses to the Combined Treatment Indicate a Reduced Recruitment of MDSCs to the Liver but No Reduction of Metastases in the Lung

To investigate for the systemic anti-tumor immune response, we assessed the number of superficially visible metastases on the lungs of the animals upon staining. The results did not reveal significant reduction of the number of lung metastases as compared to the controls (**Figure 5**). While no macroscopically visible tumors were found in the livers of the animals of all groups, histology of the liver tissue of tumor bearing, untreated mice did show patches of cell infiltrates along the vessels, which were found to stain positive for the myeloid cell marker CD11b (**Figure 6**). The prevalence of such cells was also seen in livers from mice which received irradiation. However, in livers from mice which were treated with Cabozantinib with and without irradiation, this type of cells was reduced in prevalence or entirely absent. Hence, despite no effect on the reduction of metastases was found, the difference in recruitment of CD11b-positive cells, indicating MDSCs, points to a systemic effect.

To support these findings, we conducted *in vitro* studies assessing the expression and release of GM-CSF, which was

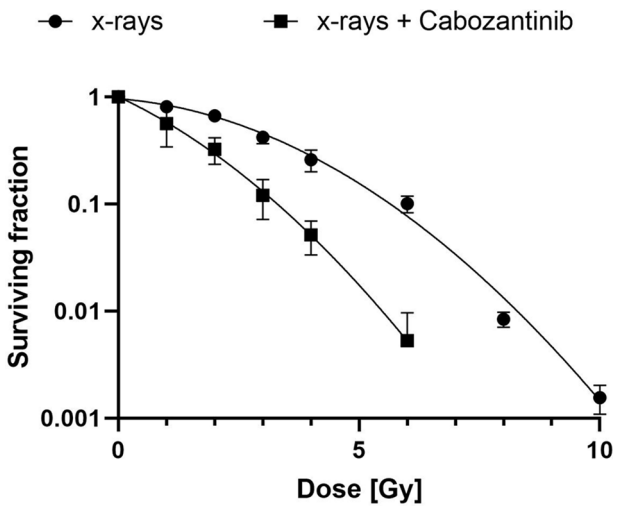

FIGURE 2 | Clonogenic cell survival after exposure to x-rays and Cabozantinib. A colony formation assay was performed as described following exposure to x-rays or x-rays and 2.5 μM of Cabozantinib. Results are derived from two (x-rays + Cabozantinib) or three (x-rays) independent experiments (mean value ± SD). A t-test comparing σ-values of α revealed a significant difference ($p<0.001$).

reported to play a major role in the recruitment and the immune-suppressive capabilities of 4T1 cells (14). Irradiation with 10 Gy alone resulted in a pronounced increase of both expression and release (significant) of GM-CSF 24h upon irradiation as compared to negative controls (**Figure 7**). Instead, when cells were treated with Cabozantinib alone, expression and release were found to be reduced and the combination of both treatments resulted in a mitigation of the effects of irradiation alone.

DISCUSSION

Treatment of triple-negative breast cancer remains a challenge since it is highly invasive and features a low response to therapeutics, often leading to relapse (10). Combined therapies may offer vast potential in treatment of metastatic disease in general when systemic immune responses are triggered. Radiotherapy has been shown to trigger such effects and it is under discussion whether an SBRT-like dose administration may be particularly efficient (12). Likewise, Cabozantinib increased the number of circulating CD8+ T-cells and decreased the presence of CD14+ myeloid cells in a Phase II study (11). In an *in vivo* prostate cancer model, Cabozantinib was reported to eradicate advanced tumors by activation of anti-tumor immunity (15). We therefore hypothesized that a combination of RT in a SBRT-like character and Cabozantinib may be beneficial in the treatment of TNBC. We investigated the potential of such therapy using the murine 4T1 model of metastatic breast cancer.

A combination of Cabozantinib in 2.5 μM with 10 Gy of x-rays, both having demonstrated to cease the growth of 4T1 cells (**Figure 1**), revealed a slightly synergistic effect as compared to the single treatments when cell death was quantified (**Figure 3**). However, irradiation mainly contributed to the reduction of living cells in the cultures. Furthermore, the addition of Cabozantinib to irradiation with x-rays resulted in an RBE of about 2 with respect to clonogenic cell survival (**Figure 2**). Hence, our data suggested a direct effect of drug regimen and irradiation on 4T1 tumor cells. Given these promising results, we investigated the effects on local tumor control and systemic effects in lung and liver in a syngenic BALB/c mouse model.

Treatment with Cabozantinib beginning at day 5 after tumor inoculation throughout the remaining 21 days of the study resulted in a significant tumor growth reduction ($p = 0.0002$). This is in line with the reported suppression of tumor growth in 4T1 tumor models upon inhibition of VEGFR-2 and c-Met (16), which are kinase targets of Cabozantinib (17). However, x-ray irradiation at a dose of 14 Gy applied to the 4T1 tumors did not lead to a significant difference to the control group with respect to tumor growth. This points to a high radioresistance in our *in vivo* model, which is in contrast to former work reporting a significantly reduced tumor growth in a similar model system, already after 12 Gy exposure to the tumor (18).

Systemically, it was shown that irradiated 4T1 tumors can attract mesenchymal stem cells (MSC) to the tumor (19), which can give rise to immune suppressive fibroblasts, which attract MDSC to the tumor and raise other features of treatment resistance (20). In the work presented here, the combination of both treatment measures did not result in further reduction of tumor growth as compared to Cabozantinib alone (**Figure 4**), showing that synergistic effects as seen in the *in vitro* studies were not reflected *in vivo*.

We also aimed at investigating the potential of the combined treatment with Cabozantinib and irradiation with respect to systemic immune responses. For Cabozantinib, anti metastatic activity was

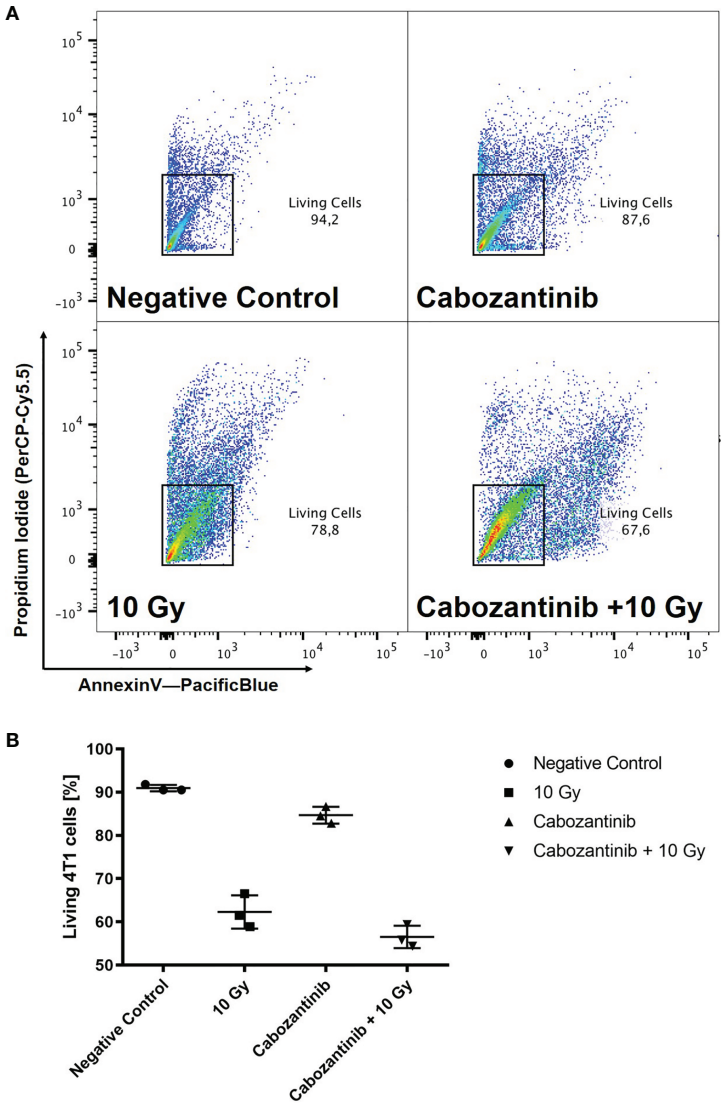

FIGURE 3 | Cell death after treatment with x-rays and Cabozantinib. Cell death was assessed as described following exposure to 10 Gy of x-rays, 2.5 μM Cabozantinib or both. Exemplary scatter plots resulting from flow cytometry analysis **(A)**. Cells positive for propidium iodide and Annexin-V were excluded to obtain living cells. The example is representative for the other biological replicates. Amount of living 4T1 cells 72h after treatments **(B)**. Results are derived from three independent experiments (mean value ± SD). A One-way ANOVA revealed significant differences for 10 Gy and Cabozantinib + 10 Gy as compared to the negative control ($p<0.0001$), but not for Cabozantinib alone ($p=0.0653$) or between 10 Gy and Cabozantinib + 10 Gy ($p=0.0917$).

reported also in immune incompetent tumor models due to the inhibitory effect on VEGF-R and c-Met (21). In our set-up, however, despite the reported anti metastatic activity of Cabozantinib (21), neither of the treatment methods nor the combination resulted in a reduction of lung metastases count (**Figure 5**).

Instead, an indication for a systemic immune-related response was found analyzing the livers of the animals. Liver histology of tumor bearing, untreated mice revealed cell infiltrates along the vessels, which were positive for the myeloid cell marker CD11b (**Figure 6**), indicating presence of MDSC (22). In the 4T1 and other tumor models, the patches of cells visible along the liver vessels have been characterized as an accumulation of immune suppressive MDSC (23). The expansion of the immune suppressive MDSC was shown to be possible with injection of GM-CSF in absence of a tumor, and adoptively transferred MDSC were also shown to home to the liver, where they closely resembled their presence in the spleen (23). In the 4T1 model specifically, the immune suppressive capability of these $Cd11b^{+}/Gr\text{-}1^{int}$ MDSC was shown to be steered exclusively by GM-CSF (14). Under influence of Cabozantinib, there was no visible presence of these cells in the liver. This is in line with the reported activity of Cabozantinib

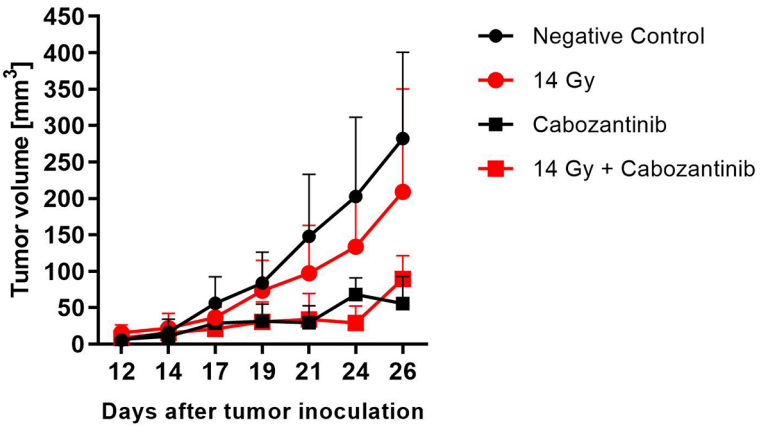

FIGURE 4 | Tumor growth after treatment with x-rays and Cabozantinib. The tumor volume was measured with a caliper and the mean value (+SD, N=8-12) is plotted against days after tumor inoculation. Mice assigned to irradiation with 14 Gy of x-rays were exposed on day 14 and those assigned to Cabozantinib administration received treatment beginning on day 5. Significance was tested using a One-way ANOVA (p=0.068).

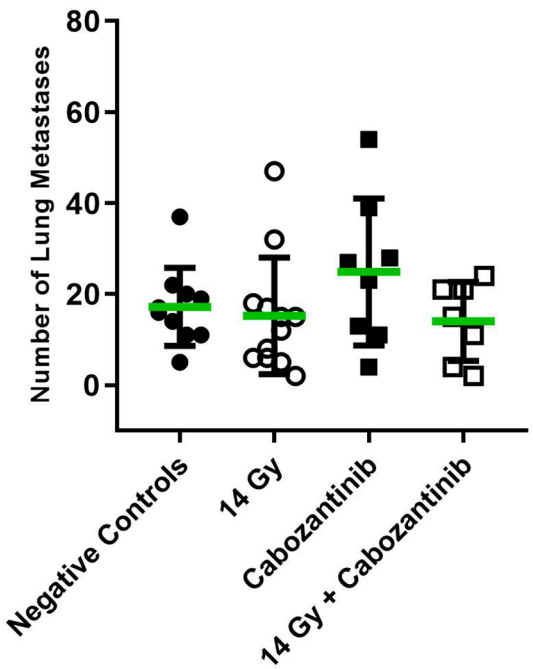

FIGURE 5 | Number of superficially visible lung metastases following the different treatment regimens. Mice were treated with 14 Gy, Cabozantinib or both. Upon scarification on day 26 and resection, lungs were stained as described and the number of superficially visible metastases were counted (N=8-12). Significance was tested using a One-way ANOVA (p=0.2771).

in antagonizing MDSC presence and with our results for gene expression and relsease of GM-CSF, which did show a reduced expression and protein presence of GM-CSF in 4T1 cells and in their supernatant, respectively (**Figure 7**).

Here, the prevalence of such cells was observed in livers from mice that received irradiation. However, in livers from mice that were treated with Cabozantinib with and without irradiation, this type of cells was reduced in prevalence or entirely absent, in line with the capability of Cabozantinib to antagonize MDSC as shown in other models (7, 8). Moreover, enhanced release of GM-CSF following irradiation of 4T1 tumors was shown to attract circulating tumor cells into the tumor bed of irradiated tumors

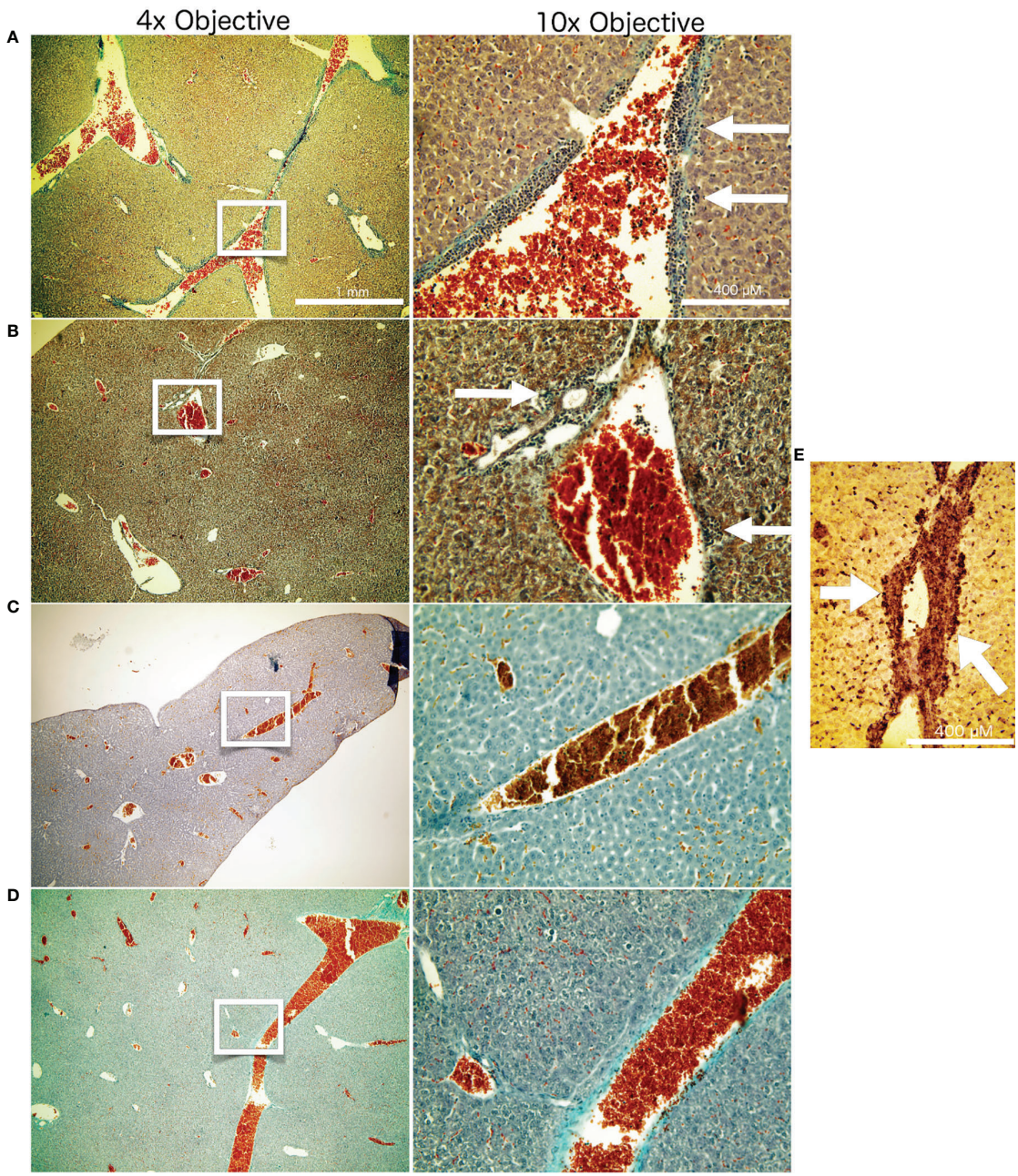

FIGURE 6 | Liver histology. Masson Goldner staining of liver tissue from the different treatment groups after termination of the experiment at day 26. The white frames on the left column of images indicate the image seen in higher magnification in the right column. Represented are examples from the respective treatment groups: Untreated negative controls **(A)**. Mice which received 14 Gy of x-ray irradiation localized to the tumor at day 14 **(B)**. Mice which received Cabozantinib at 10 mg/kg per day beginning with day 5 after tumor inoculation **(C)**. Mice which received both 14 Gy irradiation to the tumor and the diet supplemented with Cabozantinib **(D)**. White arrows indicate the patches of CD11b-positive cells, indicating MDSC. **(E)** Representative CD11b staining of a liver sample from a untreated mouse 26 days after tumor inoculation. White arrows are pointing to the patches of CD11b-positive cells adjacent to liver vessels.

and unirradiated secondary tumor sites, contributing to tumor re-growth (24). Cabozantinib, on the other hand, resulted in a reduced tumor growth (**Figure 4**), thus pointing to a role for GM-CSF and MDSC recruitment in our model and an explanation for the radioresistance of tumors treated with irradiation alone.

In conclusion, despite promising synergistic *in vitro* effects, the combination of photon radiotherapy and Cabozantinib failed to add on the effect of Cabozantinib alone with respect to tumor growth control. Furthermore, none of the treatments, in combination or alone revealed anti-metastatic effects. However,

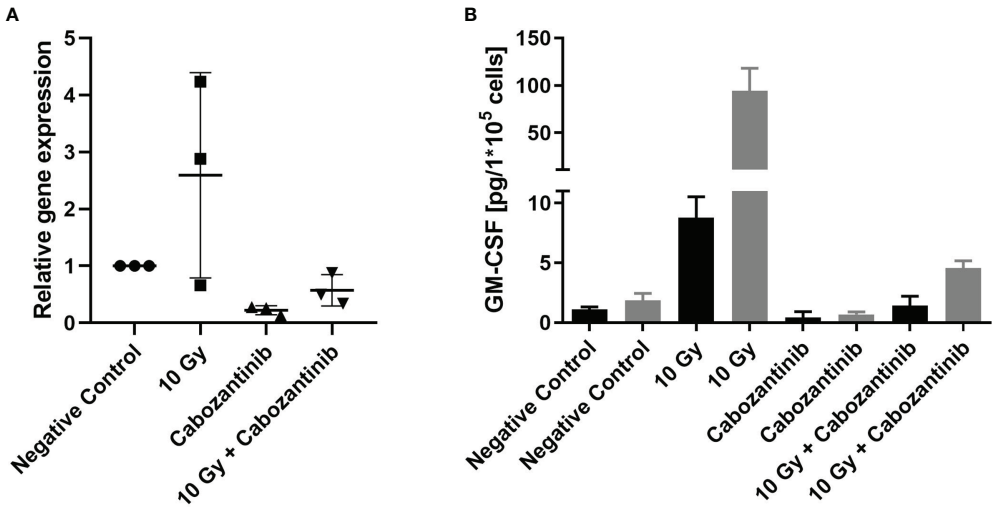

FIGURE 7 | Gene expression and protein release of GM-CSF following treatment. Cells were treated as described with irradiation and/or Cabozantinib. Gene expression analysis 24h after treatment **(A)**. Data are derived from three independent experiments each and show the n-fold as compared to each negative control. Analysis with a One-way ANOVA revealed no significant differences between the groups ($p=0.0537$). Release of GM-CSF measured in the supernatant 24h (black columns) and 48h (grey columns) after treatment **(B)**. Release of GM-CSF is normalized to the cell number. Data are derived from one experiment carried out in triplicates, which were each measured in technical duplicates. Results were found to be significant following an analysis using a One-way ANOVA ($p<0.0001$, for 24h and 48h, both negative controls vs. 10 Gy and 10 Gy vs. 10 Gy + Cabozantinib).

the ability of Cabozantinib to antagonize an increase in GM-CSF in 4T1 cells following irradiation indicates a utility in combination with radiotherapy, despite the lack of synergistic effects in terms of tumor growth or metastases control in our study.

DATA AVAILABILITY STATEMENT

The raw data supporting the conclusions of this article will be made available by the authors, without undue reservation.

ETHICS STATEMENT

The corresponding ethical approval code is 23 177-07/G 15-8-058.

AUTHOR CONTRIBUTIONS

NR, AH, and LD have substantially contributed to the conception and design of the work, as well as the acquisition, analysis and interpretation of the data. AH, MD, and CF have substantially contributed to design and revision of the manuscript. All authors contributed to the article and approved the submitted version.

FUNDING

This work was partially supported by ESA-IBER project and FAIR-phase-0.

ACKNOWLEDGMENTS

We thank Dr. Michael Scholz for helpful discussions. Technical support in carrying out the animal experiments by TRON GmbH, Mainz, is gratefully acknowledged.

SUPPLEMENTARY MATERIAL

The Supplementary Material for this article can be found online at: https://www.frontiersin.org/articles/10.3389/fonc.2021.788182/full#supplementary-material

REFERENCES

1. Galon J, Bruni D. Approaches to Treat Immune Hot, Altered and Cold Tumours With Combination Immunotherapies. *Nat Rev Drug Discov* (2019) 18:197–218. doi: 10.1038/s41573-018-0007-y
2. Adams JL, Smothers J, Srinivasan R, Hoos A. Big Opportunities for Small Molecules in Immuno-Oncology. *Nat Rev Drug Discov* (2015) 14:603–21. doi: 10.1038/nrd4596
3. Huck BR, Kötzner L, Urbahns K. Small Molecules Drive Big Improvements in Immuno-Oncology Therapies. *Angew Chem - Int Ed* (2018) 57:4412–28. doi: 10.1002/anie.201707816

4. Bristow RG, Alexander B, Baumann M, Bratman SV, Brown JM, Camphausen K, et al. Combining Precision Radiotherapy With Molecular Targeting and Immunomodulatory Agents: A Guideline by the American Society for Radiation Oncology. *Lancet Oncol* (2018) 19:e240–51. doi: 10.1016/S1470-2045(18)30096-2
5. Sharma RA, Plummer R, Stock JK, Greenhalgh TA, Ataman O, Kelly S, et al. Clinical Development of New Drug-Radiotherapy Combinations. *Nat Rev Clin Oncol* (2016) 13:627–42. doi: 10.1038/nrclinonc.2016.79
6. Durante M, Reppingen N, Held KD. Immunologically Augmented Cancer Treatment Using Modern Radiotherapy. *Trends Mol Med* (2013) 19:565–82. doi: 10.1016/j.molmed.2013.05.007
7. Kwilas AR, Ardiani A, Donahue RN, et al. Dual Effects of a Targeted Small-Molecule Inhibitor (Cabozantinib) on Immune-Mediated Killing of Tumor Cells and Immune Tumor Microenvironment Permissiveness When Combined With a Cancer Vaccine. *J Transl Med* (2014) 12:1–15. doi: 10.1186/s12967-014-0294-y
8. Lu X, Horner JW, Paul E, Shang X, Troncoso P, Deng P, et al. Effective Combinatorial Immunotherapy for Castration-Resistant Prostate Cancer. *Nature* (2017) 543:728–32. doi: 10.1038/nature21676
9. Schiff D, Desjardins A, Cloughesy T, Mikkelsen T, Glantz M, Chamberlain MC, et al. Phase 1 Dose Escalation Trial of the Safety and Pharmacokinetics of Cabozantinib Concurrent With Temozolomide and Radiotherapy or Temozolomide After Radiotherapy in Newly Diagnosed Patients With High-Grade Gliomas. *Cancer* (2016) 122:582–7. doi: 10.1002/cncr.29798
10. Medina MA, Oza G, Sharma A, Arriaga LG, Hernández JM, Rotello VM, et al. Triple-Negative Breast Cancer: A Review of Conventional and Advanced Therapeutic Strategies. *Int J Environ Res Public Health* (2020) 17:1–32. doi: 10.3390/ijerph17062078
11. Tolaney SM, Ziehr DR, Guo H, Ng MR, Barry WT, Higgins MJ, et al. Phase II and Biomarker Study of Cabozantinib in Metastatic Triple-Negative Breast Cancer Patients. *Oncologist* (2017) 22:25–32. doi: 10.1634/theoncologist.2016-0229
12. Chen Y, Gao M, Huang Z, Yu J, Meng X. SBRT Combined With PD-1/PD-L1 Inhibitors in NSCLC Treatment: A Focus on the Mechanisms, Advances, and Future Challenges. *J Hematol Oncol* (2020) 13:1–17. doi: 10.1186/s13045-020-00940-z
13. Fournier C, Scholz M, Weyrather WK, Rodemann HP, Kraft G. Changes of Fibrosis-Related Parameters After High- and Low-LET Irradiation of Fibroblasts. *Int J Radiat Biol* (2001) 77:713–22. doi: 10.1080/09553000110045025
14. Dolcetti L, Peranzoni E, Ugel S, Marigo I, Gomez AF, Mesa C, et al. Hierarchy of Immunosuppressive Strength Among Myeloid-Derived Suppressor Cell Subsets Is Determined by GM-CSF. *Eur J Immunol* (2010) 40:22–35. doi: 10.1002/eji.200939903
15. Patnaik A, Swanson KD, Csizmadia E, Solanki A, Landon-Brace N, Gehring MP, et al. Cabozantinib Eradicates Advanced Murine Prostate Cancer by Activating Antitumor Innate Immunity. *Cancer Discov* (2017) 7:750–65. doi: 10.1158/2159-8290.CD-16-0778
16. Shojaei F, Simmons BH, Lee JH, Lappin B, Christensen G. HGF/c-Met Pathway Is One of the Mediators of Sunitinib-Induced Tumor Cell Type-Dependent Metastasis. *Cancer Lett* (2012) 320:48–55. doi: 10.1016/j.canlet.2012.01.026
17. Uitdehaag JCM, De Roos JADM, Van Doornmalen AM, Prinsen BW, De Man J, Tanizawa Y, et al. Comparison of the Cancer Gene Targeting and Biochemical Selectivities of All Targeted Kinase Inhibitors Approved for Clinical Use. *PloS One* (2014) 9:1–13. doi: 10.1371/journal.pone.0092146
18. Schrand B, Verma B, Levay A, Patel S, Castro I, Benaduce AP, et al. Radiation-Induced Enhancement of Antitumor T-Cell Immunity by VEGF-Targeted 4-1BB Costimulation. *Cancer Res* (2017) 77:1310–21. doi: 10.1158/0008-5472.CAN-16-2105
19. Klopp AH, Spaeth EL, Dembinski JL, Woodward WA, Munshi A, Meyn RE, et al. Tumor Irradiation Increases the Recruitment of Circulating Mesenchymal Stem Cells Into the Tumor Microenvironment. *Cancer Res* (2007) 67:11687–95. doi: 10.1158/0008-5472.CAN-07-1406
20. Chandler C, Liu T, Buckanovich R, Coffman LG. The Double Edge Sword of Fibrosis in Cancer. *Transl Res* (2019) 209:55–67. doi: 10.1016/j.trsl.2019.02.006
21. Xiang Q, Chen W, Ren M, Wang J, Zhang H, Deng DYB, et al. Cabozantinib Suppresses Tumor Growth and Metastasis in Hepatocellular Carcinoma by a Dual Blockade of VEGFR2 and MET. *Clin Cancer Res* (2014) 20:2959–70. doi: 10.1158/1078-0432.CCR-13-2620
22. Bronte V, Brandau S, Chen SH, Colombo MP, Frey AB, Greten TF, et al. Recommendations for Myeloid-Derived Suppressor Cell Nomenclature and Characterization Standards. *Nat Commun* (2016) 7:1–10. doi: 10.1038/ncomms12150
23. Ilkovitch D, Lopez DM. The Liver Is a Site for Tumor-Induced Myeloid-Derived Suppressor Cell Accumulation and Immunosuppression. *Cancer Res* (2009) 69:5514–21. doi: 10.1158/0008-5472.CAN-08-4625
24. Vilalta M, Brune J, Rafat M, Soto L, Graves EE. The Role of Granulocyte Macrophage Colony Stimulating Factor (GM-CSF) in Radiation-Induced Tumor Cell Migration. *Clin Exp Metastasis* (2018) 35:247–54. doi: 10.1007/s10585-018-9877-y

Conflict of Interest: The authors declare that the research was conducted in the absence of any commercial or financial relationships that could be construed as a potential conflict of interest.

frontiers in Oncology

ORIGINAL RESEARCH
published: 17 February 2022
doi: 10.3389/fonc.2022.788293

Biological Effects of Monoenergetic Carbon Ions and Their Associated Secondary Particles

Dylan J. Buglewicz[1], *Kade D. Walsh*[1], *Hirokazu Hirakawa*[2], *Hisashi Kitamura*[3], *Akira Fujimori*[2] *and Takamitsu A. Kato*[1]*

[1] Department of Environmental & Radiological Health Sciences, Colorado State University, Fort Collins, CO, United States, [2] Department of Charged Particle Therapy Research, National Institutes for Quantum and Radiological Science and Technology, Chiba, Japan, [3] National Institute of Radiological Sciences, National Institutes for Quantum and Radiological Science and Technology, Chiba, Japan

OPEN ACCESS

Edited by:
Pankaj Chaudhary,
Queen's University Belfast,
United Kingdom

Reviewed by:
Laure Sabatier,
Commissariat à l'Energie Atomique et aux Energies Alternatives (CEA),
France
Mark A. Hill,
University of Oxford, United Kingdom
Elettra Valentina Bellinzona,
University of Trento, Italy

***Correspondence:**
Takamitsu A. Kato
Takamitsu.Kato@Colostate.edu

Specialty section:
This article was submitted to Radiation Oncology, a section of the journal Frontiers in Oncology

Received: 02 October 2021
Accepted: 24 January 2022
Published: 17 February 2022

Citation:
Buglewicz DJ, Walsh KD, Hirakawa H, Kitamura H, Fujimori A and Kato TA (2022) Biological Effects of Monoenergetic Carbon Ions and Their Associated Secondary Particles. Front. Oncol. 12:788293. doi: 10.3389/fonc.2022.788293

DNA double-strand breaks (DSBs) are the main factor behind carbon-ion radiation therapy (CIRT)-induced cell death. Nuclear interactions along the beam path between the primary carbon ions and targets result in nuclear fragmentation of carbon ions and recoiled particles. These secondary particles travel further distances past the Bragg peak to the tail region, leading to unwanted biological effects that may result in cytotoxicity in critical organs and secondary induced tumors following CIRT. Here, we confirmed that the density of the DSB distributions increases as the cell survival decreases at the Bragg peak and demonstrated that by visualizing DSBs, the various LET fragmentation ions and recoiled particles produced differences in their biological effects in the post-Bragg peak tail regions. This suggests that the density of the DSBs within the high-LET track structures, rather than only their presence, is important for inducing cell death. These results are essential for CIRT treatment planning to limit the amount of healthy cell damage and reducing both the late effect and the secondary tumor-associated risk.

Keywords: DNA damage, carbon ion radiotherapy, Bragg peak, gamma-H2AX, secondary particles

INTRODUCTION

The most consequential of the ionizing radiation-induced DNA damage lesions are DNA double-strand breaks (DSBs). These DSBs are known to be the major factor responsible for radiation-induced cell death when left unrepaired or misrepaired (1, 2). However, misrepair of DSBs may give rise to genomic instability, thus increasing the risk of cancer development (3). High linear energy transfer (LET) radiation includes alpha particles, carbon, and iron ions which deposit their energy within densely ionizing tracks that are created by the particle's traversal through the cell. This allows for the formation of multiple close-proximity DNA damages including DSBs, single-strand breaks (SSBs), and base damages following high LET irradiation. Such complex DNA damage has also been demonstrated in prior studies using clusters of γ-H2AX foci as a surrogate marker for DSBs by horizontal irradiation and high-resolution microscopy (4–6). Additionally, these clustered DSBs are

known to be very difficult for the cell to repair and may be a strong contributor to genomic instability (7, 8).

Carbon ion radiotherapy (CIRT) has been effective for cancer treatment due to its excellent dose distribution with maximized dosage at the Bragg peak (9). As the carbon ions approach their Bragg peak, their LET values increase, and the DNA damage qualities become more complex. Carbon ions interact with matter along their beam path, and this results in fragments and recoiled particles, such as hydrogen, helium, lithium, beryllium, and boron, that also provide doses on the beam path (10, 11). Specifically at the Bragg peak, these secondary particles consist of 50% of the doses (12). However, those secondary particles can travel longer ranges than the primary carbon ions and provide significant doses past the Bragg peak, thus producing a tail region (12). CIRT provides more dose at the tail region than seen with proton radiotherapy, as proton fragments that have lower energy are thus limited in range as compared to CIRT. In previous studies, we presented the cytotoxic effect in the post-Bragg peak tail region of carbon ions in CHO and its DNA repair mutant cells as well as in human cancer cells (13–15). Other recent reports, using a horizontal irradiation and analysis system, also visually demonstrated the cytotoxic effects following proton and carbon-ion irradiation (15, 16). DNA damage responses in micrometer order scale sensitivity have also revealed high LET like foci track damage following proton irradiation (17). It is important to address the cytotoxicity in the post-Bragg peak tail region as it may cause unwanted side effects in CIRT through cellular loss or accumulation of mutations. Currently, evidence of secondary tumor production following CIRT has not been demonstrated (18). However, if the post-Bragg peak region contains DNA damage produced by high LET radiation, it may cause long-term effects in CIRT patients. Thus, it is important to address the biological effects within the carbon-ion post-Bragg peak tail region as the current radiobiology information in this region is limited.

To address these issues and appropriately observe the biological effects from carbon-ion irradiation, we have developed a method capable of observing the DSB distribution within the full monoenergetic carbon-ion beam range including the post-Bragg peak tail region in a single biological system using γ-H2AX foci as a marker for DSBs. One of the major advantages of our method of irradiation, in which the beam source is parallel to the cell culture flasks, is that it makes it possible to view the DNA damage-induced foci along high-LET particle tracks, which would not be readily observed if the incident particles were perpendicular to the cell culture flask base to which the cells are attached. To the best of the authors' knowledge, this is the first study in which the DSB distribution for the full carbon-ion beam range including the tail region has been evaluated in a single *in vitro* biological system. Here we not only demonstrate that our system is capable of identifying the depths within the beam range that show characteristics of high-LET radiation but also demonstrate how the DSB distribution changes as the beam approaches the Bragg peak and can observe the heterogeneity of the DNA damage in the post-Bragg peak depths resulting from the secondary particles.

MATERIALS AND METHODS

Cell Culture and Irradiation Conditions

Chinese hamster ovary (CHO) cells were kindly supplied by Dr. Joel Bedford (Colorado State University, Fort Collins, CO). Cells were grown and maintained in α-MEM (Invitrogen, Carlsbad, CA, USA) supplemented with 10% heat-inactivated fetal bovine serum (Sigma, St Louis, MO, USA), supplemented with antibiotics and antimycotics at 37°C in incubators at 5% CO_2 and 100% humidity. Doubling times were approximately 12 h for this cell line. Carbon ions and iron ions were accelerated to 290 and 500 MeV/nucleon, respectively, using the Heavy Ion Medical Accelerator in Chiba (HIMAC) synchrotron at the National Institute of Radiological Sciences (NIRS), Chiba, Japan. Dose rates for carbon ions and iron ions were set at 1 Gy/min. The irradiation field is within 2.5% uniformity (19). Monoenergetic 290-MeV/nucleon carbon ions and 500-MeV/nucleon iron ions have LET values of 13 and 200 keV/μm on entrance, respectively. Cell culture flasks or chamber slides were set up in a horizontal position (approximately 5°) to carbon-ion or iron-ion beam source, respectively, prior to irradiation. X-ray irradiation was performed at 200 kVp and 20 mA with aluminum (0.5 mm)–copper (0.5 mm) filters (Shimadzu, TITAN-320, NIRS), and dose rates were set at 0.5 Gy/min. Irradiations were carried out at room temperature. The beam characteristics and dosimetry using HIMAC have been described previously (20, 21). In brief, dosimetry of the carbon ions was obtained using a combination of an ionization chamber and a fluence measurement by a gas flow-type multiwire proportional counter. The dose-averaged LET values were calculated by HIBRAC code.

Irradiation Procedure for Cell Survival Assays

Cultured cells were trypsinized and resuspended into growth medium. 60 ml of media containing 30,000 cells was placed into a T-175 cell culture flask a few hours prior to irradiation, and attachment was confirmed. Cells were irradiated at room temperature with the dose rate of 1 Gy per minute. All flasks were irradiated independently with an incident dosage of either 2, 3, 5, or 10 Gy directly at beam entry. The flasks rested flat on the cell culture area, and the beam entry point was at the bottom of the flask (non-capped end) (**Figure 1A**) (15). Immediately following irradiation, all cells were incubated for a period of 7 days for colony formation. After this culturing period, each culture flask was then washed with 0.9% NaCl, fixed in 100% ethanol, and stained with 0.1% crystal violet.

Survival Fraction Calculation for Cell Survival Assays

Survival fractions were calculated as described previously (15). In short, to quantify the survival fraction at each of our evaluated depths, they were scored for every millimeter along the width of the flask either possessing a surviving colony, defined as a colony containing >50 cells, or not possessing a surviving colony and the average value was calculated. Therefore, the survival fraction was

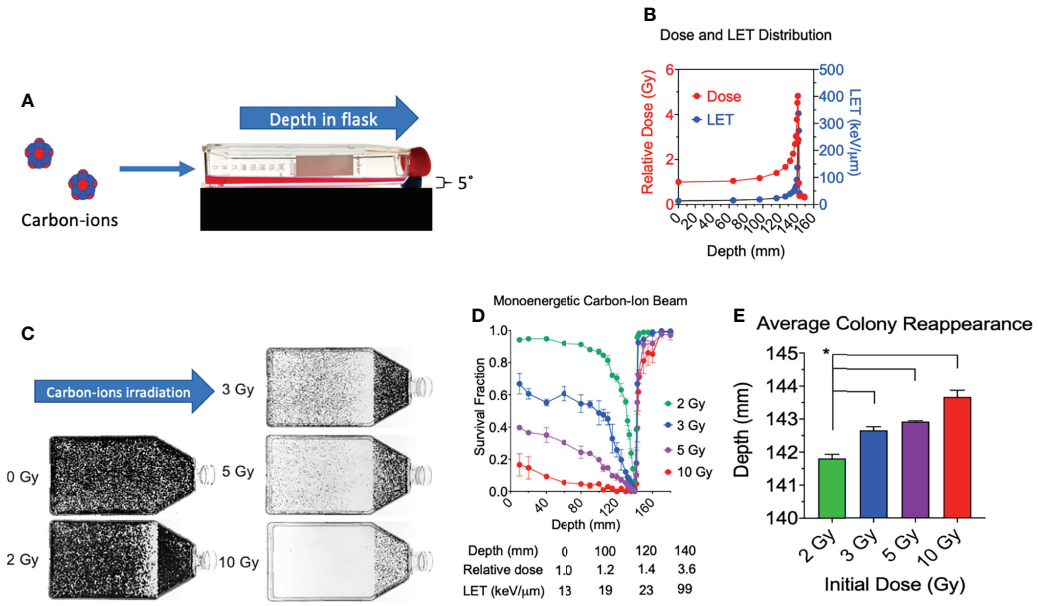

FIGURE 1 | Cell survival vs. depth of the full monoenergetic carbon-ion beam range at increasing initial doses in CHO cells. **(A)** An illustration of the horizontal irradiation setup. **(B)** Dose and LET distribution of carbon-ion 290 MeV/n. **(C)** Images of T-175 cell culture flasks following irradiation of 2, 3, 5, or 10 Gy initial dosage. **(D)** Survival fraction vs. depth following irradiation of each initial dosage. Statistical significances are illustrated in **Supplemental figure 1**. **(E)** Average colony reappearance depth at each initial dosage for the detailed analysis of cytotoxicity after Bragg peak. * indicates $p < 0.05$. Error bars indicate standard errors of the means from two or three independent experiments per each initial dosage.

calculated as the number of colonies at the specific depth divided by total millimeter along the width of the flask. This approach was repeated for a minimum of three independent experiments for each one of our initial dosages of 2 and 3 Gy with the reference at the 0-Gy dose, and two independent experiments for 5 and 10 Gy. The post-Bragg peak narrow cell culture area near the cap did not interfere with the survival fraction, as previously reported (15, 17).

To evaluate the cytotoxicity of the post-Bragg peak area in detail, a colony reappearance analysis was carried out as described previously (15, 17). The reappearance of colony formation following the Bragg peak was recorded with a ruler. Colony reappearance was defined as the average distance from the entrance for the first observable colonies after the Bragg peak. Seven equally spaced locations were analyzed for each flask to obtain a sensitive analysis of the extension of the cytotoxic range after the Bragg peak.

Irradiation Procedure for γ-H2AX Assays

For carbon-ion and X-ray irradiations: The top of each T-225 cell culture flask, i.e., the portion of the flask opposite to the cellular adherent side, was removed by a hot knife, and 6 poly-L-lysine-coated glass microscope slides were placed inside each flask in a sterilized manner and oriented, as indicated in **Supplemental Figure 2**. The positions of the slides were chosen to maximize the width and distance of the observable space within the flask. Tops were then returned to their respective flask and sealed with parafilm prior to addition of CHO cells. Cultured cells were trypsinized and resuspended into the growth medium. 60 ml of media containing 9 million cells was placed into T-225 cell culture flasks a few hours prior to irradiation, and attachment was confirmed. For iron-ion irradiations, 0.4 ml of media containing 50,000 cells was placed into each well of an 8-well Chamber Slide System (Thermo Fisher, Waltham, MA, USA) a few hours prior to irradiation and attachment was confirmed. Chamber slides were placed with 4 of the 8 wells (one side) directly facing the iron-ion beam in a horizontal orientation (approximately 5 degrees) relative to the iron-ion beam. Only wells of the side directly facing the iron-ion beam were analyzed to appropriately represent the incident iron ions (22). Carbon ions were irradiated and analyzed by this method to address the variations within the full carbon-ion beam range capable within our system while iron ions utilized the method to address only their ions upon the entrance region to maintain a high LET positive control with their LET value being 200 keV/μm.

Immunofluorescence Staining

A DSB marker, γ-H2AX foci formation assay was carried out as it was previously (23). Briefly, each slide containing cells was taken out of the flask following irradiation and was washed in cold PBS and fixed for 15 min in 4% w/v paraformaldehyde in PBS and washed again in PBS. Cells were then permeabilized for 5 min in 0.2% v/v Triton X-100 (Sigma, St Louis MO, USA) in PBS and washed twice in PBS. Slides were treated with 10% goat serum for 1 h at 37°C for blocking. Antibodies were diluted with 10% v/v goat serum in PBS. Cells were incubated with 1:300 diluted mouse anti-γ-H2AX

antibody (Millipore, Burlington, MA, USA) for 1 h at 37°C, washed three times in PBS, and incubated with 1:500 diluted Alexa Fluor 488 goat anti-mouse IgG antibody (Abcam, Cambridge, MA, USA) for 1 h at 37°C, and washed four times in PBS. DAPI (4′,6-diamidino-2-phenylindole) (Roche, Indianapolis, IN, USA) in SlowFade was then applied to stain the DNA.

γ-H2AX Foci Analysis by Zeiss Axioplan Microscopy With and Without MetaMorph Deconvolution

Microscopic images were captured with a Zeiss Axioplan microscope using a ×60 objective. 20 slices of images with every 0.5 μm were obtained to cover 2–3 μm of CHO thickness to quantify γ-H2AX foci within the 3-dimensional nucleus in a 2-dimensional image. 20 deconvoluted or non-deconvoluted images were stacked into a single-layer image to analyze γ-H2AX foci. Non-deconvoluted stacked images were analyzed for foci intensities. Deconvoluted stacked images were analyzed for foci cluster sizes and the number of individual foci. For this analysis, images taken by the Zeiss Axioplan were deconvoluted and processed using MetaMorph software (Molecular Devices, LLC, San Jose, CA, USA) *via* 2D no-neighbor deconvolution.

γ-H2AX Foci Scoring

Foci scoring was carried out blindly in each experiment with at least 50 cells/each depth analyzed or at least 50 cells/each control. Unless stated otherwise, all foci analyses are reported followed by the mean and standard error of the means from at least 3 independent experiments. Foci cluster sizes within the cells at each depth or in controls were scored as >2.4 μm in length and/or width. Foci length was measured within MetaMorph software following image processing. Foci of this size were chosen due to the largest observed foci size in our negative control, unirradiated cells, which were determined to be 0.8 μm, with a very low frequency of occurrence, and very few clusters within the cells following our high-dose low-LET control irradiation, 4-Gy X-ray, were observed as >2.4 μm. In contrast, following our high-LET control, 2-Gy iron ion, many clusters were observed as >2.4 μm. Additionally, a prior study using a higher image resolution than that used in our study demonstrated the presence of many individual γ-H2AX foci within each cluster following 2-Gy iron-ion beam irradiation (4). Thus, with use of our conventional image resolution *via* a Zeiss Axioplan microscope with deconvolution, we analyzed the individual foci number per cell (**Supplemental Figure 3**). However, the manual foci counting was difficult to reproduce due to highly clustered foci. To eliminate possible counting bias, the intensity values of each cell within each depth was obtained from the stacked image without deconvolution. Apparent, clear-tracked foci were scored as a track. Because depths lower than 90 mm possessed marginal track figures, the data were not included. In addition, depths were also defined by the relative depth percentage with respect to the physical dose peak at 141.4 mm which we defined as the relative depth = 100%.

Statistical Analysis

All experimental data were derived from at least 3 independent experiments with exception to 5- and 10-Gy cell survival, whose data were derived from 2 independent experiments. For experiments involving γ-H2AX foci, at least 50 cells per each depth or control per experiment were analyzed. Statistical significance was determined by using one-way analysis of variance (ANOVA) followed by the Bonferroni multiple-comparison test by GraphPad Prism 8 software (GraphPad, La Jolla, CA, USA). $p < 0.05$ was considered as statistical differences for all tests. Analysis was carried out between entry depth (10 mm) versus others unless stated otherwise, as with post-Bragg peak depths compared to the final depth (155 mm) versus others.

RESULTS

Physics Nature of Monoenergetic Carbon Ions 290 MeV/n

All experimental flasks were irradiated in a horizontal orientation with a carbon-ion beam source with 290 MeV/n (**Figure 1A**), as it was conducted in our previous research (15). The monoenergetic carbon ions have an initial LET value of 13.4 keV/μm and reaches 337 keV/μm at the depth of 142 mm (**Figure 1B**). The Bragg peak is at 141.4 mm. When initial 2 Gy of monoenergetic carbon ions is irradiated, the dose at the Bragg peak is approximately 9.6 Gy. The post-Bragg peak tail region at 148.8 mm is estimated to have 0.7 Gy.

Cytotoxicity of the Full Range of Monoenergetic Carbon Ions 290 MeV/n

Consistent with our prior work, we observed a decrease in survival at our first evaluated depth with an increase in initial beam entry irradiation dosage (15). Under initial beam irradiation doses of 2, 3, 5, and 10 Gy at the entrance within the flask, the distance of 140 mm presented a clear cytotoxicity without colonies (**Figure 1C**) and the lowest relative survival score (**Figure 1D**). The absorbed dose at this narrow area is more than 4 times that at the entrance dose. A clear cytotoxicity near the Bragg peak, 50% reduction of relative survival fraction compared to the initial depth of 10 mm, was observed at 132 mm for 2 Gy, 115 mm for 3 Gy, 100 mm for 5 Gy, and 40 mm for 10 Gy. The post-Bragg peak cytotoxicity, defined as survival score less than 0.9, was observed up to 142 mm for 2 Gy, 143 mm for 3 Gy, 145 mm for 5 Gy, and 160 mm for 10 Gy (**Figure 1D**).

To clarify the potential cytotoxicity at the post-Bragg peak, a detailed analysis of cytotoxicity after the Bragg peak was carried out by the distance for the reappearance of colonies. Our results also demonstrated that the average depth of colony reappearance following no colonies at the Bragg peak at 140 mm extended as the initial irradiation dosage increased (**Figure 1E**). Reappearance of colony formation was observed for the initial dosages of 2, 3, 5, and 10 Gy at the depths of 141.80 ± 0.22, 142.64 ± 0.19, 142.91 ± 0.04, and 143.69 ± 0.35 mm, respectively. The depths of colony reappearance following the Bragg peak at 140 mm for 3, 5, and 10 Gy were all found to be significant as compared to the initial dosage of 2 Gy ($p < 0.05$). These findings demonstrate that the depth of maximum cytotoxicity is

consistent throughout a wide range of initial dosages and suggest that secondary particles of carbon ions may be responsible for cell death at the post-Bragg peak region as these fragmented ions and recoiled products are known to be capable of traveling greater distances with relatively the same velocity (24).

γ-H2AX Foci Distribution in the Full Range of Monoenergetic Carbon Ions 290 MeV/n

To further investigate the biological effects on a molecular level behind our results obtained in the clonogenic assays, we observed the DSB distribution *via* the γ-H2AX assay at increasing depths within the carbon-ion beam range including the post-Bragg peak tail region. For all γ-H2AX assay experiments, we utilized an exponentially growing CHO10B2 cell line as with our survival experiments. Cells were analyzed for γ-H2AX expression at 0.5 h following their respective irradiation, as prior studies have indicated that the strongest induction of γ-H2AX foci was observed at this time point (4, 25, 26). For experimental controls, we used unirradiated cells as the negative control, 2 and 4 Gy X-ray irradiation for low-LET positive controls, and 2 Gy iron-ion irradiation for the high-LET positive control (**Figure 2A**). We utilized 2-Gy carbon-ion irradiation to address the DSB distribution within the full beam range capable in our system (10–155 mm), as this initial beam irradiation dosage demonstrated the largest survival fraction ratio between its survival fraction at the entrance (10 mm) to the Bragg peak depth (140 mm) in our clonogenic assays. For each individual experiment, at least 50 cells were analyzed at each depth as well as in each of our controls. As with our clonogenic assay, the statistical significance of each depth in these experiments and for controls was determined by comparison to the first evaluated depth closest to the beam entry at 10 mm.

Representative images show that quantities and qualities of γ-H2AX foci changed on the path of carbon-ion irradiation (**Figure 2A**). Foci analysis was carried out using three different categories including signal intensity per cell without deconvolution and the number of clusters of foci per cell, and foci track number per cell after image processing with deconvolution (**Figure 2B**). The signal intensity was a less subjective analysis than manual counting of foci. An initial 2 Gy of carbon-ion induced signal intensity of 7.9×10^5 AU (arbitrary unit) at a 10-mm entrance from a background of 1.9×10^5 AU. It was maximized at 142 mm (relative depth = 100.4%) with 24.5×10^5 AU. At the post-Bragg peak region, signal intensity decreased to 7.6×10^5 AU at 155 mm (relative depth = 110.7%); however, it was statistically higher than the background and had a similar value to the signal intensity at the entrance (**Figure 2C**).

For the qualitative analysis of foci, we used foci cluster size and track analysis. Foci cluster size was initially analyzed to determine high LET-specific cluster size. Cluster size was measured using MetaMorph software following appropriate image calibration. A cluster size smaller than 0.8 μm was

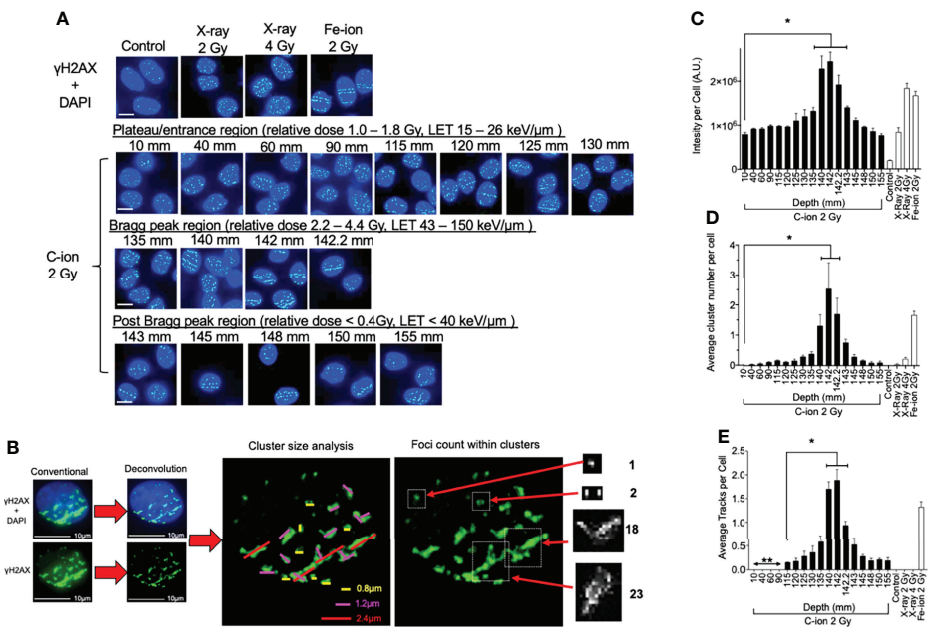

FIGURE 2 | γ-H2AX foci formation at each depth following 0.5 h post monoenergetic 290 MeV/n carbon-ion irradiation in CHO cells. **(A)** Representative images of carbon-ion-induced foci at the different depth, control, X-ray, and iron-ion irradiation. Green indicates γ-H2AX foci. Blue is DAPI-stained nuclei. Indicator bar represents 10 μm. **(B)** Deconvolution process with MetaMorph software prior to analysis and method representation of foci cluster size scoring and foci counting in each cell. Foci clusters were scored as greater than 0.8, 1.2, or 2.4 μm in width and/or length represented as yellow, pink, or red lines, respectively. Foci counting was determined by differences in pixel intensity across each cluster. **(C)** Intensity analysis of foci at different depths. **(D)** Clustered (diameter > 2.4 μm) foci analysis at the different depth. **(E)** Track foci analysis at the different depth. Bonferroni multiple-comparison test, * indicates $p < 0.05$. Error bars indicate the standard errors of the means from a minimum of 50 cells analyzed per each depth per experiment and at least three independent experiments per each irradiation treatment.

observed in all tested samples including unirradiated or low LET X-ray-irradiated controls. Cluster sizes of more than 1.2 μm were not observed for the unirradiated control but were in all irradiated samples including low LET X-ray irradiation (**Supplemental Figure 4**). However, the cluster size of more than 2.4 μm was considered as a high LET signature in this analysis as it was highly observed within our high LET control, iron ion, as well as in the carbon-ion Bragg peak region, with very few being observed within our low LET control, X-ray. There were more than 0.25 clusters per cells between 130 and 145 mm (relative depths = 91.9 and 102.5%, respectively) following carbon-ion irradiation (**Figure 2D**). At 142 mm, the number of clusters was peaked with 2.5 clusters per cell. These large clusters were also observed at the post-Bragg peak region up to 155 mm with reduced numbers, but still greater than those observed at the entrance depth of 10 mm.

Linear foci tracks were visually noticeable near the Bragg peak or high LET iron-ion irradiation with the horizontal irradiation method (**Figure 2A**). Track structures were observed following 2 Gy of carbon-ion irradiation between 115 and 155 mm and high LET iron ion with strong confidence, but not in the cells of the control, low LET X-ray irradiation, or carbon ion at the entrance region. A distance of up to 90 mm and shorter presented non-confident foci tracks, which may be a false positive of randomly distributed foci. Therefore, the actual track count was conducted beginning from 115 mm (relative depth = 81.3%). The average number of tracks peaked at 142 mm with 1.9 tracks per cell (**Figure 2E**). The average number of tracks above 0.5 was observed from 135 to 145 mm. These quantitative and qualitative analyses of foci distribution strongly suggested that DNA damage is peaked at 142 mm. This value is similar to the maximum cytotoxicity observed at 140 mm and matched well with the physical dose and LET distribution of the Bragg peak.

Differentiating the High-LET Track Structures Between Track-Positive Cells of Post-Bragg Peak Depths

At the post-Bragg peak region following 2 Gy of carbon-ion irradiation, the foci analysis showed a steep decrease, but we observed a significantly higher signal intensity and high LET signature compared to the unirradiated control (**Figures 2C–E**). To further investigate the biological effects after the Bragg peak tail region, an in-depth analysis was conducted by adding 10 Gy of carbon-ion irradiation. While high-LET foci track structures were detected in all post-Bragg peak depths (143–155 mm, relative depth = 102.1%–110.7%) following either 2- or 10-Gy carbon-ion irradiation (**Figure 3A**), track and cluster numbers decreased by a further post-Bragg peak (**Figures 3B, C**).

Additionally, visible differences of the track structures were distinctively observed after the Bragg peak up to 155 mm as sparse and dense tracks. To characterize these foci tracks, tracks containing a greater number of multiple cluster foci defined as >2.4 μm cluster foci size were analyzed. Such tracks with cluster foci were greatly observed at 143 mm, but they were dramatically decreased after 145 mm (**Figure 3C**). The number of large clusters in tracks between 2 and 10 Gy did not show

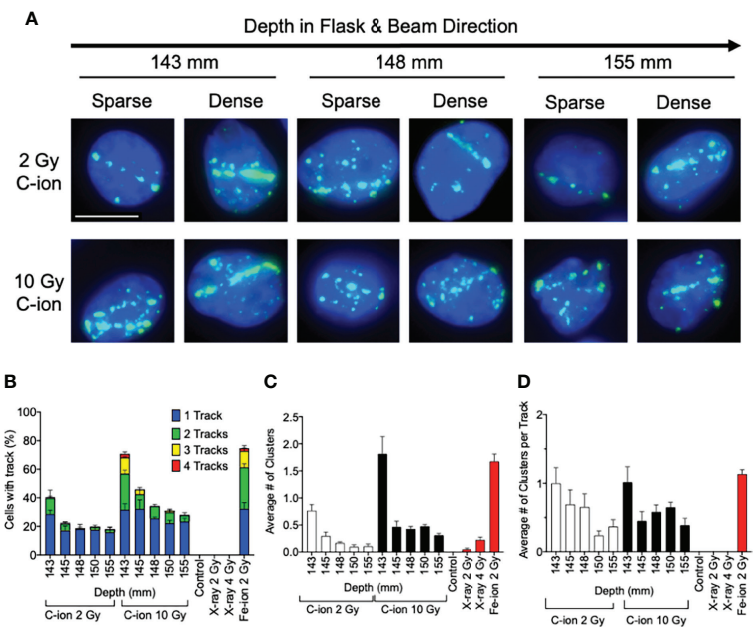

FIGURE 3 | Analysis of post-Bragg peak depths following 2- and 10-Gy carbon-ion irradiation. **(A)** Representative images of foci track structure variation (sparse or dense) at the post-Bragg peak following either 2 or 10 Gy. **(B)** Percent of cells with 0, 1, 2, 3, or 4 foci tracks in the post-Bragg peak. **(C)** Average number of clustered (diameter > 2.4 μm) foci in the post-Bragg peak. **(D)** Average number of clustered foci in the track in the post-Bragg peak. Error bars indicate standard errors of the means from a minimum of 50 cells analyzed per depth per experiment and at least three independent experiments per irradiation treatment.

statistically significant changes (**Supplemental Figure 5**). This means that the high LET-induced damage fraction is higher near the Bragg peak and lower after 145 mm, up to 155 mm in this study, which is dominated by lower LET-induced damage. This was likely due to the property differences between each of the carbon-ion nuclear fragmentation ions and recoiled particles, as it has been previously reported that heavy ions produce denser foci distributions within in their tracks than the light ions (27).

DSB Distribution Correlation With Cell Death

Firstly, for correlation against DNA damage complexity, clustered foci and tracked foci were analyzed as a function of signal intensity. Both clusters and tracks increased with signal intensity in a quadratic manner (**Figure 4A**). X-ray-induced clusters presented a much lower efficiency to produce clusters per signal intensity. On the other hand, iron ions demonstrated a much higher efficiency to produce clusters or tracks per signal intensity. The efficiency to produce a greater number of clusters or tracks was observed to be associated with the LET values of the radiation. To address the importance of the γ-H2AX foci distribution for the cellular lethality at the post-Bragg peak, cell survival scores were plotted against γ-H2AX signal intensity, cluster foci, and track-positive cells following either 2 or 10 Gy of carbon-ion irradiation (**Figures 4B, C**). Each tested parameter matched well with the survival fraction, although this was not a one-to-one ratio (**Figure 4D**). This was especially observed when entrance and post-Bragg peak data were analyzed separately. The signal intensity showed that the entrance region had more efficiency to kill cells per signal intensity compared to the post-Bragg peak region. Clusters and tracks in the post-Bragg peak were less effective to inactivate cells, but the inactivation ratio was similar between pre- and post-Bragg peak regions. Therefore, all parameters matched well with the survival fraction and initial DNA damage quantities and qualities are highly associated with cell survival.

DISCUSSION

The biological effects in cytotoxicity and DNA damage of full-range hadron beam were previously conducted utilizing a proton beam with small flasks using a relatively low proton beam energy (17). The current study utilizing the carbon-ion beam required using a much larger flask to cover the longer penetration of carbon ions. The irradiation system was developed from the previously reported cytotoxicity and genotoxicity analysis with the modifications of using multiple slides placed within each experimental flask in order to observe the DNA damage distribution in the full-range carbon-ion beam (15). Our cell survival results were consistent with prior studies describing the characteristic nature of carbon ions having a sharp increase in

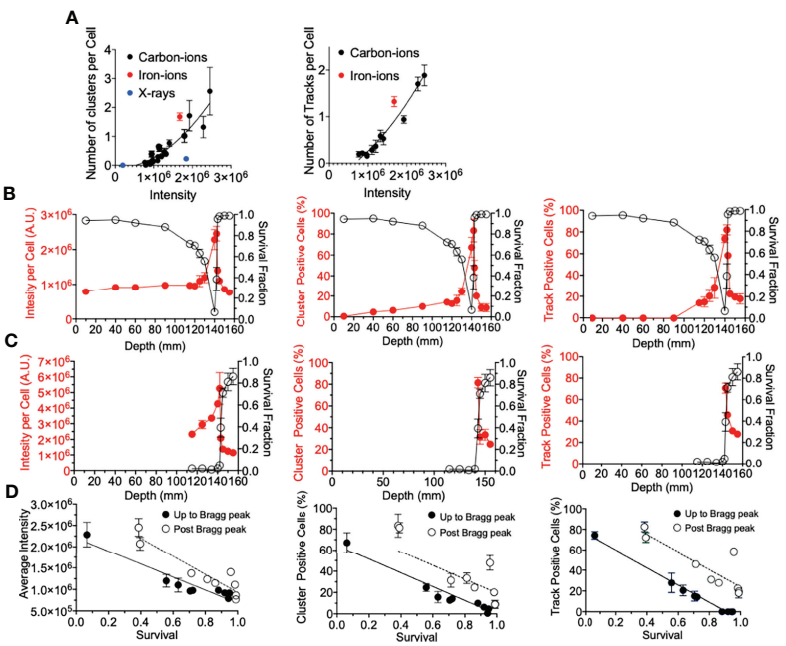

FIGURE 4 | γ-H2AX foci comparison with survival. **(A)** Number of clusters or tracks per intensity per cell. Black, red, and blue circles indicate carbon ions, iron ions, and X-ray irradiation, respectively. **(B)** Gy carbon-ion irradiation showing full beam range comparison of survival with average intensity, percent of cells with clusters, or tracks. **(C)** 10-Gy carbon-ion irradiation showing full beam range comparison of survival with average intensity, percent of cells with clusters, or tracks. **(D)** Correlation between survival and intensity, clusters, and tracks. Up to Bragg peak 10–140 mm (●) and post Bragg peak 142–155 mm (○). Linear regression analysis was carried out with GraphPad Prism 8 software. Error bars indicate standard errors of the means from a minimum of 50 individual cells analyzed per depth per experiment from at least three independent experiments per irradiation treatment.

the deposited dosage the closer the beam approaches to the Bragg peak (13, 15). We observed a sharp decrease in survival fractions the closer the depth was to the Bragg peak, with the lowest survival fraction being observed at 140 mm in depth, regardless of initial treatment dosage, and a slight difference of 2 mm with physical dose distribution (**Figures 1B, C**). Following the Bragg peak, a sharp increase in survival was observed, which suggested that the majority of the dosage was deposited at the Bragg peak. However, there was a notable decrease in survival in the post-Bragg peak regions as the initial irradiation dosage increased (**Figure 1E**). Cellular lethality was also extended after the Bragg peak in a dose-dependent manner, as was previously observed (**Figure 1E**) (15). Several potential reasons may explain this extended cytotoxicity after the Bragg peak. One possibility is due to the heterogeneity of beam quality, e.g., the monoenergetic beam is not perfectly monoenergetic meaning that some fraction of carbon ions may be of higher energy allowing for them to travel further (12). Another possible reason explaining this observation may be due to the secondary particles from nuclear fragmentation of the initial carbon ions and recoiled particles, as these fragmentation ions and recoiled particles are known to be capable of traveling longer distances past the Bragg peak (28). The studies presented that these fragment ions and recoiled particles provide non-negligible doses after the Bragg peak (10, 28). Importantly, prior studies have identified that these secondary particles are composed of proton, helium, lithium, beryllium, and boron. At the beam entrance, carbon particles dominate the relative fluence of the beam particles but the fragmentation reactions lead to an increase in the secondary particles as the beam proceeds toward the Bragg peak. At the Bragg peak, only around 50% of the primary carbon ions are believed to remain. Following the Bragg peak, the number of secondary proton and helium particles exceeds those of the carbon particles and the other secondary particles are observed to be less than 5% of the secondary proton and helium particles (10, 11). To clarify whether the extended toxicity following the Bragg peak is due to the secondary particles rather than beam uniformity, DNA damage distribution was quantitatively and qualitatively analyzed.

The main challenge of this study was the analysis of DNA damage distribution in the full-range carbon-ion irradiation up to 155 mm. To make this possible, flame-sterilized and poly-L-lysine-coated glass microscope slides were tightly placed within large T-175 flasks for cell culture. A DSB marker, γ-H2AX foci formation, was used to determine DNA damage quantities and qualities based on the number and distribution in the cellular nuclei. The number of γ-H2AX foci, which is the quantitative analysis of DNA damage, showed a sharp increase of DNA damage near the Bragg peak and peaked at 142 mm (**Figure 2C**). This may be associated with the fact that high-LET irradiation, such as carbon ions near the Bragg peak, not only produce DSBs but also are efficient at producing complex DSBs in addition to causing cluster of DSBs over larger scales because of correlation of events along the track. Moreover, as the LET of the particles increases, there is an increase in the frequency and complexity of complex DSBs produced. The complexity of DNA damage was analyzed with two parameters of foci distribution including the cluster of multiple foci at one location and foci track structure, both of which are signatures of high LET radiation exposure (29, 30). The kinetics of foci disappearance after high LET radiation exposure is known to be slower than that after low LET radiation. The complexity of DNA damage was also peaked at 142 mm (**Figures 2D, E**). Therefore, 2-mm differences between DNA damage distribution and cellular lethality were observed in both quantitative and qualitative analyses.

This difference could be explained by several reasons. The first is the geometrical difference between flask of survival and flask with cells on slides, as the slides may move during transportation and irradiation within flasks. However, slides were fixed on their location by melting the plastic with heat to avoid potential movement. The second reason can be due to the overkill effect from focused DNA damage to hit cells. LET values increased at the Bragg peak between 140 and 142.5 mm as 91 to 337 keV/mm with a peak at 142 mm with 337 keV/mm (**Figure 1B**). Ionizing radiation most efficiently produces DNA damage and kills cells at around 100 keV/mm. The LET above this value will result in overkill or, in other words, when a single particle deposits much more energy than is required to kill a cell, and this results in it killing less cells per absorbed dose. Moreover, at very high LET values, the percentage of non-hit cells has been observed to increase (31). In contrast to what was observed, we expected the cluster number per cell within the range of the carbon ion to be significantly higher than what was observed at these depths if all of our observed tracks contributed, as this would change the distribution of foci and tracks across the irradiated cell population according to the equation, $D = 0.16 \times L \times \frac{N}{A}$, where D is the dose in Gy, L is LET in keV/μm, N is the number of tracks per nucleus, and A is the nuclear area in square micrometers perpendicular to the beam (32).

As observed in survival, cytotoxicity was maximized at 140 mm, where the LET values are near 100 keV/μm and DNA damage was maximized at 142 mm with above 300 keV/μm. Our previous study also showed that the RBE value of cell survival was maximized at 200 keV/μm of iron ions with the value of around 4 and decreased after 250 keV/μm of silicon ions (33).

The last possibility is explained by the time of our analysis. DNA damage analysis was carried out 0.5 h following irradiation. γ-H2AX foci can be maximized at this time point (34, 35), but the lethality is strongly associated with repair capacity and residual DNA damages (17). Typically, higher initial damages cause higher residual damages. Clustered foci after Bragg peak may remain longer than simple foci at the entrance region. Data from 24 h following irradiation may answer this in the future studies as this may be due to a combination of decreased repairability of complex DSB at individual sites of DNA damage, in conjunction with the overlap of multiple γ-H2AX foci associated with the correlation of breaks along the radiation track, requiring multiple sites of damage to be repaired for the clustered foci to be lost. It would also be beneficial in future studies to conduct the chromosomal aberration assay within our system. Comparison between the types of chromosomal aberrations at each depth with our present data

may further answer this discrepancy as the proximity of the DSBs along the high-LET tracks may increase the frequency of chromosomal aberrations arising from misrepair between these correlated breaks as well as in the complexity of chromosomal rearrangements arising with non-symmetrical types typically resulting in clonogenic cell death (36, 37).

The analysis of DNA damage at the post-Bragg peak provided validation of our system. The cluster and track foci were observed at the post-Bragg peak region. If the extended cell death or DNA damage at the post-Bragg peak region came from heterogenic energy of initial carbon ions or possible irradiation errors, the complex type of DNA damage should be observed at any depth analyzed randomly. However, both clustered foci or track foci structures were observed up to 155 mm following 2 or 10 Gy of carbon-ion irradiation (**Figures 3B, C**). When comparing 2 and 10 Gy data, we expected the number of cells with tracks and the average number of clustered foci to increase by a factor of 5 which was not the observed case and may indicate that we did not observe all the tracks, meaning it may require more than the 150 cells per depth analyzed to provide more accurate results in this case. However, evaluating the quality of the track, not the dose, in which we normalized the average number of clusters by track allowed us to overcome this problem by evaluating per track not per cell. Thus, we observed that the cluster positive foci tracks, the clear signature of high LET radiation exposure, were gradually decreased after Bragg peak (**Figure 3D**). This suggests that DNA damage within the post-Bragg peak region is mainly from the secondary particles including nuclear fragmentations and recoiled particles rather than random carbon-ion beam artifact. Since the complexity of DNA damage was observed in the post-Bragg peak region, the lighter fragments travel further and potentially a few centimeters after the Bragg peak and some of the secondary particles have LET values more than 10 keV/μm (11, 12). This study conducted up to 155 mm based on the limitation of slide placement in the T175 flask size, but the secondary particles may travel at more than 10% of the initial Bragg peak range of 140 mm. Thus, the secondary particles from carbon ions were observed to travel much longer than the secondary particles observed after proton irradiation in our previous study (17). Furthermore, simulation analysis also supports these findings (28, 38). Our study clearly suggests that the post-Bragg peak of carbon ions contains a small but significant amount of high LET radiation fraction, which is enough to cause the cytotoxicity and potentially genotoxicity (**Figures 1E**, **2A**).

Lastly, we determine if the underlying factor between the foci distribution correlation with cell death was due to the amount of foci per cell (*via* average intensity per cell), the foci distribution per cell (*via* percentage of cluster >2.4 μm positive cells), the presence of a track structure (*via* percentage of track positive cells), or a combination of these (**Figure 4**). All three factors explained well for cell survival. While there was not a one-to-one correlation between each of these factors and cell survival, the importance of this analysis was that the relationship between γ-H2AX and survival was very similar between pre-Bragg peak and post-Bragg peak regions (**Figure 4**). This suggests that the DNA damage and cellular death after irradiation at the post-Bragg peak occur by the same mechanisms, which depends on the DSB quantities and qualities, as at the pre-Bragg peak regions.

In conclusion, the DSB distribution analysis of the full carbon-ion beam range in a single biological system conducted in this study clarified differences in the DNA damage distribution near the Bragg peak, as the γ-H2AX distribution is dramatically changed in their number and character near the Bragg peak. The cellular lethality was confirmed in the post-Bragg peak region, and this can be explained by the DSBs produced by the various LET nuclear fragments and recoiled particles as observed in the foci track structures. The signature of DNA damage from secondary particles was observed in the tail region far from the Bragg peak at least up to a 10% distance of the initial Bragg peak. These results are of great interest as the DSBs at the post-Bragg peak region may contribute to cellular death and organ dysfunction and even genetic instability, possibly resulting in cancer cell propagation. Results of this study should be carefully considered during radiation treatment planning to limit the amount of healthy cell damage in patients. As our system of irradiation also demonstrated that the biological response can dramatically change in millimeter differences, a limitation to the current irradiation system is that the biological response is critically dependent on both the dose delivered and radiation quality (LET), both of which also vary significantly with depth and therefore position on the flask. Thus, to further address the variation in relative biological effectiveness in the post-Bragg peak region and relate this to the spectrum of particles and associated energies of the fragments, more detailed cell survival studies with cells plated at a range of depth with the beam normal to the plated cell population should also be performed at and beyond the Bragg peak, backed up with detailed modeling of the carbon ion and associated fragments as a function of the depth in future studies.

DATA AVAILABILITY STATEMENT

The original contributions presented in the study are included in the article/**Supplementary Material**. Further inquiries can be directed to the corresponding author.

AUTHOR CONTRIBUTIONS

Conceptualization, TK. Methodology and formal analysis, DB, KW, HK, and TK. Resource data curation, DB, KW, HH, HK, AF, and TK. Writing—original draft preparation, DB and TK. Writing—review and editing, DB, KW, HK, AF, TK. Funding acquisition, AF, TK. All authors contributed to the manuscript revision and read and approved the submitted version.

FUNDING

This research was partially funded by Dr. Akiko Ueno Radiobiology Fund (TK) and the Japan Ministry of Education, Culture, Science and Technology (MEXT) Grants-in-Aid for Scientific Research on Innovative Areas (JP15K21745, AF).

ACKNOWLEDGMENTS

We thank the QST HIMAC facility. We thank Dr. Joel Bedford for kindly supplying cell lines.

SUPPLEMENTARY MATERIAL

The Supplementary Material for this article can be found online at: https://www.frontiersin.org/articles/10.3389/fonc.2022.788293/full#supplementary-material

Supplementary Figure 1 | Survival fraction vs depth following irradiation of each initial dosage. Red and blue arrows indicate survival fraction at 142 and 143 mm, respectively, to demonstrate how survival fraction decreases in the post Bragg peak at increased initial irradiation treatment dosage. Areas highlighted in gray or green represent a significant decrease ($P<0.05$) or significant increase ($P<0.05$) compared to the closest analyzed depth near beam entry at 1.0 cm, Bonferroni multiple comparisons test.

Supplementary Figure 2 | Depiction of slide placement to determine beam depth in flask following carbon-ion irradiation.

Supplementary Figure 3 | Foci number per cell after initial 2 Gy of carbon-ion irradiation. Counting was conducted manually with deconvoluted images. Red dots indicate data from individual cells. Mean and standard deviation are shown.

Supplementary Figure 4 | Number of clusters per cell after initial 2 Gy of carbon-ion irradiation. Cluster sizes were divided into up to 0.8 μm, between 0.8-1.2 μm, and larger than 2.4 μm. Depiction of slide placement to determine beam depth in flask following carbon-ion irradiation.

Supplementary Figure 5 | Cluster size within tracks after initial 2 Gy or 10 Gy of carbon-ion and 2 Gy of iron-ion irradiation. Cluster sizes were divided into up to 0.8 μm, between 0.8-1.2 μm, and larger than 2.4 μm. Depiction of slide placement to determine beam depth in flask following carbon-ion irradiation.

REFERENCES

1. Lomax ME, Folkes LK, O'Neill P. Biological Consequences of Radiation-Induced DNA Damage: Relevance to Radiotherapy. *Clin Oncol (R Coll Radiol)* (2013) 25:578–85. doi: 10.1016/j.clon.2013.06.007
2. Cornforth MN, Bedford JS. A Quantitative Comparison of Potentially Lethal Damage Repair and the Rejoining of Interphase Chromosome Breaks in Low Passage Normal Human-Fibroblasts. *Radiat Res* (1987) 111:385–405. doi: 10.2307/3576926
3. Jeggo P, Lavin MF. Cellular Radiosensitivity: How Much Better Do We Understand It? *Int J Radiat Biol* (2009) 85:1061–81. doi: 10.3109/09553000903261263
4. Nakajima NI, Brunton H, Watanabe R, Shrikhande A, Hirayama R, Matsufuji N, et al. Visualisation of Gamma H2AX Foci Caused by Heavy Ion Particle Traversal; Distinction Between Core Track Versus Non-Track Damage. *PloS One* (2013) 23(8). doi: 10.1371/journal.pone.0070107
5. Oike T, Niimi A, Okonogi N, Murata K, Matsumura A, Noda SE, et al. Visualization of Complex DNA Double-Strand Breaks in a Tumor Treated With Carbon Ion Radiotherapy. *Sci Rep* (2016) 6:7. doi: 10.1038/srep22275
6. Nakajima NI, Hagiwara Y, Oike T, Okayasu R, Murakami T, Nakano T, et al. Pre-Exposure to Ionizing Radiation Stimulates DNA Double Strand Break End Resection, Promoting the Use of Homologous Recombination Repair. *PloS One* (2015) 10:15. doi: 10.1371/journal.pone.0122582
7. Asaithamby A, Hu B, Chen DJ. Unrepaired Clustered DNA Lesions Induce Chromosome Breakage in Human Cells. *Proc Natl Acad Sci USA* (2011) 108:8293–8. doi: 10.1073/pnas.1016045108
8. Kramer M, Kraft G. Calculations Of Heavy-ion Track Structure. *Radiat Environ Biophys* (1994) 33:91–109. doi: 10.1007/BF01219334
9. Tsujii H, Kamada T. A Review of Update Clinical Results of Carbon Ion Radiotherapy. *Jpn J Clin Oncol* (2012) 42:670–85. doi: 10.1093/jjco/hys104
10. Haettner E, Iwase H, Kramer M, Kraft G, Schardt D. Experimental Study of Nuclear Fragmentation of 200 and 400 MeV/u (12)C Ions in Water for Applications in Particle Therapy. *Phys Med Biol* (2013) 58:8265–79. doi: 10.1088/0031-9155/58/23/8265
11. Endo S, Takada M, Tanaka H, Onizuka Y, Tanaka K, Miyahara N, et al. Measurement of Microdosimetric Spectra Produced From a 290 MeV/n Spread Out Bragg Peak Carbon Beam. *Radiat Environ Biophys* (2010) 49:469–75. doi: 10.1007/s00411-010-0285-1
12. Kodaira S, Kitamura H, Kurano M, Kawashima H, Benton ER. Contribution to Dose in Healthy Tissue From Secondary Target Fragments in Therapeutic Proton, He and C Beams Measured With CR-39 Plastic Nuclear Track Detectors. *Sci Rep* (2019) 9:3708. doi: 10.1038/s41598-019-39598-0
13. Genet SC, Maeda J, Fujisawa H, Yurkon CR, Fujii Y, Romero AM, et al. Comparison of Cellular Lethality in DNA Repair-Proficient or -Deficient Cell Lines Resulting From Exposure to 70 MeV/n Protons or 290 MeV/n Carbon Ions. *Oncol Rep* (2012) 28:1591–6. doi: 10.3892/or.2012.1982
14. Fujisawa H, Genik PC, Kitamura H, Fujimori A, Uesaka M, Kato TA. Comparison of Human Chordoma Cell-Kill for 290 MeV/n Carbon Ions Versus 70 MeV Protons *In Vitro*. *Radiat Oncol* (2013) 8:91. doi: 10.1186/1748-717X-8-91
15. Buglewicz DJ, Banks AB, Hirakawa H, Fujimori A, Kato TA. Monoenergetic 290 MeV/n Carbon-Ion Beam Biological Lethal Dose Distribution Surrounding the Bragg Peak. *Sci Rep* (2019) 9:6157. doi: 10.1038/s41598-019-42600-4
16. Cuaron JJ, Chang C, Lovelock M, Higginson DS, Mah D, Cahlon O, et al. Exponential Increase in Relative Biological Effectiveness Along Distal Edge of a Proton Bragg Peak as Measured by Deoxyribonucleic Acid Double-Strand Breaks. *Int J Radiat Oncol Biol Phys* (2016) 95:62–9. doi: 10.1016/j.ijrobp.2016.02.018
17. Horendeck D, Walsh KD, Hirakawa H, Fujimori A, Kitamura H, Kato TA. High LET-Like Radiation Tracks at the Distal Side of Accelerated Proton Bragg Peak. *Front Oncol* (2021) 11:690042. doi: 10.3389/fonc.2021.690042
18. Mohamad O, Tabuchi T, Nitta Y, Nomoto A, Sato A, Kasuya G, et al. Risk of Subsequent Primary Cancers After Carbon Ion Radiotherapy, Photon Radiotherapy, or Surgery for Localised Prostate Cancer: A Propensity Score-Weighted, Retrospective, Cohort Study. *Lancet Oncol* (2019) 20:674–85. doi: 10.1016/S1470-2045(18)30931-8
19. Torikoshi M, Minohara S, Kanematsu N, Komori M, Kanazawa M, Noda K, et al. Irradiation System for HIMAC. *J Radiat Res* (2007) 48(Suppl A):A15–25. doi: 10.1269/jrr.48.A15
20. Kanai T, Endo M, Minohara S, Miyahara N, Koyama-Ito H, Tomura H, et al. Biophysical Characteristics of HIMAC Clinical Irradiation System for Heavy-Ion Radiation Therapy. *Int J Radiat Oncol Biol Phys* (1999) 44:201–10. doi: 10.1016/S0360-3016(98)00544-6
21. McMillan DD, Maeda J, Bell JJ, Genet MD, Phoonswadi G, Mann KA, et al. Validation of 64Cu-ATSM Damaging DNA *via* High-LET Auger Electron Emission. *J Radiat Res* (2015) 56:784–91. doi: 10.1093/jrr/rrv042
22. Desai N, Davis E, O'Neill P, Durante M, Cucinotta FA, Wu H. Immunofluorescence Detection of Clustered Gamma-H2AX Foci Induced by HZE-Particle Radiation. *Radiat. Res.* (2005) 164:518–22. doi: 10.1667/rr3431.1
23. Gerelchuluun A, Maeda J, Manabe E, Brents CA, Sakae T, Fujimori A, et al. Histone Deacetylase Inhibitor Induced Radiation Sensitization Effects on Human Cancer Cells After Photon and Hadron Radiation Exposure. *Int J Mol Sci* (2018) 19. doi: 10.3390/ijms19020496
24. Arico G, Gehrke T, Gallas R, Mairani A, Jakel O, Martisikova M. Investigation of Single Carbon Ion Fragmentation in Water and PMMA for Hadron Therapy. *Phys Med Biol* (2019) 64:15. doi: 10.1088/1361-6560/aafa46
25. Zhao J, Guo Z, Pei S, Song L, Wang C, Ma J, et al. pATM and γh2ax Are Effective Radiation Biomarkers in Assessing the Radiosensitivity of 12C6+ in Human Tumor Cells. *Cancer Cell Int* (2017) 17:49. doi: 10.1186/s12935-017-0419-5
26. Kato TA, Okayasu R, Bedford JS. Comparison of the Induction and Disappearance of DNA Double Strand Breaks and Gamma-H2AX Foci After Irradiation of Chromosomes in G1-Phase or in Condensed Metaphase Cells. *Mutat Res.-Fundam Mol Mech Mutagen* (2008) 639:108–12. doi: 10.1016/j.mrfmmm.2007.11.006
27. Hilgers G, Bug MU, Rabus H. Measurement of Track Structure Parameters of Low and Medium Energy Helium and Carbon Ions in Nanometric Volumes. *Phys Med Biol* (2017) 62:7569–97. doi: 10.1088/1361-6560/aa86e8

28. Francis Z, Seif E, Incerti S, Champion C, Karamitros M, Bernal MA, et al. Carbon Ion Fragmentation Effects on the Nanometric Level Behind the Bragg Peak Depth. *Phys Med Biol* (2014) 59:7691–702. doi: 10.1088/0031-9155/59/24/7691
29. Fujii Y, Yurkon CR, Maeda J, Genet SC, Okayasu R, Kitamura H, et al. Influence of Track Directions on the Biological Consequences in Cells Irradiated With High LET Heavy Ions. *Int J Radiat Biol* (2013) 89:401–10. doi: 10.3109/09553002.2013.767990
30. Jakob B, Splinter J, Taucher-Scholz G. Positional Stability of Damaged Chromatin Domains Along Radiation Tracks in Mammalian Cells. *Radiat. Res.* (2009) 171:405–18. doi: 10.1667/RR1520.1
31. Goodhead DT, Belli M, Mill AJ, Bance DA, Allen LA, Hall SC, et al. Direct Comparison Between Protons and Alpha-Particles of the Same LET: I. Irradiation Methods and Inactivation of Asynchronous V79, HeLa and C3H 10T1/2 Cells. *Int J Radiat Biol* (1992) 61:611–24. doi: 10.1080/09553009214551421
32. Tracy BL, Stevens DL, Goodhead DT, Hill MA. Variation in RBE for Survival of V79-4 Cells as a Function of Alpha-Particle (Helium Ion) Energy. *Radiat Res* (2015) 184:33–45. doi: 10.1667/RR13835.1
33. Kato TA, Tsuda A, Uesaka M, Fujimori A, Kamada T, Tsujii H, et al. *In Vitro* Characterization of Cells Derived From Chordoma Cell Line U-CH1 Following Treatment With X-Rays, Heavy Ions and Chemotherapeutic Drugs. *Radiat Oncol* (2011) 6:116. doi: 10.1186/1748-717X-6-116
34. Kato TA, Nagasawa H, Weil MM, Little JB, Bedford JS. Levels of Gamma-H2AX Foci After Low-Dose-Rate Irradiation Reveal a DNA DSB Rejoining Defect in Cells From Human ATM Heterozygotes in Two at Families and in Another Apparently Normal Individual. *Radiat. Res.* (2006) 166:443–53.
35. Hamada N, Imaoka T, Masunaga S, Ogata T, Okayasu R, Takahashi A, et al. Recent Advances in the Biology of Heavy-Ion Cancer Therapy. *J Radiat Res* (2010) 51:365–83. doi: 10.1269/jrr.09137
36. Loucas BD, Shuryak I, Cornforth MN. Three-Color Chromosome Painting as Seen Through the Eyes of mFISH: Another Look at Radiation-Induced Exchanges and Their Conversion to Whole-Genome Equivalency. *Front Oncol* (2016) 6:52. doi: 10.3389/fonc.2016.00052
37. Loucas BD, Cornforth MN. The LET Dependence of Unrepaired Chromosome Damage in Human Cells: A Break Too Far? *Radiat Res* (2013) 179:393–405. doi: 10.1667/RR3159.2
38. Gunzert-Marx K, Iwase H, Schardt D, Simon RS. Secondary Beam Fragments Produced by 200 MeVu(-1) C-12 Ions in Water and Their Dose Contributions in Carbon Ion Radiotherapy. *New J Phys* (2008) 10:075003. doi: 10.1088/1367-2630/10/7/075003

Conflict of Interest: The authors declare that the research was conducted in the absence of any commercial or financial relationships that could be construed as a potential conflict of interest.

Advantages of publishing in Frontiers

OPEN ACCESS
Articles are free to read for greatest visibility and readership

FAST PUBLICATION
Around 90 days from submission to decision

HIGH QUALITY PEER-REVIEW
Rigorous, collaborative, and constructive peer-review

TRANSPARENT PEER-REVIEW
Editors and reviewers acknowledged by name on published articles

Frontiers
Avenue du Tribunal-Fédéral 34
1005 Lausanne | Switzerland

Visit us: www.frontiersin.org
Contact us: frontiersin.org/about/contact

REPRODUCIBILITY OF RESEARCH
Support open data and methods to enhance research reproducibility

DIGITAL PUBLISHING
Articles designed for optimal readership across devices

FOLLOW US
@frontiersin

IMPACT METRICS
Advanced article metrics track visibility across digital media

EXTENSIVE PROMOTION
Marketing and promotion of impactful research

LOOP RESEARCH NETWORK
Our network increases your article's readership